5. Velocity, Vorticity, and Mach Number

The objective of this chapter is to provide a comprehensive statement of the experimental methods that can be used to transduce the velocity and its companion quantity: vorticity ($\nabla \times \vec{u}$). Velocity measurements can be understood to represent *spatially integrated* and *pointwise* values. Thermal transient anemometry (Sect. 5.6) and sonic anemometers (Sect. 5.7) represent the former. Pressure-based velocity measurements (Sect. 5.1), thermal anemometry (Sect. 5.2), and particle-based techniques (Sect. 5.3) represent the latter. In addition, particle image velocimetry (PIV, Sect. 5.3.2), planar Doppler velocimetry (Sect. 5.3.3), and molecular tagging velocimetry (Sect. 5.4) also provide spatial distributions of the pointwise measurements for the *instant* at which the image is formed. The vorticity measurements rely on some form of the above pointwise measurements. A general overview of optical methods is presented in Sect. 5.5.1.

5.1 **Pressure-Based Velocity Measurements** .. 216
5.1.1 Measurement of Total Pressure Head with Pitot Tubes 218
5.1.2 Dynamic Head from Separate Measurements of Total and Static Pressures 226
5.1.3 Direct Measurement of Dynamic Head (Combined Pitot-Static and Other Probes) 226
5.1.4 Measurement of Dynamic Head and Flow Direction (Multihole Probes) 228

5.2 **Thermal Anemometry** 229
5.2.1 Introduction 229
5.2.2 Sensors 231
5.2.3 Anemometer Electronics 258
5.2.4 Calibration Procedures in Subsonic Flows 266
5.2.5 Measurement of Velocity and Temperature Fluctuations 273
5.2.6 Calibration Procedures in Compressible Flows 278
5.2.7 Special Techniques 279
5.2.8 A Comprehensive Technique for X-Array Calibration and Data Processing 283

5.3 **Particle-Based Techniques** 287
5.3.1 Tracer Particles 287
5.3.2 Laser Doppler Technique 296
5.3.3 Particle Image Velocimetry 309
5.3.4 Doppler Global Velocimetry 342
5.3.5 Laser Transit Velocimetry 353

5.4 **Molecular Tagging Velocimetry (MTV)** 362
5.4.1 The Photochemistry of MTV: Molecular Tracers and Chemical Mechanisms 363
5.4.2 The Experimental Implementation of MTV: Tagging Methods, Detection and Processing 373
5.4.3 Examples of MTV Measurements 377
5.4.4 Summary and Conclusions 382

5.5 **Vorticity** 382
5.5.1 Optical Techniques in Strophometry – Vorticity Measurements Methods . 383
5.5.2 High-Resolution Dual-Plane Stereo PIV (DSPIV) 400
5.5.3 Measurements of the Vorticity Vector and Other Velocity Gradient Tensor-Based Turbulence Properties 408
5.5.4 Transverse Vorticity Measurements with a Four-Sensor Hot-Wire Probe 429

5.6 **Thermal Transient Anemometer (TTA)** 434
5.6.1 Operational Description 434
5.6.2 Representative Results 435

5.7 **Sonic Anemometry/Thermometry** 436
5.7.1 Definition 436
5.7.2 Measurement Principles 437
5.7.3 Device Characteristics, Accuracy, and Limitations 439
5.7.4 Data-Acquisition Requirements 444
5.7.5 Use and Calibration Procedures 444
5.7.6 Manufacturers and Costs 445
5.7.7 Device Comparison 445

References 446

5.1 Pressure-Based Velocity Measurements

Measurement of dynamic head, in conjunction with use of the Bernoulli equation, is perhaps the most commonly used means of determining fluid velocity in a steady, mid-to-high velocity flow. The fabrication of suitable pressure probes is simple and inexpensive, the transducer range may be selected to suit the flow under consideration and a differential measurement of total and static head is sufficient for incompressible flows, in which the density is known. It is, however, an intrusive technique, and one which requires some subtlety for accurate results over a range of flow types and Reynolds numbers using finite-sized probes. With correct use and under appropriate corrections high-accuracy velocity measurements may be obtained.

Governing Equations

The technique rests on the general (5.1), known as the *Bernoulli equation*, which is valid along a single streamline in steady, inviscid flows where the continuum approximation holds.

$$\frac{\mathrm{d}p}{\rho} + U\,\mathrm{d}U = 0\,. \tag{5.1}$$

Here U is the local mean magnitude of the velocity along the streamline, ρ is the local fluid density and p is the local pressure. Equation (5.1) may be integrated along the streamline to give the general form for compressible flow of an ideal gas:

$$\frac{p_0}{p} = \left(1 + \frac{\gamma - 1}{2} M^2\right)^{\frac{\gamma}{\gamma-1}}\,, \tag{5.2}$$

where p_0 would be the pressure in the fluid after an isentropic, adiabatic deceleration along the streamline to a zero-velocity condition. This quantity is commonly called the *stagnation* or *total* pressure despite its non-scalar nature (a dependence on coordinate system) and consequently the true (scalar) pressure p is often referred to as the *static pressure*.

The pressure–density relation

$$\frac{1}{2}\rho U^2 = \frac{1}{2}\gamma M^2 p \tag{5.3}$$

has been utilized in writing (5.2), where the Mach number $M = U/a$, the speed of sound is $a = \sqrt{\gamma p/\rho}$, and γ is the ratio of specific heats. For small Mach numbers, binomial expansion gives

$$p_0 - p = \frac{1}{2}\rho U^2 \left(1 + \frac{M^2}{4} + \frac{(2-\gamma)M^4}{24} + \ldots\right) \tag{5.4}$$

and the familiar incompressible ($M = 0$) form

$$p_0 - p = \frac{1}{2}\rho U^2\,, \tag{5.5}$$

where $1/2\rho U^2$ is termed the dynamic head or dynamic *pressure*. Thus, for incompressible flow, measurements of density, and total and static pressures can be used to obtain the local velocity.

Note that truncation of the binomial expansion of (5.2) causes an error in the determination of dynamic head of 0.2% for $M \leq 0.09$ if only the first term of the expansion is retained (i. e., the incompressible Bernoulli equation), for $M \leq 0.55$ if two terms are used and through $M = 1$ for three or more terms (assuming zero measurement error).

In compressible flow, the continuum approximation may be violated if the ratio of the molecular mean free path λ to the characteristic flow dimension (here the diameter of the probe d), i. e., the Knudsen number $\mathrm{Kn} = \lambda/d$, is sufficiently large that boundary interactions instead of inter-molecular collisions determine relaxation times. Using the Chapman–Enskog solution of the Boltzmann equations to obtain the viscosity, the conditions under which the continuum approximation holds ($\mathrm{Kn} < 0.01$) can be written in terms of the Mach number and Reynolds number based on d as

$$\mathrm{Kn} = \frac{\lambda}{d} = \left(\frac{\pi\gamma}{2}\right)^{1/2} \frac{M}{\mathrm{Re}_\mathrm{d}} \ll 1\,. \tag{5.6}$$

Only continuum flow in an ideal fluid will be considered here. For a detailed discussion of pressure-based velocity measurement in non-continuum gases, see *Chue* [5.1, Sect. 1.8].

In the case of a continuum supersonic freestream, a probe of finite size will cause the formation of a detached shock (Fig. 5.1d), hence a total pressure probe will measure the reduced stagnation pressure p_{02} in the decelerated subsonic flow of region 2. Because of the non-isentropic nature of the compression through the shock wave, the Bernoulli equation cannot be used. The freestream Mach number M_∞ can be found by means of the Rayleigh supersonic pitot formula and a measurement of the freestream static pressure p_∞:

$$\frac{p_\infty}{p_{02}} = \left[\frac{2\gamma M_\infty^2 - (\gamma - 1)}{\gamma + 1}\right]^{1(\gamma-1)} \times \left[\frac{\gamma + 1}{2} M_\infty^2\right]^{-\gamma/(\gamma-1)}\,. \tag{5.7}$$

If the upstream reservoir pressure is known and the flow is isentropic up to the shock, normal shock relations give

$$\frac{p_{0\infty}}{p_{02}} = \left[\frac{2\gamma M_\infty^2 - (\gamma-1)}{\gamma+1}\right]^{1/(\gamma-1)} \times \left[\frac{2+(\gamma-1)M_\infty^2}{(\gamma+1)M_\infty^2}\right]^{\gamma/(\gamma-1)} , \tag{5.8}$$

or, of course, for downstream pressure measurements (5.2) may be used. If required, U_∞ can be determined from (5.3). Thus both the freestream Mach number and velocity can be obtained more easily from separate measurements of the stagnation pressure p_{02} and freestream static pressure than from a difference measurement of dynamic head in compressible flow.

Measurement Techniques

The measurement technique selected will depend on the flow under consideration, and potentially the ability to physically place an apparatus into the flow. In confined flows or flows with large velocity gradients (such as wall-bounded flows) where probe size may be limited by spatial resolution concerns, and where the variation of pressure with distance from the wall is known or negligible, a Pitot (impact) tube may be used with a static pressure tapping at the wall, or a static pressure tube. (Measurements of static pressure have been addressed in Chap. 4 *Pressure of Measurement Systems*, and it will be assumed that all static pressure measurements have been acquired and corrected using the techniques described therein.) In free flow, a Pitot-static tube may be used to obtain reasonably closely collocated measurements of static and total pressures, with the limitation that these probes are relatively large and thus may present blockage issues. Larger, multihole probes may be used to determine both the magnitude and direction of the velocity vector.

For all methods of determining the velocity, measurement errors will be introduced unless:

- measuring devices are small enough that there is negligible disturbance to the incoming flow because of the presence of the device and any associated support or traversing mechanism (i. e., blockage and interference are negligible, all measurement devices are *small*),
- the devices are correctly aligned to the flow velocity vector within the range of yaw acceptance (note that this condition may be violated in a highly turbulent flow),
- the stagnation pressure device is small enough that the assumption of deceleration of a single streamline holds (approximately),
- the stagnation pressure device Reynolds number is sufficiently large that the assumption of isentropic, inviscid streamline deceleration is valid,
- the dimensions of the device are negligible compared to the incoming flow lengthscales, i. e., the pressure can be considered approximately uniform across the measurement face,
- measurements are averaged over a sampling time selected to be long enough to give convergence of the reading to the true velocity, having accounted for the response of the probe (where, in general, the smaller the orifice, the longer the response time),
- the flow is free of particulates, condensation, etc., which could adversely affect the device readings.

Well-designed measurement devices will minimize the effects of violating these conditions.

In addition, the accuracy of the measurements will depend on the accuracy of the transducer. The sensitivity of the velocity to errors in the differential measurement of stagnation and static pressures for compressible and incompressible flows are given in (5.9) and (5.10), respectively:

$$\frac{\mathrm{d}U}{U} = \frac{1}{\gamma M_\infty^2}\frac{p\,\mathrm{d}p_0 - p_0\,\mathrm{d}p}{p_0 p} , \tag{5.9}$$

$$\frac{\mathrm{d}U}{U} = \frac{1}{2}\frac{\mathrm{d}(p_0-p)}{p_0-p} . \tag{5.10}$$

Devices to measure the (static) pressure have been considered in Chap. 4: static pressure wall tappings (Sect. 4.1) and static pressure tubes (Sect. 4.2). That chapter also addresses suitable hardware for determining velocity from pressure measurements in Sect. 4.3. Here the use of Pitot/impact tubes is described for the measurement of total pressure in Sect. 5.1.1, and in conjunction with a separate static pressure device to obtain the dynamic head in Sect. 5.1.2, while Sect. 5.1.3 covers combined probes such as the Pitot-static tube for the local measurement of dynamic pressure, and Sect. 5.1.4 introduces multihole probes from which both the velocity direction and magnitude may be determined. Some fundamental ideas will carry over from Chap. 4 and between sections, especially the correction methods for measurements of steady pressure. It has been noted in Chap. 4 that there is subtlety in the order of application of the various corrections to measured data, and this must be emphasized when the velocity is to be determined from the dynamic head, the difference between

two measured quantities, p_0 and p, that may not be the true values in the flow. In situ calibration may be required to maximize probe accuracy. The reader is referred to *Bryer* and *Pankhurst* [5.2] and *Chue* [5.1] for further details on most sections.

The convention of aligning x with the mean velocity direction and y with the direction of traverse of the probe (i. e., parallel to the probe support axis, Fig. 5.1) will be adopted. Reynolds decomposition will be used to write $u_x = U + u'$, $u_y = V + v'$ and $u_z = W + w'$, where U, V, and W are the mean (time-averaged) component velocities and a prime denotes a fluctuating velocity.

5.1.1 Measurement of Total Pressure Head with Pitot Tubes

Consider the probes of Fig. 5.1a–c for the measurement of total pressure p_0 commonly deemed *Pitot probes* after *Henri de Pitot* [5.3] (see also Sect. 5.1.3 for details of other total pressure devices). In what follows, it will be assumed that the only errors are introduced into measurement of p_0, i. e., p and ρ are measured accurately. In general, the results will hold for both impact-type and Pitot-static probes (Sect. 5.1.4), with the flow around the latter more severely disturbed due to the larger thickness (a higher ratio of inner to outer diameter, $\theta = d_{\text{in}}/d$) required to accommodate both static and stagnation pressure connections (Fig. 5.7c).

For a Pitot probe of a particular geometry, dimensional analysis shows that, given a completely accurate measurement of static pressure, the dynamic pressure measured by a transducer attached to the probe $p_{0\text{m}} - p$, will be related to the true velocity as a function of the following variables

$$C_{\text{p}} = \frac{p_{0\text{m}} - p}{\frac{1}{2}\rho U^2} = f\left(\tilde{\phi}, \text{Re}_{\text{d}}, M, \frac{\overline{u'^2}}{U^2}, \frac{\overline{v'^2}}{U^2}, \frac{\overline{w'^2}}{U^2}, \alpha, \frac{y}{d}\right) , \quad (5.11)$$

where $\tilde{\phi}$ is some measure of the incoming flow angle relative to the yaw sensitivity of the probe, Re_{d} is the local probe Reynolds number, M is the incoming Mach number, α relates the lengthscale of incoming shear to the probe diameter, y/d considers proximity to a surface and the components of relative turbulent intensity are given by $\overline{u'^2}/U^2$, etc.; the effect of turbulence scale relative to the probe can be considered in the yaw behav-

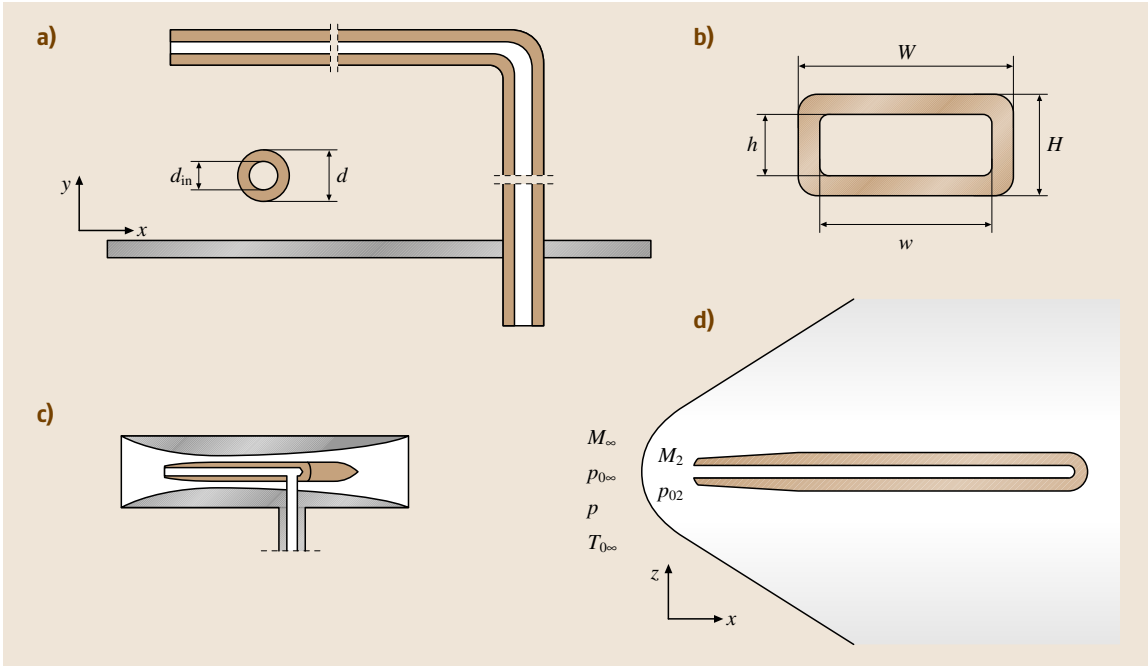

Fig. 5.1a–d Probes for the measurement of total head: **(a)** blunt-nosed cylindrical Pitot probe; **(b)** flattened Pitot probe; **(c)** Kiel probe; and from shock relationships: **(d)** Pitot probe in supersonic flow with known freestream static pressure p_∞ or reservoir pressure $p_{0\infty}$

ior. If $C_p = 1$ then the true total pressure is measured by the probe (and Bernoulli's equation holds uncorrected), but in general the magnitude of each of the parameters and their influence on the velocity determined from the measurements must be assessed.

Probe Selection and the Effect of Geometry

The finite size of practical Pitot probes violates the conditions of strict applicability of the Bernoulli equation. Rather than measuring the total pressure due to the stagnation of a single streamline, the probe will measure a uniform pressure imposed by the flow pattern at its nose. Depending on the probe Reynolds number (see the section on this topic below), a stagnation streamsurface will form inside or in front of the probe and the resulting flow pattern will determine the measured total head. If the probe is not fully aligned with the incoming flow, a further complexity to this tip flow is introduced and must be accounted for.

Spatial averaging in inhomogeneous flows may be limited by by using small-diameter probes to approximate the single-streamline condition, and the disturbance of the incoming streamlines due to the presence of the probe may be reduced through appropriate design of the probe and its mounting/traversing mechanism. However the dimensions of the probe may be limited by structural constraints and the poor temporal response of small-orifice designs. Blockage considerations may further constrain the dimensions of the probe, such that d/D must be small (Sect. 5.1.2).

The probe tip geometry will influence the flow in the region of the stagnation point and hence also impact on the measurement error. Standard probe designs include a cylindrical square-ended design (Fig. 5.1a) and a flattened cylinder (appropriate for measurement close to a surface) (Fig. 5.1b). For multiple simultaneous measurements rakes of probes may be used (although note that care must be taken to avoid mutual interference, especially in supersonic flow).

The effect of the ratio of inner to outer probe diameters θ will be detailed later, however historically $\theta = 0.6$ has been used by many investigators and thus many of the Pitot corrections have been formulated for this type of probe.

Directional Sensitivity

A Pitot probe may experience an incoming flow that is not parallel to its centerline either through physical misalignment to the predominant flow direction (which may be eliminated by careful experimental setup) or because of large variations in the angle of a turbulent or unsteady flow. The directional sensitivity of the probe will depend on the tip shape, probe diameter ratio θ, and the Mach and Reynolds numbers, and may be different in the yaw (z) and pitch (y) directions because of the presence of the probe support, Fig. 5.1 (note also that flattened probes are particularly sensitive to pitch because of their geometry). The zero-yaw condition corresponds to the maximum pressure reading (of interest when the direction of the flow is also to be determined, Sect. 5.1.3) and for commonly used designs $C_p \approx 1$ for a wide angular range, such that exact alignment with the flow direction is not critical to accurate measurements.

For simple square-ended probes, *Liepmann* and *Roshko* [5.4] suggest that an accuracy of $\approx 1\%$ of dynamic head ($C_p \geq 0.99$) may be obtained for yaw angles up to $\pm 20°$, decreasing with decreasing relative orifice size d_{in}/d and increasing rounding of the nose. *Bryer* and *Pankhurst* [5.2,5] note that the acceptable yaw angle also increases slightly with increasing Mach number.

Chue [5.1] has summarized the yaw characteristics of several commonly used nose shapes (shown here in Fig. 5.2). The Kiel probe (Fig. 5.1c) gives the best yaw response by a factor of approximately two.

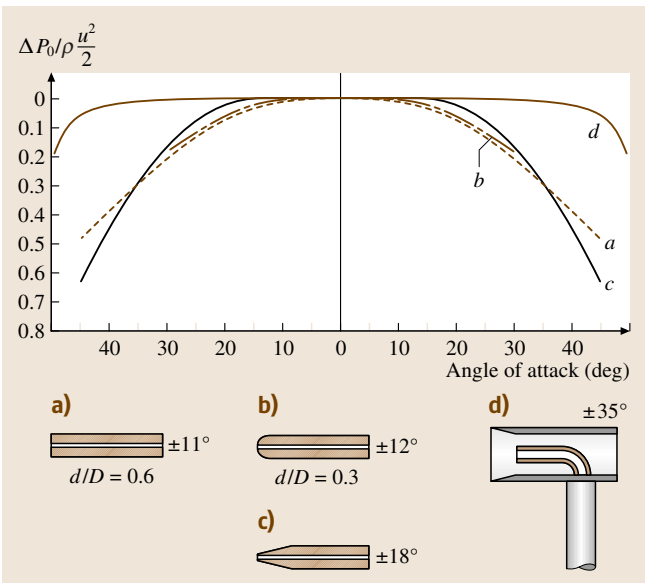

Fig. 5.2a–d Yaw sensitivity of commonly used Pitot probe tip designs: **(a)** square-ended Pitot probe with $\theta = 0.6$; **(b)** round-nosed Pitot/Pitot-static probe with $\theta = 0.3$; **(c)** Pitot probe with tapered tip, suitable for supersonic measurements; **(d)** Kiel probe (after *Chue* [5.1])

Probe Reynolds Number: The Effect of Viscosity

For real, viscous fluids, the assumption of inviscid (isentropic) flow on which the Bernoulli equation relies must be revisited. When the probe Reynolds number $\mathrm{Re_d} = dU_{\mathrm{local}}/\nu$ is low (where U is the local flow velocity and ν is the kinematic viscosity), in particular, viscosity may affect the flow around the probe tip such that measured total pressure $p_{0\mathrm{m}}$ differs significantly from the true impact pressure since the stagnation streamsurface may extend forward of the probe tip. This is commonly corrected by means of a calibration process, since there is not a simple extension of the Bernoulli equation to a viscous fluid.

Early measurements were taken with the round, square-ended design of Fig. 5.1a by *Barker* [5.8], *Hurd* et al. [5.7] and *MacMillan* [5.9]. For incompressible flow and $\mathrm{Re_d} \to 0$ the effect of viscosity is to increase the measured impact pressure (and hence also measured velocity) above the true value, i. e., $C_\mathrm{p} > 1$. There is some discussion in the literature of whether or not C_p ever falls below zero in the mid-Reynolds number range [5.7] or whether this is an artefact of experimental method [5.9]. The exact form of C_p appears to be sensitive to the mode of calibration, the condition of the probe tip (square ends reduce C_p relative to spherical/hemispherical tip values) and the ratio of inner to outer probe diameter (large θ reduces C_p).

Chue suggested that d_{in} is the more-appropriate dimension to use at low probe Reynolds number, $\mathrm{Re_{d_{in}}} < 10$, and under this scaling it appears that there is reasonably good collapse for most probe tip de-

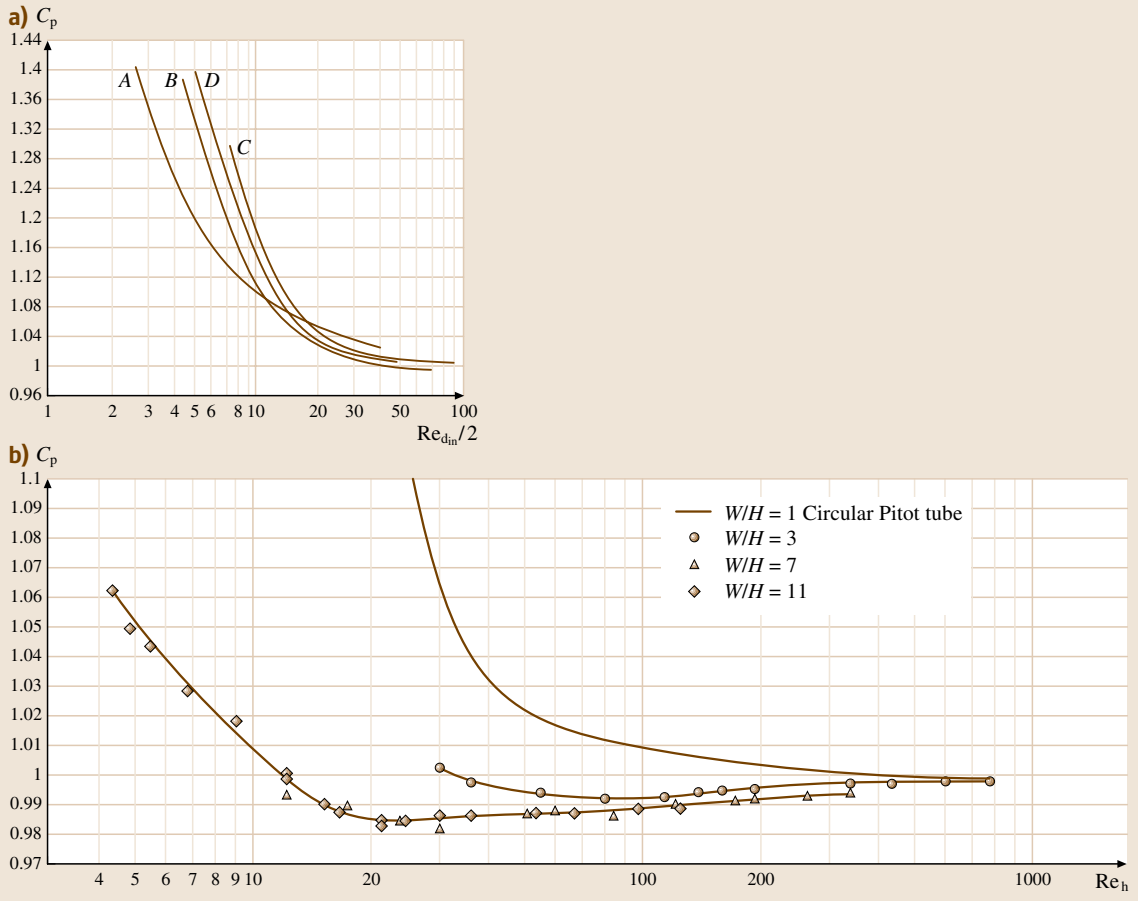

Fig. 5.3a,b Viscous correction for: **(a)** cylindrical probes: *A. Sherman* [5.6], *B. Hurd* et al. [5.7], *C. MacMillan*, *D. Barker* [5.8] (after *MacMillan* [5.9]); **(b)** flattened, boundary-layer-type probes (after *MacMillan* [5.10])

signs to the low-Reynolds-number numerical results of *Lester* [5.11]. For vanishingly small Reynolds number, inertial effects are negligible and the pressure distribution becomes independent of density, $C_p = A/\mathrm{Re}_d$.

Figure 5.3a shows the variation of C_p calibrations with $\mathrm{Re}_{d_{in}}$ for cylindrical probes and square [5.6] and round [5.7–9] noses.

With reasonable accuracy, the effect of viscosity at low probe Reynolds number may be represented by

$$\begin{aligned} C_p &= \frac{4.14}{\mathrm{Re}_{d_{in}}} \quad \mathrm{Re}_{d_{in}} < 1 \quad \textit{Hurd} \text{ et al. [5.7]} \\ &= 1 + \frac{2.5}{\mathrm{Re}_{d_{in}}^{1.25}} \quad 1 < \mathrm{Re}_{d_{in}} < 10 \quad \textit{Lester} \text{ [5.11]} , \end{aligned} \tag{5.12}$$

where the results of *Hurd* et al. [5.7] have been reformulated in terms of the inner probe diameter and a curve fit to *Lester*'s [5.11] data has been suggested. For higher Reynolds numbers,

$$\begin{aligned} C_p &= \frac{\mathrm{Re}_d}{1.07\mathrm{Re}_d - 7.4} && 12 < \mathrm{Re}_d < 60 \\ & && \textit{Mikhailova} \text{ and } \textit{Repik} \text{ [5.12, 13]} \\ &= 1 + \frac{10}{\mathrm{Re}_d^{1.5}} && \mathrm{Re}_d > 30 \\ & && \textit{Zagarola} \text{ [5.14]} \\ &= 1 \pm 2\% && \mathrm{Re}_d > 600 \\ & && \textit{Chue} \text{ [5.1]} . \end{aligned} \tag{5.13}$$

For a hemispherical nose design, *Merriam* and *Spaulding* [5.15] have shown that the diameter ratio does not affect C_p for $0.2 < \theta < 0.74$. The results of *Sherman* [5.6] for a round-nosed probe at low Reynolds number are shown as curve A in Fig. 5.3a. For $\mathrm{Re}_d > 20$ they agree well with the theoretical solution of *Homann* [5.16] for the stagnation region of a sphere:

$$C_p = 1 + \frac{6}{\mathrm{Re}_d + 0.455\sqrt{\mathrm{Re}_d}} . \tag{5.14}$$

The effect of viscosity is perhaps more often important for square-ended flattened probes (Fig. 5.1b) since this kind of probe is often used close to surfaces where the velocity may be low. Common probe dimensions lie in the region of $0.3 < h/H < 0.6$ and $3 < W/H < 11$. The results of *MacMillan* [5.10], shown here in Fig. 5.3b, reveal that a single C_p versus $\mathrm{Re}_{d_{in}}$ curve is appropriate for aspect ratio $W/H \geq 7$. C_p falls below unity for increasing non-axisymmetry. However note that h/H was varied for these experiments so the effect of θ has not been taken into account. *Mikhailova* and *Repik* [5.13] attempted to relate the calibration curves for flattened probes to those for circular probes by defining a complex equivalent diameter with a theta-dependent coefficient (not given here).

For compressible flow, a calibration coefficient for the total pressure alone C_μ may be defined

$$C_\mu = \frac{p_{0m} - p_0}{\frac{1}{2}\rho U^2} = C_p - \frac{p_0 - p}{\frac{1}{2}\rho U^2} . \tag{5.15}$$

In subsonic compressible flow the effect of compressibility should be to decrease the calibration coefficient below its incompressible value, as a superposition of viscous and compressibility effects [from (5.4)]. However, the available subsonic data of *Sherman* [5.6] show negligible effect of compressibility, thus the incompressible form, $C_\mu = C_p - 1$, assessed at the appropriate Reynolds number, should be applied to subsonic, compressible flow measurements [5.1].

For supersonic flow, the calibration coefficient is more appropriately written in terms of the (subsonic) flow conditions downstream of the probe-induced bow shock (Fig. 5.1d):

$$C_\mu = \frac{p_{02m} - p_{02}}{\frac{1}{2}\rho U_2^2} \tag{5.16}$$

and evaluated as for subsonic flow. (If there is strong shear then the bow shock may no longer be normal to the stagnation streamline and the pressure measured by the probe can no longer be simply expressed.) An estimate of the velocity behind the shock U_2 for the Reynolds number at which the correction must be evaluated can be obtained using the Rayleigh supersonic Pitot formula [(5.7) with the measured stagnation pressure p_{02m}] for M_∞ and the normal shock relation of (5.17) for the Mach number behind the shock

$$M_2 = \left(\frac{1 + \frac{\gamma-1}{2} M_\infty^2}{\gamma M_\infty^2 - \frac{\gamma-1}{2}} \right)^{\frac{1}{2}} . \tag{5.17}$$

The velocity follows after a temperature measurement:

$$U_2 = \frac{M_2\sqrt{\gamma R T_{02}}}{\sqrt{\frac{T_{02}}{T_2}}} = \frac{M_2\sqrt{\gamma R T_{02}}}{\left(1 + \frac{\gamma-1}{2} M_2^2\right)^{\frac{1}{2}}} . \tag{5.18}$$

Note that, for an adiabatic flow, $T_{02} = T_{01}$ so that the freestream temperature measurements may be used.

Direct experimental calibrations of p_{02m}/p_{02} versus Re_d in general retain the influence of Mach number and/or probe shape. *Chue* [5.1] has proposed the approximate curve of Fig. 5.4 for hemispherical, flat, and

internally chamfered probes, noting that the Mach number does not seem to influence the calibration within the scatter of the available data. For $Re_{d\infty} > 200$ the effect of viscosity is small. Note, however, that $Re_{d\infty}$ is the freestream Reynolds number, which will not capture the subtleties of the flow downstream of the shock wave. This calibration should be treated as approximate. A somewhat improved collapse may be obtained by using p_{02m}/p_{02} versus $Re_{d2}\sqrt{\rho_2/\rho_\infty}$, where Reynolds number Re_{d2} is assessed downstream of the shock, as the abscissa [5.17].

Effect of Turbulence

In a turbulent flow, the impact pressure at a point in the flow includes a contribution from the turbulent fluctuating velocity that increases the reading above its true value in the following way [5.18]:

$$p_{0m} = p + \frac{1}{2}\rho\left(U^2 + \overline{u'^2} + \overline{v'^2} + \overline{w'^2}\right) , \qquad (5.19)$$

where the overbar denotes a time average and quasi-steady flow is assumed. Although the detailed nature of the turbulence and the size of the characteristic scale relative to the probe diameter probably influences the measured stagnation pressure to some degree, *Christiansen* and *Bradshaw* [5.19] suggest that (5.19) is appropriate and *Tavoularis* and *Szymczak* [5.20] demonstrated negligible effect of characteristic scale (at least for low turbulence intensity)

$$\frac{\sqrt{\overline{u'^2}}}{U} < 10\% .$$

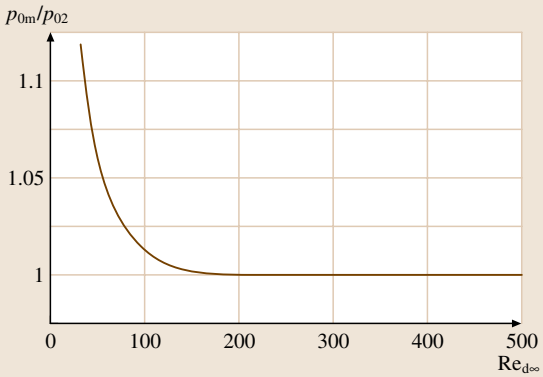

Fig. 5.4 Variation of the ratio of the measured to the true stagnation pressure downstream of the probe-induced shock versus the upstream Reynolds number (after *Chue* [5.1])

However for large-scale fluctuations and coherent structures, the instantaneous yaw angle must be considered in the response. *Zagarola* [5.14] included the response of the probe to normal fluctuations, i. e., the directional sensitivity, through the constant K_t, which was proposed to have a value $K_t \approx 0.3$ by *Ozarapoglu* [5.21].

$$p_{0m} - p = \frac{1}{2}\rho U_m^2 = \frac{1}{2}\rho\left(U^2 + \overline{u'^2}\right) + \frac{1}{2}\rho(1 - K_t)\left(\overline{v'^2} + \overline{w'^2}\right) . \qquad (5.20)$$

For $\overline{v'^2}$, $\overline{w'^2} \ll \overline{u'^2}$, (5.20) can be simplified to give

$$U = \sqrt{U_m^2 - \overline{u'^2}} \qquad (5.21)$$

or (for low turbulence intensity $\overline{u'^2}/U_m^2$)

$$\frac{U - U_m}{U_m} = -\frac{\overline{u^2}}{2U_m^2} . \qquad (5.22)$$

For example, *Dickinson* [5.22] proposed that this form is suitable for $y^+ = yu_\tau/\nu > 50$ in turbulent pipe flow.

Thus, correction for the effect of turbulence requires either simultaneous measurement of the fluctuating velocity, e.g., by hot-wire anemometry (which most probably negates the need for pressure-based velocity diagnostics), or the use of a known or empirical form of the distribution of $\overline{u'^2}$, $\overline{v'^2}$, and $\overline{w'^2}$.

Special attention should be paid to whether or not other corrections applied to the measurements implicitly include the effect of turbulence, and the magnitude of the turbulence correction relative to other corrections required. In a pipe with diameter D, *McKeon* et al. [5.23] found that, for Pitot probes with $d/D = 0.002$–0.014 and high Reynolds numbers ($d^+ < 2500$), the turbulence correction was an order of magnitude smaller than other corrections and could be neglected, however *Monty* [5.24] found that this was not the case for Pitot-static tubes with $d/D = 0.015$ at lower Reynolds numbers.

Effect of Shear

If a Pitot probe is to be used in a free shear flow, two additional effects on the impact pressure must be considered: the nonlinear effect of spatial integration of the inhomogeneous flow field across the probe face and displacement of the stagnation streamline induced by the finite size of the probe. Both are consequences of the violation of the single-streamline assumption and both lead to an indicated velocity that is higher than the true

value corresponding to the location of the centerline of the probe (i. e., an apparent deflection of incoming streamlines towards the region of lower velocity). The magnitude of this effect can be assessed either in terms of an implied error in probe position $\Delta y = y - y_{cl}$, the offset of the probe centerline relative to the position of the streamline under measurement, or as the difference between measured and true velocity, ΔU, at y_{cl}, where

$$\frac{\Delta U}{U(y_{cl})} = \frac{U(y_{cl}+\Delta y) - U(y_{cl})}{U(y_{cl})} = 2\alpha\frac{\Delta y}{d} - \beta\frac{(\Delta y)^2}{d^2} + \ldots \quad (5.23)$$

The shear parameters α and β are given by

$$\alpha = \frac{d}{2U(y_{cl})}\left.\frac{dU}{dy}\right|_{cl}, \quad (5.24)$$

$$\beta = -\frac{1}{2}\frac{d^2}{U(y_{cl})}\left.\frac{d^2U}{dy^2}\right|_{cl}, \quad (5.25)$$

and the subscript 'cl' implies that the variables are assessed on the probe centerline. In boundary-layer flows both α and β takes their maximum values near the wall and are necessarily zero in the freestream, and $\alpha = 0$ on the centerline of a pipe. Figure 5.5a,b shows the variation of α and β, respectively, for a cylindrical probe of 0.3 mm diameter in pipe flow at $Re_D = \overline{U}D/\nu = 75\times10^3$ and 4×10^6, where $\overline{U}$ is the bulk velocity [5.25].

Integration of a linear velocity profile across a circular probe yields the following expression for the apparent offset of the probe centerline due to spatial integration, Δy_{int}:

$$\frac{\Delta y_{int}}{d_{in}} = \frac{1}{2\alpha}\left(\sqrt{1+\frac{\alpha^2}{4}} - 1\right). \quad (5.26)$$

Thus for a probe with $\theta = 0.6$, this offset can be seen to have a maximum value of $\Delta y_{int}/d = 0.035$ when $\alpha = 1$, falling with decreasing α. This effect is usually small compared to the other shear-induced corrections, and hence is often neglected.

In addition, account must be made for a displacement of the effective stagnation streamline in the direction of the region of lower velocity due to the presence of a finite-sized probe in a shear flow. In practice, account is taken of this effect by applying a displacment correction to the probe position $\Delta y/d$, which is intuitively a function of the local shear α. Theoretical approaches that consider a sphere in potential flow due to *Hall* [5.26]

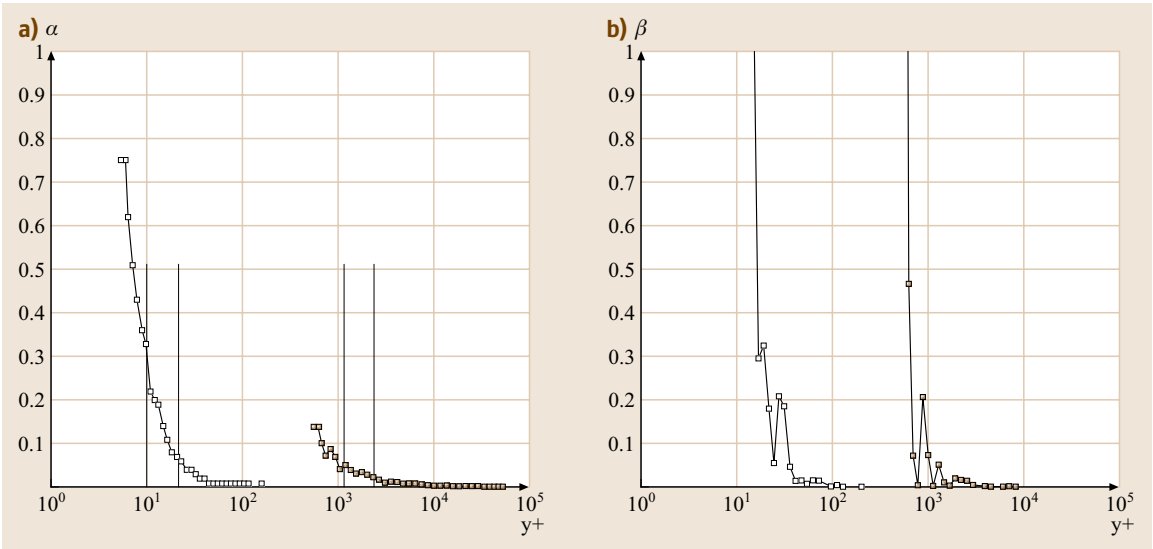

Fig. 5.5a,b The variation of shear parameters **(a)** α (5.24) and **(b)** β (5.25) in pipe flow. *Open symbols*: $Re_D = 75\times10^3$ and *closed symbols* $Re_D = 4\times10^6$ (after *McKeon* [5.25])

and *Lighthill* [5.27] give expressions of the form

$$\frac{\Delta y}{d} = A_1 \tanh(A_2\alpha) = C_1\alpha - C_2\alpha^3 + O(\alpha^5) \,. \tag{5.27}$$

However early experimental work [5.28, 30–32] led to the conclusion that a constant displacement correction,

$$\frac{\Delta y}{d} = \varepsilon_\mathrm{d} \tag{5.28}$$

was appropriate, with $\varepsilon_\mathrm{d} = 0.08–0.18$ for cylindrical probes (apparently independent of θ, $\mathrm{Re}_{d_\mathrm{in}}$, and the velocity gradient). The effect of θ can be taken into account using the expression of *Young* and *Maas* [5.31]):

$$\frac{\Delta y}{d} = 0.131 + 0.082\theta \,. \tag{5.29}$$

More recently, *Tavoularis* and *Szymczak* [5.20] proposed $\varepsilon_\mathrm{d} = 0.16$ for $\theta = 0.6$ and $\alpha \geq 0.03$, based on experiments covering $0.002 \leq \alpha \leq 0.14$. These authors noted that, as $\alpha \to 0$, so does the error in U_m, even though the positional error remains constant. For rectangular probes, *Quarmby* and *Das* [5.29] suggest $\varepsilon_\mathrm{d} = \Delta y/H = 0.19$, in qualitative agreement with early work by *Young* and *Maas* [5.31].

However the most commonly used version of this correction is due to *MacMillan* [5.28], who investigated the effect of shear on cylindrical probes with $\theta = 0.6$ in the pipe Reynolds number range $\mathrm{Re}_D = (20–100)\times 10^3$ and found

$$\varepsilon_\mathrm{d} = 0.15 \,. \tag{5.30}$$

In many situations (or at least over the range of shear parameter in which Pitot probes are commonly used) this correction is sufficient and simple to apply.

Intuition, however, suggests that the full correction must be a function of α [5.1, 23, 33], such that it tends to zero in uniform flow (consider the problem that arises on a pipe centerline with a constant ϵ_d). *McKeon* et al. [5.23] proposed the following, empirical form (the *Princeton displacement correction*):

$$\frac{\Delta y}{d_\mathrm{p}} = 0.15 \tanh\left(4\sqrt{\alpha}\right) \,. \tag{5.31}$$

Equation (5.31) takes a similar form to the potential flow theory of (5.27) and has been demonstrated to provide the best collapse between data taken with probes of different diameter (in pipe flow), and for larger values of α than the MacMillan correction. As such it is recommended that this correction be used if high measurement accuracy is required.

A comparison of the different displacement corrections for cylindrical and square Pitot probes is given in Fig. 5.6. It should be noted that the accuracy of the corrected data depends critically on the error in probe location and the practical difficulty of separating out shear and turbulence effects in experiment. In addition, a correction for wall proximity must be applied for $y/d < 2$.

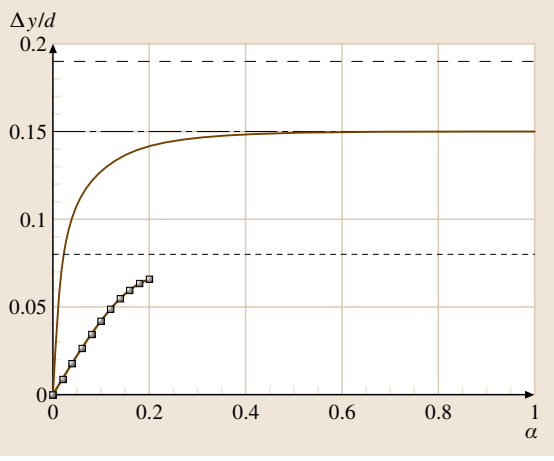

Fig. 5.6 The variation of different suggestions for the displacement correction with shear parameter α. *Solid line*: Princeton displacement correction [5.23]; *dot-dash line*: *MacMillan* correction [5.28]; *symbols*: *Lighthill* (potential theory) [5.27]; *long dashes*: correction for rectangular probes (*Quarmby* and *Das* [5.29]); and *short dashes*: lower limit of constant corrections ϵ_d in the literature ($0.08 \leq \epsilon_\mathrm{d} \leq 0.18$ for cylindrical probes)

Effect of Wall Proximity

When a Pitot probe is used near a solid boundary an additional correction is required. Consider a probe resting on a wall in uniform flow: the resultant streamline deflection is in the opposite sense to that due to shear, i. e., towards the region of higher velocity. The cumulative effect for a probe in proximity to a wall in shear flow such that $d/D \ll 1$, then, is a reduction in the velocity-gradient-induced displacement correction.

MacMillan [5.28] suggested that measurements can be corrected for the proximity of the wall by application of the following (Reynolds-number-independent) adjustment to the velocity:

$$\frac{\Delta U}{U} = 0.015 \exp\left[-3.5\left(\frac{y}{d} - 0.5\right)\right] , \tag{5.32}$$

which should be used in addition to the displacement correction (5.30) for $y/d < 2$. Although the MacMil-

lan corrections take the simplest form of the available formulations, they have been shown to overcorrect data taken in high-Reynolds-number pipe flow [5.23]. For flattened probes, the results of *Quarmby* and *Das* [5.29] indicate that (5.32) may be used with reasonable confidence when the largest probe dimension, i. e., the probe width H, is used instead of the circular probe diameter (although note that these authors found some Reynolds number dependence of the correction).

The experiments of *McKeon* et al. demonstrated that data within one probe diameter of the wall could not be used with the same confidence as further away from the wall. They proposed the *Princeton wall correction* for the effect of both shear and wall proximity in the near-wall region, based on the Preston probe pressure data of [5.34]. Assuming that a probe resting on the wall reads the true pressure at a distance from the wall of

$$\frac{y}{d} = \frac{1}{2} + \frac{\delta_w}{d} , \tag{5.33}$$

δ_w is the required wall correction, which will depend on probe Reynolds number. The correction is best given by

$$\begin{aligned} \frac{\delta_w}{d} &= 0.150 \quad \text{for } d^+ < 8 \\ &= 0.120 \quad \text{for } 8 < d^+ < 110 \\ &= 0.085 \quad \text{for } 110 < d^+ < 1600 , \end{aligned} \tag{5.34}$$

and should be applied for $1 < y/d < 2$ only. Further from the wall the free shear displacement correction of (5.31) should be used. When tested on pipe flow data taken with probes with four different diameters, excellent collapse was demonstrated for $10 < d^+ < 4000$.

Note that nearer the wall, $y/d \leq 1$, neither wall correction gives appropriate collapse of data from different diameter probes. In this region the accuracy of measurements made using Pitot probes degrades significantly and errors in probe position become critically important. This is especially unfortunate since near-wall measurements are often used to determine wall shear stress or

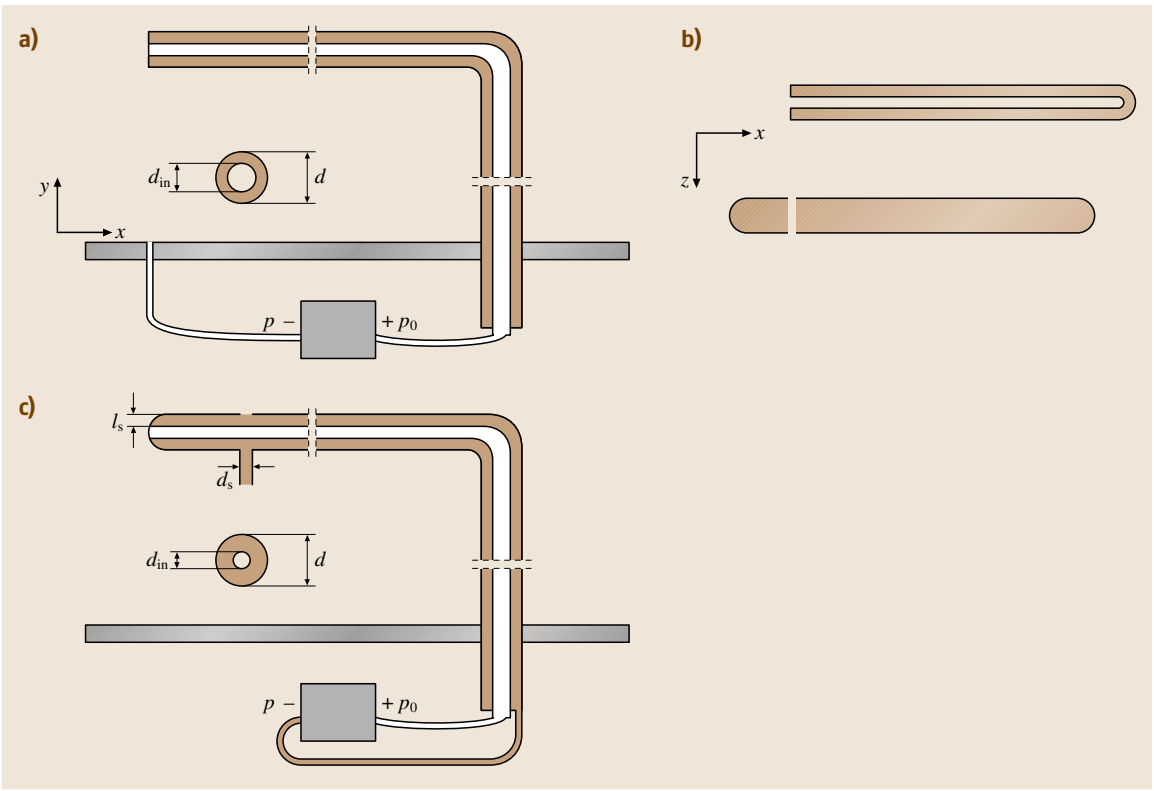

Fig. 5.7a–c Determination of the velocity from measurements of the dynamic head: **(a)** Pitot (impact) tube and static pressure wall tapping; **(b)** Pitot probe and static tube; **(c)** Pitot-static probe

slope of the mean velocity profile (Fig. 5.9). Experimentalists should be aware of the limitations of this measurement technique in the very near-wall region, particularly at high Reynolds numbers where the probe diameter becomes large relative to the viscous scale.

5.1.2 Dynamic Head from Separate Measurements of Total and Static Pressures

Separate measurements of total and static pressures from a Pitot probe (above) and either a wall tapping or static tube (Chap. 4) can be used to determine the Mach number or velocity from the Bernoulli equation [(5.2) and (5.5), respectively]. These configurations are shown in Fig. 5.7a,b using a single transducer to obtain the dynamic head. It has been noted above that, while a differential measurement to give the dynamic pressure is most suitable for incompressible flow, it is the ratio p_0/p that is required to obtain the Mach number (in which case the total and static pressure measurements must separated).

Additional corrections may need to be made when separate measuring devices are used for the total and static pressures.

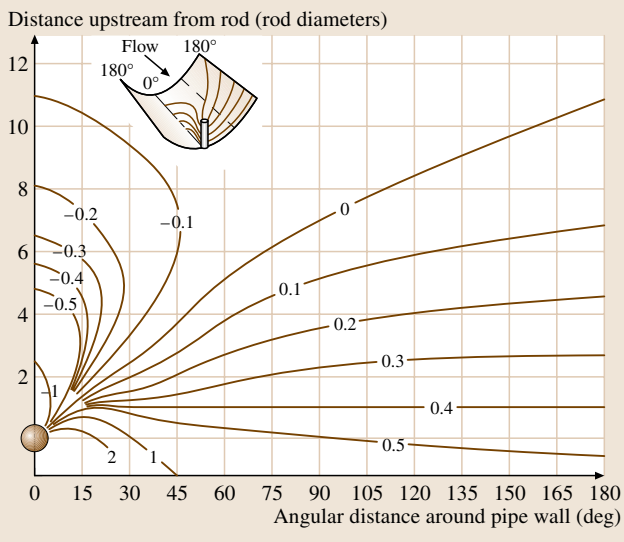

Fig. 5.8 Effect of blockage due to the probe support strut on the measurement of the static pressure by a tapping in a pipe wall. The worst case for the strut (under full extension to the pipe centreline) in relative mean velocity error $(1/B)\Delta U/U$, where $B = 2d/(\pi D)$, is given in terms of the streamwise and azimuthal separation of strut. (After *Hubbard* [5.35])

The probe body and strut and the static pressure device must be selected and located such that there is negligible interference effect between them. *Hubbard* [5.35] considered the blockage effects of the strut on a wall pressure tapping in a pipe with diameter $D = 300\,\text{mm}$. The relative mean velocity error $(1/B)\Delta U/U$, where $B = 2d/(\pi D)$, for the strut alone (under full extension to the pipe centerline) in terms of streamwise and azimuthal separation of strut and tapping is replicated here in Fig. 5.8. This represents the worst-case error since the blocking mass will be a maximum on the centerline for a retracting strut. Note that the sign of the induced error depends on the streamwise separation of the tapping from the probe strut and that, in practice, the measured pressure is often obtained by T-ing together two or more tappings offset in the spanwise direction from the impact tube streamwise measurement location.

The decrease in measured static pressure caused by the blockage because of the probe body must also be taken into account, varying from zero when the probe tip is far downstream of the location of static pressure measurement to a value that can be calculated from the Venturi effect when it is several diameters upstream [5.35].

In general, measurements with the Pitot tube in proximity to the wall require special attention, as indicated at the end of the previous section. The dramatic effect of the wall tapping correction together with the Pitot displacement and wall corrections on a high-Reynolds-number pipe mean velocity profile [5.25] is shown in Fig. 5.9, where $y^+ = yu_\tau/\nu$ and $U^+ = U/u_\tau$, and it has been shown [5.23] that there is a change to the inferred value of the von Kármán constant κ in the logarithmic law of the wall in pipe flow of the order of 5% compared to the analysis with no corrections.

5.1.3 Direct Measurement of Dynamic Head (Combined Pitot-Static and Other Probes)

Combined dynamic pressure probes may be used to obtain the flow velocity in situations where the complexity or size of separate measuring devices is undesirable. For unconfined flows, the Pitot-static probe of Fig. 5.7c is commonly used, utilizing coaxial tubing to combine a Pitot probe inside a static tube. Well-designed Pitot-static probes may be used to obtain accuracies of the order of 0.1% of dynamic head [5.36] or down to the limit of transducer sensitivity [5.2].

In general, the errors that arise when using these probes are a simple combination of the effects described

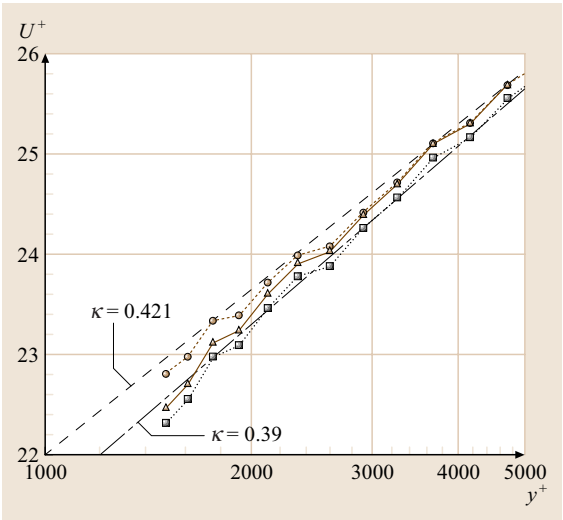

Fig. 5.9 Mean velocity profiles from *McKeon* [5.25] at $\mathrm{Re}_D = 10 \times 10^6$ under the *MacMillan* [5.28] displacement correction. *Shaw* [5.37] static pressure correction (*squares*). *McKeon* and *Smits* [5.38] static pressure correction (*triangles*), with MacMillan wall term (*circles*). Log laws with $U^+ = 1/\kappa y^+ + B$ and $\kappa = 0.421$ (*dashed line*) and $\kappa = 0.390$ (*dot-dashed line*)

for the separate measurement of total and static pressure above and in Chap. 4. Due to the complexity of design these probes tend to have a larger diameter than equivalent Pitot probes and a lower ratio of inner to outer diameter θ. Consequently, use near walls is not recommended due to a large wall-proximity effect, and care must be taken in flows with large velocity gradients (shear). The influence of viscosity on the dynamic pressure through the measurement of total head is as detailed in Sect. 5.1.1, but the impact of turbulence will depend on the correlation between the total and static pressure fluctuations.

The effect of yaw is shown in Fig. 5.10, which gives the percentage error in measured dynamic head, $100C_{pm}$, where $C_{pm} = (p_{0m} - p_m)/(1/2\rho U^2)$, due to errors in the measured total and static heads with yaw angle for a standard Pitot-static probe. It should be noted that the zero-yaw case no longer corresponds to the highest recorded velocity since there is a balance between the competing effects on the total and static pressures. The effects of pitch and yaw have been shown to be the same within approximately $\pm 1\%$ [5.2].

Chebbi and *Tavoularis* [5.39] have demonstrated that a severe reduction in Reynolds number (in this case over four orders of magnitude to a low Reynolds number $\mathrm{Re}_d = 0.14$) also dramatically increases the yaw sensitivity of a Pitot-static probe with a rounded tip and $\theta = 0.28$, reducing the range of negligible error by an order of magnitude. In general, it is unlikely that the Reynolds number effect is important, since $\mathrm{Re}_d = 0.14$ lies well outside the normal Reynolds number range in which Pitot probes are used.

The tip and stem influence the measured dynamic head through the static pressure as detailed in Sect. 4.2.2 and shown in Fig. 4.8. In the Prandtl probe design, a cancellation of the errors occurs through the location of the static pressure holes; tip-to-static-hole and static-hole-to-stem separations of $6d$ and $8d$, respectively, are used in a standard modified Prandtl design.

Other types of combined probe include the compact, cantilever-type Pitot cylinder, wedges, and cones. In the former, cylindrical design, coaxial tubes are used in conjunction with static and total tappings located at the same lengthwise distance along the cylinder, but separated circumferentially (and the outer cylinder is sealed with a rounded tip). The probe is inserted transverse to the incoming flow and rotated such that the total pressure tapping is aligned with the incoming flow. The relationship between the angular location of the static pressure tappings and local static pressure is determined by calibration since the flow may deviate from the ideal potential-flow solution due to the influence

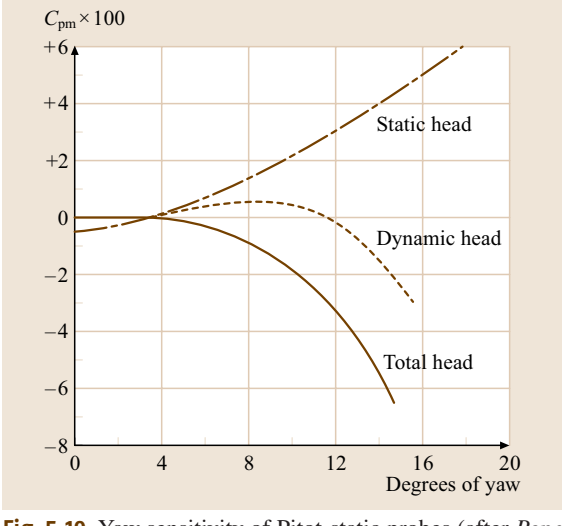

Fig. 5.10 Yaw sensitivity of Pitot-static probes (after *Pope* and *Harper* [5.36]), demonstrating the percentage error in the measured dynamic pressure, i. e., $100C_{pm}$, due to the effect of angular misalignment on the total, static, and dynamic head readings

of the tapping size or Reynolds and Mach number effects (shocks will occur in the accelerating flow over the front half of the cylinder for freestream Mach numbers $0.55 \leq M < 1.0$). The total pressure reading is independent of Reynolds number for $Re_d > 4000$, but a function of the separation of the tapping from the probe tip when this is less than five probe diameters [5.1]. *Chue* [5.1] states that the accuracy of the cantilever probe is 5% of the impact pressure per degree of yaw, implying that this kind of probe is most useful for higher flow velocities. [Note that, with two static tappings symmetrically situated around the cylinder circumference from the total tapping, the local flow direction can also be obtained by the null-reading method (Sect. 5.1.4) provided that the Mach number is low enough to preclude shocks on the cylinder surface.]

Mach number can be determined in an isentropic supersonic flow using the relationship between reservoir pressure and surface pressure on a wedge (or cone) via the oblique (conical) shock relationships [5.4].

For more details of other probe designs, the reader is referred to *Bryer* and *Pankhurst* [5.2], and *Chue* [5.1].

5.1.4 Measurement of Dynamic Head and Flow Direction (Multihole Probes)

So-called *multihole* probes are often used to obtain the flow direction, the static pressure and the dynamic head in flows where the incoming angle is unknown and/or has a large variation in the flow domain, for example, in turbomachinery and wake flows. Probes typically consist of a central, stagnation pressure hole or tube, downstream from which a number of pairs of static pressure holes/tubes are symmetrically displaced, with equal and opposite angles between the orifice faces and the flow. Figure 5.11a,b shows conical five- and seven-hole probes; other typical designs include hemispherical and wedge arrangements.

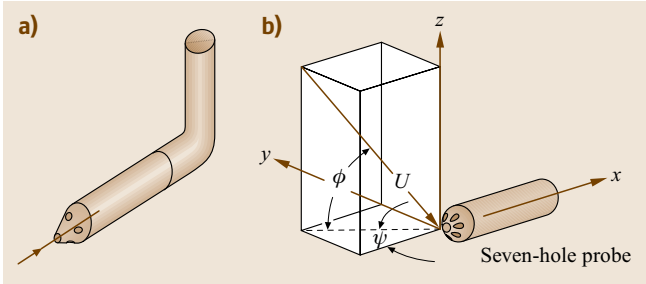

Fig. 5.11a,b Schematic of **(a)** a five-hole truncated-cone probe, and **(b)** a conical seven-hole probe, demonstrating the angular determination of the velocity vector

Multihole probes may be used in either *null-reading* (for symmetric probes) or *calibrated* modes. In the former method, the angular orientation of the probe is altered about the yaw and/or pitch axes until both static holes in a pair give the same pressure reading and the stagnation hole is aligned with the flow direction. The flow angle can then be determined from the rotations required to null the probe, which (when appropriately connected to a set of transducers and with simple probe calibrations) then gives measurements of total, static and dynamic heads, and hence the velocity vector. This method is extremely time-consuming and relies on the assumption that the flow is locally symmetric about the probe (a constraint either on probe manufacturing tolerances or the size of the probe relative to the lengthscale of any shear in the flow), however in this case the Reynolds and Mach number dependence of the measurement can be simply obtained. Note that the sensitivity of this type of probe is designed to give a more pronounced variation with angle than could be obtained by using the yaw response of the types of probe described earlier in the chapter.

Alternatively, the probe can be calibrated by forming single-valued dimensionless pressure ratios (which are a function of angle and independent of Reynolds number) in flows where either a suitable rotation mechanism is not available or leads to movement of the tip of the probe during the nulling process. For use in flows where the flow angle may lead to separation over one or more tappings (approximately 30° for most probes [5.40]), the calibrations are typically subdivided based on where the highest pressure is measured. (In practice, the calibrations become double-valued when the angle is large enough to give a significant separation in the tip region.) *Sumner* [5.41] has compared the accuracy of measurements for which the calibrations are found by interpolation and curve-fit polynomials between calibration points for seven-hole probes, finding that the former gave better results in the presence of flow separation and that results were sensitive to the grid of calibration points used.

If there is angular variation in only one plane, a three-hole Cobra probe may be used, consisting of a stagnation tube flanked by two in-plane static pressure tubes. *Chue* [5.1] proposes that the flow direction within a boundary layer may be determined to within 0.2° by the calibration method if the pitching angle does not exceed 6°.

A five-hole probe, Fig. 5.11a, may be used to determine the angular variation in both pitch and yaw directions with a magnitude of less than 30° [5.42]. At larger angles, where the five-hole probe becomes ineffective for angle determination by calibration, a seven-hole probe, Fig. 5.11b, may be more suitable (although note that the nulling method becomes prohibitively time-consuming for this type of probe). For a conical design, the cone angle is typically 30° or 45°, with the tappings spaced at 60° intervals.

Zilliac [5.40] suggests that a calibrated seven-hole probe offers a measurement accuracy of 1% in velocity and 0.5° in angle (comparable to a five-hole probe in nulling mode) also noting that since six tubes pack closely around the central stagnation tube there is only a small concomitant increase in probe size. In subsonic compressible flows, the calibration method may be used at flow angles up to 70° to determine flow angle with accuracy ±2° and Mach number to ±0.04 with 95% certainty [5.43]. *Takahashi* [5.44] has investigated the suitability of seven-hole probes for unsteady flow measurements.

While the use of multihole probes is ubiquitous in the aerospace and turbomachinery communities, there are serious limitations on these techniques that preclude their use for highly accurate measurements. The sources of error are many, including most seriously the effects of instantaneous yaw and all-component fluctuation intensity in turbulent flow, the large disturbance presented by the probe (the connections for multiple pressure lines mean that multihole probes are necessarily relatively large) and the effects of flow separation. It is not clear how the empirical corrections described in earlier sections of this chapter apply to the complex flow fields induced around a probe tip that is not aligned with the flow. While an attempt is often made to address these issues during the calibration process, the requirement for both known flow angle and velocity probably implies a laminar or at least low turbulence calibrating flow. Strictly speaking, calibration in a nonturbulent freestream justifies use of the probe only in a similar, nonturbulent flow.

In addition, multihole probes are not suitable for use in flows where there is a significant gradient in total pressure or in which the Mach number is sufficiently high that there is the potential for asymmetric shocks to form in front of the probe, or over only some of the tappings. (The effect of the latter phenomenon may be mitigated by reducing the separation between small tappings and/or using probe shapes, such as a wedge, for which analytic solutions exist.)

Further details on multihole probes may be found in *Bryer* and *Pankhurst* [5.2].

This section has described devices for the determination of the magnitude of the velocity (or Mach number), assuming at least approximate alignment of probes with the incoming flow. In general, the flow angle may be determined from Pitot and static probes through yaw calibrations if the flow conditions are otherwise known, or multihole yawmeters may be rotated until the same readings are obtained by holes on either side of the probe centerline, the *null-reading* method. For further information on these techniques and appropriate hardware, the reader is referred to *Chue* [5.1].

5.2 Thermal Anemometry

Hot-wire anemometry is a versatile technique that can be used for the measurement of velocity and temperature fluctuations in the time domain for investigations in turbulent flows. With appropriate designs hot-wire anemometry is useful over wide speed ranges from low subsonic to high supersonic flows. The method is capable of detecting turbulent perturbations with a large dynamic response because of the very small hot-wire thermal inertia and its correction in the anemometer. The hot-wire can be operated in three popular methods: constant current, constant temperature, and the new constant voltage. The response of the sensor and that of the associated operating electronic circuit are analyzed. Also included are calibration techniques and approximations for low turbulence levels.

5.2.1 Introduction

Thermal anemometry is used when one wishes to measure rapidly varying velocities with good spatial and time resolution. An example is given in Fig. 5.12 for a supersonic boundary layer. The method relies on the changes in heat transfer from a small heated sensor exposed to the fluid in motion. The sensor is made with a material whose electric resistivity depends on the temperature. It usually has the shape of a small cylindrical wire or a thin film. Experiments can be made in gases, from low subsonic to high supersonic velocities, and transparent, opaque, and even electrically conducting liquids. Instantaneous wall shear stresses can also be measured using sensors mounted flush to the surface. The measurement

of other flow properties such as temperature, density, composition, is also part of thermal anemometry. Some aspects of these property measurements are considered in the present chapter.

Heat is introduced in the sensor by Joule heating, and is lost primarily by forced convection. The heating rate is $R_w I_w^2$, where I_w is the current intensity in the sensor and R_w the sensor resistance when heated. The cooling rate is of the form $(T_w - T_a)\phi_{conv}(U\ldots)$, where T_w is the temperature of the wire when heated, and T_a is the temperature of the wire at the same location when unheated. In liquids and low subsonic gas flows, T_a is simply the temperature of the surrounding fluid. When compressibility effects are present, T_a becomes the recovery temperature T_r of the sensor. The function $\phi_{conv}(U\ldots)$ mainly depends on the fluid velocity normal to the wire. The role of the other parameters will be discussed in Sects. 5.2.3 and 5.2.4, and for the moment the forced convection effect is simply written $\phi_{conv}(U)$. A small fraction of the heat supplied to the wire is, however, conducted towards the supports holding the sensor, resulting in a nonuniform temperature distribution along its length. The quantities T_w or R_w are in reality spatial averages over the sensor. This problem is neglected for the moment, but it will be considered later in this section.

For a steady flow, the heat balance between the heating and the cooling rates has the simple form

$$R_w I_w^2 = (T_w - T_a)\Phi_{conv}(U)\,. \tag{5.35}$$

The velocity U can be deduced from the electrical quantities R_w and I_w, if T_w can be related to R_w and similarly T_a to R_a, where R_a is the resistance of the unheated sensor. Such relations exist for most sensors. Often an assumed linear dependence is adequate to describe $R(T)$ around the operating point, so that

$$R_w = R_0[1 + \chi(T_w - T_0)] \quad \text{and}$$
$$R_a = R_0[1 + \chi(T_a - T_0)]\,, \tag{5.36}$$

where T_0 is a reference temperature, R_0 the resistance of the sensor at that temperature, and χ the temperature coefficient of resistivity of the wire material around T_0, and T_0 is often chosen close to T_a. The value of χ is positive for metallic materials. For example, for tungsten, $\chi \simeq 4.0\times10^{-3}\,\mathrm{K}^{-1}$, resulting in 100% increase of the sensor resistance when the operating temperature T_w is increased by 250 K over T_a. The value of χ is negative for thermistors. For polysilicons, χ can be positive or negative, depending on the material used for the doping and its concentration.

A significant parameter that controls the operation of the sensor is the relative difference in temperature, $(T_w - T_a)/T_a$, or the relative difference in resistance, $(R_w - R_a)/R_a$. The latter is preferred because of its direct deduction from electrical quantities. It is simply denoted a_w and called the overheat ratio of the sensor,

$$a_w = \frac{R_w - R_a}{R_a}\,. \tag{5.37}$$

When needed, the relative difference in temperature can be expressed in terms of a_w as

$$\frac{T_w - T_a}{T_a} = a_w \frac{1 + \chi(T_a - T_0)}{\chi T_a}\,. \tag{5.38}$$

In practice, for air or other gases, a_w is in the range 0.05–1.0. Beyond this value, the sensor could be permanently deformed or oxidized. For example, platinum has an excellent resistance to oxidation, but is naturally soft and weak. Its tensile strength can be increased by the addition of iridium or rhodium. On the other hand, tungsten, which presents a high tensile strength, oxidizes above 600 K. For water or other fluids, a_w is limited to around 0.10 because of the occurrence of vapor bubbles from boiling.

The simple balance (5.35) holds for steady flows only. If a flow is unsteady, which is always the case if the flow is turbulent, thermal energy is unsteadily stored in the sensor, and the instantaneous heat balance becomes

$$m_w c_w \frac{\mathrm{d}T_w}{\mathrm{d}t} = R_w I_w^2 - (T_w - T_a)\Phi_{conv}(U)\,, \tag{5.39}$$

where m_w is the mass of the sensor and c_w is the specific heat of the sensor material. Conduction effects are not included in (5.39).

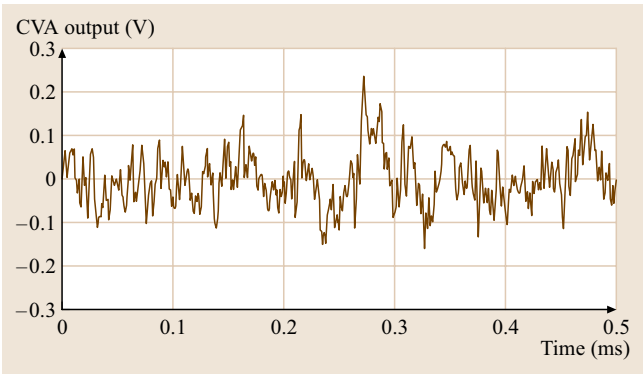

Fig. 5.12 Time trace of a turbulent signal provided by hot-wire anemometry based on experiments conducted with a constant-voltage anemometer (CVA) in a Mach 2.3 boundary layer

When the sensor is an element of an appropriate electrical system, the change in resistance can be used to generate a measurable signal. Three operating modes are possible.

- The current intensity in the sensor is maintained constant, $I_w = \text{constant}$, which leads to the constant-current anemometer (CCA). Any change of U creates a change in R_w and the measurable signal is directly this resistance change.
- The resistance of the sensor is maintained constant, $R_w =$ a constant, which leads to the constant-resistance anemometer, usually called a constant-temperature anemometer (CTA) because of (5.36). The measurable signal when a change in U occurs is then the change in current intensity I_w to be fed to the sensor to fulfill the imposed condition.
- The voltage across the sensor is maintained constant, $V_w = R_w I_w = \text{constant}$, which leads to the constant-voltage anemometer (CVA). The measurable signal is then the change in current intensity I_w to be fed to the sensor under that new imposed condition.

The main difference between these three operating modes is linked to the handling of thermal inertia of the sensor, represented by the left-hand side of (5.39). In usual applications, the frequencies of the flow fluctuations to be measured are much higher than the natural frequency of the sensor, so that electronic compensation is needed. In a CCA and CVA, this is achieved by a first-order high-pass filter integrated in the amplifying unit. In a typical CCA application, the filter's response is tuned to compensate exactly the thermal lag of the sensor. The overall bandwidth is then only limited by the amplifier's characteristics, mainly its gain–bandwidth product. With a CVA, the thermal lag is partially compensated during measurements and is fully compensated when postprocessing the data. This permits high productivity for large-bandwidth applications because no adjustment is required when the experiment is running. In a CTA, the temperature of the sensor is maintained constant by a feedback loop, so that its thermal inertia is, in principle, automatically compensated. In this case, the maximum bandwidth is limited by the amplifier's properties and some characteristics of the practical setup. Full compensation can be made after carefully tuning the circuit. These points will be analyzed in Sect. 5.2.3.

In any of these three operating modes, the temperature T_a is a major parameter, as it modifies the difference $T_w - T_a$. In fact, changing T_a is almost the same as changing T_w. This point is most important when using a CTA, which maintains $R_w = \text{const}$, hence $T_w = \text{const}$, whatever T_a. For example, in a subsonic flow, if the temperature T_a of the incoming flow increases at fixed U, the current intensity needed by the sensor decreases as $T_w - T_a$ decreases. A benefit, however, is that thermal anemometry can be used to measure temperature changes occurring in turbulent flows.

The Section is organized as follows. Section 5.2.2 describes the nature and shape of typical sensors, and their geometrical disposition relative to the incident flow, in order to obtain specific flow characteristics. The steady heat-transfer laws expressing the cooling rate of the sensors are then indicated for various fluids and flow conditions. They are most useful when interpreting the electrical signals available at the anemometer output. For unsteady flows, the thermal lag of the sensor is an inherent limiting parameter and some estimates of this lag are indicated. Finally, two important topics are considered: the heat loss towards the supports holding the sensor and the spatial resolution of the sensing element.

Section 5.2.3 deals with the electronic circuits used in the CCA, CTA, and CVA. Treatment of the thermal lag of a sensor is examined with special attention. For example, it is shown how constant-voltage operation reduces the time constant compared to constant-current operation. The frequency response as well as the electronic noise of anemometers are analyzed and compared. Effects of connecting cables are also considered.

Section 5.2.4 refers to calibration procedures in low subsonic flows including the effect of fluid temperature drifts, and Sect. 5.2.5 deals with the measurement of temperature fluctuations.

Section 5.2.6 refers to calibration procedures in high supersonic flows.

Section 5.2.7 presents some special methods, such as the use of the time of flight between sensors or the use of pulse-width-modulated wires, and also the benefit of a flying anemometer when the main flow direction is not well defined, for example in separated zones or near jet edges.

Thermal anemometry has been used for many years, with many improvements over the years. Accordingly, the literature is very rich. Acknowledgement of previous works will often be made and some comprehensive books or reviews on the subject have been contributed by *Corrsin* [5.45], *Bradshaw* [5.46], *Hinze* and *Freymuth* [5.47], *Blackwelder* [5.48], *Perry* [5.49], *Fingerson* [5.50], *Lomas* [5.51], *Bruun* [5.52], *Lekakis* [5.53], and *Comte-Bellot* [5.54–56].

5.2.2 Sensors

Materials and Sensor Geometries

The sensing elements used in thermal anemometry are either wires or films. Conventional wires are typically 0.5–5 μm in diameter and nominally 0.5–2 mm long. Films are about 0.1 μm thick and deposited on fine cylinders of quartz, about 25–50 μm in diameter, on quartz wedges, or on thin acetate or kapton foils. Furthermore, a very thin quartz coating deposited on the sensor provides both protection against a hostile environment and isolation when operating in a conductive medium. The micromachined hot wires usually have a flat trapezoidal cross section, which can be as small as $0.5 \times 0.5\,\mu\mathrm{m}^2$. Their lengths are in the range 1–200 μm. The most common materials for wires and films are listed in Table 5.1.

The upper part of Table 5.1 refers to the classical and easy-to-manipulate metallic elements. Their electric resistances at ambient temperature, $T_a \simeq 293$ K, are in the range 3–10 Ω. The temperature resistivity coefficient χ is a very important parameter and needs to be controlled since the wire manufacturing process can influence the value. Handbooks generally indicate values only corresponding to macroscopic amounts of pure material, for example, $\chi = 0.0045\,\mathrm{K}^{-1}$ for tungsten, whereas the measured values for hot-wires can be over a wide range $0.0036–0.0047\,\mathrm{K}^{-1}$. Very useful references on the subject are available in *Van Dijk* and *Nieuwstadt* [5.65].

The lower part of Table 5.1 refers to the wires and films more recently developed using micromachining technology. Their electric resistances are much larger, around 0.5–5 kΩ, meaning that the classic electronic circuitry of the CCA, CTA, or CVA should be redesigned to meet that new requirement.

Incidentally, it is interesting to measure the true wire diameter, for example with an electron microscope. Indeed, *Lemay* and *Benaïssa* [5.66] reported wire diameters which are 15–20% higher than the values stated by the manufacturer for 0.5 and 1 μm Pt–10%Rh wires. *Dersken* and *Azad* [5.67] observed that, even for specially built wires (platinum plated, tungsten core, gold plated ends), a 2.84–3.85 μm range was observed for a nominal value of 2.5 μm, and a 4.82–5.77 μm range for a nominal value of 5 μm. These differences in diameter translate into variations of the cold resistance R_a of the wire and can also be detected in that way.

Regarding the sensor dimensions, one has to prefer large aspect ratios. For hot-wires, this ratio is defined by l/d, where l is the wire length and d the wire diameter. A large aspect ratio, above 300, permits a wire to be cooled by the velocity component normal to it, with negligible heat transfer to its supports. For a fixed aspect ratio, a smaller diameter obviously leads to a shorter wire, resulting in more-local measurements, and a higher-frequency response. However, fine wires are expensive and brittle, and therefore reserved to turbulence measurements close to walls, where fine turbulent scales have to be resolved.

Table 5.1 Physical properties of sensor materials at 293 K (approximate values for MEMS polysilicons doping, P is phosphor and B boron)

Material	Resistivity (Ωm)	Temperature coefficient of resistivity χ (K^{-1})	Density ρ ($\mathrm{kg/m^3}$)	Specific heat c ($\mathrm{J\,kg^{-1}K^{-1}}$)	Thermal conductivity k ($\mathrm{W\,m^{-1}K^{-1}}$)	Ref.
Copper	1.6×10^{-8}	$+4.0\times10^{-3}$	8900	385	400	[5.57]
Nickel	7.0×10^{-8}	$+6.0\times10^{-3}$	8900	438	90	
Platinum	1.1×10^{-7}	$+3.9\times10^{-3}$	21500	130	70	[5.58]
Pt/10% Rh	1.9×10^{-7}	$+1.7\times10^{-3}$	19900	150	40	[5.59]
Silver	1.6×10^{-8}	$+3.8\times10^{-3}$	10500	235	428	[5.57]
Tungsten	6.0×10^{-8}	$+4.5\times10^{-3}$	19300	140	170	[5.58]
Silicon	2.3×10^{3}	-7.5×10^{-2}	2330	705	148	[5.60]
Polysilicon						
High P doping	5×10^{-5}	$+1.0\times10^{-3}$			50	[5.61]
Low P doping	5×10^{-5}	-2.5×10^{-3}				
B doping	2×10^{-5}	$+8.5\times10^{-4}$			60	[5.61,62]
B doping $2\times10^{16}\,/\mathrm{cm}^2$	5×10^{-5}	$+8.0\times10^{-4}$				[5.63,64]

At its ends, the sensor is connected to fine but sufficiently strong supports that act only as the electrical conductor and mechanical support. For conventional hot-wires, these elements are usually called *prongs* or *needles*, and *stem* respectively. The two parallel prongs are usually 5–10 mm long and taper down to around 100 μm near the wire. The prongs are epoxy-fitted inside the stem, whose diameter can be as small as 1 mm. To decrease the aerodynamic perturbations brought by these elements, longer prongs, up to 20 mm, were suggested by *Comte-Bellot* et al. [5.68] and *Strohl* and *Comte-Bellot* [5.69]. Specially miniaturized probes were developed by *Willmarth* and *Sharma* [5.70] and *Ligrani* and *Bradshaw* [5.71].

For microelectromachined sensors (MEMS), the successive connecting elements are called *shanks*, *beam*, and *handle*. According to *Jiang* et al. [5.72], the two parallel supporting shanks are 100 μm long, 20 μm wide, and 0.5 μm thick. The silicon beam is 1 mm long, 200 μm wide, and 75 μm thick. The handle is thick, around 500 μm. Similar values are reported by *Ebefors* [5.64] for a three-sensor probe.

Often the sensor does not span the entire distance between the needles. The inactive part close to the ends of the sensor should have a low electrical resistance in order not to participate in the sensor response. This part is often called the *stub*. For platinum wires extruded by the Wollaston process, the silver sheath is etched away to provide the active part, and preserved near the two ends. The same procedure holds for tungsten wires, which are copper-plated before soldering. Superconducting endings have also been suggested by

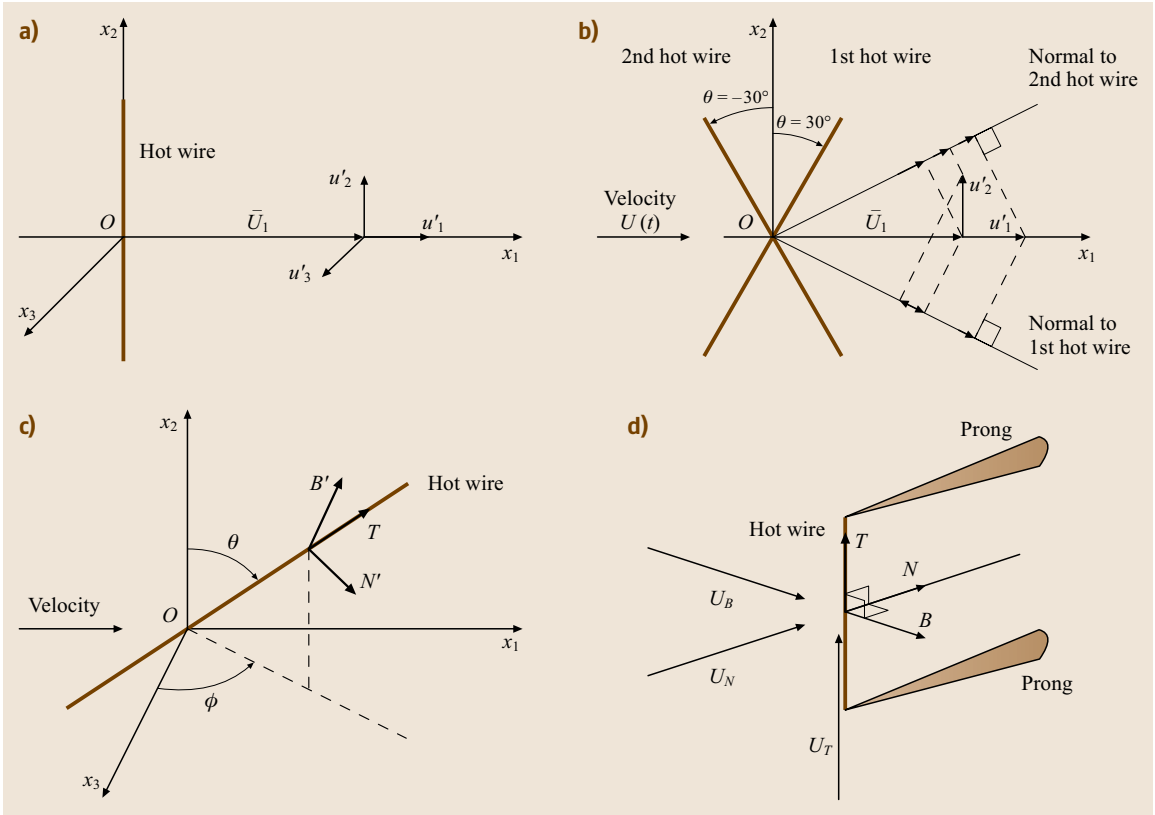

Fig. 5.13a–d Wire positions relative to the space-fixed $O_{x_1x_2x_3}$ coordinates: **(a)** single wire set normal to O_{x_1}, which is also $\overline{U}_1$; **(b)** X-wires in the $O_{x_1x_2}$ plane with $\theta = 30°$ for the first wire and $\theta = -30°$ for the second wire; **(c)** long wire with yaw angle θ and pitch angle ϕ in spherical coordinates; N′, B′, T is the wire-fixed frame, N′ corresponds to an increment in θ, B′ to an increment in ϕ, and T is along the wire [a long wire is cooled by the resulting normal velocity $U_n = (U^2_{N'} + U^2_{B'})^{1/2}$]; **(d)** short wire with its supporting prongs, N, B, T is the prong-fixed frame. The effective cooling velocity is given by (5.172) and (5.173)

Castaing et al. [5.73] for experiments in helium II at 4 K. For polysilicon sensors, various doping concentrations are used for the active and nonactive parts, as suggested by *Jiang* et al. [5.74]. Let us recall that common dopants are phosphorus and boron, and that heavier doping results in lower resistivity by increasing the number of charge carriers. The average grain size of boron-doped polysilicon layers can be estimated from atomic force microscopy (AFM), and a clear illustration is given by *McConnell* et al. [5.61].

Sensors Setup Relative to the Flow

Identification of the principal mean flow direction is an important prerequisite for hot-wire or hot-film measurements. This direction, when known, is usually taken as the x_1-coordinate axis and corresponds therefore to $\overline{U}_1$. Three basic positions can be given to a wire, as illustrated by Fig. 5.13: Fig. 5.13a the wire can be placed in the $O_{x_1x_2}$ plane and normal to x_1; Fig. 5.13b the wire can be placed in the $O_{x_1x_2}$ plane and yawed on x_2 by angle θ, hence inclined on O_{x_1} by $\pi/2-\theta$; Fig. 5.13c the wire can be outside the $O_{x_1x_2}$ plane and inclined relative to this plane with a pitch angle ϕ. The angles θ and ϕ are the standard spherical coordinate angles. These wire positions are defined relative to the space-fixed coordinates $O_{x_1x_2x_3}$. For short wires, auxiliary angles referring to the probe itself are introduced and are defined in Fig. 5.13d.

Use of these sensor positions, or combinations of these positions, leads to the following possibilities:

- Single hot-wires placed normal to $\overline{U}_1$ mainly respond to the instantaneous longitudinal velocity U_1 when the velocity fluctuations are of small amplitude. This instantaneous velocity can be written as $U_1 = \overline{U}_1 + u'_1$ using the Reynolds decomposition, where u'_1 is the longitudinal velocity fluctuation. The transverse fluctuations u'_2 and u'_3 behave as second-order terms in this setup and can be neglected. Obviously, $\overline{U}_1$ should be different from zero, otherwise the transmitted signal suffers rectification, since the hot-wire is just as much cooled by the flow coming from the right-hand side as from the left.
- Cylindrical hot-films work similarly to single hot-wires, but they are more robust when experimenting in water, oils, or liquid metals and even in slightly dirty gases. A thin quartz coating deposited on sensors prevents hydrolysis of the neighboring liquid.
- X wires are made of two inclined wires lying in the $O_{x_1x_2}$ plane and often placed symmetrically relative to $\overline{U}_1$, as in the letter X, i. e., θ (first wire) = $-\theta$ (second wire). Figure 5.13b illustrates this case for $\theta = 30°$. In practice, the midpoints of both wires are slightly separated along O_{x_3} to reduce aerodynamic and thermal interferences [5.75]. For small-amplitude velocity fluctuations, the wire responses are

$$\begin{aligned} &\overline{U}_1 \cos\theta + u'_1 \cos\theta - u'_2 \sin\theta \quad \text{for the 1st wire} \\ &\overline{U}_1 \cos\theta + u'_1 \cos\theta + u'_2 \sin\theta \quad \text{for the 2nd wire} \end{aligned} \tag{5.40}$$

and the sum and difference of the fluctuating parts of these signals give $u'_1(t)$ and $u'_2(t)$. If the wires are not perfectly symmetric relative to $\overline{U}_1$, a weighted sum and a weighted difference provide $u'_1(t)$ and $u'_2(t)$. In extreme cases, it is possible to place one of the wires normal to the flow. This wire thus directly gives $u'_1(t)$ and an appropriate combination of its response with that of a slanted wire gives $u_2(t)$ [5.76]. Note that u'_1 and u'_2 are in the plane defined by the X wires. The other transverse fluctuating component u'_3 together with u'_1, can be obtained by rotating the X-wires by 90° around the direction of $\overline{U}_1$. These classic setups are described in most textbooks (*Hinze* [5.47], *Bruun* [5.52], and *Bailly* and *Comte-Bellot* [5.77]). After proper calibration, an X probe can also be used in a two-dimensional (2-D) flow with unknown mean velocity directions (Sect. 5.2.4). A two-dimensional flow means that $U_3 \simeq 0$. The instantaneous velocity vector can be obtained, as well as the two mean components, $\overline{U}_1$ and $\overline{U}_2$, and the velocity fluctuations, u'_1 and u'_2, even when they are large. However, the incident velocity vector should always give positive velocity components relative to each wire to avoid spurious signals due to rectification. This condition defines the correct approach *quadrant*. The term *quadrant* comes from the use of two mutually orthogonal wires. In practice the acceptance angle is less than 90° because of the nearby needles supporting the wires.
- V probes work similarly to X probes. They permit measurements in close proximity to a wall. A cantilevered V probe has even been suggested by *Hishida* and *Nagano* [5.78, 79].
- Triple-sensor probes provide information about the instantaneous velocity vector at a point, hence the three velocity components, U_1, U_2, U_3 simultaneously, after proper manipulation of the three wire outputs. $\overline{U}_1$, $\overline{U}_2$, and $\overline{U}_3$ can then be obtained, along with the three velocity fluctuations u'_1, u'_2, and u'_3. Velocity component relative to each wire should always stay positive, and this defines the correct

approach *octant* to be respected. The term *octant* comes from the use of three mutually orthogonal wires. In practice the acceptance cone is smaller because of the prongs holding the wires. A fourth hot wire can be added to the probe to enlarge the acceptance cone. A recent survey is given by *van Dijk* and *Nieuwstadt* [5.80].

- Multiple hot wires, from 4 to 12, can provide one or more components of the vorticity vector as discussed by *Wallace* and *Foss* [5.81].
- Arrays of around 10 single wires permit to scan the free edges of turbulent flows, as pioneered by *Sunyach* [5.82] for jets using thermal marking. The technique was applied to boundary layers by *Chen* and *Blackwelder* [5.83] and adapted to micromachined sensors by *Jiang* et al. [5.74]. *Kang* et al. [5.84] achieved space–time correlation of active-grid-generated turbulence with an array of X-wires. *Delville* et al. [5.85] used two rakes of 12 X-probes each to analyze the large structures of a plane mixing layer on the basis of a proper orthogonal decomposition (POD). *Citriniti* and *George* [5.86] used an array of 138 single wires to reconstruct the velocity field of a round jet.
- Wall films permit one to obtain the instantaneous wall shear stress $\tau_w = \mu \partial U_1/\partial x_2$. Large arrays of wall films can be made as these sensors are non intrusive. Around 100 hot-films are most useful when investigating transition on flat or curved surfaces, separation bubbles over airfoils, or shock oscillations in transonic regimes. Laboratory experiments are reported by *Hall* et al. [5.87] using CTA, and flight experiments by *Moes* et al. [5.88] using CVA.

Many types of hot-wire probes are available commercially nowadays, but probes can be fabricated in most laboratories. Valuable advice is given by *Lomas* [5.51], e.g., for welding and soft-soldering wires on fine needles. Regarding films, even if the very first ones were successfully made by a paint and fire technique, the sensors are now made by specialized manufacturers by vapor deposition or atomic sputtering. They are reproducible within 1% and this greatly reduces the labor of calibrating large arrays. For polysilicon sensors, only a few laboratories are currently equipped to make them, but mass production is possible as a single silicon wafer can encompass a large number of sensors.

Because hot-wire anemometers have to compete with laser anemometers which are advantageously located outside the flows, hot-wire probes should be as non-intrusive as possible. In low subsonic flows, miniaturized hot-wire probes are recommended. *Willmarth* and *Sharma* [5.70] and *Ligrani* and *Bradshaw* [5.71] reported experiments with wires having lengths as small as 100 μm and diameters of 0.5 μm. For larger probes, prongs can be placed at 45° to the flow, as suggested by *Comte-Bellot* et al. [5.68], and *Strohl* and *Comte-Bellot* [5.69]. This location permits compensation of the flow deceleration due to the blocking effect of the stem – which is maximal for a stem aligned with $\overline{U}_1$, and the flow acceleration occurring between the prongs – which is maximal for prongs normal to $\overline{U}_1$. Estimates of the aerodynamic perturbations were also obtained by *Adrian* et al. [5.89] on the basis of an inviscid irrotational flow around the probe elements. Historically, *Hoole* and *Calvert* [5.90] were the first to reveal the aerodynamic perturbation resulting from a probe by comparing the wire response for a probe (prongs and stem) facing the flow or held normal to the flow, with the wire position kept unchanged.

In supersonic flows, the prongs are always aligned with the flow to withstand shock waves. Slightly slack wires with a drop of rubber cement at the soldering points provide satisfactory protection against vibration and fatigue failure as recommended by *Kovasznay* [5.91]. Slack is introduced when soldering the wire, or later if a tiny screw permits the change of prong separation, as suggested by *Bonnet* [5.92]. Control of the adjustment is made by inspecting the spectra which should not contain the sharp peaks associated with strain-gauging above 100 kHz. Measurements in transonic flows remain however very difficult due to large fluctuating aerodynamic loads and temperature fluctuations.

For MEMS sensors, strong aerodynamic perturbations were reported by *Jiang* et al. [5.74] when changing the yaw and pitch angles of their probes, in a similar way as *Hoole* and *Calvert* [5.90] did with conventional probes. Additional investigations would be of considerable interest, as the shanks, beams and handle are relatively large and close to the sensors in that new type of technology [5.93].

Steady Convective Heat Loss Laws in Subsonic Flows

The simplified heat balance (5.35) is now rewritten including all the flow and wire parameters except the aspect ratio, which will be considered later in this section. Using dimensionless analysis, this balance is of the form

$$\mathrm{Nu} = \mathrm{Nu}\left(M, \mathrm{Re}, \mathrm{Gr}, \mathrm{Pr}, \gamma, \frac{T_w - T_a}{T_a}\right) , \qquad (5.41)$$

where M is the flow Mach number, Nu, Re, and Gr are the Nusselt, Reynolds and Grashoff numbers, respectively, based on the wire diameter

$$M = \frac{U}{c}\,, \quad \mathrm{Nu} = \frac{R_\mathrm{w} I_\mathrm{w}^2}{\pi l k (T_\mathrm{w} - T_\mathrm{a})}\,,$$
$$\mathrm{Re} = \frac{\rho U d}{\mu}\,, \quad \text{and} \quad \mathrm{Gr} = g\beta(T_\mathrm{w} - T_\mathrm{a}) d^3 \left(\frac{\rho}{\mu}\right)^2 . \tag{5.42}$$

The physical properties involved for the fluid are the thermal conductivity (k), the density (ρ), the Newtonian coefficient of dynamic viscosity (μ), the thermal coefficient of expansion at constant pressure (β), the ratio of the heat capacities at constant pressure and constant volume ($\gamma = C_\mathrm{p}/C_\mathrm{v}$), and the Prandtl number ($\mathrm{Pr} = \mu C_\mathrm{p}/k$). The incident flow velocity is simply noted U instead of U_1 or U_n. The temperature at which the physical properties are taken will be discussed later in this section.

Reference to a Nusselt number shows that conduction terms and boundary conditions, hence temperature gradients, prevail in the energy equation. Indeed, for hot-wires, the Reynolds number is usually in the range $2 \le \mathrm{Re} \le 40$, before the onset of vortex shedding.

Several cases of flows are of interest as follows.

Heat-Transfer Laws for Subsonic Air Flows. M and γ obviously have no effect, Pr is fixed, for air $\mathrm{Pr} \simeq 0.70$ over a large temperature range, and T_a is the ambient fluid temperature. Furthermore, forced convection often prevails – the criterion for neglecting buoyancy effect is examined at the end of this section. Equation (5.41) simplifies therefore to

$$\mathrm{Nu} = \mathrm{Nu}\left(\mathrm{Re}, \frac{T_\mathrm{w} - T_\mathrm{a}}{T_\mathrm{a}}\right) . \tag{5.43}$$

Several heat-transfer relationships for forced convection have been reported for very long wires (l/d in the range 2000–8000) (e.g., by *McAdams* [5.94], *Van der Hegge Zijnen* [5.95], *Collis* and *Williams* [5.96], *Davis* and *Fisher* [5.58], *Bradbury* and *Castro* [5.97], *Kramers* [5.98]). The McAdams analysis already concerned 13 data sets in 1950, and in a more-recent survey in 1972, *Andrews* et al. [5.99] listed about 40 experiments. All these laws have the form

$$\mathrm{Nu} = (A_\mathrm{N} + B_\mathrm{N}\mathrm{Re}^n)\left(\frac{T_\mathrm{w} + T_\mathrm{a}}{2}\right)^m , \tag{5.44}$$

where A_N, B_N, n, and m are constant. There are, however, some tiny differences:

1. the power for the Reynolds number n varies slightly around $n \simeq 0.50$,
2. a temperature loading depending on m is introduced or not, with a maximum value of $m \simeq 0.17$; it is attributed to the flow distortion around the wire caused by the addition of heat, and
3. the physical properties of the fluid are evaluated at either the incoming flow temperature T_a or at the *film* temperature $T_\mathrm{f} = (T_\mathrm{w} + T_\mathrm{a})/2$.

In what follows, the distinction is made by using the subscripts a and f respectively.

The most-favored correlation formulae are due to *Collis* and *Williams* [5.96] and *Bradbury* and *Castro* [5.97]

$$\mathrm{Nu_f} = \left(0.24 + 0.56\mathrm{Re_f^{0.45}}\right) T_\mathrm{f}^{0.17}$$
$$\text{for } 0.02 \le \mathrm{Re_f} \le 44$$
$$\mathrm{Nu_f} = 0.48\mathrm{Re_f^{0.51}} T_\mathrm{f}^{0.17}$$
$$\text{for } 44 \le \mathrm{Re_f} \le 140 \tag{5.45}$$

and *Kramers* [5.98]

$$\mathrm{Nu_a} = 0.39 + 0.51\mathrm{Re_a^{0.50}} \quad \text{for } 2.5 \le \mathrm{Re_a} \le 1475\,. \tag{5.46}$$

We recall that the temperature dependence of the physical properties of air around $T_\mathrm{a} = 293\,\mathrm{K}$ may be expressed by the power laws [5.100, 101]

$$\frac{\rho(T)}{\rho(T_0)} = \left(\frac{T}{T_0}\right)^{-1}$$
$$\frac{\mu(T)}{\mu(T_0)} = \left(\frac{T}{T_0}\right)^{m}$$
$$\frac{k(T)}{k(T_0)} = \left(\frac{T}{T_0}\right)^{n} . \tag{5.47}$$

with $m \simeq 0.765$ and $n \simeq 0.885$. Power laws are convenient when taking logarithmic derivatives of heat-transfer laws, especially in supersonic flows.

The Collis and Williams or Kramers laws concern the average Nusselt number around the wire. An extensive survey of the local values of the Nusselt number for hot wires was conducted by *Dennis* et al. [5.102], using both experimental data and numerical predictions. The highest value is at the forward stagnation point, and its relative importance increases almost linearly with the Reynolds number. Similar results for large cylinders are available in textbooks, e.g., by *Eckert* and *Drake* [5.103].

Regarding MEMS sensors, very preliminary heat-transfer laws are indicated by *Jiang* et al. [5.72]. Surprisingly, the exponent n in U^n depends on the anemometer type, $n = 1.0$ for CCA and $n = 0.6$ for CTA. Further research is definitely needed to clarify this point. However, an exponent n larger than the $n \simeq 0.50$ usually

Table 5.2 Physical properties of usual fluids and substrates for hot-films at 293 K

Fluid/ substrate	Prandtl number Pr	$C_p/C_v = \gamma$	Density ρ (kg/m^3)	Specific heat C_p (J kg^{-1}K^{-1})	Thermal conductivity k (W m^{-1}K^{-1})	Dynamic viscosity μ (kg m^{-1}s^{-1})
Air	0.71	1.40	1.2	1005	0.0257	1.82×10^{-5}
Helium	0.70	1.66	0.17	5180	0.157	1.86×10^{-5}
Water	7.0		1000	4180	0.60	1.00×10^{-3}
Mercury	0.022		13600	140	9.3	1.55×10^{-3}
Quartz			2650	710	6–11	
Kapton			1420	1090	0.10–0.35	
Perspex			1190	1470	0.21	
Tufnol			1320	1500	0.29	
Plywood			580	2500	0.13	

admitted for circular cylinders could be possible, because the rectangular or trapezoidal cross section of this new type of sensor gives rise to shed eddies and separated zones. In textbooks, exponents in the range 0.60–0.75 are reported for elongated hexagonal cylinders, although for larger Reynolds numbers [5.104].

Equations (5.46) and (5.36) lead to the practical form

$$\frac{R_w I_w^2}{R_w - R_a} = A + BU^{0.50} \tag{5.48}$$

with

$$A = 0.39\frac{\pi l k_a}{\chi R_0} \quad \text{and} \quad B = 0.51\frac{\pi l k_a}{\chi R_0}\left[\frac{\rho_a d}{\mu_a}\right]^{0.50} . \tag{5.49}$$

Equation (5.48) is known as King's law. It concerns the wire itself, not the anemometer outputs. In order to retrieve King's law from anemometer outputs, all the resistances present in the circuits have to be taken into account, for example, the top bridge resistance in the arm containing the sensor in a CTA circuit.

In King's law, A and B are improperly called *constants*. Obviously they are not; they depend on the wire diameter and on the fluid temperature. If the temperature dependencies of the physical parameters (5.47) are introduced in (5.49), one obtains

$$\frac{dA}{A} = 0.886\frac{dT_a}{T_a}$$
$$\frac{dB}{B} = (0.886 - 0.50 - 0.38)\frac{dT_a}{T_a} = 0.006\frac{dT_a}{T_a} . \tag{5.50}$$

Coefficient B therefore varies far less with temperature than coefficient A. This result is particularly interesting at large values of U when A can be neglected compared to $BU^{0.50}$. *Uberoi* and *Corrsin* [5.105] confirmed these trends when experimenting on hot jets.

Regarding buoyancy effects, a criterion that permits one to ensure that forced convection prevails has been established by *Collis* and *Williams* [5.96] for a cross-flow

$$\mathrm{Re_f} > \mathrm{Gr_f^{1/3}} . \tag{5.51}$$

For example, taking $T_a \simeq 293$ K, $a_w \simeq 1$, $g = 9.81$ ms^{-2} and $\beta = 1/273$, and using (5.47) and Table 5.2, this criterion gives $U \geq 0.07$ m/s whatever the wire diameter.

When a mixed convection regime occurs, heat exchange laws become complicated. *Hatton* et al. [5.106] suggested an explicit correlation based on a vectorial addition of the forced and natural Reynolds numbers

$$\mathrm{Nu_f} = \left(0.384 + 0.581\mathrm{Re_{eff}^{0.439}}\right)\left(\frac{T_f}{T_a}\right)^{0.154} , \tag{5.52}$$

where

$$\mathrm{Re_{eff}^2} = \mathrm{Re_f^2}\left(1 + 2.06\frac{\mathrm{Ra^{0.418}}}{\mathrm{Re_f}}\cos\theta_z + 1.06\frac{\mathrm{Ra^{0.836}}}{\mathrm{Re_f^2}}\right) , \tag{5.53}$$

where Ra is the Rayleigh number, $\mathrm{Ra} = \mathrm{Gr}\cdot\mathrm{Pr}$, and θ_z is the angle from the vertically upward direction of the forcing flow.

Heat-Transfer Laws for Other Gases in Subsonic Flows. *Andrews* et al. [5.99], and *Pitts* and *McCaffrey* [5.107] at the National Bureau of Standards carried out extensive studies of heat exchanges for hot wires and hot films using various gases such as argon, helium, methane, propane and carbon dioxide, in the Reynolds number range below and just near vortex shedding. For all gases, except helium, the law valid for air was approximately verified once the proper temperature dependencies of the gas molecular properties were taken

into account. The Prandtl number effect is found to be relatively weak. The case of helium, for which accommodation effects are strong, is singular and a special correction was elaborated.

Heat-Transfer Laws for Liquid Flows. Equation (5.43) now involves the Prandtl number, for example Pr = 7.1 for water, 0.0225 for mercury, 0.01 for molten sodium, and in the range 20–5000 for oils. These fluids are useful either in industrial heat exchangers or in laboratory experiments to model the Earth's outer core. According to *Hill* and *Sleicher* [5.110, 111] who revisited many previous measurements done for long cylinders, the heat-transfer law that *Kramers* [5.98] suggested is particularly useful

$$\mathrm{Nu_a} = 0.42\mathrm{Pr}^{0.20} + 0.57\mathrm{Pr}^{0.33}\mathrm{Re_a}^{0.50} \,. \qquad (5.54)$$

Buoyancy effects in liquids have also been analyzed. *Gebhart* and *Pera* [5.112] considered a large range of Prandtl numbers of 6.3–63. The criterion for forced convection to prevail is similar to that of *Collis* and *Williams* [5.96]

$$\mathrm{Re_f} > \mathrm{Gr_f}^{1/n} \quad \text{where } n \text{ is between 2 and 3} \,. \qquad (5.55)$$

Regarding the heat transfer laws, *Gebhart* and *Pera* [5.112] indicated a set of curves for the Nusselt number in terms of both the Péclet and Rayleigh numbers (Pe = Re · Pr, Ra = Gr · Pr).

All the above results hold only for Newtonian fluids. Otherwise, very different phenomena are observed. Investigations made with cylindrical hot films, by *Smith* et al. [5.113] or *James* and *Acosta* [5.114] among others, showed that the Nusselt number decreases when the polymer concentration increases, at a given Reynolds number. Moreover, a cylinder normal to the flow is cooled less than a cylinder oblique to the flow. The explanation given by *Lumley* [5.115] invoked the expansion of polymer molecules in pure strain (stagnation region, hot-film set normal to the flow) so that the viscosity increases, the boundary layer on the film becomes thicker and the heat transfer is reduced.

Heat-Transfer Laws in Compressible Flows

Kovasznay [5.116], *Morkovin* [5.100], *Morkovin* and *Phinney* [5.117] and also *Laufer* and *McClellan* [5.59] pioneered the possibility of using hot-wires for supersonic flows. For a wire normal to the flow, a detached bow shock forms in front of the wire. Subsequently, the wire is in a subsonic flow, and the heat-transfer laws mentioned above regain some importance. The fluid-mechanics equations also correlate the flow parameters upstream and downstream of the shock. Especially, momentum and total temperature are conserved through the shock. Figure 5.14 illustrates the shock which exists in front of a wire for two different flows, a Mach 3 air flow and a Mach 10 helium flow. In the latter case, the bow shock becomes much thicker and forms closer to the wire. However, hot-wire anemometry remains possible in these hypersonic flows. This situation has been particularly investigated by *Spina* and *McGinley* [5.108]. The strong needles supporting the wire also create shocks, but these are attached to the needle tips, and their effect on the wire can be reduced if the inactive regions, even if short, exist at both ends of the active part of the wire.

Heat-transfer laws at high velocities have received considerable attention, for Mach number up to 6, and Reynolds numbers up to 400. Many experimental data were obtained and analyzed by *Kovasznay* [5.116], *Laufer* and *McClellan* [5.59], and *Spangenberg* [5.118], who reported very complete data tables, *Morkovin* and *Phinney* [5.117], and *Dewey* [5.119, 120], who drew many valuable curves, *Baldwin* et al. [5.121], *Gaviglio* [5.122], *Barre* et al. [5.123], and *Stainback* and *Nagabushana* [5.124], with a large bibliography, and *Spina* and *McGinley* [5.108] for gases other than air.

Regarding the temperature to be used for the physical parameters μ and k entering the Reynolds and Nusselt numbers, one can think of using the conditions behind the detached shock wave, ρ_2, U_2 and T_2, as being *the apparently free stream* for the wire, as suggested by *Kovasznay* [5.116] and used by *Laufer* and *McClellan* [5.59]. Here the subscript 2 refers to values after the shock, as usual in compressible flows, not to a lateral velocity component. On the other hand, the total temperature T_t was suggested by *Baldwin* et al. [5.121]

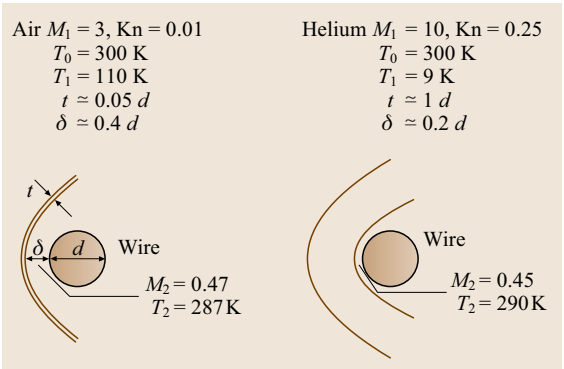

Fig. 5.14 A hot-wire probe in a supersonic flow. Two examples: Mach 3 air flow, Mach 10 helium flow (after *Spina* and *McGinley* [5.108] and *Elizarova* et al. [5.109])

or *Dewey* [5.119, 120]. Of course, the temperature T_2 is close to T_t as can be deduced from the basic relations

$$T_t = T_\infty \left(1 + \frac{\gamma - 1}{2} M^2\right) = T_2 \left(1 + \frac{\gamma - 1}{2} M_2^2\right) \tag{5.56}$$

and

$$M_2^2 = \frac{M^2 + 2/(\gamma - 1)}{2\gamma M^2/(\gamma - 1) - 1} , \tag{5.57}$$

where T_∞ is the freestream static temperature before the shock, also denoted by T_1 or simply T (this should not be confused with the temperature existing outside a boundary layer, this external zone being often called *freestream*). For example, differences between T_t and T_2 are 6.6%, 3.8%, and 3.2% for $M = 2$, 4, and 6, respectively. The temperature T_t also has the advantage of being a constant in adiabatic shock flows and very nearly constant across most boundary-layer and wake flows. Furthermore, $\rho_2 U_2 = \rho_\infty U_\infty$. These remarks lead us to choose the references in the following way. Density and velocity are based on freestream conditions, also called static conditions. Viscosity and thermal conductivity are based on the total temperature T_t, also called the stagnation or reservoir temperature.

The temperature difference entering into the Nusselt number makes use of the recovery temperature T_r, which is the temperature of the unheated wire placed in the flow. It therefore resembles the temperature T_a of the incoming flow at subsonic velocities. It is the temperature above which an additional cooling by the flow is possible. The useful dimensionless numbers are therefore

$$\mathrm{Nu_t} = \frac{R_w I_w^2}{\pi l k_t (T_w - T_r)} , \quad \mathrm{Re_t} = \frac{\rho_\infty U_\infty d}{\mu_t} ,$$
$$M = M_\infty = \frac{U_\infty}{\sqrt{\gamma R T_\infty / m}} , \tag{5.58}$$

where the subscript 't' refers to an evaluation at the stagnation temperature, the subscript '∞' at the freestream static temperature, and the subscript 'r' at the recovery temperature. $R = 8314\,\mathrm{J\,kg^{-1}\,K^{-1}}$ is the universal gas constant, and m the molar mass of the gas considered: $R/m = 287$ for air, $R/m = 2078$ for helium.

A general heat-transfer law in supersonic flow is therefore of the form

$$\mathrm{Nu_t} = \mathrm{Nu_t}(M, \mathrm{Re_t}, \gamma, \Theta) . \tag{5.59}$$

The ratio γ is usually fixed in an experiment ($\gamma = 1.4$ for air, $\gamma = 1.66$ for helium). Θ represents the wire temperature loading, denoted $(T_w - T_r)/T_r$ by *Kovasznay* [5.116] or *Smits* et al. [5.125], and T_w/T_r by *Morkovin* [5.100]. Some attempts to extract Θ from the Nusselt number have been made in special cases, e.g., by *Kovasznay* [5.116] for CCA, and by *Smits* et al. [5.125], *Spina* and *McGinley* [5.108], or *Weiss* et al. [5.126] for CTA. Keeping the general form (5.59) is much more rewarding (Sect. 5.2.6).

Concerning the wire Reynolds number $\mathrm{Re_t}$, let us be precise in that it is connected to the unit Reynolds number of a wind tunnel, $\mathrm{Re_{WT}} = \rho_\infty U_\infty / \mu_\infty$, by

$$\mathrm{Re_t} = \mathrm{Re_{WT}} d \frac{\mu_\infty}{\mu_t}$$
$$= \mathrm{Re_{WT}} d \left(1 + \frac{\gamma - 1}{2} M^2\right)^{-0.765} . \tag{5.60}$$

The wire resistance R_r at the recovery temperature T_r, is also of special interest. Since an electric current, even if very small, could modify the resistance R_r to be measured, it is advisable to obtain R_r from the plot of the measured hot-wire resistance R_w with the electric power injected into the wire at different overheats and extrapolating the curve towards zero dissipation [5.127]. It is also helpful to have some knowledge of the recovery factor η and the ratio of T_r to T_t, which depends on both the Mach and the Reynolds numbers for air flows, as

$$\eta = \frac{T_r}{T_t} \quad \eta = \eta(M, \mathrm{Re_t}) . \tag{5.61}$$

Some physical insight of η is obtained when introducing the Knudsen number. A Knudsen number expresses the continuous or rarefied flow conditions. *Stalder* et al. [5.128], using the kinetic theory of gases to relate density, viscosity and sound speed in terms of molecular velocity and molecular mean free path, arrived at the following very useful expression

$$\mathrm{Kn_\infty} = \frac{\text{molecular mean free path}}{\text{wire diameter}} \simeq \sqrt{\frac{\pi\gamma}{2}} \frac{M}{\mathrm{Re_\infty}} , \tag{5.62}$$

where $\mathrm{Re_\infty} = \rho_\infty U_\infty d / \mu_\infty$ is the freestream Reynolds number for the wire. Here the freestream conditions prevail as a Knudsen number expresses a geometric ratio. The continuous regime is for $\mathrm{Kn_\infty} \leq 0.01$. Slip flow is characterized by $0.01 \leq \mathrm{Kn_\infty} \leq 1$ and free molecular flows exist for $\mathrm{Kn_\infty} \geq 1$. Let us observe that, as η is related to M, $\mathrm{Re_t}$, and R_∞, it is superfluous to introduce a Knudsen number in the Nusselt equation (5.59).

Values for η are reported by *Laufer* and *McClellan* [5.59], *Morkovin* [5.100], and *Baldwin* et al. [5.121]. They are also available in *Spina* and *McGinley* [5.108], *Gaviglio* [5.122], *Dewey* [5.120], and

Stalder et al. [5.128]. In that work the recovery factor is denoted by r and is defined by $T_r = T\{1 + [(\gamma - 1)/2]rM^2\}$, but r can be connected to η by (5.56).

With some simplifications, η is roughly constant, $\eta \simeq 0.97 \pm 0.01$ as long as $M \leq 2$ and $\mathrm{Kn}_\infty \leq 0.2$, and η rises sharply with M and Kn_∞ afterwards, reaching values of around 1.15. For these η values in excess of one, *Stalder* et al. [5.128] invoked the small amount of energy per molecule transported from a body for the case of free-molecule flow. For marked slip flows, *Dewey* [5.119] could normalize η in terms of two analytical functions that approach the free-molecule flow and the continuum flow respectively. That expression is also available in *Eckert* and *Drake* [5.103]. These results present even more interest nowadays because of a large incentive for hypersonic flights [5.108, 129].

Plots giving $\mathrm{Nu_t}$ in terms of $\mathrm{Re_t}$, with the additional Knudsen number Kn_∞ as a parameter, were prepared by *Baldwin* et al. [5.121] as early as 1960. Similar plots were drawn and supplemented with new data by *Dewey* [5.120], and referenced afterwards by *Fingerson* and *Freymuth* [5.50] and *Eckert* and *Drake* [5.103] among others.

The Baldwin–Dewey diagram is reproduced in Fig. 5.15. In the upper part of the figure, where the values of the Nusselt number are large, the curves are close to straight lines, $\mathrm{Nu_t} \sim \mathrm{Re_t}^{1/2}$ with an additive constant slightly decreasing with the Mach number. The Knudsen number is less than 0.01, the fluid acts as a continuum and the heat exchange is large. In the lowest part of the figure, for large Knudsen numbers and small Nusselt numbers, the Mach number dependence is strongly represented as an important parameter. In this regime, $\mathrm{Nu_t}$ becomes proportional to $\mathrm{Re_t}$ rather than $\mathrm{Re_t}^{1/2}$; detailed values are available in *Dewey* [5.119]. When doing experiments, it is thus important to locate the M, $\mathrm{Re_t}$, and Kn_∞ values in these diagrams, and to estimate the most appropriate exponent n for the $\mathrm{Re_t}$ number dependence.

A great simplification occurs when $M \geq 1.2$: the Nusselt number becomes independent of the Mach number, and the main remaining parameter is the Reynolds number. Furthermore, if the Reynolds number stays reasonably high, $\mathrm{Re_t} \geq 20$, the flow is not too far from continuum conditions, and the slope relating the Nusselt number to the Reynolds number is close to 1/2.

All the heat-transfer laws we have just listed constitute useful guidelines in different occasions: to interpret calibration curves, see Sects. 5.2.4, 2.6, to obtain the wire sensitivity coefficients to small turbulent fluctuations, see the following sections, and to estimate the time constant of a wire.

Wire Sensitivity Coefficients for Subsonic Flows and Small Fluctuations

Fluctuations whose amplitude do not exceed 10% are usually assimilated as *small fluctuations*. The fluctuating wire response may then be obtained by a first-order Taylor expansion around a mean operating point. Fluctuations are assumed to follow the tangent to the response curve rather than the response curve itself. The slopes which appear are then conveniently expressed in terms of the dimensionless ratios (fluctuation)/(mean value). The reason is that these ratios are directly connected to

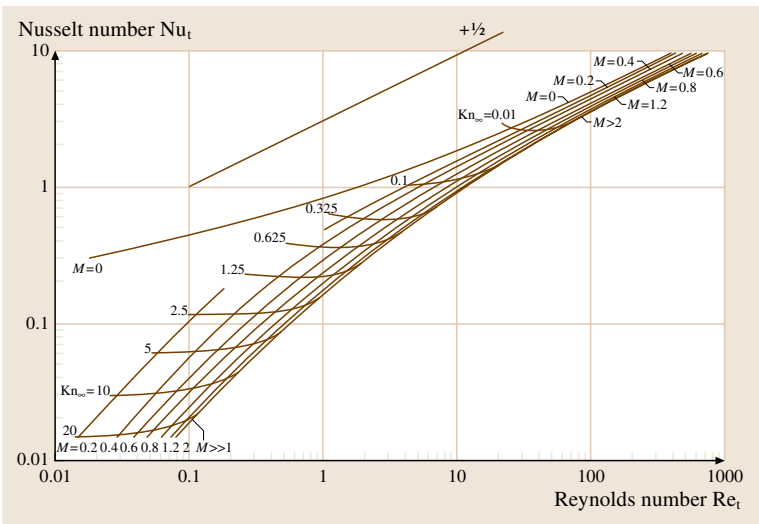

Fig. 5.15 The Baldwin–Dewey diagram for heat loss from hot wires in compressible flows. The Nusselt and Reynolds numbers are defined by (5.58) (after [5.120, 121])

the logarithmic derivatives of the heat transfer laws. This is the standard procedure in compressible flows, but for introductory purposes it is useful to treat two subsonic cases:

1. a single normal wire placed in a non-isothermal flow, and
2. a yawed wire placed in an isothermal flow.

Single Normal Wire in Non-isothermal Flows. In a subsonic incident flow with velocity and temperature fluctuations u_1' and θ_a' around an operating point, $\overline{U}_1$, $\overline{T}_a$, the response of a single normal wire can be expressed as

$$\frac{r_w'}{\overline{R}_w} = S_{U_1}^{CC}\frac{u_1'}{\overline{U}_1} + S_{T_a}^{CC}\frac{\theta_a'}{\overline{T}_a}$$

for constant-current (CC) operation ,

$$\frac{i_w'}{\overline{I}_w} = S_{U_1}^{CT}\frac{u_1'}{\overline{U}_1} + S_{T_a}^{CT}\frac{\theta_a'}{\overline{T}_a}$$

for constant-temperature (CT) operation ,

$$\frac{i_w'}{\overline{I}_w} = S_{U_1}^{CV}\frac{u_1'}{\overline{U}_1} + S_{T_a}^{CV}\frac{\theta_a'}{\overline{T}_a}$$

for constant-voltage (CV) operation , (5.63)

where the factors S are the sensitivity coefficients. The superscript (CC, CT, or CV) denotes the way the hot-wire is operated and the subscript (U_1 or T_a) the nature of the flow parameter. For example,

$$S_{U_1}^{CT} = \frac{\overline{U}_1}{\overline{I}_w}\left(\frac{\partial \overline{I}_w}{\partial \overline{U}_1}\right) \quad \text{at constant } \overline{R}_w \text{ and } \overline{T}_a \tag{5.64}$$

or

$$S_{T_a}^{CV} = \frac{\overline{T}_a}{\overline{I}_w}\left(\frac{\partial \overline{I}_w}{\partial \overline{T}_a}\right) \quad \text{at constant } \overline{V}_w \text{ and } \overline{U}_1 \ . \tag{5.65}$$

Note that (5.63) and the following equations in this section refer only to the wire. The sensitivity coefficients based on the anemometer outputs are considered in Sect. 5.2.3 as the components of the electronic circuits are implied in their expressions.

The S coefficients introduced in (5.63) are obtained by taking the derivative of (5.48), in which $U^{0.50}$ can be more generally written U^n to permit some deviation from the simple square-root law.

First, we assume that A and that B do not depend on T_a. This gives

$$\frac{dR_w}{\overline{R}_w} + 2\frac{dI_w}{\overline{I}_w} - \frac{\overline{R}_w}{\overline{R}_w - \overline{R}_a}\frac{dR_w}{\overline{R}_w} = n\frac{B\overline{U}_1{}^n}{A + B\overline{U}_1{}^n}\frac{dU_1}{\overline{U}_1} - \frac{\overline{R}_a}{\overline{R}_w - \overline{R}_a}\frac{dT_a}{\overline{T}_a} \ . \tag{5.66}$$

Inserting into (5.66) the $R(T)$ relation specified by (5.36) and the wire overheat ratio $\overline{a}_w$ defined by (5.37) yields

$$-\frac{1}{\overline{a}_w}\frac{dR_w}{\overline{R}_w} + 2\frac{dI_w}{\overline{I}_w} = n\frac{B\overline{U}_1{}^n}{A + B\overline{U}_1{}^n}\frac{dU_1}{\overline{U}_1} - \frac{\chi\overline{T}_a}{1 + \chi(\overline{T}_a - T_0)}\frac{dT_a}{\overline{T}_a} \ . \tag{5.67}$$

This equation is advantageously valid no matter how the wire is operated. The constraint relative to the chosen type of anemometer can now be introduced, i. e.,

$$\frac{dI_w}{\overline{I}_w} = 0 \quad \text{for CC} \ , \qquad \frac{dR_w}{\overline{R}_w} = 0 \quad \text{for CT} \ ,$$
$$\frac{dR_w}{\overline{R}_w} + \frac{dI_w}{\overline{I}_w} = 0 \quad \text{for CV} \ . \tag{5.68}$$

Finally, noting the fluctuations $r_w' = dR_w$, $i_w' = dI_w$, $u_1' = dU_1$, and $\theta_a' = dT_a$, yields

$$S_{U_1}^{CC} = -\overline{a}_w\frac{nB\overline{U}_1{}^n}{A + B\overline{U}_1{}^n} \ ,$$
$$S_{T_a}^{CC} = \frac{\chi\overline{T}_a}{1 + \chi(\overline{T}_a - T_0)}$$
$$S_{U_1}^{CT} = \frac{1}{2}\frac{nB\overline{U}_1{}^n}{A + B\overline{U}_1{}^n} \ ,$$
$$S_{T_a}^{CT} = -\frac{1}{2\overline{a}_w}\frac{\chi\overline{T}_a}{1 + \chi(\overline{T}_a - T_0)}$$
$$S_{U_1}^{CV} = \frac{\overline{a}_w}{1 + 2\overline{a}_w}\frac{nB\overline{U}_1{}^n}{A + B\overline{U}_1{}^n} \ ,$$
$$S_{T_a}^{CV} = -\frac{1}{1 + 2\overline{a}_w}\frac{\chi\overline{T}_a}{1 + \chi(\overline{T}_a - T_0)} \ . \tag{5.69}$$

Figure 5.16 shows the dependence of the coefficients S as a function of the mean wire overheat $\overline{a}_w$, for $n = 1/2$. One can observe the very large sensitivity of a wire to temperature for CT operation at small overheats. Regarding the S^{CV} sensitivities, which are smaller than the S^{CC} or S^{CT} values, one should remember that the S given by (5.69) refer only to the wire. The effect of the complete electronic circuits will be examined in Sect. 5.2.3.

Equation (5.67) also permits one to derive the relations that exist between the wire sensitivities of the three anemometers, whatever the turbulent fluctuation considered

$$S^{\mathrm{CT}} = -\frac{1}{2\overline{a}_{\mathrm{w}}} S^{\mathrm{CC}} , \quad S^{\mathrm{CV}} = -\frac{1}{1+2\overline{a}_{\mathrm{w}}} S^{\mathrm{CC}} ,$$
$$S^{\mathrm{CV}} = \frac{2\overline{a}_{\mathrm{w}}}{1+2\overline{a}_{\mathrm{w}}} S^{\mathrm{CT}} . \qquad (5.70)$$

If a temperature loading factor m is introduced, see (5.44), a similar development can be conducted. Equation (5.67) then takes the modified form

$$-\frac{1}{\overline{a}_{\mathrm{w}}}(1+\epsilon)\frac{\mathrm{d}R_{\mathrm{w}}}{\overline{R}_{\mathrm{w}}} + 2\frac{\mathrm{d}I_{\mathrm{w}}}{\overline{I}_{\mathrm{w}}}$$
$$= n\frac{B\overline{U}_1{}^n}{A+B\overline{U}_1{}^n}\frac{\mathrm{d}U_1}{\overline{U}_1}$$
$$-\frac{\chi\overline{T}_{\mathrm{a}}}{1+\chi(\overline{T}_{\mathrm{a}}-T_0)}(1+\epsilon)\frac{\mathrm{d}T_{\mathrm{a}}}{\overline{T}_{\mathrm{a}}} , \qquad (5.71)$$

where $\epsilon = m\overline{a}_{\mathrm{w}}(1+\overline{a}_{\mathrm{w}})/(2+\overline{a}_{\mathrm{w}})$. The sensitivity coefficients, denoted by a star with the temperature load included, become

$$S^{\mathrm{CC}\star}_{U_1} = S^{\mathrm{CC}}_{U_1}(1+\epsilon)^{-1} , \quad S^{\mathrm{CC}\star}_{T_{\mathrm{a}}} = S^{\mathrm{CC}}_{T_{\mathrm{a}}}$$
$$S^{\mathrm{CT}\star}_{U_1} = S^{\mathrm{CT}}_{U_1} , \quad S^{\mathrm{CT}\star}_{T_{\mathrm{a}}} = S^{\mathrm{CT}}_{T_{\mathrm{a}}}(1+\epsilon)$$
$$S^{\mathrm{CV}\star}_{U_1} = S^{\mathrm{CV}}_{U_1}\left(1+\frac{\epsilon}{1+2\overline{a}_{\mathrm{w}}}\right)^{-1} ,$$
$$S^{\mathrm{CV}\star}_{T_{\mathrm{a}}} = S^{\mathrm{CV}}_{T_{\mathrm{a}}}(1+\epsilon)\left(1+\frac{\epsilon}{1+2\overline{a}_{\mathrm{w}}}\right)^{-1} . \qquad (5.72)$$

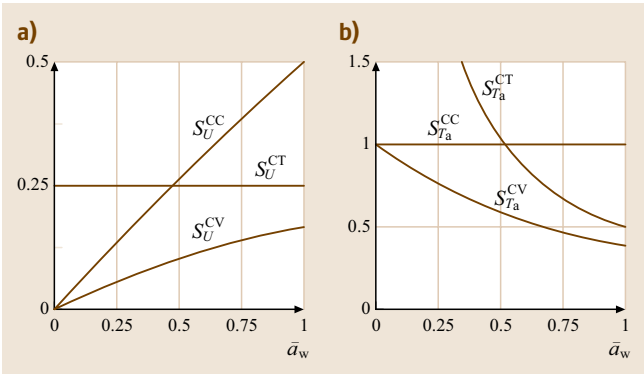

Fig. 5.16a,b Sensitivity coefficients in subsonic flows, **(a)** to velocity fluctuations, **(b)** to ambient temperature fluctuations, for a wire operated in constant-current, constant-temperature, or constant-voltage mode

Corrective terms appear more or less on all anemometers, but they are at most $2m/3$ when $\overline{a}_{\mathrm{w}} = 1$, and even smaller for a CV-operated wire.

Finally, if the dependence of A and B on the fluid temperature is introduced, as suggested by (5.50), a similar development can be conducted and yields, for example,

$$S^{\mathrm{CC}}_{T_{\mathrm{a}}} = \frac{\chi\overline{T}_{\mathrm{a}}}{1+\chi(\overline{T}_{\mathrm{a}}-T_0)} - 0.80\overline{a}_{\mathrm{w}}\frac{A}{A+B\overline{U}^n} . \qquad (5.73)$$

The difference with the value indicated in (5.69) is therefore negligible at high velocities and low overheat ratios.

Yawed Wire in Isothermal Flows. For a wire yawed at an angle θ on x_2, see Fig. 5.13, the velocity cooling the wire is now $U_1\cos\theta - U_2\sin\theta$. The sensitivity coefficient to U_1 and U_2 can be defined for small-amplitude fluctuations and obtained by deriving (5.48) with respect to U_1 and U_2 for a fixed θ. This gives

$$\frac{r'_{\mathrm{w}}}{\overline{R}_{\mathrm{w}}} \quad \text{or} \quad \frac{i'_{\mathrm{w}}}{\overline{I}_{\mathrm{w}}}$$
$$= S_{U_1}(\text{yawed wire})\frac{u'_1}{\overline{U}_1} + S_{U_2}(\text{yawed wire})\frac{u'_2}{\overline{U}_1} \qquad (5.74)$$

with

$$S_{U_1}(\text{yawed wire}) = S_{U_1}(\text{normal wire}) \qquad (5.75)$$

and

$$S_{U_2}(\text{yawed wire}) = -S_{U_1}(\text{yawed wire})\tan\theta . \qquad (5.76)$$

Wire Sensitivity Coefficients for Compressible Flows and Small Fluctuations

In a compressible flow, a single wire placed normal to the incident flow responds to changes in three fundamental variables, velocity U, density ρ, and total temperature T_{t}. However, other triplets of variables can be used and they will also be examined.

Use of ρ, U, T_{t}. *Morkovin* [5.100] established the expressions of the sensitivity coefficient to ρ, U, and T_{t} variables by taking the logarithmic derivative of the general equation (5.59). For newcomers to the field, *Bradshaw* [5.46] gave a clear view for a CT-operated wire and the benefit of using log derivatives. The algebra for the derivation is straightforward, but rather long.

One has to use the definitions of $\mathrm{Nu_t}$, $\mathrm{Re_t}$ and M given by (5.58), and two additional basic aerodynamic relations

$$M^2 = \frac{U^2/c_t^2}{1-(\gamma-1)U^2/2c_t^2}$$
$$\frac{\mathrm{d}M}{M} = \frac{1}{\alpha}\left(\frac{\mathrm{d}U}{U} - \frac{1}{2}\frac{\mathrm{d}T_t}{T_t}\right) \qquad (5.77)$$

with

$$c_t^2 = \gamma\frac{RT_t}{m}\,, \quad \text{and} \quad \alpha = 1+\frac{\gamma-1}{2}M^2\,. \qquad (5.78)$$

Morkovin treated the CC and CT cases separately, but a unified approach is possible, which can moreover encompass the CV case as well. This general equation is

$$-\frac{1}{\overline{A}_w}\frac{\mathrm{d}R_w}{\overline{R}_w} + 2\frac{\mathrm{d}I_w}{\overline{I}_w} = (\mathrm{X})\frac{\mathrm{d}\rho}{\overline{\rho}} + (\mathrm{XX})\frac{\mathrm{d}U}{\overline{U}} + (\mathrm{XXX})\frac{\mathrm{d}T_t}{\overline{T}_t} \qquad (5.79)$$

with

$$(\mathrm{X}) = \frac{\overline{\mathrm{Re}_t}}{\overline{\mathrm{Nu}_t}}\frac{\partial\overline{\mathrm{Nu}_t}}{\partial\overline{\mathrm{Re}_t}} - \frac{1}{\overline{a}_w}\frac{\overline{\mathrm{Re}_t}}{\overline{\eta}}\frac{\partial\overline{\eta}}{\partial\overline{\mathrm{Re}_t}}$$
$$(\mathrm{XX}) = \frac{\overline{\mathrm{Re}_t}}{\overline{\mathrm{Nu}_t}}\frac{\partial\overline{\mathrm{Nu}_t}}{\partial\overline{\mathrm{Re}_t}} + \frac{1}{\overline{\alpha}}\frac{\overline{M}}{\overline{\mathrm{Nu}_t}}\frac{\partial\overline{\mathrm{Nu}_t}}{\partial\overline{M}} - \frac{1}{\overline{a}_w}\frac{\overline{\mathrm{Re}_t}}{\overline{\eta}}\frac{\partial\overline{\eta}}{\partial\overline{\mathrm{Re}_t}} - \frac{1}{\overline{a}_w}\frac{1}{\overline{\alpha}}\frac{\overline{M}}{\overline{\eta}}\frac{\partial\overline{\eta}}{\partial\overline{M}}$$
$$(\mathrm{XXX}) = n_t + 1 - \frac{1+\overline{A}_w}{\overline{A}_w}\chi' - m_t\frac{\overline{\mathrm{Re}_t}}{\overline{\mathrm{Nu}_t}}\frac{\partial\overline{\mathrm{Nu}_t}}{\partial\overline{\mathrm{Re}_t}} - \frac{1}{2\overline{\alpha}}\frac{\overline{M}}{\overline{\mathrm{Nu}_t}}\frac{\partial\overline{\mathrm{Nu}_t}}{\partial\overline{M}} + m_t\frac{1}{\overline{a}_w}\frac{\overline{\mathrm{Re}_t}}{\overline{\eta}}\frac{\partial\overline{\eta}}{\partial\overline{\mathrm{Re}_t}} + \frac{1}{2\overline{\alpha}}\frac{1}{\overline{a}_w}\frac{\overline{M}}{\overline{\eta}}\frac{\partial\overline{\eta}}{\partial\overline{M}}$$

where χ' is the exponent of a power law for the temperature dependence of the wire resistance

$$\frac{R_w}{R_0} = \left(\frac{T_w}{T_0}\right)^{\chi'}, \quad \chi'=1.15 \quad \text{when } \chi=0.0041\,\mathrm{K}^{-1}\,, \quad \chi'=1.05 \quad \text{when } \chi=0.0036\,\mathrm{K}^{-1} \qquad (5.80)$$

and is hence advantageously close to one. The χ' values are deduced from χ and (5.36) by a simple Matlab routine; m_t and n_t denote the power exponents for the temperature dependence of viscosity and thermal conductivity, already introduced in (5.47), hence $m_t \simeq 0.765$, and $n_t \simeq 0.885$. Finally, $\overline{A}_w$ is a generalized overheat parameter defined by

$$\overline{A}_w = \frac{1}{2}\frac{\overline{I}_w}{\overline{R}_w}\left(\frac{\partial\overline{R}_w}{\partial\overline{I}_w}\right) \quad \text{at constant flow}\,. \qquad (5.81)$$

The factor $\overline{A}_w$ depends on the wire overheat ratio $\overline{a}_w$ and its determination is examined later in this section.

The interesting characteristic of (5.79) is that the left-hand side concerns the wire, and the right-hand side concerns the flow, once the wire overheat ratio $\overline{a}_w$ is chosen. This form is similar to that which was developed earlier for subsonic flows (5.67). It therefore permits the treatment of any anemometer type, CCA, CTA or CVA. The appropriate constraint, listed in (5.68), has to be taken into account. This leads to the following expressions for the sensitivity coefficients at the wire level

$$S_\rho^{\mathrm{CC}} = -\overline{A}_w(\mathrm{X})\,, \qquad S_\rho^{\mathrm{CT}} = \frac{1}{2}(\mathrm{X})\,,$$
$$S_\rho^{\mathrm{CV}} = \frac{\overline{A}_w}{1+2\overline{A}_w}(\mathrm{X})\,,$$
$$S_U^{\mathrm{CC}} = -\overline{A}_w(\mathrm{XX})\,, \qquad S_U^{\mathrm{CT}} = \frac{1}{2}(\mathrm{XX})\,,$$
$$S_U^{\mathrm{CV}} = \frac{\overline{A}_w}{1+2\overline{A}_w}(\mathrm{XX})\,,$$
$$S_{T_t}^{\mathrm{CC}} = -\overline{A}_w(\mathrm{XXX})\,, \qquad S_{T_t}^{\mathrm{CT}} = \frac{1}{2}(\mathrm{XXX})\,,$$
$$S_{T_t}^{\mathrm{CV}} = \frac{\overline{A}_w}{1+2\overline{A}_w}(\mathrm{XXX})\,. \qquad (5.82)$$

Obviously, the quantities (X), (XX) and (XXX) are complex, but a few remarks are helpful:

1. The leading term is the derivative of the Nusselt number with respect to the Reynolds number. This term has already been obtained at low subsonic speed. Moreover, if the temperature dependence of the physical properties are neglected, i. e., $m_t = n_t = 0$, and if the wire overheat stays less than about 0.50, then $\overline{A}_w = \overline{a}_w$, and the relations (5.69) are recovered.
2. The recovery factor η can often be taken as a constant, unless one works in a rarefied gas. The derivatives of η relative to the Mach and Reynolds numbers can then be neglected. *Morkovin* [5.100] estimated that the error is often less than 6%.
3. When the Mach number is greater than 1.2, the Baldwin–Dewey plots [5.119, 121], sketched in Fig. 5.15, show that the heat transfer no longer depends on the Mach number. Furthermore, there is the simple relation $S_\rho = S_U = \hat{S}_{\rho U}$ concerning the sensitivity coefficients.
4. When the Mach number is in the range 0.5–1.2, one has to estimate the log derivative of the Nusselt number with respect to the Mach number, in addition to the usual Nusselt dependence on the

Reynolds number. Using Fig. 5.15, one can appreciate this Mach number effect, by noting the Nusselt number change along a parallel to the ordinate axis at the chosen Reynolds number. For example, for $\mathrm{Re_t} \simeq 20$ and around $M = 0.90$, the Nusselt number decreases by about 15%. Incidentally, the values reported by *Morkovin* [5.100] in his Fig. VI-2 are much too high. *Baldwin* et al. [5.121] also referred to an earlier work by *Scadron* and *Warshawsky* [5.130] and pointed out that a possible correlation could be $\mathrm{Nu_t} = 0.431\mathrm{Re_t^{0.50}}(1+M^2)^{-0.50}$.

Use of ρU, M, T_t. This ρU, M, T_t triplet is the favorite for experimentalists because of the direct presence of the Mach number, which is the key parameter of any experiment. The sensitivity coefficients fitting that new group, noted $\hat{S}$, can be related to the S defined by (5.82). Writing the differential response for any anemometer, we have on one hand

$$\frac{r'_\mathrm{w}}{\overline{R}_\mathrm{w}} \text{ or } \frac{i'_\mathrm{w}}{\overline{I}_\mathrm{w}} = \underbrace{\frac{\overline{\rho}}{\overline{R}_\mathrm{w}}\frac{\partial \overline{R}_\mathrm{w}}{\partial \overline{\rho}}}_{S_\rho}\frac{\mathrm{d}\rho}{\overline{\rho}} + \underbrace{\frac{\overline{U}}{\overline{R}_\mathrm{w}}\frac{\partial \overline{R}_\mathrm{w}}{\partial \overline{U}}}_{S_U}\frac{\mathrm{d}U}{\overline{U}} + \underbrace{\frac{\overline{T}_\mathrm{t}}{\overline{R}_\mathrm{w}}\frac{\partial \overline{R}_\mathrm{w}}{\partial \overline{T}_\mathrm{t}}}_{S_{T_\mathrm{t}}}\frac{\mathrm{d}T_\mathrm{t}}{\overline{T}_\mathrm{t}} \tag{5.83}$$

and on the other hand

$$\frac{r'_\mathrm{w}}{\overline{R}_\mathrm{w}} \text{ or } \frac{i'_\mathrm{w}}{\overline{I}_\mathrm{w}} = \underbrace{\frac{\overline{\rho U}}{\overline{R}_\mathrm{w}}\frac{\partial \overline{R}_\mathrm{w}}{\partial(\overline{\rho U})}}_{\hat{S}_{\rho U}}\frac{\mathrm{d}(\rho U)}{\overline{\rho U}} + \underbrace{\frac{\overline{M}}{\overline{R}_\mathrm{w}}\frac{\partial \overline{R}_\mathrm{w}}{\partial \overline{M}}}_{\hat{S}_M}\frac{\mathrm{d}M}{\overline{M}} + \underbrace{\frac{\overline{T}_\mathrm{t}}{\overline{R}_\mathrm{w}}\frac{\partial \overline{R}_\mathrm{w}}{\partial \overline{T}_\mathrm{t}}}_{\hat{S}_{T_\mathrm{t}}}\frac{\mathrm{d}T_\mathrm{t}}{\overline{T}_\mathrm{t}} \,. \tag{5.84}$$

In (5.84), $\mathrm{d}(\rho U)$ can be developed and $\mathrm{d}M$ transformed using (5.77), hence

$$\frac{r'_\mathrm{w}}{\overline{R}_\mathrm{w}} \text{ or } \frac{i'_\mathrm{w}}{\overline{I}_\mathrm{w}} = \hat{S}_{\rho U}\left(\frac{\mathrm{d}\rho}{\overline{\rho}} + \frac{\mathrm{d}U}{\overline{U}}\right) + \hat{S}_M\frac{1}{\alpha}\left(\frac{\mathrm{d}U}{\overline{U}} - \frac{1}{2}\frac{\mathrm{d}T_\mathrm{t}}{\overline{T}_\mathrm{t}}\right) + \hat{S}_{T_\mathrm{t}}\frac{\mathrm{d}T_\mathrm{t}}{\overline{T}_\mathrm{t}} \tag{5.85}$$

and identifying with (5.83) gives

$$\hat{S}_{\rho U} = S_\rho \qquad \hat{S}_M = \alpha(S_U - S_\rho) \qquad \hat{S}_{T_\mathrm{t}} = S_{T_\mathrm{t}} + \frac{1}{2}(S_U - S_\rho)\,. \tag{5.86}$$

The most interesting result is that, when $M \geq 1.2$ and $\eta \simeq 1$, the derivatives involving M and η in (X) and (XX) are negligible, and (5.86) simply become

$$\hat{S}_{\rho U} = S_\rho = S_U\,, \quad \hat{S}_M = 0\,, \quad \hat{S}_{T_\mathrm{t}} = S_{T_\mathrm{t}}\,. \tag{5.87}$$

In fact, this result seems to hold already in transonic flows. Using a CC-operated wire, *Barre* et al. [5.123] and *Dupont* and *Debiève* [5.131] did a complete survey in the freestream of a wind tunnel for $0.7 \leq M \leq 2.3$, $4 \leq \mathrm{Re_t} \leq 20$, $0 \leq \overline{a}_\mathrm{w} \leq 0.50$. Using a CT-operated wire, *Horstman* and *Rose* [5.132] reported experiments in a transonic boundary layer and found that $S_\rho \simeq S_U$ holds even for $\mathrm{Re_t} \leq 20$ and $a_\mathrm{w} \geq 0.50$. Similar results were obtained by *Jones* et al. [5.133] who investigated the Mach number range $0.05 \leq M \leq 1.0$ in a specially designed probe calibration tunnel [5.134].

In these conditions, a hot-wire response simplifies to

$$\frac{r'_\mathrm{w}}{\overline{R}_\mathrm{w}} \text{ or } \frac{i'_\mathrm{w}}{\overline{I}_\mathrm{w}} = \hat{S}_{\rho U}\frac{\mathrm{d}(\rho U)}{\overline{\rho U}} + \hat{S}_{T_\mathrm{t}}\frac{\mathrm{d}T_\mathrm{t}}{\overline{T}_\mathrm{t}}\,. \tag{5.88}$$

Operating a normal wire at different overheats modifies the relative ratio between $\hat{S}_{\rho U}$ and $\hat{S}_{T_\mathrm{t}}$. With one wire, one can obtain the variances and the correlation coefficient for the fluctuations $\mathrm{d}(\rho U)$ and $\mathrm{d}T_\mathrm{t}$. This requires a minimum of three values of $\overline{a}_\mathrm{w}$, but a larger number, around ten, allows the use of a polyfit technique and yields greater accuracy. This approach is used in many supersonic experiments [5.127, 135]. An automated stepping procedure to change $\overline{a}_\mathrm{w}$ was developed by *Walker* et al. [5.136], *Weiss* et al. [5.126], or *Norris* and *Chokani* [5.137]. With two wires, placed in the close vicinity of each other, the instantaneous values of $\rho U(t)$ and $T_\mathrm{t}(t)$ can be obtained and recorded [5.124, 136, 138]. These quantities are most useful when comparisons are made with turbulence predictions, because the density-weighted averages introduced by Favre are of common use in compressible flows [5.77].

The separation of ρ and U fluctuations remains difficult, however, even when several wires are used, because of the inherent equality $S_\rho = S_U$, which makes the reduction matrix singular. Nevertheless, in some cases, it would be beneficial to know the velocity fluctuations themselves, for example when comparing hot-wire anemometry to Doppler laser velocimetry or to particle image velocimetry. Physical assumptions are therefore needed.

For example, in a boundary layer, the strong Reynolds analogy, suggested by *Morkovin* [5.139], *Gaviglio* [5.122, 140], or *Smith* and *Smits* [5.138] is most useful. It states that when a fluid particle leaves the wall

region where hot and slow motions prevail it carries with it a positive temperature fluctuation $T' > 0$, hence $\rho' < 0$, and a negative longitudinal velocity fluctuation $u' < 0$, so that the correlation between ρ' and u' is high and positive

$$\overline{\rho' u'} \simeq 0.80 \sqrt{\overline{\rho'^2}} \sqrt{\overline{u'^2}} \,. \tag{5.89}$$

In addition, the assumption of a constant stagnation temperature and constant static pressure permits one to relate the root-mean-square (rms) values of ρ' and u' by

$$\frac{\sqrt{\overline{\rho'^2}}}{\overline{\rho}} = (\gamma - 1) M^2 \frac{\sqrt{\overline{u'^2}}}{\overline{U}} \,. \tag{5.90}$$

The Kovasznay Modes. Another triplet of fundamental variables are the modes introduced by *Kovasznay* [5.91] and extensively used by *Morkovin* [5.100]: the vorticity mode ω, the entropy (spotiness) mode σ, and the acoustic mode π. The sensitivity coefficients of a wire to each of these modes, denoted by a double hat, can also be expressed in terms of the sensitivity coefficients S given by (5.82), independently of the anemometer type, by

$$\begin{aligned}
\hat{\hat{S}}_\sigma &= -S_\rho + \alpha S_{T_t} \,, \\
\hat{\hat{S}}_\omega &= S_U + \alpha(\gamma - 1) M^2 S_{T_t} \,, \\
\hat{\hat{S}}_\pi &= S_\rho + \frac{n_x}{M} S_U + \alpha(\gamma - 1)(1 + n_x M_x) S_{T_t} \,,
\end{aligned} \tag{5.91}$$

where n_x is the direction of the sound wave.

Use of the Kovasznay modes allows reasonable assumptions to be made. For example in the freestream of wind tunnels, sound waves predominate, due to sound radiation from the supersonic, turbulent, boundary layer on the nozzle walls [5.126]. Temperature spottiness, leading to an entropy mode, comes from incomplete mixing in upstream reservoirs of high-speed wind tunnels.

The General Overheat A_w. The parameter $\overline{A}_w$, which expresses the temperature load of the wire, is easily obtained from $\overline{R}_w$ and $\overline{I}_w$ measurements at different overheat values $\overline{a}_w$, if the flow conditions are unchanged, see (5.81) and *Morkovin* [5.100]. A series of 10–12 values is needed to accurately compute the derivative involved in the definition of $\overline{A}_w$.

Most importantly, the factor $\overline{A}_w$ does not depend on the anemometer type. For example, it is possible to compute $\overline{A}_w$ in the *Smits* et al. experiments [5.125], although this was not explicitly done by the authors. Indeed, the $S^{CT}_{T_t}$ coefficient given by (5.82) should be the same as that which can be deduced from any other explicit relation. In particular, *Smits* et al. [5.125] wrote

$$\mathrm{Nu}_t = A f(\tau) + B g(\tau) \mathrm{Re}_t^n \,, \tag{5.92}$$

with

$$\begin{aligned}
&f = 1 - 0.65\tau \,, \quad g = 1 - 0.085\tau \,, \\
&\tau = \frac{(T_w - T_r)}{T_t} \,.
\end{aligned} \tag{5.93}$$

Therefore, we have on one hand, from (5.82)

$$S^{CT}_{T_t} = n_t + 1 - \frac{1 + \overline{A}_w}{\overline{A}_w} \chi' - n m_t \frac{B g \mathrm{Re}_t^n}{A f + B g \mathrm{Re}_t^n} \tag{5.94}$$

and on the other hand, from (5.92) and (5.93)

$$\begin{aligned}
S^{CT}_{T_t} = n_t - \frac{\eta}{\tau} - (\eta + \tau) \frac{A f' + B g' \mathrm{Re}_t^n}{A f + B g \mathrm{Re}_t^n} \\
- n m_t \frac{B g \mathrm{Re}_t^n}{A f + B g \mathrm{Re}_t^n} \,,
\end{aligned} \tag{5.95}$$

where $\tau = \eta \overline{a}_w$ and $\eta + \tau = \eta(1 + \overline{a}_w)$. After identification, the choice of $\mathrm{Re}_t = 85$, and the use of the fitted values $A = 0.27$, $B = 0.35$ and $n = 0.55$, one obtains for $\overline{A}_w$

$$\begin{aligned}
\frac{1}{\overline{A}_w} = -1 \\
+ \frac{1}{\chi'} \left[\frac{1}{\overline{a}_w} - \eta(1 + \overline{a}_w) \frac{0.518}{4.30 - 0.48 \overline{a}_w} + 1 \right] \,.
\end{aligned} \tag{5.96}$$

Equation (5.96) advantageously makes A_w an explicit function of $\overline{a}_w$. Figure 5.17 indicates the results deduced from this equation, assuming $\chi' = 1$ and $\eta \simeq 0.95$. Other experimental data by *Morkovin* [5.100], *Comte-Bellot* and *Sarma* [5.127], or *Weiss* et al. [5.141] are also reported, concerning CC-, CT-, or CV-operated wires. Very clearly, $\overline{A}_w \simeq \overline{a}_w$ as long as $\overline{a}_w \leq 0.50$, and $\overline{A}_w > \overline{a}_w$ when $\overline{a}_w \geq 0.50$.

The increase of $\overline{A}_w$ with $\overline{a}_w$ corresponds to a decrease of the Nusselt number. This decrease is made explicit by *Smits* et al. [5.125] by means of the two functions f and g. The fitted values of A and B already used above give a relative decrease of Nu_t from 1.0 to 0.88 when $\overline{a}_w$ increases from 0 to 1. *Spina* and *McGinley* [5.108] also observed a very strong Nu_t variation in a Mach 10 helium tunnel, with $g = 1 - 0.50\tau$. *Weiss* et al. [5.126] in the freestream of a Mach 2.54 wind tunnel found $f \simeq 1 - 0.72\tau$ and $g \simeq 1 - 0.18\tau$.

The temperature load that has just been considered appears to act in a way which is opposite to that we have

indicated for subsonic flows when the film temperature is used (5.45). Indeed expressing the physical properties at the film temperature $T_f = (T_w + T_a)/2$ rather than at T_a leads to $Nu_f < Nu_a$ and the need to adjust the factor $(T_f/T_a)^{0.17}$.

Practical Values of the Sensitivity Coefficients for Supersonic Flows. For sufficiently large Mach and Reynolds numbers and a continuum flow, the sensitivity coefficients can be obtained from (5.86) and (5.82) with the appropriate simplifications listed in point 3. after (5.82). Hence

$$(X) = (XX) = \frac{1}{2} \quad \text{and}$$

$$(XXX) = n_t + 1 - \frac{1+\overline{A}_w}{\overline{A}_w}\chi' - \frac{1}{2}m_t \,. \tag{5.97}$$

In practice, one has only to measure A_w according to (5.81) or to use Fig. 5.17. For air $n_t = 0.885$, $m_t = 0.765$, and for a tungsten wire $\chi' \simeq 1.10$.

The sensitivity coefficients that can be expected in compressible flows are indicated in Fig. 5.18. For CC- and CT-operated wires, the curves agree with experimental data collected by *Gaviglio* [5.122], *Bonnet* [5.92], *Smits* et al. [5.125], and *Smits* and *Dussauge* [5.142]. Similar results have been established by *Kosinov* [5.143]. Extension to the CV-operated wire is therefore permitted from (5.82) on the same basis. In these data, convective heat transfer rates are important. When this is not the case, discrepancies may occur, because of thermal conduction end losses, as indicated by *Ko* et al. [5.144] among others.

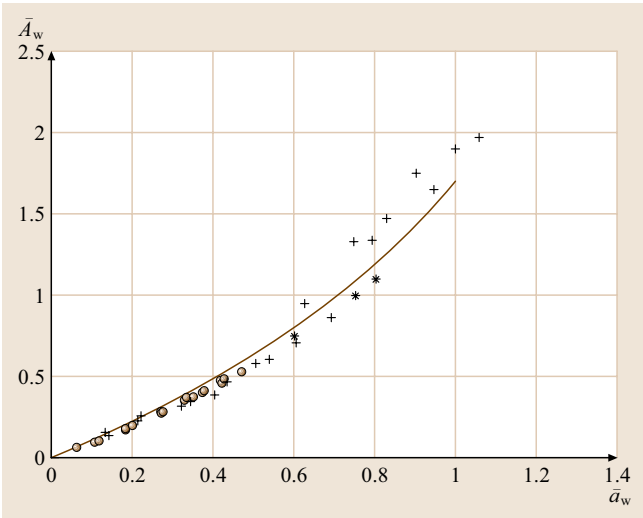

Fig. 5.17 The factor $\overline{A}_w$ as a function of the overheat ratio $\overline{a}_w$: *stars*: CCA *Morkovin* [5.100], *circles*: CCA and CVA *Comte-Bellot* and *Sarma* [5.127], *pluses*: CTA and CVA, *Weiss* et al. [5.141], *line*: (5.96)

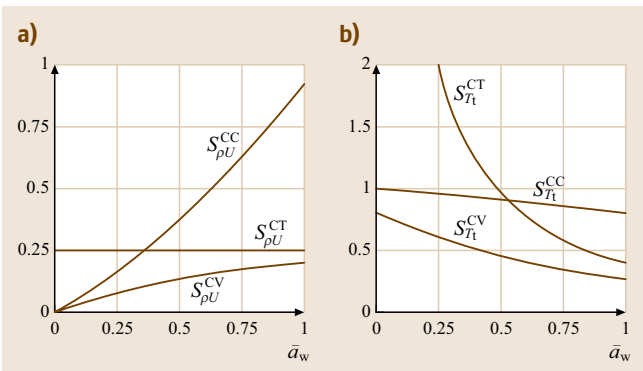

Fig. 5.18a,b Sensitivity coefficients in supersonic flows when $M > 1.2$, **(a)** to velocity or mass flux fluctuations, **(b)** to total temperature, for a wire operated in constant-current, constant-temperature, or constant-voltage mode

Time Constant for Small Fluctuations

When thermal energy is unsteadily stored in a wire, the instantaneous heat balance (5.39) has to be rewritten as

$$m_w c_w \frac{dT_w}{dt} = (R_w - R_a)I_w^2 - \Phi_{conv}(T_w - T_a) + R_a I_w^2 \,, \tag{5.98}$$

where m_w is the wire mass, and c_w is the heat capacity of the material constituting the wire. As a consequence the wire does not respond instantaneously to the forcing function Φ_{conv}. The difference between the response of an *ideal* wire, devoid of heat capacity, and the response of a CC-, CT-, or CV-operated wire, is therefore essential. Moreover, the amplitude of the turbulent fluctuation is an important parameter. We therefore consider the case of small-amplitude fluctuations in this section and the general case in the next section.

Constant-Current Operation. The thermal balance of an ideal wire having the same cold resistance R_a and heated with the same current intensity I_w as the real wire is

$$0 = (R_w^\star - R_a)I_w^2 - \Phi_{conv}(T_w^\star - T_a) + R_a I_w^2 \,, \tag{5.99}$$

where $T_w^\star$ and $R_w^\star$ are the instantaneous temperature and resistance of this ideal wire, respectively. Substituting

Φ_{conv} from (5.98) into (5.99), and using the $R(T)$ relation specified by (5.36) gives

$$\frac{m_w c_w}{\chi R_0}\frac{1}{I_w^2}\frac{1}{R_a}\frac{dR_w}{dt}+\frac{R_w-R_a}{R_w^\star-R_a}=1\,. \tag{5.100}$$

The resistance R_w is therefore related to $R_w^\star$ by a first-order linear differential equation, where one coefficient, $R_w^\star - R_a$, is a random function of time.

For small-amplitude fluctuations, i. e.,

$$\begin{aligned} R_w &= \overline{R}_w + r'_w \quad \text{with } r'_w \ll \overline{R}_w \quad \text{and} \\ R_w^\star &= \overline{R}_w^\star + r'^\star_w \quad \text{with } r'^\star_w \ll \overline{R}_w^\star\,, \end{aligned} \tag{5.101}$$

a first-order expansion of (5.100) gives $\overline{R}_w = \overline{R}_w^\star$ and

$$M_w^{CC}\frac{dr'_w}{dt}+r'_w=r'^\star_w \quad \text{with}$$
$$M_w^{CC}=\frac{m_w c_w}{\chi R_0}\frac{1}{I_w^2}\frac{\overline{R}_w-R_a}{R_a}\,. \tag{5.102}$$

The response to a step function is an exponential, and the simplest notion of a time constant M_w^{CC} applies. The amplitude attenuation is therefore given by

$$\left[1+\omega^2\left(M_w^{CC}\right)^2\right]^{-1/2}\,,$$

or $-20\,\text{dB/decade}$, or $-6\,\text{dB/octave}$.

Often, M_w^{CC} is simply denoted M_w. Furthermore, the wire Nusselt number can be introduced in (5.102) in place of I_w^2. This leads to the compact form

$$M_w^{CC}=(1+\overline{a}_w)\frac{d^2}{4}\frac{\rho_w c_w}{k_a}\frac{1}{\text{Nu}_a}\,. \tag{5.103}$$

For $a_w \simeq 0$, the expression (5.103) was already obtained by *Scadron* and *Warshasky* [5.130] when working on thermocouples. Nu_a can be measured or estimated using a heat-transfer law, e.g., Kramers law valid for air or liquids (5.46). The wire characteristics are listed in Table 5.1 and the fluid and/or substrate properties in Table 5.2. For example, $M_w^{CC} \simeq 0.50\,\text{ms}$ for a $5\,\mu\text{m}$ tungsten wire, operated at $\overline{a}_w = 0.80$ in a $U = 50\,\text{m/s}$ air flow. The amplitude attenuation is then around $-30\,\text{dB}$ at $10\,\text{kHz}$. Direct measurements of M_w^{CC} are discussed in Sect. 5.2.3.

Regarding the dependence of M_w^{CC} on the wire diameter at a given velocity, (5.103) leads to the approximate form $M_w^{CC} \sim d^{3/2}$.

For a cylindrical hot-film sensor, the frequency response was analyzed by Lowell and Patton, as early as 1955, and by *Kidron* [5.145]. When the bulk of the cylinder responds as a whole, $\rho_w c_w$ can be replaced by $\rho_s c_s$ in (5.103), where the subscript 's' refers to the substrate. Useful properties for the substrate are indicated in Table 5.2, especially the thermal conductivity k_s. For example, $M_{\text{film}}^{CC} \simeq 4.0\,\text{ms}$ for a $25\,\mu\text{m}$ cylindrical hot-film, with a quartz core, operated at $\overline{a}_w = 0.80$ in a $U = 50\,\text{m/s}$ air flow. This film needs therefore an important frequency correction. In water, the situation is greatly improved because of a substantial increase of the heat transfer rate due to water's larger thermal conductivity. For example, $M_{\text{film}}^{CC} = 0.17\,\text{ms}$ for a $50\,\mu\text{m}$ film placed in a $U = 2\,\text{m/s}$ water flow and operated at $\overline{a}_w = 0.10$.

When hot-films are placed on wedges, the response becomes more complicated because part of the thermal energy through the wire leaks towards the substrate. *Bellhouse* and *Schultz* [5.146] investigated a one-dimensional case where the heat loss takes place along a normal to the substrate. They clearly pointed out that the dynamic sensitivity cannot be obtained from a steady flow calibration. *Brison* et al. [5.147] considered a two-dimensional case, where the thermal transfer may also take place in the longitudinal direction. They showed, in particular, that a film should not be placed too close to the stagnation point of a wedge, because the high transfer rates to the external flow which prevail in that region serve as a heat sink for the substrate and therefore for the film.

Constant-Temperature Operation. In principle, since R_w is maintained constant whatever the flow conditions, the time constant concept is not required for an idealized CTA. However, since the condition of constant resistance can only be maintained by an appropriate electronic circuit, the way this circuit handles that function is an essential aspect of the actual CTA. This topic is considered in Sect. 5.2.3.

Constant-Voltage Operation. The *real* wire now has to respect $R_w I_w = V_w$, and the *ideal* wire $R_w^\star I_w^\star = V_w$, with $V_w =$ constant. Equation (5.98) keeps its form, and (5.99) becomes

$$0=(R_w^\star-R_a)I_w^{\star 2}-\Phi_{\text{conv}}(T_w^\star-T_a)+R_a I_w^{\star 2}\,. \tag{5.104}$$

Combining (5.98) and (5.104) yields

$$\frac{1}{V_w^2}\frac{m_w c_w}{\chi R_0}\frac{dR_w}{dt}=\frac{1}{R_w}-\frac{1}{R_w^\star}\frac{R_w-R_a}{R_w^\star-R_a}\,. \tag{5.105}$$

For small-amplitude fluctuations, a first-order expansion gives $\overline{R}_w = \overline{R}^{\star}_w$, $\overline{I}_w = \overline{I}^{\star}_w$, and

$$M_w^{CV} \frac{dr'_w}{dt} + r'_w = r'^{\star}_w \qquad (5.106)$$

with, for the new time constant,

$$M_w^{CV} = \frac{\rho_w c_w}{\chi R_0} \frac{1}{\overline{I}_w^2} \frac{(\overline{R}_w - R_a)}{2\overline{R}_w - R_a} = \frac{M_w^{CC}}{1 + 2\overline{a}_w} . \qquad (5.107)$$

Equation (5.107) clearly shows that M_w^{CV} is smaller than M_w^{CC}. This result was anticipated by *Sarma* [5.148] and established by *Comte-Bellot* [5.55] and *Comte-Bellot* and *Sarma* [5.127]. *Sarma* [5.149] and *Reimann* et al. [5.150] explained that, if R_w decreases due to flow, I_w increases, and this increased I_w partially restores the hot-wire resistance. These small M_w^{CV} values constitute a noticeable benefit in favor of the CV operation. For example, for the 5 µm tungsten wire considered above, M_w^{CV} goes down from 0.50 ms to 0.19 ms at $\overline{a}_w = 0.80$. Figure 5.19 reports results obtained in supersonic conditions.

Dynamic Nonlinearity: Large Fluctuations

Constant-Current Operation. Equation (5.100) cannot be linearized when the turbulent fluctuations present large amplitudes. *Corrsin* [5.45] pointed out that higher harmonics are generated by *parametric excitation* because of the coefficient $(R^{\star}_w - R_a)$, which is a random function of time. Using Fourier series, he computed the amplitude and phase of the second harmonic that appears for a sinusoidal input. Extension to random signals featuring turbulence was made by *Comte-Bellot* and *Schon* [5.151] on an analog computer. Obviously, the electronic compensation circuit of a CCA cannot discriminate between the true turbulence components and the wrong higher harmonics due to the wire behavior. As a consequence, errors on odd turbulence moments are large, such as on the skewness factors which are third-order moments. Nowadays, (5.100) can easily be solved by a Matlab procedure. Results are presented in Sect. 5.2.3.

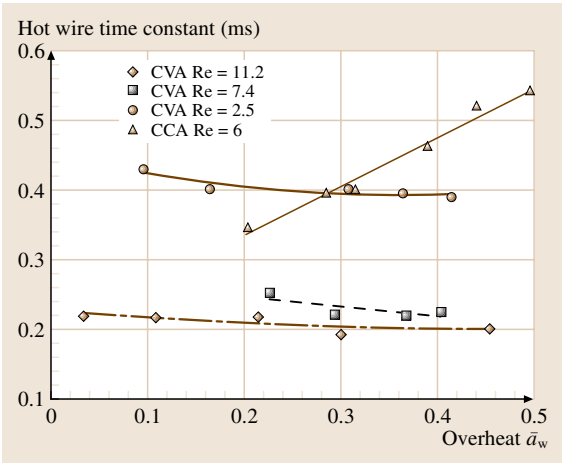

Fig. 5.19 Time constant for a CCA- and CVA-operated wire in supersonic flows (after *Comte-Bellot* and *Sarma* [5.127]). At similar Re and $\bar{a}_W$, $M_W^{CV} < M_W^{CC}$ (5.107)

Constant-Temperature Operation. Similarly to Sect. 5.2.2, the role of the electronic circuit is crucial, see Sect. 5.2.3.

Constant-Voltage Operation. For large-amplitude fluctuations, the full equation (5.105) has to be considered and higher harmonics could be generated. A systematic analysis has however not yet been performed. See also Sect. 5.2.3.

Sensors of Finite Length – End Losses

A real hot-wire is held by supports that are at ambient or near-ambient temperature, see Fig. 5.20. Thermal conduction can therefore take place axially along the wire towards the supports, resulting in a marked temperature maximum near the middle of the wire. This behavior was clearly illustrated by *Champagne* et al. [5.152] who deduced the temperature profile along a wire from its infrared emission. Very simply, one can observe a wire under a magnifying glass while gradually increasing the heating current intensity. The central part of the wire is the first to turn red.

The partial differential equation governing the temperature T at a location ξ_3 along the wire or the stubs is determined by the local heat balance between the

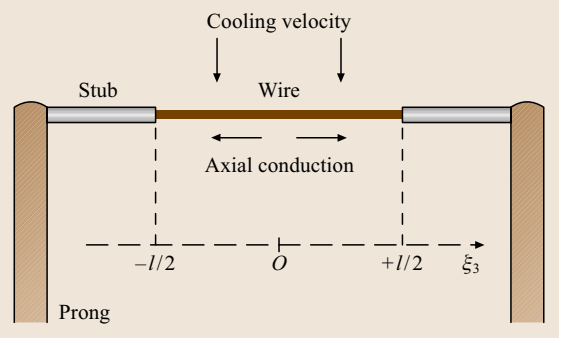

Fig. 5.20 Sketch of a short wire with stubs and prongs

ohmic heating, the convective cooling, and the axial heat conduction. This balance, which is presented in most reviews on hot-wire anemometry [5.49, 51, 52], may be written

$$\rho c \frac{\pi d^2}{4} \frac{\partial T}{\partial t} = R_1 I_w^2 - \mathrm{Nu}_1 \pi k_a (T - T_a) + \frac{\pi d^2}{4} k \frac{\partial^2 T}{\partial \xi_3{}^2} . \quad (5.108)$$

This is an extension of (5.39), the axial conduction towards the supports now being introduced. The subscript 'w' has been dropped to generalize (5.108) for a point located on the wire as well as on the stubs. Hence, d is the wire diameter d_w when ξ_3 concerns the wire, and the stub diameter d_s when ξ_3 concerns one of the two stubs, and similarly for the thermal conductivity k, the specific heat c, and the Nusselt number, which involves a Reynolds number based on the wire (or stub) diameter. The subscript '1' refers to a value per unit length (not to be confused with the top resistance of the Wheatstone bridge). The subscript 'w' is kept only for I_w as the current intensity is the same through the wire and the stubs.

The spatial average of R_1 over the wire and the stubs constitutes the input to the anemometer whatever its type, CCA, CTA, or CVA. This average is noted $\langle R \rangle$ and is given by

$$\langle R \rangle = \int_{-s-l/2}^{+s+l/2} R_1(\xi_3)\, \mathrm{d}\xi_3 . \quad (5.109)$$

It is therefore very important to examine how T and R_1 are distributed along the wire and the stubs, when the main parameters are changed, such as changes in the material, the wire aspect ratio, the relative importance of the stubs, the flow velocity normal to the wire, the flow temperature, and the current intensity through the wire.

Equation (5.108) can be rewritten in a compact form as

$$\tau \frac{\partial T}{\partial t} = \frac{\partial^2 T}{\partial \xi_3^2} - C(T - T_a) + D , \quad (5.110)$$

where

$$\tau = \frac{\rho c}{k} , \quad C = 4 \left(\mathrm{Nu}_1 \frac{k_a}{k} - \frac{\chi R_{01}}{\pi k} I_w^2 \right) \frac{1}{d^2} ,$$
$$D = 4 R_{a1} \frac{1}{\pi k} I_w^2 \frac{1}{d^2} . \quad (5.111)$$

R_{01} is the wire (or stub) resistance per unit length at the reference temperature T_0. Similarly R_{a1} is the wire (or stub) resistance per unit length at the flow temperature T_a, and $\mathrm{Nu}_1 = R_1 I_w^2 / \pi k_a (T - T_a)$ is the local Nusselt number per unit length. Locally, Nu_1 is assumed to be that of a long wire, as indicated for subsonic and supersonic flows in Sect. 5.2.2. The incident velocity therefore occurs in the factor C, the incident flow temperature in the factor D, and the wire current as well as the wire diameter in the two factors C and D.

The basic case of a wire directly soldered onto relatively massive prongs, which can be assumed to stay at temperature T_a, can be treated analytically when the incident flow is steady, uniform and isothermal. This was investigated very early by *Betchov* [5.153], *Corrsin* [5.45] or *Davies* and *Fisher* [5.58]. The solution of (5.110) that verifies the boundary conditions $T = T_a$ for $\xi_3 = \pm l/2$ gives the temperature profile $T(\xi_3)$

$$T(\xi_3) - T_a = \frac{D}{C} \left(1 - \frac{\cosh \sqrt{C} \xi_3}{\cosh \sqrt{C} l/2} \right) . \quad (5.112)$$

One can observe from (5.110) that the factor D/C is the temperature difference $(T - T_a)$ which would be established for an infinitely long wire. The space average of $T(\xi_3)$ along the wire is

$$\langle T \rangle - T_a = \frac{D}{C} \left(1 - \frac{\tanh \sqrt{C} l/2}{\sqrt{C} l/2} \right) . \quad (5.113)$$

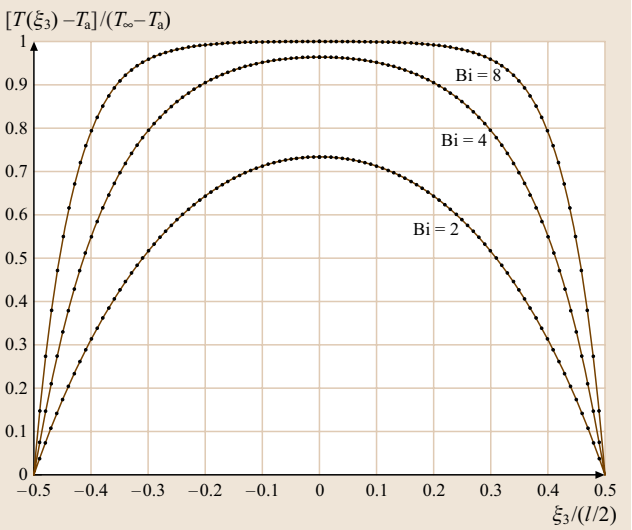

Fig. 5.21 Temperature distribution along a wire placed in a uniform perpendicular flow for different Biot numbers $\mathrm{Bi} = \sqrt{C} l/2$ with C defined by (5.111). Both ends are assumed to be at the ambient temperature T_a

Table 5.3 Steady end losses for different wires and flows, according to (5.114) when $\langle a \rangle = 0.80$

Velocity (m/s)	Material	l (mm)	d (μm)	l/d	Re_t	Nu_t	R_{01} (Ω/m)	I_w (mA)	$\mathrm{Bi} = \sqrt{C}l/2$	ϵ_{th} (%)
Air										
30	Pt	1	2.5	400	5	1.5	22400	25	3.7	7.5
30	Pt	2	5	400	10	2.0	5600	57	8.4	6.5
30	Pt	1	5	200	10	2.0	5600	57	4.2	13
30	W	1	2.5	400	5	1.5	11200	33	4.7	12
30	W	2	5	400	10	2.0	2800	75	5.4	11
30	W	1	5	200	10	2.0	2800	75	2.7	20
60	W	2	5	400	20	2.7	2800	87	6.2	9
10	W	2	5	400	5	1.5	2800	66	2.3	20
[a] $M = 2.5$ [a]	W	1.2	5	240	20	1.5	2800	65	2.8	20
[b] $M = 6$	W	1.2	5	240	7	0.7	2800	60	1.1	38
Helium										
[c] $M = 10$	W	1.2	5	240	15	1	2800	135	5.4	10

The supersonic conditions are: [a] $T_t \simeq 293\,\mathrm{K}$ and $p_t \simeq 1\times10^5\,\mathrm{Pa}$ [5.141]; [b] $T_t \simeq 450\,\mathrm{K}$ and $p_t \simeq 9\times10^5\,\mathrm{Pa}$ [5.129]; and [c] $T_t \simeq 300\,\mathrm{K}$ and $p_t \simeq 25\times10^5\,\mathrm{Pa}$ [5.108]

Figure 5.21 shows the temperature profile along a wire, according to (5.112) for different values of $\sqrt{C}l/2$, and the corresponding mean values given by (5.113). For the anemometer, the change in $\langle R \rangle$, which is related to the change in $\langle T \rangle$ by $\langle R \rangle = R_a + \chi R_0(\langle T \rangle - T_a)$, is the quantity of interest.

The heat loss q to both supports can be deduced from (5.112)

$$q = -2k_w \frac{\pi d^2}{4} \left.\frac{\partial T}{\partial \xi_3}\right|_{\xi_3 = l/2} = 2k_w \frac{\pi d^2}{4} D \frac{\tanh \sqrt{C}l/2}{\sqrt{C}} \qquad (5.114)$$

and the fraction ϵ_{th} relative to the input ohmic heating is

$$\epsilon_{th} = \frac{q}{\langle R \rangle I_w^2} = \frac{1}{1+\langle a \rangle} \frac{\tanh \sqrt{C}l/2}{\sqrt{C}l/2}\,, \qquad (5.115)$$

where $\langle a \rangle = (\langle R \rangle - R_a)/R_a$.

The dimensionless quantity $\sqrt{C}l/2$ is the Biot number Bi. It expresses the ratio between the heat-transfer coefficient of a solid at its surface and the heat conductance to the center of the solid (it is most important in food processing). Here it is based on the half-wire length $l/2$ and should be as large as possible to favor the cooling of the wire by the incident flow. Referring to the definition of C (5.111), one sees that $\sqrt{C}l/2$ depends on l/d as well as on the flow conditions and the wire diameter. In practice one therefore has to consider both l/d and $\sqrt{C}l/2$. In other words, a *long* wire involves more than the unique condition $l/d \to \infty$.

Estimates of ϵ_{th} are given in Table 5.3 for different wires and flows. Use is made of the physical data listed in Table 5.2, of Kramers' law (5.46) for subsonic flows, and of the Baldwin–Dewey diagram for supersonic flows, Fig. 5.15. Table 5.3 clearly shows that end losses become large when the Nusselt number decreases. This is the case for low-density flows. *Dewey* [5.119], *Davies* and *Fisher* [5.58], and *Lord* [5.154] studied this interesting case, even carrying out experiments in a vacuum. *Lord* [5.154] established a correction which can be applied during calibration. It was later used with success by *Ko* et al. [5.144]. *Pitts* and *McCaffrey* [5.107] also did a careful analysis of end losses for tungsten wires, $d = 4\,\mu\mathrm{m}$, $l = 1.25\,\mathrm{mm}$, and 0.1 μm-thick platinum films on quartz cylinders, $d = 50\,\mu\mathrm{m}$, $l = 1\,\mathrm{mm}$, in air and many other gases for a Reynolds number range of 2–35. The end losses were analyzed in terms of the A and B variations in King's law. These results confirm that Nu_∞ for a wire of infinite length is always less than Nu_m for a wire of finite length. The fractional decrease of A from A_∞ to A_m is very important, on the order of 50%; the fractional decrease of B stays around 5%.

When stubs exist between the wire and the prongs, the topic is conveniently investigated using a numerical technique to solve (5.108) or (5.110). *Morris* and *Foss* [5.155] studied a 1 mm active region of a 5 μm tung-

sten filament with 50 μm copper-plated stubs, where the velocity was 7.5 m/s and $\langle a \rangle = 0.7$. They found that the temperature at the end of the sensor was 13.2 K above ambient and the mean wire temperature was 210 K above ambient. *Li* et al. [5.156] studied longer stubs and different wires, and obtained in some cases a temperature 60 K above ambient for the stubs, close to that measured by *Champagne* et al. [5.152].

Recently, *Löfdahl* et al. [5.157] computed the temperature distribution along a MEMS-fabricated hot-wire sensor. The wire length was 400 μm, its cross section was 2 μm × 2 μm, and the supports were 100 μm long with a cross section of 2 μm × 20 μm. A nonuniform temperature distribution along the supports was clearly observed, with a rise of around 30 K. In addition, the convective heat transfer from the wire was found to constitute about 50–60% of the total heat generated. A conventional hot-wire has a corresponding value of 80–85%.

Fingerson and *Freymuth* [5.50] reported results for cylindrical hot-films. They found, very interestingly, that steady end losses are strongly decreased, roughly by a factor of 16, compared to tungsten wires with the same aspect ratio. Indeed, the main path for heat towards the supports is the conductive metallic film deposited on the quartz core, and this film is very thin, hence precluding heat losses. Cylindrical hot-film sensors can therefore be used with relatively low aspect ratios, on the order of 20–50.

When velocity, temperature or current intensity fluctuations are present, the problem becomes more complex, and a small-perturbation analysis is generally adopted. *Betchov* [5.153] used an analytical approach for velocity and current changes for a CC operated wire. Similarly, *Bremhorst* et al. [5.158] considered velocity, ambient temperature and current fluctuations. *Lord* [5.159] proposed a methodical approach for both a CC- and a CT-operated wire. *Beljaars* [5.160] and *Li* [5.161] considered a CT-operated wire and calculated the new dynamic response using a numerical technique. For velocity fluctuations, a 5% step down is found around 1000 Hz. This frequency is roughly the inverse of the time scale of the stub. *Perry* [5.49] reported differences between velocity fluctuations and temperature fluctuations, as well as between hot and cold wires. More results are given in Sect. 5.2.5.

Spatial Resolution

The velocity fluctuations that occur in a turbulent field vary in space from one point to another. The length scales of these variations cover a continuous spectrum from the largest scales of size L, where kinetic energy is produced, down to the smallest ones, of the size of the Kolmogorov scale η, where kinetic energy is dissipated into heat. A perfect flow analysis would require a very short wire able to respond to the smallest scales of the flow. Instead, a wire has a non-negligible length and responds to an averaged value of the turbulent fluctuations over its length. The wire response will thus depend strongly on its length l as well as on the energy contents at all scales, from L to η.

For free turbulent flows, such as jets or wakes, the scale L is roughly the lateral dimension of the flow, hence the simple relation $l \ll L$ usually holds. On the other hand, η can be very small as is related to L by $\eta/L \simeq \mathrm{Re}_L^{-3/4}$ [5.77]. For example, for a jet with $\overline{U} = 20$ m/s, $u'/\overline{U} \simeq 20\%$ and $L = 0.10$ m, one has $\eta \simeq 0.05$ mm. Obviously, $\eta \ll l$ and the wire drastically smooths out the fine turbulent velocity fluctuations.

For the inner part of wall turbulent flows, L becomes of the order of the wall distance and η approaches L in the viscous sublayer [5.77, 162]. Thus, $l \simeq L \simeq \eta$, and measurements will become erroneous for all structure sizes. Furthermore turbulence is highly anisotropic in the near-wall region.

In what follows, the first part deals with isotropic turbulence where analytical developments can be conducted. This is an important case as local isotropy is a reasonable assumption for many flows at high Reynolds numbers. In addition, some guidelines are obtained regarding the ratios L/l and η/l. In a second part, the wall region with its high anisotropy is considered. This case requires systematic experiments and/or the use of databases provided by direct numerical simulations (DNS) of the flow.

Spatial Resolution of Hot-Wires in Homogeneous Isotropic Turbulence.

Spatial Resolution for a Single Normal Wire in Isotropic Turbulence. For a single wire normal to O_{x_1} and parallel to the x_3 direction, the wire reading attributed to the wire midpoint O' is given by

$$u_1^{\mathrm{m}}(O') = \frac{1}{l} \int_{-l/2}^{l/2} u_1(0, 0, \xi_3)\,\mathrm{d}\xi_3 \,. \tag{5.116}$$

The ξ_i refer to coordinates centered at O' with ξ_3 along the wire. The superscript $()^{\mathrm{m}}$ denotes the mapping due to the wire. The sensitivity coefficient along the wire is assumed to be constant, and the tangential and binormal cooling of the wire is neglected. The mean square value

of u_1^{m} is thus given by the double integral

$$\overline{u_1^{2\mathrm{m}}}(O') = \frac{1}{l^2}\iint\limits_{\mathcal{D}} \overline{u_1(0,0,\xi_3)u_1(0,0,\xi_3')}\,\mathrm{d}\xi_3\,\mathrm{d}\xi_3' \,, \tag{5.117}$$

where $\mathcal{D}$ is the domain $-l/2, \le \xi_3,\ \xi_3' \le l/2$. Equation (5.117) can be transformed by introducing $r_3 = \xi_3' - \xi_3$ and the transverse correlation function $g(r_3)$ between longitudinal velocity fluctuations at two different points on the wire. One of the integrals can then be computed and (5.117) simplifies into

$$\overline{u_1^{2\mathrm{m}}}(O') = \overline{u_1^2}\frac{2}{l^2}\int\limits_0^l (l-r_3)g(r_3)\,\mathrm{d}r_3 \,. \tag{5.118}$$

This result was first obtained by *Dryden* et al. [5.163], who detailed all the cross terms in (5.117), and later by *Frenkiel* [5.164] who directly processed the equation as indicated above. Incidentally the method is similar to that used by *Taylor* in his study of particle diffusion through turbulence [5.77]. Equation (5.118) shows the role of the velocity correlation drop along the wire, even when measuring $\overline{u_1^2}$, which is mostly associated with large structures. This can be illustrated by using a composite correlation function that includes a transverse large scale L_{g} and a transverse Taylor scale λ_{g} connected to L_{g} by $\lambda_{\mathrm{g}}/L_{\mathrm{g}} = (15/\mathrm{Re_L})^{1/2}$ [5.77]. Writing $g(r_3)$ as

$$g(r_3) = \frac{1}{2}\left[\exp\left(-\frac{r_3}{L_{\mathrm{g}}}\right) + \exp\left(-\frac{r_3^2}{\lambda_{\mathrm{g}}^2}\right)\right] \,, \tag{5.119}$$

(5.118) gives $\overline{u_1^2}^{\mathrm{m}}(O')/\overline{u_1^2} = 0.91$, 0.86 and 0.74 for $\lambda_{\mathrm{g}} = 2l, l$ and $l/2$, respectively, when $L_{\mathrm{g}} = 4l$. Clearly the correlation drop over the wire length significantly affects the measurements.

The spatial resolution of a wire is of great concern when measuring spectra. The Fourier decomposition of the turbulent field around the wire midpoint O' is given by

$$u_i(\xi_1,\xi_2,\xi_3) = \iiint \hat{u}_i(k_1,k_2,k_3) \times \exp[i(k_1\xi_1 + k_2\xi_2 + k_3\xi_3)]\,\mathrm{d}k_1\,\mathrm{d}k_2\,\mathrm{d}k_3 \,, \tag{5.120}$$

where k_1, k_2, k_3 are the wavevector components and $\hat{u}_i$ is the Fourier contributions in the sense of generalized functions. The subscript i is $i = 1$, 2 or 3. The Fourier frame has coordinate axes parallel to the space-fixed coordinates O_{x_1,x_2,x_3}. The wire response according to (5.116) becomes

$$\hat{u}_1^{\mathrm{m}}(k_1,k_2,k_3) = \frac{\sin(k_3 l/2)}{k_3 l/2}\hat{u}_1(k_1,k_2,k_3) \tag{5.121}$$

and the spectral tensor $\Phi_{11}^{\mathrm{m}}(k_1,k_2,k_3)$ mapped by the wire is

$$\Phi_{11}^{\mathrm{m}}(k_1,k_2,k_3) = \left[\frac{\sin(k_3 l/2)}{k_3 l/2}\right]^2 \Phi_{11}(k_1,k_2,k_3) \,, \tag{5.122}$$

where $\Phi_{11}(k_1,k_2,k_3)$ represents the exact spectral tensor relative to the longitudinal velocity fluctuations. For isotropic turbulence the general form of the spectral tensor is

$$\Phi_{ij}(k_1,k_2,k_3) = \frac{E(k)}{4\pi k^4}\left(k^2\delta_{ij} - k_i k_j\right) \,, \tag{5.123}$$

where $E(k)$ is the kinetic energy spectrum of turbulence

$$\frac{\overline{u_i^2}}{2} = \int\limits_0^\infty E(k)\,\mathrm{d}k \quad \text{with } k = \left(k_1^2 + k_2^2 + k_3^2\right)^{1/2} \,. \tag{5.124}$$

The one-dimensional spectrum $E_{11}^{\mathrm{m}}(k_1)$ obtained from the response of the wire is the integral of $\Phi_{11}^{\mathrm{m}}(k_1,k_2,k_3)$ over k_2 and k_3

$$E_{11}^{\mathrm{m}}(k_1) = \int\limits_0^\infty\int\limits_0^\infty \left[\frac{\sin(k_3 l/2)}{k_3 l/2}\right]^2 \frac{E(k)}{4\pi k^4}\left(k^2 - k_1^2\right)\mathrm{d}k_2\,\mathrm{d}k_3 \,. \tag{5.125}$$

This is related to the usual power spectral density of a signal recorded in time by the Taylor hypothesis, which links k_1 to the frequency f, $|k_1| = 2\pi f/\overline{U}_1$. Equation (5.125) can be evaluated numerically once $E(k)$ is given, as suggested by *Wyngaard* [5.165]. However, the former approach by *Uberoi* and *Kovasznay* [5.166] sheds light on the physics behind the errors. Indeed, one of the integrals in (5.125) can be analytically computed whatever the form of $E(k)$. This is done by using polar coordinates in the k_2–k_3 plane, with the radius $\sigma = (k_2^2 + k_3^2)^{1/2}$ and the angle ϕ between k_2 and σ, and by introducing y such that $y = k_3 l/2 = \sigma l \sin\phi/2$, hence

$d\phi = dy[(\sigma l/2)^2 - y^2]^{-1/2}$. This yields

$$E_{11}^{m}(k_1) = 4\int_0^\infty \left[\frac{E\left(\sqrt{k_1^2+\sigma^2}\right)}{4\pi\left(k_1^2+\sigma^2\right)^2}\sigma^3 \times \int_0^{\sigma l/2} \left(\frac{\sin y}{y}\right)^2 \frac{dy}{[(\sigma l/2)^2 - y^2]^{1/2}} \right] d\sigma \, . \tag{5.126}$$

Using the new variable $k = (\sigma^2 + k_1^2)^{1/2}$, which gives $k\,dk = \sigma\,d\sigma$ at fixed k_1, (5.126) can be written as

$$E_{11}^{m}(k_1) = \frac{1}{2}\int_{k_1}^\infty W \frac{E(k)}{k^3}\left(k^2 - k_1^2\right) dk \, , \tag{5.127}$$

where the weighting function W is given by

$$W(\sigma\frac{l}{2}) = \frac{\pi}{2}\int_0^{\sigma l/2} \left(\frac{\sin y}{y}\right)^2 \frac{dy}{[(\sigma l/2)^2 - y^2]^{1/2}}$$

$$\text{with } \sigma\frac{l}{2} = \sqrt{\left(k^2 - k_1^2\right)}\frac{l}{2} \, . \tag{5.128}$$

When $W \simeq 1$, (5.127) provides the correct expression of the one-dimensional longitudinal velocity spectrum [5.77]

$$E_{11}(k_1) = \frac{1}{2}\int_{k_1}^\infty \frac{E(k)}{k^3}\left(k^2 - k_1^2\right) dk \, . \tag{5.129}$$

The graph of the weighting function W is drawn in Fig. 5.22. As long as $[\sqrt{(k^2 - k_1^2)}l/2] \leq 1$, $W \simeq 1$ and subsequently $W \simeq [\sqrt{(k^2 - k_1^2)}l/2]^{-1}$. The value at which W starts to be less than one depends on l as well as on k_1 and k. This zone and its border in the k–k_1 plane are sketched in Fig. 5.23. The spectrum $E(k)$ is also indicated on the right of the figure along with the construction which shows the spectral zone of $E(k)$ for which $W < 1$ at given l and k_1.

Wyngaard [5.165] used a Pao spectrum for $E(k)$

$$E(k) = C_K \epsilon^{2/3} k^{-5/3} \exp\left(-\frac{3}{2}C_K(k\eta)^{4/3}\right) \, , \tag{5.130}$$

where C_K is the Kolmogorov constant, $C_K \simeq 1.5$, and ϵ is the dissipation rate of kinetic energy. Figure 5.24 illustrates the errors for a Pao spectrum and for different wire lengths expressed in terms of the Kolmogorov scale η. These values agree with those of Wyngaard when $k_1 l$ is transformed into $k_1\eta$ for the abscissa. However, the Pao spectrum describes only the high-wavenumber contributions. In comparison, the Karman–Saffman–Pao form describes an entire spectrum whose inertial range is given by the $k^{-5/3}$ law [5.77]. Its expression is

$$E(k) = 1.45\frac{u'^2}{k_e}\frac{(k/k_e)^4}{\left[1+(k/k_e)^2\right]^{17/6}} \times \exp\left[-\frac{9}{4}(k\eta)^{4/3}\right] \, . \tag{5.131}$$

The maximum of $E(k)$ occurs at $\sqrt{12/5}k_e$ or below, depending on k_e. Moreover, one can compute the integral length scale L using the classic relation for isotropic turbulence

$$L = \frac{3\pi}{4}\frac{\int_0^\infty k^{-1}E(k)\,dk}{\int_0^\infty E(k)\,dk} \, . \tag{5.132}$$

Hence L, which depends on k_e, is adjustable. For example, L/η takes the values 3.2, 4.5, 7.9, 12.8 and 22, for $k_e\eta = 1, 1/2, 1/5, 1/10, 1/20$, respectively. Graphs comparing the Pao and the Karman–Saffman–Pao spectra are available in *Ewing* et al. [5.167].

Figure 5.25 shows the attenuation that affects $E_{11}^{m}(k_1)$ for a given wire length and different values of the integral length scale L, for a Karman–Saffman–Pao

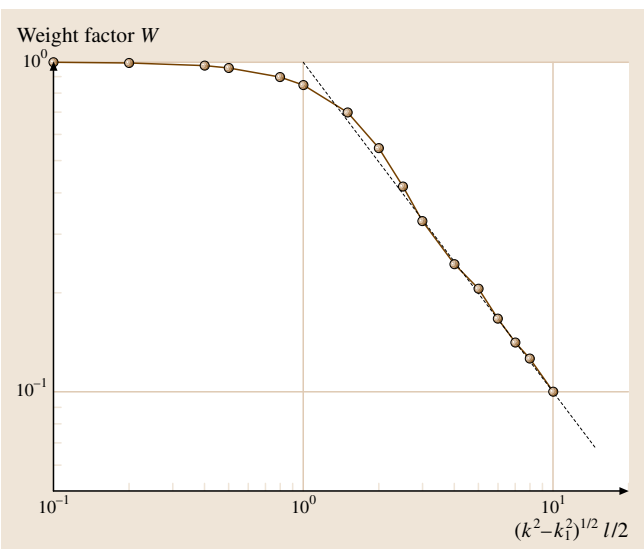

Fig. 5.22 Spatial resolution: the weighting function W for a single wire and isotropic turbulence (5.128)

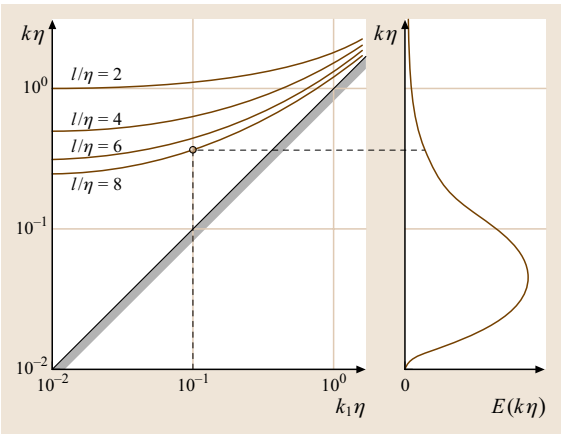

Fig. 5.23 Curves limiting the $W = 1$ and $W < 1$ zones for different wire lengths l. Under each curve $W = 1$ and above each curve $W < 1$. The dotted lines between this plot and $E(k)$ show the highest wavenumber for which $W = 1$ at a selected $k_1\eta$ when $l/\eta = 8$

spectrum. It is clear that the attenuation is large at small values of L.

In this analysis some simplifications were introduced, such as the constant value of the wire sensitivity along its length. Attempts to introduce this additional parameter were conducted by *Elsner* et al. [5.168]. The increased sensitivity in the central section of the wire is beneficial since it reduces the apparent wire length.

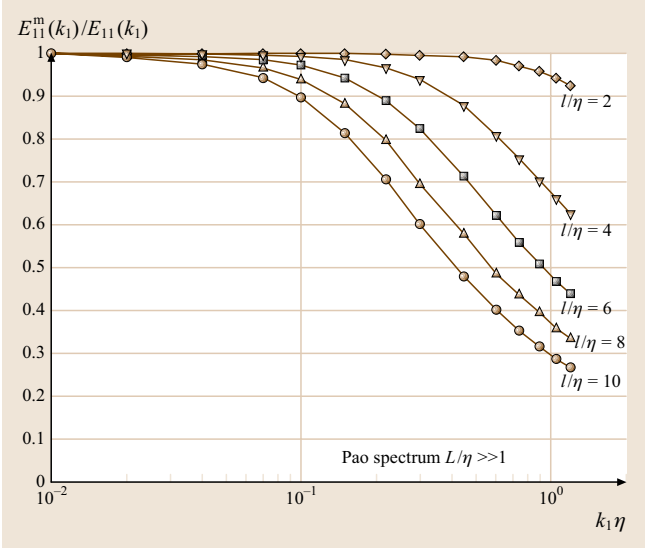

Fig. 5.24 Spatial resolution: the effect of wire length on the one-dimensional velocity spectra, for a Pao spectrum

Spatial Resolution for Two Parallel Wires in Isotropic Turbulence. Two wires of length l, normal to O_{x_1}, parallel to O_{x_3} and separated along O_{x_2} by a distance s_2, are currently used to obtain the derivative $\partial u_1/\partial x_2$. The spatial resolution of this array was considered very early by *Frenkiel* [5.164] who established the errors affecting the rms values and more recently by *Ewing* et al. [5.167] who considered the spatial filtering of the probe taking into account changes in the spectral model.

An analysis similar to that conducted in the section above is again possible. The Fourier decomposition is made relative to the midpoint O' of the array, hence giving for the wires (denoted by I and II)

$$\hat{e}^{\mathrm{m}}_{\mathrm{I}} = \frac{1}{l}\int_{-l/2}^{l/2} \mathrm{d}\xi_3 \iiint \hat{u}_1(k_1,k_2,k_3)\exp\left(-\mathrm{i}k_2\frac{s_2}{2}\right) \times \exp(-\mathrm{i}k_3\xi_3)\,\mathrm{d}k_1\,\mathrm{d}k_2\,\mathrm{d}k_3$$

$$\hat{e}^{\mathrm{m}}_{\mathrm{II}} = \frac{1}{l}\int_{-l/2}^{l/2} \mathrm{d}\xi'_3 \iiint \hat{u}_1(k_1,k_2,k_3)\exp\left(+\mathrm{i}k_2\frac{s_2}{2}\right) \times \exp(-\mathrm{i}k_3\xi'_3)\,\mathrm{d}k_1\,\mathrm{d}k_2\,\mathrm{d}k_3\,. \qquad (5.133)$$

This yields for the one-dimensional spectrum $D^{\mathrm{m}}_{1,2}$ of $(\hat{e}_{\mathrm{I}} - \hat{e}_{\mathrm{II}})/s_2$, which approaches the lateral derivative $\partial u_1/\partial x_2$ of the longitudinal fluctuations

$$D^{\mathrm{m}}_{1,2}(k_1) = \iint \left[\frac{\sin(k_3 l/2)}{k_3 l/2}\right]^2 \left[\frac{\sin(k_2 s_2/2)}{k_2 s_2/2}\right]^2 \times \Phi_{11}(k_1,k_2,k_3)\,\mathrm{d}k_2\,\mathrm{d}k_3\,. \qquad (5.134)$$

A similar result was obtained by *Ewing* et al. [5.167]. The same integration procedure as before yields

$$D^{\mathrm{m}}_{1,2} = \frac{1}{4}\int_{k_1}^{\infty} \mathrm{WD}\frac{E}{k^3}\left(k^2 - k_1^2\right)^2 \mathrm{d}k\,, \qquad (5.135)$$

where the weighting function, denoted by WD, reads

$$\mathrm{WD}\left(\sigma\frac{l}{2}\right) = \frac{4}{\pi}\frac{1}{(\sigma l/2)^2}\int_0^{\sigma l/2}\left[\left(\sigma\frac{l}{2}\right)^2 - y^2\right]^{1/2} \times \left(\frac{\sin y}{y}\right)^2\left(\frac{\sin\Delta}{\Delta}\right)^2 \mathrm{d}y \qquad (5.136)$$

with

$$\sigma\frac{l}{2} = \sqrt{\left(k^2 - k_1^2\right)}\frac{l}{2} \quad \text{and}$$

$$\Delta = \frac{s_2}{l}\left[\left(\sigma\frac{l}{2}\right)^2 - y^2\right]^{1/2}$$

and y as introduced earlier for (5.126). When WD = 1 the exact spectrum is recovered:

$$D_{1,2}(k_1) = \frac{1}{4}\int_{k_1}^{\infty} \frac{E}{k^3}\left(k^2 - k_1^2\right)^2 \mathrm{d}k \,. \tag{5.137}$$

Equation (5.136) takes into account both the length l of the two parallel wires (assumed to be identical) and the lateral separation s_2 of the wires. Figure 5.26 shows the weighting function WD for $s_2/l = 0.5$ and 1.0, and also the case where the wire length is neglected. It is clear that this simplification is not acceptable. Both the l and s_2 effects have to be considered. For further estimates, approximate curves can be used. In the case of Fig. 5.26, with the wire length included, WD may simply be represented by

$$\mathrm{WD} \simeq \exp\left[-0.15\left(\sigma\frac{l}{2}\right)^2\right] \quad \text{for } \frac{s_2}{l} = 0.5$$
$$\mathrm{WD} \simeq \exp\left[-0.24\left(\sigma\frac{l}{2}\right)^{2.7}\right] \quad \text{for } \frac{s_2}{l} = 1.0 \,. \tag{5.138}$$

Figure 5.27 illustrates the errors on $D_{1,2}^{\mathrm{m}}$ for $s_2/l = 0.50$ (a usual case) and $l/\eta = 2-4-6$. A von Karman–Saffman–Pao spectrum is used with $k_\mathrm{e}\eta = 0.10$, hence $L/\eta = 12.8$. One of the main results is that measurements of the lateral derivatives require a correction even at low k_1 values. This point was already stressed by *Wyngaard* [5.169], *Antonia* et al. [5.170], *Antonia* and *Mi* [5.171], and *Ewing* et al. [5.167]. The last of these works provides clear plots of the joint effects of the wire length and separation for a Lin spectrum which rolls off faster than a Pao spectrum in the dissipation range. As practical information, an attenuation of the order of 10% appears on the transverse velocity derivatives when $l/\eta \simeq s_2/\eta \simeq 3$.

Spatial Resolution for an X Array in Isotropic Turbulence. For X-wires, let us consider the case of two identical wires of length l, placed in the $O_{x_1x_2}$ plane, inclined at 45° to O_{x_1}, and separated by s_3 along O_{x_3}. Wire I should respond to $u_1 - u_2$, and wire II to $u_1 + u_2$ (Fig. 5.13). When taking into account the exact geometry of the probe, and making use of the Fourier decomposition, the responses are in reality

$$u_1^{\mathrm{m}} - u_2^{\mathrm{m}} = \iiint \exp\left(+\frac{\mathrm{i}k_3 s_3}{2}\right) \times \frac{1}{l}\int_{-l/2}^{l/2} \exp[\mathrm{i}(k_1\xi_1 + k_2\xi_2)]\,\mathrm{d}s(\hat{u}_1 - \hat{u}_2)\,\mathrm{d}k_1\,\mathrm{d}k_2\,\mathrm{d}k_3 \,,$$
$$u_1^{\mathrm{m}} + u_2^{\mathrm{m}} = \iiint \exp\left(-\frac{\mathrm{i}k_3 s_3}{2}\right) \times \frac{1}{l}\int_{-l/2}^{l/2} \exp\left[\mathrm{i}\left(k_1\xi_1' + k_2\xi_2'\right)\right]\mathrm{d}s'(\hat{u}_1 + \hat{u}_2)\,\mathrm{d}k_1\,\mathrm{d}k_2\,\mathrm{d}k_3 \tag{5.139}$$

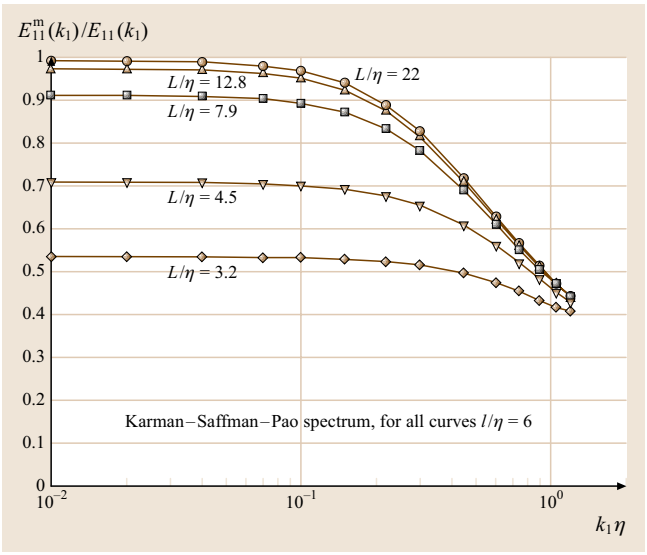

Fig. 5.25 Spatial resolution: the effect of the integral length scale L included in a Karman–Saffman–Pao spectrum on the one-dimensional velocity spectra, for a wire of fixed length

or, after integration by $\mathrm{d}s$ and $\mathrm{d}s'$ along each wire,

$$u_1^{\mathrm{m}} - u_2^{\mathrm{m}} = \iiint \left(\hat{u}_1 - \hat{u}_2\right)\frac{\sin\left[(k_1+k_2)l/(2\sqrt{2})\right]}{(k_1+k_2)l/(2\sqrt{2})} \times \exp\left(+\frac{\mathrm{i}k_3 s_3}{2}\right)\mathrm{d}k_1\,\mathrm{d}k_2\,\mathrm{d}k_3 \,,$$
$$u_1^{\mathrm{m}} + u_2^{\mathrm{m}} = \iiint \left(\hat{u}_1 + \hat{u}_2\right)\frac{\sin\left[(k_1-k_2)l/(2\sqrt{2})\right]}{(k_1-k_2)l/(2\sqrt{2})} \times \exp\left(-\frac{\mathrm{i}k_3 s_3}{2}\right)\mathrm{d}k_1\,\mathrm{d}k_2\,\mathrm{d}k_3 \,. \tag{5.140}$$

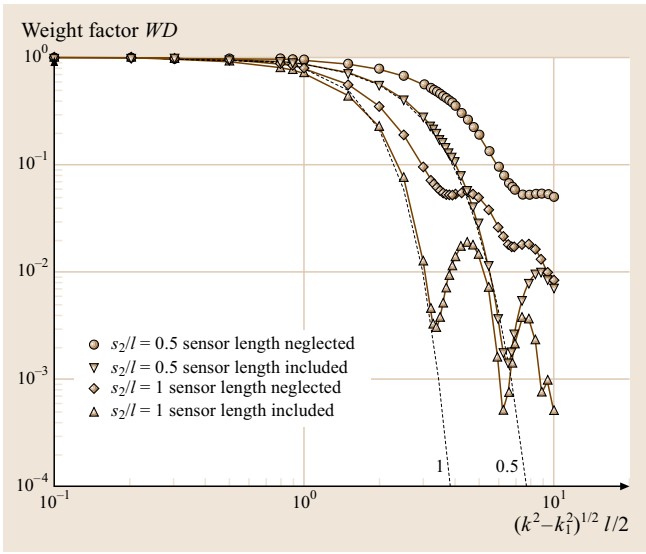

Fig. 5.26 Spatial resolution: the weighting function WD for two parallel wires and isotropic turbulence (5.136)

As above, spatial averaging along the wires reduce the readings by roughly the same amount even if different wavevectors enter into the wire responses: $k_1 + k_2$ for the first wire and $k_1 - k_2$ for the second. In addition, there is a mutual effect between u_1 and u_2. This effect is most easily shown when neglecting the wire length effect. Indeed, in Fourier space, the sum and difference of

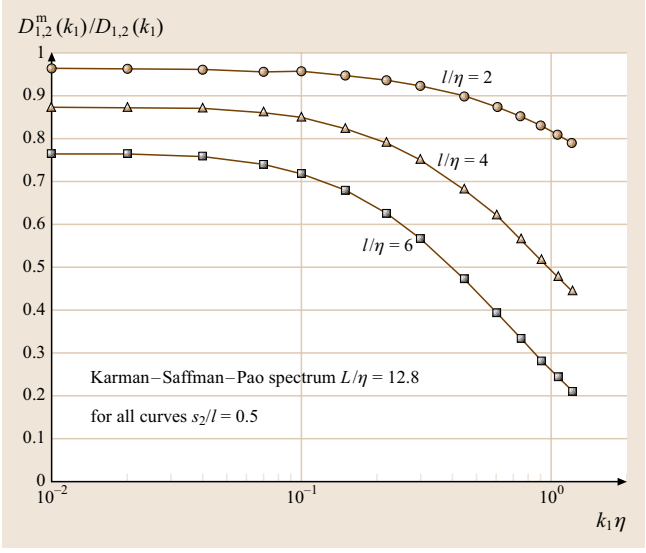

Fig. 5.27 Effect of wire length and wire separation on the one-dimensional $\partial u_1/\partial x_2$ spectra

(5.140) yields

$$\hat{u}_1^{\mathrm{m}} = \hat{u}_1 \cos\left(\frac{k_3 s_3}{2}\right) - \mathrm{i}\hat{u}_2 \sin\left(\frac{k_3 s_3}{2}\right) ,$$
$$\hat{u}_2^{\mathrm{m}} = \hat{u}_2 \cos\left(\frac{k_3 s_3}{2}\right) - \mathrm{i}\hat{u}_1 \sin\left(\frac{k_3 s_3}{2}\right) , \qquad (5.141)$$

which clearly shows that $\hat{u}_2$ enters into $\hat{u}_1^{\mathrm{m}}$ and that $\hat{u}_1$ enters into $\hat{u}_2^{\mathrm{m}}$. The measured spectra are therefore

$$\Phi_{11}^{\mathrm{m}} = \cos^2\left(\frac{k_3 s_3}{2}\right)\Phi_{11} + \sin^2\left(\frac{k_3 s_3}{2}\right)\Phi_{22}$$
$$\Phi_{22}^{\mathrm{m}} = \cos^2\left(\frac{k_3 s_3}{2}\right)\Phi_{22} + \sin^2\left(\frac{k_3 s_3}{2}\right)\Phi_{11} . \qquad (5.142)$$

Numerical 2-D integration is here required to treat different Φ_{ij} forms. *Wyngaard* [5.165] used a Pao spectrum and an X-probe with $l/\eta = 1, 3$ and 10 and $s_3/\eta = 0.5$ and 1. He found that the lateral component u_2' is hardly affected by the wire separation and that the longitudinal component u_1' can be increased for small wire separations. It therefore appears that accurate measurements of the longitudinal component would best be made using a single wire, reserving an X-array for the lateral component.

Some Experimental Results. Many experiments have been conducted in grid turbulence or in flows with characteristics close to isotropy, such as jets, far wakes, central zones of channel/pipe flows, and upper parts of the atmospheric boundary layer. The objective was either to improve the probe design or to correct measurements when inappropriate probes were used.

Wyngaard [5.165] conducted experiments in atmospheric turbulence and also in a curved mixing layer, with $\eta \simeq 0.06$ mm and $l/\eta = 2, 4$ and 6. The corrections he developed for the isotropic case appear to provide reasonable support for his data analysis.

Derksen and *Azad* [5.67] found that the isotropic correction of Wyngaard was also satisfactory for measurements in a pipe flow at $x_2/R = 0.10$ from the wall, $x_2^+ = 150$, with around 15 different wires with $d = 3.6$–$5.4\,\mu$m, $l = 0.3$–2.8 mm, and $l/\eta = 3$–20.

Elsner et al. [5.168] reported systematic measurements in grid turbulence for spectra and kinetic-energy dissipation. In those experiments $\eta = 0.25$ mm, and $l = 0.5$–3.9 mm. The mean dissipation rate for longitudinal fluctuations ϵ_1 was equivalently obtained from the second moment of the one-dimensional spectra and from the time derivative of the longitudinal velocity fluctuations. Some typical errors are -30% if $l/\eta = 10$ and

-10% if $l/\eta = 2$. A convenient linear regression line of ϵ_l versus the wire length was obtained, giving the true turbulent energy dissipation at an extrapolated zero wire length.

Zhou et al. [5.173] conducted extensive investigations of the kinetic and thermal dissipation rates in grid turbulence, with $\eta = 0.32$–0.73 mm. Several configurations of X-wires and pairs of parallel wires were used with $l = 0.5$ mm, $l/d \simeq 200$, s_2/η and s_3/η in the range 2.8–7.8. After correction, the theoretical value $\overline{(\partial u_1/\partial x_2)^2} = 2/15$, with all terms normalized by the Kolmogorov scales, was recovered except for wire separations smaller than 3η, where aerodynamic and thermal interferences were claimed to be significant.

Antonia and *Mi* [5.171] considered a heated jet and also revisited the case of atmospheric turbulence studied by *Wyngaard* [5.165]. The corrections implying isotropy appeared to provide reasonable support for the analysis.

Browne et al. [5.174] considered the far wake of a cylinder and used an X wire made of two wires whose separation can be accurately set and measured. The conditions were $\eta = 0.45$ mm, $l = 0.75$ mm, and $s_3/\eta = 0.38$–7.2. They observed that $\overline{u_1^2}$ decreases and that $\overline{u_2^2}$ increases when the wire separation increases: a result which differs from *Wyngaard* [5.165]. However, in that type of flow, isotropy is only approached at high wavenumbers as pointed out by *Antonia* et al. [5.170]. The large-scale structures of the flow exhibit strong organization which could affect the results.

Spatial Resolution in Anisotropic Turbulence. Analytical developments are obviously not possible in highly anisotropic turbulent fields, such as the wall region of turbulent boundary layers. Systematic experimental investigations or computer simulations are therefore needed. An advantage of computer simulations is that the cooling of the wire by the three velocity components can be included.

Ligrani and *Bradshaw* [5.175] reported extensive measurements in the region $x_2^+ = 5$–100 in a boundary layer whose freestream velocity was 7.3 m/s with wire diameters in the range $d = 0.62$–$5\,\mu$m with $l/d = 260$–600 and $l^+ = 3.3$–60. The superscript '+' denotes normalization by the wall variables, i. e., friction velocity u_τ and kinematic viscosity ν. The greatest effect concerns the maximum value of $(\overline{u_1^2})^{1/2}/u_\tau$ which was found to decrease from 2.8 to 2.0 when the wire length increased. Skewness and flatness factors were less affected. The probability density function of the longitudinal velocity was also investigated; a slight decrease was observed at large negative u_1 values for long wires. A stronger effect was noted by *Johansson* and *Alfredsson* [5.176] in a channel flow. Large negative $u_1(t)$ amplitudes correspond to ejection events that are naturally at small scales and hence are strongly affected by spatial averaging.

Klewicki and *Falco* [5.177] made an extensive compilation of previous works regarding the statistics of small-scale structures in boundary layers. In addition, they performed measurements using a probe for which the separation s_2 between the two parallel sensors could be varied systematically. In particular, the variance of $\partial u_1/\partial x_2$ in the buffer layer, at $x_2^+ = 38$ or 53, was found to be attenuated by only about 5% for $s_2/\eta \simeq 3$ but the attenuation increased rapidly to about 35% for $s_2/\eta \simeq 6$. In these experiments $\overline{U}_1 = 0.60$–23 m/s in the freestream and the Reynolds number based on the momentum thickness was $R_\theta = 1010$–4850.

Moin and *Spalart* [5.178] launched the use of direct numerical simulation (DNS) databases to evaluate X-wire responses. These early computations concerned a channel flow with $\mathrm{Re} = 3300$ and $\mathrm{Re}_\mathrm{h}^+ = 180$. However, only one wire separation, $s_3/\eta = 1$, was used and wires were assimilated to points.

Suzuki and *Kasagi* [5.172] extended the computations of Moin and Spalart to different types of probes. In these computations $\mathrm{Re}_\mathrm{h}^+ = 150$, $l^+ = \sqrt{2}(1-10)$, and $s_3^+ = 1-10$. A single wire placed near the maximum streamwise turbulent intensity was found to give a ra-

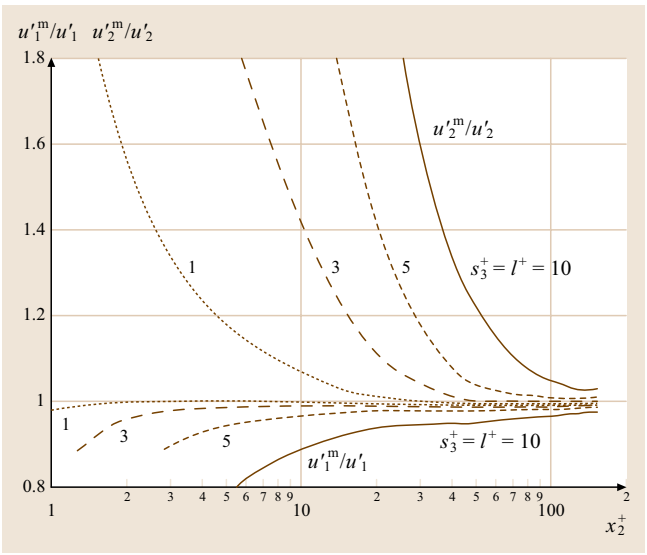

Fig. 5.28 Spatial resolution of an X-wire close to a wall: errors on the rms values of u_1' and u_2' (after *Suzuki* and *Kasagi* [5.172])

tio between the measured and exact value of 0.95 for $l^+ = 10$, and 0.90 for $l^+ = 20$. Figure 5.28 reports the corresponding ratios for u'_1 and u'_2 for conventional X-probes (wires inclined at ±45°) and several l^+ and s_3^+ values. The u'_2 component appears to be much more affected than u'_1, which is probably a strong anisotropy effect as this tendency is the opposite of that reported by Wyngaard.

Antonia et al. [5.179, 180] analyzed the lateral velocity derivatives obtained with two parallel wires in a channel flow, both experimentally and numerically. The conditions were $\mathrm{Re_h} = 3300$, $\mathrm{Re_h^+} \simeq 180$, $d = 1.3\,\mu\mathrm{m}$, $l = 0.3\,\mathrm{mm}$, $l/d = 230$, and $\eta = 0.2\,\mathrm{mm}$ at $x_2^+ = 2$. In the wall region, for x_2^+ in the range 5–40, only a wire spacing of $s_3^+ = 2$–4 was found to be adequate.

Close to walls, many other characteristics are also of great interest such as the components of the vorticity vector. Such investigations require the use of special probes made of between four and nine sensors. Their responses are extensively analyzed by *Wallace* and *Foss* [5.81] and later on in this Handbook. In addition to the spatial resolution regarding the velocity fluctuations in the probe volume, the velocity gradient effect, and the aerodynamic perturbations have also to be considered.

Finally, the additional cooling of sensors by nearby walls is also an important topic. It is considered later in this Handbook.

5.2.3 Anemometer Electronics

Constant-Current Anemometer (CCA)

Historically, CCA was successfully used as early as 1920 to investigate wind velocity and wind direction in the atmosphere by *Huguenard* et al. [5.181] and *Simmons* and *Bailey* [5.182]. Its fast response compared to wind vanes or cup anemometers was a strong motivation for its adoption. Flows through pipes or orifices were also attempted by *King* [5.183], *Thomas* [5.184], and *Richardson* [5.185]. The use of several wires simultaneously was of great benefit to treat large directional changes and even flow reversals. The extension to flows with rapid time changes was made possible by the pioneering work of *Dryden* and *Kuethe* [5.186] who showed that an *RC* circuit could be incorporated into the amplifier to compensate for the thermal inertia of the wire.

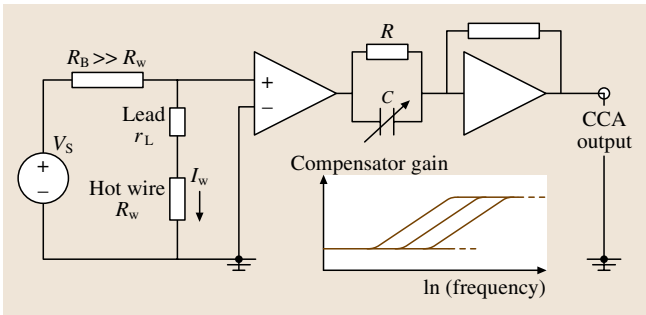

Fig. 5.29 Block diagram of a constant-current anemometer (CCA). *RC* is the adjustable compensating circuit integrated in a high-gain amplifier

The simplest circuit for a CCA is shown in Fig. 5.29. *VS* is a stable direct-current (DC) low-noise voltage source, and R_B a large ballast resistor that keeps the current I_w in the wire fairly constant despite changes in the wire resistance. An adjustable resistor placed in series with R_B permits the adjustment of I_w, and the potential drop across a precision resistor also in series with the hot-wire yields I_w. A more-functional circuit places the wire in a Wheatstone bridge. The bridge allows the measurement of the resistance of the cold wire, adjustment of the wire overheat, and also, possibly, the correction of the cable inductance by adding an appropriate capacitance or inductance in a specific arm of the bridge, similar to a CTA. A regulated constant-current supply can also be used in place of a voltage source; very stable ones are commercially available.

The amplifier, which has to be high gain and ultralow noise, is always made of several stages, and the *RC* compensating circuit with a gain increasing with frequency often covers two stages. The frequency responses offered by commercial CCA systems can reach 300 kHz. Some higher-frequency responses, up to 500 kHz, have recently been reported by *Repkov* et al. [5.187]. These authors also added to their circuit a microprocessor which permits measurements in a short-time-duration wind tunnel with protection against wire burn-out.

The compensated CCA output signal $e'^{\star}(t)$ is retrieved from the measured signal $e'(t)$ according to (5.102)

$$e'^{\star}(t) = e'(t) + M_w^{\mathrm{CCA}} \frac{\mathrm{d}e'}{\mathrm{d}t} \quad \text{with } M_w^{\mathrm{CCA}} = M_w^{\mathrm{CC}} \,. \tag{5.143}$$

The adjustment of M_w^{CCA} is done in situ, using a square-wave-intensity signal superposed onto the heating current. *Dryden* and *Kuethe* [5.186] and more recently *Perry* [5.49] have shown that step changes in U, T_a, or I_w are equivalent as long as the fluctuations stay small. The correct adjustment is obtained when a square output is restored. Multiple time records and

phase averaging greatly improve the accuracy of the adjustment.

The static sensitivity coefficients S^{CCA} expressed at the CCA output are such that

$$\left(\frac{e'}{\overline{E}}\right)_{\mathrm{CCA}} = S^{\mathrm{CCA}}_{U_1}\frac{u'_1}{\overline{U}_1} \quad \text{and}$$
$$\left(\frac{e'}{\overline{E}}\right)_{\mathrm{CCA}} = S^{\mathrm{CCA}}_{T_\mathrm{a}}\frac{\theta'_\mathrm{a}}{\overline{T}_\mathrm{a}} \,. \tag{5.144}$$

These S^{CCA} are easily connected to the wire sensitivity coefficients S^{CC} defined in Sect. 5.2.2. For a CCA working without a bridge, there is the simple relation

$$S^{\mathrm{CCA}} = S^{\mathrm{CC}} \,. \tag{5.145}$$

For a CCA involving a bridge, with R_1 in the top arm on the side of the hot-wire, one has

$$S^{\mathrm{CCA}} = S^{\mathrm{CC}}\frac{\overline{R}_\mathrm{w}}{\overline{R}_\mathrm{w} + r_\mathrm{L} + R_1} \,. \tag{5.146}$$

The electronic noise of a CCA circuit is easy to estimate when the wire is directly connected to the amplifier input through a cable lead of resistance r_L. Neglecting the stray noise picked up through the inductance and capacity of the wire and its lead (twisted cables are advised, as well as separate circuits for the wire heating and the transmitted wire signal), the noise sources are the thermal noise of the wire and lead, and the input voltage noise of the amplifier. The signal-to-noise ratio

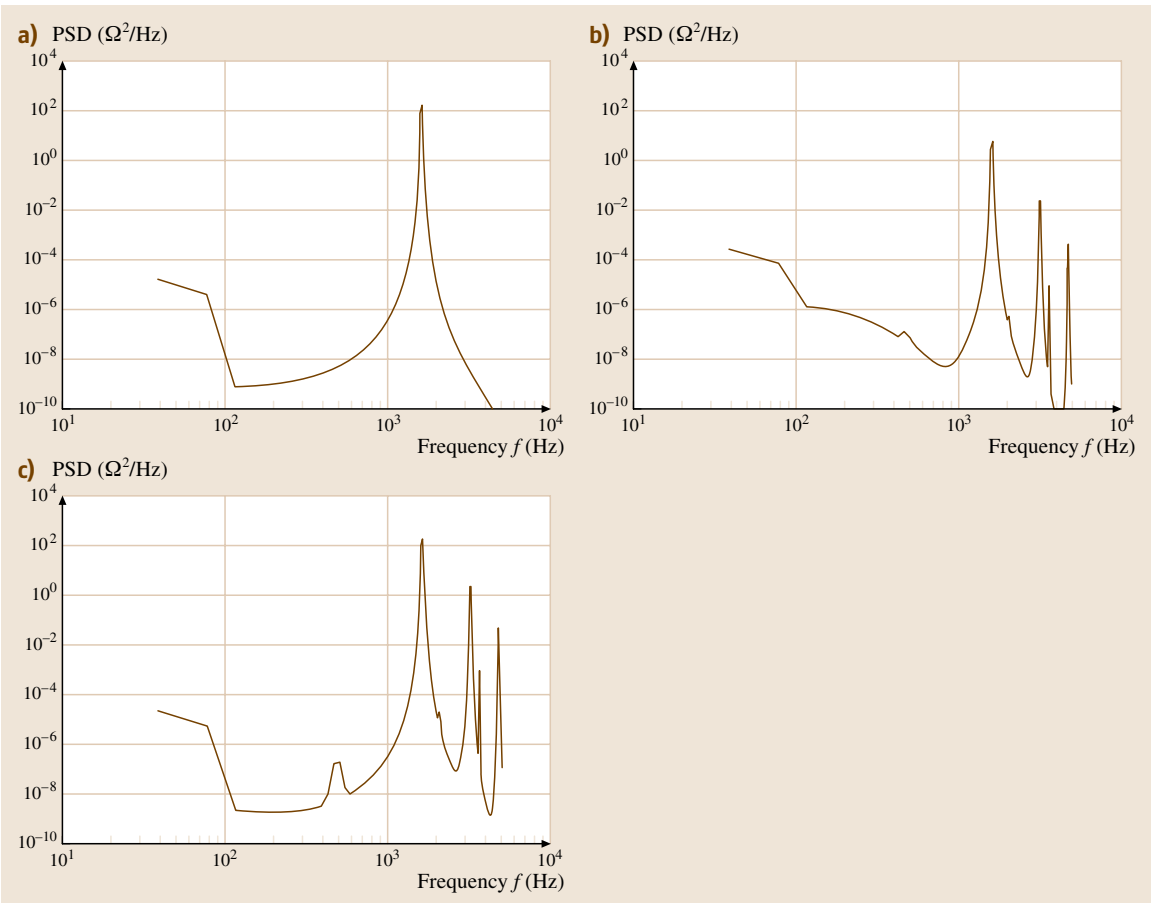

Fig. 5.30a–c Higher harmonics generated by parametric excitation in a CCA: **(a)** PSD of the input signal $R^\star_\mathrm{w}$, **(b)** PSD of the solution R_w of (5.100), **(c)** PSD of the linearly corrected CCA output r'_w based on (5.102). $R^\star_\mathrm{w} = 10 + \sqrt{2}\cos\omega t$, $M_\mathrm{w}\omega = 5$, skewness factors are 0.0002, 0.0200, and -0.2724 for $R^\star_\mathrm{w}$, R_w, and r'_w, respectively

(SNR) at frequency f is therefore of the form

$$\mathrm{SNR}|^{\mathrm{CCA}} = \frac{S_{\mathrm{w}}^{\mathrm{CCA}}}{2\pi f M_{\mathrm{w}}^{\mathrm{CCA}}} \frac{\overline{E}}{\hat{e}_{\mathrm{n}}} \frac{\hat{u}_1}{\overline{U}_1} , \qquad (5.147)$$

where $\hat{e}_{\mathrm{n}}$ is the total resulting noise in $\mathrm{V}/\sqrt{\mathrm{Hz}}$, as usual in noise analysis, and $\hat{u}_1$ the turbulence spectrum in $\mathrm{ms}^{-1}/\sqrt{\mathrm{Hz}}$. In $\hat{e}_{\mathrm{n}}$, the most important term is the amplifier noise.

If the wire is placed in a Wheatstone bridge, the SNR estimate is more complicated because it involves all the resistances constituting the bridge. *Kidron* [5.188] and *Freymuth* [5.189] did the complete analysis, and managed to show that a CCA circuit behaves similarly to a CTA circuit. Expression (5.157), which is indicated later on in Sect. 5.2.3, can then be used. *Bestion* et al. [5.190] made systematic comparisons for supersonic flows and observed no significant differences between $\mathrm{SNR}|^{\mathrm{CCA}}$ and $\mathrm{SNR}|^{\mathrm{CTA}}$.

Finally, when the incident fluctuations are large, the higher harmonics generated by parametric excitation at the wire level (Sect. 5.2.2), are not at all suppressed by the compensating circuit. Even worse, they are amplified as if they were true turbulence. Figure 5.30 represents the power spectral density (PSD), for the input signal $R_{\mathrm{w}}^{\star}$, for the solution R_{w} of (5.100), and for the CCA output signal $Q(t)$ corrected by applying the linear thermal lag correction defined by (5.143). In that assumed corrected CCA output $Q(t)$, the second harmonic is of the order of 10^{-2} relative to the fundamental, and overly large negative values on the velocity skewness appear, of the order of -0.27 for amplitude fluctuations of 15% and $M_{\mathrm{w}}^{\mathrm{CCA}}\omega \simeq 5$. These results agree with those obtained by *Comte-Bellot* and *Schon* [5.151] with an analog computer.

Bremhorst and *Graham* [5.191] also considered the case of large velocity changes. However, their approach remained based on a first-order system, only taking into account the $M_{\mathrm{w}}^{\mathrm{CCA}}$ changes with the velocity. Second and higher harmonics could not therefore be observed in their analysis.

Constant-Temperature Anemometer (CTA)

A typical CTA circuit is shown in Fig. 5.31. The two vital elements are the Wheatstone bridge and the feedback amplifier. The sensor is placed in one arm of the bridge. The voltage difference across the bridge is a measure of the change in wire resistance with the incident velocity or with the flow temperature, and it constitutes the input to the operational amplifier. The designed amplifier has an output current feedback to the top of the bridge, and hence to the wire to restore its resistance. For example, the top bridge voltage E increases when the flow velocity increases or when the fluid temperature decreases, hence increasing the current intensity in the wire. The feedback amplifier usually consists of several stages of voltage gain and a unity-gain current booster.

The resistance ratio R_2/R_1 is called the bridge ratio. It is often chosen larger than one, e.g., 5, 10, or 20. The amplifier current is thus mainly introduced into the active arm containing the wire rather than into the opposite passive arm. Furthermore, the top resistance R_1 is often chosen to be large, $R_1 = 10\,\Omega$, $20\,\Omega$, or even $50\,\Omega$, to increase the top bridge voltage E and its fluctuations, and to ease their acquisition. However, for any asymmetric bridge the Wheatstone bridge accuracy is decreased, as explained in basic textbooks [5.192]. The wire overheat is set up by adjusting resistance R_3.

In principle, since R_{w} is maintained constant, the thermal lag of the wire is automatically suppressed (5.39). Such an advantage was recognized as very useful at an early stage, by *Ziegler* in 1934 [5.193], *Weske* in 1943 [5.194], or *Ossofsky* in 1948 [5.195]. However, it was not until the mid 1960s that reliable CTA devices became available with the development of high-

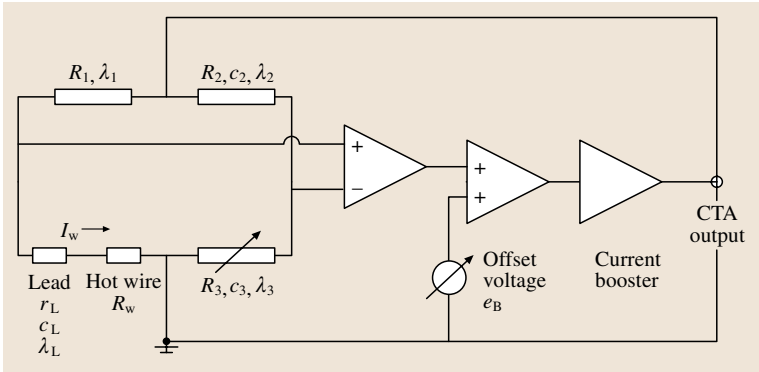

Fig. 5.31 Block diagram of a constant-temperature anemometer (CTA). The wire overheat is adjusted by modifying resistance R_3. The adjustable capacities and inductances placed in arms 2 and 3 of the bridge, c_2, λ_2, c_3, λ_3, and the offset voltage e_{B}, make the CTA stable

quality solid-state operational amplifiers. Many circuits were then suggested, some even without a Wheatstone bridge [5.196], and many aspects of the control theory involved in the CTA response were analyzed over the years by *Freymuth* in 1967 [5.197], *Davis* and *Davies* in 1968 [5.198], *Perry* and *Morrison* in 1971 [5.199], *Wood* in 1975 [5.200], *Freymuth* again in 1977 and 1998 [5.201, 202], and *Watmuff* in 1995 [5.203]. Possibilities offered by recent computer-controlled CTA are described by *Fingerson* [5.204] or *Jorgensen* [5.205].

Let us now analyze the CTA performance in more detail. Concerning the frequency response, it is first rewarding to examine the case of an ideal CT anemometer, without any additional circuits, as done by *Hinze* [5.47]. This is just a first-order system approach. From the change of the wire resistance, the error signal to the amplifier input can be computed taking into account the time constant of the wire and the amplifier response involving a closed loop. This yields for the time constant of the wire under CT operation

$$M_{\mathrm{w}}^{\mathrm{CTA}} = \frac{M_{\mathrm{w}}}{1+2G\overline{a}_{\mathrm{w}}\overline{R}_{\mathrm{w}}g_{\mathrm{tr}}}\,, \tag{5.148}$$

where g_{tr} is the transconductance of the bridge, G the amplifier gain, M_{w} the time constant of the wire alone, and $\overline{a}_{\mathrm{w}}$ the overheat ratio. *Comte-Bellot* [5.54,206] computed a similar expression, which shows the roles of the resistances R_1, R_2, and R_3 of the bridge

$$M_{\mathrm{w}}^{\mathrm{CTA}} = \frac{M_{\mathrm{w}}}{1+2G\overline{a}_{\mathrm{w}}\frac{\overline{R}_{\mathrm{w}}}{\overline{R}_{\mathrm{w}}+R_1}\frac{R_2}{R_2+R_3}}\,. \tag{5.149}$$

The time constant in constant-temperature operation is therefore much smaller than that in constant-current operation, as G can be on the order of 1000. However, the wire overheat ratio $\overline{a}_{\mathrm{w}}$ has to be sufficiently high, and a value of $\overline{a}_{\mathrm{w}} = 0.80$ is often advised by the manufacturers. At low overheat ratios, when $\overline{a}_{\mathrm{w}} \to 0$, the time constant of the anemometer system approaches that of the wire M_{w}, and this precludes measurements as no compensation is provided by the CTA circuit. Expression (5.149) also shows that a symmetric bridge yields the smallest possible value for $M_{\mathrm{w}}^{\mathrm{CTA}}$, thus permitting the best frequency response.

A realistic analysis of the CTA must, of course, go beyond that of a first-order system. The reason is that many parameters play a role in the dynamic response, and all are essential to the CTA stability and high-frequency response. It is useful to list them:

1. the time response of the hot-wire of the form $(1+M_{\mathrm{w}}s)^{-1}$ with a Laplace transform ($s = \mathrm{i}\omega$); this supposes small-amplitude fluctuations [5.45] (Sect. 5.2.2),
2. the resistance of the hot-wire prongs, around 0.50 Ω, and the resistance r_{L} of the connecting cable, around 0.20 Ω/m,
3. the inductance of the coaxial connecting cable λ_{L}, around 0.40 μH/m,
4. the capacitance of the coaxial connecting cable c_{L}, around 60 pF/m,
5. the bridge resistances,
6. the trim inductors introduced in the bridge,
7. the trim capacitors introduced in the bridge,
8. the roll-off frequency and gain of the feedback amplifiers, the gain can be frequency dependent,
9. the offset value applied to the last feedback amplifier.

Let us remark that λ_{L} has a greater effect than c_{L}, as $1+\mathrm{i}\omega\lambda_{\mathrm{L}}/R_{\mathrm{w}} \simeq 1+0.3\mathrm{i}$ whereas $1-\mathrm{i}\omega R_{\mathrm{w}}c_{\mathrm{L}} \simeq 1.00$, for a 5 m-long cable and a frequency of 100 kHz, using the values indicated in 3 and 4 in the above list. Furthermore, λ_{L} can be balanced out by a capacitor c_2 placed in parallel to resistor R_2 in the opposite arm of the bridge, and such that $c_2 = \lambda_{\mathrm{L}}/R_1R_3$ according to the alternating-current (AC) equilibrium condition for a Maxwell bridge [5.192]. Another possibility would be to place an inductance in series with the top resistance R_1, then $\lambda_1 = R_2\lambda_{\mathrm{L}}/R_3$, or in series with resistance R_3, then $\lambda_3 = R_2\lambda_{\mathrm{L}}/R_1$. Trim capacitors are easier to manufacture, so that the solution using c_2 is usually preferred.

Freymuth [5.197, 201, 207, 208] made significant contributions taking into account points 1, 7, 8 and 9. For small-amplitude fluctuations, he showed that a CTA is well represented by a third-order system with a differential equation of the form

$$\begin{aligned}&\frac{M_{\mathrm{w}}M''}{G}\frac{\mathrm{d}^3e'}{\mathrm{d}t^3} + \frac{M_{\mathrm{w}}}{G}\left(M' - G\frac{\overline{R}_{\mathrm{w}}}{\overline{R}_{\mathrm{w}}+R_1}R_2c_2\right)\frac{\mathrm{d}^2e'}{\mathrm{d}t^2}\\ &\quad + \frac{M_{\mathrm{w}}}{G}\frac{e_{\mathrm{B}}}{\overline{E}}\frac{\mathrm{d}e'}{\mathrm{d}t} + e'\\ &= s_{\mathrm{u}}u' + s_{\mathrm{sq}}sq'\,,\end{aligned} \tag{5.150}$$

where M_{w} is the time constant of the wire, M' and M'' are time constants that characterize the frequency response of the feedback circuit (M' in s, and M'' in s^2), G is the amplifier gain, e_{B} is the offset voltage, c_2 is a capacitance in the arm opposite to the wire, s_{u} is the dimensional sensitivity to a velocity change, and s_{sq} is the sensitivity to a square wave applied to the bridge (the derivative of sq is also involved), e' is the voltage fluctuation at the top of the bridge, $\overline{E}$ is the mean voltage at the top of the

bridge, and t is the time. Let us recall that a first-order system exhibits an exponential decay, a second-order system an oscillating decay, and a third-order system both types of decay simultaneously.

For a given amplifier and a given wire working in fixed conditions, M', M'', and M_w are fixed. Therefore, the only way to adjust the CTA dynamic response is to act on G, e_B, and c_2. In particular e_B, which is around 5–10 mV, is present in a damping term. *It is also advisable to make all adjustments at the expected maximum flow velocity. This is because M_w decreases when U increases, hence the damping term in front of de'/dt decreases, and the system may oscillate.*

Freymuth [5.201] also analyzed the CTA response for a sinusoidal forcing velocity and for an electronic step voltage and showed that the best optimized cut-off frequency, f_c is given by

$$f_c = \frac{1}{2\pi}\left(\frac{G}{M'' M_w}\right)^{1/3} \qquad (5.151)$$

and that the transient response to an electronic step voltage should present a high-amplitude pulse followed by an undershoot without oscillation. In practice, this electronic test is performed by applying a square-wave signal to the bridge; Fig. 5.32 illustrates this response for a wire and a film. Recently, *Khoo* et al. [5.209] and *Teo* et al. [5.210] reported many results for wires and films, using either voltage or velocity perturbations.

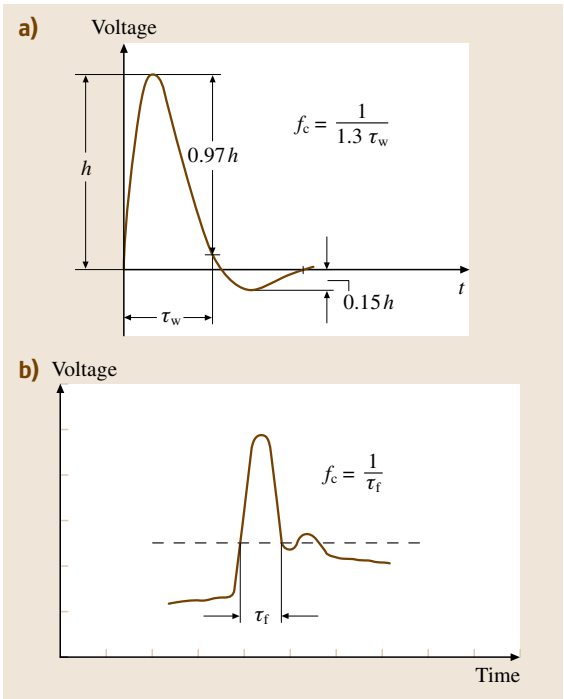

Fig. 5.32a,b The square-wave test response of a hot-wire probe **(a)** and hot-film probe **(b)** operated by a CTA (after *Bruun* [5.52])

The time constants M' and M'' in (5.150) were interpreted by *Freymuth* [5.211] in terms of a two-stage feedback amplifier with each stage characterized by a first-order frequency response. The gains of these stages were denoted by G_1 and G_2, their first-order time constants by M_1 and M_2, and their gain–bandwidth products were such that $\mathrm{GBP}_1 = G_1/2\pi M_1$ and $\mathrm{GBP}_2 = G_2/2\pi M_2$. Then, $G = G_1 G_2$, $M' = M_1 + M_2$, and $M'' = M_1.M_2$, and f_c becomes

$$f_c = (f_w \mathrm{GBP}_1 \mathrm{GBP}_2)^{1/3}\,. \qquad (5.152)$$

For a wire frequency f_w that is usually of the order of 100 Hz and gain–bandwidth products of the order of 3 MHz, $f_c \simeq 100$ kHz. This is quite close to the maximum CTA frequency announced by manufacturers. The offset voltage e_B is also clearly applied to the second amplifier.

Watmuff [5.203] performed a systematic investigation of all points 1 to 9. Using Laplace transforms, he started with a model deliberately of higher order than is anticipated, with a transfer function of the form

$$P(s) = P_7 s^7 + P_6 s^6 + P_5 s^5 + P_4 s^4 + P_3 s^3 + P_2 s^2 + P_1 s + P_0\,. \qquad (5.153)$$

He used a compact matrix notation and conducted computer simulations to explore the behavior of representative configurations. The polynomial form for the poles of (5.153) is really seventh order when all points 1 to 9 are taken into account. It becomes fifth order when points 4 and 7 are not taken into account. Interestingly, Watmuff observed that his fifth-order system has only three dominant modes, a pair of complex poles and a simple one. The two higher simple modes remain well behaved and are beyond the frequency range of interest. This aspect confirms therefore *Freymuth*'s results [5.201, 202].

Watmuff [5.203] also provided a good understanding of the square wave test used to optimize a CTA. In particular, he showed that a satisfactory response cannot be obtained by adjusting the offset when the cable inductance is too high. Another interesting result concerns the subminiature wires that often lead to CTA instabilities.

Weiss et al. [5.212] suggested the use of the Fourier transform of the square-wave response to obtain the amplitude of the transfer function of the CTA, and to correct

the measured spectra during postprocessing. Figure 5.33 illustrates how the frequency response can be substantially extended, up to around 300 kHz. Even the case of small overheat ratios can be treated satisfactorily. The technique was used by *Weiss* et al. [5.141, 213] in a Mach 2.5 boundary layer and allowed the corrected CTA spectra to agree with the CCA and CVA measurements. This was not the case in previous investigations [5.127, 214].

The sensitivity coefficients S^{CTA} expressed at the CTA output (top of the bridge) are defined by

$$\left(\frac{e'}{\overline{E}}\right)_{\mathrm{CTA}} = S^{\mathrm{CTA}}_{U_1}\frac{u'_1}{\overline{U}_1} \quad \text{and} \quad \left(\frac{e'}{\overline{E}}\right)_{\mathrm{CTA}} = S^{\mathrm{CTA}}_{T_a}\frac{\theta'_a}{\overline{T}_a}\,. \tag{5.154}$$

for velocity or temperature fluctuations. They are such that

$$S^{\mathrm{CT}A} = S^{\mathrm{CT}} \tag{5.155}$$

whatever the cable resistance r_L and the top bridge resistance R_1. Indeed one has the simple equation

$$I_w = \frac{E}{(R_1 + R_w + r_L)}\,, \quad \text{which gives} \quad \frac{\mathrm{d}I_w}{\overline{I}_w} = \frac{\mathrm{d}E}{\overline{E}}\,. \tag{5.156}$$

This simplification should not let one believe that any cable can be used, as cable capacitance and inductance have to be taken into account in the CTA dynamic response. Optimized cables are therefore often advised by CTA manufacturers.

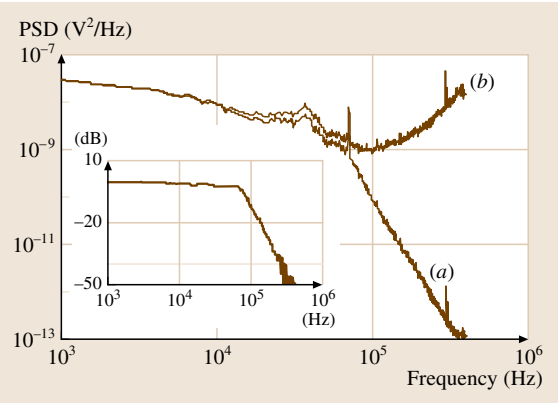

Fig. 5.33 Use of a CTA transfer function to measure the freestream power spectra in a Mach 2.5 wind tunnel: (*a*) original spectrum, (*b*) corrected spectrum, insert corresponding to bridge frequency response. The CTA noise in f^2 is only visible on curve (*b*) (after *Weiss* et al. [5.212])

Because $e_B \neq 0$, the Wheatstone bridge is not perfectly balanced. *Weiss* [5.215] analyzed how this could affect S^{CTA}_U and $S^{\mathrm{CTA}}_{T_a}$. He showed that both S^{CTA} values are lower than those of a perfectly balanced bridge, and that the degree of discrepancy increases with increasing offset voltage and decreasing overheat ratio. However, a direct calibration procedure may take this effect into account.

The electronic noise of a CTA has been analyzed by *Kidron* [5.188] and *Freymuth* [5.189]. The signal-to-noise ratio (SNR), at frequency f, may be expressed as

$$\mathrm{SNR}|^{\mathrm{CTA}} = \frac{1}{2}\,\frac{1}{2\pi f M_w}\,\frac{m\overline{a}_w}{(1+m)^2}\,\frac{\overline{E}}{\hat{e}_n}\,\frac{\hat{u}}{\overline{U}}\,, \tag{5.157}$$

where m denotes the ratio R_1/R_w, $\hat{u}$ the spectrum of the fluctuating velocity u', and $\hat{e}_n$ the spectrum of the equivalent noise e'_n of the bridge and amplifier occurring at the amplifier input. The spectrum $\hat{u}$ is expressed in $\mathrm{ms}^{-1}/\sqrt{\mathrm{Hz}}$ and the spectrum $\hat{e}_n$ in $\mathrm{V}/\sqrt{\mathrm{Hz}}$. Some adaptation has been made from the original paper [5.201] to transform the M^{CTA}_w value, which involved the bridge, into M_w, which characterizes the wire itself. Equation (5.157) shows that a high SNR requires $m \simeq 1$ in addition to a high $\overline{a}_w$ value.

Regarding the CTA output noise spectrum itself, which is the square of the denominator in (5.157), a growth in f^2 is expected. This behavior was observed only recently as experiments require very low-turbulence freestream wind tunnels and CTA with very large bandwidths. *Saddoughi* and *Veeravalli* [5.216] reported experiments in subsonic flows, and *Weiss* et al. [5.212] [5.141] in the freestream of a Mach 2.5 wind tunnel. The f^2 growth was followed by a final decay which was very abrupt as the high-frequency amplitude response of a CTA circuit described by (5.150) varies as f^{-3}, which corresponds to a Butterworth filter of third order [5.201].

Although the arguments presented in this section mostly concern hot-wires, they can apply to hot-films in the case of a bulk response of the film and its quartz core. When this is not the case, the high-frequency f^{-3} law for hot-wires becomes a $f^{-2/5}$ law for hot-films, according to the analysis performed by *Freymuth* [5.217] and the experimental data collected by *Fingerson* and *Freymuth* [5.50] and *Fingerson* [5.204].

Last but not least, *Freymuth* [5.217] carried out a nonlinear analysis of the CTA response. He used the full equation (i. e., not linearized) for the amplifier and the wire responses. This led him to a nonlinear third-order equation with variable coefficients that he solved

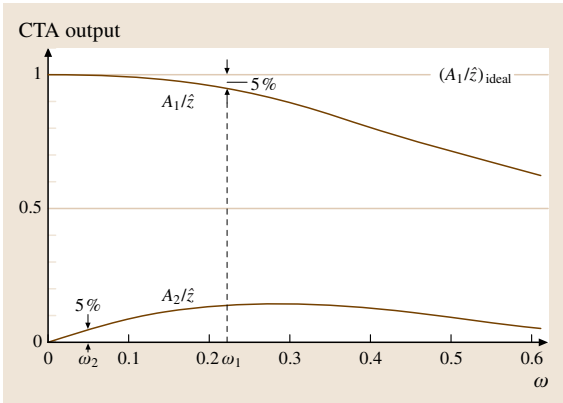

Fig. 5.34 Normalized fundamental component $A_1/\hat{z}$ and second harmonic $A_2/\hat{z}$ of a CTA output for an input function $z = \hat{z}\sin(\omega t)$ with $\hat{z} = 0.4$ (after *Freymuth* [5.217])

by iteration. Figure 5.34 shows the second harmonic A_2 generated in the case of a relatively large sinusoidal change in the flow velocity. Since the numerical estimate of Freymuth is rather complex, the problem could be revisited because the velocity signal and the electronic signal could differ from each other when nonlinearities are included.

Constant-Voltage Anemometer (CVA)

The block diagram of a CVA is shown in Fig. 5.35. This recent technique was conceived and developed by *Sarma* [5.148, 218]. Prototypes have been tested in several investigations mostly dealing with high-speed transitional and turbulent boundary layers, in the laboratory [5.127, 150, 219–221] and in flight using remote control [5.88].

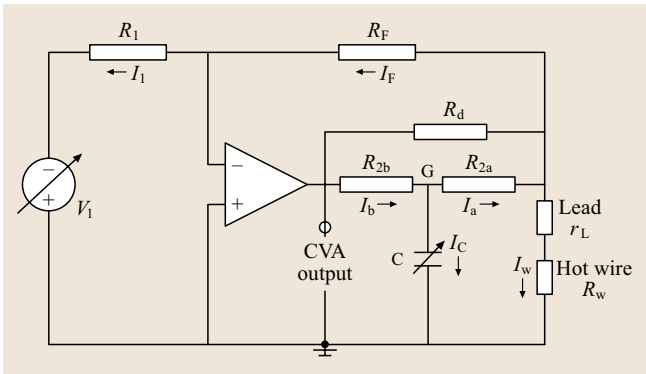

Fig. 5.35 Block diagram of a constant-voltage anemometer (CVA). The output signal is large due to the large resistance $R_{2a} + R_{2b} = R_2 \simeq 100\,\Omega$

The sensor, either a wire or a film, is placed in the feedback loop of the operational amplifier. The voltage across it, $V_w = R_w I_w$, can be adjusted and measured, and once set it is independent of the hot-wire resistance R_w. Any change in wire resistance due to fluid flow produces a change of current in the wire, whose only path is through resistance R_2. The anemometer output V_s is closely related to the voltage drop in resistor R_2. The circuit parts involving R_{2a}, R_{2b}, and C with $R_{2a} + R_{2b} = R_2$ permit a linear frequency increase of the CVA output and therefore the thermal lag compensation of the wire. The time constant T_C associated with this compensation is

$$T_C = \frac{R_{2a} R_{2b}}{R_2} C \,. \tag{5.158}$$

The Ohm–Kirchhoff laws applied to the network give

$$\begin{aligned}
-R_1 I_1 + V_1 &= 0 \,, \\
V_w - R_F I_F &= 0 \,, \\
I_F &= I_1 \,, \\
V_w &= R_w I_w \,, \\
V_s - R_{2b} I_b &= V_G \,, \\
V_G - R_{2a} I_a &= V_w \,, \\
V_G - \frac{I_C}{\mathrm{i} C \omega} &= 0 \,, \\
I_b &= I_a + I_C \,, \\
I_a &= I_w + I_F \,.
\end{aligned} \tag{5.159}$$

An infinite gain–bandwidth product is assumed for the operational amplifier, the resistor R_d, which is large compared to R_2, is neglected. The analysis including lead resistance r_L will be considered later on in this text. From (5.159) one can easily deduce

$$V_w = V_1 \frac{R_F}{R_1} \tag{5.160}$$

which shows that the wire voltage V_w is indeed constant, as V_1 is a stable reference voltage. The adjustment of V_w is done by adjusting V_1, manually or in a automated way by a PC. After some algebra, one can also obtain from (5.159) the CVA output signal V_s at frequency ω

$$\frac{V_s}{V_w} = 1 - \frac{R_2}{R_{2a}} + R_2 \left(\frac{1}{R_w} + \frac{1}{R_F} + \frac{1}{R_{2a}} \right) (1 + \mathrm{i}\omega T_C) \tag{5.161}$$

with T_C given by (5.158). Also,

$$\overline{V}_s = \left[1 + R_2 \left(\frac{1}{\overline{R}_w} + \frac{1}{R_F} \right) \right] V_w \,, \tag{5.162}$$

permitting one to deduce $\overline{R}_w$ from $\overline{V}_s$ by

$$\overline{R}_w = R_2 \left[\frac{\overline{V}_s}{V_w} - \left(1 + \frac{R_2}{R_F}\right) \right]^{-1} . \quad (5.163)$$

The output change v'_s due to a flow change at frequency ω, is obtained from (5.161) by derivation with respect to R_w, if the fluctuation amplitudes are small. Taking also into account the wire thermal lag M_w^{CVA} in CV operation, this gives

$$v'_s = -R_2 \overline{I}_w \frac{r'_w}{\overline{R}_w} \frac{1 + i\omega T_C}{1 + i\omega M_w^{CVA}}$$
$$\text{with } M_w^{CCV} = M_w^{CV} . \quad (5.164)$$

The factor $R_2 \overline{I}_w$ clearly shows that the CVA output is very large, as resistance R_2 can be chosen to be large, of the order of 100 Ω. A factor of 20 can therefore be gained compared to a CCA, and a factor of 2 compared to a CTA with a 50 Ω top resistance. The factor $1 + i\omega T_C$ shows the increase in gain of the CVA output with frequency. Resistor R_d, which has been neglected, has a damping role to limit that increase. Details are available in *Sarma* [5.148] and *Kegerise* and *Spina* [5.222,223]. In addition, a high-order low-pass Butterworth filter is placed just before the CVA output, and below its frequency limit, around 650 kHz, the CVA fluctuating output $e'(t)$ is identical to v'_s, and for the mean values, $\overline{E} = \overline{V}_s$.

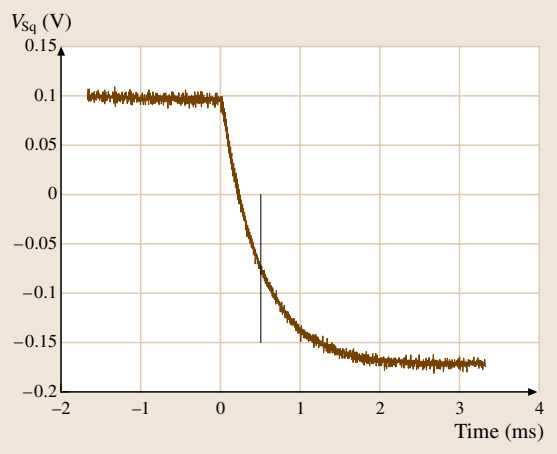

Fig. 5.36 Time trace of a 16 Hz square-wave signal applied to a 5 µm tungsten wire placed in the potential core of a $U = 15$ m/s jet with $\overline{a}_w = 0.25$. The curve shows the quality of the exponential fit. The *vertical line* corresponds to a 63% reduction and indicates the M_w^{CVA} value, 0.48 ms in the present case

As a whole, the system is of order one and the gain demand in CV operation is smaller than in CC operation, as $M_w^{CVA} < M_w^{CCA}$, so that a CVA can be stable and have a high frequency response.

The time constant M_w^{CVA} is measured in situ using a square-wave test and an auxiliary circuit developed by *Sarma* and *Lankes* [5.224]. An example is shown in Fig. 5.36.

In order to correct for M_w^{CVA}, one can select a T_C value which provides for the exact $1 + i\omega M_w^{CVA}$ compensation in (5.164). On current prototypes around 40 values are available [5.225]. However, a drawback is that the bandwidth of the CVA decreases when T_C increases, as the gain–bandwidth product of an operational amplifier is fixed. Another approach is therefore preferred. It consists of making a partial hardware correction in the CVA during the experiments, with a fixed T_C value, and to complete the correction later, during data processing, as suggested by *Kuppa* et al. [5.226] and *Sarma* et al. [5.225]. Denoting these two signals by $e'_{raw}(t)$ and $e'_{corr}(t)$, respectively, *Comte-Bellot* and *Sarma* [5.127] explained the relation to apply to $e'_{raw}(t)$ to restore $e'_{corr}(t)$ in terms of the i-th and $(i-1)$-th samples acquired at a sampling frequency of f_s

$$e'_{corr}(i) = \frac{e'_{raw}(i) + f_s \left\{ M_w^{CVA} \left[e'_{raw}(i) - e'_{raw}(i-1) \right] + T_C e'_{corr}(i-1) \right\}}{1 + T_C f_s} . \quad (5.165)$$

This two-step procedure has several advantages:

1. it increases the productivity during data acquisition,
2. it ensures a constant frequency bandwidth whatever the flow conditions or wire overheat, and
3. it permits slightly different M_w^{CVA} values to be tested within experimental accuracy (±2%).

A point, however, not yet investigated is how high the sampling frequency has to be in order to allow a first-order scheme. Further investigation on this topic is encouraged.

The CVA output sensitivity coefficients to flow changes, denoted by S^{CVA}, can be obtained from (5.162) and (5.164) and related to the wire sensitivity S^{CV} in CV operation. Also one has to note that $r'_w/\overline{R}_w = -i'_w/\overline{I}_w$. For example, this gives for velocity fluctuations

$$\left(\frac{e'_{corr}(t)}{\overline{E}} \right)_{CVA} = S_U^{CVA} \frac{u'(t)}{\overline{U}_1}$$
$$\text{with } S_U^{CVA} = \left[1 + \overline{R}_w \left(\frac{1}{R_2} + \frac{1}{R_F} \right) \right]^{-1} S_U^{CV} . \quad (5.166)$$

The factor in the brackets is advantageously close to 1.0, as $R_2 = 100\,\Omega$, $R_F = 300\,\Omega$, and $\overline{R}_w \simeq 10\,\Omega$. The correction is therefore rarely needed.

The lead resistance r_L slightly modifies the sensitivity coefficient given by (5.166) as well as the time constant given by (5.164) because the constant voltage condition is $(R_w + r_L)I_w =$ constant and not simply $R_w I_w =$ constant. This topic has been investigated by *Comte-Bellot* et al. [5.227] who established the following useful compact form, which is valid for velocity fluctuations as well as for temperature fluctuations,

$$S^{CVA}\,(\text{with lead}) = LS \times LM \times S^{CV} \tag{5.167}$$

with

$$LS = \left[1 + (\overline{R}_w + r_L)\left(\frac{1}{R_2} + \frac{1}{R_F}\right)\right]^{-1} \times \left[1 + \frac{r_L}{\overline{R}_w(1 + 2\overline{a}_w)}\right]^{-1} \tag{5.168}$$

(the CVA circuit resistances R_2 and R_F have been included in LS) and

$$LM = \left(1 + \frac{r_L}{\overline{R}_w}\right)\left[1 + \frac{r_L}{\overline{R}_w(1 + 2\overline{a}_w)}\right]^{-1} . \tag{5.169}$$

Very advantageously, $LS \times LM \simeq 1$ because LS is slightly greater than one, and LM slightly less than one. The correction can therefore be often omitted.

Because of the constant-voltage operation the capacitance of the cable does not introduce any limitation on the dynamic response and also does not pick up extraneous noise, as pointed out by *Sarma* [5.148]. Inductance may also have a similar neutral behavior. Indeed the CVA has consistently exhibited superior noise immunity over CTA and CCA in tests in high radiofrequency interference (RFI) and electromagnetic interference (EMI) environments in hypersonic wind tunnels as reported by *Lachowicz* et al. [5.220] and *Blanchard* et al. [5.228]. This advantage makes it possible for fast setup of the CVA. Only the lead resistance of the cable needs to be considered, as presented above.

The electronic noise of a CVA prototype was analyzed by *Weiss* and *Comte-Bellot* [5.221]. Equation (5.159) are in this case completed with the Nyquist–Johnson noise sources of all resistances, and with the input voltage and current noise of the operational amplifier. Experiments were also conducted with different carbon resistances and tungsten wires operating with no flow, at the setting $T_C = 0.10\,\text{ms}$ generally used. The rms noise value was found to decrease as the wire resistance increased, hence permitting an upper noise limit to be determined from experiments on an unheated wire. Regarding the noise power spectra, an increase with the square of the frequency was observed, as in other anemometers. An explicit relation was obtained for the signal-to-noise ratio, $SNR|^{CVA}$ at frequency f

$$SNR|^{CVA} = \frac{1}{2\pi f M_w^{CVA}} \frac{R_{2a}}{R_{2a} + \overline{R}_w} \frac{\overline{a}_w}{2(1 + 2\overline{a}_w)} \frac{V_w}{\hat{e}_n} \frac{\hat{u}_1}{\overline{U}_1} \tag{5.170}$$

with $\hat{e}_n$ the noise spectrum in $V/\sqrt{Hz}$, e.g., $\hat{e}_n \simeq 2.7 \times 10^{-9}\,V/\sqrt{Hz}$ in [5.221], and $\hat{u}_1$ the turbulent spectrum also in $V/\sqrt{Hz}$. It was also shown that $V_w = R_F V_1 / R_1 \pm e'_n$, denoting the fluctuations of e_n by e'_n. The value of R_{2a}, which is proprietary to the manufacturer, can be assumed to be around $R_2/2$, and hence still large relative to R_w, so that $R_{2a}/(R_{2a} + \overline{R}_w) \simeq 1$. Equation (5.170) is therefore easy to use. It permits the estimation of SNR values when investigating the low-energetic fine-scale turbulent structures or the background perturbations of wind tunnels.

Finally, for large-amplitude fluctuations, the higher-order harmonics generated by parametric excitation at the wire level (5.105), are compensated as if they were turbulence. A suggestion to reject them would be to deduce $R_w(t)$ from $V_s(t)$, and then $R^\star(t)$ by inverting (5.105) [5.229]. Nowadays time data are acquired at high sampling frequencies and this procedure could lead to satisfactory results. Attempts in that direction would be most useful. A similar procedure could also work for a CCA, but it has never been suggested, despite the long history of the CCA. Also, as M_w^{CVA} is less than M_w^{CCA}, the inversion of (5.105) could be done with greater accuracy.

5.2.4 Calibration Procedures in Subsonic Flows

The calibration of a hot-wire probe associated with its anemometer establishes the relationship between the anemometer output voltage and the magnitude and direction of the incident velocity vector. A quiescent flow is the best to quickly record accurate data. In air, the potential region of a plane or circular jet, or the freestream of a wind tunnel are often chosen. Nowadays, the flow velocity and probe angle are easily controlled by a personal computer (PC), and the anemometer outputs are acquired in an automated way.

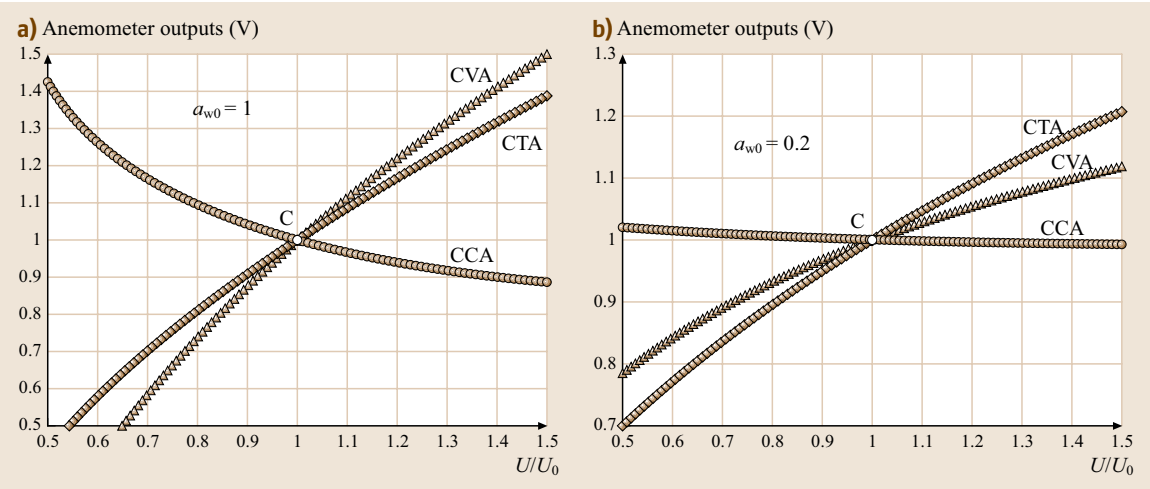

Fig. 5.37a,b Comparison of the CCA, CTA, and CVA response curves to velocity changes: **(a)** for $\overline{a}_w = 1.0$, **(b)** for $\overline{a}_w = 0.20$, at the reference velocity $U_0 = 10\,\mathrm{m/s}$. The vertical voltage shifts (in V) are 0.831, 4.157, and 8.314 for **(a)**, and 0.288, 2.208, and 4.800 for **(b)**, for the CCA, CTA and CVA respectively. For the CTA, $R_1 = 40\,\Omega$, for the CVA $R_2 = 100\,\Omega$

Preliminaries

The responses of anemometers generally exhibit nonlinearities for large velocity or fluid temperature changes. Part of the nonlinearity comes from the wire and the other part comes from the anemometer electronics. Although both effects are included in calibration curves, a hint of the shape of the curves is useful prior to the systematic acquisition of calibration data. This can be achieved by using a simple heat-loss law for the wire, such as King's law (5.48). Figure 5.37 reports Matlab simulations for a single wire placed normal to a flow, for the three types of anemometer, CCA, CTA and CVA, and two mean wire overheat values, $\overline{a}_w = 0.20$ and 1.0 at the reference velocity $U_0 = 10\,\mathrm{m/s}$. All anemometer outputs are translated along the y-axis in order to coincide at C. The curvature inherent to each curve is hence

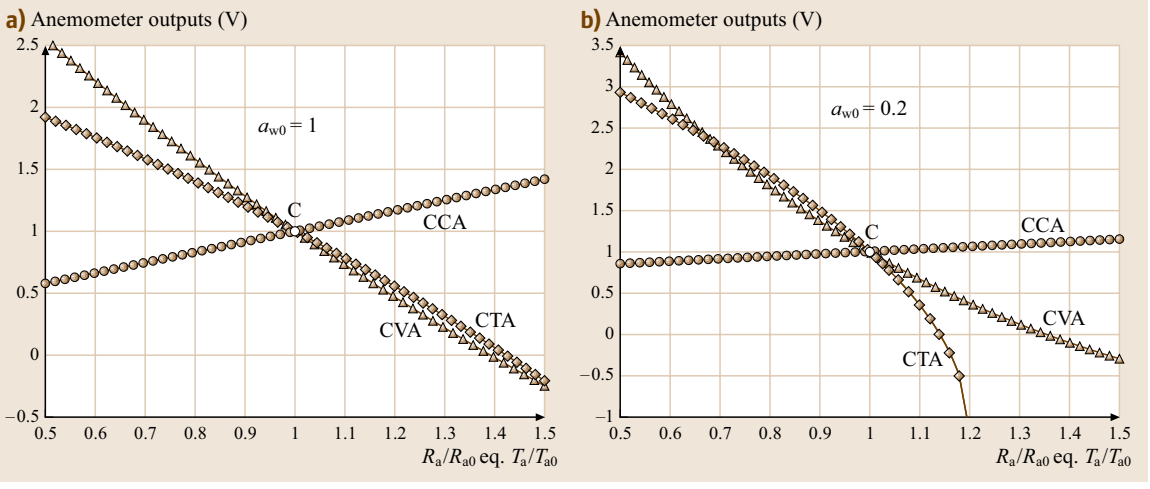

Fig. 5.38a,b Comparison of the CCA, CTA, and CVA response curves to ambient temperature changes: **(a)** for $\overline{a}_w = 1.0$, **(b)** for $\overline{a}_w = 0.20$, at the reference temperature $T_{a0} = 293\,\mathrm{K}$, $R_{a0} = 5\,\Omega$. The vertical voltage shifts and the values of R_1 and R_2 are the same as in Fig. 5.37

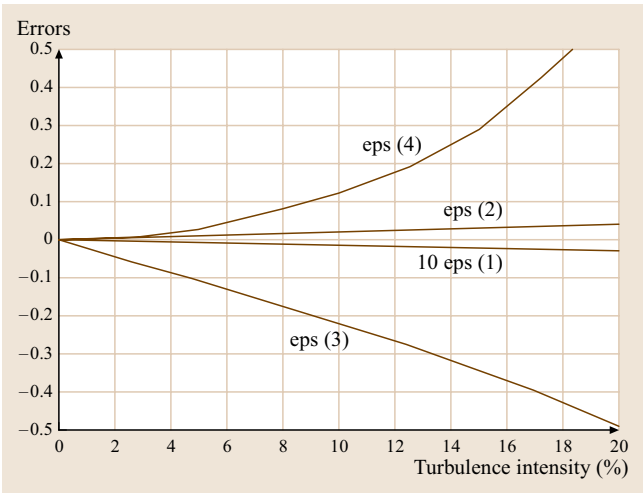

Fig. 5.39 Errors made by linearizing the anemometer calibration curve around the operating point as a function of the turbulence level. Example of a CTA; eps(1) to eps(4) are defined by (5.171)

preserved and permits a direct visual appraisal of the nonlinear effects. For example, at $\overline{a}_w = 1.0$, the CVA is seen to be able to keep an almost linear response over a $\pm 10\%$ velocity change. A satisfactory linear response also appears on the CTA, but strong nonlinearities occur in a CCA.

The wire response to a change in R_a, which corresponds to a change in the fluid temperature T_a, can similarly be investigated; results are presented in Fig. 5.38. An exact linear response appears with a CCA and a satisfactory one for a CVA whatever $\overline{a}_w$. On the contrary, a CTA presents a strong nonlinear response at low overheat ratios, already visible at $\overline{a}_w = 0.20$.

Figure 5.39 shows for a CTA the errors that exist if only the tangent to the velocity calibration curve at the operating point is used to interpret the measurements. The operating point is such that $U_0 = 10\,\mathrm{m/s}$, $a_{w0} = 1.0$, and $E_0 = 4.157\,\mathrm{V}$ (with $R_1 = 40\,\Omega$ for the top bridge resistance). The synthetic input turbulence u' is a random Gaussian noise, with 10^6 values, its mean and rms values are 0 and 1.0, and the skewness and flatness factors are 0 and 3, respectively. The turbulence level is varied between 0 and 20%. The errors considered are defined by

$$\mathrm{eps}(1) = \frac{\overline{E} - E_0}{E_0} ,$$

$$\mathrm{eps}(2) = \left(\frac{\sqrt{\overline{e'^2}}}{\overline{E}} - S_{U_1} \frac{\sqrt{\overline{u'^2}}}{U_0} \right) \left(\frac{\sqrt{\overline{e'^2}}}{\overline{E}} \right)^{-1} ,$$

$$\mathrm{eps}(3) = \frac{\overline{e'^3}}{\left(\overline{e'^2}\right)^{3/2}} , \quad \mathrm{eps}(4) = \frac{\overline{e'^4}}{\left(\overline{e'^2}\right)^2} - 3 \qquad (5.171)$$

with

$$e'(t) = E(t) - \overline{E} \quad \text{and}$$

$$S_{U_1} = \frac{1}{4} \frac{B\sqrt{U_0}}{A + B\sqrt{U_0}} = 0.215 .$$

The errors that affect the mean or the rms values are small, less than 1%, and are hence negligible. On the other hand, the flatness factors and more so the skewness factors show large errors. Their measurement therefore requires the use of the full calibration curve. This means that the calibration curve has to be inverted with accuracy at each sampling point used in the data-acquisition routine to deduce the velocity from the anemometer output.

Results from the application of a time-varying sinusoidal input signal u' is also instructive. The higher harmonics that necessarily appear have low power content, for example 10^{-2} and 10^{-4} down from the fundamental. Errors on the PSD spectra are therefore small. Double correlation functions, which are Fourier transforms of PSDs, are also expected to be free of error. However, the skewness factors are in error, giving for example $\mathrm{eps}(3) \simeq -0.23$ because of the cross-product, which involves the square of the fundamental and the first harmonic.

Static nonlinear effects can be similarly simulated for the two other types of anemometers, the CCA and CVA. For the operating point considered above ($U_0 = 10\,\mathrm{m/s}$, $a_{w0} = 1.0$), at a Gaussian turbulence level of 10% for all the three anemometers, eps(1) and eps(2) are both less than 1%, the higher harmonics have the same low relative order of magnitude as indicated above, eps(3) values are -0.22 for CTA, -0.34 for CVA and $+0.47$ for the CCA, and eps(4) values are 0.12 for CTA, 0.28 for CVA and 0.48 for CCA. For these higher moments, inversion of the calibration curve is therefore recommended whatever the type of anemometer.

Calibration of a Single Wire Normal to the Flow

For a single normal wire, only the incident velocity has to be changed. It is often measured by a Pitot tube connected to a pressure transducer. It is common practice to carry out around 20–30 readings over the selected velocity range. The description of the calibration curves can be made by using

1. power relationships, close to King's law or a similar law with added terms

2. simple or extended polynomial fits
3. spline fits.

Bruun et al. [5.231] compared the accuracy of the different techniques. Technique 3 seems the best. It relies on a flexible strip (a drafting spline) that provides a smooth curve through and between points on the graph. The data range is subdivided into subintervals, and each interval is fitted with a cubic spline.

To ensure smoothness the empirical fit must provide a monotonic relationship between the anemometer output and the velocity including the derivatives of all orders. For example, for a CTA or CVA, the fit must verify $\mathrm{d}^n E_{\text{output}}/\mathrm{d}U_1^n > 0$ for $n = 1$, < 0 for $n = 2$, and > 0 for $n = 3$, and so on. The calibration curve can then easily and accurately be inverted to deduce the velocity in the flow under investigation from the anemometer output.

For small turbulence levels, the local slope to the calibration, at the mean operating point, gives the sensitivity coefficient $S_{U_1}^{\text{CCA}}$, $S_{U_1}^{\text{CTA}}$, $S_{U_1}^{\text{CVA}}$, defined in Sect. 5.2.3.

For very low velocities the reference velocity using pressure differentials is not accurate enough. The probe is therefore displaced to a quiet environment at a known speed. A rotating arm was used by *King* [5.183, 232], a horizontal translating carriage by *Baille* [5.233], a sliding carriage with adjustable inclination by *Tewari* and *Jaluria* [5.234] to study directional effect of buoyancy. *Khoo* et al. [5.235] kept the probe fixed and placed it in the air gap between a top rotating disc and a bottom stationary disc. Their setup permits direct calibration under the cooling influence of a nearby wall.

De Haan [5.236] investigated the use of acoustic waves for the *dynamic* calibration of a hot-wire. An acoustic standing wave was superposed on the mean velocity. Experiments were conducted at a frequency of 2.5 kHz for a mean speed in the range 6–18 m/s for 18 wires differing in length, diameter and stub importance. The rms velocities measured by the wire, and based on a *static* calibration, were found to agree to within 4% with those deduced from the microphone readings.

In the absence of mean velocity, the wire can be placed at an acoustic velocity antinode within a resonant tube, but due to the rectified signal transmitted by the anemometer, data processing must only be performed on the incoming velocity maxima. The acoustic pressure at the pressure antinode is measured by a microphone flush-mounted at the wall. Acoustic velocity u' and pressure p' are simply related by $u' = p'/\rho_0 c_0$, where ρ_0 and c_0 are the density and speed of sound, respectively. The velocity is changed by adjusting the level of the acoustic source, which is usually a loudspeaker.

Calibration in liquids is mostly performed in a towing tank or in a large circular channel with a rotating arm. Many setups are described in the *Lomas* book [5.51]. A moving container filled with the test liquid and displaced along the wire was used by *Dring* and *Gebhart* [5.237]. This method allows the easy experimentation of different liquids at different temperatures.

Calibration of X-Wires in Subsonic Flow

For an X-probe, an additional angular calibration of each wire with respect to its yaw angle θ is needed at different velocities. This is done by placing the X-probe on a small rotating rig, with the probe center kept unchanged [5.238].

For low turbulence intensities, the θ range can be limited to $\pm 10°$. Then S_{U_1}(yawed wire) and S_θ(yawed wire) defined in Sect. 5.2.3 can be evaluated and used. Weighted sum and difference of the two anemometer outputs then give $u_1'(t)$ and $u_2'(t)$. Furthermore, the $u_2'(t)$ signal is almost unaffected by the nonlinear wire response to U_1 [5.239].

For high turbulence levels, a larger θ range is needed, and the interval $\pm 35°$ is commonly used. An example of a calibration map, borrowed from *Abdel* et al. [5.230], is given in Fig. 5.40. Similar plots are reported by *Lueptov* et al. [5.240] or *Johnson* and *Eckelmann* [5.241] among others.

The calibration data can be used to create a look-up matrix that contains, in discrete form, the relation-

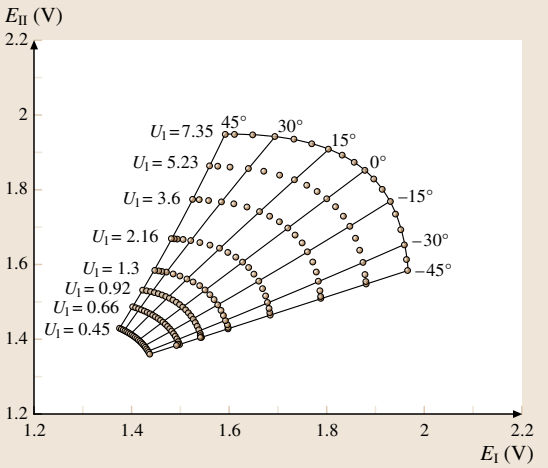

Fig. 5.40 Typical yaw angle calibration of a CTA-operated X-probe at different velocities U_1 (m/s) (after *Abdel* et al. [5.230])

ship between the two anemometer outputs, E_{I} and E_{II}, and the velocity components, $U_1(t)$ and $U_2(t)$, or their equivalents in plane polar coordinates, $|U|(t)$ and $\theta_U(t)$, for the velocity magnitude and flow angle, respectively. This method makes no assumption regarding the wire geometry or the wire response. When conducting turbulence measurements, the reconstruction of the velocity field, $U_1(t)$ and $U_2(t)$, needs bilinear interpolation schemes with high-resolution grids. This important topic is discussed by *Lueptow* et al. [5.240], *Chew* and *Ha* [5.242], *van Dijk* and *Nieuwstadt* [5.80]. Historically, *Willmarth* and *Bogar* [5.243], and *Willmarth* [5.244] pioneered the method and showed that a unique velocity vector in the plane of the X-wire can be obtained and followed in time. Very recently *Burattini* and *Antonia* [5.245] compared different X-wire calibration schemes and concluded that the look-up-table approach is more reliable than the effective-angle calibration scheme.

The calibration data can be also expressed, for each wire, in terms of a relationship involving King's law. The concept of an effective velocity, U_{eff}, is therefore widely used to represent the velocity cooling the wire

$$U_{\mathrm{eff}}^2 = U_{\mathrm{N}}^2 + U_{\mathrm{B}}^2 + k^2 U_{\mathrm{T}}^2 \,. \tag{5.172}$$

U_{N} and U_{T} are defined in Fig. 5.13d. The factor k takes into account the effects due to the finite wire length and the prong orientation with respect to the flow, usually $k \simeq 0.10-020$ [5.52]. *Chew* and *Ha* [5.238] studied more precisely how k depends on the velocity and on the probe angle. *Bruun* and *Tropea* [5.246] examined the yaw effect on A, B, and n in King's law. When reducing data for turbulence measurements, two equations have to be resolved at each time to recover the velocity vector. This computation is easier to perform when one considers the variables $|U|(t)$ and $\theta_U(t)$. The ratio of the two equations, one for each wire, gives $\theta_U(t)$. Subsequently, either equation gives $|U|(t)$. The procedure is greatly simplified if the X-probe is made of two mutually orthogonal wires, as U_{N} for the first wire becomes U_{T} for the second wire, and U_{N} for the second wire becomes U_{T} for the first wire. However, there are always four solutions to the system, and only the correct one must be kept, the one in the approach quadrant (Sect. 5.2.2). This approach is mostly used with constant-temperature anemometers and details are reported by *Kawall* et al. [5.247], *Hishida* and *Nagano* [5.78, 79], *Bruun* [5.52], or *Lekakis* et al. [5.248] among others. A comparison between the two approaches, look-up matrix and effective velocity, was made by *Browne* et al. [5.249] and they found that the effective velocity gave surprisingly good results even in high-intensity turbulent flows.

Calibration of Three- and Four-Wire Probes in Subsonic Flows

The probe calibration now requires data collection for each wire, with respect to the velocity U_1, yaw angle θ, and pitch angle ϕ. So the amount of data to collect and save is very large. Examples are available in *Lakshminarayana* and *Davino* [5.250] for turbomachinery flows or in *Pompeo* and *Thomann* [5.251] for wall turbulence. When conducting turbulence measurements, the data are exploited using the lookup-table method or the concept of effective cooling velocity.

Van Dijk and *Nieuwstadt* [5.80] recently compared the two approaches and strongly supported the look-up-table method as a very good tool to process hot-wire measurements, since rapid computer processing is readily available. Among the pioneers of the techniques, let us cite *Pailhas* and *Cousteix* [5.252], and *Döbbeling* et al. [5.253]. Special surfaces fitting the calibration data were computed by *Samet* and *Einav* [5.254] and applied to measurements in a swirling jet issuing into a coflowing stream.

The effective velocity approach was, however, used successfully by *Lekakis* et al. [5.248] who experimented with orthogonal and non-orthogonal probes, and by *Kawall* et al. [5.247], *Lekakis* et al. [5.248], or *Gieseke* and *Guezennec* [5.255]. In three-dimensions (3D), the effective cooling velocity also contains the binormal component U_{B}, hence U_{eff} is given by

$$U_{\mathrm{eff}}^2 = U_{\mathrm{N}}^2 + h^2 U_{\mathrm{B}}^2 + k^2 U_{\mathrm{T}}^2 \tag{5.173}$$

with $h \simeq 1.02-1.05$ [5.52]. The three equations provided by the anemometer outputs are now solved in two steps. Firstly, the ratios of the second and third equations by the first equation give the yaw and pitch angles for the velocity vector. Then, either equation gives the velocity magnitude. The resolution is much more direct if the three wires constituting the probe are mutually orthogonal. In any case, eight solutions are numerically possible, and only one is correct, the one in the approach octant. Addition of a fourth wire increases the acceptance cone as shown by *Lemonis* and *Dracos* [5.256] and by *Döbbeling* et al. [5.257] who could extend the acceptability range to a hemisphere. The acceptance angle was also analyzed by *Lavoie* and *Pollard* [5.258] who reported convincing results in the near field of a turbulent jet. When using the effective cooling velocity approach, there is also the need to refer to the matrix ω_{ij}, which relates the wire-fixed frame $O'_{x'_i}$, i. e.,

$(N'B'T)$, to the space-fixed frame O_{x_j}, i. e., (O_{x_1,x_2,x_3}). This is not difficult, just cumbersome. From Fig. 5.13, one has

$$\omega_{ij} = \cos\left(O'_{x'_i}, O_{x_j}\right) = \begin{cases} \cos\theta\sin\phi - \sin\theta + \cos\theta\cos\phi\,, \\ \cos\phi + 0 - \sin\phi\,, \\ \sin\theta\sin\phi + \cos\theta + \sin\theta\cos\phi\,. \end{cases} \tag{5.174}$$

Hence, the velocity components in the wire-fixed frame, $U_{N'}$, $U_{B'}$, U_T, are related to those in the space-fixed frame, U_1, U_2, U_3, by

$$\begin{aligned} U_{N'} &= U_1\cos\theta\sin\phi - U_2\sin\theta + U_3\cos\theta\cos\phi \\ U_{B'} &= U_1\cos\phi + 0 - U_3\sin\phi \\ U_T &= U_1\sin\theta\sin\phi + U_2\cos\theta + U_3\sin\theta\cos\phi \end{aligned} \tag{5.175}$$

and conversely, U_1, U_2, U_3 are related to $U_{N'}$, $U_{B'}$, U_T by

$$\begin{aligned} U_1 &= U_{N'}\cos\theta\sin\phi + U_{B'}\cos\phi + U_T\sin\theta\sin\phi \\ U_2 &= -U_{N'}\sin\theta + 0 + U_T\cos\theta \\ U_3 &= U_{N'}\cos\theta\cos\phi - U_{B'}\sin\theta + U_T\sin\theta\cos\phi\,. \end{aligned} \tag{5.176}$$

It is interesting to note that these relations are similar to those used when studying the 3-D turbulence spectra [5.77], with a wavenumber vector playing the same role as a vector coinciding with the hot-wire. Finally, a simple 2-D matrix permits the expression of a rotation around the wire to pass from the prong-frame (N B T) to the wire-frame (N', B', T), with T common to the two frames. This additional degree of freedom has to be kept for each wire as the prongs location relative to the wire is important [5.68, 90].

Wall Sensors in Subsonic Flows

Wall sensors are most conveniently calibrated by using the wall region of a fully developed pipe or channel flow, where the measured pressure gradient can serve as a direct measure of the wall shear stress. Examples are given by *Cousteix* and *Juillen* [5.259], *Haritonidis* [5.260] and *Cook* [5.261, 262] for metallic films, and by *Huang* et al. [5.263] and *Lin* et al. [5.62] for MEMS. Turbulent boundary layers can also be used. The wall sensor is calibrated against a reference method (skin friction balance, oil-film interferometry) or well established wall laws [5.264]. A properly calibrated Preston tube can also be used [5.265]. The flow between a fixed plate and a rotating plate was developed by *Brown* and *Davey* [5.266] as a very convenient and inexpensive calibration device. The Stewartson solution for the mean flow and the wall shear was used and adopted also by *Khoo* et al. [5.235].

For metallic elements, the calibration curves are observed to be of the form

$$\frac{R_w I_w^2}{R_w - R_a} = A + B\tau_w^{1/3}\,. \tag{5.177}$$

Such a reference equation was analytically established by Lévêque in 1928 and by Fage and Falkner in 1931, and revisited by *Knudsen* and *Katz* in 1958 [5.104], *Cousteix* and *Jullien* [5.259], or *Bailly* and *Comte-Bellot* [5.77]. A numerical heat-transfer model was recently developed by *Cole* and *Beck* [5.267]. The main assumption is always that the thermal boundary layer of the heated sensor lies entirely within the linear region of the velocity profile, usually called the viscous sublayer. Experiments supporting this are those of *Brown* and *Davey* [5.266], *Reichert* and *Azad* [5.268] or *Alfredsson* et al. [5.269] among others. Coefficient B depends on the probe and flow characteristics, and the additive constant A depends mainly on the heat conduction leakage to the substrate. In air it can represent as much as 50% of electric power injected [5.270]. Very interestingly, *Sarma* and *Moes* [5.271] suggested a method to measure in situ the heat loss to the substrate for a multiple hot-film array operated by CVAs. In water, leakage to the substrate is much less severe. Recently, *Mangalam* [5.272] reported many successful experiments conducted with CVAs on autonomous underwater vehicles.

For miniature MEMS devices, (5.177) is not supported by direct measurements. *Lin* et al. [5.62] reported laws where the electric power varies as $\tau_w^{0.67}$ for nitride-based sensors and as $\tau_w^{0.85}$ for parylene diaphragm sensors. The authors invoked an additional heat-transfer mechanism and developed an appropriate model for it. *Ruedi* et al. [5.273] also reported significant difficulties regarding the repeatability of calibration sets and explored various reasons for them, such as the drift of ambient temperature or quite small overheat ratios for the sensor. Even after reduction of these effects, the power dissipated by the film was closer to a linear dependance on τ_w than to the classic $\tau_w^{1/3}$ law.

Regarding the frequency response of the hot-film, *Cook* [5.262] reported very interesting measurements in an oscillating flow generated by controlling the area of a sonic throat. They used a quartz-substrate gauge, a glue-on gauge with a thin flexible substrate,

and a surface film with a cavity underneath. Interestingly, a laminar case was first studied [5.261] and they could observe that the skin friction preceded the freestream velocity by 45°, as theoretically established by *Lighthill* [5.274]. For turbulent flows, the phase advance went down to around 15–20°. This experiment was one of those simulated by *Cole* and *Beck* [5.267]. Their numerical approach permits to simulate different thermal diffusivities for the substrate and different ratios D/a, where D is the substrate depth and a is the half-length of the hot-film in the flow direction, for example $D/a \simeq 6$ for comparison with the experimental data of Cole and Beck. To this day, the highest frequency achieved is only around 20 Hz, the limitation being due to the maximum number of time steps in the computation.

In hot-film arrays, an individual calibration of the sensors is rarely needed as commercial sensors are manufactured with nearly identical characteristics. In special cases, for example to study the flow around a cylinder, *Desgeorges* et al. [5.275] individually calibrated 251 hot films simply by rotating the cylinder to bring each sensor successively to the same angular position relative to the flow.

Mean Fluid Temperature Drifts in Subsonic Flows

In many flows, the mean temperature $\overline{T}_a$ changes from day to day because of the environment, or during an experiment because of the heat released by the machines powering the wind tunnels, or from point to point in non-isothermal flows such as hot jets. The velocity calibration obtained at temperature $\overline{T}_{a0}$ is not valid at another temperature $\overline{T}_a$. The reason is that the curves expressing the relationship between the anemometer output and the velocity are shifted down for a CTA or a CVA and up for a CCA when $\overline{T}_a > \overline{T}_{a0}$, and vice versa when $\overline{T}_a < \overline{T}_{a0}$. For the CTA, *Koppius* and *Trines* [5.276] collected many data for a long wire $l/d \approx 770$ over a temperature range of 283–353 K. *Nitsche* and *Haberland* [5.265] and *Thünker* et al. [5.277] considered hot-wires and hot-films, and they could combine a refrigerated flow and a heated flow to make measurements over a very large temperature range, 250–425 K. These extreme flow conditions are typical of thermo and cryo wind tunnels.

There are several ways to account for the temperature difference $\overline{T}_a - \overline{T}_{a0}$:

1. Velocity calibration curves can be collected at a number of different fluid temperatures, covering the range of interest. All the curves are stored and the adequate curve is used in the course of turbulence measurements, which require the local temperature $\overline{T}_a$ to be independently measured. A thermocouple is sufficient for a global temperature drift of a wind tunnel. For non-isothermal flows, local measurements are needed and they require a *cold* hot-wire, usually operated in a CCA mode with a small ($\simeq 1$ mA) current. The procedure has to be repeated for every wire in a multiple-wire probe. Interpolation procedures also have to be developed to cover intermediate temperatures. An example is given by *Meyer* [5.278] for two wires making an X-probe and a third cold wire.
2. When only one velocity calibration curve has been recorded, at temperature $\overline{T}_{a0}$, only an analytical correction can be attempted to recover it from measurements carried out at T_a. The correction is essentially based on King's law. For a CTA, *Lemonis-Dracos* [5.256] expressed the correction procedure as

$$\overline{E}^{\mathrm{CTA}}_{\mathrm{corr}} = \overline{E}^{\mathrm{CTA}}_{\mathrm{meas}} \left[\frac{(\overline{T}_w - T_{a0})}{(\overline{T}_w - \overline{T}_a)} \right]^{1/2} , \qquad (5.178)$$

which comes directly from the dependence $\overline{I}^2_w \sim (\overline{R}_w - \overline{R}_a)$ at fixed $A + B\overline{U}^n_1$ in King's law. *Benjamin* and *Roberts* [5.279] revisited this correction for a large temperature change, 300–500 K, and found that the physical properties of the fluid which could affect A and B could be ignored, and even that the approximate form deduced from (5.178) by a first-order expansion

$$\overline{E}^{\mathrm{CTA}}_{\mathrm{corr}} \simeq \overline{E}^{\mathrm{CTA}}_{\mathrm{meas}} \left[1 - \gamma_c \frac{(\overline{T}_{a0} - \overline{T}_a)}{(\overline{T}_w - \overline{T}_a)} \right]$$

$$\text{with } \gamma_c = 0.50 \qquad (5.179)$$

performs even better than (5.178). One can also obtain (5.179) using the sensitivity coefficient $S^{\mathrm{CTA}}_{T_a} = -1/(2\overline{a}_w) = -\overline{R}_a/2(\overline{R}_w - \overline{R}_a) \simeq -\overline{T}_a/2(\overline{T}_w - \overline{T}_a)$ defined in Sects. 5.2.2 and 5.2.3. *Meyer* [5.278] examined the case of yawed wires and found that $\gamma_c \simeq 0.45$ when the yaw angle reaches around ±30°. *Cimbala* and *Park* [5.280] also made use of King's law, and added other factors to take into account a DC offset and a gain. A relatively small temperature range was inspected, 300–308 K. *Kostka* and *Vasanta Ram* [5.281] and *Vasanta Ram* [5.282] operated in the temperature range 293–333 K, using wires of four different aspect ratios: 718, 306, 248 and 106. Their reduced

data show that the overall Nusselt number Nu_{a0}, with physical properties evaluated at a fixed temperature, $\overline{T}_{a0} = 313\,K$, decreases linearly with the temperature difference $\overline{T}_a - \overline{T}_{a0}$.

3. *Hollasch* and *Gebhart* [5.283], working with liquids, suggested establishing the correction by changing the wire temperature T_w rather than the fluid temperature T_a.
4. Automatic compensation of ambient-temperature drift can be introduced in the electronic circuit. This has mostly been developed for CTA. Three approaches have been analyzed by *Drubka* et al. [5.284]: the constant-overheat mode, the constant-resistance-difference mode, the constant-output-voltage mode. All of them, however, require an additional temperature-compensating probe, placed in the flow and integrated in the Wheatstone bridge, and complex electronics. The simple King's law with constant coefficients is also assumed.
5. The need for an additional sensor is eliminated by *Sarma* and *Comte-Bellot* [5.285] in a CVA setup. An automated procedure permits to obtain in situ the heated and cold resistances of a hot-wire in each measurement cycle. The *high* V_w step, with $I_w \simeq 100\,mA$, permits the turbulence to be recorded and M_w^{CVA} to be measured, while the *low* V_w step, with $I_w \simeq 1\,mA$, yields R_a and T_a. Fig. 5.41 shows a typical set of calibration curves obtained for different fluid temperature T_a and the possibility to reduce all the different calibration curves into a unique calibration curve by using the ratio

$$\mathrm{PDR} = \frac{R_w I_w^2}{(R_w - R_a)}\,, \tag{5.180}$$

which involves the power injected in the wire and the difference in the hot and cold resistance of the wire. The PDR is therefore in essence a Nusselt number.

Truzzi et al. [5.286] used this method to measure the unsteady flow in the near-orifice region of synthetic jets. The method requires only one hot-wire. This is a definite advantage over previous methods established for CCA or CTA where an additional temperature sensor is needed.

5.2.5 Measurement of Velocity and Temperature Fluctuations

In subsonic non-isothermal flows, velocity fluctuations are accompanied by fluctuations in the fluid temperature. A single hot-wire placed normal to the mean incident velocity therefore has a response of the form

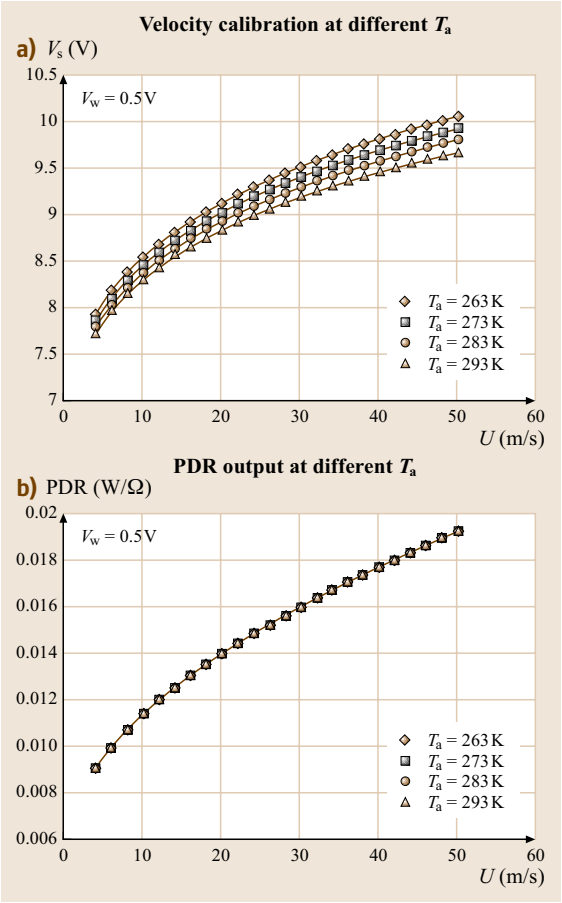

Fig. 5.41a,b Calibration curves collected at different fluid temperatures T_a for a CVA, and correction made by using the PDR ratio defined by (5.180)

$$E(t) = f\left[\overline{U}_1 + u_1'(t), \overline{T}_a + \theta_a'(t)\right], \tag{5.181}$$

where $E(t)$ is the anemometer output, $\overline{U}_1 + u_1'$ the incident longitudinal velocity and $\overline{T}_a + \theta_a'$ the incident fluid temperature. For small fluctuations, (5.181) can be rewritten

$$\frac{e'(t)}{\overline{E}} = S_{U_1}\frac{u_1'}{\overline{U}_1} + S_{T_a}\frac{\theta_a'}{\overline{T}_a}\,, \tag{5.182}$$

where the factors S are the sensitivity coefficients of the chosen anemometer to velocity and temperature. As early as 1947, *Corrsin* [5.287] pointed out the possibility to adjust the wire overheat $\overline{a}_w$ to modify the relative value of the ratio S_{T_a}/S_{U_1} in a constant-current anemometer and, hence, the relative weight of the velocity and temperature contributions in (5.182). A set of independent algebraic equations was obtained and its

resolution provided the turbulence levels $\overline{u_1'^2}$, $\overline{\theta_a'^2}$ and the velocity–temperature correlation $\overline{u_1'\theta_a'}$. This method is still in use. Furthermore, in the limit $\overline{a}_w \to 0$, the corresponding *cold* wire acts as a resistance temperature sensor and gives the temperature fluctuations. In practice, one has to see how small $\overline{a}_w$ can be set compared with the anemometer noise. This also leads to the use of very fine wires, down to 0.25 µm. With two wires operated simultaneously, one can dispose of two equations similar to (5.181) or (5.182); adequately combining them gives the instantaneous fluctuations $u_1'(t)$, $\theta_a'(t)$, and the mean values $\overline{U}_1$, $\overline{T}_a$. Most of these techniques can also be extrapolated to higher combinations of sensors, such as a X-wire associated with a cold wire to obtain $\overline{u_1'^2}$, $\overline{u_2'^2}$, $\overline{\theta_a'^2}$, $\overline{u_1'u_2'}$, $\overline{u_1'\theta_a'}$, and $\overline{u_2'\theta_a'}$. In this section we examine the most important topics related to these techniques.

The Multiple Overheat Ratio Method with One Wire

From the sensitivities S_{U_1} and S_{T_a} given in Sects. 5.2.2 and 5.2.3 one easily obtains the ratio S_{T_a}/S_{U_1}

$$\frac{S_{T_a}}{S_{U_1}} = -\frac{2}{\overline{a}_w}\frac{B\sqrt{\overline{U}_1}}{A+B\sqrt{\overline{U}_1}}\chi\overline{T}_a\left[1-\chi\left(\overline{T}_a-T_0\right)\right] \simeq -\frac{2}{\overline{a}_w} \qquad (5.183)$$

independent of the anemometer type. The approximate value $-2/\overline{a}_w$ is for $A \ll B\sqrt{\overline{U}_1}$, $T_a \simeq T_0$ and $\chi \simeq 1/T_a$. This clearly shows that adjusting the overheat ratio $\overline{a}_w$ permits modification of the ratio S_{T_a}/S_{U_1}. Squaring (5.182), using the approximate sensitivity ratio $-2/\overline{a}_w$ and averaging, yields

$$\frac{1}{S_{T_a}^2}\frac{\overline{e'^2}}{\overline{E}^2} = \frac{\overline{\theta_a'^2}}{\overline{T}_a^2} - \overline{a}_w\frac{\overline{u_1'\theta_a'}}{\overline{U}_1\overline{T}_a} + \frac{\overline{a}_w^2}{4}\frac{\overline{u_1'^2}}{\overline{U}_1^2}\,. \qquad (5.184)$$

The anemometer type appears only in the left-hand side of this equation through the sensitivity coefficient S_{T_a}. A minimum of three values of the overheat ratio $\overline{a}_w$ is required to extract $\overline{\theta_a'^2}/\overline{T}_a^2$, $\overline{u_1'^2}/\overline{U}_1^2$, and $\overline{u_1'\theta_a'}/\overline{U}_1\overline{T}_a$. More values permit the data to be smoothed and yield greater accuracy, as is done in supersonic flows where temperature is an inherent variable to be determined.

The *Cold* Wire Method

In the limit $\overline{a}_w \to 0$, the wire operates as a resistance sensor and advantageously isolates the temperature fluctuation θ_a'. However, different problems have to be examined: the residual velocity contamination, the time constant, end effects, and electronic noise.

Using King's law (5.48), and assuming $R_w \simeq R_a$ except in the difference $R_w - R_a$, the condition on $\overline{a}_w$ shows that the sensitivity ratio at a fixed velocity varies as the inverse square of the current I_w through the wire

$$\frac{S_{T_a}}{S_{U_1}} \simeq -2\left(A+B\sqrt{\overline{U}_1}\right)\frac{1}{I_w^2} \quad \text{for a CCA}\,, \qquad (5.185)$$

and as the inverse square of the wire voltage V_w

$$\frac{S_{T_a}}{S_{U_1}} \simeq -2\left(A+B\sqrt{\overline{U}_1}\right)\frac{R_a^2}{V_w^2} \quad \text{for a CVA}\,. \qquad (5.186)$$

A CTA cannot operate a cold wire because its response is strongly nonlinear at low overheats and its feedback loop also loses effectiveness (Sect. 5.2.3).

Equation (5.185) clearly shows that very small current intensities have to be used. Accordingly, the wire output signal is small and a fine wire is preferred. Tungsten wires are commercially available with $d = 3.2$ and 4.3 µm and platinum and platinum–rhodium wires with $d = 2.5$, 1.0, 0.63, and even 0.25 µm. The current to realize a *cold* wire is around 0.20 mA for $d = 2.5$ µm, 0.15 mA for $d = 1.0$ µm, 0.10 mA for $d = 0.63$ µm and 0.05 mA for $d = 0.25$ µm. The overheat ratio is then less than 0.01. For a wire length of around 0.5 mm, the cold wire resistance is of the order of 10 Ω for $d = 2.5$ µm, 60 Ω for $d = 1.0$ µm, 150 Ω for $d = 0.63$ µm, and 1200 Ω for $d = 0.25$ µm. Extrafine wires are reserved for low-speed laboratory experiments requiring high-frequency responses and low noise. Special circuits have also to be developed to accept such large values of the wire resistance. Data are reported among others by *Yeh* and *Van Atta* [5.288], *Fulachier* [5.289], *Paranthoen* et al. [5.290], *Browne* et al. [5.291], *Mydlarski* and *Warhaft* [5.292], and *Tagawa* et al. [5.293] and *Mestayer* and *Chambaud* [5.294].

The wire resistance changes with flow temperature are small and they require high amplification factors or the use of special bridges. A first attempt by *Yeh* and *Van Atta* [5.288] made use of a high-frequency carrier as in AC strain gauge bridges. *Lin* and *Lin* [5.295] developed a special bridge, and *Tavoularis* [5.296] used a reference voltage source. Output signals on the order -0.10 V/K were obtained. Present commercial systems permit outputs up to -0.5 V/K. The coefficient χ that links resistance and temperature also has to be accurately known. *Van Dijk* and *Nieuwstadt* [5.65] examined different techniques, including the common one that makes use of an oven.

The electronic noise of the circuit and the signal-to-noise ratio should also be estimated prior to measurements. These values will be those which finally determine the current intensity through the wire. The use of a low-pass filter that keeps only the significant part of the signal is beneficial, for example, a low-pass filter set at 5 kHz was used by *Browne* et al. [5.291] and *Lemay* and *Benaïssa* [5.66]. When a known frequency prevails, such as in a pulsed jet or in an acoustic resonating cavity, a narrow-band pass filter can be associated to that known frequency. *Huelsz* and *Ramos* [5.300] reported results with a ±5 Hz filter around 130 Hz in an acoustic refrigerator.

Values of the time constant M_w of *cold* wires are reported in Fig. 5.42. The measurement of M_w at small overheat can be obtained in different ways.

- Use of the time step response of the wire to an externally injected square wave signal, as is done for hot-wires. This is advantageously made in a low-turbulence environment. Some difficulties can be encountered due to the electronic noise.
- Measurement of the frequency response of the wire to a sine-wave injection, then $M_w = 1/(2\pi f_c)$, where f_c is the frequency at which a −3 dB reduction occurs in the wire response.
- Use of the response of the wire placed alternatively in a hot/cold flow at a known frequency. *Antonia* et al. [5.297] placed the cold wire downstream of a larger-diameter cylinder that was pulsed at different frequencies with a short-duration voltage pulse. *Paranthoen* et al. [5.290] vibrated the wire across a cold/hot interface.
- Extrapolation towards $\overline{a}_w = 0$ of M_w data obtained at slightly higher $\overline{a}_w$ values. This can be a way to get around the electronic noise that precludes accurate measurements. Preliminary CVA data were successful using the interval $\overline{a}_w = 0.08–0.20$.
- Radiative heating of the sensor, as suggested by *Kidron* [5.145]. The radiant flux should be well focussed on the wire itself, avoiding stubs for platinum wires etched from Wollaston or prongs for bare tungsten.

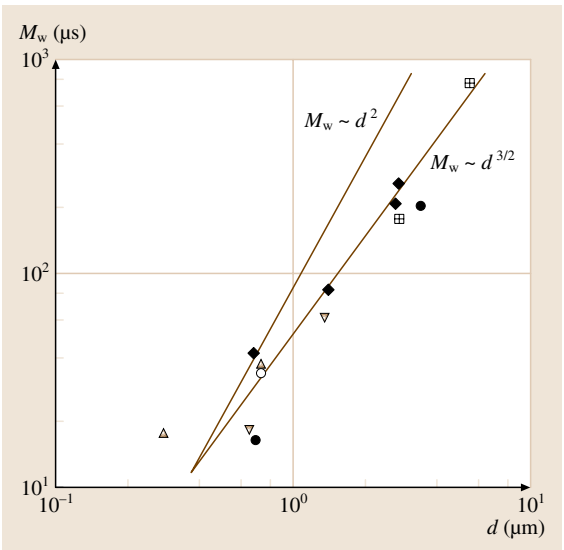

Fig. 5.42 Time constant of cold wires for $\overline{U}_1 \simeq 5$ m/s, *dagger*: *Antonia* et al. [5.297], *open circle*: *Browne* et al. [5.291], △ *LaRue* et al. [5.298], *upwards triangle*: *Lemay* and *Benaïssa* [5.66], *filled circle*: *Tagawa* et al. [5.293] *plus*: *Fulachier* and *Dumas* [5.299] *plus in circle*: CVA experiments (see references for the wire material, l/d ratio, and the presence or absence of stubs)

Estimates of M_w can be obtained from (5.103), although established for wires with infinite aspect ratio. Letting $\overline{a}_w \to 0$ gives

$$M_w = \frac{\rho_w c_w d^2}{4 k_a \mathrm{Nu}_a} \,. \tag{5.187}$$

Usually, for a regular *hot* wire, $M_w \sim d^{3/2}$ because $B_N\,\mathrm{Re}^{1/2}$ is dominant compared to A_N in the Nusselt law (5.44). For a *cold* wire A_N can play a role, as the wire is far less sensitive to the flow, thus the law $M_w \sim d^2$ can also be expected. Both the $d^{3/2}$ and d^2 laws are reported in Fig. 5.42. The former seems to fit the experimental data better irrespective of the presence or absence of stubs and the influence of the wire aspect ratio.

The spatial resolution of a cold wire relative to the temperature field is also an important topic to be considered. For isotropic turbulence, it can be investigated similarly to that was made for the velocity field (Sect. 5.2.2). Indeed *Uberoi* and *Kovasznay* [5.166] entitled their work *field mapping by the wire* without reference to the nature of the turbulent fluctuation. Only the spectral tensor $\Phi_{\theta_a}(k_1, k_2, k_3)$ and the three-dimensional spectrum $G(k)$ adapted to a scalar field have to be used. They are such that

$$\Phi_{\theta_a}(k_1, k_2, k_3) = \frac{G(k)}{k} \quad \text{with } \overline{\theta_a^2} = \int_0^\infty G(k)\,\mathrm{d}k \,. \tag{5.188}$$

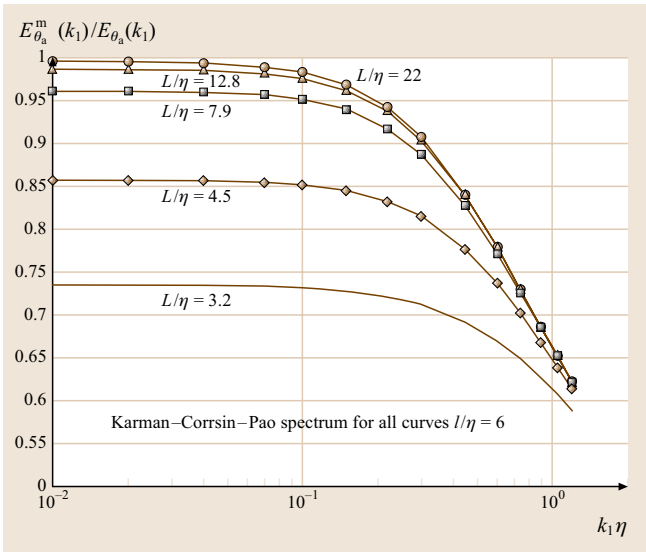

Fig. 5.43 Spatial resolution of a cold wire for the one-dimensional temperature spectra

The measured one-dimensional spectrum is therefore

$$\Phi^{m}_{\theta_a}(k_1) = \frac{1}{2}\int_{k_1}^{\infty} W\frac{G(k)}{k}\,dk \qquad (5.189)$$

with W still given by (5.128). When $W = 1$ the form established by *Kovasznay* et al. [5.301] for $\Phi^{m}_{\theta_a}(k_1)$ is recovered. In what follows a Karman–Corrsin–Pao spectrum is used for $G(k)$, being very flexible to fit laboratory or atmospheric data. Within a numerical factor (omitted for simplicity and of no consequence for the spatial resolution error based on the ratio of measured and exact values) $G(k)$ is

$$G(k) \sim \frac{\overline{\theta_a^2}}{k'_e}\frac{(k/k'_e)^2}{\left[1+(k/k'_e)^2\right]^{11/6}}\exp\left[-\frac{9}{4\,\mathrm{Pr}}(k\eta)^{4/3}\right]. \qquad (5.190)$$

Moreover, one can compute the integral length scale L_{θ_a} using the relation

$$L_{\theta_a} = \frac{\pi}{2}\frac{\int_0^\infty k^{-1}G(k)\,dk}{\int_0^\infty G(k)\,dk}. \qquad (5.191)$$

Here, k'_e is adjusted in order to have $L_{\theta_a}\eta = 3.2$, 4.5, 7.9, 12.8 and 22, as for the velocity field examined in Sect. 5.2.2. This leads to $k'_e\eta = 0.99$, 0.465, 0.183, 0.092, and 0.045, respectively. These values are very close to those used for the velocity spectra, $k_e\eta = 1$, 1/2, 1/5, 1/10, and 1/20. For atmospheric data, inner and outer scales based on the lower and upper limits of the $k^{-5/3}$ law are often preferred to k'_e and η, but the form of (5.190) still holds.

Figure 5.43 reports errors concerning the one-dimensional temperature spectra for different values of $L/\eta = L_{\theta_a}/\eta$ and a fixed wire length, $l = 6\eta$. A unity Prandtl number has been chosen. A smaller value, such as $\mathrm{Pr} = 0.70$ for air, would just lead to smaller errors as the exponential tail of $G(k)$ reduces the presence of small scales more strongly. On the whole, the errors for the temperature field appear slightly smaller than for the velocity field. A possible reason stems from the fact that Fourier components can be aligned with the wavevector for the temperature field, rather than only normal to it as for the velocity field, hence decreasing the impact of the k_3 components.

The errors on the lateral derivatives of the temperature field measured using two parallel cold wires can be similarly obtained. The measured spectrum taking into account both the wire length and the wire separation is found to be

$$D_{\theta_a,2} = \frac{1}{4}\int_{k_1}^{\infty} \mathrm{WD}\frac{G(k)}{k}\left(k^2 - k_1^2\right)dk \qquad (5.192)$$

with WD still given by (5.136). Results are reported in Fig. 5.44. Again, the errors appear to be smaller than the errors concerning a velocity field. For the longitudinal

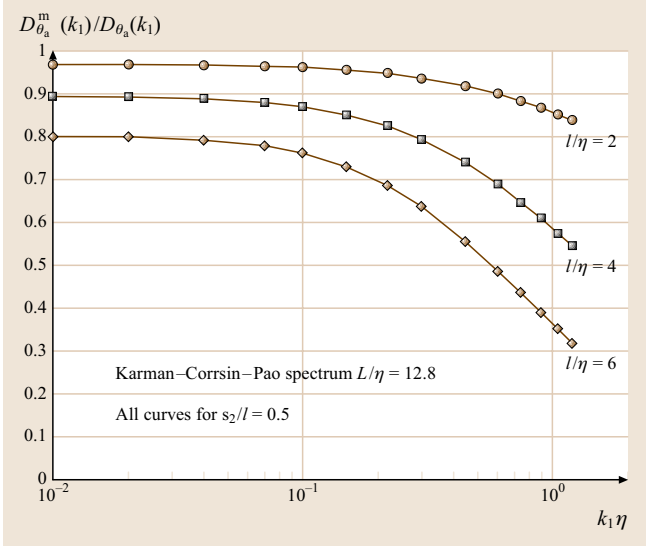

Fig. 5.44 Spatial resolution of two cold wires for the one-dimensional $\partial\theta_a/\partial x_2$ spectra

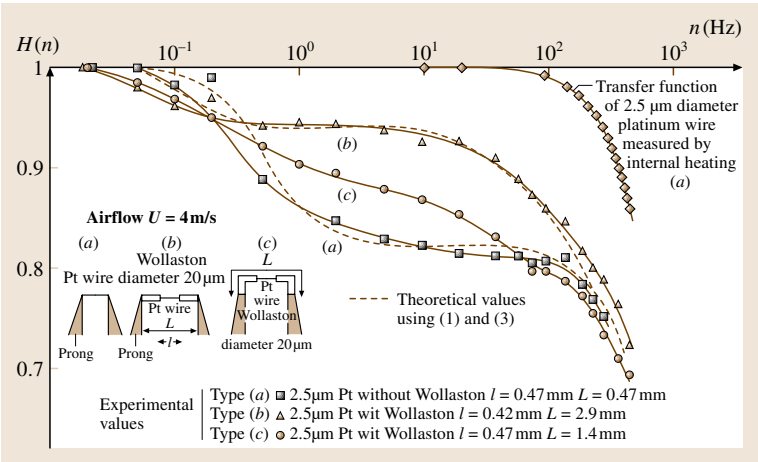

Fig. 5.45 Influence of Wollaston length and stubs on the transfer function $H(f)$ for a *cold* wire (after *Paranthoen* et al. [5.290])

derivatives, deduced from one-dimensional spectra using a single wire and the Taylor hypothesis, errors will be those that exist in the one-dimensional spectra weighted by k_1^2.

For anisotropic turbulence, no investigation has been conducted yet. Some progress using numerical simulations would be most welcome. Also, the case of *hot* wires with a mixed velocity–temperature response would be worth considering.

Finally, end losses for *cold* wires have been investigated by several researchers. As only a small part of the ohmic heating is convected away by the flow, thermal conduction towards the ends of the wire is large. Most important is the dynamic effect pointed out by *Perry* et al. [5.302], *Paranthoen* et al. [5.290, 303], and *Tsuji* et al. [5.57], with a low plateau appearing in the wire transfer function. This effect depends strongly on the aspect ratio of the wire and on the way in which the wire is bonded at its ends, in particular whether stubs are used or not (Fig. 5.45). Long stubs noticeably improve the wire response. In Paranthoen's results the wire aspect ratio is around 190, deliberately chosen small to point out the effect. Usually, fine wires present a higher aspect ratio, around 400 for a 1 μm wire that is 0.40 mm long.

The Multiple Overheat Ratio Method with Two Wires

Two wires, labeled I and II, simultaneously operated at two different overheats and closely located, give the following responses

$$E_\mathrm{I} = f_\mathrm{I}(U_1, T_\mathrm{a}) ,$$
$$E_\mathrm{II} = f_\mathrm{II}(U_1, T_\mathrm{a}) , \qquad (5.193)$$

for large turbulent changes, or

$$\left(\frac{e'}{\overline{E}}\right)_\mathrm{I} = \left(S_{U_1}\right)_\mathrm{I}\frac{u_1'}{\overline{U}_1} + \left(S_{T_\mathrm{a}}\right)_\mathrm{I}\frac{\theta_\mathrm{a}'}{\overline{T}_\mathrm{a}} ,$$
$$\left(\frac{e'}{\overline{E}}\right)_\mathrm{II} = \left(S_{U_1}\right)_\mathrm{II}\frac{u_1'}{\overline{U}_1} + \left(S_{T_\mathrm{a}}\right)_\mathrm{II}\frac{\theta_\mathrm{a}'}{\overline{T}_\mathrm{a}} , \qquad (5.194)$$

for small fluctuations. In the former case, a complete database permits one to obtain U_1 and T_a. The technique is similar to that indicated for X-wires (Sect. 5.2.4). Direct readings, as suggested by *van Dijk* and *Nieuwstadt* [5.65] or polynomial fits as suggested by *Artt* and *Brown* [5.304] can be used. In the latter case, the properly weighted sum and difference of the responses give $u_1'(t)$ and $\theta_\mathrm{a}'(t)$. A *cold* wire can be used as wire II, hence simplifying the data processing.

Calibration in Velocity and Temperature

The calibration of a wire for joint velocity and temperature measurements relies on the recording of the anemometer output while varying first the velocity at a fixed temperature and then the temperature at a fixed velocity. This requires a wind tunnel equipped with controlled heating and cooling systems. An open jet with a temperature range of 280–320 K, and a velocity range of 2–50 m/s can cover most of the subsonic needs. The probe is placed in the potential core of the jet. Obtaining smooth calibration curves or accurate look-up tables requires sufficient data points, as explained in Sect. 5.2.4 for two velocity components.

Instead of U_1 and T_a, other doublets of variables can be used. The Pitot tube reading $h = \rho_\mathrm{a}U_1^2/2$ and the thermocouple indication T_a are directly provided by an experiment; hence they are convenient measurements

for this purpose. This was suggested by *Comte-Bellot* and *Mathieu* [5.305] when working on heated wall jets. The sensitivity coefficients associated with the variables h and T_a, denoted by $\hat{S}$, can be related to S by referring to U_1 and T_a. Writing the differential response for any anemometer, we have on one hand

$$\frac{r'_w}{\overline{R}_w} \quad \text{or} \quad \frac{i'_w}{\overline{I}_w} = \underbrace{\left(\frac{\overline{U}_1}{\overline{R}_w}\frac{\partial \overline{R}_w}{\partial \overline{U}_1}\right)_{\text{cst}T_a}}_{S_{U_1}} \frac{dU_1}{\overline{U}_1} + \underbrace{\left(\frac{\overline{T}_a}{\overline{R}_w}\frac{\partial \overline{R}_w}{\partial \overline{T}_a}\right)_{\text{cst}U_1}}_{S_{T_a}} \frac{dT_a}{\overline{T}_a} \tag{5.195}$$

and on the other hand

$$\frac{r'_w}{\overline{R}_w} \quad \text{or} \quad \frac{i'_w}{\overline{I}_w} = \underbrace{\left(\frac{\overline{h}}{\overline{R}_w}\frac{\partial \overline{R}_w}{\partial \overline{h}}\right)_{\text{cst}T_a}}_{\hat{S}_h} \frac{dh}{\overline{h}} + \underbrace{\left(\frac{\overline{T}_a}{\overline{R}_w}\frac{\partial \overline{R}_w}{\partial \overline{T}_a}\right)_{\text{cst}h}}_{\hat{S}_{T_a}} \frac{dT_a}{\overline{T}_a} . \tag{5.196}$$

The increment dh can be developed in (5.196). For an incompressible fluid with thermal expansion obeying the Boussinesq assumption, and hence at constant surrounding pressure, one has $\partial\rho/\overline{\rho} = -\partial T_a/\overline{T}_a$, and therefore

$$\frac{r'_w}{\overline{R}_w} \quad \text{or} \quad \frac{i'_w}{\overline{I}_w} = \hat{S}_h\left(-\frac{dT_a}{\overline{T}_a} + 2\frac{dU_1}{\overline{U}_1}\right) + \hat{S}_{T_a}\frac{dT_a}{\overline{T}_a} . \tag{5.197}$$

Identifying with (5.195) gives

$$\begin{aligned} S_{U_1} &= 2\hat{S}_h , \\ S_{T_a} &= \hat{S}_{T_a} - \hat{S}_h . \end{aligned} \tag{5.198}$$

Another *doublet* is the mass flow rate $\rho_a U_1$ and the fluid temperature T_a. The former quantity is, for example, measured using a Brooks meter where a known fraction of the incident flow is derived and passed through a capillary tube where it is heated. The mass flow rate is deduced from the temperature rise and the heat capacity of air. The fluid temperature is measured with a thermocouple, placed in the main duct before the junction. The corresponding sensitivity coefficients, denoted by $\tilde{S}$, can be derived in a similar way as above, which gives

$$\begin{aligned} S_{U_1} &= \tilde{S}_h , \\ S_{T_a} &= \tilde{S}_{T_a} - \tilde{S}_{\rho_a U_1} . \end{aligned} \tag{5.199}$$

Sets of calibration curves or look-up tables will then use h and T_a, or $\rho_a U_1$ and T_a, as their parameters.

5.2.6 Calibration Procedures in Compressible Flows

Wires in Compressible Flows

A complete calibration procedure for high subsonic and supersonic flows, which would be similar to that in subsonic flows, is not easy to perform. One would need to change ρ, U and T_t or ρU, M and T_t independently, and this is only possible in specialized facilities. *Jones* [5.134] described such a facility which covers the ranges: $M = 0.05–1.0$, $P_t = 0.2\times10^5–1.0\times10^5$ Pa, and $T_t = 848–1098$ K for a 5.7 cm nozzle exit diameter. *Bonnet* and *Knani* [5.306] built a 1 cm supersonic calibration jet that permits the ranges $M = 1.3–3$, $P_t = 3\times10^5–14\times10^5$ Pa, and $T_t = 250–280$ K.

In practice, changes of the density ρ and mass flow ρU are made by acting on the total pressure P_t [5.122]. The Mach number M is changed by using different nozzles, as reported by *Bonnet* [5.92]. *Laufer* and *McClellan* [5.59] used a servo-driven stainless-steel flexible-plate nozzle. *Gaviglio* placed the hot-wire at different positions along the axis of a long supersonic nozzle [5.122].

Modification of T_t is less simple, because it implies an adjustment of P_t to keep ρU constant through the nozzle. Indeed, the mass flow rate for a nozzle of Mach number M and area A is given by [5.307]

$$A\rho U = AMP_t\left(\frac{\gamma}{rT_t}\right)^{1/2} \times\left(1+\frac{\gamma-1}{2}M^2\right)^{-(\gamma+1)/2(\gamma-1)} \tag{5.200}$$

where $r = R/m$ (5.58). Equation (5.200) shows that, if T_t is increased, P_t should also be increased. Often this adjustment is not possible, and the sensibility coefficient relative to T_t is computed using the term (XXX) in (5.82). This requires knowledge of n_t and m_t for the fluid, χ' for the wire, and $\overline{A}_w$ for the operating conditions. This method was used by many authors, *Rose* [5.135], *Ko* et al. [5.144], and *Gaviglio* [5.122]. Results concerning the sensitivity coefficients in supersonic flows are given in Sect. 5.2.2 and Fig. 5.18.

Calibration of inclined hot-wires in supersonic flows is usually attempted using the same procedure as in subsonic flow, by yawing the probe through an angle of about $\pm10°$. Very satisfactory results are described by *Konrad* and *Smits* [5.308] who developed special

probes. However, some difficulties were indeed encountered in earlier experiments. Wire overheat effects were reported by *Bonnet* and *Knani* [5.306]. *Fernando* et al. [5.309] investigated the problem of flow interference, where the shock waves from one wire and the wires' supports interfere with the flow on the other wire. The possible effect of the bowed shape of the wire is invoked by *Smits* and *Muck* [5.310]. Some density variation along the wire is also possible, as studied by *Reshotko* and *Beckwith* [5.311] and revisited by *Smits* and *Muck* [5.310]. The simple cosine law of the subsonic flows was therefore not so obvious for supersonic conditions, and careful analysis was advised prior to systematic measurements.

Rose and *Johnson* [5.312] preferred to use closely matched yawed wires, at approximately $\pm 45°$ to the flow direction and to measure the instantaneous difference between the two signals to obtain u_2'. The procedure is similar to that suggested by (5.40) in subsonic flows, as ρ' and θ_t' disappear in the difference. The wires were considered matched when their visual appearances were similar and their cold resistances were within 5% of each other. In principle, this direct measure of u_2' should be very pertinent for comparison with laser Doppler velocimetry (LDV) [5.313].

Attention should also be paid to the errors due to large fluctuations, as developed in Sect. 5.2.4. Since calibrations are difficult in compressible flows, sensitivity coefficients obtained with small perturbations in incompressible flows or subsonic flows are often used for the purpose (5.97). This implies that only rms, the PSD, or double correlation functions can be reasonably investigated.

Wall Sensors in High-Speed Flows

A direct calibration of wall films can also be made against a Preston tube in high subsonic and supersonic conditions. *Bradshaw* [5.314] and *Spina* et al. [5.315] analyzed the several assumptions which have to be fulfilled, and most importantly the existence of a logarithmic region. These two review articles also offer reliable skin-friction formulae that can be used whenever the global characteristics of a flow are known.

A comparison between wall hot-film and other experimental techniques for wall shear-stress measurements, such as laser interferometry, liquid crystals, or infrared imaging, was made by *Hall* et al. [5.87]. The Mach range was from 1.5–2.5 and the unit Reynolds number was 3.3×10^6–13.1×10^6 /m. The thin films provided the most reliable and quantitative indicator of the details of the transition process.

Uncalibrated sensors are usually sufficient to detect boundary-layer transition, flow separation, or shock oscillation on airfoils, because of the important magnitude changes occurring on the anemometer signals. This is an advantage when doing in-flight experiments. The very stable CVA appears particularly well adapted to this objective. Experiments are reported by *Moes* et al. [5.88] over a Mach number range of 0.68–0.80 at an altitude of 6000 m, with a 45 Ni hot-film array, the anemometers being tuned in situ to take into account the 15% decrease of the *cold* resistance compared to its value at ground level.

5.2.7 Special Techniques

The Flying Hot-Wire

One of the main restrictions of stationary hot-wire anemometry is its inability to provide measurements when reversing flow occurs. This is overcome by displacing a probe, usually an X-wire, through the flow to be investigated. At a time t the probe is assumed to be at a known position x_p, y_p, z_p and to move at a known velocity U_p, V_p, W_p. The probe responds to the relative velocity, U_r, V_r, W_r, and the flow velocity, U, V, W is connected to the measured velocity U_r, V_r, W_r by

$$U = U_p + U_r \quad V = V_p + V_r \quad W = W_p + W_r \,. \tag{5.201}$$

The probe velocity should be sufficient to ensure that all signals correspond to a velocity vector remaining within the approach quadrant of the X wire probe.

The name of *flying* probe comes from the investigation of atmospheric turbulence using a probe attached to an aeroplane, as reported by *Payne* and *Lumley* [5.316], and *Sheih* et al. [5.317]. In the laboratory the probe motion can be of various types:

- Linear, as developed by *Panchapakesan* and *Lumley* [5.318, 319] to study the external zones of air or helium jets, or by *Kelso* et al. [5.320] to investigate a flow past a fence,
- Circular, as used by *Coles* and *Wadcock* [5.321] to study the flow past an airfoil, by *Cantwell* and *Coles* [5.322] to analyze the near wake of a cylinder, by *Walker* and *Maxhey* [5.323] to investigate grid turbulence, and by *Hussein* et al. [5.324] to study turbulent jets. This last work reported interesting comparisons between a stationary hot-wire, a flying hot-wire and LDV measurements,
- Curvilinear, as developed by *Thomson* and *Whitelaw* [5.325] and *Al-Kayiem* and *Bruun* [5.326]

with bean-shaped trajectories to approach separation bubbles over airfoils.

The flying hot-wire technique requires the development of an electronic timer circuit to obtain a cyclic operation, which includes routines to initiate the motion, to acquire data during the effective passage, to move the probe back to its initial position, possibly by another path than that used for measurements, and to respect a rest position so that all flow disturbances disappear. The data from each sweep then permit to obtain phase averages for every measuring point. A full calibration of the X-wire probe is required. Many practical details of the implementation of a flying hot-wire system are available in *Bruun* [5.52].

Nowadays, flying hot-wire anemometry is in competition with laser Doppler anemometry and particle image velocimetry in laboratory experiments. However, it might keep its place for the study of atmospheric turbulence. For example, the work by *Otten* et al. [5.327] is most interesting as the aircraft speed is in the range 100–200 m/s, hence involving compressible flow around the probe.

Three-Wire Pulsed Anemometers

When heat is rapidly produced in a wire by an electric voltage pulse of a few microseconds, a tracer of heated air is introduced into the flow. This thermal wake can be detected by a sensor acting as a resistance probe placed downstream of the heated wire. Furthermore, two wires placed on either side of the pulsed wire permit the determination of the velocity direction and to solve the forward–reverse ambiguity of the flow.

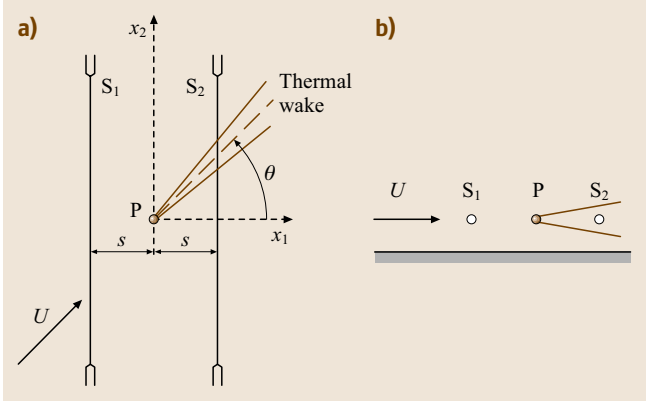

Fig. 5.46a,b Sketch of a three-wire pulsed probe. P is the pulsed wire, S_1 and S_2 are the sensors detecting the thermal wake: **(a)** general set up with sensors perpendicular to the pulsed wire, **(b)** special set up for laminar or acoustic flows

Figure 5.46 illustrates a pulsed probe. Usually the two sensor wires are parallel and their axes are perpendicular to the axis of the pulsed wire (Fig. 5.46a). This permits the thermal wake to impact either on one of the sensors even in the presence of turbulence. The sensors, kept parallel and perpendicular to the pulsed wire, can also be slightly inclined onto the pulsed wire. It was shown that this setup improves the directional response of the global probe. *Jaroch* [5.328], *Castro* and *Haque* [5.329], and *Castro* and *Dianat* [5.330] suggested setting the angle to about 30°. Sensor wires parallel to the pulsed wire Fig. 5.46b are appropriate when the thermal wake remains along a known line and downstream of one of the two sensors. This is possible for separated laminar flows or acoustic fields. Close to a wall where strong velocity gradients exist the pulsed wire has to be placed parallel to the wall. The nearby wall also permits the development of *through-wall* probes where all the prongs supporting the wires stem from the wall, as reported by *Castro* and *Dianat* [5.330].

Sketches and pictures of probes are available in *Bradbury* and *Castro* [5.331], *Westphal* et al. [5.332], *Jaroch* and *Dahm* [5.333], and *Castro* and *Dianat* [5.330] among others. A 5–10 μm tungsten wire is often used for the pulsed wire to sustain the thermal loading, while 2–5 μm wires are used for the sensors. The wire length is in the range 6–10 mm, and the spacing s is in the range 1–2 mm. The working velocity range is 1–10 m/s. The repetition frequency of the pulse is rather low, around 50 Hz, because the pulsed wire is required to cool completely between pulses.

The time of flight, T, of the wake from the pulsed wire to one of the sensing wires has to be linked to the magnitude of the velocity $|U|$ and to the yaw angle θ. The velocity vector is supposed to lie in the plane of the sensors. This requires a preliminary probe orientation, comparable to the use of X-wire probes (Sect. 5.2.2). There is also an acceptance angle for the pulsed probe which is connected to the length l of the sensors and the spacing s between the pulsed wire and either one of the sensors. Obviously, the maximum possible yaw angle is $\theta_{\max} = \tan^{-1}(l/2\,s)$. With $l = 10$ mm and $s = 1$ mm, this leads to $\theta_{\max} \simeq 75°$.

The velocity magnitude $|U|$ and the time of flight T could be thought of as simply connected through a convective process, which would give

$$T = \frac{s}{|U|\cos\theta} \quad \text{and} \quad U_1 = \frac{s}{T}\,. \tag{5.202}$$

Calibrations show that the cosine law is approximately obtained at fixed values of $|U|$ [5.329, 334]. Regarding the time of flight T, more-complex expressions than (5.202) are reported at fixed θ. For example *Handford* and *Bradshaw* [5.334] or *Castro* and *Haque* [5.330] indicated

$$U = a\frac{1}{T} + b\frac{1}{T^2} + c\frac{1}{T^3} + d\frac{1}{T^4} \,. \tag{5.203}$$

The reason for this difference is that many physical mechanisms other than convection are involved in the generation, development, and reception of the thermal wake.

- The turbulent dispersion brought due to all three turbulent velocity fluctuations enlarge the wake. An estimate necessarily involves the statistical properties of the turbulence field. Very roughly, the assumption of a short-time dispersion gives a displacement in the i direction $\delta_i \simeq u_i' T \simeq 0.2\,\mathrm{mm}$ for a turbulence intensity around 20%, for $U = 10\,\mathrm{m/s}$ and $T = 0.1\,\mathrm{ms}$. The viscous diffusion of the wake adds a small widening of the wake, on the order of 0.02 mm as given by $\delta \simeq (\nu T)^{1/2}$ for $\mathrm{Pr} = 1$.
- When the thermal wake hits the sensor, the impact only concerns a small fraction of the length of the wire, around 0.2 mm as estimated above, when the sensors are normal to the pulsed wire. The thermal conduction along the axis of the sensor wire becomes important, with heat conducted towards both the supporting prongs. This problem is more complicated than that considered in Sect. 5.2.2 where the whole wire was submitted to a flow. This topic has mostly been considered by *Bradbury* and *Castro* [5.331].
- Close to a wall the contours of constant temperature after the release of a heat *puff* are additionally distorted by the velocity shear as they move downstream. *Castro* and *Dianat* [5.330] established analytical results for a uniform shear flow. These contours are ellipses, highly elongated along the O_{x_1} direction by up to 0.4 mm when arriving at the sensing probe, and slightly tilted up towards the rapidly moving fluid. As a consequence, only a smeared temperature front arrives on the sensor. Incidentally, these contours are very similar to those established by *Tennekes* and *Lumley* [5.162] for the dispersion of particles in a uniform shear flow.
- Finally, the thermal inertia of the sensor introduces a time delay in its response. *Bruun* [5.52] established an interesting relation that gives the time $t_{\max}$ at which the maximum amplitude of the signal occurs, taking into account the relative importance of the thermal lag of the sensor M_S to that of the pulsed wire M_P

$$t_{\max} = \frac{s}{U} + \frac{M_P M_S}{M_p - M_S} \log \frac{M_P}{M_S} \,. \tag{5.204}$$

To achieve the best measurement of the time of flight, *Handford* and *Bradshaw* [5.334] advise working on the signal slope, in order to differentiate the time signal provided by the sensor. The flight time is then deduced from the point at which the slope value passes through a preset level. This method was found to be nearly independent of the flow speed.

The number of flight times that are necessary to achieve a prescribed accuracy depends strongly on both the turbulence characteristics that are studied, mean velocities or Reynolds stresses, and on the level and scale of turbulence present. An order of magnitude is 2000 flight times, which gives a total acquisition time of around 40 s.

During measurements, the most appropriate orientation of the pulse-wire probe within the flow also has to be selected. Alignment with the streamwise direction $\theta = 0$ provides accurate measurements of $\overline{U}_1$ and $\overline{u_1'^2}$. Other angles θ are introduced to obtain $\overline{U}_2$, $\overline{u_2'^2}$, and $\overline{u_1' u_2'}$. Pitch angles are also sometimes needed. Many details are given by *Castro* and *Cheun* [5.335], and *Jaroch* [5.328].

The pulsed probes have proved their capabilities in the highly recirculating zones close to obstacles. *Bradbury* [5.336] obtained complete streamline patterns in the very near wake of a flat plate placed normal to a 7.5 m/s flow. *Castro* and *Haque* [5.329] added a central splitter and investigated the normal and tangential Reynolds stresses and the momentum balance. Experiments in an axisymmetric free jet were reported by *Jaroch* [5.328]. The measurements of $\overline{U}_1$ and $\overline{u_1'^2}$ with single hot-wire and different types of pulsed-wire probes agreed very well. Some scatter appeared on other quantities such as $\overline{U}_2$, $\overline{u_2'^2}$, or $\overline{u_1' u_2'}$. To reduce this, he advised the use of pulsed-wire probes with the largest and most symmetric acceptance cone. *Venas* et al. [5.337] conducted experiments in wall jets and reported satisfactory agreement with laser Doppler anemometer data.

One-Wire Pulsed Anemometers

Another technique to measure flow velocity uses the response of a wire first heated with a very short electrical pulse and then left to relax and cool. The velocity can be deduced from the time history of the evolution, which is a function of the velocity component U nor-

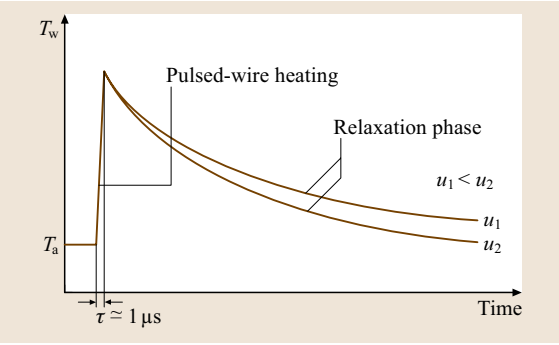

Fig. 5.47 Time evolution of the pulsed wire temperature during pulse and relaxation periods, for two speeds, U_1 and U_2 with $U_1 < U_2$: pulse duration 1 µs, current intensity when pulsing $I_{wp} = 1$ A. The pulse heats the wire by around 50 K. (After *Mathioulakis* et al. [5.339])

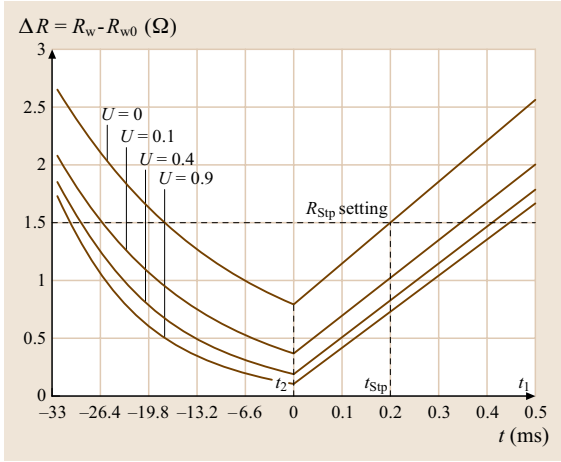

Fig. 5.48 Resistance variation in one balanced cooling–heating cycle for the heat pulse integrator method. Pulse duration 20 µs, current intensity when pulsing $I_{wp} = 0.5$ A. Note the asymmetric shape of the curve. (After *Li* and *Gow* [5.341])

mal to the wire. This idea was introduced by *Calvet* and *Liousse* [5.338] in 1971 for free convection flows, and received a renewal of attention after 1994 through the works of *Mathioulakis* et al. [5.339], *Grignon* et al. [5.340], *Li* and *Gow* [5.341], *Foss* et al. [5.342], *Foss* and *Hicks* [5.343], *Morris* and *Foss* [5.155], and *Hicks* et al. [5.344].

In the first set of papers, by Calvet, Liousse, Mathioulakis and Grignon, the wire is at ambient temperature before the pulse triggering, and after the pulse the wire is left to relax back to the ambient temperature. Figure 5.47 illustrates the temperature evolution of the wire for two incident velocities.

In that case, the characteristic time τ_1 for the temperature rise during the pulse period is obtained by neglecting the convection term in the heat balance of the wire given by (5.98). This leads to

$$\tau_1 = \frac{\pi d^2}{4}\rho_w c_w l \frac{1}{R_a \chi I_{wp}^2}\,, \qquad (5.205)$$

where I_{wp} is the constant current applied during the pulse.

During the relaxation period, the characteristic time τ_2 is the time M_w^{CCA} given by (5.103). For clarity, this equation is rewritten, as it shows that the velocity dependence appears through a Nusselt number

$$\tau_2 = (1 + a_w)\frac{d^2}{4}\frac{\rho_w c_w}{k_a}\frac{1}{\mathrm{Nu}_a}\,, \qquad (5.206)$$

where I_w is the constant floor current through the wire. Obviously $\tau_1 \ll \tau_2$. The temperature rise is sharp and almost linear, and the temperature relaxation is close to an exponential law. In their experiments the authors advantageously used a long wire, $l/d = 700$, with $d = 5\,\mu m$ and $l = 3.5$ mm to avoid end losses. The pulse frequency was around 1 kHz, which appeared sufficient for the free convection flows investigated, as the velocity was in the range 0.1–1 m/s. The current I_w was set low enough that the wire was *cold* between pulses and the ambient temperature could be measured.

The velocity U is obtained from (5.206) using (5.45) or (5.46). A regression was applied to the $R_w(t)$ variation during relaxation. Fitting the curve by an exponential law was found possible despite some discrepancies at short times because of thermal diffusion close to the hot wire. *Breton* [5.345] and *Grignon* et al. [5.340] developed analytical models to investigate the interactions that take place between convection, diffusion, and conduction at the wire level.

In the work of Li and Gow, the wire is not allowed to reach the ambient condition before it is reheated. The wire then works as a *heat integrator*, although a balanced cooling–heating cycle is permitted as illustrated in Fig. 5.48. Several parameters of interest were also investigated: the pulse width, the length of the interpulse period compared to the relaxation time of the wire, and the time it takes for the wire to reach some imposed high temperature. In Fig. 5.48 this set temperature point is noted Stp. As an application, the case of a 35 mm cylinder made of Tufnol and placed in a 5–10 m/s flow was considered. The cylinder was pierced to allow the

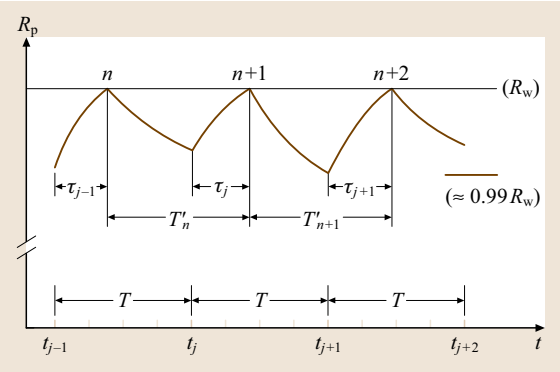

Fig. 5.49 Sketch of the heating and relaxing time traces for a one-wire pulsed probe, during three cycles. A ceiling value R_w is imposed, T is the clock period which imposes reheating. The heating and relaxing curves differ from one cycle to the next due to a velocity change. (After *Foss* et al. [5.342])

installation of 32 equally spaced wires mounted normal to the circular section. The wires, 20 µm platinum, were almost touching the cylinder surface, hence their cooling by the flow was close to that of hot-wire wall sensors. The pulse frequency was around 100 Hz. The results they found revealed good agreement with the survey conducted by *Bellhouse* and *Schultz* [5.146].

In the works by Foss, Hicks and coworkers, the wire is almost not allowed to cool between pulses, roughly by only 0.01%. The pulsing frequency is therefore very high, around 100 kHz in their most recent developments. The heating and relaxing time traces show different concavities, but their durations become roughly the same order because the convection by the flow becomes important during both the heating and relaxing periods. Figure 5.49 illustrates three cycles. Because of the imposed ceiling resistance R_w and the duration of the puls,e which has to change when the velocity varies, their system has been called a *pulse-width-modulated constant-temperature anemometer* (PWM-CTA). Block diagrams and details for the time acquisitions and connection with the velocity are available in *Foss* et al. [5.342]. Calibration of the system has been performed up to around 30 m/s and mean velocity profiles have been acquired in the shear layer of a subsonic jet.

A PWM-CTA has distinctive features. Fundamentally, it is a digital anemometer although the heat transfer and power dissipation processes that govern its behavior are analogue in character. Unlike a conventional CTA it does not require an A/D converter to transfer its output for further processing. Also, a PWM-CTA does not need a feedback loop, which is unstable in a conventional CTA. The electronic noise per se is not a relevant issue, but the comparator that is used to define the times τ_j in a cycle results in an inherent uncertainty. Further developments of these important topics are presented later in this Handbook.

5.2.8 A Comprehensive Technique for X-Array Calibration and Data Processing

Calibration

This section presents a calibration/processing strategy that is intended to provide an efficient and an accurate procedure to recover Q and γ from E_1 and E_2 (the slant-wire voltages), where Q is the velocity magnitude in the plane of the X and γ is the angle of the flow (in the plane defined by the X-array) (Fig. 5.50). This section provides an alternative approach to that presented in Sect. 5.2 of the Handbook. It is noted that the use of analytic expressions ensures the monotonicity of the calibration data: $\partial E/\partial Q$ and $|\partial E/\partial\gamma|$ are uniformly positive over the calibrated range of Q and γ. E_1 and E_2 are the output voltages from the two slant wires of the array. The velocity and angle ranges are to define a *complete calibration* such that the Q and γ values of the investigated flow field are adequately included in the calibration data.

An example of a *complete* calibration data set would be one for which 13 angles ($\gamma = +36°, +30°\ldots0°, \ldots -30°, -36°$) were used to position the probe axis with respect to the calibration stream and a series of velocity values were obtained at each angle. These data could be fit with (using the CTA as an example):

$$E_j^2 = A_j(\gamma) + B_j(\gamma)Q^{n_j(\gamma)} \qquad (5.207)$$

for the 13 γ values (where $j = 1, 2$ for the two wires of the X-array).

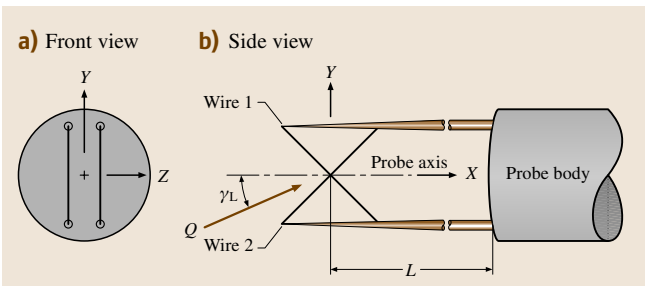

Fig. 5.50 Definition sketch for an X-array

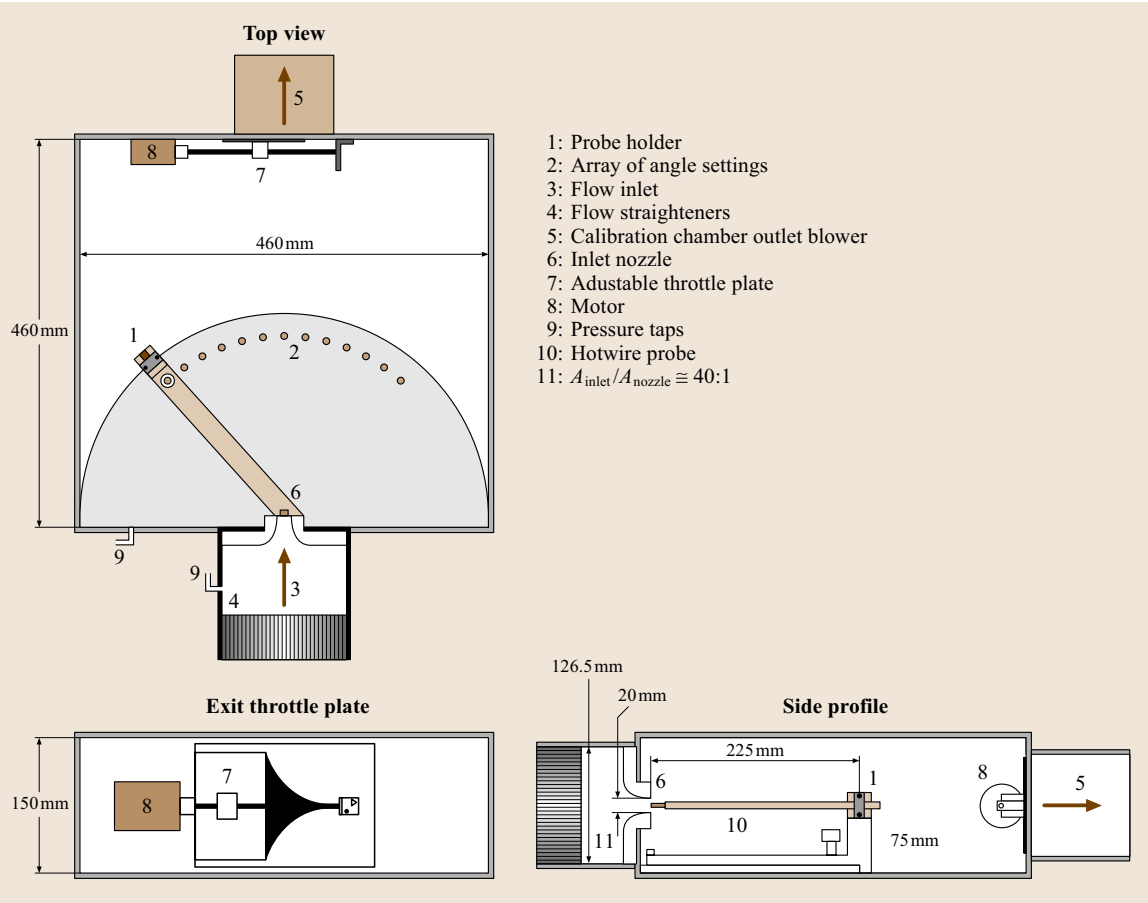

Fig. 5.51 Transient flow calibration device

The effective velocity formulation [(5.172) of Sect. 5.2.4] *collapses* the angle information of (5.207) into the single coefficient k. Experience [5.346] shows that A and n are distinctly not constant over all angles even for an X-array that meets the stringent *Strohl* and *Comte-Bellot* [5.69] geometric conditions. These earlier results are confirmed by the data of this section. The deviations in the A, B, and n values are most pronounced when the velocity approaches tangency with respect to the sensor. As a result, the use of an effective velocity (which implicitly assumes constant A and n values with the variable B reflected in the k value) cannot provide as precise a fit to the calibration data over all γ values as that provided by (5.207).

Equations of the form (5.207) also ensure the monotonicity noted above.

The requirement for an extensive body of calibration data can be effectively met using a *controlled transient* calibration tunnel to obtain the data in a minimum time. Figure 5.51 shows a representative configuration for such a calibration device. Figure 5.52 presents the transient data for each slant wire. Note that the *jagged* traces are a result of acquiring the voltages during the transient opening of the throttle plate shown in Fig. 5.51.

The analytic form of (5.207) will *smooth* the jagged data into a monotonically increasing distribution as shown in Fig. 5.53. Specifically, the processed data of Fig. 5.52 are presented in the form of $E(Q, \gamma)$ for the range $2 \leq Q \leq 18$ m/s in Fig. 5.53. It is apparent that a smooth calibration data set is achieved. The stepper-motor-controlled throttle plate was driven for a period of 40 s to develop the velocity range of 2–18 m/s. The complete calibration (13 angles) can nominally be executed in 15 min.

The A, B, and n values at each γ are selected to provide the minimum standard deviation between the

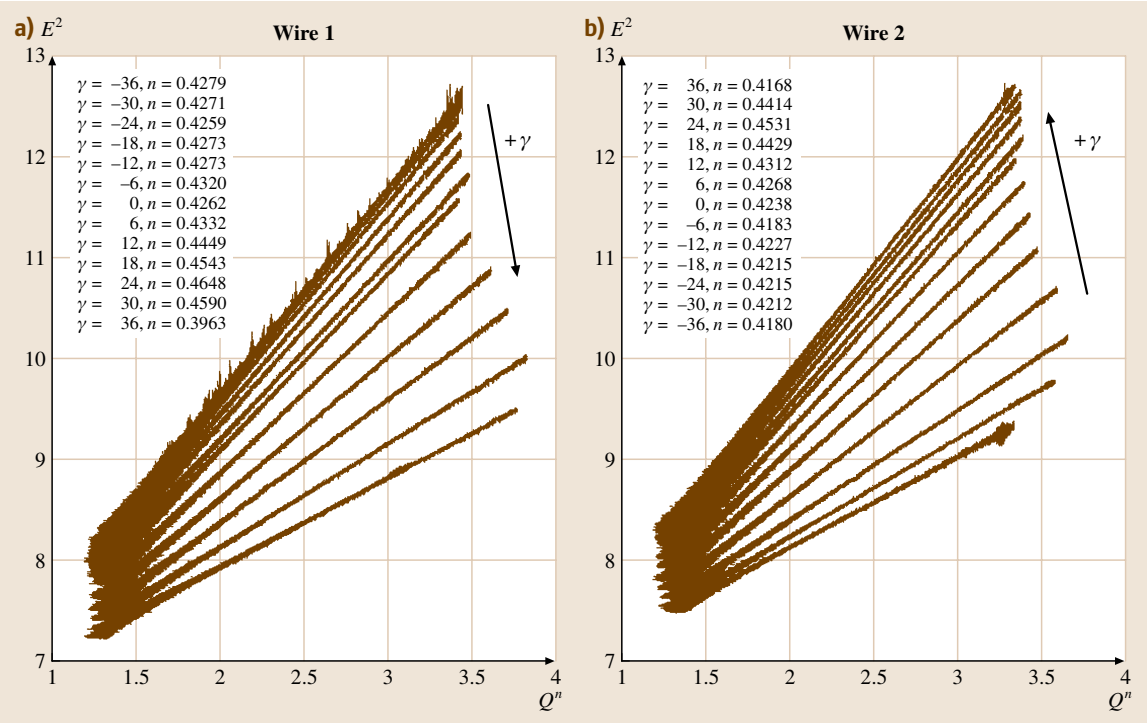

Fig. 5.52a,b Initial calibration data for the two slant-wire sensors. **(a)** $E_1^2 = f_1(Q^n; \gamma)$. **(b)** $E_2^2 = f_2(Q^n; \gamma)$

measured and the analytical values (5.208). Figure 5.54 presents $A(\gamma)$, $B(\gamma)$, and $n(\gamma)$; it is apparent that all three coefficients should be allowed to vary with respect to the calibration angle γ.

The velocity magnitudes are obtained from the pressure differences between the tap that is forward of the nozzle and the tap in the receiver chamber. (It has been confirmed that the upstream tap provides a true value for the stagnation pressure.) This use of the Bernoulli equation is predicated upon a *steady-state* condition. Specifically, that

$$\int_{S_1}^{S_2} \frac{\partial V}{\partial t}\,\mathrm{d}s \ll \frac{1}{2}\left[V^2(S_2) - V^2(S_1)\right] + \frac{1}{\rho}\left[p(S_2) - p(S_1)\right]. \qquad (5.208)$$

This assumption has been evaluated by comparing the results of:

- a steady-state calibration – a 10 s acquisition at each velocity setting, with
- the results of three different transient conditions: 40, 50, 60 s durations for the acquisition period.

Figure 5.55 shows these data for the representative condition of wire 2 at $\gamma = 18°$. A fixed value of ΔE^2 has been added to the E^2 values of the transient data in order to separate these distributions on the figure. It is apparent that the transient condition does not violate the use of the Bernoulli equation. Obviously, a much longer calibration period would be required if a steady-state calibration protocol were used for all Q and γ values. These data also verify the use of (5.207) to average the unsteady oscillations properly about the correct mean values.

Processing Algorithm

Flow field measurements, of course, invert the calibration process. Voltages (E_1 and E_2) are measured and the Q and γ values are sought. The recommended algorithm can best be described graphically. The computational method described in this section was developed by *Browne* et al. [5.249] and independently by *Morris* [5.347]. It is also readily implemented via software postprocessing of the time series of voltage values.

Consider a voltage pair: $E_1 = 2.734\,\mathrm{V}$ and $E_2 = 2.653\,\mathrm{V}$. From Fig. 5.53, it is apparent that these voltage values will intersect the 13 curves, resulting in

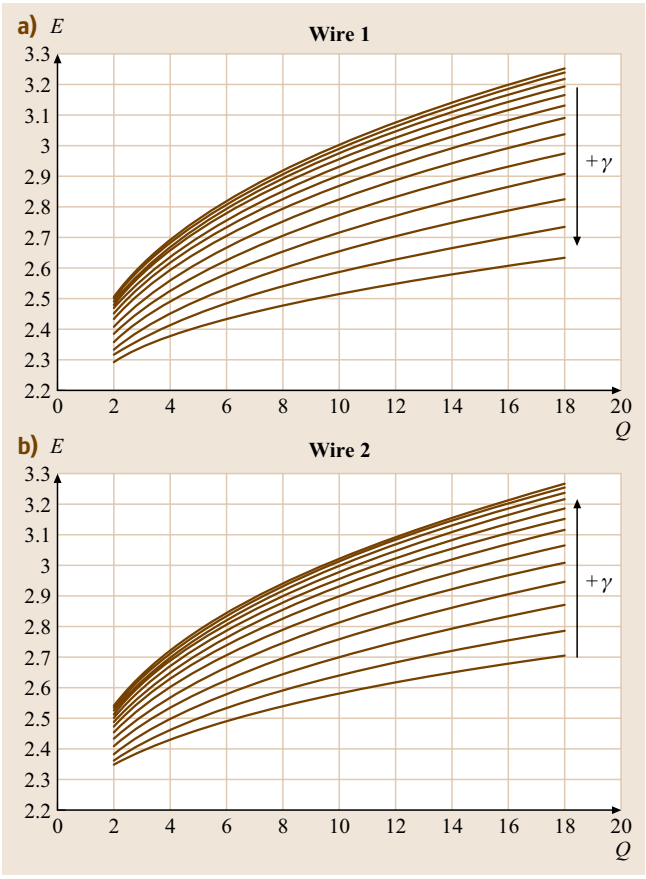

Fig. 5.53a,b A complete set of smoothed calibration data for $0 \le Q \le 18\,\mathrm{m/s}$ and $-36 \le \gamma \le 36°$. **(a)** $E_1 = g_1(Q;\gamma)$. **(b)** $E_2 = g_2(Q;\gamma)$

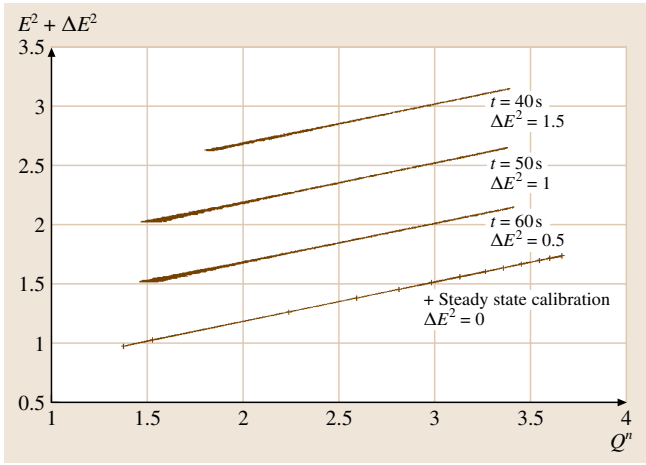

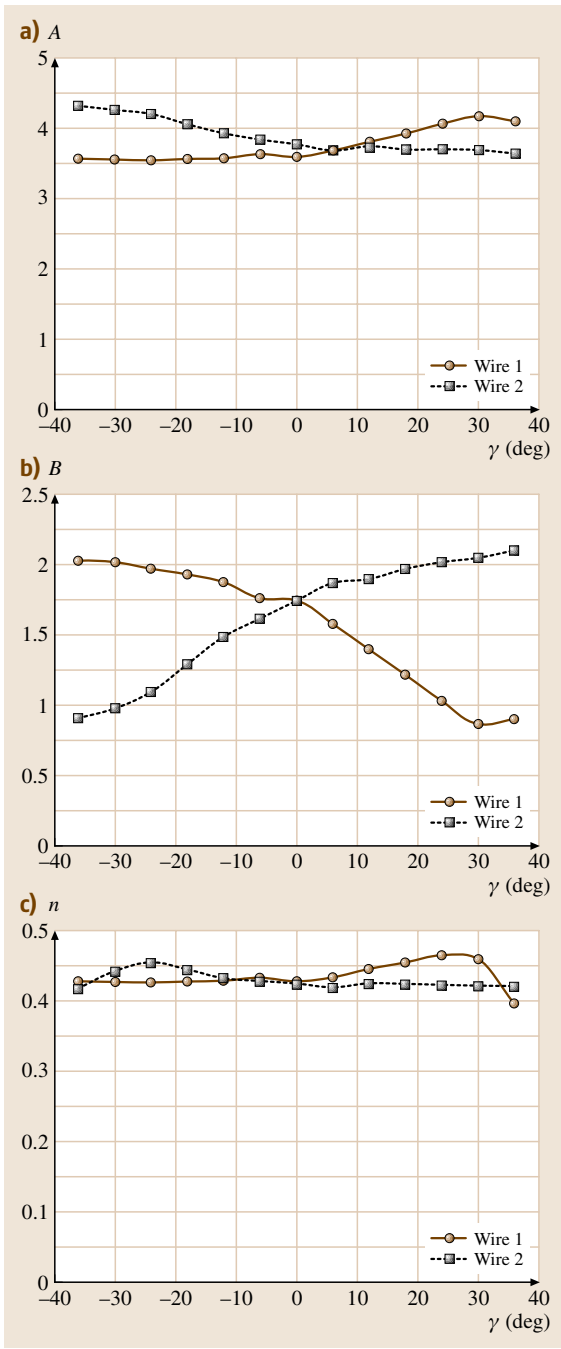

Fig. 5.54a–c Best-fit A, B, and n values for the slant-wire sensors 1 and 2

Fig. 5.55 Confirmation of the transient velocity calibration protocol. Note: these data are for slant-wire $\gamma = 18°$ ◀

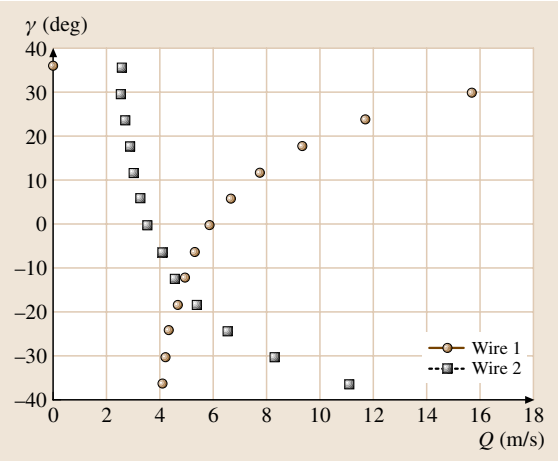

Fig. 5.56 Q and γ values that are separately compatible with the measured E_1 and E_2 values

26 discrete velocity values. The 13 (Q, γ) values for each sensor can then be plotted on common axes, as shown in Fig. 5.56. Consider that smooth curves are used to interpolate between the discrete data points from each sensor.

It is apparent that the true (Q, γ) values for the measured (E_1, E_2) values are defined by the intersection of the two curves. Computationally, one could fit a second- or third-order polynomial through the three or five points closest to the intersection point to determine the intersection values. As shown in Fig. 5.57, both interpolation curves provide a precise indication of the (Q, γ) values that correspond to the (E_1, E_2) values. The inferred velocity magnitudes differ by 0.6% and the angles differ by 0.11°. These values are within the tolerances one would expect from an X-array measurement.

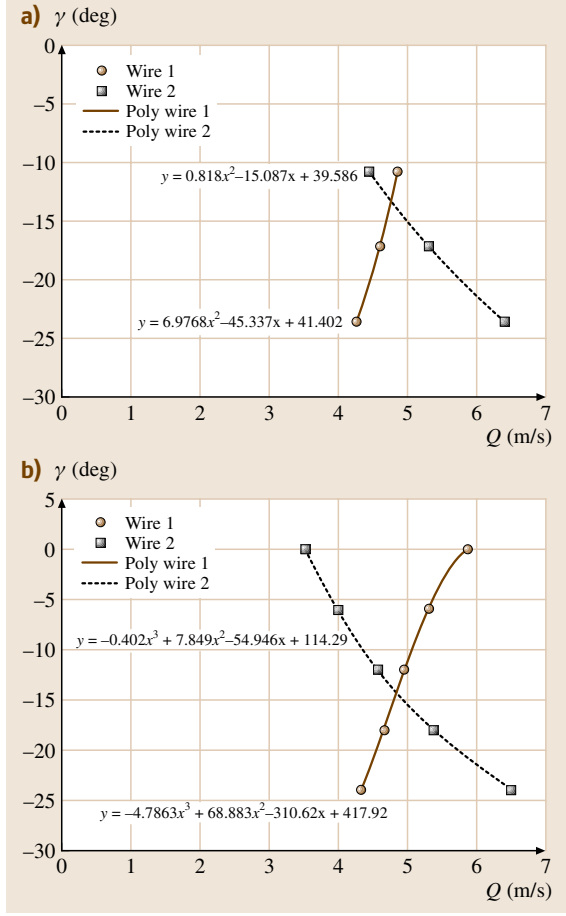

Fig. 5.57a,b Derived (Q, γ) values from the measured (E_1, E_2) values: **(a)** three-point second-order fit ($Q = 4.88$ m/s, $\gamma = -14.6°$), **(b)** five-point third-order fit. ($Q = 4.85$ m/s, $\gamma = -14.4°$)

Summary

The $A(\gamma)$, $B(\gamma)$, and $n(\gamma)$ values of Fig. 5.54 indicate that an accurate calibration requires a complete calibration of an X-array probe. If one adopts the practice of acquiring a complete calibration *before* and *after* a data set (to confirm the integrity of the data), then an efficient as well as a complete calibration process is advantageous. The transient calibration described above provides these attributes.

5.3 Particle-Based Techniques

5.3.1 Tracer Particles

In this Section four optical measurement techniques for flow velocity based on tracer or seed particles in the flow will be described: laser Doppler anemometry/velocimetry (LDA, LDV), particle image velocimetry (PIV), Doppler global velocimetry (DGV), and laser transit velocimetry (LTV). These techniques rely on the

presence of particles in the flow that not only follow all flow velocity fluctuations but are also sufficient in number to provide the desired spatial or temporal resolution of the measured flow velocity. Of course it is desirable that these tracer particles are at the same time good light-scattering centers, since this improves the signal quality for a given incident laser power. The fact that flow tracking demands small particles and light scattering improves with increasing particle size already suggests the need for optimization when choosing tracer particles. The following section deals therefore with the tracer particle issues common to all of the measurement techniques, in particular the particle motion in flows is examined, the scattering properties of particles, their generation and their introduction into the flow.

Particle Motion in Flows

Within the approximation of low Reynolds number, the equation of motion of a small spherical particle immersed in a fluid flow is given as

$$\begin{aligned}
&\frac{4}{3}\pi a^3 \rho_\mathrm{p} \frac{\mathrm{d}\boldsymbol{v}}{\mathrm{d}t} \\
&= \underbrace{\frac{4}{3}\pi a^3 \rho_\mathrm{f} \frac{\mathrm{D}\boldsymbol{V}}{\mathrm{D}t}}_{\text{non-inertial force}} + \underbrace{\frac{4}{3}\pi a^3 (\rho_\mathrm{p} - \rho_\mathrm{f})\boldsymbol{g}}_{\text{net body force}} \\
&\quad \underbrace{-6\pi\mu a \left[(\boldsymbol{v}_\mathrm{p} - \boldsymbol{U}) - \frac{1}{6}a^2 \nabla^2 \boldsymbol{U}\right]}_{\text{quasi-steady viscous force}} \\
&\quad \underbrace{-6\pi\mu a^2 \int_0^t \frac{\mathrm{d}}{\mathrm{d}\tau}\left[(\boldsymbol{v}_\mathrm{p} - \boldsymbol{U}) - \frac{1}{6}a^2 \nabla^2 \boldsymbol{U}\right] \frac{\mathrm{d}\tau}{\sqrt{\nu(t-\tau)}}}_{\text{time history (Basset) force}} \\
&\quad \underbrace{-\frac{2}{3}\pi a^3 \frac{\mathrm{d}}{\mathrm{d}t}\left[(\boldsymbol{v}_\mathrm{p} - \boldsymbol{U}) - \frac{1}{10}a^2 \nabla^2 \boldsymbol{U}\right]}_{\text{added mass force}} + \underbrace{\boldsymbol{L}}_{\text{lift force}} ,
\end{aligned} \tag{5.209}$$

where $a\ (= 1/2d_\mathrm{p})$ is the tracer particle radius, $\boldsymbol{U}$ is the velocity of the surrounding fluid, and $\boldsymbol{g}$ is the gravitational acceleration. The lift force originates from the finite circulation around the sphere. It can either be due to an intrinsic rotation of the sphere immersed in a uniform flow (Magnus effect) or to rotational flow such as when a particle is immersed in a shear layer. In the latter case the fluid exerts a net force in the direction of the velocity gradient. This equation is known as the Basset–Boussinesq–Oseen (BBO) equation and details of its derivation can be found in *Crowe* et al. [5.348]. Solutions for this equation have been given by *Hjemfelt* and *Mockros* [5.349] and by *Chao* [5.350]. A more recent discussion of this equation and solutions for turbulent flow has been given by *Mei* [5.351] and a summary of tracer particle issues in general can be found in *Melling* [5.352].

Table 5.4 Commonly used tracer particles for PIV experiments

Fluid	Material	Diameter (μm)	Density (kg/m^3)
Air	DEHS	1–3	10^3
–	Glycol–water solution	1–3	10^3
–	Vegetable oil	1–3	10^3
–	TiO_2	0.2–0.5	$1–4\times10^3$
Water	Latex	5–50	10^3
–	Sphericell	10–100	$0.95–1.05\times10^3$
–	Silver-coated hollow glass spheres	30–100	$> 10^3$

For very small particle tracers as used in LDA or PIV the first part of the quasi-steady viscous term (Stokes drag) dominates the right-hand side of the equation. In the approximation that $\mathrm{D}\boldsymbol{U}/\mathrm{D}t = \mathrm{d}\boldsymbol{v}_\mathrm{p}/\mathrm{d}t$ (5.209) allows the difference between the particle velocity $\boldsymbol{v}_\mathrm{p}$ and that of the surrounding fluid $\boldsymbol{U}$ to be estimated as

$$\boldsymbol{v}_\mathrm{p} - \boldsymbol{U} = \frac{2}{9}\frac{a^2(\rho_\mathrm{p} - \rho_\mathrm{f})}{\mu}\frac{\mathrm{d}\boldsymbol{v}_\mathrm{p}}{\mathrm{d}t} . \tag{5.210}$$

The velocity difference $\boldsymbol{v}_\mathrm{p} - \boldsymbol{U}$ is referred to as the slip velocity. Clearly from (5.210) the choice of neutrally buoyant particles $(\rho_\mathrm{p} - \rho_\mathrm{f})/\rho_\mathrm{f} = 0$ leads to particle tracers that accurately follow the flow. While this condition can be easily satisfied for liquid flows, it cannot be achieved so easily in gas flows, where a typical value of the density ratio is $\rho_\mathrm{p}/\rho_\mathrm{f} = \boldsymbol{O}(10^3)$, and therefore particles with a smaller diameter ($0.5\,\mu\mathrm{m} < d_\mathrm{p} < 5\,\mu\mathrm{m}$) are employed. Larger particles used in liquid flows approximating the neutral buoyancy condition can be selected from a wide choice of materials, for instance hollow glass spheres or polyamide particles of relatively large diameter ($5\,\mu\mathrm{m} < d_\mathrm{p} < 50\,\mu\mathrm{m}$) can be used. Table 5.4 summarizes seeding particle properties in relation to different flow experiments.

From the above relations in the case that $\rho_\mathrm{p}/\rho_\mathrm{f} \gg 1$ (gas flows), a single exponential decay law is commonly used to model the particle response to a stepwise variation in the flow velocity. The characteristic response

time τ reads

$$\tau = \frac{2}{9} a^2 \frac{\rho - \mathrm{p}}{\mu} \,. \tag{5.211}$$

The particle response time should be kept smaller than the smallest time scale of the flow. Moreover in high-speed flows, especially if shock waves are present, exact flow tracing can never be achieved. At least within limited regions downstream of shock waves (Fig. 5.59), where the flow decelerates abruptly, the particle tracers decelerate along an exponential decay curve (Fig. 5.60). The thickness of a shock wave occurring at sea level atmospheric conditions is of the order of 0.1 µm. Further information regarding the response of particles across shock waves can be found in *Dring* [5.354] or *Tedeschi* et al. [5.355]

The fidelity of the flow tracers in turbulent flows is quantified by the particle Stokes number S_k, defined as the ratio between τ and the characteristic flow time scale τ_f. The most critical conditions are met when particle tracers are immersed in turbulent flows with a high Reynolds number, where a wide range of turbulent scales is present. From a practical point of view it can be stated that the condition $S_k < 0.1$ returns an acceptable flow tracing accuracy with errors below 1%.

Among the requirements for the choice of the seeding material, health and safety aspects have to be taken into account. The material should not be hazardous or toxic if inhaled, it should not be corrosive or reactive when in contact with parts of the flow facility or other instrumentation. Finally, seeding material that naturally evaporates leaving minimum residues introduces less contamination of the facility and its optical interfaces.

Scattering Properties of Tracer Particles

Small particles are required to fulfil the fluid-mechanical requirements of tracers. However, as an opposing requirement, the particles should scatter enough light in order to be visible. Typical particle dimensions are on the order of a micrometer for gas (i. e., air) flows, and tens of micrometers for liquid (i. e., water) flows. This means that the scattering of light by these particles occurs in the so-called Mie regime, where the particle diameter d_p is larger than the light wavelength λ. Another approach is to use tracer particles that contain a fluorescent dye; the light that is absorbed by the dye is emitted at a longer wavelength, which makes it possible to distinguish tracer particles from other objects (e.g. interfaces).

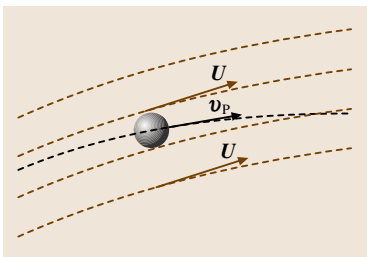

Fig. 5.58 Velocity discrepancy between the particle and the surrounding fluid velocity

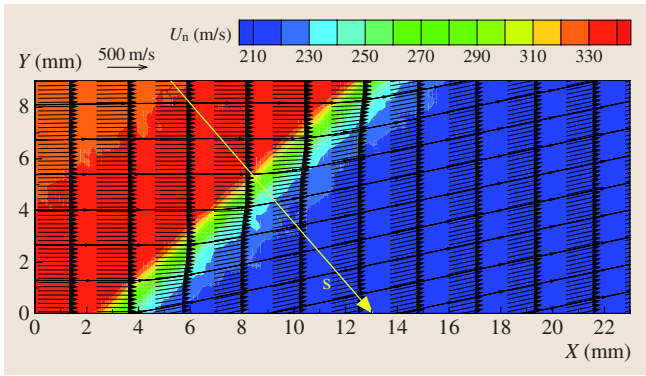

Fig. 5.59 PIV measurement of the flow across a planar shock wave. (After *Scarano* and *van Oudheusden* [5.353])

Mie Scattering. The particle scattering cross section depends on the particle diameter, the wavelength of the

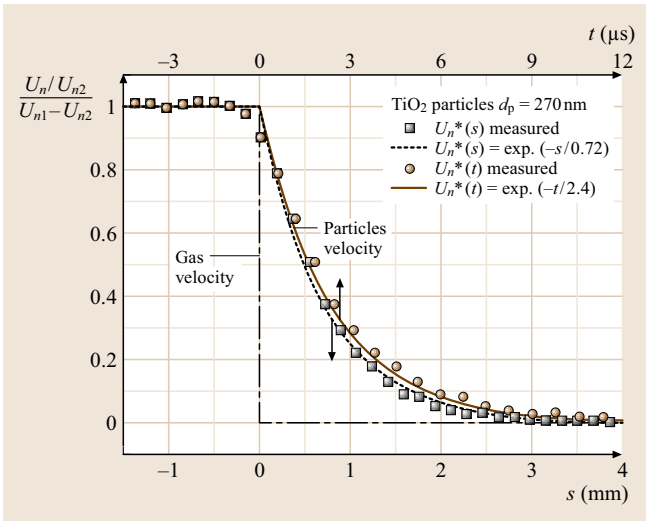

Fig. 5.60 (Particle) velocity profile and time evolution normal to the shock wave. Across shock waves the particle velocity lag is not the only source of error. Often the velocity measurement is affected by the limited spatio-temporal resolution of the measurement technique. This appears as a smoothing effect of the velocity profile at the shock location. (After *Scarano* and *van Oudheusden* [5.353])

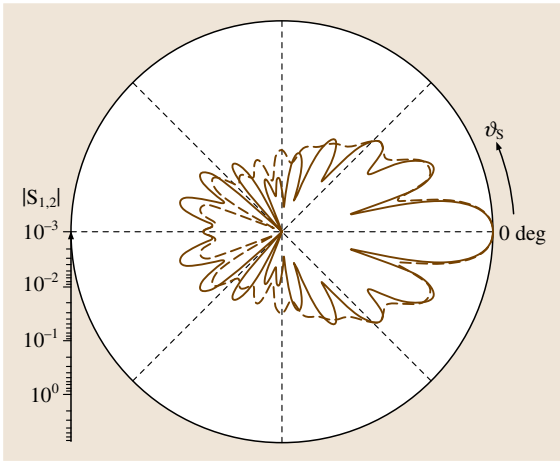

Fig. 5.61 Scattering function for a Mie parameter value of 10 computed for a water droplet in air ($m = 1.334$); *solid line*: perpendicular polarization, *dashed line*: parallel polarization (after *Albrecht* et al. [5.356])

light, and the refractive index of the particle (m) (relative to the refractive index of the surrounding medium). The Mie parameter $x_M = \pi d_p/\pi$ governs the scattering amplitude. The scattering cross section shows a very strong variation as a function of the scattering angle (υ_s). A typical Mie scattering diagram is shown in Fig. 5.61. Most of the light is scattered in the forward direction, and an appreciable amount of light is scattered in the backward direction; at a scattering angle of 90°, e.g., for single-camera PIV with the optical axis normal to the light-sheet plane, the scattering amplitude is generally very low. This is why PIV needs a much stronger light source than LDA (which operates in near-forward or near-backward scattering mode). For very small tracer particles (of less than a few μm) the light scattering cross section also depends on the direction of polarization relative to the scattering direction. As most continuous wave lasers used for LDA and frequency-doubled Nd:YAG lasers used for PIV emit polarized light, one should find the appropriate orientation of the doubling crystal of the laser.

In the Mie regime ($d_p > \lambda$) the scattering cross section is roughly proportional to the d_p^2 (i. e., the particle surface area), but when the particle diameter becomes less than the wavelength of light ($x_M < 3$) the scattering cross section is proportional to d_p^4 (Fig. 5.62. This implies a practical lower limit for tracer particles to a fraction of micrometer.

The scattering cross section also depends on the particle material refractive index relative to the refractive index of the surrounding medium. For small liquid droplets and solid particles in a gas (e.g., air) the relative change in refractive index is about 1.3–1.5, but in a liquid it is about 1.2 or less; this is why LDA and PIV in liquid flows generally requires larger tracer particles in comparison to air. The use of hollow glass spheres in liquids combines the advantages of (near-)neutral buoyancy and a large change in refractive index at the internal glass/bubble interface. The reflectivity of particles can also be improved by means of a metal coating. Silver-coated glass beads have a high reflectivity, but apart from the high specific gravity (about that of water) it is unknown whether the coating remains intact when suspended in water.

Fluorescent Tracer Particles. Tracer particles can be labeled with a fluorescent dye (e.g., Rhodamine); the

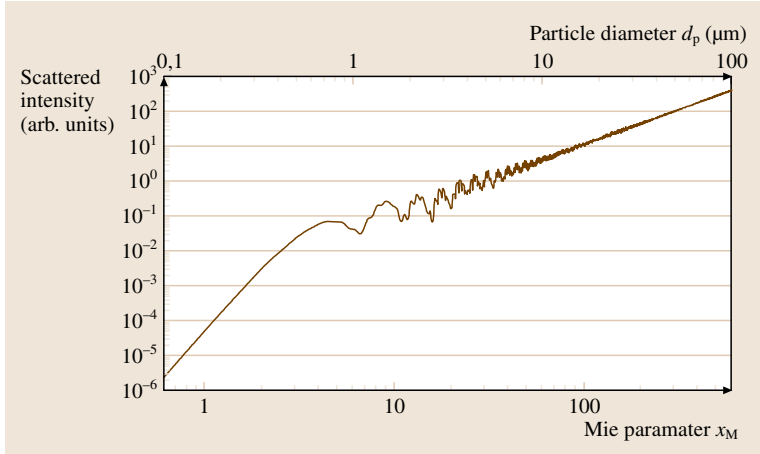

Fig. 5.62 Scattering intensity as a function of the Mie parameter x_M computed for a water droplet in air ($m = 1.333$, $\lambda_w = 514.5$ nm) at a scattering angle of $\vartheta_s = 30°$ and a circular receiver aperture of radius 10 mm (after *Albrecht* et al. [5.356])

Table 5.5 Summary of fluorescent dye properties (from *Rottenkolber* et al. [5.358])

Attribute	Rhodamin 6G	Rhodamin B	Sulforhodamin	DCM
Maximum absorption wavelength (nm)	524	544	529	481
Maximum emission wavelength (nm)	≈ 580	≈ 600	≈ 650	≈ 650
Quantum yield	High	Medium	Low	High
Lifetime (e^{-2}-decay) (ns)	6.4	2.5	5.8	1.6
Lifetime (99%-decay) (ns)	14.5	8.4	12.3	5.2
Onset (ps)	< 25	< 18	< 35	< 14

dye absorbs the incident light, which is then re-emitted at a longer wavelength. For example, when the green (532 nm) light of a Nd:YAG laser illuminates tracer particles doped with Rhodamine, the particles not only scatter the laser light, but also emit orange–red (550–680 nm) light. This makes it possible to separate the tracer particles from other scattering objects, such as walls, bubbles, droplets and other particles, by means of an appropriate optical filter that blocks the light with the wavelength of the incident light (viz., light sheet) and passes the fluorescent light. Fluorescent tracer particles are commonly used for PIV in multiphase flows, in near-wall measurements, and in microscopic measurements [5.357].

The emission of fluorescent light is isotropic, so there is no dependence of particle image intensity as a function of viewing angle with respect to the light sheet orientation (see above). The fluorescent intensity depends on the amount of fluorescent dye in the tracer particle; this is generally proportional to the particle volume, which implies that the brightness decreases in proportion to d_p^3 (as opposed to Mie scattering, which decreases in proportion to d_p^2). The duration of the fluorescence is typically ≈ 10 ns (viz., instantaneous), although prolonged exposure induces photo-bleaching that reduces the fluorescence intensity. Also, the fluorescent light is incoherent, which implies that such particles are unsuitable for holographic recording approaches.

PIV can also be combined with instantaneous thermometry by using tracer particles that contain liquid crystals. When combined with a color camera one can measure the local temperature from the color of the light scattered by these tracer particles [5.360, 361].

Fluorescent tracer particles have also been successfully used for laser Doppler measurements, the main issue being the fluorescent onset time and lifetime, since these will determine the dynamic range of detectable velocities. Using ultrashort laser pulses and time-resolved fluorescence spectroscopy, *Rottenkolber* et al. [5.362] have determined the characteristics of four common fluorescent dyes, as summarized in Table 5.5.

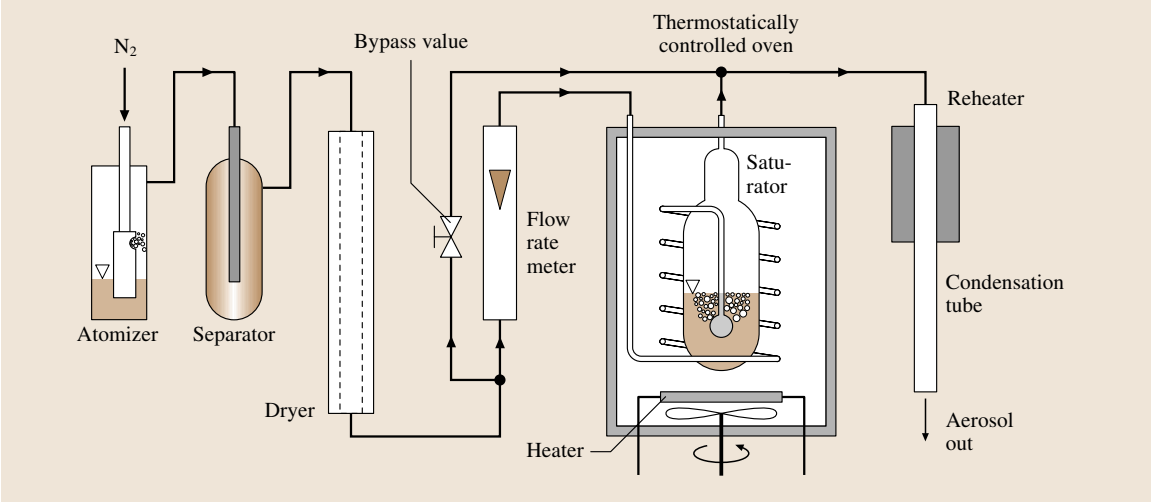

Fig. 5.63 Modified Sinclair–La Mer aerosol generator (after *Helsper* and *Mölter* [5.359])

Particle Generation

Some of the best suited particles for laser Doppler and PIV measurements, such as polymers, hollow SiO_2 microballoons or metallic-coated spheres, are quite complex to fabricate but are commercially available. Since these particles are not always inexpensive, they are better suited for closed loop systems. When larger quantities of particles are required, more economical solutions are sought and dedicated particle generators offer a good solution, some of which are also commercially available. In many cases however, the user provides his own particle generation hardware; details of several such solutions are provided below.

Particle generation can be divided according to solid and liquid particles. Solid particles or powders are used to seed liquid flows or in applications such as combustion, where liquid droplets would evaporate. In either case a monodispersed size distribution and a spherical particle shape are desirable, the latter condition being automatically fulfilled by small liquid droplets.

Droplet Generation

Condensation. Droplet generation through condensation can be spontaneous in a highly saturated vapor stream; however, the necessary control of size and concentration is really only achievable if the vapor pressure, the condensation temperature, and the seed nuclei concentration are all controlled. Such a generator, which is a modification of the classical *Sinclair* and *La Mer* [5.363] generator, is pictured in Fig. 5.63, adapted from *Helsper* and *Mölter* [5.359] and commercially available as a monodispersed aerosol generator (Palas MAGE-2000).

Fog generators, as are used in theatrical productions or discotheques, have also been used for particle seeding or flow visualization in wind tunnels. These devices also

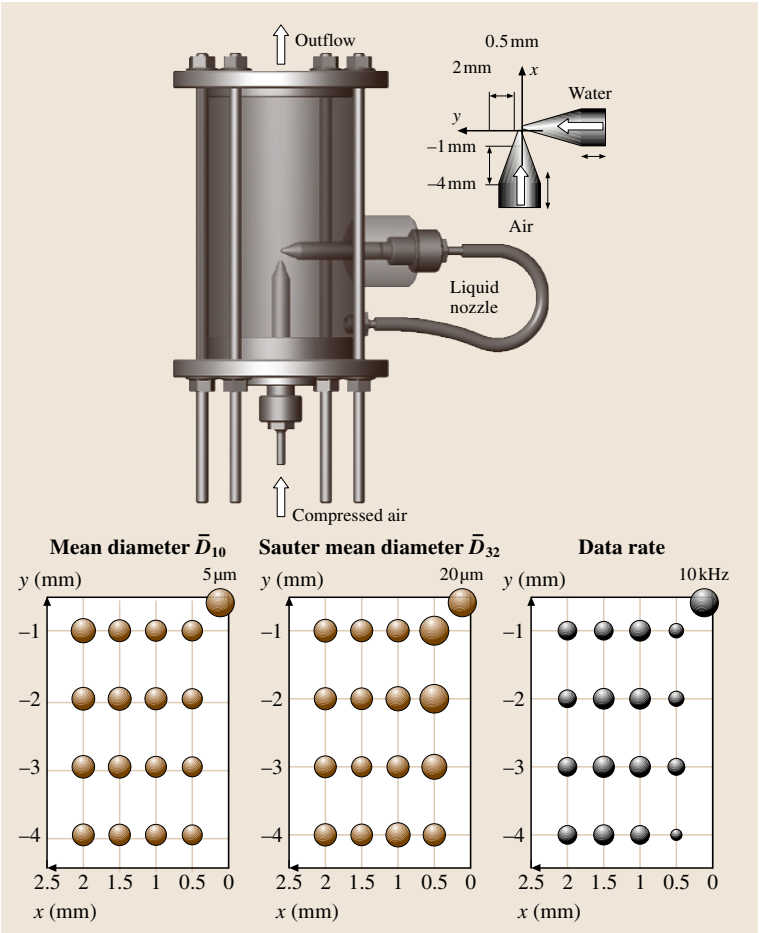

Fig. 5.64 A twin-fluid atomizer showing data rate, mean diameter and Sauter mean diameter as a function of nozzle alignment

work on the principle of condensation. Oil is evaporated on a heated plate and condenses to fine droplets in the gas flow; however, the size distribution is wide and the delivery rate is not as well controlled. These devices do not work well in very dry atmospheres, since the fog immediately evaporates. The longevity of the droplets can be controlled through the choice of fluid and its vapor pressure. Such devices are also commercially available and are a good choice where high particle rates are required, for example in large wind tunnels.

Atomization. By far the most common method of seeding gas flows is through liquid atomization. Of the many atomizer types available [5.364] the common nebulizer type used in inhalation devices is the most suitable. This is known as a twin-fluid or air-assist atomizer and draws liquid from a reservoir into a high-speed gas jet, where the liquid stream undergoes prompt atomization. Since this type of atomization results in a polydisperse spray, an impactor or separator is used to remove large droplets from the flow stream.

The droplet size depends primarily on the atomizing airflow rate and on the liquid used. Typical mean particle sizes range from 0.2 μm using DEHS (di-ethyl-hexyl-sebacat) to 4–5 μm with water. Fluids like olive oil or water with alcohol lie between. Particle rates as high as 10^{13} m^3/s are possible from a single nozzle (AGF 2.0, Palas GmbH), although a cascade of nozzles can also be used to vary concentration at almost constant flow rate (six-jet atomizer model 9306, TSI Inc.). Where necessary, bypass air can be used to dilute the flow to concentration levels appropriate for the particular experiment.

For many applications, the common inhalation or medication nebulizer offers an economical solution and can be easily obtained through medical suppliers. These units are available with reservoirs ranging from 20 cl to 1 l. An impactor plate is often built into such devices and a mean particle diameter of about (4±2) μm with water can be expected.

The actual construction of such twin-fluid atomizers is quite varied, several designs being suitable for construction in ones own laboratory. One such design is pictured in Fig. 5.64. A high-speed airstream from a central nozzle creates a low static pressure and draws liquid from a reservoir into the air jet, where it is atomized. The alignment of the air nozzle with the liquid nozzle influences the number density of the droplets but not the drop size distribution, as illustrated in Fig. 5.64 for water and various operating conditions.

A popular atomizer design is the Laskin nozzle, as described in detail by *Echols* and *Young* [5.365] and as shown in Fig. 5.65. High-speed submerged air jets are created by small holes (1 mm) in the nozzle tube (10 mm diameter). These exit the nozzle tube just below a collar (16 mm diameter), which has 2 mm holes tangent to the nozzle. The exact location of these holes is quite critical for proper functioning of the unit. The dimensions of the nozzle tube and the collar are not as critical. There should be sufficient clearance between the bottom of the nozzle tube and the bottom of the container, at least 25 mm. The air holes should be no more that 25 mm below the free surface of the liquid.

The number of particles is controlled through the number of activated nozzles. The droplet size distribution is only slightly dependent on the feed air pressure but does depend on the liquid used, oils leading to a smaller size distribution than water. Dilution air can be used to adjust the final output concentration or to achieve isokinetic introduction of the particles into the

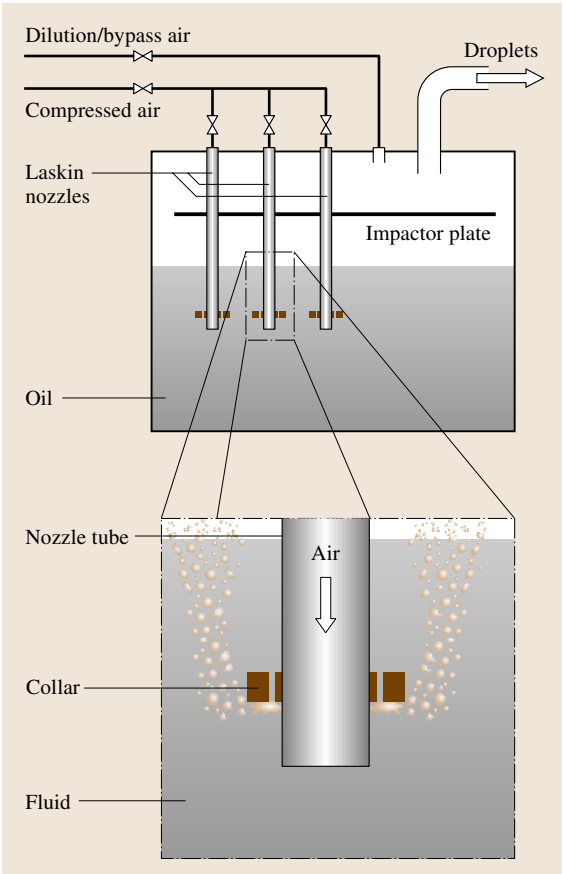

Fig. 5.65 Schematic of a Laskin nozzle unit for droplet seeding

flow stream. Laskin nozzles exhibit mean droplet diameters of about 1 μm with vegetable oils. Such atomizers can also be designed to withstand back-pressures of several bar, necessary when delivering tracer particles into flows under pressure.

A highly monodispersed stream of droplets can be generated by exploiting the inherent instabilities of a laminar liquid jet, as first analyzed by *Rayleigh* [5.366]. Although the droplet quantity is far below that typically required for flow seeding, this generator is in widespread use as a standard with which phase Doppler instruments can be aligned and adjusted. Such devices are commercially available (e.g., TSI model 3450) but also exist in a wide variety of custom designs [5.367].

The principle of this generator is pictured in Fig. 5.66a. Rayleigh showed that a round liquid jet of diameter D will disintegrate into droplets due to surface tension forces. This instability exists for wavelengths in the range $3.5–7D$, whereby the wavelength $\lambda = 4.508D$

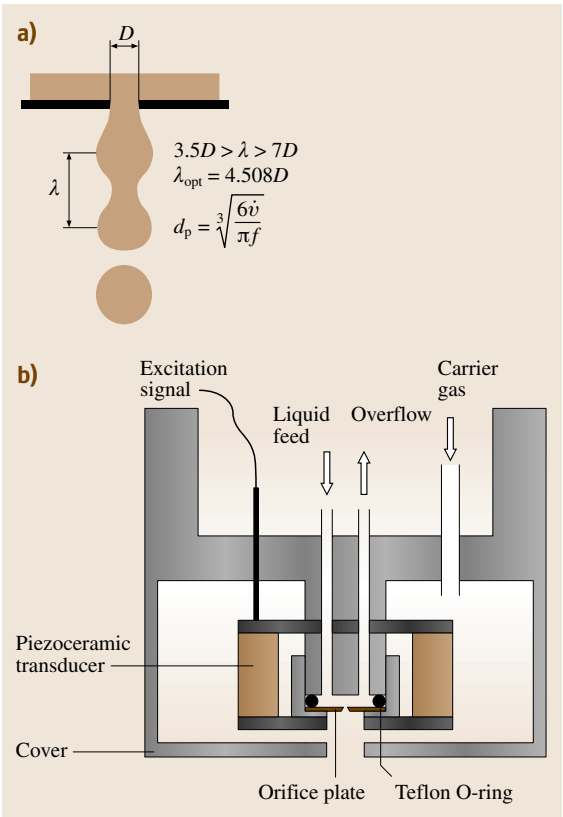

Fig. 5.66a,b Monodisperse droplet generation using the Rayleigh instability. **(a)** Principle of Rayleigh instability of a round liquid jet; **(b)** vibrating orifice generation head

exhibits unstable behavior. If the liquid jet is now externally perturbed at a wavelength in this range, the instabilities will lock on to this wavelength and a highly periodic stream of mono-dispersed droplets results. The size of each droplet is given directly by

$$d_\mathrm{p} = \left(\frac{6\dot{v}}{\pi f}\right)^{1/3} . \qquad (5.212)$$

Since both the volume flow rate $\dot{v}$ and the excitation frequency f can be exactly controlled, the drop size is adjustable to within micron accuracy.

Solid Particle Generation

Atomization. Solid particles can be produced by atomization of suspensions using techniques described in the previous section. After atomization, the liquid or solvent evaporates, leaving a solid particle. Typical suspensions are latex particles (polysterol or polyvinyltoluol) with very narrow size distributions. Such particles are usually available in 10% solutions with sizes of 10–20 μm. They are made in a polymerization process, which results in standard deviations in size of only a few percent. The suspension must be diluted before atomization such that the probability of obtaining more than one latex particle per droplet becomes very low. Also this method of aerosol generation has been accepted as a standard. Other solid particles have been atomized in this manner, in particular TiO_2 and ZrO_2 in a 5% ethyl alcohol suspension for investigations in flames [5.368].

From Powders. There are several methods of obtaining a flow of tracer particles from a powder. In all cases, however, coagulation tends to reduce the number concentration and shift the size distribution towards larger particles. Thus, it is often important to use dry delivery gas and also dry, hydrophobic powders. Two different dispersion devices will be briefly described.

The first of these is the rotary brush seeder, pictured in Fig. 5.67a. In this device a packed column of powder is fed into a rotating brush, which lifts off the top layer of powder and transports it into a high-speed stream (170 m/s) of carrier gas, usually air. This high-speed gas stream also provides sufficient energy to break up larger coagulate particles further. The rate of particle delivery is controlled by the bulk powder feed rate, the brush rotation rate, and the volume flow rate of carrier gas. Typically, powders are quartz dust, calcium, glass spheres, and titanium dioxide.

A second method of dispersing a bulk powder into a gas stream is the cyclone aerosol generator, pictured in Fig. 5.67b. *Glass* and *Kennedy* [5.369] have used such

a device for dispersing 0.1–1 μm Al_2O_3 particles. *Anderson* et al. [5.370] have used this design for tracer particle generation for PIV studies. The cyclone acts not only as a dispersion method but also as a particle size separator, depending on the diameter of the outlet tube.

A summary of various solid aerosol materials commonly used for seeding purposes is given in Table 5.6.

Introducing Particles into the Flow

Achieving optimum flow seeding is generally acknowledged as the most difficult part of LDA and PIV experiments. Once the flow is uniformly seeded with required concentration, the experiment has a high chance of success. The seeding procedure consists of different steps, which may vary depending on the flow facility. For water flows in a confined environment or within closed-loop flow the seeding procedure consists in dispersing the seeding material in the fluid. It is best practice to increase the seeding concentration gradually from a low level until reaching the desired one. If seeding exceeds the optimum level, multiple scattering and opacity compromise the setup of the experiment. For air flows the seeding material first needs to be entrained in the working fluid and then inserted upstream of the measurement region. Particles of a given diameter can be selected from a polydisperse particle distribution in the seeded fluid through centrifugation or making use of impact plates. The procedure of dispersing the seeded fluid within the stream is equally important. The seeding distribution system should not perturb the flow and at the same time should provide a homogeneous seeding level in the flow. This is usually accomplished with two-dimensional rakes of orifices placed upstream of screens and meshes in the wind tunnel settling chamber. In some cases a homogeneous seeding concentration cannot be achieved because of physical processes in the flow affecting the fluid density (e.g., compressible flows, flames). A homogeneous flow seeding does not show the underlying structure of the flow. Figure 5.68a is a PIV recording of the flow around a square cylinder developing as a von Kármán wake behind the model. The darker and brighter stripes are due to the light refraction and reflection through the transparent model. Conversely, in high-speed flows inhomogeneous seeding distribution is unavoidable due to the combined effect of density variations and strong inertia forces locally centrifuging seeding particles from the core of vortices. This is illustrated in Fig. 5.68b, where a Mach 2 stream develops around the model of a rocket propelled with a supersonic jet [5.372].

With atomized droplets, their lifetime before complete evaporation is of particular interest, since this

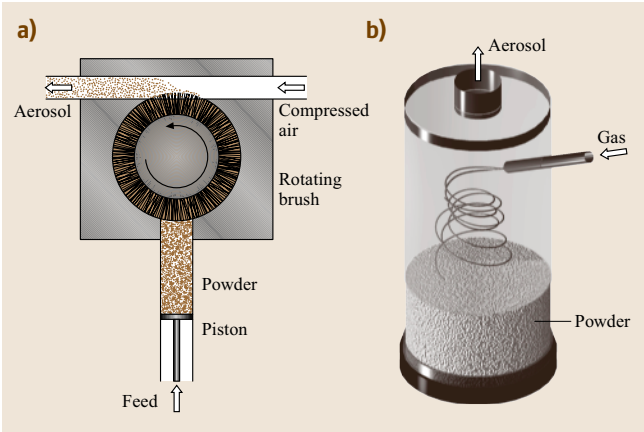

Fig. 5.67a,b Aerosol generation from powder. **(a)** Operation principle of a rotary brush seeder. **(b)** A cyclone aerosol generator

determines how far upstream the particle injection can be placed. The evaporation rate can be controlled through the choice of liquids. For instance, a 5–10% addition of glycerin to water can extend the droplet lifetime tremendously.

Deposition of particles on walls is one major obstacle to tracer-based measurement techniques in large wind tunnels, since the cost of cleaning such an installation can be enormous. For this reason water droplets are often the preferred tracer; however, other liquids exist which leave almost no deposits and are nontoxic, e.g., DEHS. Window deposition is also a limiting factor for measurements in motored and fired engines. For this reason the window design should afford quick and easy removal/cleaning. It is not unusual to experience measurement times of only tens of seconds before window cleaning is again necessary, meaning that external systems must be used to keep all engine components and fluids at operating temperatures. Recessed windows or protecting air curtains in front of windows have both

Table 5.6 Properties of various solid seeding materials (after *Agarwal* and *Johnson* [5.371])

Material	Density (g/cm^{-3})	Index of refraction	Melting point (°C)
DOP	0.98	1.49	
PSL	1.05	1.59	
NaCl	2.16	1.54	801
Al_2O_3	3.96	1.79	2015
TiO_2	4.26	2.6–2.9	1750
SiC	3.2	2.6	2700
ZrO_2	5.6	2.2	2980

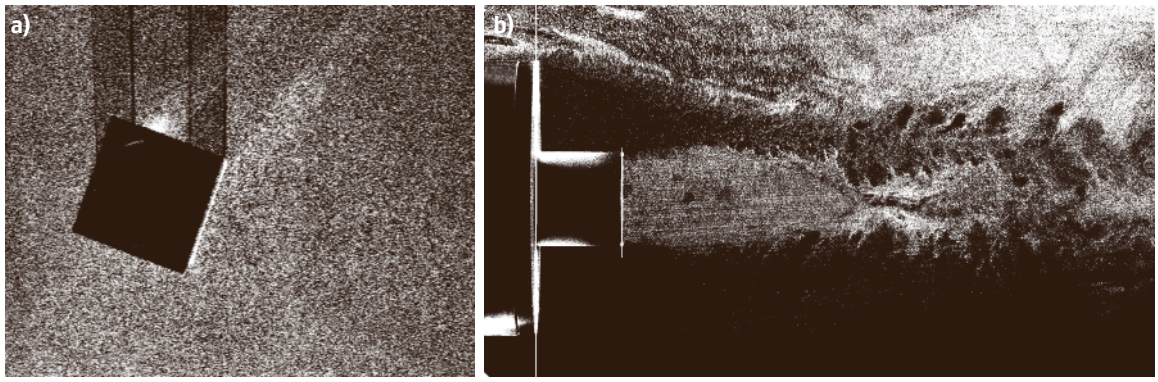

Fig. 5.68a,b Example of homogeneous seeding density in a low-speed bluff-body wake **(a)** and inhomogeneous seeding in a high-speed supersonic flow **(b)**. (After *Scarano* et al. [5.372])

been used to avoid window dirtying; however, these measures are not always possible without disturbing the measured flow field.

Recommendations

A common erroneous tendency is to increase the seeding level beyond optimum in order to compensate for a drop in the signal-to-noise ratio. Such a drop can be due to several effects that should be checked before deciding to increase the seeding level:

1. contamination of optical interfaces for illumination and imaging
2. misalignment of receiving optics (LDA) or between the light sheets or incorrect (too long) time separation between pulses (PIV)
3. excessive seeding concentration causing medium opacity
4. blurred particle images due to incorrect setting of the imaging focal plane (PIV).

5.3.2 Laser Doppler Technique

Measurement Principles

The laser Doppler technique, most frequently referred to as a laser Doppler anemometer (LDA) or laser Doppler velocimeter (LDV) is a widespread technique for pointwise velocity measurements in a flow with fluid markers. Some decisive advantages of the technique over more-conventional probe-based techniques can be mentioned: non-intrusiveness, directional sensitivity, high spatial and temporal resolution, and high accuracy. A first laser Doppler instrument was presented by Cummins et al. and by *Yeh* and *Cummins* in 1964 [5.373], in which an optical configuration, subsequently known as the reference-beam mode, was introduced. The currently used dual-beam mode was introduced almost simultaneously by *Lehmann* [5.374] and *vom Stein* and *Pfeifer* [5.375], the latter of which were granted a patent. In this configuration, two in-going laser beams crossing at an intersection angle were used to form a measurement volume and the scattered light from both beams was collected on a single detector. These were the basic innovations leading to the present-day laser Doppler instrument.

The basic principle of the technique invokes the Doppler effect twice, once when the incident laser light, characterized by the wavelength λ_b and frequency f_b (subscript 'b' for beam), impinges on a moving tracer particle and once when light with a frequency f_p (subscript 'p' for particle) is scattered from the moving tracer particle and received by a stationary detector with the frequency f_r (subscript 'r' for receiver). This is illustrated in Fig. 5.69, and the corresponding relation for the detected frequency of scattered light is given by

$$f_r = f_b \frac{\left(1 - \frac{\boldsymbol{v}_p \boldsymbol{e}_b}{c}\right)}{\left(1 - \frac{\boldsymbol{v}_p \boldsymbol{e}_{pr}}{c}\right)} \approx f_b + \frac{\boldsymbol{v}_p(\boldsymbol{e}_{pr} - \boldsymbol{e}_b)}{\lambda_b}$$
$$\text{for } |\boldsymbol{v}_p| \ll c,\ c = f_b \lambda_b \,, \qquad (5.213)$$

where c is the speed of light in the medium surrounding the particle and $\boldsymbol{v}_p$ is the particle velocity. The second term in (5.213) contains the Doppler shift of the incident wave frequency. The difference of the normal vectors appears when the direction of propagation of the incident and scattered wave differs. The Doppler shift is directly proportional to this difference and to the velocity of the particle. For typical flow systems and for receiver placements that maxi-

mize the magnitude of the vector different, the Doppler shift is of the order 1–100 MHz, which compared to the frequency of laser light (approximately 10^{14} MHz) is very small and virtually impossible to resolve directly. One exception is direct detection through the use of frequency-dependent absorption cells, leading to the Doppler global velocimeter described in Sect. 5.3.4.

The most common approach to circumvent the necessity of resolving the Doppler shift directly is known as the dual-beam configuration, in which a measurement volume is formed at the intersection of two incident waves and the scattered waves are detected with a single detector, as illustrated in Fig. 5.70a. Applying (5.213) to each of the input beams, the frequencies at the detectors can be written

$$f_1 = f_b + \frac{\boldsymbol{v}_p(\boldsymbol{e}_{pr} - \boldsymbol{e}_1)}{\lambda_b}\,, \quad f_2 = f_b + \frac{\boldsymbol{v}_p(\boldsymbol{e}_{pr} - \boldsymbol{e}_2)}{\lambda_b}\,. \tag{5.214}$$

The difference (beat) frequency f_D is obtained through the optical mixing of waves with frequencies f_1 and f_2 on the detector. This frequency is commonly called the Doppler frequency and, using the vector relation illustrated in Fig. 5.70b, can be expressed as

$$f_D = f_1 - f_2 = +\frac{\boldsymbol{v}_p(\boldsymbol{e}_1 - \boldsymbol{e}_2)}{\lambda_b} = \frac{2\sin(\Theta/2)}{\lambda_b}|\boldsymbol{v}_p|\cos\alpha = \frac{2\sin(\Theta/2)}{\lambda_b}v_{p\perp}\,, \tag{5.215}$$

where $v_{p\perp}$ is the particle velocity component perpendicular to the beam bisector. Noteworthy is the fact that the difference frequency is independent of the receiver position and that it is linearly proportional to the velocity component in the x direction. Furthermore, the intersection angle Θ and the wavelength can be determined very accurately from the optical arrangement, eliminating the need for a dedicated calibration of the device. Equation (5.215) is therefore the direct link between the frequency of modulated light intensity at the detector and the desired flow velocity component.

The fringe model is an alternative explanation of the laser Doppler principle, in which the wavefronts of two coherent beams interfere in the intersection volume, forming interference fringes with a spacing Δx, as illustrated in Fig. 5.71. Tracer particles passing through the volume will scatter modulated light according to the passing of the constructive and destructive interference fringes, yielding the Doppler frequency at the

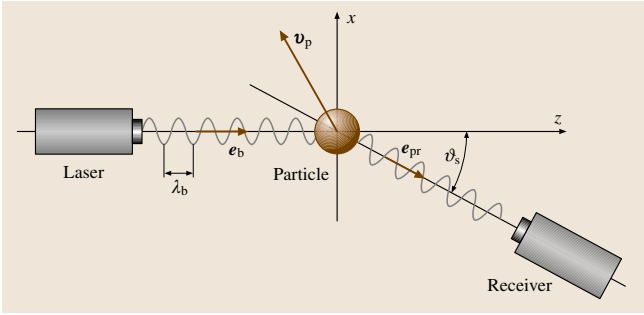

Fig. 5.69 Defining geometry for applying the Doppler effect in the laser Doppler technique

detector. This frequency is determined for each individual tracer particle passing through the volume, yielding flow velocity readings in time.

The fringe model clearly indicates the need to maintain high fringe contrast to yield a maximum modulation in the resulting signal from the receiver. This contrast is best when the intensity and polarization direction of the two incident beams are equal, and of course that the light is spatially and temporally coherent – the main reasons for using a laser as a light source.

One further requirement is to distinguish the sign of the particle velocity, since the Doppler frequency alone does not contain this information, as indicated in Fig. 5.72a. The same signal will be obtained for a par-

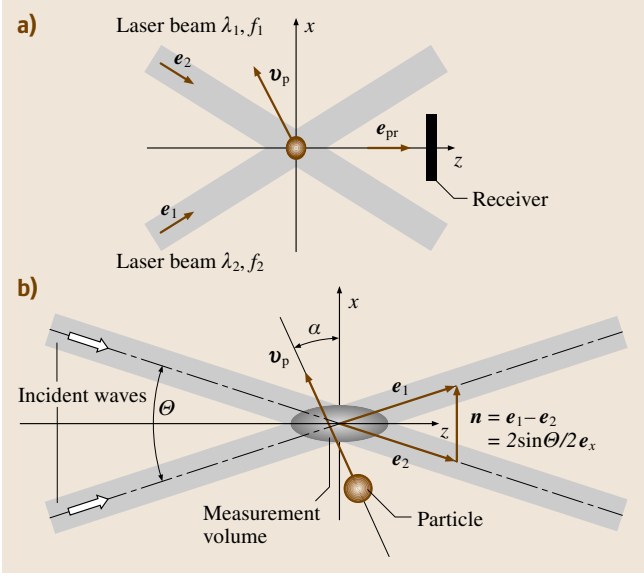

Fig. 5.70 **(a)** Dual-beam configuration. **(b)** Vector relations relevant to determining the Doppler frequency

ticle crossing the fringes in either direction. To achieve directional sensitivity the frequency of one of the incident beams is shifted by an amount f_s compared to the other beam, which results in a moving fringe pattern. A tracer particle with zero velocity in the measurement volume will result in a received frequency of f_s, while any movement of the particle will result in a frequency larger or smaller than f_s, depending on the direction relative to the fringe movement. This is illustrated in Fig. 5.72b.

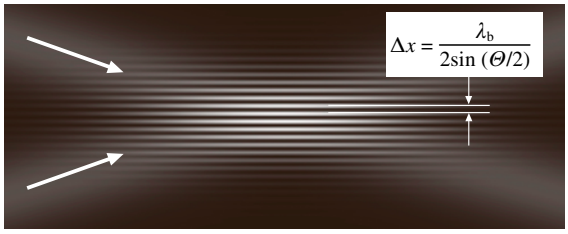

Fig. 5.71 Interference pattern in the measurement volume – fringe model

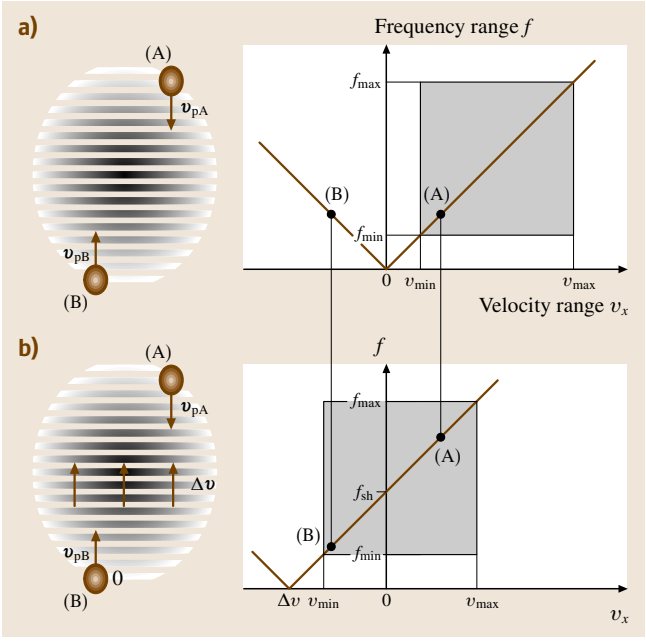

Fig. 5.72a,b Measured frequencies for particles crossing the measurement volume in positive (A) and negative (B) x directions: **(a)** without frequency shift; and **(b)** with frequency shift

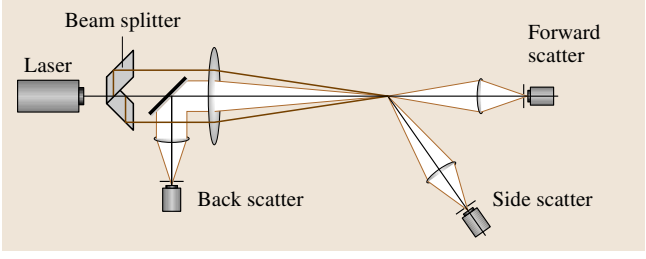

Fig. 5.73 Possible optical configurations of a laser Doppler system

The magnitude of the shift frequency must be chosen such that the highest expected velocity in the negative x direction, i. e., in the direction of the moving fringes, is still significantly smaller that the velocity of the fringes (Δv). How this achieved is outlined next.

Optical Systems

There exist a very large number of different optical configurations to realize the laser Doppler technique, the choice of which depends largely on factors specific to the intended application. These include the available optical access, possible particle seeding, velocity range, required spatial and temporal resolution, number of velocity components to be measured, etc.

Fundamentally the laser Doppler technique can work with the detector placed at any scattering angle with respect to the incident beams; however the discussion in Sect. 5.3.1 indicated that the scattered light intensity from tracer particles is usually much stronger in the forward direction. This suggests that the receiving optics should be placed on the opposite side of the measurement volume to the transmitting optics. While this is desirable for better signal strength, the available optical access does not always allow this. Often a receiving optics integrated into the transmitting optics is more convenient to position and at the same time requires only one optical access to the measurement point. This fundamental distinction between forward and backscatter is illustrated schematically in Fig. 5.73, whereby also side-scatter arrangements are sometimes used for limiting the measurement volume in its length.

Practically most laser Doppler systems are now realized with a fiber-optic link between the bulk optical components of the system and the measurement probe. A typical system is illustrated in Fig. 5.74, showing a Bragg cell used for splitting the laser beam into two beams, one shifted in frequency compared with the other (for directional sensitivity). A color-splitting prism follows, resulting in two or three colors from an all-lines laser to be separated. The use of two or three colors allows systems to be configured to measure two or three velocity components of the tracer particle movement simultaneously. The individual beams (up to six) are then transmitted to a measurement head via single-mode

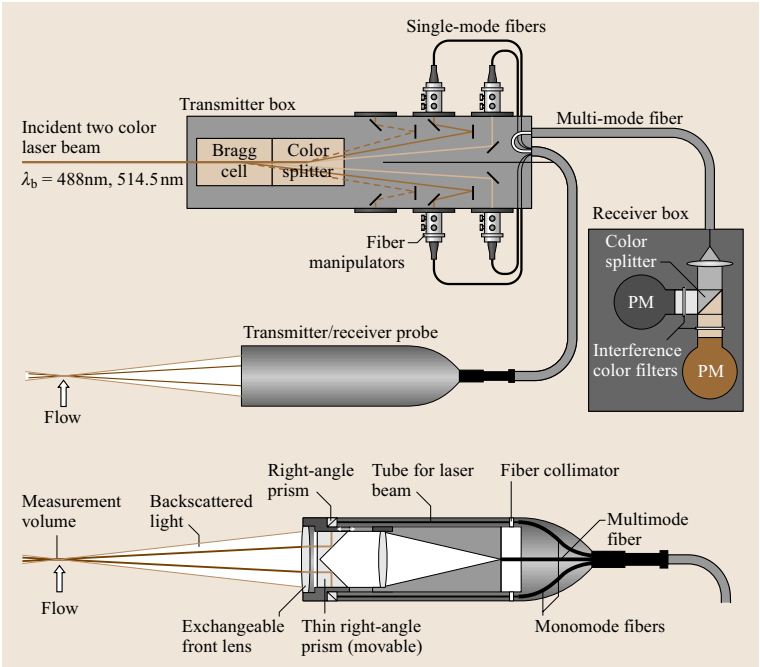

Fig. 5.74 Two-color, four-beam laser Doppler system, suitable for measuring two velocity components. The green ($\lambda = 488$ nm) and blue ($\lambda = 514.5$ nm) lines of an argon-ion laser have been used

polarization-preserving fibers, since both coherency and polarization are prerequisites for interference in the measurement volume. Fiber links of 5 or 10 m are not uncommon; hence only the probe head must be mounted and traversed to position the measurement volume in the flow field.

The Bragg cell can be understood as an acoustic diffraction grating from which the zero and first-order beams are used. Typical frequency shifts of the first-order beam are 40 MHz or 80 MHz, which then also becomes the frequency shift or the frequency of the moving fringes in the intersection volume. Particles passing through the volume will then result in signal frequencies that are smaller or larger, depending on their direction. Some laser Doppler systems employ an electronic down-mixing of this signal to shift the frequencies to lower ranges, more compatible with signal processing electronics. As an example, for a Bragg cell operated at 40 MHz and a mixing with a reference signal of 35 MHz, an effective frequency shift of 5 MHz is achieved.

The scattered light from tracer particles passing through the measurement volume is collected through a lens system and focused onto a photodetector using

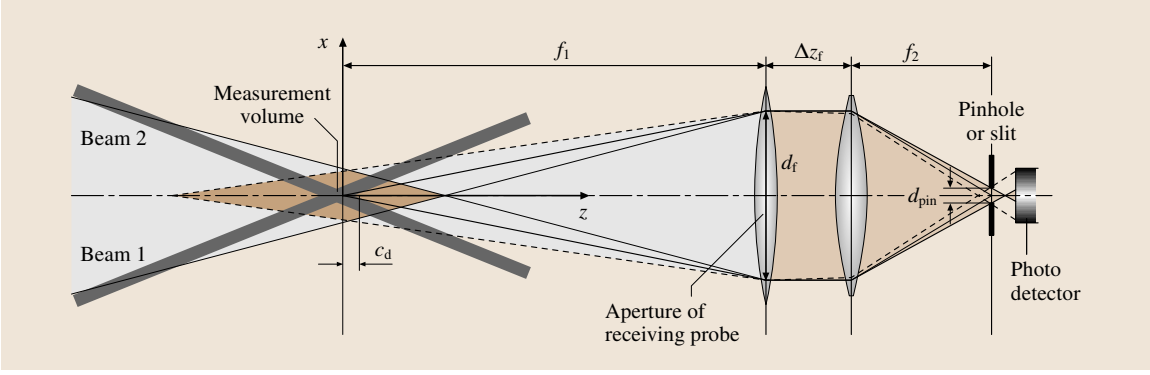

Fig. 5.75 Configuration of the receiving optics

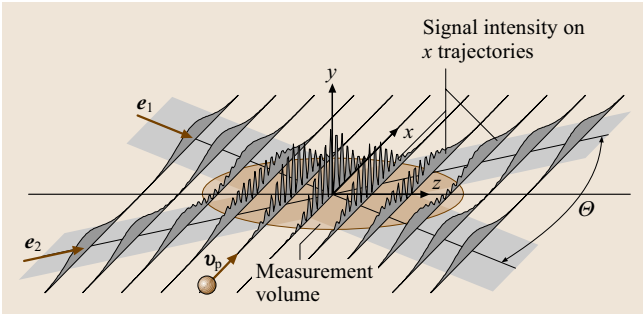

Fig. 5.76 Signal generation in the measurement volume

a receiving optics. The photodetector, typically a photomultiplier or photodiode, converts the scattered light intensity into an electrical signal with proportional voltage. The receiving optics may be integrated into a single probe together with the transmitting optics, as shown in Fig. 5.74; however the optical characteristics are separate and can be represented by the two-lens system shown in Fig. 5.75. Using this lens arrangement, the measurement volume is imaged onto a pinhole, slit or fiber. This pinhole acts as an aperture and can limit the effective dimensions of the measurement volume, either in diameter (forward or backscatter) or in length (side scatter). The magnification of the lens system is given as $\beta = -f_2/f_1$ (where f_1 and f_2 are the focal lengths of the lens system shown in Fig. 5.75), which together with the pinhole diameter determines the observation area at the beam intersection plane.

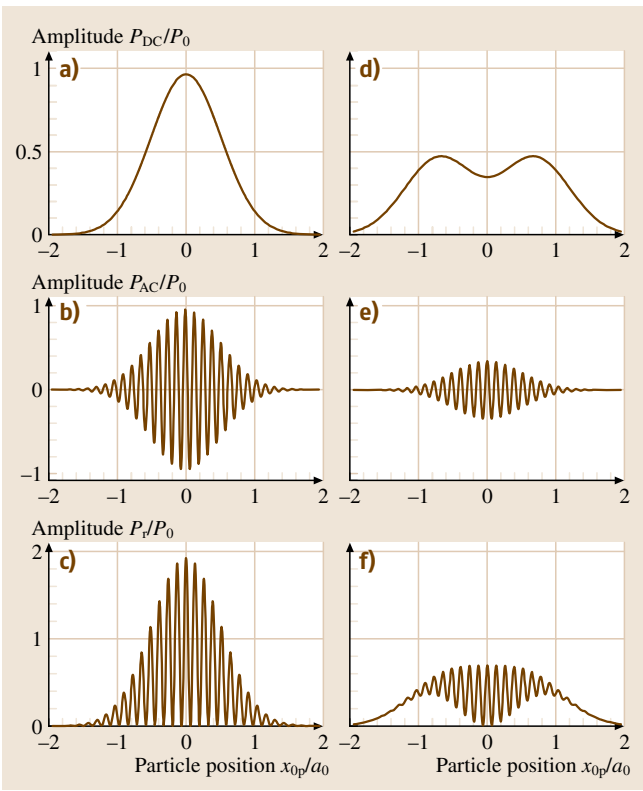

Fig. 5.77a–f Detector signals and their corresponding DC and AC parts for two different particle trajectories ($\boldsymbol{v}_p = \boldsymbol{e}_x v_{px}$, $S_{1r} = S_{2r}$). **(a–c)** $\boldsymbol{r}_{p0} = (0, 0.1b_0, 0.1c_0)^T$, **(d–f)** $\boldsymbol{r}_{p0} = (0, 0.2b_0, 0.7c_0)^T$

The spatial resolution achieved with the laser Doppler technique depends both on the optical system and on the signal-processing electronics. The size of the measurement volume created at the intersection of the two incident beams depends on the degree of beam focussing. Laser beams are Gaussian beams and, when focused with a lens, they exhibit a beam waist, the diameter (d_{w1}) of which depends on the focal length of the lens (f), the wavelength (λ_b), and the diameter of the beam at the beam waist before the lens (d_{w0}):

$$d_{w1} = \frac{4f\lambda_b}{\pi d_{w0}} \,. \tag{5.216}$$

A Gaussian beam exhibits a Gaussian intensity profile in its cross section; hence there is no distinct border between illuminated and non-illuminated at the edge of the beam. The diameter given in (5.216) refers to the diameter at which the intensity has fallen to e^{-1} of the maximum intensity on the beam axis.

In most laser Doppler systems the focal length of the front lens in the transmitting optics determines the standoff or working distance between the probe and the measurement position. This distance is often dictated by the application at hand and by the available optical access. However this focal length can also be applied with (5.216) to give the dimensions of the measurement volume. The nominal size of the measurement volume can be approximated as an ellipsoid with half-axes and volume given as

$$a_0 = \frac{d_{w1}/2}{\cos\Theta/2} \,, \quad b_0 = \frac{d_{w1}}{2} \,, \quad c_0 = \frac{d_{w1}/2}{\sin\Theta/2} \,,$$
$$V_0 = \frac{4}{3}\pi a_0 b_0 c_0 \,, \tag{5.217}$$

and the number of interference fringes in the volume will be

$$N_{fr} = \frac{a_0}{\Delta x} = \frac{2d_{w1}\tan(\Theta/2)}{\lambda_b} \,. \tag{5.218}$$

Typically the diameter of the measurement volume will range between 40 µm and 200 µm and the length will

be 5–10 times larger, depending on the intersection angle. If smaller measurement volumes are desired, beam expansion must be used before the front lens to increase d_{w0}, which decreases d_{w1}. The length of the measurement volume may also be truncated by using a side-scatter receiving arrangement in combination with a pinhole aperture in front of the photodetector, as indicated above. However, the volume in which tracer particles can be detected can still be larger or smaller than the nominal measurement volume. To underline the difference between the detection volume and the measurement volume, the signal generation is examined in more detail.

As illustrated in Fig. 5.76, the signal generation in the measurement volume depends on the trajectory of the particle. The trajectory influences both the low-frequency (DC/pedestal) and modulated (AC/Doppler frequency) portion of the signal. This is shown for two exemplary trajectories in Fig. 5.77. The amplitude of the signal will depend on particle size. For particles significantly larger than the fringe spacing Δx, the modulation, or visibility, will also decrease even if the fringe contrast is 100%. This occurs because larger particles will always result in several fringes being *seen* by the detector. Whether a particle will be detected of not will depend on the detection criteria invoked in the signal processing step, which may include an amplitude or a signal-to-noise threshold on the DC and/or AC portion of the signal. Hence, the effective spatial resolution of the laser Doppler system is a complex function of many optical and electronic parameters.

This discussion also underlines the trade-off in selecting the size of tracer particles. Small particles follow flow fluctuations more accurately and result in higher modulation levels in the Doppler signal; on the other hand they also result in lower signal amplitudes ($\propto d_p^2$ in the Mie scattering range), lower signal-to-noise ratios and in the worst case may not even be detected.

Using different colors of a laser source, two or three measurement volumes can be overlaid but with differing fringe orientation. By distinguishing the signals from the different beam pairs through color filtering in the receiving optics, two or three velocity components can be simultaneously acquired. An optical arrangement suitable for three velocity components is shown in Fig. 5.78. Note that the three velocity components may not all be orthogonal to one another and may require a transformation into the probe-fixed or laboratory coordinate system.

The performance of the laser Doppler system will depend largely on the optical system. Therefore any strategy for maximizing the signal-to-noise ratio and the rate of Doppler signals should begin with the optical system. The main influencing factors include

- Input laser power
- Incident intensity (for given laser power a function of measurement volume diameter)

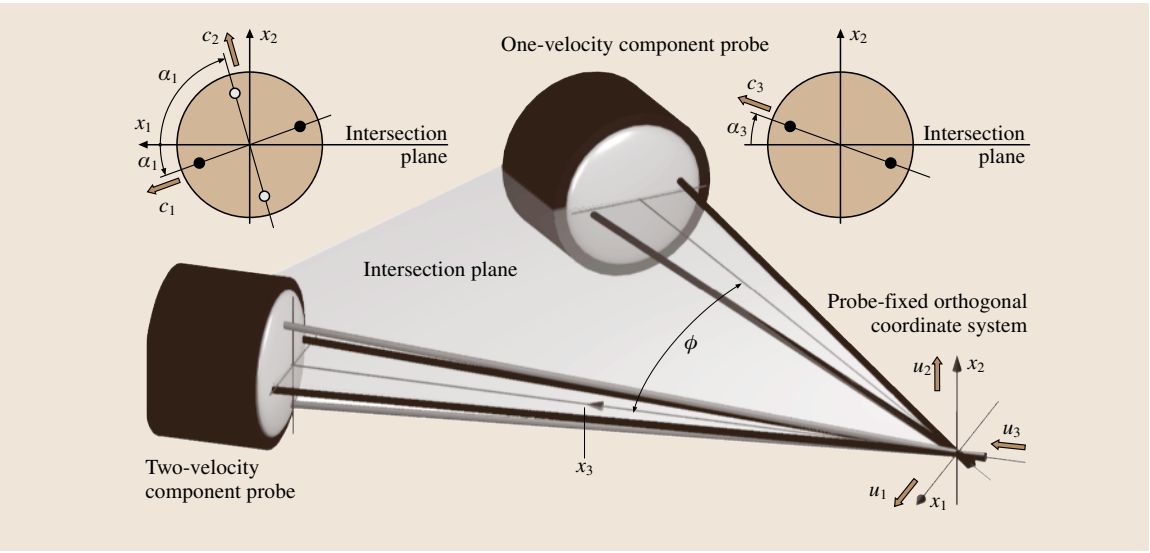

Fig. 5.78 Three-velocity component laser Doppler system, showing measured velocity components and probe-fixed, orthogonal coordinate system

- Complete intersection of the two beams, equal intensity, equal polarization, coherence
- Particle size
- Receiving aperture and alignment of the receiving optics.

In some cases these factors are choices representing conflicting requirements and additional diagnostic equipment may be necessary to achieve the best performance.

Signal Processing

Each tracer particle passing through the measurement volume results in a signal at the output of the photodetector. The signal processor has the task of detecting when a signal is present and estimating various signal parameters – Doppler frequency, arrival time, signal length, signal-to-noise ratio. Such a time series of particle signals is shown in Fig. 5.79, where a high-pass filter was used to first remove the DC part of the signal. Note that the signals arrive irregularly in time, a feature requiring special consideration in the data processing step. These signals are often referred to as burst signals, or Doppler bursts.

For the temporal resolution of the system, the number of detected or processed signals per unit time is of importance. Assuming a random and homogeneous spatial distribution of particles in the flow with concentration $\overline{n}_\mathrm{p}$, the mean number of particles in the measurement volume is

$$\overline{N}_{\mathrm{p}0} = \overline{n}_\mathrm{p} V_0 = \frac{4}{3}\pi a_0 b_0 c_0 \overline{n}_\mathrm{p} \qquad (5.219)$$

and the mean signal rate (number of signals per unit time) for particle trajectories through the measurement volume parallel to the x axis is

$$\dot{N}_0 = p b_0 c_0 \overline{n}_\mathrm{p} \overline{v}_x \,. \qquad (5.220)$$

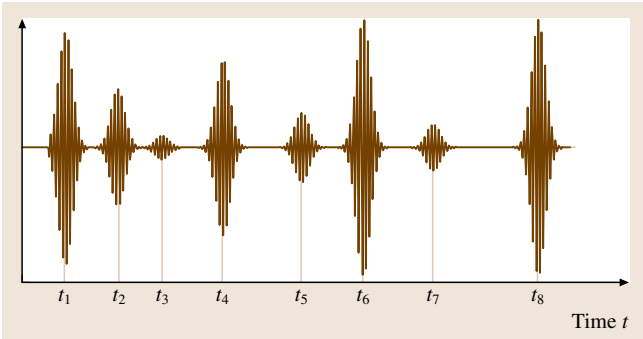

Fig. 5.79 Irregular arrival of burst signals in time

Increasing the particle concentration indefinitely does not continue to improve the temporal resolution; firstly because at high particle loadings the injection of particles start to influence the flow, but also because the signal processing may not be reliable in estimating the signal frequency when multiple particles are present simultaneously in the measurement volume. Using Poisson statistics, which is valid for random spatial distributions of particles, three concentration ranges can be distinguished:

- $\overline{N}_{\mathrm{p}0} < 0.1$: single realization with a probability of 99.5%
- $\overline{N}_{\mathrm{p}0} \geq 0.1$: multiple particle signals, in which the superposition of random amplitudes deteriorate signal quality and may lead to a lower signal rate
- $\overline{N}_{\mathrm{p}0} > 10$: a quasi-continuous signal.

Signal processors operate most effectively in the single realization mode, which places upper limits on the allowable mean particle concentration for a given measurement volume size. Smaller measurement volumes tolerate higher mean concentrations. At the same time, the same laser power distributed over a smaller measurement volume will result in higher incident intensity and higher signal amplitudes and quality. However, reducing the measurement volume indefinitely will eventually result in fewer particles being seen, reducing the temporal resolution of the system.

Superimposed on the Doppler signal is noise, including stochastic noise from the photodetector and electronics (shot noise, Johnson noise, dark current) as well as from the scattering process itself. The laser may introduce signal noise, especially laser diodes. Noise can arise from unwanted reflections associated with the flow rig or other particles. Poor grounding of the experimental apparatus or poorly designed electronics may also lead to ground noise. Except for the last source, noise contributions in the system are usually considered to be spectrally white, referring to the fact that the total noise power is distributed evenly over all frequencies up to the upper bandwidth of the system. The power of the signal fluctuations σ_s^2 divided by the power of the noise fluctuations σ_n^2 is known as the signal-to-noise ratio (SNR) and is generally expressed in decibels

$$\frac{\mathrm{SNR}}{\mathrm{dB}} = +10 \log\left(\frac{\sigma_\mathrm{s}^2}{\sigma_\mathrm{n}^2}\right) \,. \qquad (5.221)$$

In Fig. 5.80, a laser Doppler signal, a noise signal and the summation of the two in time, spectral and correlation domain is illustrated. It becomes obvious from Fig. 5.80 that the power spectral density (PSD) or the

autocorrelation function (ACF) offer excellent means to monitor SNR and to determine whether a particle signal is present or not (Sect. 23.4). The presence of noise in the signal can have both direct and indirect effects on the measurement quantities. In the worst case, the scattering signal from the particle may not be detected at all or a completely wrong frequency could be measured from a noisy signal. However, noise may also affect estimates of the signal duration, generally leading to an overestimation, which then influences the derived flow quantities in the data processing. In any case, noise increases the variance of the signal frequency estimates, regardless of which processing scheme is employed. Thus, noise at the signal processing stage essentially determines the lowest resolvable level of measurable turbulence in a flow. This level is known as the Cramèr–Rao lower bound (CRLB), and is discussed further in Sect. 23.5, as are further aspects about the estimation of noise and SNR of a signal.

The noise contribution to the signal can be decreased and the SNR increased by bandpass filtering the signal before processing; however to do this the cut-off frequencies of the filter must be carefully chosen so as not to suppress signals with widely varying Doppler frequencies due to turbulent flow fluctuations. The advantage of employing bandpass filters is that a higher particle detection rate can be achieved and the variance of the frequency estimates may decrease. Otherwise this variance will falsely appear as turbulent flow fluctuations. Nevertheless, as mentioned above, the best strategy for

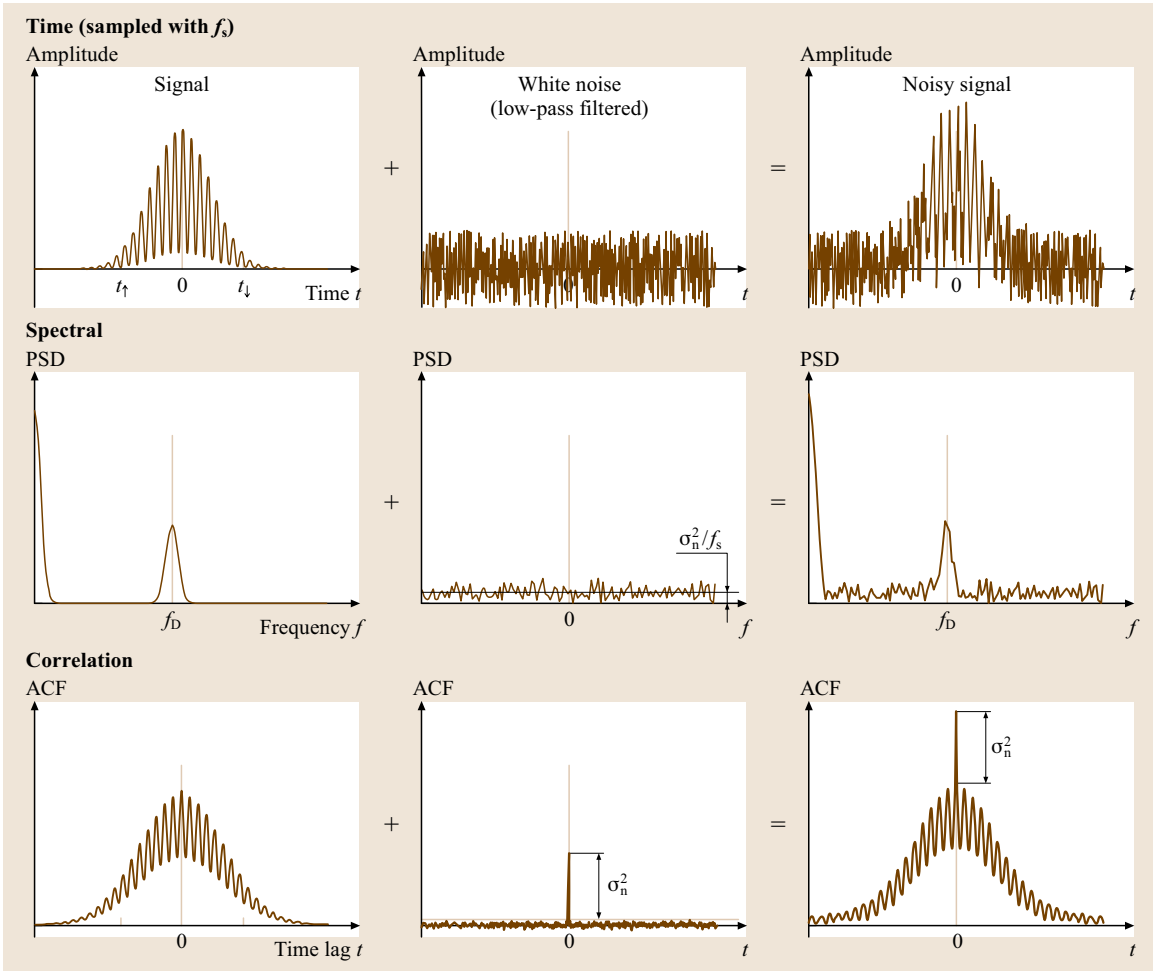

Fig. 5.80 Representation of a laser Doppler signal, a noise signa,l and a combination of the two in the time, spectral, and correlation domains

achieving a maximum signal-to-noise ratio is to design and adjust the optical system properly.

The processing of Doppler signals has seen a long history of various methods since the first instruments; however the high speed and low cost of present-day electronics has resulted in commercial processor units that exclusively use either the autocorrelation or power spectrum for both signal detection and signal parameter estimation. The main signal parameter to be estimated from each Doppler burst is the frequency f_D and, as shown in Sect. 23.5.1 of this Handbook, several estimators exist which come very close to achieving the Cramèr–Rao lower bound for the signal frequency. In fact with some a priori knowledge about the signal frequency range, and with judicious use of filters, the CRLB can even be exceeded. Modern commercial processors are able to achieve these limits.

Other signal parameters to be estimated for each burst include the arrival time, the length of the burst, and the signal-to-noise ratio. The arrival time is required for reconstruction of the velocity time series and also for checking for coincidence between signals from different channels of a two- or three-velocity component system. Coincidence is registered when a signal is detected on each channel within a given time separation, typically 10–30% of the total signal duration. This coincidence is important when the velocity values are used to estimate Reynolds stress terms, in which case only velocity component values definitely coming from the same particle should be considered.

The length of the burst, sometimes referred to as transit or residence time, is a quantity required in the data processing stage for estimating mean and fluctuating flow velocities. However the burst length may also be used as a postvalidation criterion. The burst duration can be compared with the measurement volume size divided by the measured velocity. If these do not agree within sufficient bounds, the particle is rejected from entering further statistics. Similarly, the signal-to-noise ratio can be used either as an online validation or as a postvalidation criterion. Modern signal processors allow these quantities and their acceptable limits to be adjusted through software.

With the widespread availability of fast analog-to-digital convertors and processors, customized signal-processing schemes are easily implemented, which may estimate additional signal parameters. In particular, model-based signal processing is attractive for special applications. One example is the recent use of the laser Doppler technique to estimate particle acceleration [5.376]

Data Processing

As opposed to signal processing, whose task is to estimate certain characteristic parameters from a given signal, data processing uses these estimated parameters from many signals to derive certain flow-related quantities. Two basic properties unique to laser Doppler data must be considered. First, the sample times of the flow velocity, given by the particle arrival times in the measurement volume, are irregular. This is in contrast to many other measurement instruments, which use a regular time sampling of an analog signal (analog-to-digital converter). The second important feature of laser Doppler data is that not only is the velocity sample time random, but that the short-term rate of random particle arrivals will generally be correlated with the measured flow quantity. This correlation will be referred to as the *particle-rate/velocity* correlation and without careful attention to this fact, estimators can be biased, i. e., their expectation can be incorrect.

The assumption of a homogeneous and random spatial distribution of tracer particles in the fluid leads to an exponential distribution of the distances between particles [5.377]. For a constant convective velocity, this results in an exponential distribution of interarrival times through any volume in space. Therefore, a good model of the interarrival time probability density distribution (PDF) is

$$p(\Delta t_i) = \dot{N} \exp\left[-\dot{N}(t_i - t_{i-1})\right], \qquad (5.222)$$

where $\dot{N}$ is the mean particle rate and t_i and t_{i-1} are the arrival times of consecutive particles i and $i-1$, respectively. The striking feature of the distribution is that the most probable time between two particles is zero. Even at modest mean particle arrival rates, particles will quite often appear in rapid succession. Either the signal processor must be able to evaluate the signals online or suitable input buffering must be available to avoid loss of information and to prevent processor *dead time*. On the other hand, the fact that velocity information is often available over the very short time spans of consecutive particles suggests that, in principal, information about very high-frequency velocity fluctuations is contained in the data. This is in strong contrast to data sampled at equal time intervals, for which the sampling theorem applies and for which no information above the Nyquist frequency $f_{Nyq} = 1/(2\Delta t_s)$ is available, where Δt_s is the sampling interval. In fact, with randomly sampled data, there is no equivalent to the sampling theorem or the Nyquist frequency and with suitable estimators it is possible to achieve alias-free and unbiased estimates

of signal power at frequencies far exceeding the mean particle arrival rate, as discussed below.

Arrival-time information is sometimes used in data processing as a basis for validation. Knowing the particle velocity and the dimensions of the measurement volume, an estimate of mean transit times can be made. Measured arrival times lying far below these estimates indicate that the signal processor may be delivering more than one velocity value per particle. Since moment estimators of velocity fluctuations generally assume the single realization condition, such multiple values per particle are unacceptable. These can often be recognized as peaks in the probability density function of the interarrival time, which also indicate suitable thresholds for validating each individual velocity before further processing.

Estimation of Moments. The particle-rate/velocity correlation is the main physical reason for requiring special moment estimators for laser Doppler data. The particle rate through the measurement volume is determined by the volume flux of fluid through the measurement volume and this is, in general, correlated with the measured velocity component. Therefore, the sample rate of the velocity also increases with velocity. For a given observation time, higher velocities will be sampled more frequently than lower velocities and a simple arithmetic mean of all samples will be positively biased over the true time mean of the velocity. The degree of bias will depend on how strong the correlation between the particle arrival rate and the measured velocity component is.

A correct estimator for the mean of the u flow velocity component must therefore weight each sample with a factor g, which is inversely proportional to the conditional probability density of a particle arrival at a time t_i, given the velocity u_i,

$$\hat{\overline{u}} = \frac{\sum_{i=1}^{N} u_i g_i}{\sum_{i=1}^{N} g_i} , \tag{5.223}$$

where the index i refers to the arrival time t_i and the hat ($\hat{}$) signifies that this is only an estimation of the mean.

One possible weighting factor would be

$$g_i = \frac{1}{\sqrt{u_i^2 + v_i^2 + w_i^2}} , \tag{5.224}$$

which uses the magnitude of the vector velocity and assumes a spherical measurement volume. For this, a three-velocity component laser Doppler system is necessary.

Alternatively, the residence time (or transit time) of the particle τ_i can be used as a weight factor, since this will be inversely proportional to the vector velocity magnitude [5.378].

$$g_i = \tau_i . \tag{5.225}$$

This is only possible if the signal processor provides residence time information and if it is reliable.

An estimator for the second moment is given in a similar manner

$$\hat{\sigma}_u^2 = \frac{\sum_{i=1}^{N} \left(u_i - \hat{\overline{u}}\right)^2 g_i}{\sum_{i=1}^{N} g_i} , \tag{5.226}$$

as are estimators for joint moments

$$\hat{\overline{u'v'}} = \frac{\sum_{i=1}^{N} \left(u_i - \hat{\overline{u}}\right)\left(v_i - \hat{\overline{v}}\right) g_i}{\sum_{i=1}^{N} g_i} . \tag{5.227}$$

The last estimator assumes that the u and v velocities are available at the same instant in time, meaning time coincidence is demanded during the acquisition. For independent time series, i. e., data collection without coincidence, this equation must be modified to

$$\hat{\overline{u'v'}} = \frac{\sum_{i=1}^{N} \sum_{j=1}^{M} \left(u_i - \hat{\overline{u}}\right)\left(v_i - \hat{\overline{v}}\right) g_{ui} g_{vi}}{\sum_{i=1}^{N} g_{ui} g_{vi}} . \tag{5.228}$$

As an example, if a residence time weighting is being used, g_{ui} corresponds to the residence time of the i-th particle, found from the u component signal.

The issue of choosing an appropriate moment estimator is certainly less critical now than in the past, simply because almost all commercial signal processors now provide reliable estimates of the transit time for each particle passage through the measurement volume. Transit-time weighting is the recommended estimator for all measurement situations involving spatially homogeneous particle seeding.

The necessity to use a weighted estimator can be checked by cross-correlating the measured velocity magnitude with the interarrival time fluctuations between particles. This is especially reliable if all three

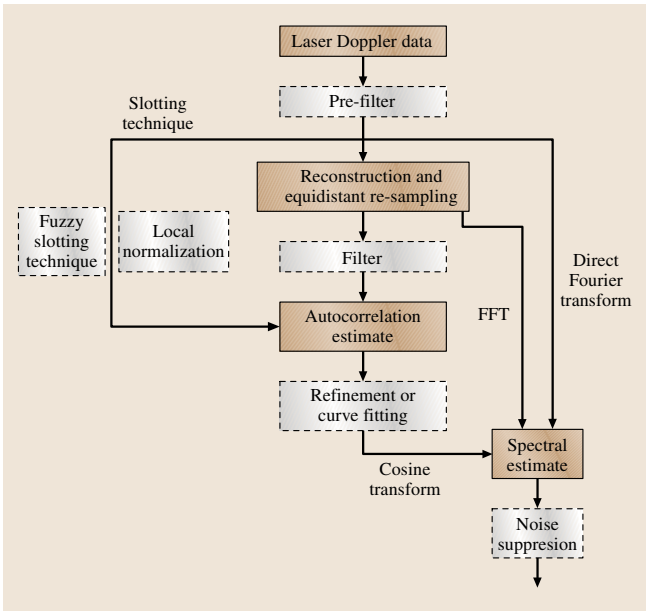

Fig. 5.81 Power spectral density estimation methods for laser Doppler data

velocity components are available. A weighted estimator is only required if a significant correlation exists between these quantities.

Estimation of Turbulent Velocity Spectra. In contrast to the rather straightforward computation of power spectral density functions for equally sampled data, as described in detail in Sect. 22.1, now the input data is randomly sampled in time and no obvious equivalent to the fast Fourier transform (FFT) is available as a computational algorithm. However, as anticipated at the beginning of this discussion, some estimators are able to exploit the random sampling to achieve estimates of turbulent kinetic energy at frequencies much higher than the mean particle arrival rate. The most common of these include

- direct transform
- slot correlation followed by a cosine transform
- reconstruction with equidistant resampling and FFT.

The relation between these techniques is pictured schematically in Fig. 5.81. In each of the algorithmic routes, additional steps (shown as dashed boxes in Fig. 5.81) are possible, representing various enhancements of these basic algorithms.

A comprehensive review and evaluation of these techniques are given in *Benedict* et al. [5.379]. They come to the conclusion that two main algorithms for estimation of the PSD and autocorrelation function (ACF) can be recommended: the fuzzy slotting technique in combination with local normalization [5.380], and the refined sample-and-hold (S+H) reconstruction [5.381].

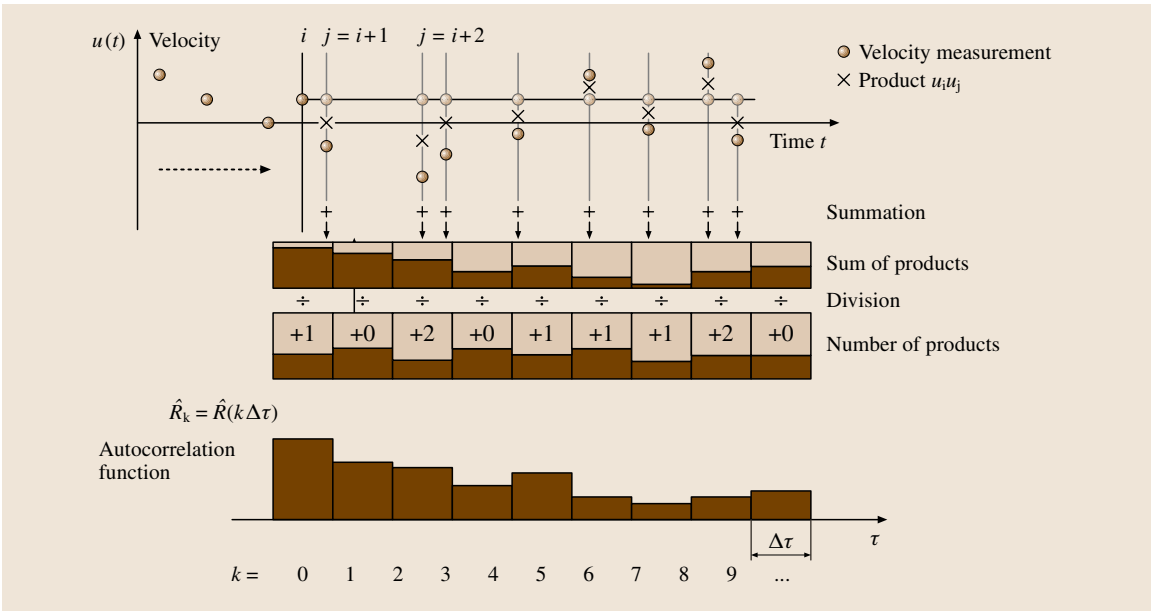

Fig. 5.82 Time series of laser Doppler velocity data and slot correlation with equidistant lag time bins $\Delta\tau$

The Slotting Technique. The slotting technique, generally credited to *Mayo* et al. [5.382], is pictured in Fig. 5.82 and computed as

$$\hat{R}_k = \hat{R}(k\Delta\tau) = \frac{\sum_{i=1}^{N}\sum_{j=J}^{N} u_i u_j b_k(t_j - t_i)}{\sum_{i=1}^{N}\sum_{j=J}^{N} b_k(t_j - t_i)},$$

$$b_k(t_j - t_i) = \begin{cases} 1 & \text{for } \left|\frac{t_j - t_i}{\Delta\tau} - k\right| < \frac{1}{2} \\ 0 & \text{otherwise} \end{cases} \quad (5.229)$$

with the velocity samples $u_i = u(t_i)$ and $u_j = u(t_j)$. The velocity product of all sample pairs with time separations falling within a given lag-time bin is added to that bin's sum as another estimate of the ACF for that lag time. After processing all possible signal pairs, each sum is divided by the number of accumulated products in that bin. The original algorithm of Mayo uses $J = 1$, which means that all sample pairs occur for k and $-k$. Calculating only positive lag times ($k \geq 0$) (5.229) can be modified to $J = i$. Note that the first ACF coefficient ($\tau = 0$) also contains self-products. With $J = i$ the self-products are over-represented compared to $J = 1$. Therefore, an additional weighting factor of 1/2 is often used for self-products when ($J = i$). However, since noise in each of the velocity estimates is unavoidable, the first slot will be increased by the variance of the noise. Since the ACF coefficient at $\tau = 0$ normally also corresponds to the variance of the process, this variance will be overestimated using the estimator given by (5.229). This also leads to a biased PSD estimate. Using only cross-products ($J = i + 1$) leads to a spectral estimate with a noise-independent expectation. In fact, only the estimation variance increases in the case of noise. However, the first slot can also be under-represented due to processor dead times. This again can lead to a bias of the $k = 0$ ACF coefficient, and thus the PSD estimate. The ACF coefficient estimates are usually considered valid for time lags in the middle of each bin.

A one-sided PSD estimator is computed from the slot correlation by taking its discrete cosine transform

$$\hat{S}_j = \hat{S}(f_j) = \hat{S}\left(\frac{j}{2K\Delta\tau}\right) = 2\Delta\tau\left[\hat{R}_o + 2\sum_{k=1}^{K-1}\hat{R}_k \cos(2\pi f_j k\Delta\tau) + (-1)^j \hat{R}_K\right], \quad (5.230)$$

where K is the index of the maximum time lag of the ACF and is chosen by the user.

A severe limitation of the standard slotting technique is its high variance (roughly constant up to moderate lag times), which leads to poor estimates of turbulence spectra. In order to reduce the variance of the slotting technique, *van Maanen* and *Tummers* [5.383] employ an ACF normalized by a variance estimate particular to each slot, called the local normalization. This results in an estimate of the correlation coefficient

$$\hat{\rho}_k = \hat{\rho}(k\Delta\tau) = \frac{\sum_{i=1}^{N}\sum_{j=J}^{N} u_i u_j b_k(t_j - t_i)}{\sqrt{\left[\sum_{i=1}^{N}\sum_{j=J}^{N} u_i^2 b_k(t_j - t_i)\right]\left[\sum_{i=1}^{N}\sum_{j=J}^{N} u_j^2 b_k(t_j - t_i)\right]}} \quad (5.231)$$

and is used as the basis for the cosine transform. The corresponding one-sided, real PSD estimator is

$$\hat{S}_j = \hat{S}(f_j) = \hat{S}\left(\frac{j}{2K\Delta\tau}\right) = 2\hat{\sigma}_u^2\Delta\tau\left[1 + 2\sum_{k=1}^{K-1}\hat{\rho}_k \cos(2\pi f_j k\Delta\tau) + (-1)^j \hat{\rho}_K\right], \quad (5.232)$$

where $\hat{\sigma}_u^2$ is an estimate of the velocity variance. While (5.231) has been shown to have significantly lower variance for small lag times than (5.230) normalized by $\hat{R}_0$, the variance at large lag times is unchanged.

Another method for reducing variance in the slotting technique has been dubbed the fuzzy slotting technique by *Nobach* et al. [5.381]. In this estimator, a lag-product weighting scheme is defined as

$$b_k(t_j - t_i) = \begin{cases} 1 - \left|\frac{t_j - t_i}{\Delta\tau} - k\right| & \text{for } \left|\frac{t_j - t_i}{\Delta\tau} - k\right| < 1 \\ 0 & \text{otherwise} \end{cases} \quad (5.233)$$

and is used instead of the top-hat function in the original algorithm (5.229). This estimator allows lag products to contribute to two slots simultaneously and weights lag products that lie close to the slot centers more heavily. The combination of this fuzzy slotting technique with local normalization is one of the recommended methods of computing the ACF.

Reconstruction with FFT. Reconstruction methods create equidistantly spaced time series by resampling according to various interpolation schemes, thereby allowing a FFT to be used in making PSD or ACF estimates. The most common scheme by far is the sample-and-hold (zeroth-order, S+H) reconstruction. This is the simplest of the polynomial class of reconstruction algorithms and is depicted schematically in Fig. 5.83. It can be written as

$$u^{(\mathrm{SH})}(t) = u(t_i) \quad \text{for } t_i \le t < t_{i+1} \text{ and } i = 1, \ldots, N\,, \tag{5.234}$$

where N is the total number of samples in a given block. The reconstruction can be performed either over the entire data set or with single data blocks. The equidistant resampling with time steps of Δt_s is performed by

$$u_i^{(\mathrm{SH})} = u^{(\mathrm{SH})}(i\Delta t_\mathrm{s}) \quad \text{for } i = 0, \ldots, N_\mathrm{R} - 1 \tag{5.235}$$

and leads to a data set of N_R samples that can be processed by a Fourier transform.

The Fourier transform with the imaginary unit i is given by

$$\underline{U}_\mathrm{n}^{(\mathrm{SH})} = \sum_{i=0}^{N_\mathrm{R}-1} u_i^{(\mathrm{SH})} \exp\left(-2\pi \mathrm{i}\frac{in}{N_\mathrm{R}}\right) \quad \text{for } n = 0, \ldots, N_\mathrm{R} - 1 \tag{5.236}$$

and leads to the full block PSD

$$\hat{S}_\mathrm{n}^{(\mathrm{SH})} = \frac{\Delta t_\mathrm{s}}{N_\mathrm{R}} \left|\underline{U}_\mathrm{n}^{(\mathrm{SH})}\right|^2 \quad \text{for } n = 0, \ldots, N_\mathrm{R} - 1 \tag{5.237}$$

and, through the inverse FFT

$$\underline{\hat{X}}_k^{(\mathrm{SH})} = \frac{1}{N_\mathrm{R}} \sum_{i=0}^{N_\mathrm{R}-1} \hat{S}_i^{(\mathrm{SH})} \exp\left(2\pi \mathrm{i}\frac{ik}{N_\mathrm{R}}\right) \quad \text{for } k = 0, \ldots, N_\mathrm{R} - 1 \tag{5.238}$$

to the full block ACF

$$\hat{R}_k^{(\mathrm{SH})} = \frac{1}{\Delta t_\mathrm{s}} \hat{X}_k^{(\mathrm{SH})} \quad \text{for } k = 0, \ldots, N_\mathrm{R} - 1\,. \tag{5.239}$$

To reduce the variance of the final PSD estimate, only $K + 2 < N_\mathrm{R}$ values of the ACF are used for further calculations. K is the maximum desired lag time for the ACF. In the refinement step outlined below, $K + 1$ values of $\hat{R}_k$ are required, and one further sample in the ACF is required for the subsequent Fourier transform to the PSD, i. e., $K + 2$ samples in total.

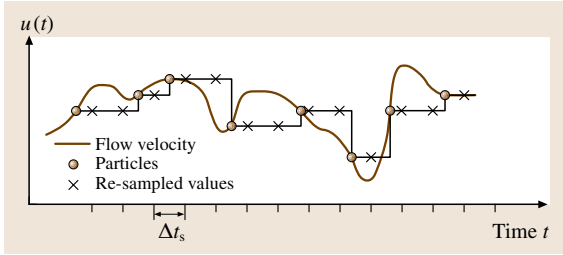

Fig. 5.83 The concept of zeroth-order reconstruction (S+H) and resampling at equal time intervals

Unquestionably the work of *Adrian* and *Yao* [5.384] was a major step forward in understanding the fundamental content of an S+H reconstructed signal. They derived an expression for the expectation of the PSD

$$k = 0, \ldots, N_\mathrm{R} - 1 E[\hat{S}^{(\mathrm{SH})}(\omega)] = \underbrace{\frac{1}{1 + \omega^2/N^2}}_{\text{filter}} \left[S(\omega) + \underbrace{\frac{2\sigma_u^2}{N^3 \lambda_u^2}}_{\text{step noise}} \right], \tag{5.240}$$

where $E[\hat{S}^{(\mathrm{SH})}(\omega)]$ is the expectation of the spectral estimate and $S(\omega)$ is the true spectrum (σ_u^2 is the variance of the velocity fluctuations and λ_u is the Taylor microscale). The second term in parentheses was termed step noise and corresponds to the spectral contribution necessary to account for the step-like jumps in an S+H signal. This contribution vanishes with the inverse of the third power of the data rate $\dot{N}^{-3}$. The factor in front of the parentheses, operating on both the true spectrum and the step noise, is a first-order, low-pass filter with a cut-

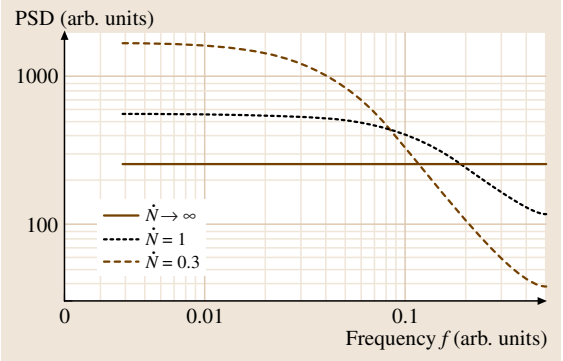

Fig. 5.84 The PSD of a white-noise process computed using a S+H reconstruction and resampling with FFT PSD estimation

off frequency of $\dot{N}/(2\pi)$. This was subsequently named the particle-rate filter and, at higher frequencies, dominates the spectrum. Actually the step noise is a form of aliasing in which the signal energy above the filter cut-off frequency is distributed evenly over the entire spectrum.

One result from *Adrian* and *Yao* [5.384] is reproduced here because of the clarity it brings to how all reconstruction methods effect spectral estimators. Simulated laser Doppler data from a white-noise process are submitted to a S+H reconstruction, resampling and a conventional FFT PSD estimation. The result is shown in Fig. 5.84. The effects of both the additive step noise and the low-pass filter are clearly evident at low particle rates; indeed the completely falsified spectrum for the lowest data rate begins to uncannily resemble that of turbulence. The conclusion of Adrian and Yao was that such spectra are reliable only up to a frequency of $\dot{N}/(2\pi)$, a substitute for the Nyquist frequency rule concerning regularly sampled data. Their assumption that the ACF of turbulent velocity fluctuations is exponential was not instrumental to this conclusion. Of course the computed spectrum below the cut-off frequency is still falsified by the step noise or any other aliased energy from higher-frequency components in the signal.

Even the nature of the interpolation curve in the reconstruction does not alter the basic limitation of the particle-rate filter. This was demonstrated by *Müller* et al. [5.385], who applied numerous other reconstruction schemes to simulated and measured laser Doppler data. These included higher-order polynomials, projection onto convex sets (POCS), fractal reconstruction, and the so-called Shannon reconstruction. Although the reconstructed signal in the time domain was visually more appealing than an S+H signal in many cases, the spectral content was altered surprisingly little.

Nobach et al. [5.386] developed a refinement that cancels the particle-rate filter effect associated with S+H reconstruction. The approach is to derive an expression for the resampled ACF in terms of the true ACF. The relation is then inverted to improve the ACF estimation. The inversion is given by

$$\hat{R}_k = \begin{cases} \hat{R}_0^{(\mathrm{SH})} & \text{for } k = 0 \\ (2c+1)\hat{R}'^{(\mathrm{SH})}_k - c\left(\hat{R}'^{(\mathrm{SH})}_{k-1} + \hat{R}'^{(\mathrm{SH})}_{k+1}\right) & \\ & \text{for } k = 1, \ldots K \end{cases} ,$$

$$c = \frac{\exp\left(-\dot{N}\Delta t_\mathrm{s}\right)}{\left[1-\exp\left(-\dot{N}\Delta t_\mathrm{s}\right)\right]^2} , \qquad (5.241)$$

where $\hat{R}$ is the refined ACF estimate based on the ACF of the reconstructed and resampled time signal $\hat{R}^{(\mathrm{SH})}$. A full derivation of this relation is given by *Nobach* et al. [5.381]. The PSD follows from a cosine transform of $\hat{R}$. In principle, a refinement can be derived for any reconstruction algorithm, but for the S+H reconstruction the refinement becomes the very simple algorithm given above and is effective enough that the advantages of other reconstruction schemes become negligible.

5.3.3 Particle Image Velocimetry

What is PIV?

Most common fluids, such as air and water, are homogeneous and optically transparent. This implies that the motion of the fluid is not readily visible; this is experienced by the modern traveler who takes a view through an airliner window and is oblivious of the air rushing at speeds around 250 m/s just outside the window. Once the fluid has been marked, for example by using smoke, small particles or a dye, the fluid motion and structure of the flow become visible; methods for flow visualization are described by *Merzkirch* [5.387], and the book by *Van Dyke* [5.388] contains excellent examples of flow visualization examples providing insight in the deep physical aspects of fluid motion. Yet, visualization methods are predominantly qualitative, and in general fluid markers are introduced at specific locations. On the other hand, single-point methods (e.g., *hot-wire anemometry* and *laser-Doppler anemometry*) provide a quantitative and accurate sample of the flow at a given point. They are however unable to capture the instantaneous flow organization, also known as *coherent flow structures*, observed in turbulent flows [5.389–391]. With the development of digital camera technology and affordable digital image processing it became possible to develop new measurement methods that could simultaneously provide the instantaneous spatial flow field description and a quantitative result [5.392]. One of the most successful measurement methods that has emerged in the past two decades is *particle image velocimetry* (PIV) [5.393, 394].

The working principle of PIV is schematically described in Fig. 5.85. The different aspects of a PIV measurement are discussed in greater detail in the remainder of this chapter. The principle of PIV is based on the measurement of the displacement of small tracer particles that are carried by the fluid during a short time interval. The tracer particles are sufficiently small that they accurately follow the fluid motion and do not alter the fluid properties or flow characteristics (Sect. 5.3).

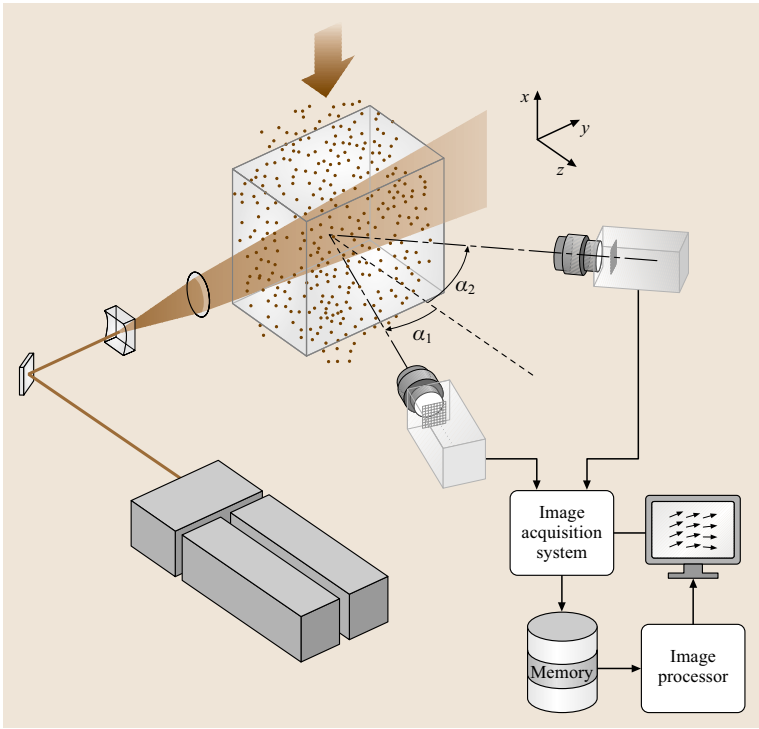

Fig. 5.85 Schematic of a typical PIV measurement system

The tracer particles are illuminated by means of a thin light sheet generated from a pulsed light source (usually a double-head pulsed laser system), and the light scattered by them is recorded onto two subsequent image frames by a digital imaging device, typically a CCD camera. By means of stereoscopic imaging it is possible to determine the three components of the flow velocity within the planar field defined by the light sheet. The simplified one-camera system suffers from the restriction that the optical axis must be aligned in the direction normal to the light-sheet plane. Moreover such systems only yield two velocity components within the measurement plane and are therefore only suitable for the investigation of flows with a negligible out-of-plane velocity component. PIV is essentially a non-intrusive measurement method; however it requires optical access for both the delivery of the light sheet and recording of the images. In order to obtain robust unbiased measurements over the flow domain, it is important that the tracer particles are homogeneously distributed within the observed flow region. This is a marked difference with respect to flow visualization methods, where fluid trac-

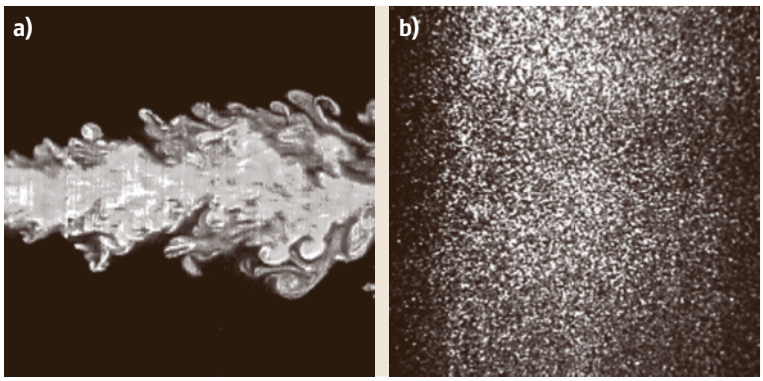

Fig. 5.86a,b Turbulent jet experiment: flow visualization of the jet by means of a dye added to the jet fluid **(a)**; PIV image of the same jet where both the jet fluid and the surrounding fluid are homogeneously seeded with tracer particles **(b)**

ers are typically introduced at very specific locations, as shown in the example of Fig. 5.86.

The recorded images are typically processed offline on a digital computer. This consists essentially of a cross-correlation analysis of the particle-image patterns in small subdomains, or *interrogation regions*, between the first and second image frame. Because of the stereoscopic viewing and the finite thickness of the light sheet, the observed particle-image displacement is slightly different for each camera, which depends on the magnitude and direction of the local velocity. The three-component displacement vector is reconstructed from the displacements observed by the two cameras. The particle-image pattern displacement divided by the image magnification and the time delay between the laser light pulses yields the local fluid velocity. This process is repeated for the entire image domain, which yields the instantaneous velocity in a planar cross section of the observed flow. Sophisticated interrogation methods have been developed that make it possible to interrogate images at high spatial resolution and to determine displacements with high accuracy. The PIV analysis typically yields 10^3-10^5 velocity measurements per image (depending on the digital image format and interrogation resolution) with a typical measurement accuracy of about 1% [5.397].

PIV is a measurement method able to partially determine the instantaneous velocity gradient tensor $\partial \boldsymbol{u}/\partial \boldsymbol{x}$ within the plane defined by the light sheet. This implies that PIV measurement can be used to determine the instantaneous out-of-plane component of the vorticity, i. e., the curl of the velocity field. This has been a major breakthrough in experimental methods that has made it possible to investigate aspects of flows experimentally that were previously impossible, with particularly interesting applications for turbulent flows where quantitative information on coherent flow structures could be inferred. In this respect PIV measurements made it possible to investigate turbulent flows from a perspective other than that of the one-point statistics, retrieving the deterministic approach to the study of turbulence and restoring the concepts of dynamical organization and emphasizing the role of coherent structures, which were not straightforward when using previous experimental methods. For example, Fig. 5.87 shows the observation of a so-called *hairpin vortex* in wall-bounded turbulent flow by means of classical hydrogen-bubble visualization and the computed out-of-plane vorticity from a PIV measurement; the same figure shows an example of an LDA measurement obtained in the same region where the heads of hairpin vortices would occur, which evidently does not reveal the turbulent flow structure.

An additional contribution of the PIV technique to experimental research is the capability to determine the flow velocity at a large number of points simultaneously, which allows a significant reduction of the time needed to acquire experimental data in wind-tunnel tests [5.398]. An example is PIV measurement of the wake behind an airplane model in a towing tank [5.399], as illustrated in Fig. 5.88. The light-sheet position is at

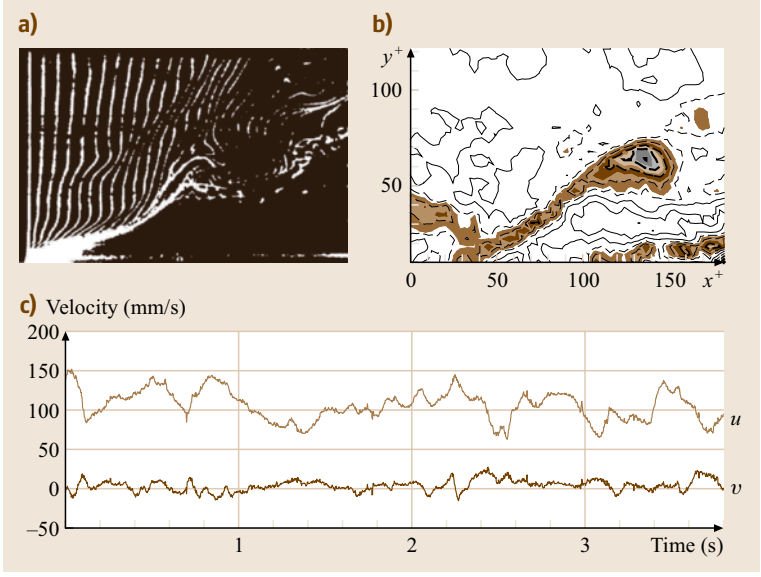

Fig. 5.87a–c Coherent structures in wall-bounded flows. **(a)** *Hairpin vortex* visualized by means of hydrogen bubbles (after *Kim* et al. [5.395]); **(b)** measured out-of-plane vorticity for a hairpin vortex measured with PIV (*Westerweel* [5.396]); **(c)** time trace of a two-component LDA measurement near the wall in a turbulent boundary layer (courtesy of A. Schwarz-van Maanen)

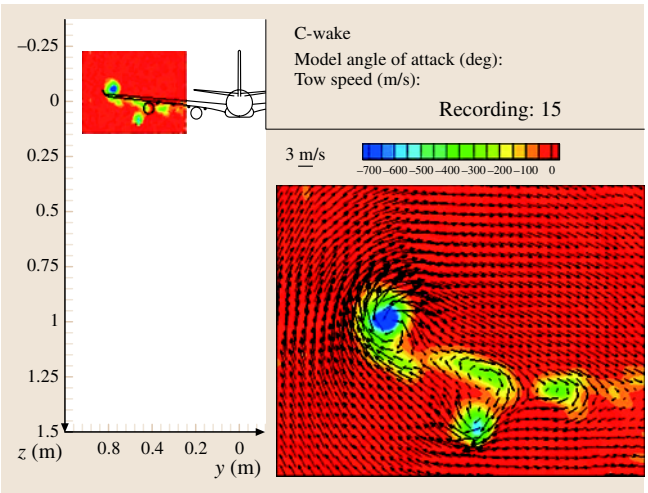

Fig. 5.88 The measured vorticity behind an airplane model in a towing tank (*Scarano* et al. [5.399])

a fixed location in the laboratory system of reference, while the aircraft model is towed through the measurement plane and beyond, releasing trailing vortices. Typically such vortex wakes are quite persistent and extend over very long distances in comparison with the wingspan. Measurements with single-point methods (such as HWA or LDA) would require a passage of the model for each measurement location, while a PIV measurement captures the wake vorticity field time history at a given station within a single experimental run.

The extension of the PIV technique into a three-dimensional measurement method has been achieved by different approaches. The most popular is the high-speed scanning method [5.400, 402] where the quasi-instantaneous three-dimensional flow structure is reconstructed from PIV recordings obtained at high repetition rate over parallel planes slightly shifted along the normal direction (Fig. 5.89a).

The instantaneous three-dimensional measurement of the flow can also be achieved by holographic recording [5.403] of an illuminated volume and the particle depth position is obtained by the reconstruction of the 3-D object from its hologram. A more-recent approach for three-dimensional measurements makes use of several viewing directions of an illuminated volume in the flow domain and a three-dimensional scattered light field reconstruction algorithm based on digital tomography [5.404]. A typical result is shown in Fig. 5.89b.

In the past decades PIV has evolved from a method that was only applied in specialized laboratories into a versatile off-the-shelf experimental tool [5.394] with a spatial resolution and accuracy that can be used for the detailed investigation of complex unsteady and three-dimensional flows. With state-of-the-art equipment it is possible to measure from large-scale supersonic flows [5.405], down to microscopic-scale low-speed flows [5.357] and even in living organisms [5.406, 407]. With the use of multiple-camera systems it is possible to combine PIV with other optical diagnostics such as *laser-induced fluorescence* (LIF), which makes it pos-

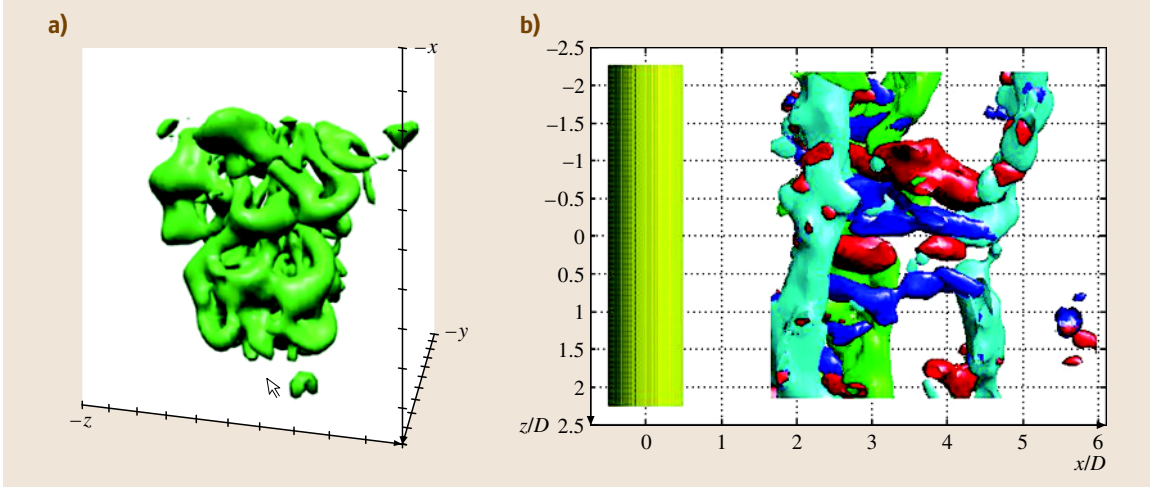

Fig. 5.89a,b Three-dimensional PIV measurements: **(a)** Turbulent jet measured by the scanning light-sheet technique and visualized with a vorticity isosurface (after *Hori* and *Sakakibara* [5.400]); **(b)** circular cylinder wake measured with tomographic PIV and visualized by color-coded vorticity components isosurfaces (after *Scarano* et al. [5.401])

sible to obtain simultaneous velocity and concentration or temperature measurements [5.408]. The use of fluorescent markers or advanced analysis methods allows an easy extension of PIV in multiphase flows [5.409–413].

Optical Systems: Seeing the Flow

Illumination.

Light Source Requirements. The measurement principle of PIV relies on a finite observation time Δt used to detect the particle motion. The particle tracers need to be illuminated and observed twice within the time separation. The first requirement for a light source suited for PIV experiments is a short duration of illumination δt. A practical criterion for the choice of the maximum duration of each illumination pulse is that particle images do not appear as streaks but rather as circular dots. This is obtained when the (imaged) particle displacement within the pulse duration (or during the imager exposure time for continuous illumination) is significantly smaller than the size of the particle image itself (see the section on imaging for the particle image size):

$$\delta t \ll \frac{d_\tau}{\boldsymbol{v}M} \,. \tag{5.242}$$

The second requirement is that the illuminated particles are distributed within a thin sheet such that they can be imaged in focus and their position in depth is dictated by the light sheet. A third requirement is that the intensity of the light source must allow the scattered light from the seeding particles to be detected by digital imaging devices. The required pulse energy E is proportional to the linear dimension L of the area of interest. Typically $E \approx 100\,\mathrm{mJ}$ is sufficient to illuminate an area with $L = 10\,\mathrm{cm}$ in air flows, while about twice that area is possible in water flows. The planar illumination requires that the thickness of the light sheet is significantly smaller than its height and width (in the order of 1%).

Lasers are used as illumination sources since they can produce a pulsed, collimated and monochromatic light beam that can be easily shaped into a thin light sheet (see the next section). The most common device used for PIV experiments is the solid-state frequency-doubled Nd:YAG laser that emits light with a wavelength of 532 nm. It produces pulse energies ranging between 10 mJ and 1 J. With its very short pulse duration (5–15 ns) this instrument is practically suited to illuminate flows without any limit on the flow speed. The standard architecture of a PIV laser consists of two separate lasers firing independently at the required pulse separation. Therefore the time separation can be freely optimized for the experimental conditions, primarily the flow speed and the imaging magnification.

However its repetition rate ranges between 10 and 50 Hz, posing the major limitation of Nd:YAG-based systems in performing time-resolved experiments except for very low-speed flows ($\boldsymbol{v} < 0.2\,\mathrm{m/s}$). In the last decade, important developments in the area of solid-state lasers have improved significantly the performance of diode-pumped Nd:YLF lasers for high-repetition-rate illumination. Currently Nd:YLF lasers are capable of emitting pulses of energy of 10–40 mJ at a repetition rate of 1–5 kHz. Their pulse duration is about 10 times longer than Nd:YAG lasers.

Light-Sheet Formation Optics. The circular-cross-section beam delivered by the light source is shaped into

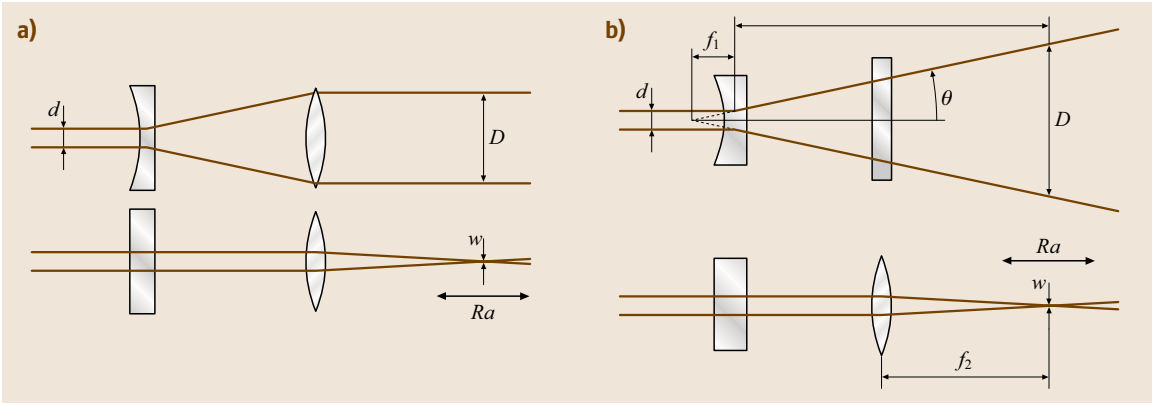

Fig. 5.90a,b Light-sheet formation optics: **(a)** constant sheet width. **(b)** linearly expanding sheet width. The Rayleigh length Ra is the length over which the light sheet has a minimum thickness w (denoted as the *waist*)

a thin sheet by means of cylindrical and spherical lenses. Common arrangements are illustrated in Fig. 5.90. In the first case (Fig. 5.90a) a cylindrical lens expands the beam along the vertical direction followed by a spherical lens that compensates the effect of the first lens. The resulting system is equivalent to a beam expander along the vertical direction. In the horizontal direction the cylindrical lens has no effect on the beam and the spherical lens will focus it at a distance equal to the focal length. This arrangement is particularly suited to achieve uniform illumination along the propagation direction. It is, however, not practical in cases for which large regions of space have to be illuminated unless a large-format spherical lens is available. The scheme illustrated in Fig. 5.90b applies for the illumination of large areas and in general when uniform illumination is not strictly required. In this case the desired sheet width can be obtained at an appropriate distance L as a function of the focal length of the cylindrical lens f_1. Systems with more than two lenses allow more-complete control of the light sheet at the cost of increased complexity.

To minimize the variation of the light sheet properties within the area of interest it is convenient to design the light-sheet optics in such a way that the beam waist does not fall within the measurement region. In fact the spatial rate of change of sheet thickness and energy density is highest around the waist. As a consequence several experimental parameters such as out-of-plane particle motion and particle brightness vary largely within the measurement area, limiting the possibility to optimize the experiment. In particular, an arrangement with the waist outside (possibly beyond) the measurement region is strictly required when performing stereoscopic measurements with a large velocity component across the light-sheet thickness.

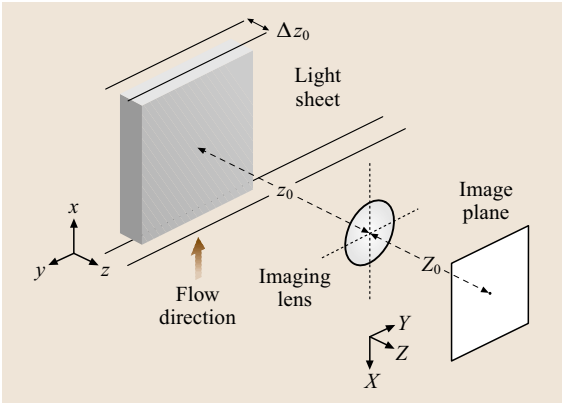

Fig. 5.91 Schematic of the optical configuration for PIV imaging. (After *Westerweel* [5.414])

Imaging. A schematic of the PIV optical configuration is shown in Fig. 5.91. The light sheet has a finite thickness Δz_0 and is assumed to be uniform along the x and y directions. An image of the tracer particles in the light sheet is formed by means of a lens on the surface of an image sensor (usually a CCD or CMOS sensor array). The lens is characterized by its focal length f, aperture number $f^{\#}$ (given by the focal length divided by the aperture diameter), and image magnification M_0, defined as the ratio of the image distance Z_0 and object distance z_0. The diameter d_τ of the image of a small tracer particle with diameter d_p in the light sheet is given by [5.393, 415]

$$d_\tau \cong \left(d_s^2 + M_0^2 d_p^2\right)^{1/2} ,$$
$$\text{with } d_s = 2.44(1 + M_0) f^{\#} \lambda , \qquad (5.243)$$

where d_s is the *diffraction-limited spot* diameter and $M_0 d_p$ the geometric image diameter. The diffraction-limited spot results from the finite resolution of the optical system due to diffraction effects; for a point source ($d_p \to 0$) or distant object ($M_0 \to 0$) the light captured by the objective is spread over a small spot also known as the *Airy* disc, with diameter d_s, surrounded by diffraction rings of decreasing brightness [5.415]. For all practical purposes in PIV, the light distribution in the Airy disc is well approximated by a Gaussian intensity distribution with an e^2 diameter of $0.74 d_s$. The first expression in (5.243) would be exact when the diffraction-limited spot and geometrical-optics particle image follow a Gaussian intensity distribution.

For typical optical parameters in PIV, e.g., $M_0 \approx 0.2$, $f^{\#} \approx 4$, $\lambda \approx 0.5\,\mu\text{m}$, $d_p \approx 10\,\mu\text{m}$, $d_s \approx 6\,\mu\text{m}$, it is found that $d_s \gg M_0 d_p$, so that $d_\tau \approx d_s$. In other words, the diffraction limit generally dominates the particle-image formation, and the particle-image diameter is quite uniform despite variations in d_p.

Equation (5.243) dictates the lower limit for the particle image diameter and applies for an aberration-free lens with a circular aperture. In practice this means that it is valid for sufficiently large $f^{\#}$, since for very small $f^{\#}$ aberrations decrease the performance of lens systems; it is good practice always to close the aperture of a lens by one or two f-stops, and to use a lens within its designed magnification range; different lens designs exist, e.g., for high-magnification imaging (viz., *macro*lenses) or for fixed magnification and working distances (*telecentric* lenses).

Moreover, the particle-image diameter follows (5.243) for particle images in focus, i. e., when the light-sheet thickness Δz_0 is smaller than the focal depth δz of the optical system (Fig. 5.91) given by [5.393]

$$\delta z \cong 4\left(1+\frac{1}{M_0}\right)^2 f^{\#2}\lambda\,. \qquad (5.244)$$

For the above example the focal depth of the imaging system is about 1 mm. In the case of μPIV the focal depth will in general be much smaller than the thickness of the illuminated volume, and the recording contains both focused particle images as well as out-of-focus particle images, which degrade the measurement precision. In this case the measurement volume is not defined by the thickness of the light sheet, but by the *correlation depth*, i. e., the depth along the optical path over which (defocused) particle images contribute significantly to the measured displacement [5.416].

Given the rather small focal depth and the strong dependence of the measurement error on particle-image diameter, it is important that the optical system is properly focused. To adjust the lens by hand while judging the focus from a monitor is often not accurate and impossible to verify. It is good practice to consider the *image contrast*, defined as the standard deviation of the image gray value divided by the mean image gray value, as a function of the focal-plane position; the position with maximum image contrast is the optimal focus position.

Stereoscopic Imaging. The use of stereoscopic imaging by means of two cameras makes it possible to reconstruct the three-component displacement vector in the plane of the light sheet. A review of stereoscopic PIV and related methods is given by *Prasad* [5.417]. The two generic configurations are the *translation method* and the *angular method* (Fig. 5.92). In the translation method the object and image planes are parallel, so that the magnification is constant, but disadvantages are that

- it is restricted to rather small viewing angles (up to about 15°), and
- the off-axis viewing is prone to optical aberrations.

The angular method allows much larger viewing angles and paraxial imaging, but the image magnification is no longer constant. This leads to a perspective deformation of the image and varying resolution over the image domain. In recent years practical and accurate methods have been developed for image reconstruction in angular stereoscopic viewing.

For an ideal imaging system with parallel object and image planes and with a thin light sheet (i. e., $\Delta z_0 \ll \delta z$), a particle at position (x, y, z) within the light sheet ($z \approx z_0$) is projected onto a position (X, Y, Z_0) with: $X/x = Y/y = M_0$. For angular stereoscopic viewing it is necessary to tilt the backplane of the camera with respect to the optical axis of the lens, according to the diagram shown in Fig. 5.93, so that all particle images are in focus; this is the so-called *Scheimpflug* configuration [5.417,418]. Since the object plane and image plane are not parallel, the image magnification varies over the

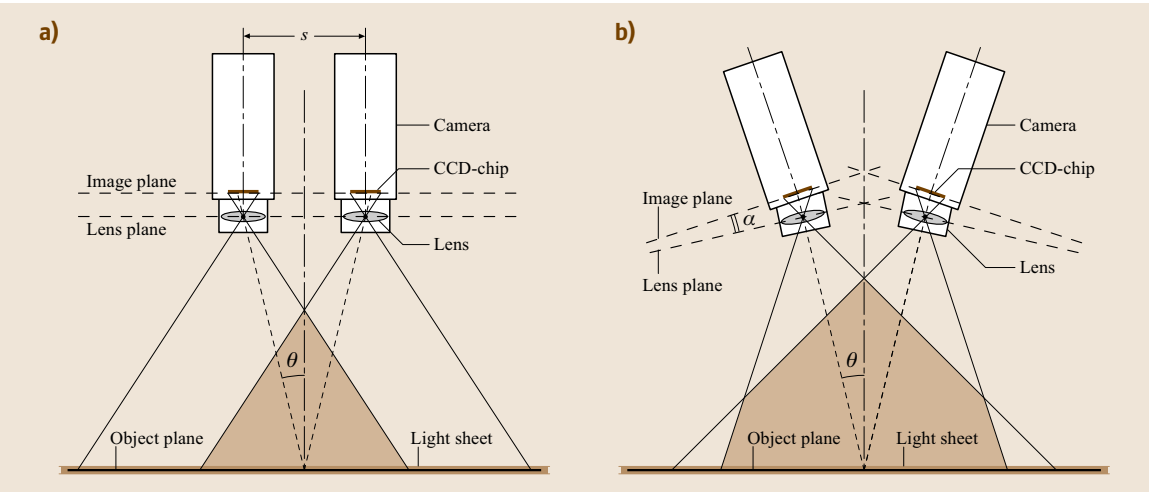

Fig. 5.92a,b Optical configurations for stereoscopic imaging: the translation method **(a)** and angular displacement method **(b)**

field of view. As a result there is a perspective deformation of the image as shown in Fig. 5.96. The geometric back-projection of (X, Y) in the image data onto (x, y) in the object plane is given by

$$x = \frac{fX \sin\alpha}{M_0 \sin\theta(X \sin\alpha + fM_0)} ,$$
$$y = \frac{fX}{X \sin\alpha + fM_0} , \qquad (5.245)$$

where the angles α and θ are defined in Fig. 5.93. This method requires accurate values for the optical and geometric parameters; inaccuracies can lead to significant systematical errors in the PIV results. A generalized approach is to use a mapping function instead [5.417, 420]

$$x = \frac{a_0 + a_1 X + a_2 Y + a_3 X^2 + a_4 Y^2 + a_5 XY + \ldots}{1 + a_1' X + a_2' Y + \ldots} ,$$
$$y = \frac{b_0 + b_1 X + b_2 Y + b_3 X^2 + b_4 Y^2 + b_5 XY + \ldots}{1 + b_1' X + b_2' Y + \ldots} , \qquad (5.246)$$

where the parameter vectors $\boldsymbol{a}$, $\boldsymbol{a}'$, $\boldsymbol{b}$, and $\boldsymbol{b}'$ are determined by means of a calibration target. When $\boldsymbol{a}' = \boldsymbol{b}' = \boldsymbol{0}$ the parameter vectors $\boldsymbol{a}$ and $\boldsymbol{b}$ can be found from an arbitrary number of calibration points by means of solving a set of linear equations. For correcting perspective image distortion (in which straight lines are imaged as straight lines) it is in principle sufficient to use second-order polynomials.

The three-component displacement vector $(\Delta x, \Delta y, \Delta z)$ for a symmetric angular configuration (i. e., $\theta_1 = \theta_2 = \theta$) is reconstructed from the two in-plane displacements $(\Delta x_l, \Delta y_l)$ and $(\Delta x_r, \Delta y_r)$ observed by the *left* and *right* camera, respectively,

$$\Delta x = \frac{\Delta x_1 - \Delta x_2}{2 \sin\theta} , \quad \Delta y = \frac{\Delta y_1 + \Delta y_2}{2} ,$$
$$\Delta z = -\frac{\Delta x_1 + \Delta x_2}{2 \cos\theta} , \qquad (5.247)$$

for $|\Delta x_1|, |\Delta y_1|, |\Delta x_2|, |\Delta y_2| \ll z_0 \sin\theta$ (Fig. 5.94). It is noted that the expression for Δz in (5.247) implies that, in a single-camera configuration (with the optical axis perpendicular to the light-sheet plane), the in-plane components of the displacement are contaminated by the out-of-plane displacement; the error is proportional to $\Delta z \tan\eta$, where η represents the viewing angle with respect to the optical axis. Given typical values for $\Delta x, \Delta z \approx 0.25$ mm and $\eta \approx 6°$ (for a point near the edge of the field of view) yields an error of up to 10% of the in-plane displacement.

A generalized method to obtain the out-of-plane component is by means of so-called *three-dimensional calibration* or *Soloff method* [5.421], where an image of the calibration target is recorded at two or more positions along the z-coordinate, and the relation between the three-dimensional position $\boldsymbol{x}$ in the object domain and the two-dimensional position $\boldsymbol{X}$ in each image plane is

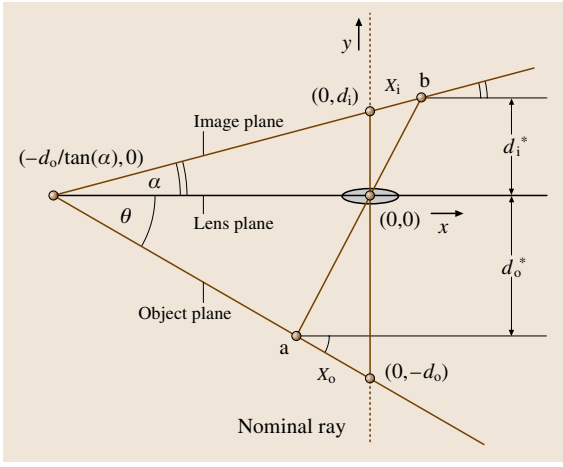

Fig. 5.93 Scheimpflug condition for tilted object and image planes

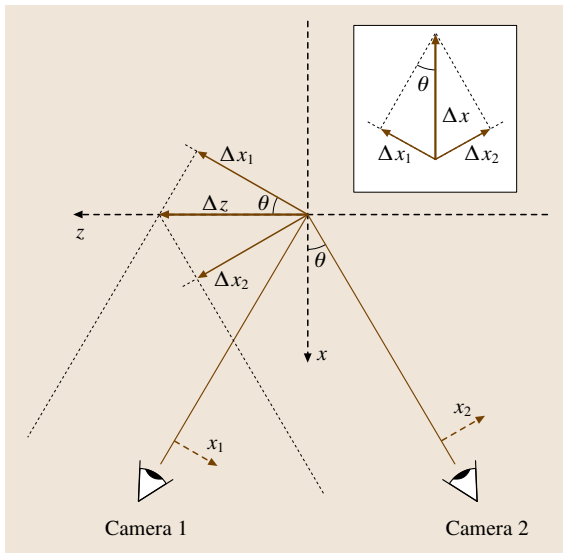

Fig. 5.94 The principle of stereoscopic PIV in which an out-of-plane displacement Δz is reconstructed from the observed motion in two cameras. In this diagram the cameras are located on opposite sides of the light sheet. (After *van Doorne* et al. [5.419])

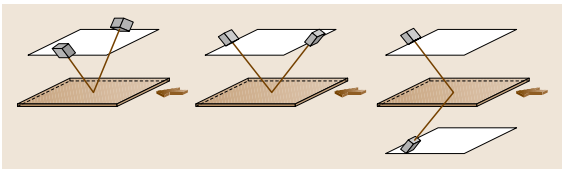

Fig. 5.95 Three generic configurations for the light sheet and cameras in stereoscopic PIV. The *arrow* indicates the direction of propagation of the light sheet

fitted to a polynomial $\boldsymbol{F}(\boldsymbol{x})$. The particle-image displacement $\Delta\boldsymbol{X}$ is then given by: $\Delta\boldsymbol{X} \cong (\nabla\boldsymbol{F})\cdot\Delta\boldsymbol{x}$, [5.417]:

$$\begin{pmatrix}\Delta X_\mathrm{l}\\ \Delta Y_\mathrm{l}\\ \Delta X_\mathrm{r}\\ \Delta Y_\mathrm{r}\end{pmatrix} \cong \begin{pmatrix}F^\mathrm{l}_{1,1} & F^\mathrm{l}_{1,2} & F^\mathrm{l}_{1,3}\\ F^\mathrm{l}_{2,1} & F^\mathrm{l}_{2,2} & F^\mathrm{l}_{2,3}\\ F^\mathrm{r}_{1,1} & F^\mathrm{r}_{1,2} & F^\mathrm{r}_{1,3}\\ F^\mathrm{r}_{2,1} & F^\mathrm{r}_{2,2} & F^\mathrm{r}_{2,3}\end{pmatrix} \begin{pmatrix}\Delta x\\ \Delta y\\ \Delta z\end{pmatrix} \qquad (5.248)$$

with $F_{i,j} = \partial F_i/\partial x_j$. The set of equations in (5.248) is solved by means of a least-squares optimization method.

Equation (5.247) shows that the random measurement error for Δz relative to the random errors in Δx and Δy is inversely proportional to $\tan\theta$. Hence, for $\theta = 45°$ the errors in the in-plane and out-of-plane components are of the same order. When stereoscopic viewing is applied for a liquid flow (viz., water) the light rays are refracted at the water–air interface. Given Snell's law, a stereoscopic viewing angle of 45° in air reduces to only

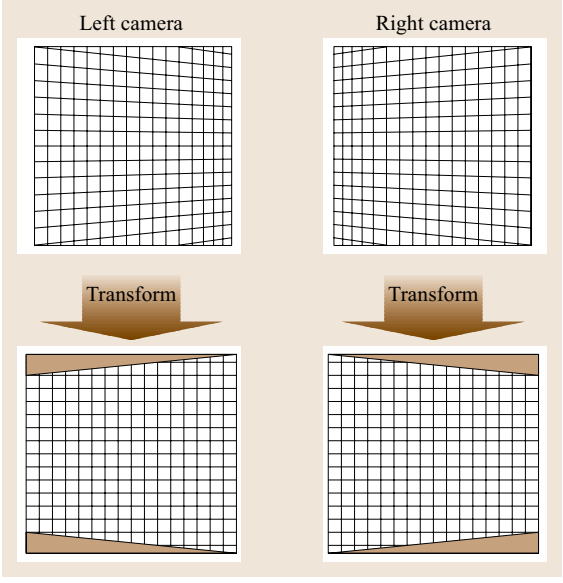

Fig. 5.96 Perspective deformation due to the angular configuration in stereoscopic viewing

32° (with a refractive index of $n = 1.33$) for water, implying that an effective 45° stereoscopic viewing angle in water is obtained for 49°, which is close to the critical angle (for $n = 1.33$), making this arrangement not viable. It is therefore common to use prisms such that the optical axis is not refracted when it crosses the wall of the test section and large viewing angles in liquids are attainable without strong image distortion [5.417].

When using a calibration-based stereoscopic reconstruction, it is important that the position of the calibration target accurately coincides with the light sheet; deviations lead to so-called *registration errors* and artefacts in the measurement results [5.419, 422]. A small deviation can be corrected by means of a procedure based on the so-called *disparity map* obtained by cross-correlating the simultaneous particle images recorded from the two views [5.418, 423].

Another aspect that can strongly influence the performance of a stereoscopic PIV system is the orientation of the cameras with respect to the light sheet. In most applications with restricted optical access it will be practical to position both cameras on one side of the light sheet; with full optical access one can position the cameras on opposite sides of the light sheet. Three generic configurations can be identified, as shown in Fig. 5.95. For the first configuration the scattering angle is around 90° for both cameras. In view of the scattering diagram shown it would be favorable to use forward or backward scattering, as is achieved in the second configuration. The level of scattering has usually increased, although it can be quite uneven between the two cameras, as forward scattering is generally an order of magnitude stronger than backward scattering. In the third configuration both cameras are positioned so that light is scattered in a forward direction and at equal scattering levels; this configuration would be favorable when working with low-power lasers or very small tracer particles, provided that sufficient optical access is available.

Non-Ideal Imaging. For non-ideal imaging systems the particle images can be distorted as a result of optical aberrations, and straight lines in the object plane become curved lines in the image plane, i. e., nonuniform imaging. Examples of optical aberrations are *coma* and *astigmatism*. Coma usually occurs for nonparaxial imaging, while astigmatism occurs when the light rays pass at significant angles through different refractive media (e.g., when no prisms are applied for stereoscopic viewing in a liquid). Nonuniform imaging is generally classified as *barrel* or *pincushion* deformation. Optical aberrations and image nonuniformity can usually be

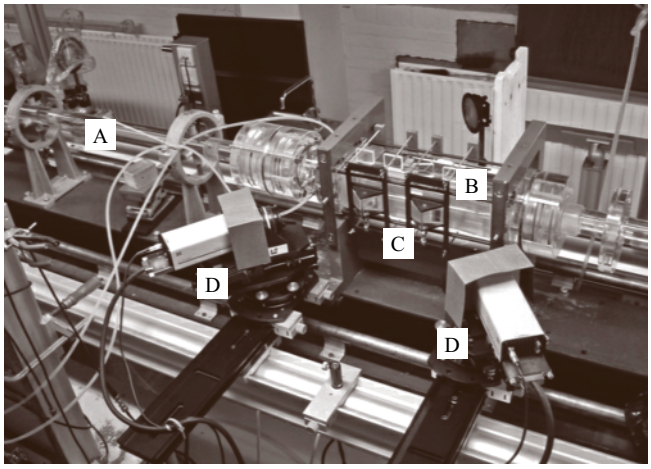

Fig. 5.97 Stereoscopic PIV setup for measurements in a pipe. A: pipe; B: water-filled rectangular box; C: water-filled prisms; D: cameras on Scheimpflug mounts (after *van Doorne* and *Westerweel* [5.419])

avoided when lenses are used within the design specifications. A small degree of image nonuniformity can be corrected by using higher-order polynomials as mapping functions (5.246).

Optical aberrations and image nonuniformity also occur when the flow is observed through curved windows, for example when imaging a flow in a cylindrical pipe. This can become very strong when such a pipe is filled with a liquid. In that case the optical distortions and image nonuniformity can be reduced considerably by enclosing the pipe section at the measurement location with a box that is filled with the same liquid. It is also beneficial to replace the pipe wall locally with a thin-walled pipe section.

As an example, Fig. 5.97 shows the optical configuration for stereoscopic PIV measurements in a pipe. The cameras are on Scheimpflug mounts on opposite sides of the light sheet in the forward scattering direction, and the setup includes a water-filled box with a thin-walled pipe section and prisms to minimize optical distortions.

Digital Image Processing. Digital image processing encompasses all computer operations on digital images. For a full account of all possible methods one is referred to the many text books that have been written on this subject [5.424, 425]. In general two approaches are distinguished in image processing:

1. image *restoration* attempts to *repair* undesirable effects due to the imaging (e.g., perspective distortion, image blur due to defocusing), whereas
2. image *enhancement* accentuates certain image features (e.g., improvement of image contrast, suppression of background illumination).

The interrogation analysis of PIV images by means of spatial correlation is based on the requirement that the image statistical properties are *homogeneous*, i. e., the image mean and standard deviation are spatially uniform and the spatial correlation is a function of the difference of two spatial locations. This implies:

1. homogeneous seeding
2. uniform illumination
3. uniform image background.

In many practical situations these requirements may not be fully met: for large flow facilities and high-speed flows it is difficult to maintain a homogeneous seeding; the Gaussian intensity profile of laser beams and the use of an uncollimated light sheet imply gradual variations of the local illumination intensity; PIV measurements near wall and other objects usually suffer from nonuniform backgrounds due to reflections. Some of these non-ideal aspects in PIV images can be compensated by means of image-processing methods, which are briefly reviewed here.

Low-Pass and High-Pass Filtering. Straightforward image-processing operations are low- and high-pass filtering. These can be implemented by means of moving average or autoregressive methods. Alternatively, these filters can also be implemented in the Fourier domain making use of the duality of multiplication and convolution [5.426]. These operations are linear, which implies that subtracting a low-pass filtered image from its original image is equivalent to a high-pass filtered image. In general, these methods are *lossy* (see later), which means that information is lost. For example, high-pass filtering generally removes a slowly varying background image, but also reduces the effective particle-image diameter, which can lead to increased discretization errors (peak locking); also, high-pass filtering does not remove sharp edges present in background images. An effective approach for the elimination of background noise and sharp edges is based on the subtraction of the statistical minimum intensity locally from each image. This procedure can be applied under the constraint that the background noise is constant during the acquisition of the series of recordings.

Histogram. In general the gray values in a PIV image are not equally distributed. The typical gray value histogram

will have a dominant peak that represents the dark image background and an exponentially decaying part that represents the particle images (Fig. 5.98). In general the number of gray values (typically 4096 gray values for a 12 bit digitizer) by far exceeds the number of gray values a human can detect, which is about 60 [5.425]. Therefore only the brightest particle images are usually observed, whereas the actual number of particle images that contribute to the spatial correlation can be much larger than what would be judged on visual inspection of PIV images. To enhance the visibility of weak particle images a nonlinear relation between intensity and pixel gray value can be applied with the aim to achieve a more-uniform distribution over the gray values. This is referred to as *histogram equalization* [5.425].

Min/Max Filtering. A method to remove a slowly varying background image and to normalize the image contrast is *min/max* filtering [5.396]. The image is filtered in two ways:

1. each pixel is replaced by the *smallest* value in an $M \times N$-pixel neighborhood (i. e., a local minimum filter), and the result is passed through an $M \times N$-pixel moving-average filter;
2. the same operation is carried out but now for the *largest* value in an $M \times N$-pixel neighborhood (this results also passes an $M \times N$-pixel moving-average filter).

The results are the so-called lower and upper *envelopes* of the pixel gray values. The lower envelope is subtracted from the original image, and the result is divided by the (scaled) difference between the upper and lower envelope. The result represents an image with zero background and homogeneous image contrast. The optimal filter size depends on the particle-image diameter and seeding density, and can be found by optimizing the fraction of valid displacement measurements [5.428].

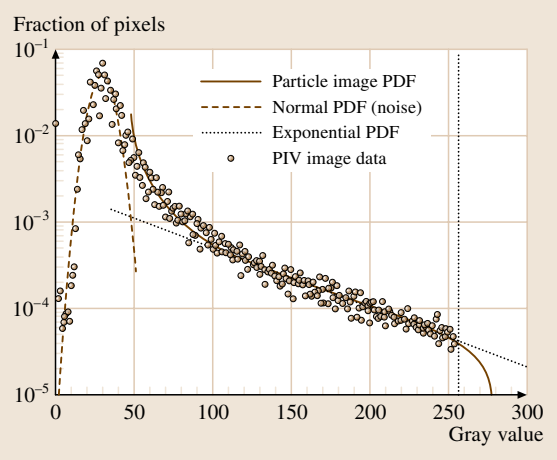

Fig. 5.98 Histogram of pixel gray values for an 8 bit digital PIV image (after *Westerweel* [5.427])

Image Compression. A typical image format in PIV is 1024×1024 px with 12 bit dynamic range (i. e., 4096 gray levels). Hence, a single stereoscopic PIV recording requires about 8 MB of storage. Recording a large time series easily takes up several gigabytes, and a full experiment can consume several hundreds of gigabytes. Standard compression algorithms, such as Joint Photographic Experts Group (JPEG), are *lossy* compression methods, in which fine image details are lost. As PIV images are completely filled with small-scale objects (viz., particle images), the use of lossy compression methods always implies a loss of performance [5.429], i. e., an increase in the number of spurious vectors and an increase of the random noise error (due to an increase of the effective particle-image diameter). Lossless compression methods, such as Lempel–Ziv–Welch (LZW), are better suited for PIV image data, although the compression ratio is modest due to the fact that there is little to no structure in PIV images (which typically appear as *white-noise* images). As a matter of fact, the best compression is PIV interrogation itself, which reduces an 8 MB stereoscopic image set to about 50 kB of displacement data.

Particle-Image Detection. Particle tracking methods and super-resolution PIV (Sect. 5.4) depend on the detection of individual particle images. As particle images generally appear as bright dots on a dark background, a common approach is to use the condition of local maximum above a selected grey value threshold: all pixels above the given threshold represent particle images. The number of detected particle images depends on the threshold value: when this threshold value is too high a significant number of particle images remain undetected, whereas a value that is too low will result in the spurious detection of background noise as particle images. In addition, nonuniform illumination makes it difficult to use a *single* threshold value for the entire image, unless image processing has been used to normalize the image (see before). For uniform illumination and monodisperse tracer particles the grey value histogram would be bimodal, and the optimal threshold value would lie in between the histogram peaks that represent the particle images and image background [5.430].

However, in practice illumination is not uniform (mainly due to the Gaussian profile of the light sheet), and the histogram will *not* be bimodal; instead it has a single background peak and an exponential tail that represents the particle images (Fig. 5.98). Inevitably, this means that the number of detected particle images depends on the threshold and that there will be a bias towards bright particle images, i. e., large tracer particles (that may have a significant slip with respect to the fluid velocity) and tracer particles that occur in the central (i. e., bright) section of the light sheet. The latter implies that a threshold reduces the effective light-sheet thickness.

Image Interrogation: Inside the Computer

Velocity from Tracer Motion. In PIV the motion of a fluid is visualized by the motion of small tracer particles added to the fluid. These tracer particles constitute a *pattern* that can be used to evaluate the fluid motion. If the tracer density is very low (i. e., the distance between distinct particles is much larger than the displacement) then it is very easy to evaluate the displacement from individual tracer particles. This mode of operation is generally referred to as *low-image-density* PIV, or *particle tracking velocimetry* (PTV). However, for most PTV algorithms the amount of information that can be retrieved from an image is very limited. By increasing the concentration of tracer particles, the displacement becomes *larger* than the particle-image spacing, and it is no longer possible to identify matching pairs unambiguously. This mode of operation is generally referred to as *high-image-density* PIV.

Low-Image-Density PIV. An intuitive approach for interrogating PIV images is by matching individual particle-image pairs. Consider the simplest interrogation algorithm, i. e., *nearest-neighbor matching*: for each particle image in frame 1 a matching particle image is searched within an interrogation domain in frame 2 (Fig. 5.99). The probability of identifying the *correct* particle-image pair is given by the probability P_0 that no *other* particle images occur within a circle with an area $A = \pi \Delta X^2$. The number of particle images that appears within a given area is a Poisson process (given that the tracer particles have a homogeneous random distribution over the flow volume), with the mean number of particle image per unit area given by: $C\Delta z_0/M_0^2$, where C is the tracer number density, Δz_0 the light-sheet thickness, and M_0 the image magnification. Then, the probability P_0 is given by

$$P_0 = F_O \, e^{C\Delta z_0/M_0^2 \pi \Delta X^2} \,, \tag{5.249}$$

where F_O is the probability that the tracer particle leaves the light sheet between the two exposures. In order to achieve a success rate P_α for the interrogation of the frames, one can use (5.242) to determine an upper limit for the displacement ΔX (assuming $F_O = 1$):

$$\Delta X < \delta \cdot \sqrt{\frac{4}{\pi} \ln\left(\frac{1}{P_\alpha}\right)} \,,$$
$$\text{with } \delta \cong 0.5 \left(\frac{C\Delta z_0}{M_0^2}\right)^{-1/2} \,, \tag{5.250}$$

where δ is the mean distance between neighboring particle images. It is easily verified that an acceptable interrogation success rate implies that $\Delta X \ll \delta$, e.g., $\Delta X/\delta < 0.26$ for $P_\alpha = 95\%$. This implies that the interrogation algorithm is only successful when the *image density*, defined as

$$N_I = \left(\frac{C\Delta z_0}{M_0^2}\right) A \quad \text{with } A = \pi \Delta X^2 \,, \tag{5.251}$$

is considerably smaller than one; the phrase *low-image-density PIV* has been coined to categorize PTV methods.

The obtained velocity vectors are randomly distributed over the image domain and rather sparse: if one would subdivide an image into interrogation domains with area A, only a fraction $N_I \ll 1$ would actually contain a particle-image pair. For example, for an 8 px displacement range and a 95% interrogation success rate, the number of measured velocity vectors would be about one thousand. More-advanced PTV interrogation algorithms make use of iterative approaches where the particle images are paired based on a velocity estimate obtained by a previous cross-correlation analysis. This approach is known as *super-resolution* analysis in the sense that information is extracted at a resolution higher than that of the interrogation windows [5.431]. In this case a much higher vector density can be achieved.

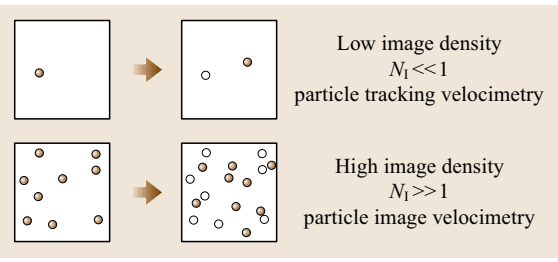

Fig. 5.99 Interrogation strategies for low image density and high image density

The limiting principle in this case is that the displacement differences within the interrogation window must always be smaller than a given parameter related to the particle-image spacing – as explained above for the nearest-neighbor matching algorithm.

High-Image-Density PIV. As explained above, one cannot rely on a simple particle-image matching algorithm to measure displacements that are larger than the mean particle-image spacing. Hence, to increase the number of samples that can be extracted it is necessary to use an approach that is capable of matching particle-image pairs when the displacement ΔX is *larger* than the mean particle-image spacing δ (Fig. 5.99). Instead, it is necessary to use a statistical approach to identify the most probable match of particle images in the two frames.

Spatial Correlation Analysis. Consider an interrogation domain in frames 1 and 2 that contains a substantial number of particle images, as shown in Fig. 5.100a. For a given particle image in the first frame each particle image in the interrogation domain in frame 2 is a possible match candidate and each pair represents a possible displacement with equal likelihood; this is represented in the displacement histogram in Fig. 5.100b where each peak represents a possible displacement and all peaks have equal amplitude to represent that each matched pair has an equal probability. This procedure is then repeated for all particle images in the interrogation domain in frame 1, and the probabilities in the displacement histogram are superimposed. Hence, the displacement peak for each of the matching pairs will soon be dominant over the displacement peaks for unrelated pairs, as shown in Fig. 5.100b.

Already two important requirements for PIV interrogation are evident:

1. the displacement of the particle images within the interrogation domain should be (nearly) uniform;
2. the interrogation domain should contain a considerable number of particle image pairs, i. e., $N_I \gg 1$; this is why this interrogation strategy is also referred to as *high-image-density PIV*.

The important difference with respect to low-image-density PIV is that the interrogation in any location normally contains sufficient particle images to obtain a valid measurement. In general, the number of velocity data extracted from high-image-density PIV is an order of magnitude larger than for low-image-density PIV, i. e., about 10^4 interrogations/image. In addition the velocity data is arranged on a regular grid, as opposed to the random data in low-image-density PIV, which is more convenient in view of post-interrogation processing of the data.

The statistical analysis to identify the most likely particle-image pairing is equivalent to find the particle-image displacement by means of a spatial cross-correlation $R(\boldsymbol{s})$ of the interrogation images $W_1(\boldsymbol{x})I_1(\boldsymbol{x})$ and $W_2(\boldsymbol{x})I_2(\boldsymbol{x})$:

$$R(\boldsymbol{s}) = \int_A W_1(\boldsymbol{x})I_1(\boldsymbol{x})W_2(\boldsymbol{x}+\boldsymbol{s})I_2(\boldsymbol{x}+\boldsymbol{s})\,\mathrm{d}\boldsymbol{x}\,, \tag{5.252}$$

where W_1 and W_2 are windowing functions that define the interrogation domains in the images I_2 and I_2, respectively.

Spatial Correlation Analysis. A theoretical analysis of PIV interrogation using spatial correlation was initially developed by *Adrian* [5.432] for double-exposure continuous images obtained from the photographic recording technique. Later this theory was extended to image pairs with cross-correlation. *Westerweel* [5.396, 414, 433] adapted the theory for analysis of digital images.

To understand the operating principle of the spatial correlation analysis, the images I_1 and I_2 are split into mean and fluctuating parts, i. e., $I_1(\boldsymbol{X}) = \langle I_1\rangle + I_1'(\boldsymbol{X})$ and similarly for I_2, where $\langle\cdots\rangle$ denotes an ensemble average over images under identical circumstances but with different particle-image patterns. Also, it is implicitly assumed that the particle images are distributed homogeneously so that $\langle I_1\rangle$ is a constant. After substitution in (5.244), $R(\boldsymbol{s})$ can be written as

$$R(\boldsymbol{s}) = R_C(\boldsymbol{s}) + R_F(\boldsymbol{s}) + R_D(\boldsymbol{s})\,, \tag{5.253}$$

where R_C is the spatial cross-correlation of the mean image intensities, R_F the cross-correlation of $\langle I_1\rangle$ and $I_2'(\boldsymbol{X})$ and vice versa, and R_D the cross-correlation of the fluctuating images intensities $I_1'(\boldsymbol{X})$ and $I_2'(\boldsymbol{X})$. This is

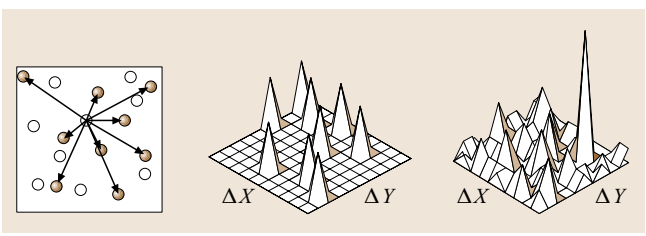

Fig. 5.100 Histogram analysis for finding the most probable displacement

also illustrated in Fig. 5.101. In practice this means that the terms R_C and R_F can be eliminated by subtracting the mean image intensity from the interrogation images. The remaining term R_D can be split into mean and fluctuating parts, where the averaging is taken over an ensemble of tracer patterns for a given (fixed) velocity field $\boldsymbol{u}(\boldsymbol{X}, t)$:

$$R_D(\boldsymbol{s}) = \langle R_D(\boldsymbol{s})|\boldsymbol{u}\rangle + R'_D(\boldsymbol{s}) \,, \tag{5.254}$$

where $\langle R_D(\boldsymbol{s})|\boldsymbol{u}\rangle$ is commonly referred to as the *displacement-correlation peak* and $R'_D(\boldsymbol{s})$ as the *random correlation term*. Figure 5.102 shows typical examples of $\langle R_D(\boldsymbol{s})|\boldsymbol{u}\rangle$ and $R'_D(\boldsymbol{s})$. Evidently $\langle R_D(\boldsymbol{s})|\boldsymbol{u}\rangle$ shows a single peak at a location $\boldsymbol{s} = \boldsymbol{s}_D$, which coincides with the local particle-image displacement within the interrogation domain (provided that the velocity field within the interrogation domain is uniform).

However, it is only possible to identify the correct displacement-correlation peak when its amplitude is larger than the highest random correlation peak in $R'_D(\boldsymbol{s})$. If this is not the case, the interrogation analysis yields a *spurious* value for the particle-image displacement.

The ratio of the highest correlation peak and that of the second highest correlation peak is a measure of the *detectability* of the displacement-correlation peak, indicated by D_0, and can be considered as a lower limit of the signal-to-noise ratio.

Theoretical analysis shows that for a (nearly) uniform velocity field the quantity $\langle R_D(\boldsymbol{s})|\boldsymbol{u}\rangle$ is given by

$$\langle R_D(\boldsymbol{s})|\boldsymbol{u}\rangle \sim N_I F_O(\Delta z) F_I(\boldsymbol{s}) F_\tau(\boldsymbol{s} - \boldsymbol{s}_D) \,, \tag{5.255}$$

where N_I is the *image density*, F_O the *loss of correlation due to out-of-plane motion* of the tracer particle (i. e., tracer particles that enter or leave the light sheet between the two exposures), F_I the *loss of correlation due to in-plane motion* of the tracer particles (i. e., tracer particles that enter or leave the interrogation domain between the two exposures), and F_τ the particle-image self-correlation. Given that the light sheet has a Gaussian intensity profile along the z-coordinate, and that the in-

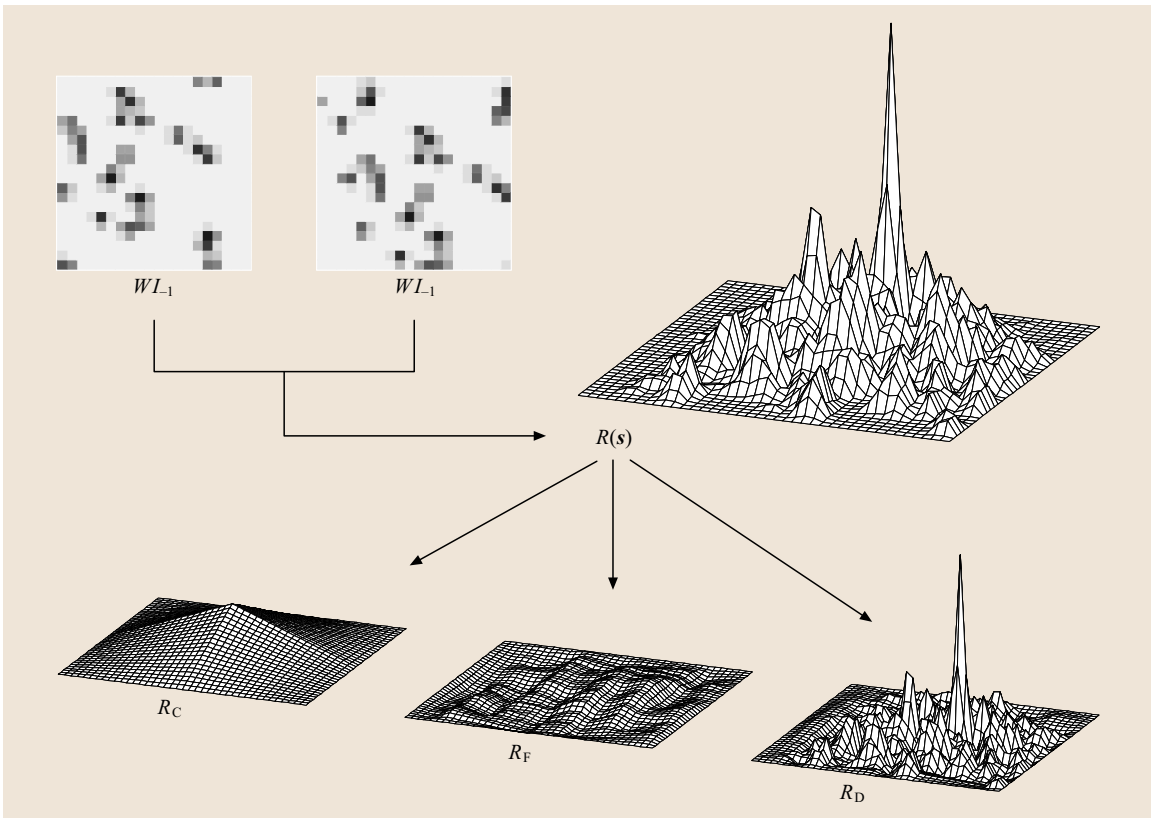

Fig. 5.101 The spatial cross-correlation $R(\boldsymbol{s})$ of interrogation images WI_1 and WI_2, (*top-hat* windowing) when split into mean and fluctuating parts, can be separated into three terms: R_C, R_F, and R_D

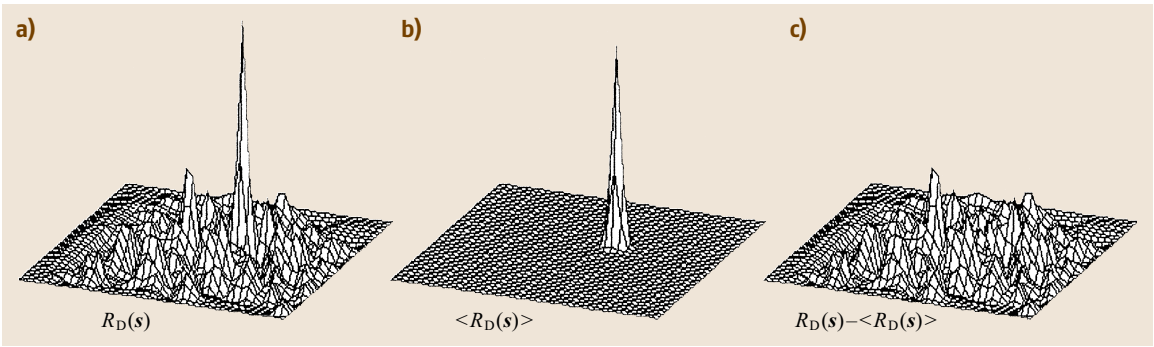

Fig. 5.102a–c Separation of the displacement-correlation term R_D **(a)** into mean **(b)** and fluctuating terms **(c)**

terrogation windows are identical (i. e., $W_1 = W_2 = W$) and uniform with an area $A = D_I \times D_I$, F_O and F_I are given by

$$F_O(\Delta z) = \exp\left(-8\frac{\Delta z}{\Delta z_0}\right), \quad \text{and}$$
$$F_I(s_X, s_Y) = \left(1 - \frac{|s_X|}{D_I}\right)\left(1 - \frac{|s_Y|}{D_I}\right), \qquad (5.256)$$

for $|s_X|, |s_Y| < D_I$. For identical particle images that have an (approximate) Gaussian shape with an e^{-2} width d_τ, the particle-image self-correlation F_τ is given by

$$F_\tau(s) = \exp\left(-4\frac{s^2}{d_\tau^2}\right) \quad \text{with } s^2 = s_X^2 + s_Y^2 . \qquad (5.257)$$

Note that F_τ has a Gaussian shape with an e^{-2} width d_τ. The expressions (5.247) and (5.249) can be used to evaluate the effect of the image density and in-plane and out-of-plane motion on the location and shape of the displacement-correlation peak.

Image Density. Figure 5.103 shows the effect of a variation in the image density N_I on the spatial correla-

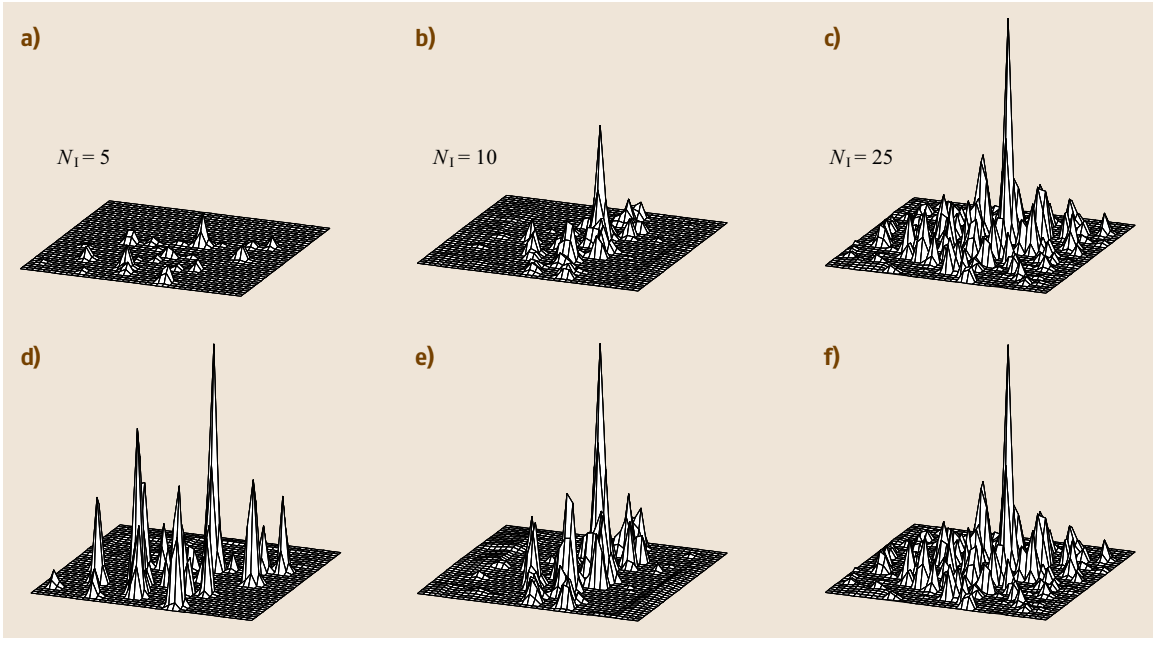

Fig. 5.103a–f The appearance of the spatial correlation as a function of image density, viz. $N_I = 5$, 10, and 25. Graphs **(d–f)** are identical to graphs **(a–c)**, but normalized with respect to the maximum peak height

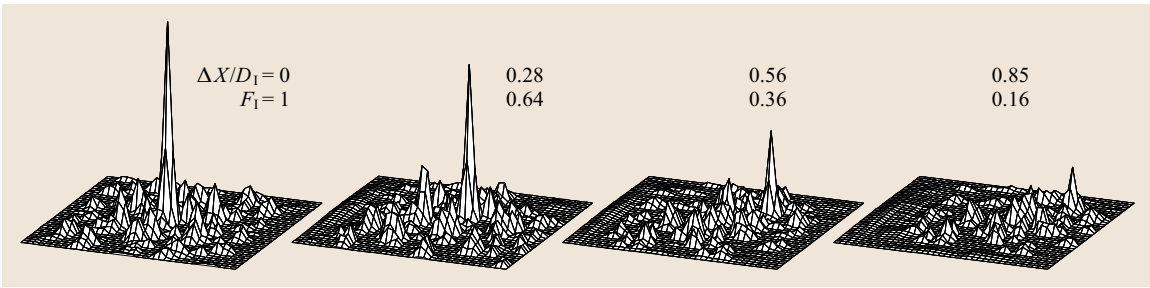

Fig. 5.104 The spatial correlation for increasing in-plane displacement (at constant image density)

tion, while the in-plane and out-of-plane displacements remain constant. As predicted by (5.247) the peak amplitude is directly proportional to N_I, i. e., the signal strength increases when the number of particle images in the interrogation domain increases. It is also clear that the *noise* (i. e., the random correlations) increases in proportion to N_I. However, when the correlation is normalized with respect to the highest peak (Fig. 5.103d–f), it is clear that the *relative* noise level (defined as the highest random correlation peak) *decreases* with increasing N_I.

In-Plane and Out-of-Plane Motion. The amplitude of the displacement-correlation peak decreases for increasing in-plane displacement. Examples of the spatial correlation for increasing in-plane displacements are shown in Fig. 5.104. The peak amplitude is proportional to the fraction of the particle images that remains within the interrogation domain; this fraction is equal to the value of $F_I(\boldsymbol{s})$ (5.249). Note that the amplitude of the displacement-correlation peak decreases for increasing displacement, while the amplitude of the noise peaks remains at the same level. Hence, for increasing in-plane displacement, the probability that the displacement peak is correctly identified reduces. Later it is shown that the location of W_2 can be shifted over (s_X, s_Y), so that the number of particle images within the interrogation domain is maximized and $F_I \approx 1$ (Sect. 5.4.2). An alternative way to achieve $F_I = 1$ is to use a larger window W_2 such that all particle image present in W_1 are also included in W_2.

Out-of-Plane Motion. Figure 5.105 shows the spatial correlation for a fixed image density and in-plane displacement, but for increasing out-of-plane displacement. The peak amplitude decreases for increasing $|\Delta z|$ and is proportional to $F_O(\Delta z)$ as defined in (5.248) (for a light sheet with a Gaussian intensity profile). Unlike the effect of in-plane motion, it is not possible to reinterrogate the image pairs and compensate for the out-of-plane motion; in practice this means that loss of correlation due to out-of-plane motion is a major limiting aspect of a planar PIV measurement.

It should also be noted that in Fig. 5.105 it was assumed that the light sheet is *identical* (perfectly overlapped) for both exposures. In practice this may not always be the case when a double-cavity laser is used; when the two laser beams do not perfectly overlap, the value of Δz in Fig. 5.105 should be replaced by $\Delta z + z^*$, where z^* is the light-sheet misalignment. In PIV measurements where the principal flow direction is perpendicular to the light-sheet plane a deliberate offset can be used to maximize F_O (this is very similar to the window offset method, although it cannot be executed in

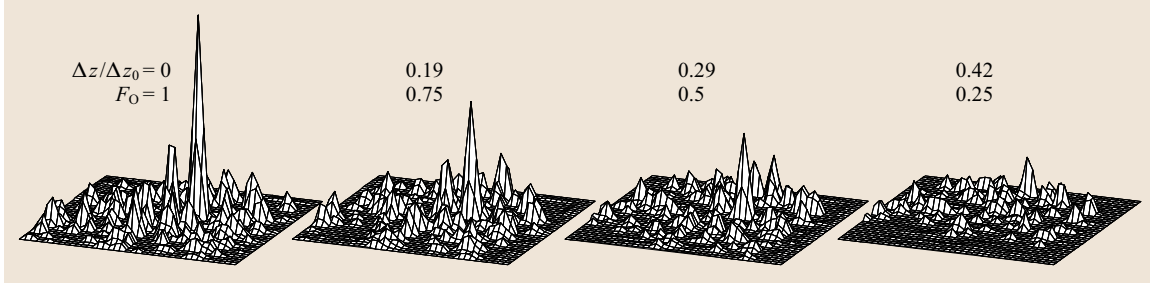

Fig. 5.105 The spatial correlation for increasing out-of-plane motion

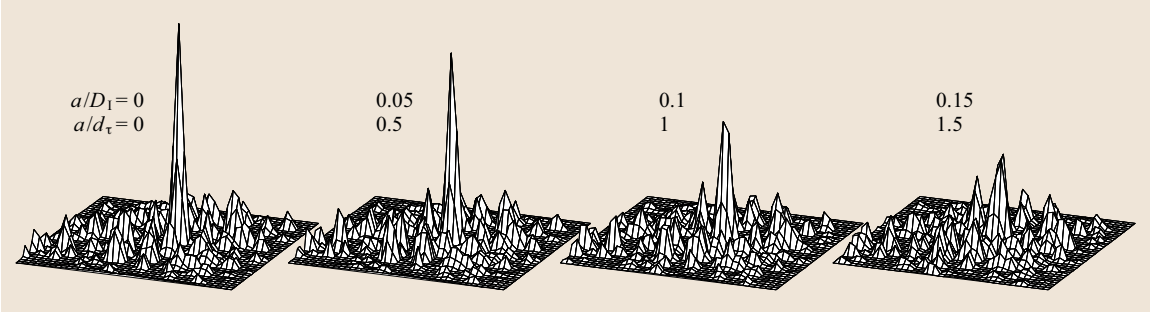

Fig. 5.106 The spatial correlation for an increasing velocity difference within the interrogation window

a postrecording phase). A practical procedure to achieve the highest correlation in relation to the light sheets overlap is to perform online cross-correlation while displacing one light sheet and monitor the height of the correlation peak.

Velocity Gradient. The effect of a local velocity gradient in the measurement field was ignored in the present theory. An extension to arbitrary flow fields is not trivial. Instead it can be assumed that there is a *small* local variation of the velocity field within the interrogation domain; this variation can be due to a large-scale gradient in the in-plane or out-of-plane fluid motion, or a local variation at a scale below the dimensions of the interrogation domain. It is then investigated to what extent such variations do not significantly affect the theory developed for purely uniform fluid motion.

Figure 5.106 shows the spatial correlation for increasing local variation $a = M_0|\Delta u|\Delta t$ within the interrogation domain of the displacement field. For increasing a the peak amplitude *decreases* while the *width* of the peak *increases*, and the total volume under the correlation peak remains (approximately) constant. The loss of correlation F_Δ due to a (small) variation of the displacement field is given by

$$F_\Delta(a) = \exp\left(-\frac{a^2}{d_\tau^2}\right) . \qquad (5.258)$$

The effects of a local variation of the displacement field are negligible when a is smaller than d_τ. For larger values of a it can happen that the displacement-correlation peak excessively broadens and splits up into several correlation peaks, and an unambiguous estimation of the displacement is no longer possible. Hence, $a/d_\tau \approx 1$ is an upper limit for which the assumption of local uniform flow holds. In the special case that the local variation of the displacement field is only due to large-scale in-plane gradients, it is possible to use window deformation methods [5.435] to recover the displacement-correlation peak for $a > d_\tau$.

PIV Design Rules. In summary, the amplitude of the displacement-correlation peak is given by

$$R(\boldsymbol{s}_D) \sim N_P N_I F_I F_O F_\Delta . \qquad (5.259)$$

For cross-correlation analysis of two image frames $N_P = 1$, but in the case of *ensemble correlation*, which can be used for steady flows (primarily in μPIV), N_P is the number of superimposed correlations. The peak amplitude in relation to the highest noise peak (or signal-to-noise ratio) can be *enhanced* by increasing N_I (and N_P), but is *impeded* by in-plane and out-of-plane loss of

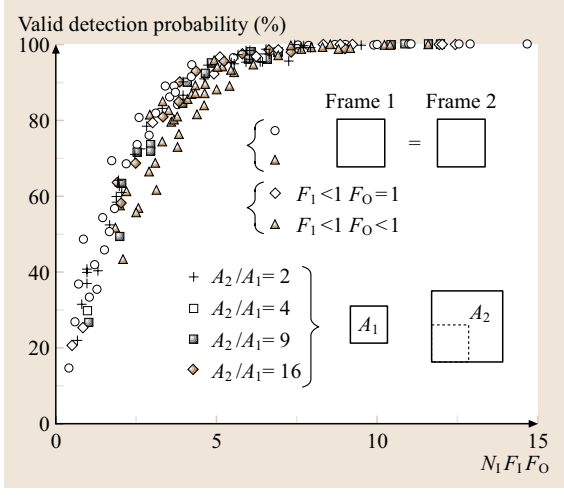

Fig. 5.107 The valid detection probability for the displacement-correlation peak as a function of the image density N_I and the in-plane and out-of-plane loss of correlation, F_O and F_I, respectively (after *Keane* and *Adrian* [5.434])

correlation and loss of correlation due to local variation of the displacement field.

The probability of obtaining a detectability D_0 defined as the signal-to-noise ratio that is larger than 1.1 as a function of the parameters N_I, F_I and F_O more or less collapses onto a single curve, as shown in Fig. 5.107. The data are based on extensive Monte Carlo simulations, and show that the detection probability for cross-correlation analysis and uniform displacements (i. e., $N_P = 1$ and $F_\Delta = 1$) reaches close to 100% when $N_I F_I F_O$ is larger than about 7.5. This result has led to the following general *design rules* for PIV measurements [5.434, 436, 437]

$$N_I > 10 \quad |\Delta X| < \frac{1}{4} D_I \,,$$
$$|\Delta z| < \frac{1}{4} \Delta z_0 \,, \quad M_0 |\Delta u| \Delta d_\tau \,, \tag{5.260}$$

i. e., when the interrogation domain contains at least 10 particle-image pairs, the in-plane and out-of-plane motion should be less than about one-quarter of the interrogation window size and light-sheet thickness, respectively, and local variations of the displacement within the interrogation domain should be less than the particle-image diameter. When these criteria are met at least 95% of the interrogations should return the correct particle-image displacement.

As mentioned before, some of the criteria in (5.252) can be relaxed, e.g., the use of a *window offset* eliminates the second rule and the use of *window deformation* relaxes the fourth rule (but only when in-plane gradients are dominant). Nonetheless, any advanced methods will rely on an initial interrogation result that should comply with these design rules.

Digital Correlation. The spatial correlation analysis described previously deals with *continuous* images. In practice one is dealing with *digital images*, i. e., the continuous image field is sampled at discrete locations and the image intensity is quantified to discrete levels. The effects of spatial discretization are not important according to the Nyquist theorem [5.426] when the image sampling rate is at least twice the bandwidth of the optical system [5.415], and the intensity quantization can be ignored when the difference between the discrete levels is small compared to the intensity variations [5.425]. *Westerweel* [5.438, 439] demonstrated that for digital PIV analysis it is not necessary to sample the images at the Nyquist rate, since the information on the particle-image displacement is represented at much smaller spatial frequencies than the detailed information of the individual particle-image locations. In practice a 32×32 px interrogation domain is typically used; when the design rule in (5.252) for in-plane motion is used, this would imply an 8 px maximum displacement. If the displacement uncertainly would be determined by the pixel dimension (i. e., a ±0.5 px error), then the relative error for digital PIV measurements would not be better than 1/8(≈ 13%). Fortunately, it is possible to obtain accurate measurements of the displacement by means of interpolating the discrete displacement-correlation peak, or so-called *subpixel interpolation* (Fig. 5.108); the typical uncertainty is 0.05–0.10 px, which implies relative errors around 1% or better. This is sufficient for application of PIV to the investigation of a wide range of unsteady and turbulent flows, and is key to the success of *digital* PIV. However, as one is operating below the Nyquist sampling rate, a number of effects emerge that are typical for digital PIV analysis that will be discussed below.

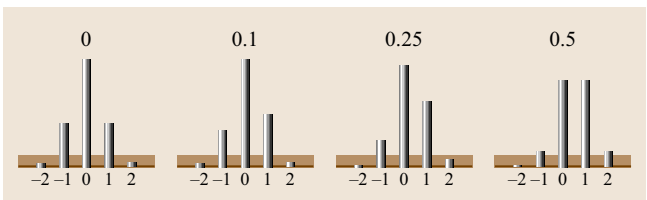

Fig. 5.108 Detailed shape of the correlation peak (in one dimension) as a function of the subpixel part of the displacement (here shown for a 1.6 pixel particle-image diameter). The *horizontal shaded region* represents the background noise level in the correlation

Pixelization. The image $I(x, y)$ is discretized by the image sensor (i. e., CCD or CMOS device) that integrates the light intensity over a small area, or *pixel*:

$$I[i, j] = \iint p(x - i \cdot d_\tau, y - j \cdot d_\tau) I(x, y) \, \mathrm{d}x \, \mathrm{d}y \,, \tag{5.261}$$

where $p(x, y)$ is the pixel spatial sensitivity. This is usually a uniform rectangular area, but more-complex forms should be used to represent the effect of *microlenses* (where the sensitivity may be nonuniform and leakage from adjacent pixels can be incorporated). The total area of $p(x, y)$ divided by d_τ^2 (for a square pixel layout) is the *pixel fill factor* β. When β is significantly smaller than one, the light sensitivity of the sensor decreases proportionally. At the same time the fill factor affects the efficiency of subpixel interpolation [5.427].

The image intensity is represented in a finite number of discrete levels. Common quantization level ranges are

256 or 4096 gray levels, i. e., 8 bit and 12 bit quantization, respectively. The quantization can be represented as additive white noise [5.425]:

$$I[i,\,j] = I^{\bullet}[i,\,j] + \varsigma[i,\,j]\,. \tag{5.262}$$

When the variance of ζ is small with respect to the variance of I, the effect of quantization can be ignored, and usually the sensor noise level is larger than the quantization noise level. Therefore $I^{\bullet}$ will simply be written as I. However, an extreme situation is a *binary* image (which contains only gray levels 0 and 1), which is sometimes used to implement a special form of spatial correlation; in that case the increased noise contribution of ζ needs to be compensated by a higher image density.

Discrete Correlation. For digital images $I_1[i,\,j]$ and $I_2[i,\,j]$ the discrete spatial correlation is given by

$$\phi[p,\,q] = \sum_i \sum_j W_1[i,\,j]\big(I_1[i,\,j] - \overline{I}_1\big) \times W_2[i+p,\,j+q]\big(I_2[i+p,\,j+q] - \overline{I}_2\big)\,, \tag{5.263}$$

where $\overline{I}_1$ and $\overline{I}_2$ are the averaged image values over the windows W_1 and W_2, respectively. Commonly, W_1 and W_2 are identical and uniform $N\times N$-px domains that are equal to 1 inside the domain and zero outside the domain. A generalized form of the discrete correlation when W_1 and W_2 are not identical is given by *Ronneberger* [5.440]; if W_2 is larger than W_1 then is no longer a constant, i. e., and vice versa.

The discrete spatial correlation $\phi[p,\,q]$ is related to the continuous spatial correlation $R_{\mathrm{D}}(\boldsymbol{s})$ by convoluting R_{D} with the self-correlation Φ_{pp} of $p(x,y)$ and then sampling the result at integer multiples of d_{r}:

$$\phi[p,\,q] \doteq \{\Phi_{\mathrm{pp}} * R_{\mathrm{D}}\}(p\cdot d_{\tau},\, q\cdot d_{\mathrm{r}})\,, \tag{5.264}$$

(ignoring trivial normalization and/or conversion factors, e.g., conversion from light intensity to gray value).

Computation of the Spatial Correlation. The spatial correlation involves a summation over $M\times N$ multiplications for each *pixel* in the correlation domain, which has to be evaluated for a total of $2M\times 2N$ px in the correlation domain; hence, the *direct* evaluation of requires a total of $(2M\times 2N)^2$ multiplications, which implies a considerable computational effort. Fortunately, there exists a very efficient algorithm to improve the processing speed for the evaluation of the spatial correlation, i. e., the *fast Fourier transform* (FFT).

The spatial correlation in (5.255) can be computed by means of a *discrete Fourier transform* (DFT) and is *identical* to the correlation provided that the domain is at least $2M\times 2N$ to contain $\phi[p,\,q]$; the proof is given in Appendix. The DFT can be computed by means of the fast and efficient FFT algorithm [5.441]. For a $U\times V$ domain the FFT algorithm requires only $4UV\log_2 UV$ multiplications (when U and V are both powers of 2), which implies an enormous reduction in the computational effort. In its most common form the domain size has to be a power of 2, but generalized algorithms exist in which the domain size can be any combination of a power of prime numbers (e.g. 2, 3, 5, which captures almost any domain size). It is however not necessary to restrict the application of FFT to interrogation domains that are only a power of 2, or prime numbers; with proper *zero padding* (Appendix A) any domain size can be selected, as long as the padded domain matches the requirements for the FFT algorithm that is being used.

It is common to use an $M\times N$ correlation domain, which implies that part of the correlation that falls outside the domain is folded back into the (periodic) domain. This only causes significant errors when the correlation attains significant nonzero values outside the central $M\times N$ domain. This only occurs when the particle-image displacement $[p,\,q]$ is *outside* the domain: $-M/2 < p < +M/2,\ N/2 < q < +N/2$. When the experimental conditions comply with the design rules in (5.252) this does not occur, and the use of an $M\times N$ correlation domain generally implies a substantial reduction of the computational effort (of roughly a factor four), compared to a $2M\times 2N$ domain, at the cost of a small but acceptable increase of the noise level.

Subpixel Interpolation. One of the most powerful aspects of digital PIV is the ability to determine the particle-image displacement at subpixel level: under optimal conditions the particle-image displacement can be estimated with a precision better than 0.1 px. This means that the measurement error can be as low as 1% (or less) for a 32×32 px interrogation domain with an 8 px particle-image displacement (in accordance to the 1/4-rule).

The peak location at subpixel level is obtained by *interpolation* of the correlation values around the correlation maximum. Figure 5.108 shows the correlation values in a narrow peak as a function of the subpixel position of the displacement-correlation peak. Note that the value $\phi_0 \equiv \phi[m_0,\,n_0]$ of the correlation maximum remains practically unchanged, while the

two adjacent correlation values $\phi_{-1} \equiv \phi[m_0 - 1, n_0]$ and $\phi_{+1} \equiv \phi[m_0 + 1, n_0]$ change considerably in amplitude. This means that the subpixel location of the maximum (i. e., the particle-image displacement) can be estimated from the correlation values $\{\phi_{-1}, \phi_0, \phi_{+1}\}$ for each coordinate.

The most commonly used method for the sub-pixel estimation of the displacement is the *three-point Gaussian peak fit*, where the subpixel part for each component of the displacement is given by [5.442]:

$$\varepsilon_X = \frac{1}{2} \frac{(\ln \phi_{-1} - \ln \phi_{+1})}{(\ln \phi_{-1} - \ln \phi_{+1} - 2 \ln \phi_0)} , \qquad (5.265)$$

The numerator in (5.257) represents the skew of the correlation peak as also shown in Fig. 5.108. Evidently, this estimator fails when:

1. any of the considered correlation values is zero or negative, or
2. when the denominator is close to zero.

The former can occur for very narrow correlation peaks, i. e., $d_\tau / d_r \ll 1$, or when then the image background is nonuniform (e.g., in the case of reflections), whereas the latter can occur for very wide correlation peaks when: $\phi_0 \approx \phi_{-1} \approx \phi_{+1}$, i. e., $d_\tau / d_r \gg 1$.

In principle the correlation values ϕ_{-2} and ϕ_{+2} would also carry information with regard to the subpixel peak position, but for very narrow peaks ($d_\tau / d_r \approx 2$) and finite image density ($N_I \approx 10$) the correlation noise level is of the order of the correlation values ϕ_{-2} and ϕ_{+2}, so that their contribution to the estimated displacement value is practically insignificant. For larger particle images ($d_\tau / d_r \gg 2$) or higher image densities ($N_I \gg 10$) it would make sense to use a larger domain for the subpixel estimation. In that case the displacement is estimated by means of two-dimensional least-squares fit of a Gaussian curve over a 5×5 kernel (or larger) domain. This has the additional advantage that the fit can be generalized to accommodate elliptical peaks with arbitrary orientation (which can occur in the case of strong local velocity gradients). However, for narrow peaks that effectively cover a 3×3 px domain, there is no significant difference between the one-dimensional (1-D) fit (5.257) applied for each component and a least-squares 2-D fit.

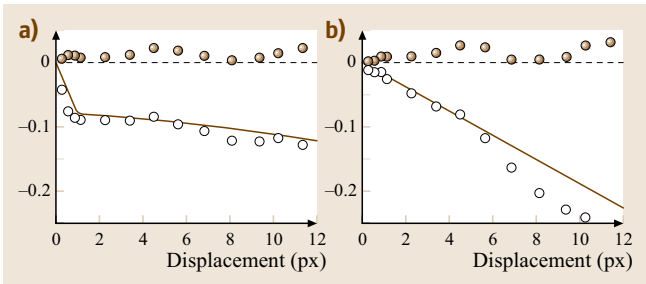

Fig. 5.109a,b The difference between the measured and actual displacement as a function of the actual displacement for uniform **(a)** and Gaussian **(b)** interrogation windows. The *open symbols* and *line* indicate the estimate using the biased correlation ϕ, while the *filled symbols* indicate the result using the unbiased estimate ϕ^* (5.259)

Bias Correction. The spatial correlation $R(\boldsymbol{s})$ defined in (5.244) is a biased estimate of the true two-point ensemble correlation for a *finite* interrogation domain; this bias is proportional to the in-plane loss of correlation $F_I(\boldsymbol{s})$, which skews the displacement-correlation peak and causes a bias in the estimated displacement towards the origin of the correlation domain (even when the displacement is uniform). This bias is proportional to the size of the interrogation domain and the width of the displacement-correlation peak [5.414, 434]. This bias can be corrected by using

$$\phi^*[m, n] = \frac{\phi[m, n]}{F_I[m, n]} , \qquad (5.266)$$

where $F_I[m, n]$ is given by (5.249) for uniform and identical interrogation windows W_1 and W_2. The difference between the measured and actual image displacement using $\phi[m, n]$ and $\phi^*[m, n]$, respectively, is shown in Fig. 5.109. It is important that the peak identification is done in $\phi[m, n]$, as the unbiased correlation $\phi^*[m, n]$ has a diverging variance for large $[m, n]$ [5.443], which can cause the appearance of dominant spurious correlation peaks near the edges of the correlation domain.

Peak Locking. Reduction of the particle-image diameter relative to the pixel size can lead to an effect commonly referred to as *peak locking*. This effect becomes apparent in the displacement histogram of PIV data, as illustrated in Fig. 5.110. Evidently, peak locking significantly reduces the accuracy of PIV measurements [5.444]; although the effect on velocity flow statistics may be within acceptable limits, this effect can lead to awkward results for instantaneous spatial derivative data such as vorticity [5.445].

The effect originates from the fact that the displacement-correlation peak increasingly deviates from its assumed Gaussian shape for decreasing d_τ / d_r, i. e., the term Φ_{pp} in (5.256) deforms the correlation

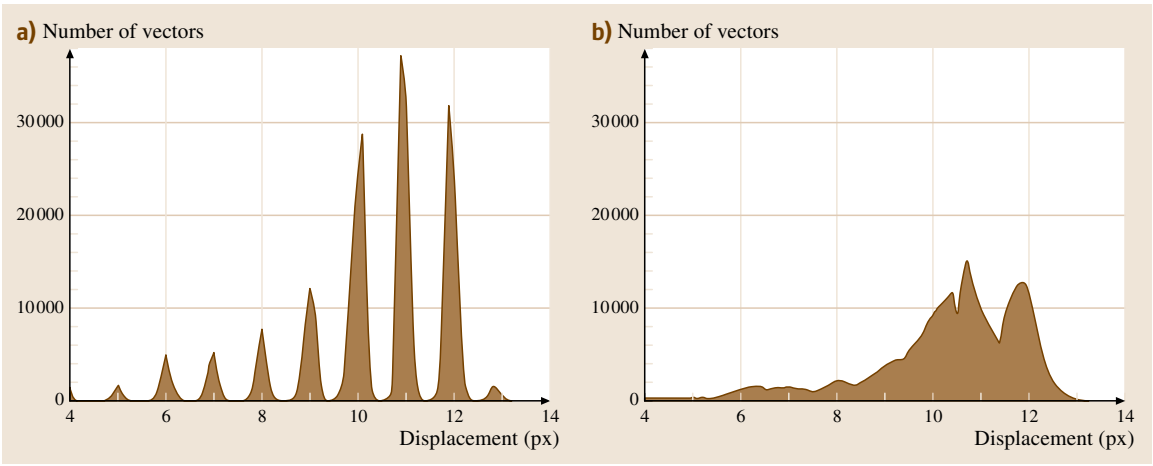

Fig. 5.110a,b PIV data from a turbulent pipe flow obtained with two different subpixel interpolation methods: **(a)** peak centroid, and **(b)** Gaussian peak fit

peak. This is illustrated in Fig. 5.111, which shows the difference between the measured and true subpixel displacements for different values of d_τ/d_r. Note that the slope of the curves near the origin in Fig. 5.111 is always negative, which implies that the measured displacement is biased towards integer pixel values.

Further analysis shows that diffraction-limited particle images are fully resolved when the particle-image diameter is at least four pixels [5.427]. This means that the continuous particle images can be fully reconstructed from the discrete samples according to the Shannon–Whittaker sampling theorem [5.426], and that peak-locking effects do not occur. Between 2 and 4 px

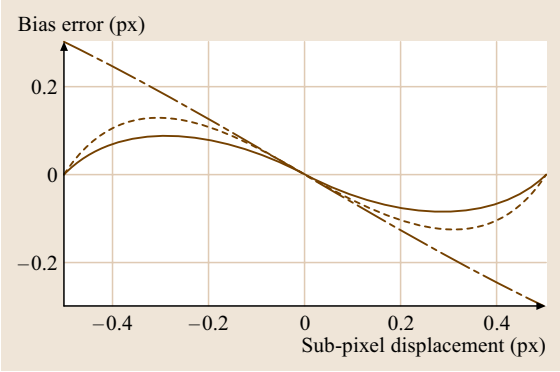

Fig. 5.111 The *bias error*, or mean difference between the measured displacement and true displacement, as a function of the subpixel fraction of the displacement for the peak centroid (*dash-dotted*), parabolic peak fit (*dashed*) and Gaussian peak fit (*solid*) (after *Westerweel* [5.396])

in diameter, the bias error is small and its magnitude depends on the pixel fill ratio [5.427]. For very small particle images, i. e., 1–2 px in diameter, the effect of peak locking becomes very strong, although the correlation peak may still contain sufficient information to recover the displacement data, i. e., ϕ_{-1} and ϕ_{+1} are sufficiently above the background noise level. It should be noted that the peak height is a function of the subpixel displacement, which enhances biasing towards integer pixel displacements. For $d_\tau/d_r < 1$ all information is retained in ϕ_0, and ϕ_{-1} and ϕ_{+1} are no longer above the background noise level, i. e., signal recovery is no longer feasible.

Numerous approaches have been suggested to eliminate the peak-locking effect, including image defocusing, (*anti-aliasing*) image filtering, alternate subpixel interpolation methods, and window subpixel reinterpolation [5.446]. Most of these methods have in common that they redistribute the image information and thus artificially increase the effective particle-image diameter. The best practice seems to be a proper choice of light source energy and optical configuration (viz., image magnification and lens aperture) to match the diffraction limit to the available image pixel resolution.

Optimization. From the preceding paragraphs it already becomes clear that the optimal particle-image diameter is somewhere between one and four pixels. Analysis shows that this is primarily determined by the information content of the estimated spatial correlation $\phi[m, n]$ and that the random error for the three-point Gaussian peak fit in (5.257) has a minimum value of about

0.05–0.10 px at $d_\tau/d_r \approx 2$ under idealized conditions. This has been confirmed by means of simulation results and controlled experiments [5.438,439,447].

The estimated correlation values $\phi[m,n]$ are not independent *samples* of $R_D(s)$, but are correlated over a finite domain with an area L^2 that is given by [5.414]

$$L^2 = \sum_m \sum_n \frac{\mathrm{cov}\{\phi[m_0,n_0],\phi[m_0+m,n_0+n]\}}{\mathrm{var}\{\phi[m_0,n_0]\}} , \tag{5.267}$$

where $[m_0,n_0]$ is the location of the displacement-correlation peak. The value of L^2 can be interpreted as the number of correlated samples in the interrogation domain, so that $(L/M)^2$ represents the relative uncertainty level for an $M\times M$ domain [5.443]. The typical behavior of L/M as a function of d_τ/d_r is shown in Fig. 5.114, which indicates two scaling regimes:

1. for small particle images ($d_\tau/d_r < 1$) the increase in pixels decreases the uncertainty, i. e., the amount of available information in the correlation peak location increases with increasing number of pixels (or decreasing d_r);
2. for large particle images ($d_\tau/d_r > 1$) the correlation peak spreads over a larger number of pixels with decreasing d_r, but this does not increase the information content of the correlation peak and therefore does not reduce L/M.

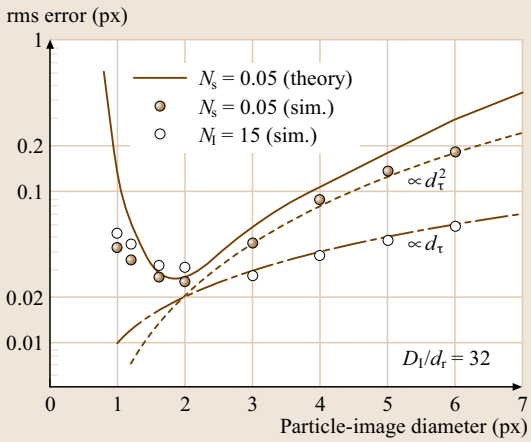

Fig. 5.112 The rms displacement error as a function of the particle image diameter (in pixel units) for 32×32 px interrogation windows and constant image density $N_I = 15$ (*open symbols*) and constant source density $N_s = 0.05$. The *solid line* represents a theoretical result, while the *dotted* and *dashed lines* represent scaling relations. (After *Westerweel* [5.433])

This special property is related to the fact that the *width* of the correlation peak is directly related to the *maximum slope* of the correlation peak (which determines the estimation uncertainty), as is the case for a Gaussian-like shape [5.448, 449]. As a result the root-mean-square (rms) error is proportional to the particle-image diameter (for resolved particle images), i. e.,

$$\sigma_{\Delta X} \cong c d_\tau , \tag{5.268}$$

with $c \approx 0.05$–7 [5.393,433,444] This relation holds for large (Gaussian-like) particle images (i. e., $d_\tau/d_r \gg 1$) and indicates that the performance improves for decreasing particle-image diameter. However, improvement breaks down when the effect of finite pixel size becomes apparent. Figure 5.112 shows the simulation results and a theoretical prediction for the rms error as a function of the particle-image diameter relative to the pixel dimension. The theoretical result is based on the image statistical properties as the only input parameters. Also, two scaling regimes for the rms error as a function of d_τ/d_r are identified: $\sigma_{\Delta X} \sim d_\tau$ for constant *image density*, and $\sigma_{\Delta X} \sim d_\tau^2$ for constant *source density*.

Hence, the optimal particle-image diameter is determined by two opposing trends, i. e., the reduction of the random error for decreasing particle image diameter and an increase for the bias and random error for decreasing particle image diameter as a result of the finite pixel dimensions; the optimal value for d_τ/d_r is about 2 (or slightly larger) based on theoretical and simulation results, but in the literature values between 2 and 4 are reported based on practical considerations.

The rms estimation error is approximately constant as a function of the displacement, but is proportional to the displacement for $|\Delta X|/d_r < 0.5$, as shown in Fig. 5.113.

The error vanishes for zero displacement as the interrogation images WI_1 and WI_2 are identical (for zero out-of-plane motion). This property can be utilized to improve the performance of subpixel interpolation by means of window matching.

The fact that the rms error is proportional to the subpixel displacement (rather than constant) implies also a bias towards integer pixel displacement values; the error fluctuations are much smaller for near-integer pixel values, but increase for increasing subpixel displacement, causing a typical variation in the histogram

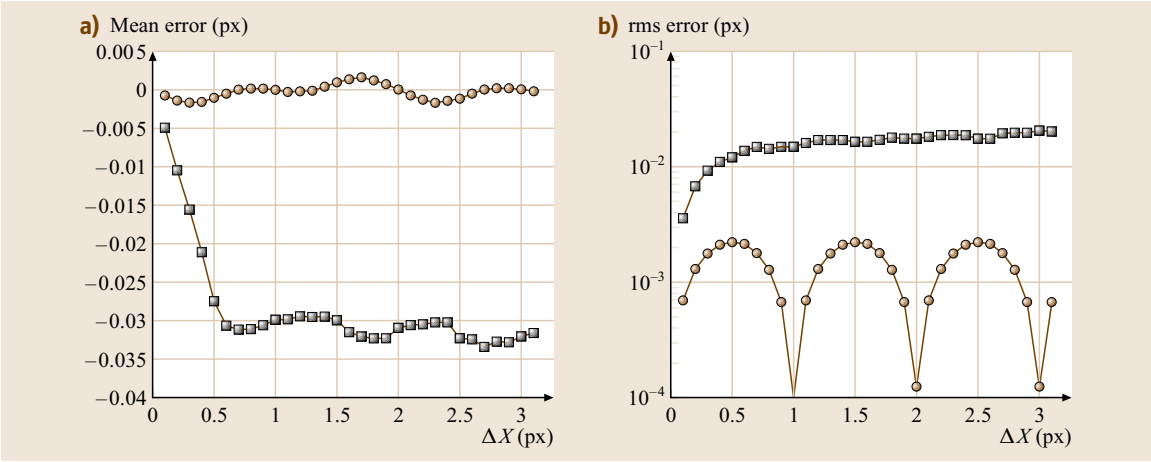

Fig. 5.113a,b Measurement error due to discretization as a function of the displacement. **(a)** Bias error; **(b)** rms error. *Squares* are relative to single-step correlation. *Circles* are relative to multistep correlation and subpixel window shift

for subpixel displacements as shown in Fig. 5.113. The vanishing of the rms error towards zero in-plane displacement (i. e., when the two interrogation images become identical) only occurs when the out-of-plane displacement is negligible. Therefore one can expect that this contribution towards peak locking will disappear for increasing out-of-plane motion, as shown by the simulation results of *Foucaut* et al. [5.450]. Hence, for flows with appreciable turbulence levels, this contribution to peak locking is usually not significant.

Dynamic Range. The lower end of the dynamic range is determined by the requirement that the corresponding displacement can be distinguished from the noise level.

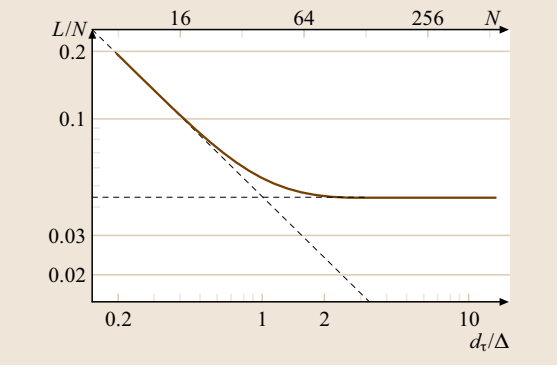

Fig. 5.114 The level of uncertainty in the estimation of the displacement from the spatial correlation as a function of the particle-image diameter (in pixels)

The minimum detectable displacement shall be denoted with $\Delta \boldsymbol{X}_{\min}$. The maximum measurable displacement $\Delta \boldsymbol{X}_{\max}$ can be directly related to the minimum F_{I} criterion stating that the in-plane displacement should not exceed one-quarter of the interrogation window size D_{I}, i. e., $\Delta X_{\max} \leq 1/4 D_{\mathrm{I}}$ (5.253). The velocity dynamic range therefore reads:

$$\frac{\Delta \boldsymbol{X}_{\max} - \Delta \boldsymbol{X}_{\min}}{\Delta \boldsymbol{X}_{\min}} = \frac{D_{\mathrm{I}}}{4 \Delta \boldsymbol{X}_{\min}} - 1 \,. \tag{5.269}$$

This expression reads as a accuracy–resolution trade off. The dynamic range can be increased with a larger window size, at the expense of the spatial resolution. The dependence of $\Delta \boldsymbol{X}_{\min}$ on other experimental parameters has been one of the most investigated topics in PIV [5.393, 396, 442]. It is strongly dependent upon the particle image diameter (see previous section) and the type of subpixel interpolation used to determine the location of the correlation peak.

A typical value of $\Delta \boldsymbol{X}_{\min} = 0.1$ px can be assumed under generic measurement conditions. Following *Willert* and *Gharib* [5.442] this can be achieved using a three-point Gaussian peak-fit model, particle images of two to three pixel diameter, displacements not exceeding 10 px, and a window size of 32 × 32 px. With the previous considerations (5.262) yields a dynamic range in the order of 10^2 for a window size of 32 × 32 px.

Detectability Enhancement. The detectability defined above is directly dependent upon the number of paired

particle images within the correlation windows and in general increases with the interrogation window size at the expense of the spatial resolution. In the following paragraphs a few methods are presented to enhance the detectability without the direct need to increase the size of the interrogation window. However it should be said that each of the proposed methods relies upon assumptions and is strictly valid only within specific hypotheses.

Local Correlation Averaging. Under several experimental conditions a high source density cannot be achieved for technical reasons. As a consequence analysis performed at low image number becomes critical, with the appearance of a large number of spurious correlation vectors. A first approach to increasing the number of particle pairs without increasing the window size consists of accumulating the effect of several instantaneous particle image recordings (basically summing up the images, i. e., taking $N_P > 1$). This approach is only valid when the flow is strictly steady. However the method has the limit that beyond a given point, individual particle images cannot be distinguished anymore. A better solution is therefore to average the correlation maps from the analysis of the single recordings [5.409,451]. In this case no upper limit is found on the number of recordings that can contribute to build the correlation signal. In μPIV this procedure is very frequently adopted to average out of the particle velocity spatiotemporal fluctuations solely due to the Brownian motion of the molecules in the fluid.

Correlation Multiplication. The correlation map produced at a given location is the result of the correlation signal from each single pixel. A possible way to enhance the correlation peak height and reduce the noisy peaks is to multiply several correlation maps for a correlated value of the velocity but uncorrelated particle image pattern [5.452]. The most common approach is to multiply each correlation map by those obtained at the neighboring locations. The method can also be applied for unsteady flows, however it has not yet been ascertained whether this approach yields a net benefit in flows with a significant velocity gradient.

Phase-Only Correlation. A recent approach specific to the drop in S/N close to optical interfaces (e.g., bright walls) is to eliminate the amplitude information during the FFT-based evaluation of the cross-correlation map. The so-called DC pedestal in the correlation map can be significantly suppressed and reliable particle correlation information could be retrieved in conditions where bright objects other than particles where included in the correlation window [5.453].

Advanced Interrogation Techniques. This discussion places severe limitations on the measurement performance of PIV when solely associated to the spatial correlation operator. Advanced techniques have been introduced that allow one to overcome the limitations posed by the application of the cross-correlation operator to interrogate the images [5.454]. The first group of techniques allows the measurement dynamic range to be increased in relation to the in-plane particle motion. The second group shows the possibility of enhancing the correlation peak. Finally the discussion touches upon possible improvements to the spatial resolution.

Window Shift Method. When the in-plane particle image displacement is estimated by means of a first

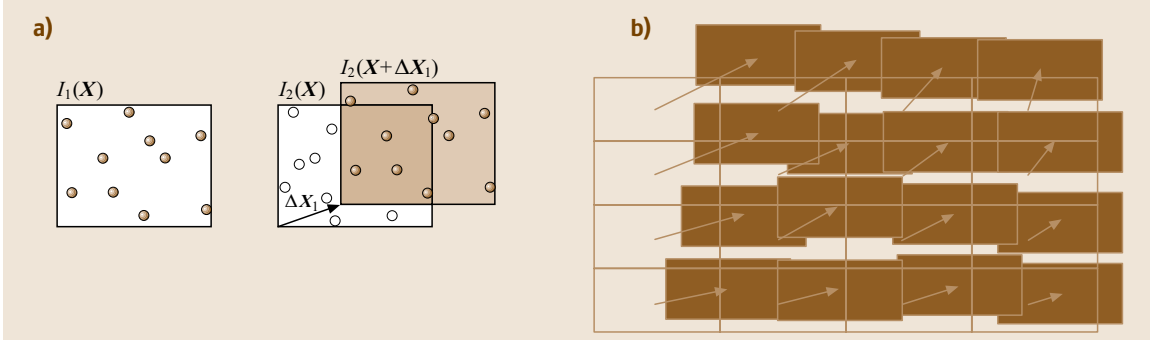

Fig. 5.115a,b Window shift technique. **(a)** The correlation is evaluated between two particles patterns shifted, accounting for the translation due to the flow motion. Shaded shifted window with the estimated displacement. **(b)** Window shift for a group of windows

correlation analysis, a relative shift between the correlation windows can be applied in order to compensate for the loss of pairs due to the average particle motion. As a result the number of particle image pairs F_I is increased. The technique can be implemented as a two-step analysis where the interrogation is repeated the second time with the window in the second exposure shifted by the value of the displacement obtained from the first interrogation [5.439]. Denoting the result from the first interrogation by $\Delta \boldsymbol{X}_1$, the subsequent interrogation will be performed with a modified form of the cross-correlation operation, which reads:

$$R_1(\boldsymbol{s}) = \int_A W_1(\boldsymbol{x}) I_1(\boldsymbol{x}) W_2[\boldsymbol{x} + \text{round}(\Delta \boldsymbol{x}_1) + \boldsymbol{s}] \times I_2[\boldsymbol{x} + \text{round}(\Delta \boldsymbol{x}_1) + \boldsymbol{s}]\, \mathrm{d}\boldsymbol{x} \,. \quad (5.270)$$

The argument of the windowing function W will be omitted in the remainder, assuming a uniform (top-hat) weighting. The increase of paired particle images reduces substantially the systematic underestimate of the particle displacement and marginally the rms uncertainty. The result of (5.263) is then added to the previously obtained displacement.

Multigrid Analysis. A logical consequence of the window shift technique is the multigrid approach: the interrogation process is repeated several times, with the interrogation window shifted after each interrogation. At this point the window size does need to comply with the 1/4 rule given in (5.253) related to the average particle in-plane motion. As a result the dynamic range is amplified; when the window-refinement multigrid window-shift technique is applied, (5.262) can be rewritten as:

$$\frac{\Delta X_{\max} - \Delta X_{\min}}{\Delta X_{\min}} = \frac{R D_I}{4 \Delta X_{\min}} - 1 \,, \quad (5.271)$$

where D_I^0 is the interrogation window size at the first interrogation and R is the window refinement defined as the ratio between the initial and final size of the interrogation window. In conclusion, for a fixed window size, the dynamic range is increased proportionally with the refinement ratio R, which typically ranges between 2 and 6. For two-dimensional flow problems, the maximum displacement can even exceed the window linear dimension (except for the first interrogation). Other factors may limit the maximum displacement, out-of-plane particle motion and high velocity gradient being the main sources of pair loss.

Subpixel Window Shift. PIV measurements obtained with digital imaging devices may be affected by errors arising from the limited resolution of the light intensity pattern and in turn of the spatial correlation map. As discussed before the estimate of the subpixel particle image, displacement is affected by an error due to imperfect interpolation of the peak or to its distorted shape [5.396]. These effects can be corrected applying the relative shift between I_1 and I_2 with subpixel precision [5.446, 454, 455]. The expression for the spatial correlation function for the subpixel window shift is a slightly modified version of (5.263):

$$R_1(\boldsymbol{s}) = \int_A W_1 \tilde{I}_1 \left(\boldsymbol{x} - \frac{\Delta \boldsymbol{x}}{2}\right) W_2 \tilde{I}_2 \left(\boldsymbol{x} - \frac{\Delta \boldsymbol{x}}{2} + \boldsymbol{s}\right) \mathrm{d}\boldsymbol{x} \,, \quad (5.272)$$

where $\tilde{I}$ indicates that the image intensity values are obtained by interpolation at subpixel locations. As addi-

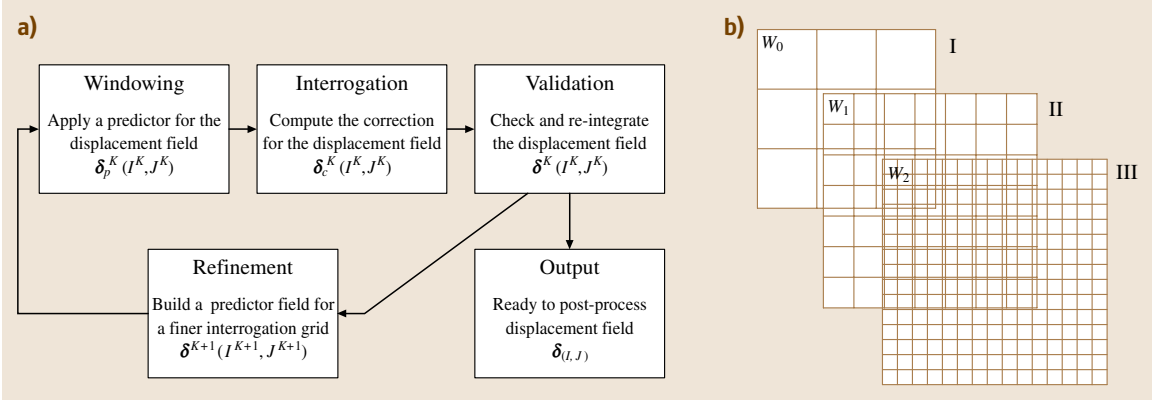

Fig. 5.116a,b Block diagram of multigrid interrogation **(a)** and graphical description of the interrogation grids **(b)**

tional advantage, the method can be implemented with second-order precision following an accurate centered interrogation scheme where the two windows are shifted backward and forward by an equal amount [5.456]. The advantage with respect to the discrete window offset technique is that the subpixel shift returns a correlation map with a fractional displacement that tends to zero, and is therefore unbiased (Fig. 5.113). The particle displacement measured after the application of the window shift is regarded as a correction term to be added to the applied shift. A drawback of the subpixel shift method is that it requires image samples at intermediate locations between pixels, obtained with image interpolation techniques at additional computational effort. Moreover the image interpolation may introduce signal degradation, especially when the particle images are barely sampled ($d_\tau/d_\mathrm{r} < 2$).

Iterative Window Deformation. This discussion has been carried out with the assumption that the motion of particles within the interrogation window can be assumed to be uniform. This rough hypothesis is never strictly valid and in most flows of interest the velocity field may exhibit significant variations within the interrogation windows. A hypothesis with more-general validity is the flow to be represented with a linear function within the interrogation window rather than a constant value, which correspond to a local representation by truncated Taylor expansion [5.457] as shown in (5.267). The expression of the spatial correlation function is therefore further modified into (5.266).

$$R_1(\boldsymbol{s}) = \int_A W_1 \tilde{I}_1 \left(\boldsymbol{x} - \tfrac{\Delta x(x)}{2}\right) W_2 \tilde{I}_2 \left(\boldsymbol{x} + \tfrac{\Delta x(x)}{2} + \boldsymbol{s}\right) \mathrm{d}\boldsymbol{x} \,, \tag{5.273}$$

where the displacement applied to the intensity pattern is now a function of space and may therefore be nonuniform. Several levels of approximation may be considered depending on the truncation of the Taylor series below, however the most common choice is to stop at the first-order term

$$\Delta \boldsymbol{x}_1(\boldsymbol{x}) = \Delta \boldsymbol{x}_1(\boldsymbol{x}_0) + \nabla[\Delta \boldsymbol{x}_1(\boldsymbol{x}_0)](\boldsymbol{x} - \boldsymbol{x}_0) + \ldots \sigma(\boldsymbol{x} - \boldsymbol{x}_0)^2 \,. \tag{5.274}$$

In (5.274), $\boldsymbol{x}_0$ denotes the position of the center of the interrogation window. It should be mpetd that the above expression can return all previous interrogation methods depending on the number of parameters used for the displacement approximation. If no parameter is considered ($\Delta \boldsymbol{x}_1 = 0$) the interrogation corresponds to the basic cross-correlation. The zeroth-order truncated expansion corresponds to the window-shift method and a first-order truncation corresponds to the window deformation technique. When the spacing of the displacement vectors is smaller than the size of the window (i. e., overlap factor of 50% or higher) the displacement distribution within the window can be represented with a piecewise linear function, which corresponds to a higher-order approximation of the flow pattern within the window.

The technique can be implemented within the multigrid approach and its main advantage with respect to the window-shifting method is an increased robustness and accuracy over highly sheared flows such as boundary layers, vortices, and turbulence in general (Fig. 5.117c). A correlation map sample from a turbulent shear flow is shown in Fig. 5.118. The correlation map (Fig. 5.118a) shows several peaks of height comparable to the peak of the most probable displacement. In this situation the detection of a false peak is very likely to occur with increased measurement uncertainty along the shear layer. These spurious peaks are approximately distributed in the direction normal to the local velocity gradient, causing a broadening of the correlation signal. The correlation map obtained by the window deformation shows a more-pronounced single peak only marginally affected by broadening.

Higher-Order Correlation Methods. The interrogation process attempts a global matching of the particle images patterns between the two exposures, which may be regarded as an optimization process:

$$\max_{\Delta X} \int_A I_1[\boldsymbol{x}] I_2[\boldsymbol{x} + \Delta \boldsymbol{x}] \mathrm{d}A \,, \tag{5.275}$$

where $\Delta \boldsymbol{X}$ is the vector parameter to be determined that maximizes the correlation function. Spatial cross-correlation analysis (even including the schemes with window deformation) only yields one vector from each interrogation window, corresponding to a weighted average of the particle displacement inside the window. When the optimization is extended from the displacement to its spatial derivatives the optimization space becomes multidimensional, where a maximum includes the particle displacement as well its gradient or higher-order derivatives:

$$\max_{\Delta \boldsymbol{X}, \mathrm{grad}(\Delta \boldsymbol{X}), \ldots} \int_A I_1[\boldsymbol{x}] I_2[\boldsymbol{x} + \Delta \boldsymbol{x}] \mathrm{d}A \,. \tag{5.276}$$

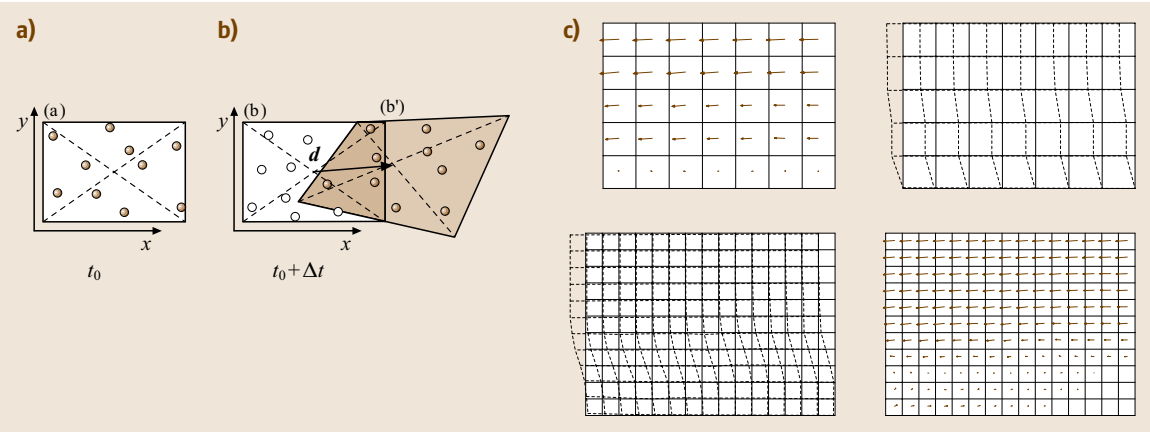

Fig. 5.117a–c Window deformation principle. **(a,b)** Tracer pattern in the first **(a)** and second **(b)** exposure (*solid circles* in **(b)** are the tracers correlated with the first exposure). **(c)** Schematic view of the multigrid window deformation method

The number of parameters involved in the optimization is given by the order of approximation of the Taylor expansion used to represent the displacement within the interrogation window. Higher-order correlation information can in principle return at each measurement cell the values of the velocity and its derivative(s) with the advantage of an increased spatial resolution. However the properties of estimators higher than first order are not yet sufficiently understood. As an example of application of higher-order correlation, the evaluation of the spatial correlation associated to the second derivatives of the displacement field can be used to reduce the filtering effect associated to the conventional spatial cross-correlation analysis [5.458] significantly.

Iterative Interrogation. Most common PIV image-analysis software nowadays performs multistep analysis of PIV recordings, which can be seen as composed out of two procedures:

1. *Multigrid analysis*, where the interrogation window size is progressively decreased. This process allows the elimination of the 1/4-rule constraint and is usually terminated when the required window size (the smallest) is applied.
2. *Iterative analysis* at a fixed sampling rate (grid spacing) and spatial resolution (window size). This process further improves the accuracy of the image deformation and enhances the spatial resolution.

The iterative analysis can be described by a predictor–corrector loop as represented schematically in Fig. 5.121. The iterative equation in its simplest form reads

$$\Delta \boldsymbol{x}_{k+1} = \Delta \boldsymbol{x}_k + \Delta \boldsymbol{x}_{\text{corr}} \,, \tag{5.277}$$

where $\Delta \boldsymbol{x}_k$ indicates the result of the evaluation at the k-th iteration used as the predictor for the $k+1$-th iteration. The correction term $\Delta \boldsymbol{x}_{\text{corr}}$ can be intended as a residual and is the displacement vector obtained by

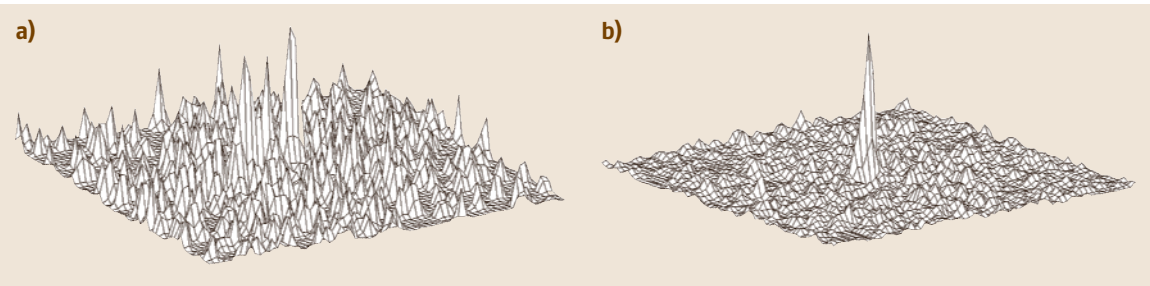

Fig. 5.118a,b Discrete spatial correlation in a turbulent shear flow. Interrogation with single-step correlation **(a)** and with the multistep window deformation technique **(b)**

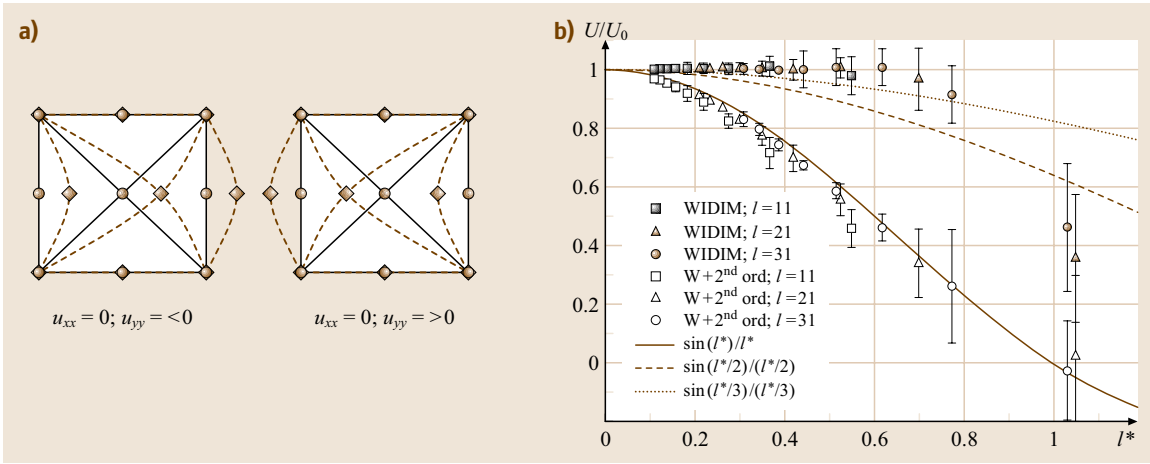

Fig. 5.119a,b Schematic representation of the second-order correlation scheme **(a)**. Comparison between the second-order correlation method spatial response and the basic correlation **(b)**

cross-correlation analysis of the deformed images I_1^k, I_2^k obtained from the original images I_1, I_2 according to the relations

$$I_1^k = \tilde{I}_1\left[\boldsymbol{x} - \frac{\Delta \boldsymbol{x}_k(\boldsymbol{x})}{2}\right], I_2^k \quad = \tilde{I}_2\left[\boldsymbol{x} + \frac{\Delta \boldsymbol{x}_k(\boldsymbol{x})}{2}\right]. \tag{5.278}$$

The procedure can be reiterated several times, however two to three iterations are already sufficient to achieve a well-converged result, which allows deformation of the images and compensation for most of the in-plane particle image motion.

Stability and Spatial Resolution of Iterative Interrogation. The overall approach described above appears very logical and its simplicity makes it straightforward to implement, which probably justifies why it has been so broadly adopted in the PIV community (PIVchallenge II and III, *Stanislas* et al. [5.397]). However when such iterative interrogation is performed without spatial filtering of the velocity field, the process tends to oscillate and eventually diverge unless the image processing is interrupted at an early stage. The instability arises from the sign reversal in the sinc shape of the response function associated to the top-hat function of the interrogation window. If two almost identical images are considered (except for artificial pixel noise) the displacement field measurement after some iterations oscillates spatially with a wavelength $\Lambda_{\text{unst}} = 2/3 D_{\text{I}}$.

The above result is consistent with the fact that the response function r_{s} of a top-hat interrogation window (the common option) corresponds to the $\sin(x/D_{\text{I}})/(x/D_{\text{I}})$ function. Therefore the range with negative values of the sinc function is responsible for the amplification of the specific wavelength. The iterative process requires therefore a stabilization by means of a low-pass filter applied to the updated result (Fig. 5.121). In line with the above definitions, the update term reads

$$\Delta \boldsymbol{x}_{k+1} = r_{\text{s}}(\Delta \boldsymbol{x}_0 - \Delta \boldsymbol{x}_k)\,. \tag{5.279}$$

The iterative process stability can be achieved with the application of a spatial low-pass filter to the velocity predictor, as shown in the block diagram of Fig. 5.121.

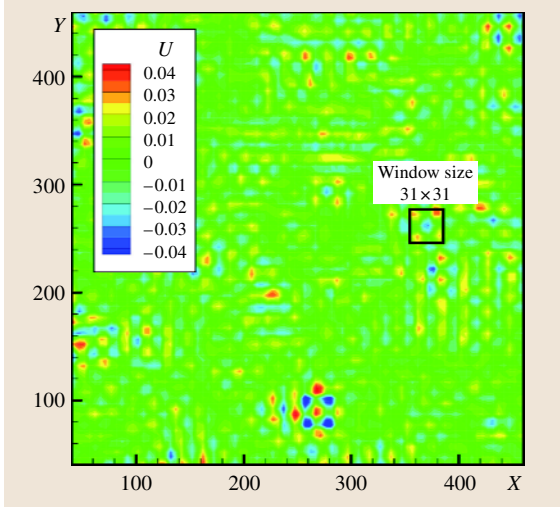

Fig. 5.120 Displacement field from iterative analysis of images with a zero-displacement field

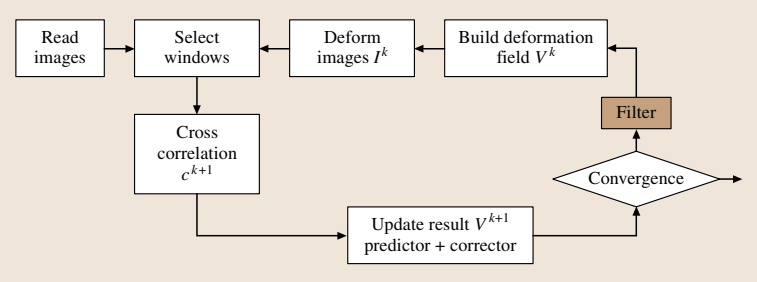

Fig. 5.121 Block diagram of the iterative image deformation interrogation method with filtered predictor

The property of the filter is to damp the growth of fluctuations at wavelengths smaller than the window size. A moving-average filter with a kernel size corresponding to that of the interrogation window is proven to be more than sufficient to stabilize the process [5.459]. The iterative equation relative to the block diagram in Fig. 5.121 can be rewritten as

$$\Delta \boldsymbol{x}_{k+1} = f(\Delta \boldsymbol{x}_k) + \Delta \boldsymbol{x}_{\text{corr}} \,. \tag{5.280}$$

Introducing the spatial response of the chosen low-pass filter r_f (in the present case we assume for simplicity that $r_\text{f} = r_\text{s}$), the filtered version of the iterative equation reads

$$\Delta \boldsymbol{x}_{k+1} = \Delta \boldsymbol{x}_k + r_\text{s}^2(\Delta \boldsymbol{x}_0 - \Delta \boldsymbol{x}_k) \,, \tag{5.281}$$

where the sign reversal is eliminated by taking the square of the response function. Other means of stabilization are nonlinear filtering such as least-squares spatial regressions [5.460] or directly weighting the interrogation window (e.g., pyramidal, Gaussian, or LFC technique as suggested by *Nogueira* et al. [5.461]). A numerical simulation of the sine-wave test shows that the single-step cross-correlation yields a spatial response that compares well with that of a moving-average filter. The iterative correlation conversely returns a spatial response with almost no modulation error up to wavelengths twice the size of the interrogation window. However without a spatial filter, the result tends to overshoot the actual amplitude and small-wavelength fluctuations are amplified. When a spatial regression filter is applied, such behavior is avoided, whereas the spatial resolution is still significantly better than that of the single-step cross-correlation in terms of modulation error.

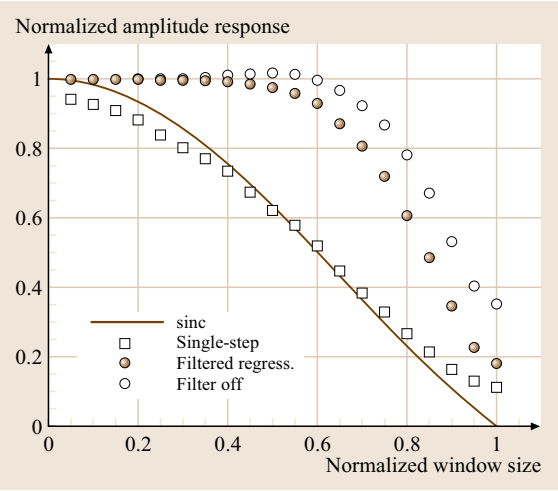

Fig. 5.122 Sine wave test: normalized amplitude response as a function of the normalized window size. *Sinc* function (*solid line*); single-step correlation (*squares*); iterative window deformation (*circles*); filtered iterative window deformation (*filled circles*)

Postprocessing

The interrogation analysis of PIV images yields an array of displacement vectors that represent the two or three component velocity field in the measurement volume (this is either a plane or a volume). The next step is *data validation*, i. e., the identification of erroneous displacement vectors. In general the signal dropout due to invalid data will be low, and the missing data is replaced in order to retain the regular array structure. The final step is then data evaluation, which can include the computation of derived quantities (e.g., vorticity and strain rate) and turbulence statistics (e.g., Reynolds stress), or the detection of specific flow structures.

Data Validation. If one would optimize a PIV measurement in accordance to the *recipe* presented in (5.253) one could end up with a result as shown in Fig. 5.123; the displacement field contains a number of displacement vectors that do not appear to fit with the surrounding displacement field. Such vectors occur when a random correlation peak exceeds the amplitude of the displacement-correlation peak, and therefore such vectors are commonly referred to as *spurious vectors*. These

vectors are often the result of insufficient particle images, large in-plane or out-of-plane displacements, or high spatial gradients of the velocity; other causes can be a strong background image (e.g., due to a surface reflection) or light-sheet inhomogeneity (e.g., a shadow cast by a larger object).

The aim of optimizing PIV is to maximize the probability of detecting the displacement-correlation peak. One could aim to increase the image density to achieve a near-100% valid detection rate, but this can lead to other undesirable effects, such as fluid opacity (due to multiple particle scattering) and multiphase effects (i. e., increase of the apparent fluid viscosity and particle–particle interactions). Therefore, a more-practical approach is to accept a small fraction (typically about 5%) of spurious vectors, and to rely on a post-interrogation detection, removal, and replacement procedure.

There are several approaches to identify spurious vectors. An intuitive approach is visual inspection of a plotted vector map. Such an approach is acceptable for the evaluation of a handful of PIV results (as was the case when PIV was first developed), but is impractical nowadays when PIV measurements tend to generate 10^3 vectors maps or more.

For the automated validation there are generally two approaches, which are based on

1. correlation signal quality
2. local *coherence* of the vector map, i. e., a comparison of each vector with measured displacements in adjacent interrogation regions

Both will be discussed below, but in general detection methods based on correlation signal quality are not very robust and the evaluation based on local *coherence* appears to be much more efficient.

Correlation Signal Quality. The quality of a PIV interrogation can be expressed by the amplitude of the displacement-correlation peak, which is proportional to $N_I F_I F_O F_\Delta$. However, the amplitude also depends on the local image properties, such as mean intensity and intensity variance, which are determined by the local light level and particle image characteristics. When the correlation is normalized by the (local) variance of the image intensity, the correlation amplitude varies between 0 and 1, where 1 means perfect correlation of the particle-image pattern. However, the amplitude also depends on the local value of F_τ, which complicates the interpretation of the correlation signal amplitude; for example, when one of the interrogation images contains an unmatched bright particle image, it simply correlates with the brightest particle image in the other interrogation image, leading to a spurious displacement with near-unity correlation coefficient.

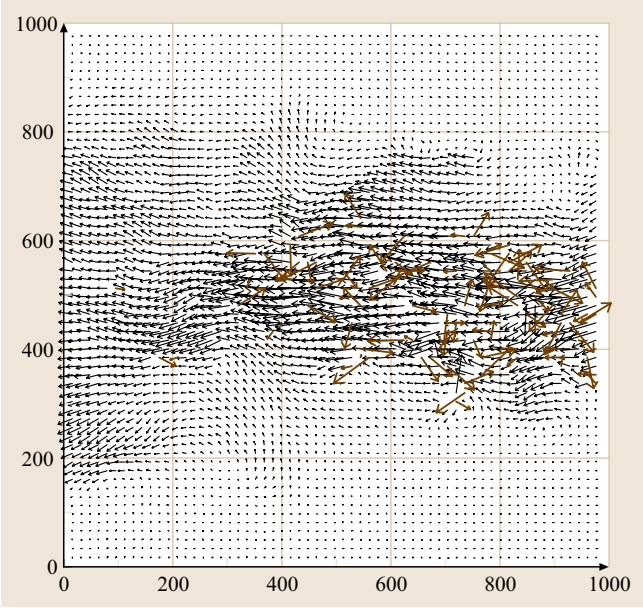

Fig. 5.123 Example of a PIV result containing spurious vectors (after *Westerweel* and *Scarano* [5.462])

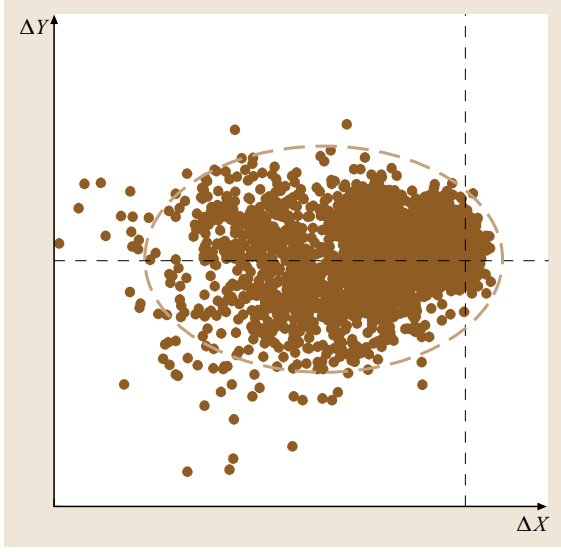

Fig. 5.124 The displacements corresponding to the vector map in Fig. 5.123. The ellipse indicates the region that contains the range of expected displacements

The signal quality is also characterized by the amplitude of the displacement-correlation peak relative to the highest random correlation peak; this ratio is generally referred to as the *peak detectability* D_0, and this measure can be regarded as a lower limit for the correlation signal-to-noise ratio. However, the detectability appears to be a reliable measure only when the image density N_I is high, while D_0 can strongly fluctuate for low N_I, leading to erroneous acceptance of spurious vectors.

Vector Field Coherence. The measured displacement field is expected to have a certain *smoothness* or *coherence*, in which spurious vectors stand out with respect to the overall or local displacement field. A first approach is to generate a scatter plot of the observed displacements; see the example in Fig. 5.124. The valid displacements appear to fall in a closed region indicated by the ellipse. Evidently, this region would be different for each flow. One can identify displacements that occur outside this region as spurious data. This type of identification represents a *global approach* in which fluctuations that are unacceptably large with respect to the mean and variance of the total flow field are discarded. However, this global approach cannot identify spurious displacements within the global fluctuation level that show up because of a strong deviation with respect to the *local* displacement field.

A local approach would be to compare each vector with the local mean displacement of the four or eight adjacent displacement vectors. A complication is that the local mean is a linear estimate that is strongly influenced by the possible presence of a spurious vector in the neighborhood of adjacent displacement vectors. This is easily avoided by using the *median* of the displacement components, which has statistical properties similar to the local mean but is quite impervious to the presence of spurious data and therefore much more robust. Hence, the *residual* r of a displacement vector $\boldsymbol{U}_0$ is defined as

$$r = \frac{|\boldsymbol{U}_0 - \boldsymbol{U}_m|}{\sigma} , \qquad (5.282)$$

where $\boldsymbol{U}_m$ is the *median* vector of the eight vectors $\{\boldsymbol{U}_1, \ldots, \boldsymbol{U}_8\}$ in the 3×3 neighborhood of $\boldsymbol{U}_0$ and σ a normalization factor; a robust estimate for σ is the median r_m of $r_i = |\boldsymbol{U}_i - \boldsymbol{U}_m|$ (with $i = 1\ldots8$). A small offset ε is added to r_m, i. e. $\sigma = r_m + \varepsilon$, where $\varepsilon \approx 0.1$ px, to improve the performance of the evaluation for very low fluctuation levels. Now, a vector is labeled as *spurious* when r is larger than a given threshold value r_c. This approach is commonly referred to as the *median test* [5.462, 463].

The optimal value for r_c depends on the experimental details, the flow conditions and the quantities to be extracted from the data. The proper choice of r_c is important: if it is chosen too small then valid data can be labeled as spurious, and if it is chosen too large then spurious data remain undetected; these erroneous detections are generally referred to as errors of the first and second kind, respectively. It depends on the objectives of the measurement whether or not it is acceptable to have a small fraction of spurious data to remain or of valid data being rejected; this should be investigated for each measurement. In general, low-order turbulence velocity statistics are quite insensitive, while derivative data (such as the vorticity) are strongly affected, by undetected spurious data.

The normalization described by *Westerweel* and *Scarano* [5.462] makes r_c relatively independent of the flow conditions, and a typical value for r_c is 2, with larger and smaller values yielding a less- and more-stringent detection, respectively.

Data Replacement. The most common strategy is to accept that there is a small fraction of spurious vectors in a PIV result, to rely on a robust validation method for the detection of spurious data, and to replace the missing vector data. This strategy can only work when the fraction of spurious vectors is low. In general, PIV data are considered of good quality when the fraction of spurious vectors is less than about 0.95. Behind this rule of thumb there is a simple statistical argument that is explained below.

For flows with fairly homogeneous statistics for the velocity fluctuations and homogeneous seeding, the occurrence of spurious vectors is randomly distributed over the measurement domain. The median test is quite insensitive to the presence of any spurious vectors when less than one-half of the adjacent interrogations return a spurious result. Consider the four directly adjacent interrogation positions in a 3×3 neighborhood. Given a probability γ that each of these interrogations yields a spurious result, the probability of finding k spurious vectors in n interrogations is given by a binomial distribution $B(k, n; \gamma)$. The probability that the four adjacent interrogations contain no more than two spurious vectors is then given by

$$\text{Prob(successful median test)} = \sum_{k=0}^{2} B(k, n = 4; \gamma) . \qquad (5.283)$$

Suppose it is required that the median test should not fail in the measurement domain. For a typical image of 1024×1024 px interrogated with 32×32 px interrogations regions with 50% overlap, this means that it should fail less than 1 in 4096 interrogations. Solving the above equation shows that γ should be less than 0.04, which is close to the rule of thumb value ($\gamma = 0.05$).

Estimation of Derivative Data. The vorticity and deformation are flow properties that can be directly obtained by numerical differentiation of the PIV velocity field. To obtain reliable estimates of these derivative properties it is important that the PIV measurement data is accurate, does not contain spurious data, and that the spatial resolution is adequate to perform a differentiation of the data. In the previous section it was shown that reliable and accurate velocity data can be obtained provided the flow is appropriately seeded with small tracer particles, and the images are recorded in correspondence to the optimization rules in (5.253). The spatial resolution of the PIV measurement is characterized by the dimension size of the interrogation window. Under ideal circumstances it is possible to use 16×16 px (or even 8×8 px) interrogation regions, which provide sufficient spatial resolution to determine the instantaneous velocity derivatives (mostly associated with small-scale turbulence). Usually an overlap of 50–75% is used between adjacent interrogation positions, which provides sufficient data density to estimate the deformation and vorticity.

Methods for the estimation of derivative data have been described by *Lourenco* and *Krothapalli* [5.464], *Abrahamson* and *Lonnes* [5.465], *Fouras* and *Soria* [5.466], *Raffel* et al. [5.467], and *Foucaut* and *Stanislas* [5.468]. Here we describe the basic approach for the estimation of the out-of-plane component of the vorticity that is commonly referred to as the *circulation method*.

The deformation tensor $\partial \boldsymbol{u}/\partial \boldsymbol{x}$ can be split into symmetric and antisymmetric parts. The symmetric part is referred to as the stress tensor, while the antisymmetric part (which has only three nonzero components) can be written as a vector, i. e., the vorticity $\boldsymbol{\omega}$ [5.469]. The vorticity vector is then defined as the curl of the velocity field:

$$\boldsymbol{\omega} = \nabla \times \boldsymbol{u} \,, \quad \text{with } \omega_z = \frac{\partial v}{\partial x} - \frac{\partial u}{\partial y} \,, \tag{5.284}$$

where u and v are the two in-plane components. For PIV data that are obtained at discrete locations the vorticity ω_z can be estimated from central first-order differences of the measured velocity data

$$\omega_z(i,\, j) \cong \frac{v(i+1,\, j) - v(i-1,\, j)}{2\Delta x} - \frac{u(i,\, j+1) - u(i,\, j-1)}{2\Delta y} \,, \tag{5.285}$$

where $(i,\, j)$ are the indices of the interrogation grid in the x- and y-directions, respectively, and Δx and Δy are the distances between mesh points. Given that a 50% overlap is used between subsequent interrogations, the estimation of the vorticity involves data over a region with an area of $3D_\mathrm{I} \times D_\mathrm{I}$. This implies that the vorticity is computed with a resolution length scale that is larger than the resolution length scale of the velocity data. This can be compensated partially by using interrogation data with a larger overlap, but this also increases the correlation of the noise in the velocity data, which deteriorates the accuracy of the vorticity estimate.

The differentiation scheme in (5.285) tends to amplify the noise in the measured velocity data. *Landreth* and *Adrian* [5.470] propose the use of a mild low-pass filter with a Gaussian kernel to attenuate the noise while retaining the velocity signal unaffected. A more-common approach is to estimate the vorticity by means of the circulation, i. e.,

$$\omega_z = \lim_{A \to 0} \frac{1}{A} \oint_C \boldsymbol{u} \cdot \mathrm{d}\ell \,, \tag{5.286}$$

where C is the contour that encloses an area A (Fig. 5.125). The discrete representation of (5.286) is [5.471]:

$$\begin{aligned} &\omega_z(i,\, j) \\ &\cong \frac{1}{4\Delta x \Delta y} \\ &\quad \times \begin{pmatrix} \Delta y \cdot v(i+1,\, j) \\ \quad + \frac{1}{2}\Delta y[v(i+1,\, j-1) + v(i+1,\, j+1)] \\ -\Delta x \cdot u(i,\, j+1) \\ \quad - \frac{1}{2}\Delta x[u(i-1,\, j+1) + u(i+1,\, j+1)] \\ -\Delta y \cdot v(i-1,\, j) \\ \quad - \frac{1}{2}\Delta y[v(i-1,\, j-1) + v(i-1,\, j+1)] \\ +\Delta x \cdot u(i,\, j-1) \\ \quad + \frac{1}{2}\Delta x[u(i-1,\, j-1) + u(i+1,\, j-1)] \end{pmatrix} . \end{aligned} \tag{5.287}$$

Note that this is *identical* to first applying a filter to the velocity data:

$$\tilde{u}(i,j)=\frac{1}{2}\left\{u(i,j)+\frac{1}{2}[u(i-1,j)+u(i+1,j)]\right\},$$
$$\tilde{v}(i,j)=\frac{1}{2}\left\{v(i,j)+\frac{1}{2}[v(i,j-1)+v(i,j+1)]\right\}, \quad (5.288)$$

which are then substituted in (5.285). For a 50% overlap the vorticity estimate involves a region with an area of $4D_I \times D_I$, which is only slightly larger than the central difference scheme using unfiltered velocity data. However, the noise in the vorticity result is substantially reduced. It can be easily verified using (5.285) and (5.288) that, for statistically independent velocity data, the rms error in ω_z is reduced by a factor of $\sqrt{3/8} \approx 0.6$. For a 1% noise level in the velocity data (i. e., a 0.1 px error and a 10 px displacement) the vorticity can be estimated with an error of about 5–10% of the rms variation of the vorticity.

Appendix: Computation of the Spatial Correlation Using the Discrete Fourier Transform

Consider an $M \times N$ px image $I[m,n]$. This image may be considered as an infinitely large image with $I[m,n]=0$ outside: $1 \le m \le M$, $1 \le n \le N$, i. e., *zero padding*. Let $\tilde{I}[m,n]$ be a periodic image with periods U and V in m and n, respectively, such that $\tilde{I}[m,n]=I[m,n]$, for $1 \le m \le U$, $1 \le n \le V$ with $U \ge M$, $V \ge N$. The two-dimensional discrete Fourier transform (DFT) $\tilde{F}[u,v]$ of $\tilde{I}[m,n]$ is given by

$$\tilde{F}[u,v] = \frac{1}{UV}\sum_{m=\{U\}}\sum_{n=\{V\}}\tilde{I}[m,n]\exp\left[-2\pi\mathrm{i}\left(\frac{mu}{U}+\frac{nv}{V}\right)\right]. \quad (5.289)$$

Here the notation of *Oppenheim* et al. [5.426] is adopted, in which $m=\{U\}$ denotes the summation of m over one period U, and similarly for $n=\{V\}$. The DFT is periodic in u and v with periods of U and V, respectively. The inverse two-dimensional DFT is defined as

$$\tilde{I}[u,v]=\sum_{u=\{U\}}\sum_{v=\{V\}}\tilde{F}[u,v]\exp\left[2\pi\mathrm{i}\left(\frac{mu}{U}+\frac{nv}{V}\right)\right]. \quad (5.290)$$

Let $\tilde{I}_1[m,n]$ and $\tilde{I}_2[m,n]$ be the periodic images associated with the interrogation images $I_1[m,n]$ and $I_2[m,n]$, respectively, constructed according to the definitions above. For each of these two signals the discrete Fourier transform is given by (5.289), denoted by $\tilde{F}_1[u,v]$ and $\tilde{F}_2[u,v]$ respectively. The cross power spectral density $\tilde{S}[u,v]$ is given by the convolution of $\tilde{F}_1[u,v]$ and $\tilde{F}_2^*[u,v]$, where the asterisk denotes the complex conjugate. Substitution of (5.289) yields

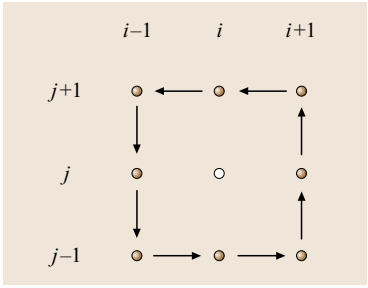

Fig. 5.125 The computation of the vorticity ω_z by means of the contour integral in (5.287) is equivalent to the central differentiation scheme in (5.285) using the filtered velocity data defined in (5.288)

$$\tilde{S}[u,v] = \frac{1}{(UV)^2}\sum_{k=\{U\}}\sum_{l=\{V\}}\sum_{m=\{U\}}\sum_{n=\{V\}}\tilde{I}_1[k,l]\tilde{I}_2[m,n] \times\exp\left[-2\pi\mathrm{i}\left(\frac{m-k}{U}u+\frac{n-l}{V}v\right)\right], \quad (5.291)$$

which, after substitution of $r=m-k$ and $s=n-l$, can be written

$$\tilde{S}[u,v] = \frac{MN}{(UV)^2}\sum_{r=\{U\}}\sum_{s=\{V\}}\exp\left[-2\pi\mathrm{i}\left(\frac{ru}{U}+\frac{sv}{V}\right)\right] \times\left\{\frac{1}{MN}\sum_{k=\{U\}}\sum_{l=\{V\}}\tilde{I}_1[k,l]\tilde{I}_2[k+r,l+s]\right\}. \quad (5.292)$$

The term between braces is recognized as the spatial correlation $\tilde{\phi}[r,s]$ of the two *periodic* images $\tilde{I}_1[m,n]$ and $\tilde{I}_2[m,n]$. The summations over k and l are taken over an area for which $\tilde{I}_1[k,l]=I_1[k,l]$, so that

$$\tilde{S}[u,v] = \frac{MN}{(UV)^2}\sum_{r=\{U\}}\sum_{s=\{V\}}\tilde{\phi}[r,s]\exp\left[-2\pi\mathrm{i}\left(\frac{ru}{U}+\frac{sv}{V}\right)\right], \quad (5.293)$$

with

$$\tilde{\phi}[r,s] = \sum_{\alpha=-\infty}^{+\infty} \sum_{\beta=-\infty}^{+\infty} \phi[r+\alpha U, s+\beta V] \,, \quad (5.294)$$

where ϕ is defined in (5.256). The most important difference with the direct computation of the spatial correlation is that the DFT applies to *periodic* fields only. For images that are defined over an $M \times N$ px domain, the spatial correlation is defined over a $2M \times 2N$ px domain. This implies that the *exact* spatial correlation $\phi[r, s]$ can be retrieved when the interrogation images are padded by zeroes over a domain that is at least *twice* the size of the original signal in each direction. This is illustrated in Fig. 5.126. Hence, proper zero padding eliminates the effect that the DFT deals with periodic signals, which is usually referred to as DFT with (quasi-)nonperiodic boundaries.

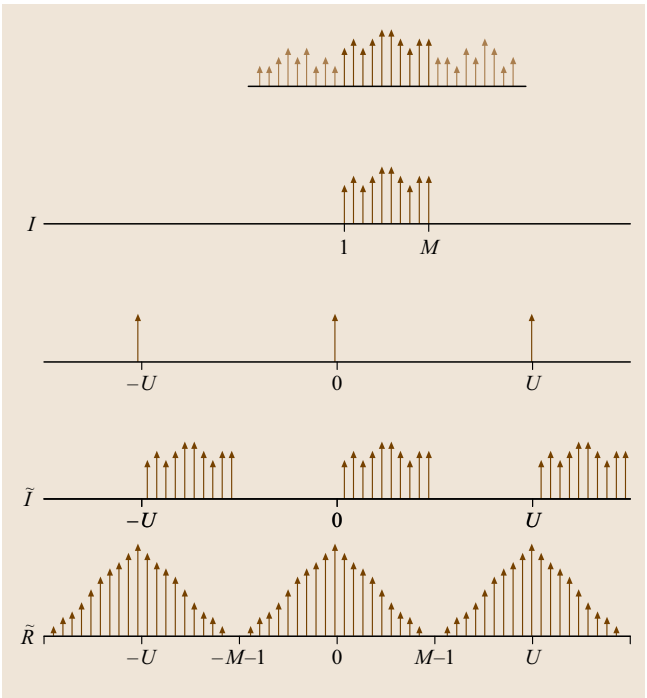

Fig. 5.126 Computation of the spatial (auto-)correlation by means of the discrete Fourier transform (DFT). *Top to bottom*: the signal, the finite domain signal (viz., interrogation image), the pulse train with a period of U, the harmonic signal $\tilde{I}$, and the spatial aut-correlation. The DFT implies a circular repetition of the original signal, so that the exact spatial correlation is only obtained when the period of the DFT domain is at least twice the signal length

In conclusion, the *exact* spatial correlation is obtained when zero padding is applied in accordance with the size of the correlation domain. So, *Fourier correlation* is not different from *direct correlation*. However, small errors are introduced when the DFT computation is done without zero padding, which can result in a significant increase of the measurement error for the subpixel displacement. Zero padding is used implicitly in the *direct* computation of the correlation, but it is unnecessary slow in comparison to the zero-padded DFT computation which can be evaluated with the fast and efficient FFT algorithm.

5.3.4 Doppler Global Velocimetry

Doppler global velocimetry (DGV), also known as planar Doppler velocimetry, is a member of a class of laser-based velocimetry techniques that use the absorption characteristics of molecular filters to determine the Doppler shift of scattered laser light. Tuning a single-frequency laser to a point midway along the side of an absorption line results in the absorption of approximately half of the light energy by the media. If the optical frequency is changed, e.g., by tuning the laser, Doppler shift in the light, etc., the amount of energy absorbed by the media changes. Thus the absorption line acts as an optical frequency-to-intensity converter, and is linear over a significant frequency range for a majority of absorption lines. Developing an optical system to monitor the instantaneous effects of this transfer function on collected scattered laser light yields a method to determine the velocity of targets passing through a specific point or points within the illuminating laser beam. This may be a single point along the beam, or an array of points within a laser light sheet as viewed by a video camera.

The direct determination of optical frequency eliminates the need to mix multiple laser light sources (e.g., reference-beam laser velocimetry, fringe-type laser velocimetry, interferometry-based laser velocimetry) or time-track individual particles (e.g., laser transit anemometry, and particle image velocimetry (PIV)). Thus any source of Doppler-shifted scattered light from a single-frequency laser may be measured to yield the velocity of the scattering object. This characteristic yields the ability to obtain average, time-dependent, or instantaneous velocity measurements from single or multiple submicron particles and even gas molecules. The limitation is the acquisition of sufficient scattered photons to activate the detector with adequate photon statistics to yield good signal-to-noise ratios. The technology also

allows the measurement-point dimensions to be defined by the viewing optical system, and eliminates the necessity to resolve single micron-sized particles. Finally, the ability to measure the velocity of very small particles and even molecules virtually eliminates measurement errors resulting from particle dynamics.

Note that molecular filter technology does have limitations, however. High-energy lasers and/or heavily seeded flows, scientific-grade cameras and integration techniques may be required to produce the signal levels needed to obtain accurate flow measurements. The overall measurement accuracy is dependent on the quality of the frequency content within the laser beam, the precision of the molecular filter calibration, the amplitude resolution and signal-to-noise ratio of the detector, the analog-to-digital converter, and the precision and geometry of the component placement.

Basic Principles

The shift in optical frequency of light scattered from a moving object is not only dependent on the velocity of the object, but also on the geometric configuration of the light source and the detector. If, as shown in Fig. 5.127, a laser beam is transmitted from the left to right along the vector direction $\hat{\boldsymbol{i}}$, and an object passes through the beam, light will be scattered in all directions. If a detector is placed along a vector direction $\hat{\boldsymbol{o}}$ to intercept a portion of the scattered light, that light will have an optical frequency shift described by

$$\Delta\nu = \frac{\nu_o \boldsymbol{V}\cdot(\hat{\boldsymbol{o}}-\hat{\boldsymbol{i}})}{c}\,, \tag{5.295}$$

where $\Delta\nu$ is the Doppler shift frequency, ν_o is the laser optical frequency, $\boldsymbol{V}$ is the velocity of the object, and c is the speed of light. The vectorial dot product in (5.295) indicates that this configuration will be sensitive to velocity along a single direction in space: the direction of $(\hat{\boldsymbol{o}}-\hat{\boldsymbol{i}})$ lying within the plane of $\hat{\boldsymbol{o}}$ and $\hat{\boldsymbol{i}}$. Thus multiple velocity components can be measured by changing the propagation direction of the laser beam ($\hat{\boldsymbol{i}}$), or by placing multiple detectors about the measurement point, e.g., $\hat{\boldsymbol{o}}_{\mathrm{A}}$, $\hat{\boldsymbol{o}}_{\mathrm{B}}$, $\hat{\boldsymbol{o}}_{\mathrm{C}}$.

The laser must have the ability to generate a single-frequency output that is tunable to allow alignment with the chosen absorption line. The laser should also be frequency stabilized to keep the optical frequency within the dynamic range of the line. The following two examples illustrate these characteristics for the application of an iodine vapor cell. The 514.5 nm output from an argon-ion laser lies close to several candidate absorption lines. The laser must include an etalon to select a single longitudinal mode that yields bandwidths that are narrow enough ($\approx$ 10 MHz) to provide a usable frequency resolution along the absorption line. Heating and/or tilting the etalon also provides a frequency tuning capability. Another commonly used laser, a pulsed, frequency-doubled Nd:YAG, provides the capability of making measurements nearly instantaneously. However, an injection seeder is needed to provide single-frequency operation.

The determination of the Doppler shift is obtained using a molecular absorption filter acting as an optical frequency discriminator to measure the frequency of the collected scattered light. Once found, the original laser frequency, typically determined using the same or a second molecular absorption filter [laser frequency monitor (LFM)], is subtracted from the measured frequency to yield the Doppler shift. The velocity is then obtained us-

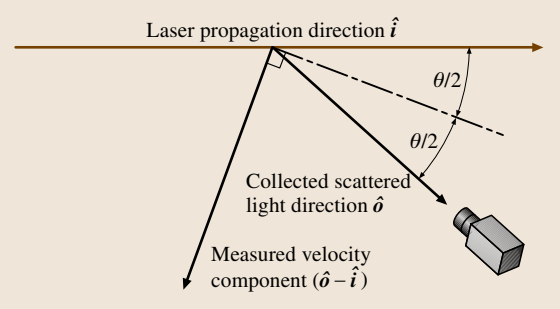

Fig. 5.127 Measurement of the velocity direction based on the orientation of the laser propagation direction and the detector location.

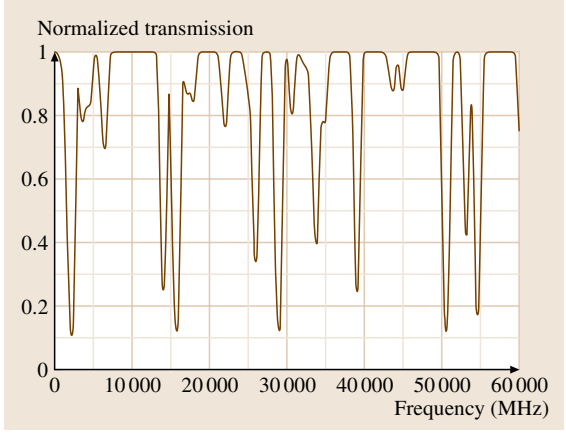

Fig. 5.128 Absorption spectra of iodine near the 514.5 nm line of an argon-ion laser (after *Forkey* et al. [5.472])

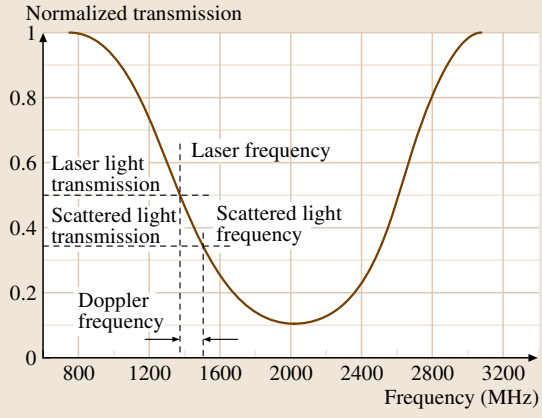

Fig. 5.129 Iodine vapor cell (IVC) transfer function

ing (5.295). The most commonly used molecular filter is an iodine vapor cell. Iodine possesses a large number of absorption lines in the green portion of the visible spectrum, which matches well with several laser systems, e.g., argon ion, doubled Nd:YAG, and doubled Yb:YAG. *Forkey* et al. [5.472], who developed a model outlining the absorption characteristics of iodine vapor with respect to optical frequency, aided the task of selecting an appropriate line. An example portion of the spectrum is shown in Fig. 5.128. A line that had a deep well with a linear slope was selected. The vapor pressure was then set to obtain the desired frequency-to-intensity characteristics.

A velocimeter can be created for flow measurement applications using these principles by projecting a single-frequency laser beam through a flow field and viewing a point(s) along the beam with a detector (Fig. 5.127). An iodine vapor cell is placed in front of the detector and the laser frequency is adjusted to a point along the edge of a linear absorption line (Fig. 5.129). When the flow is started, the collected scattered light is shifted in frequency based on the Doppler effect and the transmissivity through the iodine vapor changes (Fig. 5.129). Measurement of this change yields the information needed to determine the velocity of the scattering media. However, it also includes effects of variation in scattering intensity related to particle number density and size distribution along with inherent spatial variations in the laser beam intensity. Using a second detector to sample the collected light prior to the iodine vapor cell can eliminate these effects. This serves as the normalizing reference signal needed to determine the effects of the vapor transfer

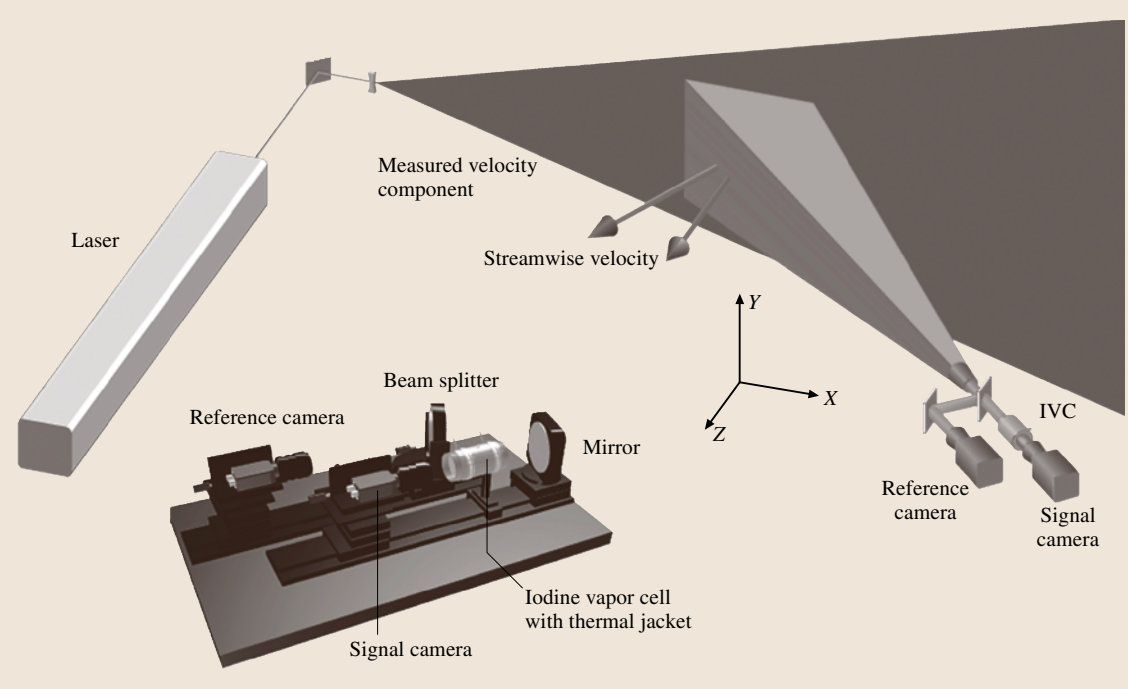

Fig. 5.130 Pictorial view of a one-component Doppler global velocimeter optical configuration

function on the collected scattered light, as illustrated for a single-component configuration in Fig. 5.130.

Molecular filter technology has been used in a variety of configurations to provide flow measurements in diverse applications. Although the primary application has been wind-tunnel testing, significant efforts have been directed toward internal flow applications in engines, and even in medical drug-delivery systems. The technology has been used to provide the *third* component measurement in laser transit anemometry and particle image velocimetry systems to eliminate the need for multiple viewing ports in internal flow applications.

Configurations and Applications

The original concept was proposed and demonstrated in the laboratory by *Komine* [5.473] and *Komine* et al. [5.474] at the Northrop Research and Technology Center. The technology was transferred to the NASA Langley Research Center in 1991, where *Meyers* and *Komine* [5.475] conducted the first wind-tunnel demonstration. The technology was advanced toward a practical wind-tunnel measurement system by capturing the video frames digitally and redirecting the laser light sheet to three orthogonal positions within the same measurement plane to obtain sequential three-component measurements [5.476, 477]. Development continued at Langley toward the goal of increasing measurement accuracy along with determining the limits of the technology through wind-tunnel testing; see *Meyers* [5.478] and *Meyers* et al. [5.479].

The ability to obtain three-component velocity measurements without the need to resolve individual seed particles opened the potential to use DGV in large wind tunnels to view the flow field over large measurement planes. The first application of multiple cameras to obtain simultaneous three-component measurements was a long-focal-length application in the NASA Ames Research Center 40×80 foot national full-scale aerodynamic complex (NFAC); see *Meyers* [5.478] and *Reinath* [5.480] (Fig. 5.131). The resolved streamwise velocity component of the 463 °C flow exiting a high speed civil transport (HSCT) engine simulator is shown in Fig. 5.132 along with the velocity profile extracted from a row of pixels along the horizontal diameter. The spatial resolution was 1.25 mm at focal distances of 15.8, 15.2, and 16.8 m, respectively, for the three-camera systems. This effort continued at NASA Ames leading to rotorcraft measurements in the 80×120 foot leg of the NFAC using a pulsed Nd:YAG-based system; see *McKenzie* [5.481] and *McKenzie* and *Reinath* [5.482]. The long-range capabilities of DGV led to the use of several configurations in the US Air Force Wright Laboratory subsonic aerodynamic research laboratory. Primarily these efforts concentrated on the investigation of leading-edge vortex interaction with vertical stabilizers on high-performance aircraft; see *Beutner* et al. [5.483], *Elliott* and *Beutner* [5.484], and *Elliott* et al. [5.485].

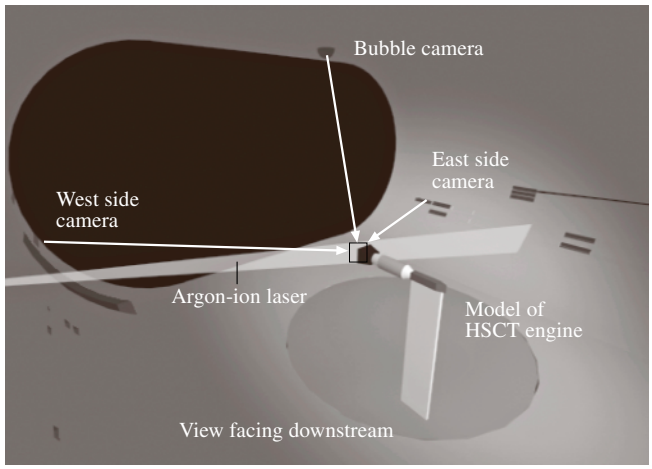

Fig. 5.131 Configuration of the three-component DGV optical system in the NASA Ames 40×80 foot NFAC to measure the flow from a high-speed jet

A research program at ThermoTrex Corporation used various elements (cesium, potassium, and rubidium) to obtain optical frequency-to-intensity conversions that led to the development of a unique long-focal-length approach, *Kremer* et al. [5.486] and *Bloom* et al. [5.487]. One of the systems used potassium in a Faraday-cell configuration where polarization rotation was used to establish the transfer function instead of using optical energy absorption. This accomplished a factor of two increase in dynamic range, but required the use of an Alexandrite laser operating at 770 nm. This pulsed system was successful in measuring the line-of-sight velocity profile of the flow about a helicopter rotor at ranges exceeding 400 m with a measurement uncertainty of 0.6 m/s.

The ability to measure the flow velocity without resolving individual seeding particles made this technology attractive for the measurement of very high-speed flows. Research at Princeton University led to the development of filtered Rayleigh-scattering techniques that were able to measure supersonic/hypersonic flows using molecular scattering, *Miles* et al. [5.488], and *Forkey*

et al. [5.472, 489]. They used a *dense* iodine vapor cell that yielded a nearly step-function response to view Doppler frequency contours as the optical frequency of the pulsed Nd:YAG laser was tuned. Conventional DGV approaches were used at NASA Langley by *Meyers* [5.478] – argon, and *Smith* et al. [5.490] and *Smith* [5.491] – Nd:YAG, Ohio State University by *Elliott* et al. [5.492] and *Clancy* et al. [5.493] – Nd:YAG, and Oxford University by *Quinlan* et al. [5.494] to investigate flows about models and in high-speed jets.

The engine measurement techniques research group of the Institute of Propulsion Technology at the DLR Research Center Köln-Porz has developed DGV systems to measure various internal flows. Applications have included jet inlet, turbine, combustor, internal combustion engine, and engine exhaust flow fields along with measurements of sprays and flames by *Röhle* and *Schodl* [5.495], *Röhle* [5.496], *Röhle* et al. [5.497], *Willert* et al. [5.498], and *Fischer* et al. [5.499]. Example results from flow measurements inside a cold combustion chamber are shown in Fig. 5.133.

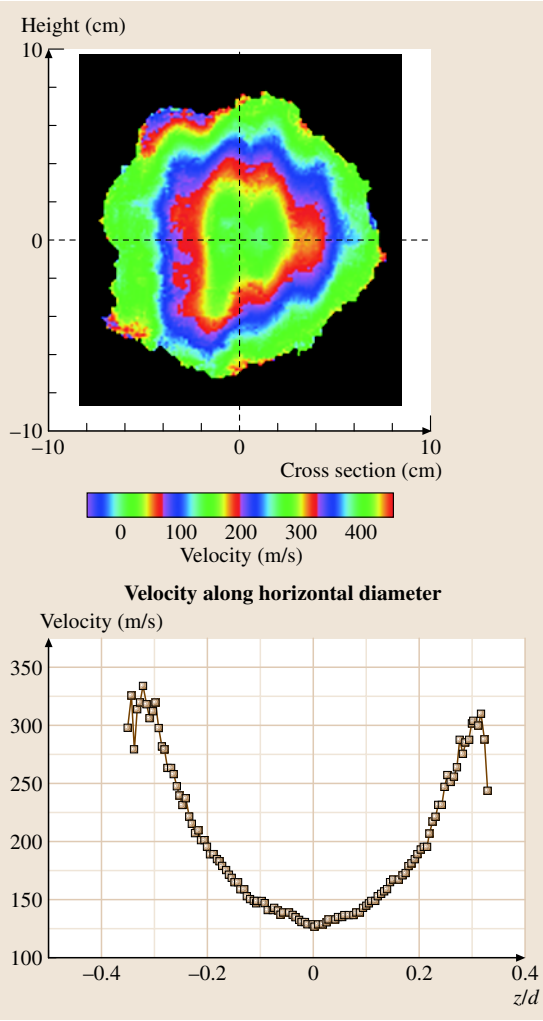

Fig. 5.132 Resolved streamwise component of velocity from the high-speed jet flow operating at 463 °C at a freestream Mach number of 0.15

A unique modification to a standard DGV configuration was developed at Cranfield University in England. *Nobes* et al. [5.500] adapted fiber-optic imaging bundles to provide three-component flow measurements along with laser frequency measurements using a single iodine vapor cell and only a pair of cameras. This approach greatly reduced system cost and complexity. It also lowered measurement uncertainty since a single iodine vapor cell could be used for all three components and the LFM function. The only disadvantage appeared to be image blurring caused by the edges of the individual fibers that limited the effective measurement spatial resolution. This approach was used by *Willert* et al. [5.501] of DLR Köln to obtain the first three-component measurements in a large cryogenic wind tunnel.

The ability to accept scattered light from multiple particles was exploited by *Kuhlman* et al. [5.502, 503] and *Kuhlman* and *Collins* [5.504] at West Virginia University, and *Crafton* et al. [5.505] at Purdue University through the development of point measurement configurations. The goal was to determine if the technology would provide continuous temporal measurements that could be interrogated for turbulence intensity and power spectral measurements. The results indicated a strong potential for measurements with better accuracy than can be obtained with fringe-type laser velocimetry.

The final category addressed is hybrid configurations that combine DGV technology with other techniques to produce systems with unique characteristics. An innovative hybrid was developed by *Förster* et al. [5.506] at DLR Köln that used DGV technology to obtain the third component in a modified laser transit anemometer system. The resulting system provided three-component point measurements within turbomachinery using a single optical access port. Taking the approach a step further, *Wernet* [5.507] from the NASA Glenn Research Center combined DGV technology with particle image velocimetry to produce a system capable of measuring three-component flow fields with a single viewing port. This work was directed toward turbomachinery and engine applications.

System Design, Calibration, and Potential Error Sources

Although the fundamental physics for molecular-filter-based laser velocimetry has been presented along with example systems/applications to illustrate the breadth of this technology, the insight needed to develop a usable system would be difficult to obtain from this information. The purpose of this section is to highlight physics/equipment anomalies and how system design, calibration procedures, and software processing techniques can minimize the effects of the anomalies. The predicted quality of the measurements can be determined through an error analysis of a system based on an iodine vapor cell with argon-ion/frequency-doubled Nd:YAG laser sources. Although specific to DGV, many of the characteristics that will be analyzed here are common to point-based systems and systems using other molecular-filter/laser combinations.

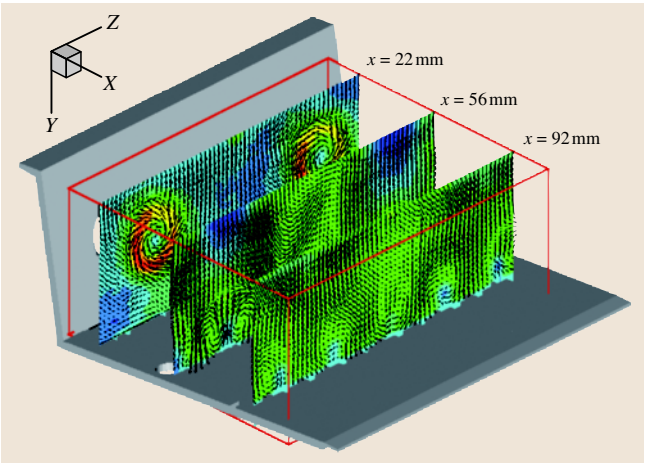

Fig. 5.133 Measurements in a double-staged isothermal combustion chamber by DLR, Köln (after *Röhle* et al. [5.497])

Laser. The search for sources of measurement uncertainty begins with the laser and the quality of its output. The laser characteristics described in the *Basic Principles* section pertain to single-frequency outputs that can be tuned to the midpoint along the edge of an iodine absorption line. The most common lasers that satisfy these requirements are continuous-wave (CW) argon-ion lasers operating at 514.5 nm, and pulsed, injection-seeded, frequency-doubled Nd:YAG lasers operating at 532 nm. It is noted that currently available continuous-wave frequency-doubled Nd:YAG lasers cannot be easily tuned and have frequency drifts of several MHz/min, and thus are not suitable. Furthermore, all lasers must be environmentally protected as any changes in ambient temperature or pressure, or vibrations in mounting structure(s) will cause them to become unstable, producing multimode operation or even cessation of lasing.

Single frequency operation is obtained in the argon-ion laser by placing a temperature-controlled etalon within the laser cavity. The etalon forms a second resonator that, if tuned to one of the resonant frequencies supported by the laser cavity, isolates a single longitudinal mode for amplification. The etalon resonant frequency is tuned by changing its temperature or by mechanically tilting it – both methods change the effective etalon thickness. The dependence of the index of refraction of the media and the component thickness on the environmental temperature results in frequency drift of the two resonant frequencies. This will reduce the laser output power as the two resonant points misalign, which may cause the output frequency to oscillate between two adjacent longitudinal modes before *hopping* to the next mode. Typically, the drift originates from the laser cavity since the etalon is normally enclosed in a temperature-controlled oven. The most efficient method to eliminate this drift is through an active feedback control system using the laser frequency measurements from the LFM as an input to control a piezoelectric transducer that actively positions a cavity mirror [5.506] to compensate for environmentally induced changes in cavity length.

The use of an injection seed laser makes it possible to operate a pulsed, frequency-doubled Nd:YAG laser in single-frequency mode. This laser-diode-pumped seed laser emits a low-power, single-frequency continuous-wave beam that is directed onto the primary laser cavity axis, thus providing a stimulating source when the primary laser is pulsed. In this manner, the primary laser acts as an amplifier of the single-frequency beam from the seed laser, thus maintaining its optical frequency characteristics. Adjusting the temperature of the seed laser will change the length of its Nd:YAG rod and thus the output frequency. The tunable range is approximately 20 GHz (an order of magnitude greater than with an argon) with a minimal loss of laser energy over multimode operation (the etalon in the argon laser reduces the output power by 50%). The main laser cavity resonant frequency is adjusted through a feedback-driven piezoelectric transducer mounted to the fully reflective mirror. The control function is derived from the measurement of the Q-switch build-up time – the shorter the time, the better the frequency overlap between the seed laser and the host, which improves single-frequency operation. The piezoelectric transducer is normally dithered to bracket

any changes in the resonant frequency caused by thermal expansion/contraction of the main cavity. Pulse-to-pulse optical frequency variations can be as large as 70 MHz, requiring the measurement of each pulse frequency with the LFM. In addition, the optical frequency is not homogeneous throughout the laser beam cross section. Unlike a gas laser whose media index of refraction in the laser cavity is virtually the same as air, a Nd:YAG laser rod has a much larger index of refraction. Thus any microscopic variation in rod length caused by fabrication or temperature variations will effectively change the laser cavity length over the cross section, yielding a resonant frequency distribution. The theoretical distribution, based on manufacturer rod face flatness and parallelism specifications, was determined to be approximately 100 MHz, a similar range to that found experimentally. The simplest method to eliminate this error source is to obtain a wind-off measurement of optical frequency with the DGV system. The resulting mean-removed frequency image represents the variation caused by the laser. This *frequency flat field* is simply subtracted from the acquired Doppler frequency measurements to yield the unbiased images.

The laser output must be monitored to insure single-frequency operation. An optical spectrum analyzer placed in the LFM can provide a real-time reading of the optical frequency spectra of an argon-ion laser. If a clean single frequency is not found, the laser should be adjusted to reestablish a single frequency. Measurement of the Q-switch build-up time in a Nd:YAG laser provides a parameter indicating single-frequency operation. The build-up time can be determined by measuring the time between the Q-switch trigger and the occurrence of the optical pulse. When the laser is operating in single-frequency mode, this build-up time is minimized.

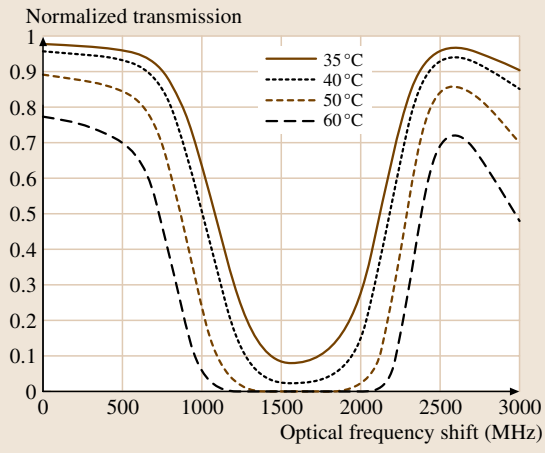

Fig. 5.134 Theoretical iodine vapor absorption line profiles as a function of cold finger temperature

Iodine Vapor Cell. The absorption of light by iodine vapor is based on the temperature-dependent shape of the selected absorption line. While the location of the optical frequency at the center of a given absorption line is fixed by the atomic characteristics of iodine, the depth and width of that line are dependent on the number of iodine molecules in the optical path. For a fixed cell length the number of molecules in vapor state, and thus the line shape, is dependent on the temperature of the coldest point within the cell (Fig. 5.134). Typically the cell body is held at a high temperature and a narrow stem extending from the body is kept at a tightly controlled lower temperature – thus defining the iodine vapor pressure. While this method is acceptable for spectroscopy applications, a variation of $\pm 0.1\,^{\circ}\mathrm{C}$ of the control temperature represents a ± 3 m/s velocity uncertainty in DGV measurements. Additionally, the inability to isolate the cells completely from hostile wind-tunnel environments results in large variations in line shape because of the inherent slow response of a heating/cooling system to counteract ambient temperature changes. This is the reason for the lack of quantitative velocity measurements in early wind-tunnel applications of the technology.

The solution to the inability to control cell temperature was the construction of a vapor-limited or starved cell [5.479, 484]. After a standard iodine vapor cell has been constructed, the desired vapor pressure is set using the above approach. Once the internal pressure has stabilized, the stem is sealed at the cell body to separate excess crystalline iodine from the cell. Setting the cell to any temperature at or above the original stem temperature yields a constant cell vapor pressure since all iodine molecules will be in the vapor state once the original stem temperature is reached. Elevating the cell temperature, for example an additional 20 °C, provides a buffer to account for the slow response of the temperature controllers to any change in environmental temperature, and maintain a constant optical frequency-to-intensity transfer function.

Optical Components: Transmitter. The creation of a laser light sheet normally involves simply placing a cylindrical-lens system in the laser beam. However, the Gaussian and approximate Gaussian power distributions found in argon-ion and pulsed Nd:YAG lasers, respectively, can produce detector saturation due to the high-intensity scattered light from the optical axis, yet

be undetectable away from the axis. Additionally, the diameter of the laser beam can produce a thick light sheet that will lessen the common volume viewed by the three receivers, potentially introducing velocity errors in areas with large velocity gradients. Thus the area viewed should be set to the half-power limits of the light sheet along with focusing the sheet thickness at the center of the viewing area. If average velocity measurements are acceptable, slowly scanning an argon beam along with on-camera integration will yield good results, as the light sheet will then have a flat intensity distribution. Note, however, that rapid scanning can impose an apparent Doppler frequency shift in the measurements.

Optical Components: Receiver. The receiver optical system, shown in Fig. 5.130b, is fairly simple. However, attention must be given to the characteristics of the optical component or significant measurement errors may occur. The first element reached by the scattered light is the beam splitter. The transmission/reflection ratio is dependent on the input light polarization in all beam splitters, including the so-called nonpolarizing variety. This is significant since the polarization of light scattered by small particles is dependent on particle size, scattering angle and to a lesser extent index of refraction. Thus any differences in input polarization, e.g., calibration setup, variations in particle size distribution, etc., will change the transmission/reflection ratio imposed by the beam splitter, and effectively rescale the system transfer function in an unknown manner. Additionally, spatially dependent transfer function variations caused by any optical element, e.g., dirt, fingerprints, interference fringes, etc., will result in local deviations in the system transfer function. These effects can be greatly reduced or eliminated by operating the system normally with particle scatter, but with the laser frequency adjusted so that all optical frequencies are outside any absorption lines. The resulting reference images are normalized by the signal images to yield the *intensity flat field*. The laser frequency is then tuned to the desired location along the absorption line and data acquired. Resultant normalized signal images are then multiplied by the intensity flat field, thus negating all polarization (assuming the particle size distribution has not changed) and spatially dependent optical transmission effects.

Other suggestions regarding the optics include the use of a cube-type beam splitter, a cold-welded iodine vapor cell, and green photographic filters placed on the cameras. Typically beam splitter plates are used to divide incoming light into two optical paths. These plates have a partially reflective coating on the input side and an antireflective coating on the other. Thin plates should be avoided as they may be physically distorted by the mounting hardware, leading to a degradation of image quality. Beam splitter plates have exhibited the property of softening/blurring the transmitted image, producing artifacts in the normalized results. Thus, beam splitter cubes are recommended since they do not exhibit this characteristic. Aligning the iodine vapor cell along the signal leg optical axis can produce fringes from the interference of scattered light from cell window surfaces. These fringes are typically circular, as the low pressure within the cell will pull the centers of the windows inward. Further, hot welding the windows to the cylinder body will induce heat stress in the windows producing additional optical distortions. Cold welding the windows to the cylinder body and misaligning the iodine vapor cell a few degrees from the optical axis will greatly reduce or eliminate these optical distortions. Placing photographic green filters on the cameras attenuates contributions from other light sources, e.g., room lights, combustion products, etc., without greatly affecting the collected scattered light intensity. The filters will not eliminate contributions from these sources, but will help since any background light energy acquired will decrease the effective dynamic range of the cameras.

Optical Components: Cameras. Camera requirements are dependent on specific techniques and applications, thus the choice of camera is difficult to specify in a generic sense. The following factors should be considered:

- Spatial resolution/image size
- Imaging rate
- Pixel-well depth/amplitude resolution
- Overall signal-to-noise ratio
- Image integration/shutter control
- CW or pulsed laser applications
- Working focal distance
- Background light/environment
- External triggering/synchronization capabilities.

In general the camera/detector system must be linear with a repeatable optical intensity-to-voltage calibration since amplitude is the measured parameter. In multiple-camera configurations, all cameras must be externally synchronized using the same synchronization waveform, precluding a master/slave approach since image acquisition must be simultaneous over exactly the same time period. Overall a cooled CCD sensor with at least a 12 bit onboard digital conversion capability and a controllable electronic shutter is recommended. However,

this may be more camera than is needed for a given experiment – RS-170-type cameras may be acceptable. In any case, it is advisable to measure the overall camera signal-to-noise ratio using the method outlined by *Meyers* et al. [5.479] since the signal-to-noise ratio quoted by camera manufacturers is typically based only on electronic noise, which is not necessarily sufficient for DGV applications.

Facility and Model. All surfaces that will scatter laser light should be painted either flat black or red (if a green photographic filter is used) to reduce spurious light sheets or flare. A light sheet impinging on any surface (including antireflective-coated windows once they become coated with dirt or particles) will produce some flare, which limits measurements to several millimeters above the surface. If on-surface measurements are desired, light should originate from under the surface. Treating surfaces will have the added benefit of reducing the secondary scatter caused by surface–particles–detector and particles–surface–detector paths. This source of background light can not be eliminated and will affect measurement accuracy as the Doppler shift imposed on this secondary scattered light will not be the same as the scattered light from particles passing through the light sheet [5.495].

Facility configuration must also be considered. If the opposing facility wall has a window that is not antireflective coated and the light sheet reflection cannot be directed outside all camera views, it should be orthogonal to the window, making the reflected light sheet coplanar with the original. As with any spurious light sheet, a measurement error will occur, as the additional scattered light from this sheet can not be eliminated. However, since it is coplanar, each measurement vector and its contribution can be estimated based on Mie scattering, if the particle size distribution is known.

Flow Seeding. Typically a flow measurement application using molecular filter velocimetry will involve

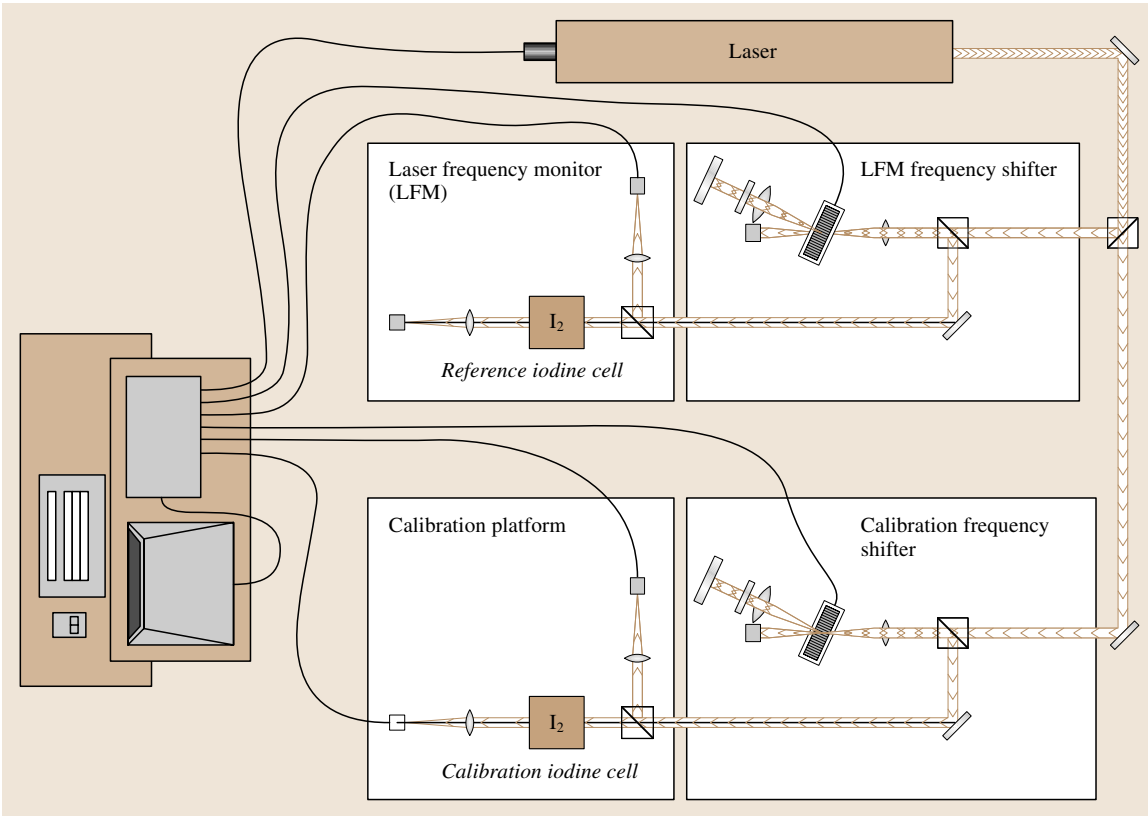

Fig. 5.135 Iodine vapor cell calibration layout using tunable Bragg cells; tuning range: 420–660 MHz, laser mode spacing: 129 MHz

seeding the flow with small particles. Particle generation techniques normally used for fringe-type laser velocimetry and PIV, such as Laskin nozzles, liquid sprays with embedded polystyrene latex, etc., typically have limited particle number densities when the plume is expanded to fill large laser light sheets. In addition, these particles tend to be fairly large and may not follow the flow with the desired fidelity. Smoke generators, such as theatrical foggers and smoke simulators used to train firefighters, will provide sufficient number densities. Care must be used if theatrical foggers are chosen as they typically generate size distributions that have extremely long tails, upwards of 20–50 μm. The recommended generator is the smoke simulator, as this device will produce 0.2–0.7 μm mineral oil particles in number densities controllable by the generator. The output can range from a barely visible wisp, to a cloud capable of filling the NASA Langley 14×22 foot subsonic tunnel in a few minutes. If testing in a supersonic flow, water condensation is a good choice as the particle size is extremely small and particles will completely fill the flow field. The presence of water, however, will affect the flow properties to a minor extent.

System Calibration: Iodine Vapor Cell. Determining an accurate optical frequency-to-transmissivity transfer function for the iodine vapor cell (IVC) is critical to the overall accuracy of DGV measurements. Example calibration procedures are outlined below.

1. Laser tuning – The output laser frequency is changed by mode-hopping (argon) or adjusting the seed laser temperature (Nd:YAG) and tracking the transfer function. This technique assumes that the change in laser frequency is a linear function of the adjustment. Through experimentation it has been determined that this approach does not provide the accuracy required for DGV applications and thus is not recommended.
2. Measuring the Doppler frequency of a rotating wheel – The IVC is placed in a DGV system that is configured to measure velocity in a single plane. The Doppler frequency profile across the wheel can be predicted from distance and rotational speed measurements. By having a Doppler shift range greater than the laser resonator frequency, the profiles may be overlapped to produce a transfer function that does not depend on knowing the absolute laser or mode hop frequencies. This approach is recommended.
3. Bragg cell frequency shift – The best accuracy has been obtained using a pair of tunable Bragg cells to change the input frequency by known amounts at each laser longitudinal mode, Fig. 5.135. The results have yielded standard deviations about a B-spline curve fit of less than 0.2% full scale. This technique is highly recommended.

Image Distortion. The determination and correction of perspective and other distortions is necessary to insure accurate overlap of the signal and reference camera images. Furthermore, accurate overlap is required to align multiple image pairs to determine standard Cartesian velocity component measurements. Standard 2-D polynomial dewarping methods using single equations to adjust an image do not account for high-spatial-frequency distortions typically present in windows and optical components. Thus a piecewise method must be used to insure accurate overlap between the camera images. Using a piecewise bilinear warping procedure [5.478], a distorted fiber optic view of a dot card target can be corrected (Fig. 5.136).

Intensity Flat Field. The intensity flat field is the amplitude calibration between the signal and reference camera images. The correction accomplishes two tasks:

1. it determines the overall beam splitter division of collected scattered light as affected by the polarization characteristics of the scattering media; and,
2. it determines any higher spatial frequency variations in the optical transfer function, e.g., dirt, interference fringes.

The intensity flat field should be obtained by acquiring a normal data image with the laser and all Doppler-shifted frequencies located outside all absorption lines.

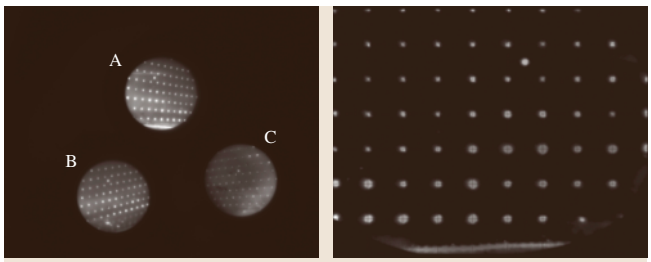

Camera view of three imaging fibres | Dewarped image of fiber A

Internal fiber bundle diameter: 0.5 mm (30 000 fibers), dot spacing 25 mm

Fig. 5.136 Image dewarping of a dot card spatial alignment target viewed by three fiber-optic imaging systems: piecewise bilinear method

Frequency Flat Field (Crystal-Based Lasers). Crystal-based lasers, such as Nd:YAG, have a distribution of optical frequencies over the output beam cross section. This distribution is caused by microscopic variations in rod length that change the effective length of the optical cavity based on the rod index of refraction and the spatial distribution of rod length. Typically, 10 arc s of parallelism and a flatness of $\lambda/10$ can yield optical frequency variations of up to 100 MHz. The distribution of optical frequencies can be measured by obtaining Doppler frequency maps under wind-off conditions. An intensity flat field should also be taken to account for any particle size changes between wind-on and wind-off conditions. The measured frequency distribution is then subtracted from the Doppler frequency maps of the flow to negate these frequency variations.

Application Sequence

Continuing with the example of using DGV to measure a flow field, the following data-acquisition and data-processing sequence is suggested. Other molecular filter velocimetry techniques and measurement applications have a similar operating sequence.

Data Acquisition.

Image Alignment. An alignment target is placed in the measurement plane and data images acquired. A target composed of a rectangular pattern of equally spaced dots is suggested, as individual dot centroid locations are more easily and accurately determined than the intersection of lines. Further, the determination of piecewise dewarping coefficients based on the centroid locations will increase spatial accuracy of the overlaid images. Using a back-illuminated perforated panel of millimeter-sized holes with small spatial separations as the alignment target may increase this accuracy further. The resulting image would be a *star* field where centroids may be more-accurately determined using the greater contrast of bright spots on a dark background (the same principle used in particle image velocimetry).

Background Images. A background data set should be acquired with all components having the same settings that would be used when acquiring velocity data – except no particles are injected. The background contains contributions from all light sources, e.g., room lights, laser flare from walls, and models. The background image levels can then be subtracted from the data images to eliminate these sources. Secondary scattering [5.495] however, can not be eliminated, thus procedures must be implemented to eliminate or minimize any extraneous laser light.

Frequency Flat Field Images (Crystal-Based Lasers Only). Inject particles into the laser light sheet without a measurable flow to determine the laser-induced optical frequency distribution. The resulting optical frequency measurement images should be subtracted from the Doppler frequency images obtained from the flow measurements to eliminate these frequency variations. Note: a separate intensity flat field image set should be obtained as the particle scattering characteristics may not be the same as during the acquisition of flow measurements.

Intensity Flat Field Images. The facility should be operating at the desired conditions for the flow measurements and the seeding particles injected into the flow. The laser should then be frequency tuned to place all optical frequencies outside of the absorption line (insure that an adjacent line is not entered). An alternate method for crystal-based lasers is to operate the laser multimode. The resulting normalized images represent the transfer function of the optical system without the effects of the iodine vapor. The normalized images obtained from the flow measurements should be multiplied by this transfer function to eliminate the spatially dependent influences of the optical elements.

Flow Measurement Images. Measurement accuracy is strongly dependent on the amplitude and spatial distribution of the collected scattered light in the data images. Higher measured amplitudes will lower the significance of noise sources, such as photon, electronic, and quantizing noise. The more uniform the flow seeding, the lower the effect that minor spatial *misalignments* of the signal image with the reference image will have on the accuracy of the normalization process. The signal amplitude can be effectively increased in CCD detectors by allowing them to integrate the incoming collected scattered light over a time period needed to charge the capacitors to a high level [5.495–497]. Integration has the added benefit of averaging laser speckle noise along with any motion of the particle stream that would reduce spatial amplitude gradients at the stream boundary [5.479]. If integration is used, whether on the detector or in the computer, electronic noise becomes more significant. Thus a cooled camera should be used to lower these noise levels. This approach also limits DGV to average or phase-locked measurements – instantaneous measurements have the potential for too great a level

of measurement uncertainty even when a high-power, pulsed laser is used. It is noted, however, that point measurement configurations using photomultipliers as detectors in conjunction with high-speed digitizers can be used for temporal measurements. These detectors are far more sensitive and have lower noise levels than cameras.

Data Monitoring. Unlike fringe-type laser velocimetry or particle image velocimetry, molecular filtered velocimetry does not have a definitive parameter that determines if a measurement is acceptable in real time. The sensitivity of the technology to single-frequency stability of the laser, uniformity of seeding, and signal strength minimums require constant monitoring of many parameters. In addition, sample data should be processed in near real time to determine if the velocity measurements are reasonable, and as an indicator of potential problems.

Summary

Molecular filter velocimetry has characteristics that make the technique advantageous for many fluid-mechanical investigations. These include high-speed flows, highly three-dimensional flows, cyclic flows, flows with a large dynamic range in velocity, and for the specific case of point Doppler velocimetry, temporal measurements such as turbulence power spectra. From an installation viewpoint, these techniques provide long focal distance, large measurement area capabilities and, through the use of fiber optics, measurements of internal flows in confined structures.

As with any measurement technique, however, there are limitations. The technique requires careful monitoring of the laser and components, heavier seeding than other laser-based methods, and no in situ indicators that the measurements will be accurate. Additionally, since the measurement accuracy is an absolute value, low-speed flow measurements may not be as accurate as other methods. Finally, although instantaneous measurements can be obtained, their use for turbulence statistics would require great care to insure minimal error.

5.3.5 Laser Transit Velocimetry

This section starts with a short overview of the history of the development of laser transit velocimetry (LTV) also known as laser two-focus velocimetry (L2F). The advantageous properties of LTV that qualify this technique for high-speed and turbomachinery flows and for near-wall measurement applications are explained. The fundamentals are then treated, describing the general principal, the statistical data evaluation and the prospects for the measurement of turbulence statistics. Next, a state-of-the-art LTV system is considered, presenting details about the optical setup, the measurement procedure and the data-processing and evaluation methods. Subsequently, three-component LTV techniques are treated with the main emphasis being placed on the recently developed three-component Doppler-L2F velocimeter. In this hybrid system the L2F principle is combined with a Doppler-frequency shift analysis by which the velocity component in the direction of the optical axis is determined. The unique measurement system is described in detail and examples of applications are presented.

In 1968, very soon after the laser Doppler (LD) method became known, an alternative optical flow velocity measuring method was introduced by *Thompson* [5.508]. This method, referred to as the *tracer particle fluid velocimetry*, was the forerunner of the kind of optical measuring devices known today as laser transit (LT) or laser two-focus (L2F) velocimeters. The idea was to measure the time of flight of tracer particles carried with the fluid passing through two separated, parallel, highly focused laser beams (Fig. 5.137). When Thompson compared his method with the known LD method, he saw the advantages of a simpler optical setup, simpler data processing, and the employment of lower-power lasers to detect the scattered light of the small tracer particles.

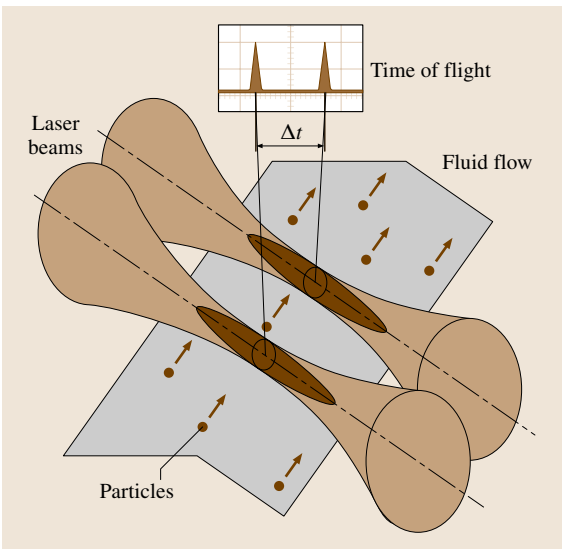

Fig. 5.137 Time-of-flight velocimeter probe volume

In Thompson's system the two beams in the probe volume had a waist diameter d of 40 µm and a separation s of a few millimeters. Photomultipliers adjusted to the probe volume generate pulse-type signals when detecting the scattered light of particles crossing the laser beams. An oscilloscope internally triggered by the photomultipliers' voltage pulses was used for the time-of-flight measurements. However, successful measurements could only be obtained when the orientation of the plane containing the two beams was adjusted parallel to the mean flow direction. In this case the probability of successful dual beam transits of the particles attains its maximum value. Under these conditions multiple traces integrated on the oscilloscope screen show two bright, pulse-type signals, one on the left side of the screen, which starts the oscilloscope trace and a second one separated from the first by $\overline{\Delta t}$ indicating the successful time-of-flight measurements (Fig. 5.138). Due to the integration the detected value $\overline{\Delta t}$ represents the mean value of the time-of-flight measurements, which together with the known separation s of the beams provides the magnitude of the mean flow velocity component perpendicular to the beams

$$\overline{u}_{\perp} = \frac{s}{\overline{\Delta t}} \,. \tag{5.296}$$

Knowing the orientation $\overline{\alpha}$ of the plane containing the two beams the mean velocity vector components $\overline{\alpha}$ and $\overline{u}_{\perp}$ in the plane perpendicular to the beam axis are determined.

The brightness of the second signal on the oscilloscope screen is a measure of the probability of successful dual-beam crossings. The level of brightness reaches its maximum value when the angle α of the beam's plane is correctly adjusted to the mean flow direction.

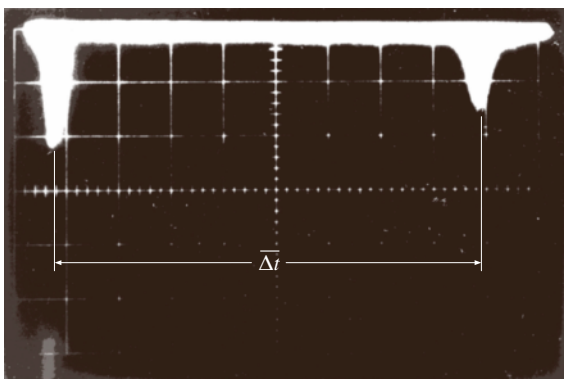

Fig. 5.138 Time-of-flight signals superimposed on an oscilloscope

The detectability of the second signal and the adjustment of the beam's plane is quite easy in flows of low turbulence intensities where the flow direction is very uniform. However, in cases where the flow turbulence intensity increases and exceeds values of about 10%, detectability of the second signal disappears almost completely, rendering this time-of-flight measuring method inapplicable.

Due to this limitation Thompson's method did not achieve much importance. Only a few authors [5.509, 510] followed his proposal and applied similar optical setups to flows where the turbulence intensities were low, the mean flow direction was well predictable and the beams plane could be set to a fixed orientation.

Then in 1973 a paper was published [5.511] describing how this laser transit velocimetry technique could also be operated in turbulent flows. It showed how the collected data could be processed to determine the two components of the mean flow velocity, turbulence intensities, Reynolds shear stresses, and also higher-order moments of the fluctuating velocity quantities.

This knowledge about its applicability to turbulent flows changed matters dramatically and, as of that point in time, this technique underwent rapid development.

While the optical arrangements proposed have not undergone significant modifications, considerable development has taken place on the signal-processing electronics. Two different development directions were initiated. One group of researchers [5.510, 512–521] applied correlators and photon correlators and a second group used time-of-flight measurements and statistical data analysis [5.522–536]. Theoretically the correlation analysis should be the superior technique, especially at high data rates (< 200 kHz), but this superiority has not been proved in practice to date where the data rate is comparatively low (< 20 kHz). As can be shown [5.520, 528, 537] under these conditions there is complete agreement between the measured cross correlogram and the time-of-flight histogram. Because of its availability in the area of nuclear physics and its simplicity the time-of-flight measurement method has attained much more importance. This technique is therefore treated in this article. The output of both techniques, either the correlogram or the histogram requires further data processing.

Many authors have theoretically analyzed the LT measurement method in detail [5.510, 512, 513, 515, 520, 521, 523, 525, 526, 531, 538–544]. Most of the main error sources are known today and they can be estimated quantitatively as a function of the probe volume geometry.

Over the years LT velocimetry has gained importance in the experimental fluid flow analysis. Due to its high signal-to-noise level resulting from the highly focused laser beams LT velocimetry extends the range of applicability of LD systems and can therefore be considered a supplementary method.

Its specific fields of application are: high-speed flows, applications with limited optical access where backscatter arrangements with low signal level are required, and applications in narrow flow channels, where background flare reduction is important. Apart from these positive features the LT velocimetry technique is in practice limited to applications in flows with turbulence intensities smaller than 30%, and hence cannot be applied in, e.g., combusting and mixing flows, where the turbulence intensities by far exceed this value.

Several LT systems are on the market and some industrial and research organizations have built their own system for in-house use. LT velocimetry has been successfully applied to long-range wind speed analysis, heat exchangers, wet steam flows, water pumps, diesel engines, plasma flows, and standard and cascade wind tunnels. Nevertheless the LT velocimetry has found its widest application in the field of turbomachinery flow investigation. Numerous papers have been published producing results of measurements in centrifugal and axial compressors as well as turbines. A rather complete overview is given in [5.532, 540]. These detailed LT velocimetry data have contributed a great deal to our improved understanding of turbomachinery internal flow. This is especially true with regard to rotor flow investigations, which are almost inaccessible for conventional measuring techniques. The comparison with theoretical data has resulted in improved mathematical models and design procedures.

Laser Transit Velocimetry Applied to Turbulent Flows

In turbulent flows the velocity vector at any location is considered as a random variable, which under stationary conditions can be described by a three-dimensional probability density function that depends generally on all three components of the velocity vector. As the LT velocimeter as well as the usual two-component LD systems are only capable of measuring the velocity components in the plane perpendicular to the optical axis, in the ideal case the measured data can only approach the two-dimensional probability density function, which can be derived from the three-dimensional function by integration over the on-axis velocity component. To be able to perform this integration, both systems must also be capable of detecting the respective velocity components from such flow vectors that have a significant on-axis component. Therefore the axial length of the probe volumes must be long enough. Since this requirement can often not be fulfilled sufficiently in practice the systems with a limited integration range require a roughly perpendicular alignment of the optical axis with respect to the expected mean flow velocity. Assuming that the LT velocimeter can be operated in such a way that the measured data can be approached by a two-dimensional probability density function, the mean values of any velocity function defined in the plane perpendicular to the optical axis, e.g., the mean velocity components, turbulence intensities, and Reynolds shear stresses, can be deduced [5.532].

Let us consider a typical LT velocimeter probe volume, as shown in Fig. 5.139. The beams waist diameter d is about 10 µm, the beam separation s is about 0.2–0.4 mm. The plane containing the two beams – the plane of beams – is rotatable and its angular position is indicated by the value α. Two photomultipliers are adjusted to the beams and deliver the start and stop signal for the time-of-flight measurements. Due to the given ratio of beam diameter and separation a certain angular capture range $\Delta\alpha$ is defined, within which particles can move and cross the two beams. When at a location in a turbulent flow the beam's plane is adjusted to a certain angle α; within the rather wide angular range of fluctuating flow directions only those particles that move along the plane within the range $\Delta\alpha$ can pass through both the beams and deliver two successive scattered light pulses. The time elapsed between the pulses yields the component of the particle velocity perpendicular to the optical axis.

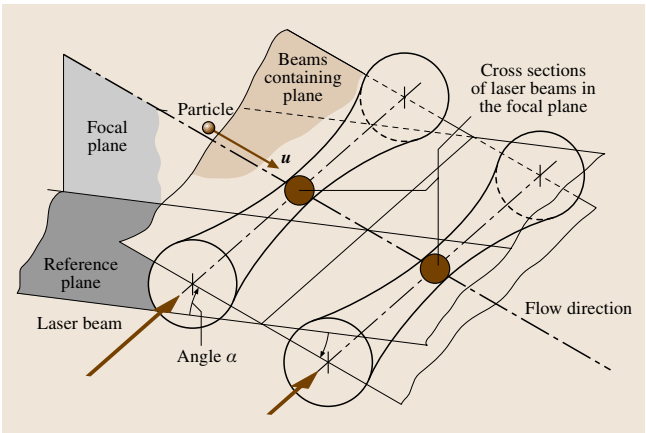

Fig. 5.139 LT velocimeter probe volume

When particles move outside this small angular range $\Delta\alpha$, they may still start a time measurement but then either there will be no stop signal within the preselected time range or a different particle will stop the measurement, hence generating incorrect measurements.

To distinguish between correct and incorrect time-of-flight measurements many measurements at the chosen position of the plane of beams are necessary. In Fig. 5.140, as an example, a probability histogram of such collected data is plotted. Due to its random distribution the incorrect measurements are represented by the baseline of nearly constant frequency level. The net distribution, which exceeds the baseline frequency, is shaped like a Gaussian curve and represents the correct time-of-flight measurements. The necessity of collecting multiple measurement events is not a real drawback since the statistical analysis in any case requires a large number of data, which determines the measurement accuracy.

By setting the plane containing the beams to other, slightly different, angles and by accumulating time-of-flight data until the preset number of started measurement events has been achieved, more velocity histograms can be constructed. This is possible as long as the chosen angles of the plane are within the range of the velocity angle fluctuations of the turbulent flow. The result of this measurement procedure is a two-dimensional probability histogram (Fig. 5.141) as a function of time-of-flight and angle settings. These data are the input data for a rather sophisticated evaluation procedure, based on nonlinear regression fits of an ideal probability density function of the flow velocity to the measured histogram [5.540, 541]. Mean values of the velocity components and turbulence intensities are the typical output, but Reynolds shear stresses and higher-order moments can also be computed.

The accuracy is mainly determined by the number of collected data, the background noise resulting from laser light reflection from surfaces in the vicinity of the probe volume, the flow turbulence, and the selected beam separation. In the case of low turbulence intensities ($< 5\%$) the accuracy of the velocity magnitude and angle determination is very high (measurement error $< 1\%$ of the flow magnitude and less than $0.2°$ of the flow angle), better than can be achieved by LDA systems, although the measurement error increases with flow turbulence. When turbulence intensities exceed 30% the LT velocimeter is practically not applicable because of difficulties in distinguishing between correct and incorrect measurement events.

Optics

The schematic assembly of the LT velocimeter that pioneered the first application in turbulent flows [5.511] is shown in Fig. 5.142. An argon laser was used as a light source. The linear polarized laser beam was transformed by a quarter-wave plate into circular polarization. In this way the following rotatable Rochon prism splits the laser beam into two beams of different linear polarization but

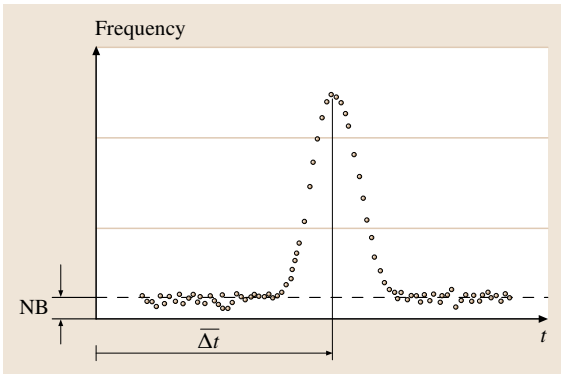

Fig. 5.140 Time-of-flight data histogram collected at a given setting of the plane of beams (incorrect measurements are indicated by the noise band NB)

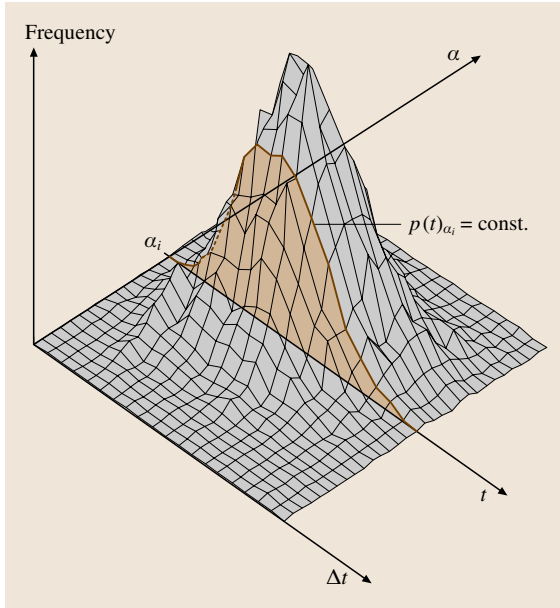

Fig. 5.141 Two-dimensional histogram of measured time-of-flight data collected at different angle α settings of the plane of beams

of equal intensity, independent of the angular position of the Rochon prism. One output beam follows the direction of the incident laser beam while the other is deflected from that direction by an angle δ (compare detail A).

As the focal point of the following lens L1 is located at the point of division, both beams leave the lens parallel to each other and are focused in the second focal plane.

The two beams are then relayed by the inner part of lens L2 to the measuring volume, which is to be placed in the selected measuring position in a flow field (e.g., in a wind tunnel) (compare detail B).

Particles that traverse the beams in this area each emit scattering light pulses and the part which is scattered back is detected by the outer area of lens L2 and sent via a spatial filtering device to two photodetectors, each assigned to a beam in the measuring volume.

The spatial filtering device serves to keep the background radiation, which arises in narrow channels as a result of reflection of the laser beams off the channel walls, to a minimum. The use of microscope optics makes the spatial filtering very effective. Due to the enlargement the two very small backscattered beams can be adjusted very precisely to the two holes of the aperture.

This optical setup for two-component measurements has not changed significantly over the years as its optical design was already rather optimized. It was rather emerging technologies such as fibres and laser diodes that initiated the development of improved LT systems, which were easier and more reliable to handle and operate [5.540].

Electronics

When the photomultipliers detect the scattered light pulses from particles crossing the assigned laser beam in the probe volume, voltage output pulses are generated. To compensate for losses in the signal transfer chain (Fig. 5.143) the photomultiplier output signal must first be amplified. Fast amplifiers are required as, especially at high velocities, the scattered light pulses become very short – pulse widths of only a few nanoseconds.

Depending on the velocity and the size of the particles and the position where they cross the beams the amplitude of the scattered light pulse varies greatly. At low speeds many photons are integrated and strong Gaussian-shaped pulses are generated, whereas at very high speeds only a few single photons are transferred to the photomultipliers. Because of this high dynamic range of pulse amplitude and pulse width signal filters are required by which an optimized signal can be attained when the time-constant adjustment is matched to the specific experimental conditions. The range of the adjustable time constants of the filters is typically 2 ns to 1 µs. With this filter technique the signal-to-noise ratio can be essentially improved, hence allowing a more-effective reduction of background noise.

Discriminators are implemented to transform these signals with varying amplitude into uniform pulses,

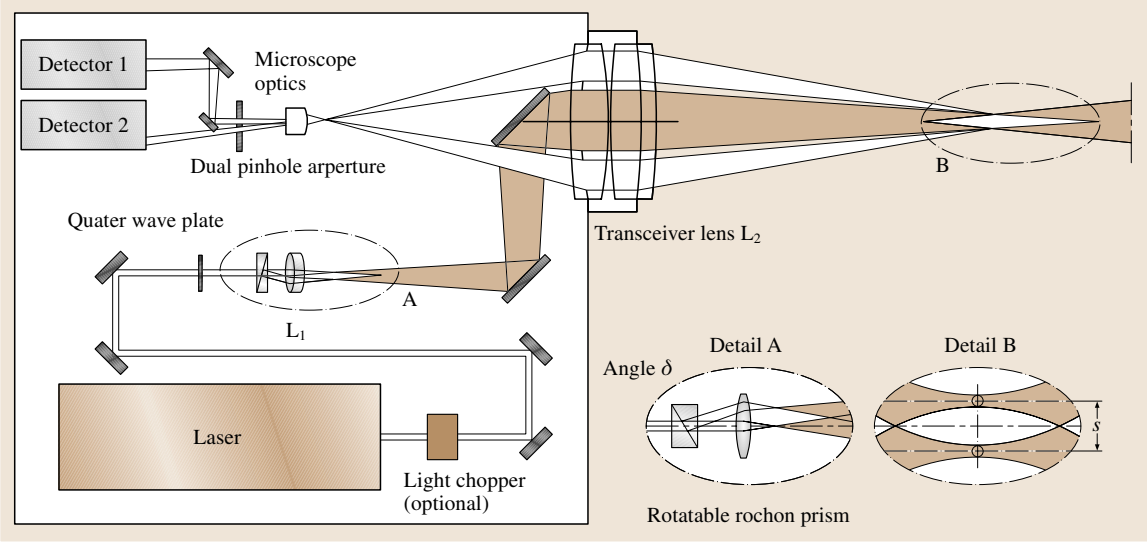

Fig. 5.142 Schematic of the LT velocimeter optics

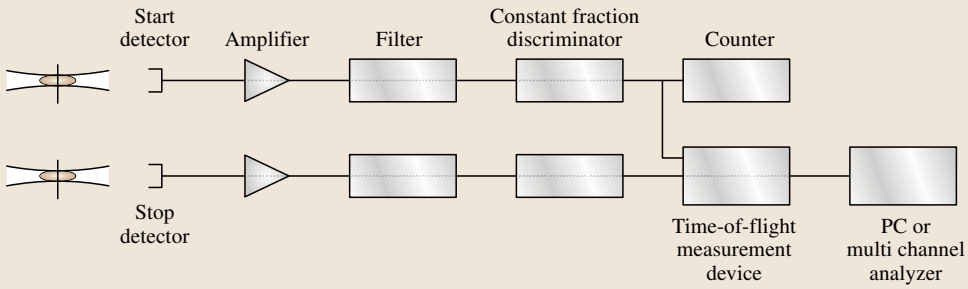

Fig. 5.143 Schematic of the LT velocimeter electronics

which are needed as input signals for precise time-of-flight measurements.

When the output pulses of the discriminator are generated, by employing simple leading-edge triggers, timing errors may occur due to the varying amplitude of the input pulses (Fig. 5.144). Therefore constant-fraction discriminators are preferably implemented, which operate with a special triggering method that allows the output pulses to be generated exactly at the instant of the maximum of the input signal, independent of the amplitude. The constant-fraction technique can only work precisely if an internal delay time is adjusted according to the time constant of the signal. Since this time constant is defined by the aforementioned signal filters the setting of filters and constant-fraction discriminator is combined.

The output signals from the discriminator are the input signals for the further time-of-flight analysis. This can either be performed by cross-correlation techniques or by direct time-of-flight measurements in combination with statistical data analysis.

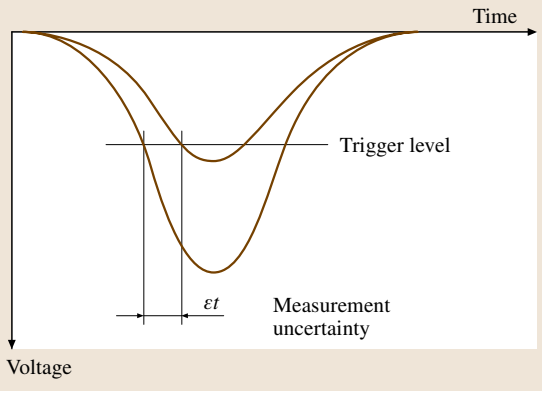

Fig. 5.144 Measurement uncertainty as a function of varying signal amplitude

In the early stages of development of the LT technique time-to-amplitude converters and multichannel analyzers were used (these are very common for time measurements in nuclear physics). Nowadays, fast counters are in use for time-of-flight measurements and statistical analysis is completely PC-based with an integrated custom-developed, dedicated PC card.

A normalization of the measured histogram taken at each angle setting of the plane of the beams is necessary to enable the construction of the desired two-dimensional histogram. The reference value for this normalization is the number of measurement events started. These are indicated by valid start signals delivered by the time-of-flight measuring system and acquired by a preset counter. After having reached the preset number, which has to be selected by the operator depending on the actual measurement conditions, the counter interrupts the data acquisition. The straightforward way of operation is to set the preset number to the same value for all angle settings of the beam's plane.

The measured two-dimensional histogram of data is then used as the input for further data evaluation.

Experimental Operation

The probe volume geometry of a LT velocimeter, the waist diameter d, and the beam separation s are determined by the diameter D of the incident laser beam, the splitting angle δ of the Rochon prism, and the focal length f_1 of the lens L1 (Fig. 5.142), assuming that the imaging scale of the lens system L2 is 1:1.

The Gaussian waist diameter ($1/e^2$ diameter) is

$$d = \frac{4}{\pi}\lambda\frac{f_1}{D}\,, \tag{5.297}$$

where λ is the wavelength of the laser beam, and the beam separation is

$$s = f_1\delta\,. \tag{5.298}$$

The angular range $\Delta\alpha$ in the LT system that is capable of detecting successful dual-beam crossings is only a few degrees and is given by

$$\Delta\alpha \sim \frac{d}{s} = \frac{4\lambda}{\pi\delta D} . \qquad (5.299)$$

The sensitive axial length of the probe volume l depends on the laser power P, the beam waist diameter d, the diameter d_p of the particles considered, the effectiveness of spatial filtering, and the amplitude discrimination of the photomultiplier signals.

For a laser power P of 0.5 W and particles with diameters of 0.5–1 μm it turns out from practical experience that the axial length l is about 10–40 times the beam waist diameter d. That means, for a typical diameter of $d = 10\,\mu\text{m}$,

$$l \approx 0.1\text{–}0.4\,\text{mm} . \qquad (5.300)$$

While in the case of LD systems the fringe spacing (and this determines the probe volume diameter) is matched to the expected velocity magnitude it is very advantageous in the case of LT system to match the beam separation s to the expected turbulence intensities [5.532]. In this way an LT system can be optimized with respect to the measuring accuracy and time required to perform the measurements. Assuming a constant beam diameter of $d = 10\,\mu\text{m}$, a beam separation of $s = 0.35\,\text{mm}$ is recommendable for turbulence intensities of 3% and the separation should be changed to $s = 70\,\mu\text{m}$ when the flow turbulence reaches 16%. With the reduced beam separation at higher turbulence intensities the corresponding angular capture range $\Delta\alpha$ increases from $\Delta\alpha = 1.5°$ to $\Delta\alpha = 8.0°$ so that the number of successful dual beam crossings (and with it the measurement time) becomes equal in the two different flow cases. Additionally, with the wider angular range $\Delta\alpha$ the angular step width of the beam's plane settings can also be extended so that in both flow cases the total number of angle settings can also be kept constant and likewise the total measurement time. With respect to the measurement accuracy, 10–02 angle settings placed within the angular fluctuation range of the turbulent flow are sufficient. In practice more angle settings are often needed to make the angular scanning range wide enough so that the unknown flow angle at a new measurement position most probably falls within this range. The measured data give a clear indication whether the range was correct and sufficiently wide. Otherwise measurements must be repeated with a modified angular setting range.

Applications in periodically fluctuating flows, e.g., rotor flow analysis in turbomachines, require special

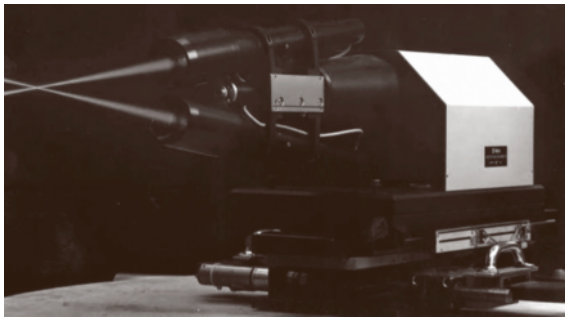

Fig. 5.145 3C-L2F optical head

synchronizing electronics to enable phase-resolved velocity measurements. Either a one-per-revolution or a blade-frequency signal is needed as an input. The synchronizer divides the blade period periodically in up to 64 windows. When a measurement event is indicated by a valid time-of-flight measurement, at that instant of time the window number assigned to the measurement event is identified and the measurement data are then directed to a corresponding storage. After the data collection all 64 storages are filled with data. The data, collected in each individual storage, determine the two-dimensional probability histogram, which is required for further data evaluation. The result is the velocity information (mean value and turbulence intensities) distributed in 64 circumferential positions over the blade period. In principle, measurement can be performed in a single, selected blade passage, however in practice – because of the saving in terms of measurement time – the data from all blade passages are mixed together and further calculations provide representative mean values.

When the rotor blades move through the probe volume, strong light reflections occur and may destroy the

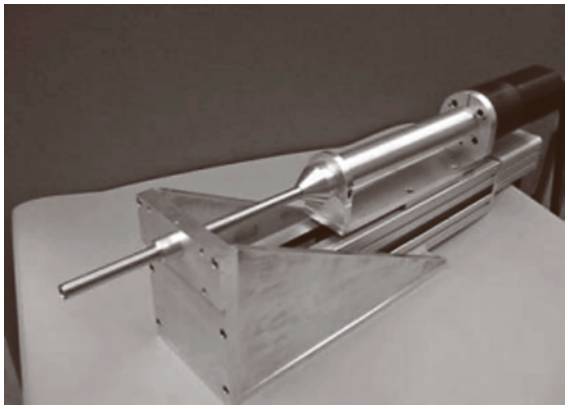

Fig. 5.146 3C-Doppler L2F probe

photomultiplier. In order to avoid this problem either the laser beam is switched off during the short blade-passage time by means of Pockels or Bragg cells, or the photomultipliers are gated by changing the polarization of the high voltage between the cathode and first dynode. During this blade-passage time – a small part of the blade period – the data collection is interrupted.

Three-Component Systems

To date the two-component LT technique has been best suited to overcoming serious access problems, since it is a back-scattering technique with a confocal optical beam path. This is the main reason why the two-component LT technique is well established in the experimental flow analysis of turbomachines, where the optical access problems are most severe.

This statement is not valid when three-component measurements are considered. Standard three-component velocimeters consist of two separate optical units – one or two velocity-component measuring devices – which are angularly displaced and operate on a common probe volume. For reasons of measurement accuracy of the velocity components the displacement angle should be at least 30°, which leads to a solid angle of greater than 40° necessary for optical access. This condition cannot be fulfilled in most turbomachinery applications.

A specially designed three-component LT system [5.540, 545] is on the market today and in use at various European institutions. This system (Fig. 5.145) is set up with two independent two-component LT systems with a tube-type optical head construction. The two tubes are mounted on a mechanical rotation unit inclined to the rotational axis at an angle of 7.5°. The location where the laser beams intersect is on the rotational axis and determines the probe volume. From the two-component data of the two independent LT systems the three velocity components can be deduced. Since the system is designed to adjust to the maximum sensitivity of the radial component measurement automatically, the solid angle required for optical access is only 20°, remarkably smaller than that needed for a standard three-component arrangement.

Even though this three-component system is well suited for turbomachinery measurements in general there are extreme applications where either this small

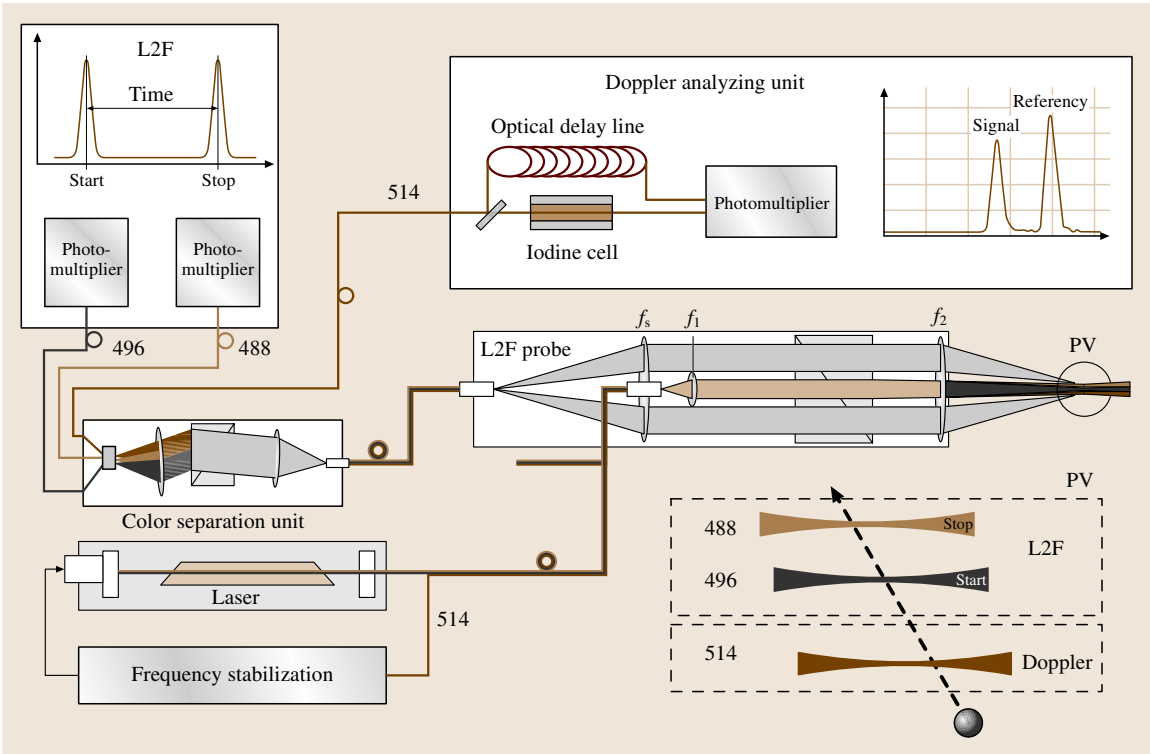

Fig. 5.147 Schematic of the 3C-Doppler L2F device

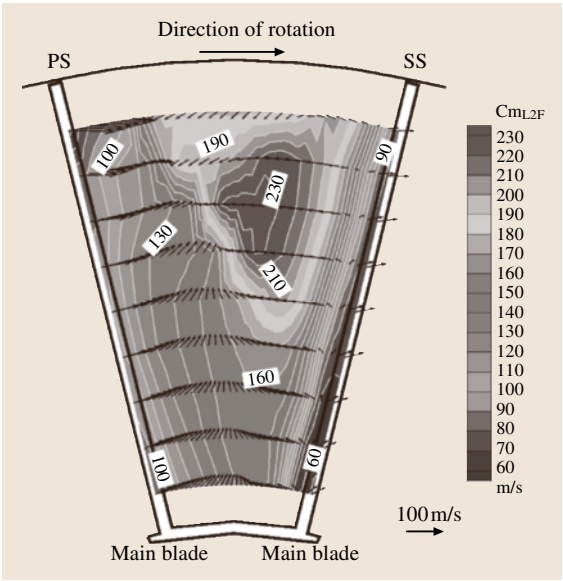

Fig. 5.148 Absolute velocity distribution measured at 0% meridional length just in front of the blades

solid angle for optical access is still too large or where not enough space is available to place and operate the optical head. In these cases only two-component systems can be used because they only need an 11° solid angle for optical access.

Recently a new three-component system was developed, called the 3C-Doppler-L2F, which operates with the same confocal optical setup as the two-component LT system, thus enabling three-component measurements even under difficult conditions, e.g., in centrifugal compressors, to be carried out. This technique combines the principle of the LT method with the principle of the Doppler global velocimetry [5.546, 547]. From the time-of-flight data, the standard two-component measurements provide the velocity vector component in the plane perpendicular to the optical axis. An additional frequency analysis of the scattered light determines the Doppler frequency shift, which represents the velocity component along the optical axis. The Doppler shift is measured by using the frequency-dependent absorption of iodine.

The system was developed for an application in a transonic centrifugal compressor and designed in the shape of an optical probe with an outer diameter of 25 mm and a probe throw of about 100 mm. The 3C-Doppler-L2F probe is shown in Fig. 5.146.

The setup of the 3C-Doppler-L2F device is shown in Fig. 5.147. A frequency-stabilized argon-ion laser with an intracavity etalon is used as a light source. While operating in multicolor mode, the Ar^+ laser was frequency stabilized using the green line ($\lambda = 514$ nm). The laser was fibre linked to the probe head. Lens f_1 collimates the laser beam emerging from the fibre end and guides the multicolor beam to a dispersion prism where the various colors experience different angular deflections, so that with the aid of lens f_2, parallel beams with differing colors and separations are focused in the probe volume (PV).

The multicolor light scattered by the particles traversing these beams is collected by the outer area of lens f_2 and sent through the same dispersion prism, where the various colors are again deflected such that the light produced at the various places in the probe volume is projected on a single focal point by lens f_3 and thus may be coupled into a multimode receiving fibre, which additionally functions as a aperture for spatial filtering. The receiving fibre guides the multicolor scattered light to a color-separation unit where the various colors of the detected light are separated and launched into the three assigned fibres.

The scattering light pulses from the 488 nm and 496 nm laser beams in the probe volume are guided to a L2F processing unit, where the start and stop signals for the time-of-flight measurements are generated. The signals are processed by standard commercially available L2F signal processors and provide the two-velocity component $v_\perp$ and angle α in the plane perpendicular to the optical axis

The velocity component v_Z along the optical axis is deduced from the Doppler-frequency shift analysis using the scattering light pulses from the 514 nm laser beam in the probe volume. In this Doppler analyzing unit the 514 nm scattering light is collimated and split by a nonpolarizing beam splitter into two beams of equal intensity, One beam is guided through an iodine cell, providing signal light pulses while the other beam is guided through a multimode fibre that serves as an optical delay line. Along this path the reference light pulses are transmitted. Both pulses are detected by a single photomultiplier with a constant time delay determined by the fibre. The amplitude ratio of these pulses is proportional to the transmission $T(v)$ of the iodine cell, from which the scattered light frequency can be derived. The measurement uncertainty of the v_Z-component is ± 0.5 m/s.

The 3C-Doppler L2F system was applied to a centrifugal compressor in order to measure the flow field in the rotating flow channels of a transonic splitter blade impeller of advanced design [5.548, 549]. These flow

data are very much desired for the validation of 3-D Navier–Stokes numerical simulations.

In Fig. 5.148 the velocity distribution between two main blades measured just in front of the rotor leading edge is plotted. The three-component absolute velocities are represented by the vector plot of the velocity components within the measurement plane and the color-coded out-of-plane velocity component CmL2F. The triangularly shaped area in the central upper part of the plot is the region where the relative intake velocity is supersonic. The steep gradient on the left side of this region indicates the location of a compression shock where the supersonic relative velocity suddenly changes to subsonic. The splitter blades, which are centered between two main blades (Fig. 5.148), are not shown in this plot since their leading edge is located further downstream at 30% of the meridional length. Their upstream influence on the flow at the location in front of the rotor, however, is presumably indicated by the in-plane flow vectors pointing upwards between the two main blades. Another successful application in a low-pressure turbine demonstrates the outstanding capability of the three-component Doppler L2F system.

Outlook

Nowadays planar velocimetry systems such as the particle image velocimetry and global Doppler velocimetry are common, as they are very efficient and therefore cost saving. These planar systems in comparison to point measurement techniques also supply additional information such as visualization of flow structures, and for this very reason are very much in use today. However for planar systems the problem of optical accessibility is more severe and cannot be solved in some applications. Therefore we are convinced that point measurement techniques, and LD and LT velocimetry, will continue to be of importance in the future, especially in turbomachinery flow research.

5.4 Molecular Tagging Velocimetry (MTV)

Molecular tagging velocimetry (MTV) is a whole-field optical technique that relies on molecules that can be turned into long-lifetime tracers upon excitation by photons of appropriate wavelength. These molecules are either premixed or naturally present in the flowing medium (i. e., unseeded applications). Typically a pulsed laser is used to *tag* the regions of interest, and those tagged regions are interrogated at two successive times within the lifetime of the tracer. The measured Lagrangian displacement vector provides the estimate of the velocity vector. This technique can be thought of as essentially a *molecular* counterpart of particle image velocimetry (PIV), and it can offer advantages compared to particle-based techniques where the use of seed particles is not desirable, difficult, or may lead to complications. Figure 5.149 illustrates one implementation of the technique where the particular tracer used is a water-soluble phosphorescent supramolecule. A planar grid of intersecting laser beams, formed from a pulsed excimer laser (20 ns pulse width, 308 nm wave-

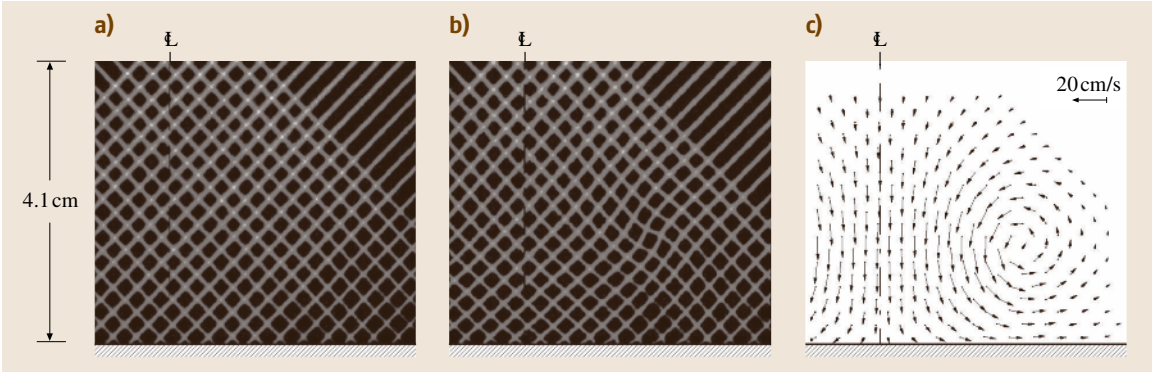

Fig. 5.149a–c Typical MTV image pairs and the resultant velocity field [5.550]. The flow shown is from a vortex ring impacting on a flat wall at normal incidence. The axis of symmetry is indicated by the dashed lines. **(a)** The grid imaged 1 μs after the laser pulse. **(b)** The same grid imaged 8 ms later. **(c)** The velocity field derived from **(a)** and **(b)**

length), turns on the luminescence of the supramolecules that are premixed in a water flow of a vortex ring approaching a solid wall at normal incidence [5.550]. The displacement of the tagged regions is determined, in this case, using a direct spatial correlation method. The conventional planar imaging shown in Fig. 5.149 provides information on two components of the velocity vector, the projection onto the viewed plane. Stereo imaging can produce the complete three components of the velocity vector [5.551].

While the earliest use of MTV can be traced back at least three decades, this technique has seen significant advances over the past 15 years [sometimes under alternate titles such as laser-induced photochemical anemometry (LIPA) and flow tagging velocimetry]. The ability to non-intrusively tag the molecules in a flowing medium and observe their subsequent evolution offers other possibilities besides velocimetry in fluid flows. Depending on the tracer properties and the method of implementation, molecular tagging can be used for flow visualization, simultaneous quantification of velocity and scalar (concentration or temperature) fields, and novel methods in the study the Lagrangian evolution of scalar fields, entrainment, and mixing. As we describe the various elements involved in using molecular tagging techniques, and in particular molecular tagging velocimetry, we draw attention to several review articles that have appeared in the past [5.552–555], in addition to a special issue of *Measurement Science and Technology* on this topic [5.556].

5.4.1 The Photochemistry of MTV: Molecular Tracers and Chemical Mechanisms

A molecular complex is suitable for molecular tagging applications if its lifetime as a tracer is long enough relative to the flow convection time scale to allow sufficient displacement of the tagged regions during the interrogation time. The photophysical properties of the tracer, in turn, dictate the wavelength and number of photon sources needed to create the tracer (i. e., the tagging process) and those needed for interrogation.

All MTV techniques are based on the chemistry of molecules in electronic excited states. Normally residing in dark or ground states, molecules enter excited states when they absorb energy from the environment. Electronically excited molecules are generally very reactive, eventually returning either to their original ground state or to a new ground-state molecule. The departure of a molecule from its excited state may occur in the absence of a reacting partner (called an intramolecular decay process) or with the help of a second molecule (called an intermolecular decay process), as shown schematically in Fig. 5.150.

Figure 5.150a depicts the intramolecular processes that govern the decay of an isolated excited state molecule to its ground state. Competing photon emission (radiative) and thermal (nonradiative) relaxation pathways are described by the radiative (k_r) and nonradiative (k_{nr}) rate constants, respectively. The radiative rate constant is an intrinsic property of the molecule and it reflects the probability of the excited state emitting a photon of a given frequency; k_r is directly related to the ability of the molecule to absorb light, described by the oscillator strength or the molar absorptivity constant [5.557–559]. k_{nr} encompasses all decay pathways that do not lead to photon emission. Nonradiative decay most typically entails the conversion of an excited state's electronic energy into high-energy vibrations of the ground-state molecule [5.560–562]. Vibrational relaxation to the equilibrated ground state molecule (M) is accompanied by the concomitant release of heat ($k_{nr}^{(M)}$); alternatively, the excess vibrational energy may be manifested in the creation of a different ground-state molecule ($k_{nr}^{(P)}$), called the photoproduct. The

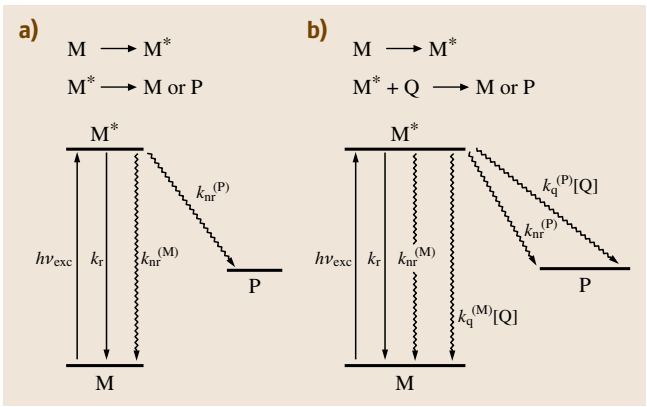

Fig. 5.150 **(a)** Simple excited-state diagram for intramolecular decay processes of a molecule in an excited state M*. The radiative rate constant k_r and nonradiative rate constant $k_{nr}^{(M)}$ describe the conversion of M* to its ground state M by photon and thermal emission, respectively. $k_{nr}^{(P)}$ is the rate constant describing the return of M* to a new molecule P. **(b)** The excited state diagram including intramolecular and intermolecular decay processes of a molecule in an excited state M*. The quenching rate constants $k_q^{(M)}$ and $k_q^{(P)}$ describe the intermolecular conversion of M* by quencher Q to its ground state M or a new ground-state molecule P

overall nonradiative decay rate constant k_{nr} is simply $k_{nr} = k_{nr}^{(M)} + k_{nr}^{(P)}$.

The interplay between k_r and k_{nr} determines the fundamental properties of molecules in excited states [5.557, 563]. The intensity of the luminescence I_0 is directly dependent on the luminescence efficiency, usually called the emission quantum yield Φ_e, which is the ratio of the number of photons emitted per photons absorbed. The emission quantum yield is directly related to k_r and k_{nr} by the following expression

$$I_0 \sim \Phi_e = \frac{k_r}{k_r + k_{nr}} = k_r \tau_0 \,, \tag{5.301}$$

where τ_0 is the observed lifetime of the electronic excited state, and

$$\tau_0 = \frac{1}{k_r + k_{nr}} \,. \tag{5.302}$$

Nonradiative relaxation pathways usually dominate (i. e., $k_{nr} \gg k_r$) and, as can be seen from (5.301), molecules under this condition will remain dark upon excitation. However, when thermal emission is inefficient with regard to photon emission (i. e., $k_r \gg k_{nr}$), excited states will literally light up or luminesce.

Two types of luminescence are of significance to MTV techniques: fluorescence and phosphorescence. In the ground state, virtually all molecules reside in electronic states in which the electrons are paired. For this situation, a molecule is said to be in a singlet ground state. Quantum-mechanical rules dictate that the most probable transitions to excited states will be to other singlet excited states. Fluorescence is the radiative process that accompanies the relaxation of a molecule from a singlet excited state to its singlet ground state. Because singlet-to-singlet transitions are quantum-mechanically allowed, they occur with a high probability. Hence k_r is large, ranging from 10^8 to $10^{10}\,s^{-1}$. From the perspective of (5.301) and (5.302), there are two consequences of such large values of k_r. Nonradiative decay channels k_{nr} are generally not competitive with k_r (i. e., $k_r \gg k_{nr}$). As deduced directly from (5.301), the emission intensity of a fluorescent excited state is therefore intense. Moreover, the lifetime of a fluorescent excited state will also approach that of k_r^{-1} (5.302); thus fluorescent lifetimes are short, on the order of 1–100 ns with most fluorescent lifetimes being ≈ 2–10 ns.

Conversely, phosphorescence is long-lived because the transitions between the excited state and ground state are forbidden. In a phosphorescent excited state, the electrons are triplet-paired or aligned with each other. Here the absorption process occurs between the singlet ground state and an excited state of different spin. Quantum-mechanically this is a forbidden transition, and hence k_r is small. The radiative decay rates can therefore approach seconds and the phosphorescence lifetimes can be large (owing to the small k_r). However, the phosphorescence intensity from the spin-forbidden excited state may be significantly weaker than fluorescence because k_{nr} will become competitive with k_r on the micro- to millisecond time scale. Moreover, because the absorption cross section of the triplet state is small, it is usually not produced by direct absorption. Alternatively, the triplet excited state is usually populated from a correspondent singlet state by the intersystem crossing (ISC) process. Because the triplet has a lower energy than the singlet, the wavelength for phosphorescence is significantly red-shifted from the absorption profile. Thus, whereas the wavelength difference between the absorption and emission profile (known as the Stokes shift) may be relatively small for fluorescence, a large shift between the wavelengths of absorption and phosphorescence is typically observed.

Equations (5.301) and (5.302) only consider the intramolecular decay processes of the excited-state molecule in the absence of external reactants. Because electronically excited molecules are highly energetic, they are susceptible to intermolecular reactions in which M^* physically or chemically interacts with species in its environment (called quenchers Q) [5.564] to again return to ground state M or to another molecule P (Fig. 5.150b). When quenching processes are present, (5.301) and (5.302) must be modified by adding $k_q[Q]$ to their denominators,

$$I \sim \Phi_e = \frac{k_r}{k_r + k_{nr} + k_q[Q]} \,, \tag{5.303}$$

$$\tau = \frac{1}{k_r + k_{nr} + k_q[Q]} \,, \tag{5.304}$$

where k_q is the quenching rate constant and the concentration of the reacting partner [Q] accounts for the bimolecular nature of the quenching process. It follows from this formalism that quenching pathways are dissipative and their presence will diminish the luminescence intensity and shorten the excited-state lifetime. The Stern–Volmer relation quantitatively defines the attenuation in luminescence lifetime and intensity under quenching conditions as

$$\frac{I_0}{I} = \frac{\tau_0}{\tau} = 1 + \tau_0 k_q[Q] \,, \tag{5.305}$$

where I_0, I, and τ_0, τ are the luminescence intensity and lifetime in the absence and presence of Q, respectively. Owing to the short lifetimes of singlet excited

states, significant concentrations (typically 0.01 molar or greater) of Q are required to quench fluorescence. This is not the case for phosphorescence. The long lifetimes of phosphorescent excited states makes them especially susceptible to quenching at extremely small concentrations of Q.

Most of the imaging techniques based on molecular tagging may be understood in the context of the simple relations defined by (5.301–5.305). Below is a description of the chemistry behind these techniques.

The Different Mechanisms of MTV

The four basic mechanisms that encompass current MTV techniques are shown in Fig. 5.151. Sometimes referred to as laser-induced photochemical anemometry (LIPA), mechanism A describes measurements based on the image produced by a photochromic dye and is the only MTV technique that relies on measuring absorbance. Light excitation produces a high-energy form of the dye, which is usually more strongly absorbing than the ground-state molecule M (usually from transparent to opaque); the dye molecules in the flow are therefore tagged by the darkened image. Mechanism B describes the Raman excitation plus laser-induced electronic fluorescence (RELIEF) technique. In a RELIEF experiment, a high-energy form of the molecule, M′ (specifically vibrationally excited oxygen), is also responsible for creating the image. But unlike in LIPA, M′ emits photons upon subsequent irradiation. The RELIEF image is therefore revealed by detecting luminescence rather than absorbance. Mechanism C relies on the production of a luminescent molecule P upon excitation of a ground-state molecule M. For the technique with the moniker photoactivated non-intrusive tracing of molecular motion (PHANTOMM), a laser dye is produced. Variants of the technique arise from the production of different P species: ozone in the oxygen tagging velocimetry (OTV) technique, hydroxyl radicals in the hydroxyl tagging technique (HTV), and two techniques based on the photorelease of NO. In each case, a luminescent image is produced upon excitation with a *write* laser and the image is detected by irradiating with a subsequent *read* laser pulse. Within mechanism C we also include the reverse approach such as photobleaching where, instead of releasing a luminescent tracer, a nonluminescent species is produced from fluorescent dyes, thereby creating a *negative* image. Mechanism D is the most straightforward of the MTV techniques. An excited-state molecule M* is produced by excitation. An image is detected by directly monitoring the long-lived phosphorescence from M* upon its radiative return to its ground state M. Details of each of the MTV techniques are presented next.

Mechanism A: MTV by Absorbance. Originally introduced by *Miller* [5.565] for visualizing flows, photochromic chemicals were extensively used first by Hummel and his group for velocity measurements [5.566–569] and subsequently were more-thoroughly applied to the MTV technique by *Falco* and *Chu* [5.570] under the acronym LIPA. In a photochromic process, laser excitation of molecule M produces an electronically excited molecule M*, which then relaxes by nonradiative decay ($k_{nr}^{(M)}$ and $k_{nr}^{(P)}$). Whereas most of the vibrational energy is released as heat ($k_{nr}^{(M)}$), some vibrational energy is channeled into the making and/or breaking of bonds ($k_{nr}^{(P)}$) to produce a high-energy form

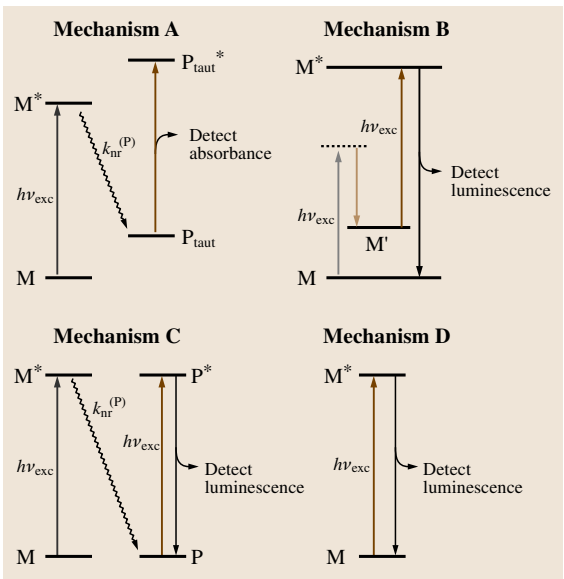

Fig. 5.151 The different mechanisms of MTV. M and M* designate a molecule in its ground and electronic excited state, respectively, and P indicates the formation of a new molecule. Consistent with Fig. 5.150, *solid arrows* describe radiative transitions and *wavy arrows* indicate nonradiative transitions. The excitation lines are color-coded to emphasize the number of different frequencies typically needed for each experiment. The different diagrams summarize the photochemistry and photophysics that give rise to the various MTV techniques under the various acronyms of LIPA based on photochromism (type A), RELIEF (type B), PHANTOMM, OTV, HTV (type C), and direct luminescence (type D)

of the molecule P_{taut}; in chemical terms, this high-energy molecular species is called a tautomer (the same molecular framework connected by a different bonding pattern). This tautomeric process is adaptable to MTV because the absorption spectra of M and P_{taut} are different. The color change accompanying the M-to-P_{taut} conversion can be detected by exciting with a white-light source. In the context of MTV description, the long-lifetime tracer in this case is the newly produced P_{taut}, which can persist for several seconds to minutes.

The photochromism of commercially available substituted benzyl pyridines and spiropyran dyes have been used for most velocimetry measurements to date. The structure of these dyes and their overall photochemistry are depicted in Fig. 5.152. The nature of the X_i substituent on either tracer may be varied to tune the precise spectroscopic and photophysical properties of the dye. In the benzyl pyridine and spiropyran systems, M is colorless to slightly yellow, whereas P_{taut} is dark blue. This color change results from the increased conjugation (the alteration of single and double bonds) of the molecular framework upon conversion to the high-energy tautomer. For the molecules on the left side of Fig. 5.152, electrons in the π system of the dye (those electrons associated with the alternating single and double bonds) are confined to a single six-membered ring (highlighted by the dark outline). Excitation to M* followed by subsequent nonradiative decay causes the making and breaking of bonds such that the π system is extended. The increase in the conjugation allows the electrons to delocalize over a longer part of the molecule, resulting in a red shift of the absorption spectrum from the ultraviolet to the visible spectral region as explained by quantum-mechanical particle-in-a-box formalisms [5.571]. Use of photochromic chemicals requires two photon sources. When solutions of the photochromic tracers are irradiated with a *write* laser, typically a UV laser (e.g., with a wavelength of 351 nm), P_{taut} is produced and an opaque image is generated along the path of excitation. A second light source (usually a white-light source) is then needed to see or *read* the image.

There are several advantages of molecular tagging by a photochromic tracer. The nonradiative conversion from M* to P_{taut} occurs rapidly, within the duration of a nanosecond laser pulse, and hence the image is formed promptly upon laser irradiation. The conversion of P_{taut} back to M occurs reversibly so the tracer is reusable. Moreover, P_{taut} persists for several seconds to minutes before thermally converting back to M. Thus, flows moving at slow speeds may be studied and the photochromic tracer can be used repeatedly. Though yet to be implemented in fluid flow studies, there are numerous other photochromic imaging systems offering a wide range of available chemical and spectroscopic properties. A purported drawback of this mechanism is the insolubility of these photochromic dyes in water. While it is true that most studies using photochromics have been performed in organic liquids (typically kerosene), relatively minor chemical modifications to many photochromic dyes would enable them to dissolve easily in water [5.572].

Despite these advantages (i. e., long lifetime, reusable), there is one drawback of photochromic systems that limits their overall utility for MTV. Because the image is produced by a change in absorbance, the difference between the incident and transmitted light must be measured, a task which greatly complicates data collection and analysis. Indeed, emitted light (against a black background) is more easily and accurately detected than transmitted light, and consequently images based on luminescence are more amenable to MTV. For this reason, the major advances in the MTV technique in recent years have been made with the luminescence-based imaging schemes of mechanisms B, C, and D. Nevertheless, MTV with photochromics have been used effectively in fluid-dynamics studies [5.570, 573–579].

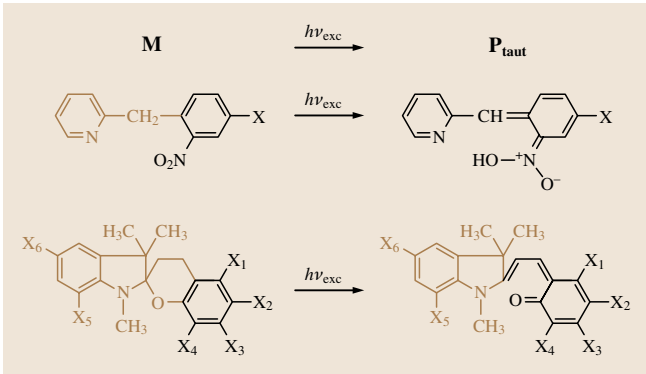

Fig. 5.152 Photochemical transformations of two popular photochromic dyes used for MTV: the substituted benzyl pyridines (*top*) and spiropyran dyes (*bottom*). The molecules are labeled with respect to the M and P_{taut} designations of Fig. 5.150 (mechanism A). The *bold lines* show the molecular framework responsible for the color change upon laser excitation

Mechanism B: MTV by Vibrational Excited-State Fluorescence. The Raman excitation plus laser-induced electronic fluorescence (RELIEF) technique was designed by *Miles* and coworkers [5.580–584] for molecular tagging in unseeded air flows. The technique is schematically described in Fig. 5.151 (mechanism B).

The oxygen in the air flow is tagged by a laser to produce oxygen in a vibrational excited state, which is long-lived and its displacement can subsequently be interrogated, or *read*, by exciting to an electronic excited state that is emissive. The mechanism is ingenious in its design because the long-lifetime tracer needed to follow the flow is derived from the vibrational excited state of oxygen; the short-lived fluorescence of the electronic excited state of oxygen is used only to interrogate the vibrationally excited molecule.

RELIEF is the most spectroscopically sophisticated MTV technique. The spectroscopic underpinning of RELIEF is based on the stimulated Raman effect [5.585], which is familiar to most as a method to Raman-shift the wavelength of light from a laser pump source. In normal Raman scattering, laser irradiation of frequency ν_0 results in the spontaneous population of a vibrational excited level. The populations are small, however, and vibrational excited states are not produced in sufficient concentration to be viable for velocimetry. At high laser irradiances (electric fields of $> 10^9$ V/m) nonlinear effects dominate, such that a substantial fraction of the exciting radiation of frequency ν_0 is converted into radiation of frequency $\nu_0 \pm n\nu$, where ν is the vibrational frequency of the molecule. Most of the power (sometimes as much as 50%) is transferred to the first Stokes line, $\nu_0 - \nu$. In the context of Fig. 5.152, the exciting nonlinear radiation $\nu_0 - \nu$ pumps the system from its ground to its first vibrational level by driving the system through a virtual excited state (indicated by the dashed lines). For oxygen, the process involves the population of the first vibrational level ($\upsilon = 1$) of the $^3\Sigma_g^-$ electronic ground. The formation of the long-lifetime tracer, i. e., the vibrationally excited oxygen, is rapid and occurs within the laser pulse of order 10 ns. This vibrational level can be very long-lived, approaching 27 ms at 1 atm [5.586]. However, for MTV applications, the usable lifetime is in the 100 ms range owing to collisional deactivation of vibrationally excited oxygen by water and carbon dioxide [5.587]. In most applications to date, the time delay between tagging and interrogation has been of order 10 µs or less. From the $^3\Sigma_g^-(\upsilon = 1)$ vibrational excited state, oxygen can be excited to its $^3\Sigma_u^-$ (or sometimes referred to as the B) excited state (responsible for the famous Schumann–Runge bands of oxygen [5.588] from which 200–400 nm fluorescence may be observed for interrogation purposes.

The requirement of three frequencies (i. e., two to tag, one to interrogate) makes the RELIEF technique challenging to implement. The power transferred to the first Stokes line at $\nu_0 - \nu$ is related exponentially to the incident laser power. The intense light at the difference frequency needed to produce sufficient concentrations of the vibrationally excited oxygen is provided by mixing the 532 nm second harmonic of a Nd:YAG laser and the 580 nm output of a dye laser, or a Raman-cell frequency shifter, also driven by the 532 nm line of the same Nd:YAG laser. For interrogation, the 193 nm output of an ArF excimer laser is needed to promote the vibrationally excited oxygen molecules into the fluorescent Schumann–Runge manifold. On the detection side of the experiment, the overall imaging of the flow is complicated by the fact that the $^3\Sigma_u^-$ fluorescent excited state of oxygen is predissociative, leading to the homolytic cleavage of the oxygen–oxygen bond [5.589]. Bond cleavage is of course a nonradiative decay process, hence the overall quantum efficiency for fluorescence is small. In addition, the electronic communication between excited and ground states is poor (owing to poor Franck–Condon factors) so that the efficiency for fluorescence is further compromised. Despite these challenges, MTV measurements with RELIEF have been successfully carried out in gas-phase, oxygenated flows [5.581–583, 590, 591].

Mechanism C: MTV by Photoproduct Fluorescence. The photoactivated non-intrusive tracking of molecular motion (PHANTOMM) method is based on tracers that would otherwise luminesce if not for the attachment of a deactivating, or caging, group. First introduced by *Lempert* et al. [5.592] for liquid-phase flows, the overall technique relies on two sources of photons. Laser excitation leads to the photolytic removal of the deactivating group to produce a fluorescent dye with high emission quantum efficiencies. In the context of MTV description, the long-lifetime tracer in this case is the uncaged laser dye, which can persist for a very long time. The laser dye is spatially produced only where the *write* laser has excited the flow. The displacement of the tagged regions is revealed by illuminating the flow with a *read* laser to reveal the fluorescence from the uncaged dye. The uncaged dye can be tracked indefinitely since the photolytic removal of the deactivating group is irreversible. For this reason, the PHANTOMM technique can accommodate very slow flow speeds and has been utilized in several novel applications [5.593–599].

An obvious question is why does the laser dye need to be photogenerated in the first place? Returning to the discussion of Sect. 5.4.2, fluorescence is short-lived; thus a fluorescent image that is directly produced by laser excitation will exist for only 1–10 ns. The glowing image is too short-lived to lead to sufficient displace-

ment over the convection timescale of most flows. The PHANTOMM technique overcomes this limitation by uncaging the fluorescent dye. From a chemical perspective, PHANTOMM is the luminescent counterpart to LIPA. In both techniques, an initial excitation pulse is used to produce a tracer, which can be followed in time; with LIPA the tracer is absorbing and hence tracked by the detection of transmitted light, whereas in PHANTOMM the tracer is tracked by detecting emitted light.

The detection of a fluorescent image offers several advantages to the PHANTOMM technique. Because the transition between the singlet excited state and singlet ground state is allowed for strongly absorbing materials such as organic laser dye molecules, k_r approaches $10^9\,s^{-1}$. This rate of radiative relaxation is so large that the nonradiative decay channels k_{nr} are generally not competitive (i. e., $k_r \gg k_{nr}$). From (5.301), the emission intensity of the PHANTOMM image is therefore intense. Also because fluorescence lifetimes are short [on the order of $\approx 1-10\,ns$ (5.302)], the excited state (and hence the tagged region in the PHANTOMM technique) is not readily quenched by oxygen. This can be understood within the context of (5.305). The quenching rate for oxygen is diffusion controlled (i. e. , $k_q = 10^9\,mol^{-1}s^{-1}$), and its concentration in solution is typically 10^{-3} mol. With an excited-state lifetime of $\approx 10^{-9}\,s^{-1}$, a maximum quenching of 0.1% will be observed. Thus the fluorescence image is not affected by air, a fact long known to the practitioners of laser-induced fluorescence (LIF). The short lifetime of the fluorescence of uncaged dye offers another significant advantage for increasing signal gain. Once uncaged, a dye can be excited multiple times, allowing for multiple photons to be detected from an individual activated dye over time durations that are short with respect to fluid motion. *Lempert* et al. [5.592] have estimated that the photogenerated fluorescein dye (with its natural radiative lifetime of 4.5 ns and quantum yield of 0.90) can emit 150 photons over the duration of a conventional flashlamp-pumped dye laser (FWHM = 2 μs), which is a time scale that is frozen with respect to fluid motion in most liquid applications.

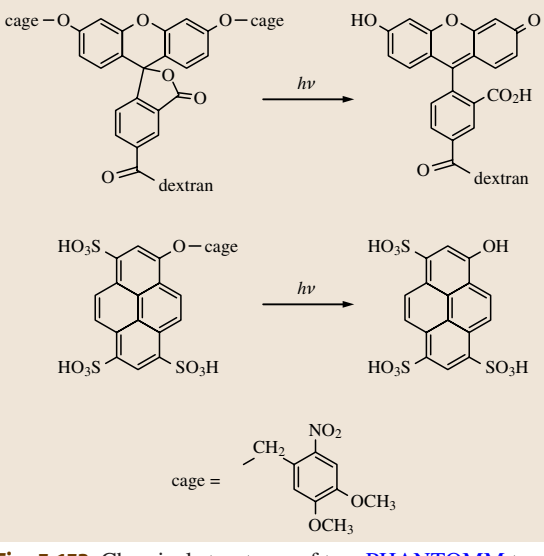

Fig. 5.153 Chemical structures of two PHANTOMM tracers before and after photolytic cleavage of the deactivating group. The photochemistry of the top caged tracer produces a fluorescein dye, whereas that of the bottom caged tracer yields a pyrene fluorophone

A variety of caged fluorescent dyes is currently available commercially from Molecular Probes, Inc. (Eugene, Oregon, USA). Two such tracers are shown in Fig. 5.153. In each case the dye is modified with a methoxynitroaromatic deactivating, or caging, group. The covalent attachment of the deactivating group renders the latent fluorescent dye nonemissive. The tracers can be activated with the third harmonic of a Nd:YAG laser (355 nm) to produce dyes with luminescence properties of fluorescein and pyrene. Though the precise mechanism for the photolytic removal of the deactivating group has yet to be determined, it likely occurs via well-known resonance structures involving the nitro group to yield an aldehyde through a photochemistry that appears to be initiated by π to π^* excitation of the deactivating group [5.600]. However, even though the excitation light may be absorbed within the appended group, it cannot be contained there and it is free to flow to all bonds in the molecule on vibrational time scales (sub-picosecond). The nonspecificity of the excitation process means that the photolytic removal of the group does not occur immediately upon laser excitation; specifically, the deactivating group falls off the dye on millisecond time scales [5.592], which establishes the upper limit for the flow speeds that can be investigated. Moreover, as emphasized in Fig. 5.153, the luminescent dye is produced irreversibly by cleavage of a covalent bond. Thus the overall tracer can be used only once. A significant advance to the overall approach will be creation of photoactivated dyes that can be uncaged promptly and reversibly.

Interestingly, the PHANTOMM concept, though not so named at the time, was first implemented by *Boedeker* [5.601], and further utilized by *Goss*

et al. [5.602], using a much simpler tracer molecule than those shown in Fig. 5.153. Water will photodissociate to OH and H radicals upon two-photon excitation at 248 nm [5.603]. Subsequent excitation with a second laser at 308 nm yields the fluorescence characteristic of the Q_1 transitions [5.604] of the OH radical. With regard to the PHANTOMM construct, the caged tracer is water, the deactivating group or cage is an H radical, and the fluorescent dye is the OH radical. The need for two-photon excitation to release the OH radical makes the technique difficult to implement. Nevertheless, Boedecker's approach permits gas-phase flows to be imaged by the PHANTOMM technique with the caveat that the OH radical tracer has a short lifetime and thus is restricted to high-speed flows. Related studies by *Goss* et al. [5.605] have expanded Boedeker's approach to permit high-speed combusting flows to be imaged by luminescence from C, C_2, and CN tracers produced by the photolysis of hydrocarbons.

Under the acronym hydroxyl tagging velocimetry (HTV), Pitz and coworkers have advanced the use of OH radical fluorescence by replacing the two-photon *write* pulse with a one-photon pulse [5.606–611]. In this adaptation, single-photon dissociation of vibrationally excited water molecules to produce the OH radical is achieved by the 193 nm excitation wavelength of an ArF excimer laser. The tagged regions are imaged with the OH radical fluorescence excited by the 248 nm wavelength of a KrF excimer laser. Though not yet implemented, the 308 nm excitation frequency of a XeCl excimer laser should also be suitable to image the OH radical fluorescence. The technique has been used to image the flow fields of combusting H_2–air flames. At lean concentrations of H_2, OH radical lifetimes approach 1 ms. For rich H_2 flames, however, the lifetime of the OH radical drops to ≈ 200 ns owing to its reaction with H_2 to produce H_2O and a H radical. The advantage of single-photon generation of OH radical from H_2O is that larger spatial regions can be tagged with single-photon excitation. HTV has recently been used in a noncombusting supersonic flow where water was sprayed upstream to provide moist air and adequate OH signal level [5.609].

In the ozone tagging velocimetry (OTV) technique of Pitz and coworkers [5.608, 612, 613] the *caged dye* is ozone, which is created from oxygen O_2 by the same reaction chemistry that produces ozone in the upper atmosphere. The basic photochemistry of the OTV technique is shown below:

$$O_2 + h\nu(\lambda = 193\,\text{nm}) \rightarrow O(^3P) + O(^3P)$$
$$O(^3P) + O_2 \rightarrow O_3\,,$$
$$O_3 + h\nu(\lambda = 248\,\text{nm}) \rightarrow O(^3P) + O_2^*$$
$$O_2^* \rightarrow O_2 + h\nu_{\text{fluor}}\,.$$

Two sources of photons are therefore needed for this approach. The 193 nm light from an ArF excimer laser impinging on air causes oxygen to dissociate into two oxygen radicals. These $O(^3P)$ radicals react with undissociated oxygen to produce ozone O_3, which is the long-lifetime tracer and the tagging reagent. After a known delay time, the position of the O_3 tag line is revealed by the application of a 248 nm pulsed laser sheet produced from a KrF excimer laser. The 248 nm excitation undoes the chemistry of the 193 nm laser line, causing ozone to photodissociate to an $O(^3P)$ radical and O_2, which fluoresces via the Schumann–Runge transitions that are accessed by the KrF interrogation laser. The long imaging lifetimes are derived from the ozone tracer, which is stable in air at room temperature. However, at increased temperatures, ozone is unstable with respect to thermal decomposition; thus, the OTV technique is not suitable for hot flows (e.g., beyond 600 K). In addition, the formation of O_3 from O_2 with the 193 nm laser pulse is not rapid and occurs over a time scale of $\approx 20\,\mu$s. In a situation similar to the uncaging of fluorescein in the PHANTOMM technique, the delay between laser tagging and the generation of enough ozone to obtain a fluorescent image with sufficient signal-to-noise ratio dictates the fastest flow speeds that can be accommodated.

Another tracer molecule that can be produced from uncaging is nitric oxide NO. The fluorescence of NO has long been used in LIF measurements [5.587]. As with all the techniques described in this section, implementation of the tracer for MTV applications requires its generation from a parent molecule. Whereas many other smallmolecular tracers exhibit only short lifetimes due to energy-transfer processes or high reactivity, NO is stable on the millisecond time scale, thus allowing relatively slow flows to be imaged. There are two caged NO molecules that have been employed to date for this MTV mechanism. NO_2 may be dissociated in the focused beam of a 308 nm XeCl laser [5.614]. The NO generated may be imaged by the fluorescence of NO, generated by its excitation with a Raman-shifted 226 nm line from a KrF excimer laser. NO may also be generated from tert-butyl nitrite seeded in an air or nitrogen flow [5.615, 616]. NO is released upon excitation with either a 193 nm ArF laser or a 248 nm KrF excimer laser. The photodissociation cross section of the tert-butyl nitrite at 248 nm is a factor of ≈ 2 smaller than compared to 193 nm, but the pulse energies of the KrF

lasers are generally higher. Finally, NO may be generated by irradiating air with an intense laser beam in a method known as air photolysis and recombination tracking (APART) [5.617–619]. The tracer results from the creation of NO from reaction of N_2 and O_2 in the field of illumination of a focused ArF excimer laser beam (193 nm wavelength). This MTV scheme is attractive because the air flow may be imaged without any kind of seeding.

A different implementation of mechanism C for MTV applications relies on the laser-enhanced ionization (LEI) of an atomic species naturally present in the flow or seeded into it [5.620]. The LEI technique relies on the excitation a neutral atom or molecule to an excited state near its ionization limit. A second photon can then be used to ionize the atom or molecule, thus producing a depletion of the neutral species, which is typically fluorescent. The detected region is revealed by an attenuation of the luminescence intensity. Pertaining to the mechanism described in this section, the LEI technique yields a *negative* image, in contrast to the foregoing techniques of this section. Instead of releasing a luminescent tracer, the ionizing laser pulse produces a nonluminescent species. Detection of a quenched luminescence against a bright background complicates the implementation of MTV and limits the overall dynamic range of the technique. Most recently, the LEI technique has been improved by using the secondary laser to produce a luminescent image [5.621]. In this implementation, neutral strontium ions seeded into a flame are ionized by first resonantly exciting ($\lambda_{exc} = 460.733$ nm) neutral strontium atoms from their ground state ($5s^2$, $^1S_0$) to a Rydberg state ($5s^15p^1$, $^1P_1$), followed by subsequent ionization of this excited species to produce strontium ions with the 308 nm output of an excimer laser. Fluorescence from the strontium ions is detected at 407.8 nm upon excitation with a 421.552 nm *read* laser pulse. The precise excitation frequencies are produced from XeCl-pumped dye lasers. The technique is somewhat cumbersome to implement as two pump and two dye lasers are needed to produce the fluorescent image; one laser system for the production of the strontium ions and another to produce the laser-induced fluorescence image. The short lifetime of strontium ions (of the order of 60 µs due to ion–electron recombination processes) makes this approach suitable for imaging supersonic and hypersonic flows.

Yet another alternate implementation of mechanism C includes a photobleaching approach. Continuous excitation of organic dyes reduces the ability of the dye molecules to absorb photons and emit fluorescence, thereby reducing the effective concentration of active dye molecules and a reduction of fluorescence emission from the bleached regions. The detrimental effects of photobleaching have been addressed previously in quantitative LIF studies [5.622–624]. A first-order description of the photobleaching process defines the bleaching effectiveness in terms of a rate that is proportional to the excitation source photon flux and properties of the dye molecule, i. e., absorption cross section and bleaching quantum efficiency [5.622]. As a result, effective photobleaching over a short timescale requires a high-intensity laser source. In comparison with the PHANTOMM concept, this is a reverse approach where, instead of releasing a luminescent tracer, a nonluminescent species is produced from fluorescent dyes, thereby creating a *negative* image. As already described previously, however, detection of reduced luminescence against a bright background complicates the implementation of MTV and limits the overall dynamic range of the approach. Nevertheless, MTV measurements based on photobleaching have been successfully carried out [5.625–628].

Mechanism D: MTV by Direct Phosphorescence. Molecular tagging based on direct photoluminescence is the easiest technique to implement. A single laser is used to produce a luminescent excited state, which is extremely long-lived and its displacement by the flow can be imaged by simply monitoring the emanating luminescence. In the context of MTV description, the long-lifetime tracer in this case is the excited-state molecule itself. The emission of a photon returns the molecule back to its ground state where the tracer may be re-excited; thus the tracer is reusable.

The overall approach of the MTV technique based on mechanism D is similar to LIF, but the tracer has a long enough lifetime to permit sufficient displacement of the luminescence-tagged regions with the flow. The requisite long lifetimes of the tracer necessarily require the luminescence to be phosphorescence-based. This presents two obstacles to the development of MTV tracers for mechanism D. Successful imaging systems with long lifetimes must display the intrinsic property of a small k_r, but k_{nr} must be even smaller if the emission quantum yield is to approach its theoretical limiting value of unity (5.301, 302) and produce intense luminescence intensities. This requirement demands that efficient nonradiative decay pathways be eliminated in the design of imaging reagents. However, this property does not necessarily ensure a viable MTV technique; even if k_{nr} remains small with regard to k_r, long-lived

excited-state molecules have enough time to react with other molecules in their environment by quenching. As discussed in the context of (5.303) and (5.304), quenching leads to decreased emission intensity and lifetime, respectively.

For MTV applications based on mechanism D, quenching is an issue pervading most measurements. Water, oxygen, and residual metals in the environment are good quenchers of luminescence. As described by (5.305), the lifetime and intensity of an excited state decrease with increasing concentration of these quenchers. Thus a primary challenge in the design of any successful imaging system is to minimize these quenching pathways. The most problematic quencher in engineering applications is oxygen, owing to its efficiency and prevalence in the environment. Oxygen quenches phosphorescent excited states by an energy-transfer mechanism. The problems with oxygen in the MTV technique can be explicitly demonstrated by considering (5.305). Typically the quenching rate for oxygen is diffusion controlled (i. e., $k_q = 10^9\,\mathrm{mol}^{-1}\mathrm{s}^{-1}$), and its concentration in solution is typically 10^{-3} mol and in air is 10^{-2} mol. According to (5.305), the lifetime and intensity of a tracer possessing an inherent 1 ms photoluminescence lifetime (τ_0) will be attenuated by 10^3 in oxygenated solutions and will be reduced by over 10^4 in air.

Indeed, in the absence of oxygen, MTV measurements can be performed with a variety of organic phosphors. Some of the popular tracers such as biacetyl and acetone, which have often been used for flow visualization and LIF concentration measurements, can also be used as MTV tracers. The potential of biacetyl for this purpose has been known for sometime [5.629–631], and detailed multipoint measurements have been carried out with it [5.632–639]. Biacetyl (also called 2,3-butanedione) has a broad absorption spectrum with maxima at 270 and 420 nm. It is nontoxic and its relatively high vapor pressure (40 Torr at room temperature) allows a molar seeding of $\approx 5\%$. Biacetyl phosphoresces with a high quantum yield (0.15) and with a lifetime approaching 1.5 ms in nitrogen and helium flows. Nevertheless, oxygen completely quenches the green phosphorescence of biacetyl, even when present at only trace levels, rendering it impractical for general use in oxygenated flows such as air. More recently, *Lempert* and coworkers have demonstrated the acetone-based MTV approach and applied it to high-speed microjet flows [5.640, 641].

Long-lived, unquenchable tracers for MTV applications may be constructed by connecting small molecular subunits in intricate ways to lead to elaborate molecular architectures [5.642–645]. These supramolecules contain multiple sites with complementary function – a photoactive center capable of emitting visible light at one site and a docking site for the photoactive center at the other. This strategy centers on manipulating the fundamental parameters governing the luminescence intensity of a photoactive center such that molecular recognition of a constituent at the docking site causes k_r to be much greater than k_{nr} and k_q [5.646]. In this manner, it is possible to develop tracers with long-lived, bright phosphorescence that are not quenched.

Examples of such tracers are those based on lanthanide ions such as europium (Eu^{3+}) and terbium (Tb^{3+}) that have been developed for the study of two-phase flows. These ions exhibit luminescence from transitions involving electrons residing in orbitals buried deep within the ion. For this reason, the luminescent excited state is shielded from the external environment. Although oxygen will physically contact the lanthanide ion upon collision, it cannot communicate with the luminescent excited state owing to poor electronic coupling [5.647, 648] and oxygen quenching of lanthanide luminescence is not predominant. However, water is an excellent quencher of lanthanide luminescence because its O−H bonds act as good thermal receptacles for the excited-state energy of lanthanide-based active sites [5.649]. The deleterious effect of water can be circumvented by encapsulating the lanthanide ion in a molecular cage – a cryptand ligand (Fig. 5.154). The two nitrogens and five oxygens comprising the three straps of the 2.2.1 cryptand ligand occupy seven of the nine coordination sites of the lanthanide ion; the two remaining coordination sites are important

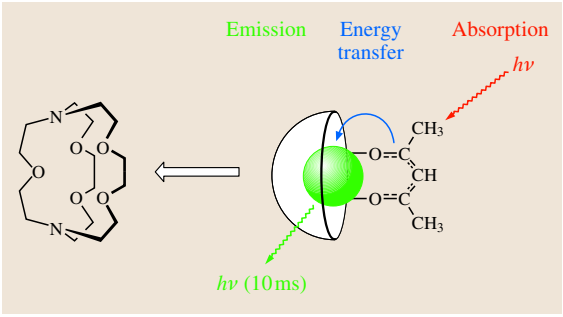

Fig. 5.154 A cryptand molecular cage encapsulates the photoluminescent Tb_3^+ ion (indicated by the *shaded ball*) with two remaining coordination sites occupied by light-harvesting groups, thereby allowing the photoactive Tb_3^+ center to be indirectly excited

for docking a light-harvesting group described below. The excited states of lanthanide ions are intrinsically bright lumophores, but they show little or no luminescence under direct irradiation because the excited states are spin-forbidden, and therefore they have low absorbance [5.650]. Docking or coordination of a light-absorbing group like acetylacetonate (acac) at the two unoccupied coordination sites opens up a conduit for energy to flow from the light-harvesting group to the lanthanide ion [5.651] and results in the green luminescence of the Tb^{3+} ion, which subsequently decays with its natural lifetime of 1.7 ms. This absorption-energy transfer-emission process [5.652] allows the lanthanide ion to be excited indirectly with intensities 10^3–10^4 times greater than in its absence. Thus this tracer emits brightly, possesses a long lifetime and its excited state is not quenched by oxygen or water. These properties have allowed successful use of this tracer in a study of two-phase flows using the MTV technique [5.552].

Interest in developing tracers with even longer lifetimes has led to a class of supramolecules called cyclodextrins (CDs). Cyclodextrins are cyclic oligosaccharides [5.653], formed from connecting six, seven, or eight D-glucose rings (a common sugar) in a head-to-tail arrangement (α-, β-, and γ-, respectively) (Fig. 5.155).

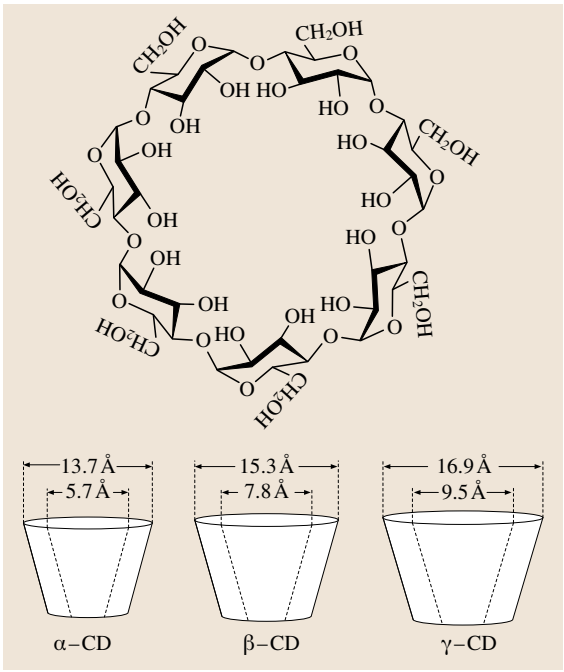

Fig. 5.155 A cyclodextrin and the dimensions of the CD cup for the α, β, and γ forms

The molecule is cup-shaped with its size determined by the number of sugars in the structure. The CD most often used in MTV applications [5.550] is β-CD, which is constructed from seven sugar subunits, resulting in an outer cup dimension of 15.3 Å and an inner cup dimension of 7.8 Å. Hydroxyl groups of the sugar rings encircle the outer rims of the CD cup, imparting water solubility. To increase the solubility even more, an additional glucosyl subunit is hung off of the rim (called Gβ-CD). The hydrocarbon rings of the D-glucose subunits of the cup walls define a water-repelling or hydrophobic interior that allows it to absorb water-insoluble or hydrophobic compounds. Thus the cyclodextrin is a miniature bucket that dissolves in water but will fill itself with hydrophobic compounds.

The CD cup can be filled with a lumophore such as 1-bromonaphthalene (1-BrNp). This molecule has a bright fluorescence with a 9 ns lifetime. The purpose of attaching the bromine to the molecule is to induce a crossing from the fluorescing, singlet excited state to a triplet ex-

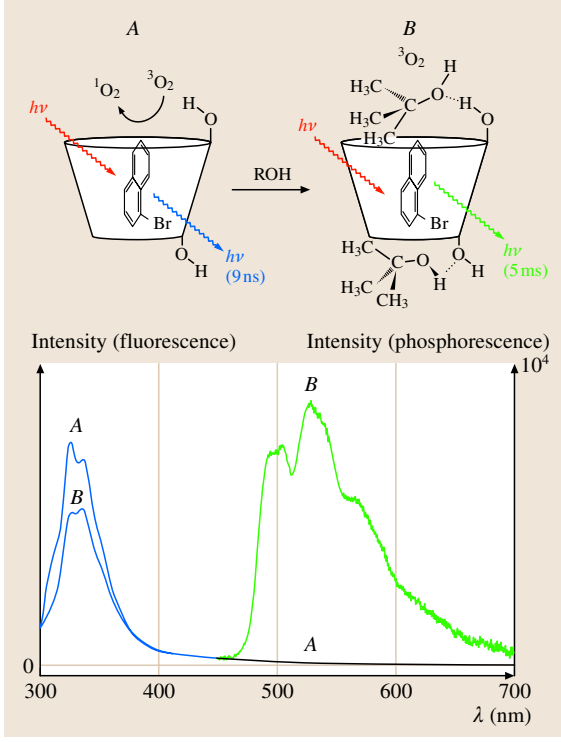

Fig. 5.156 Phosphorescence from 1-bromonaphthalene (1-BrNp) included within a CD is observed only when alcohols are present. In the absence of alcohol (*A*), only blue fluorescence is observed. Green phosphorescence is triggered upon addition of an alcohol such as tert-butanol (*B*)

cited state. The bright green phosphorescence (10 ms is the natural lifetime but the lifetime may decrease to ≈ 5 ms when intense irradiation sources are used) from 1-BrNp is efficiently quenched by oxygen, even when the lumophore is included within a CD cup, as shown in Fig. 5.156 (spectrum A) where only the short-lived blue fluorescence of the 1-BrNp is observed. The phosphorescence can be recovered when certain alcohols (indicated collectively by ROH) are added to the solution. Exhaustive equilibria, photophysical, and kinetics studies for a series of alcohols [5.654] reveal that a ternary complex (1 − BrNp • Gβ − CD • ROH) is formed among the alcohol, CD, and 1-BrNp. The mechanism that gives rise to the triggered phosphorescence by alcohols is shown in Fig. 5.156. In short, the alcohol hydrogen-bonds to the rim of the CD cup, and the aliphatic end of the alcohol flips over the hydrophobic interior of the CD. Accordingly, the alcohol acts as a lid for the CD cup, thereby shielding 1-BrNp from oxygen (Fig. 5.157). Phosphorescence enhancements can be very large, approaching 10^4–10^5, depending on the fit of the alcohol lid to the top of the CD cup [5.655].

The details of the MTV implementation and other applications of the phosphorescent supramolecules described above can be found in *Gendrich* et al. [5.550]. The choice of the alcohol and its concentration strongly influence the phosphorescence lifetime and intensity. For MTV studies, cyclohexanol and neopentanol are the alcohols of choice, and the excitation sources used to date are the 308 nm of the XeCl excimer laser or the 266 nm of quadrupled Nd:YAG laser. Since phosphorescence emission is produced only when all components (Gβ-CD, 1-BrNp, and alcohol) of the ternary complex are present, it is possible to devise in addition to pure velocimetry other applications for molecular-tagging passive-scalar mixing regions, or chemical reaction interfaces, and monitor their Lagrangian evolution. In more-recent studies [5.656, 657] the original glucosyl subunits (i. e., in Gβ-CD) have been replaced by maltosyl subunits (Mβ-CD). The measured properties of both glucose- and maltose-based triplexes are quite similar and the two can be used interchangeably. The three components of these phosphorescent complexes are commercially available; the various alcohols and the lumophore (1-BrNp) are readily found in catalogs of most scientific chemical companies, and maltosyl beta CD is available from Cyclodextrin Technologies Development, Inc. (Gainesville, FL, USA) under the trade name Trappsol.

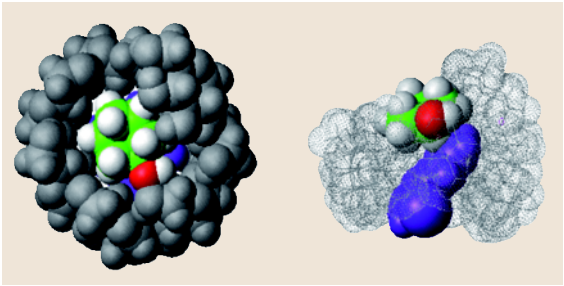

Fig. 5.157 Top and side views of computer-generated molecular model of the tracers from 1-BrNp, CD, and cyclohexanol. The CD is speckled in the side view so that the inside of the cup may be viewed. The purple molecule is 1-BrNp and the multicolored molecule is cyclohexanol. In the top view, the cyclohexanol obscures the 1-BrNp. It is this *blocking action* that prevents oxygen from quenching the phosphorescence of the 1-BrNp

5.4.2 The Experimental Implementation of MTV: Tagging Methods, Detection and Processing

The specific complexities in the photophysics of the various molecular tracers used for MTV determine the wavelength and number of photon sources needed for tagging and those needed for interrogation. Regardless of these complexities, implementation of MTV for fluid flow studies involves certain common issues that are discussed in this section.

Tagging Methods

Molecular tagging along single or multiple parallel lines is the simplest method of tagging and has been utilized in a large fraction of MTV studies to date. The experiment is typically configured to create tagged lines perpendicular to the primary flow direction and the velocity is estimated from the displacement of these lines. Two examples of single-line tagging are shown in Figs. 5.158 and 5.159. Figure 5.158 depicts the displacement of a tagged line that is created by RELIEF (MTV mech-

Fig. 5.158 Typical single-line RELIEF image pair taken in a turbulent free air jet with 0 μs (*lower line*), and 7 μs (*upper line*) time delay. The *line* is approximately 1.2 cm long (after [5.590], with permission of Cambridge Univ. Press)

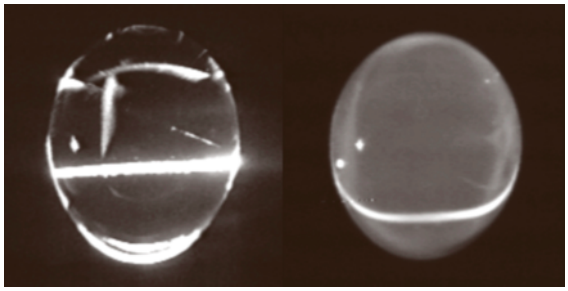

Fig. 5.159 Single-line tagging image pair inside a free-falling 5 mm-diameter water droplet using caged fluorescein [5.658]. The time delay between the initial tagging (*left*) and displaced image (*right*) is 29.5 ms

anism B) in a turbulent air jet. The resulting velocity data have been used to elucidate certain characteristics of turbulent velocity fluctuations [5.590]. Figure 5.159 illustrates the image pair from single-line tagging using caged fluorescein (MTV mechanism C). These image data have been used to characterize the internal circulation inside a falling water droplet [5.593, 594, 658]. An example of multi-line tagging using phosphorescent supramolecules (MTV mechanism D) in a water tunnel is provided in Fig. 5.160. This figure illustrates the trailing-edge region of a NACA-0012 airfoil oscillating sinusoidally at a high reduced frequency of $k = 8.8$ and amplitude of 2° [5.659]. The time delay between tagging and interrogation is selected to be long (about 20 ms) to allow a large displacement of the tagged lines so that the flow patterns caused by vortical structures and vortex sheets can be easily observed.

When using line tagging, it is important to recognize that this tagging method allows the measurement of only one component of velocity, that normal to the tagged line. In addition, the estimate of this velocity component has an inherent error associated with it, which is connected with the ambiguity in the unique determination of the displacements of various portions of a (continuous) tagged line. Following the analysis of *Hill* and *Klewicki* [5.660], the error can be written in the form $\Delta u/u = (\upsilon/u)(\partial u/\partial y)\Delta t$, where u is the estimated velocity component normal to the tagged line, Δu is the error in the estimated velocity, υ is the flow velocity component parallel to the tagged line, and Δt is the time delay between tagging and interrogation. Clearly an a priori knowledge of the flow field is necessary in order to provide an estimate of the error. It can be observed, however, that this inherent error is identically zero only in flows where the velocity component υ along the tagged line is zero (i. e., unidirectional flows) or where the velocity gradient along the line $\partial u/\partial y = 0$. In a general flow field where these constraints are not met, the error can be reduced by decreasing the delay time Δt, but it cannot be made arbitrarily small, since Δt needs to be large enough for the resulting displacement of the tagged line to be measured with adequate accuracy. While bearing these issues in mind, it is sometimes possible to take advantage of an a priori knowledge of the flow field under investigation to design the experimental parameters such that the inherent error discussed here becomes minimal compared to other measurement errors. Representative examples of fluid flow measurements obtained with line tagging methods include studies of jets [5.581–583, 590, 640, 641], boundary layers [5.660, 661], pulsatile flow through tubes [5.569], particle-laden coaxial jets [5.662], buoyancy-induced flow in directional solidification [5.663–665], and axial flow within concentrated vortex cores [5.666, 667]. MTV with line tagging has also found extensive use in microfluidic applications where the flow is primarily unidirectional [5.596, 599, 627, 668, 669].

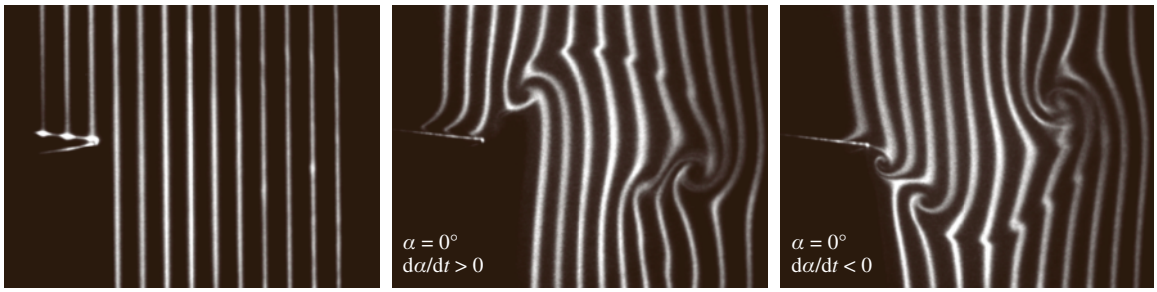

Fig. 5.160 Multiline tagging in the trailing region of a NACA-0012 airfoil pitching sinusoidally with an amplitude of 2° [5.659]. The tagging pattern (*left image*) right after the laser pulse is a series of parallel lines with a spacing of 3 mm (about 0.025 chord length). The displaced lines are shown at zero angle of attach during pitch-up (*middle image*) and pitch-down (*right image*)

In order to measure two components of the velocity in a plane unambiguously, the luminescence intensity field from a tagged region must have spatial gradients in two, preferably orthogonal, directions. For single-point velocimetry, this can be achieved using a pair of crossing laser beams and measuring the displacement of the beam intersection; a grid of intersecting laser beams allows multipoint velocity measurements as illustrated in Fig. 5.149. This tagging scheme, first suggested by *D'Arco* et al. [5.573] and later improved upon and utilized by *Falco* and *Chu* [5.570], is now commonly used.

The methods used to date for generating a grid of intersecting laser beams typically rely on standard optics (i. e., beam splitters, mirrors, spherical and cylindrical optics, and beam blockers). For example, the tagging pattern shown in Fig. 5.149 is generated by manipulating the main beam of an excimer laser to increase its aspect ratio using a cylindrical lens, followed by splitting the outgoing laser sheet with a 50:50 beam splitter and redirection by mirrors, and then passing them through a pair of beam blockers [5.550]. Spherical lenses are used as needed to control the spatial scaling of the entire grid pattern. The maximum density of grid intersections is limited by different factors depending on the type of molecular tracer that is used. In some cases the energy requirements to create the tag and detection sensitivity set the limit. *Miles* et al. [5.591] have reported a single intersection created with RELIEF, whereas *Pitz* et al. [5.609] recently achieved a 7×7 grid pattern with their HTV approach using OH (Fig. 5.161). When using phosphorescent tracers for MTV in both gas- and liquid-phase flows, the energy in each tagging beam is typically in the range 1–2 mJ or less per pulse and the maximum grid density has been limited not by the available laser energy but by the pixel density of the imaging detector arrays used [5.550, 635, 670]. For 640×480 px detector arrays, tagging with a grid pattern in the range 30×30 has been achieved. Recent work with higher-resolution detectors (1280×1024 px array) tags the phosphorescent molecules in a water flow with about a 70×70 grid pattern [5.657].

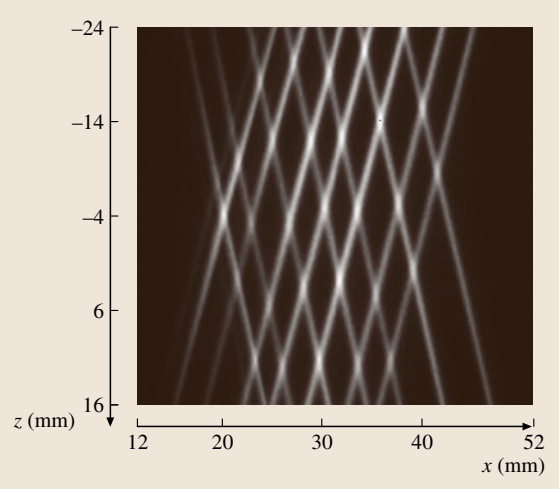

Fig. 5.161 A 7×7 grid of tagged OH lines in a supersonic flow (Mach number 2) over a cavity [5.609]

It is useful to note that tagging by a nonuniform laser illumination in the form of a grid is needed when the molecular tracer is present uniformly in the fluid. This method is only a special case of a more-generalized approach to induce a spatially nonuniform luminescence intensity in a tagged region. For example, the nonuniform passive-scalar field typical of most turbulent flows can sometimes be used as a natural source of luminescence nonuniformity without the need for grid illumination, or further enhancement of the effect of grid illumination. Examples of this type are discussed in *Koochesfahani* et al. [5.553] and *Gendrich* et al. [5.550].

Detection

The most common implementation of MTV uses a single detector; the initial (or reference) tagging pattern is recorded once, usually at the beginning of the experiment, and then the *delayed* images are acquired. This approach works well as long as the initial tagging pattern remains spatially invariant throughout the experiment. Otherwise, any variations in the initial tagging pattern (e.g., due to laser-beam pointing instability, vibration of the optics, nonuniform tracer concentration, etc.) is misinterpreted as flow velocity fluctuations and reduces the measurement accuracy of the instantaneous velocity.

To minimize these potential problems, *Gendrich* et al. [5.550] implemented a two-detector imaging system for their work with phosphorescent tracers. The MTV image pairs are acquired by a pair of CCD detectors that view the same region of interest in the flow through a beam splitter. Using a reference target, the two cameras are aligned to within one pixel, and the remaining residual displacement field between the two detectors is quantified to subpixel accuracy and accounted for in subsequent data processing (for details see [5.550]). Immediately after the pulsed laser fires to tag the molecules in the flow, the first detector records an initial image of the tagged regions. After a prescribed time delay, the second detector records

a second image of the tagged regions displaced by the flow. Such a two-image system offers advantages over the typical single-image system in that no assumption needs to be made a priori about the intensity field in a tagged region and one can properly take into account the variations in the initial tagging pattern. Two-detector imaging has been used in many MTV studies, especially those based on phosphorescent tracers [5.638, 659, 664–667, 669–675].

These one- or two-detector schemes address conventional planar imaging for obtaining information on two components of the velocity vector over the viewed plane (or one velocity component in the case of line tagging). When stereo imaging is used to obtain the out-of-plane velocity component as well (*Krüger* [5.615]; *Bohl* et al. [5.551]), the number of detectors needed increases by a factor of two. With advances in detector technology, the two-detector MTV approach can now be accomplished with a single *dual-frame* camera that allows the acquisition of two images of the tagged regions with a programmable time delay between them [5.657, 666]. This capability not only simplifies the implementation of conventional MTV imaging but also provides for a significant reduction of effort in aligning multiple cameras for stereo imaging [5.666].

Processing

A common method for finding the displacement of tagged lines or grids has been to locate the center of each line by various techniques [5.592, 660, 667]. One approach is to use the best fit to an assumed laser line shape, for example, a Gaussian intensity distribution [5.592]. Another is to use a second-order curve fit following Gaussian smoothing [5.660]. *Hill* and *Klewicki* [5.660] report the rms accuracy in determining the displacement of a tagged line to be 0.35 px. The performance of these methods for finding line centers tend to suffer when the intensity distribution of the tagged regions cannot be assumed in advance, for example, due to a nonuniform tracer distribution, difficulties associated with laser-beam transmission through a flowing medium, photobleaching effects, etc. *Sadr* and *Klewicki* [5.676] have recently explored a spline-based method and report an improvement in subpixel accuracy by about a factor of three.

Another approach for finding the displacement of tagged regions is based on a direct digital spatial correlation technique, and offers certain advantages over the traditional line-center methods. In particular, it is a more-general scheme that is independent of the specific intensity distribution within a tagged region and can accommodate arbitrary tagging patterns including those due to nonuniform scalar mixing fields. The details of this approach and its performance are described in *Gendrich* and *Koochesfahani* [5.677]. A small window, referred to as the source window, is selected from a tagged region in the earlier undelayed image, and it is spatially correlated with a larger roam window in the second delayed image. A well-defined correlation peak occurs at the location corresponding to the displacement of the tagged region by the flow; the displacement peak is located to subpixel accuracy using a multidimensional polynomial fit (see the example in Fig. 5.162). This approach is similar to that used in DPIV processing of particle image pairs and, because of the averaging process inherent in the correlation procedure, it is more robust to the presence of noise and typically more accurate than line-center methods. Based on both experiments and an extensive statistical study, it has been found that the displacement of the tagged regions can be typically determined with a 95% confidence limit of 0.1 subpixel accuracy (i. e., 95% of the displacement measurements are accurate to better than 0.1 px). This corresponds to an rms accuracy of 0.05 px, assuming a Gaussian distribution for error. For high values of image signal-to-noise ratio, the 95% confidence level can be as low as 0.015 px (0.0075 px rms). An example of the application of this procedure is provided in Fig. 5.149; the velocity vectors shown in this figure are *raw* and have not been filtered or smoothed.

The spatial correlation method described above has also been applied to processing line tagging images in an investigation of flows in microchannels [5.668, 669].

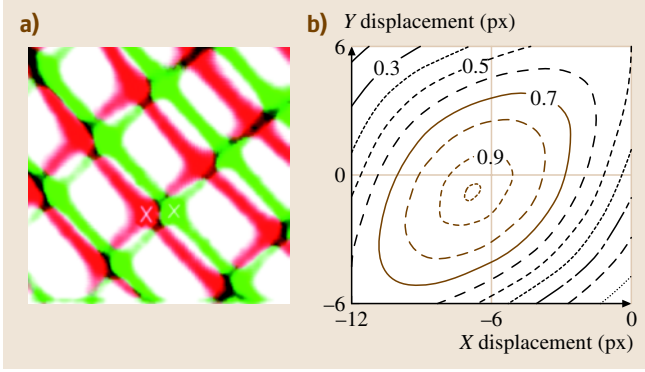

Fig. 5.162 **(a)** Superposed experimental MTV image pair: *green lines* are the grid at $t = 0$, *red lines* are the grid after $\Delta t = 6$ ms delay. **(b)** Correlation coefficient contours for the indicated intersection in **(a)** (after *Koochesfahani* et al. [5.553])

In this case, a one-dimensional correlation procedure is used and accuracies similar to *Gendrich* and *Koochesfahani* [5.677] are obtained. A modified version of the two-dimensional spatial correlation method of *Gendrich* and *Koochesfahani* [5.677] has been introduced by *Zheng* and *Klewicki* [5.678] where the subpixel accuracy is determined not based on the original multidimensional polynomial fit but using two decoupled polynomials. This approach offers a faster computational algorithm at the expense of reduced accuracy. Other processing methods such as the image correlation velocimetry approach of *Tokumaru* and *Dimotakis* [5.679] have also been applied to MTV image pairs [5.608].

MTV velocity data are obtained originally on an irregularly spaced measurement grid. In order to take advantage of standard data display and processing techniques, the data need to be remapped onto a regular grid with uniform spacing. One method that has been used for this purpose is based on a least-squares fit to low-order polynomials. The details of the procedure and its performance characteristics are given by *Cohn* and *Koochesfahani* [5.680]. The velocity field on a regular grid is then used to compute the vorticity field in the same manner as in DPIV data. Typically a finite-difference approach, for example, second-order central difference, is utilized [5.671,680]. The accuracy of the measured vorticity depends on the accuracy in the velocity measurement and the data grid spacing. Vorticity measurement accuracies in the range $1–2\,s^{-1}$ (95% confidence limit) have been reported [5.670,673].

An example of MTV data obtained by the procedures described above is given in Fig. 5.163. This example shows the instantaneous whole-field measurement of two components of the velocity vector over a plane in a study of unsteady boundary-layer separation caused by the interaction of a vortex ring impinging on a solid wall. This interaction generates an unsteady adverse pressure gradient on the wall, which results in boundary-layer separation and the formation of a secondary vortex. An LIF visualization of this flow right after the formation of the secondary vortex is depicted in Fig. 5.163a (only the right half of the flow is included). Figure 5.163b shows the corresponding instantaneous MTV velocity data (1 mm grid spacing with the first grid 0.5 mm away from the wall) and the computed vorticity field. These data have sufficient resolution to study the behavior of the unsteady boundary layer on the wall and the progression of the boundary-layer separation process [5.671].

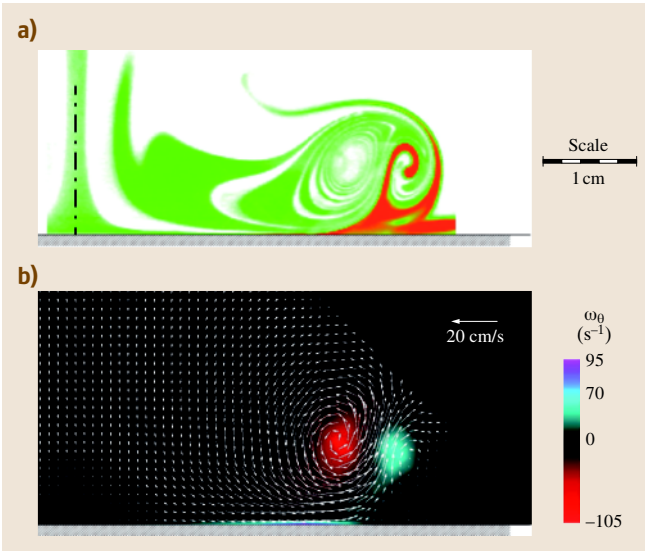

Fig. 5.163 (a) LIF image of the *right-half* of a downward-moving vortex ring impinging on a solid wall. The ring and wall-layer fluids are marked by green- and red-emitting laser dyes, respectively. (b) Velocity and vorticity fields measured using MTV (after *Koochesfahani* et al. [5.553])

5.4.3 Examples of MTV Measurements

The references cited in this work present the development and application of molecular tagging velocimetry in flows over a wide range of speeds, from liquid-phase microfluidic flows with speeds that are measured in μm/s to gas-phase flows at supersonic speeds. The scope of the measurements covers a range from the instantaneous profile of one component of velocity vector along a tagged line to whole-field three-component velocity data over a plane obtained with stereo imaging. Some of the flows that have been successfully investigated include pulsatile flow in tubes, electro-osmotically and pressure-driven microfluidics, internal circulation in droplets, unsteady boundary-layer separation, vortex flows and mixing enhancement, convective flows in directional solidification, flows during intake and compression inside motored internal combustion (IC) engines, flows in engine testing facilities, high-temperature reacting flows, free and wall-bounded turbulent flows, and highly three-dimensional vortex flows with strong out-of-plane motions where the primary flow direction is normal to the tagged plane.

In this section we provide several examples to highlight some of the measurement capabilities that have been achieved with molecular tagging velocimetry

based on phosphorescent tracers (MTV mechanism D). These examples consider only velocimetry applications. The unique properties of some molecular tracers have led to novel methods for studying scalar mixing in turbulent flows using caged fluorescent dyes [5.681,682] and high-sensitivity temperature measurements with phosphorescent supramolecules [5.656]. In addition, MTV has been extended to multivariable mapping such as simultaneous velocity–concentration [5.674] and velocity–temperature [5.657, 683, 684] experiments.

Boundary-Layer Resolved Measurements of Leading-Edge Separation on a Pitching Airfoil

When an airfoil dynamically pitches to high angles of attack the viscous boundary layer near the leading edge eventually separates and causes catastrophic events such as dynamic stall. The evolution of the flow within the boundary layer at the onset of separation has been captured with molecular tagging velocimetry [5.672], providing the first detailed map of the events that occur within the boundary layer near the surface of a pitching airfoil. The results shown in Fig. 5.164 are from measurements carried out in a 60×60 cm water tunnel using a 12 cm chord NACA-0012 airfoil pitching at a constant rate (nondimensional pitch rate = 0.1) from 0 to 60° angle of attack. The chord Reynolds number is about 12 000. Since the range of spatial scales in this problem is too large to be captured in a single field of view, these measurements are carried out over multiple fields of view with decreasing size. Repeatability of this flow allows the data to be compiled into a single finely resolved data set for each 0.25° change in angle of attack.

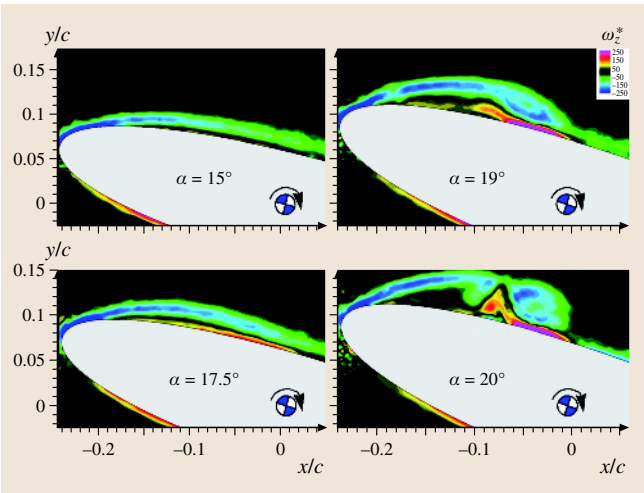

Fig. 5.164 Evolution of the vorticity field at the onset of leading-edge separation on an airfoil pitching to high angles of attack [5.672]

The nondimensional vorticity field computed from this data set is shown in Fig. 5.164 at four angles of attack near the onset of leading-edge separation. These results illustrate the ability of MTV to image fluid flows near walls. Among the details that are resolved in these measurements are the occurrence of a thin reversed-flow region near the airfoil surface, and the eruption of the boundary-layer vorticity away from the wall in a highly localized manner in both time and space. Complementary two-dimensional Navier–Stokes computations have also been carried out at the flow conditions of these experiments. A conclusion from these experimental data is that the process of boundary layer separation occurs over a shorter time scale, and is more eruptive, than that captured by the computations.

Measurement of Buoyancy-Driven Convective Flow During Unidirectional Solidification

Solidifying a binary alloy under off-eutectic conditions is often accompanied by convection in the melt. The convection mechanisms caused by solutal and thermal forces for such conditions can produce inhomogeneities and imperfections such as solute-rich channels in the final fully solidified ingot casting. While the convective phenomena involved in the formation of these imperfections are not completely understood, it is generally accepted that they are best described in terms of complex dynamic fields and that most experimental methods applied to date are poorly suited to measure these fields. One means of learning more about these phenomena has been the use of transparent analogs of metallic alloys. One such analog is the binary aqueous ammonium chloride (NH_4Cl–H_2O) system. Some of the complex features of convective phenomena associated with solidification in the aqueous ammonium chloride include: the vertical growth of a solid–liquid interface with concurrent early development of numerous fine structures of salt fingers followed by the appearance of a small number of plumes ejecting fluid jets from channels in the mushy zone of the growing dendritic crystal mass. These features are illustrated in the shadowgraph images in Fig. 5.165 [5.664, 665].

Measurement of this flow field by particle-based techniques can be problematic since the presence of particles could interfere with the solidification process and create unwanted nucleation sites. In addition, the mushy

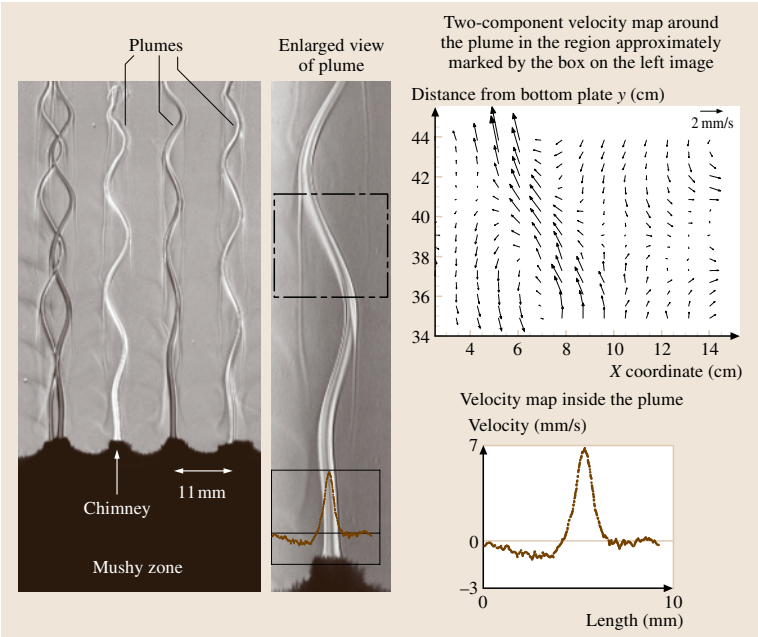

Fig. 5.165 Shadowgraph image of organized plumes above an advancing solidification front and the velocity fields measured by MTV [5.664, 665]. The velocity profile at the bottom of plume is measured using line tagging

zone acts as a very fine-scale porous medium and traps the particles that are contained within the liquid above. As a result, the fluid within the plume is often devoid of particles. The MTV approach using phosphorescent supramolecules have been used to measure the velocity field within and around the plumes [5.664, 665]. The portion of the flow near the bottom of the plume is mostly unidirectional (vertically upward flow) and single line tagging is sufficient to map the velocity profile within the plume. Farther up, however, two-component velocity maps are obtained using molecular tagging by an intersecting grid of laser lines. A unique aspect of these measurements is that the time delay between tagging and interrogation needs to be long due to the slow flow speeds involved. The 60 ms delay time used in these measurements is about a factor of 12 longer than the phosphorescence lifetime (i. e., $1/e$ point) of the tracer used, resulting in a significant reduction of phosphorescence emission intensity and necessitating the use of an intensified camera for detection.

Figure 5.165 shows the measured instantaneous velocity profile across a single plume as it exits the chimney, and the velocity map around the plume farther up. The upward jet-like velocity field within the plume is captured along with a nonsymmetric downward flow around the plume. Note the peak velocity is only 7 mm/s and the width of the plume is about 2 mm.

Measurements in a *Steady Flow Rig* Model of an IC Engine

The steady flow rig configuration is commonly used in the internal combustion (IC) engine research community to study the fundamentals of the intake flow. The particular geometry used here consists of a quartz cylinder of radius $R_0 = 41$ mm, placed axisymmetrically around a nozzle with a valve body placed axisymmetrically inside the jet nozzle. In this case the flow exiting through the valve opening, which simulates the intake flow into an IC engine geometry, is in the form of an

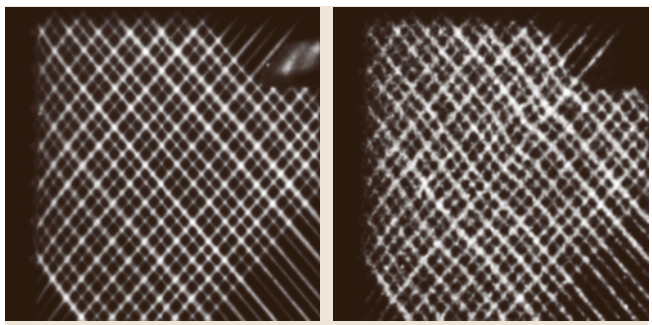

Fig. 5.166 Example of the tagging pattern for the gas flow into the steady flow rig (after *Stier* and *Koochesfahani* [5.635]). Images were acquired by a gated image-intensified camera

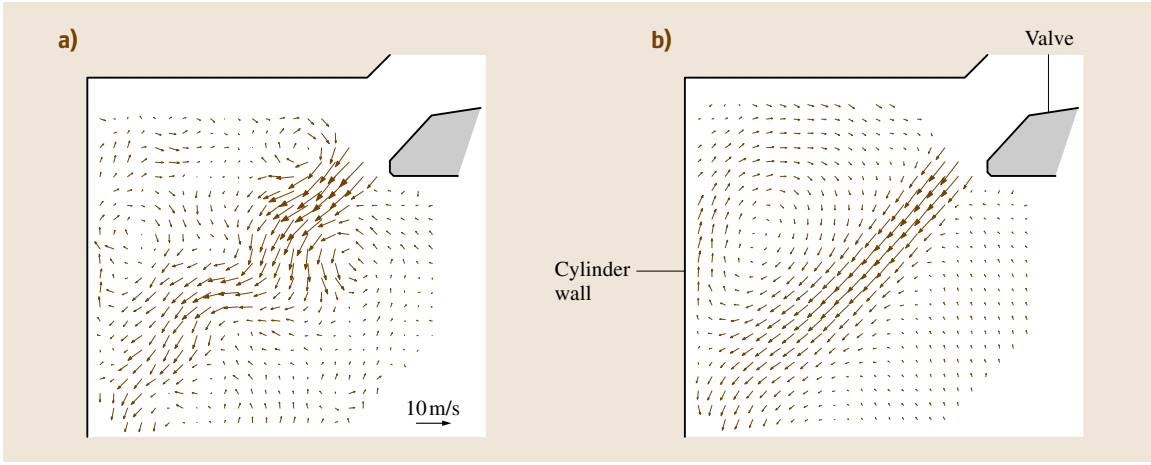

Fig. 5.167a,b Intake flow into a steady flow rig model of an IC engine measured with MTV using nitrogen seeded with biacetyl (after *Stier* and *Koochesfahani* [5.635]). **(a)** The instantaneous velocity field derived from the image pair in Fig. 5.166 using a spatial correlation procedure. **(b)** Time-averaged velocity field based on 320 instantaneous realizations

annular jet. In this study, the valve opening (valve lift) is set at $L = 9$ mm and the maximum intake speed is about 10 m/s. The instantaneous accelerations in the shear layer at the interface between the intake jet and adjacent fluid can be as high as 5000 g, making it difficult to rely on the results of particle-based techniques. The details of this work can be found in *Stier* and *Koochesfahani* [5.635].

Figure 5.166 shows a 3×3 cm field of view in the nitrogen/biacetyl flow being investigated and the regions tagged by a grid pattern generated from an excimer laser ($\lambda = 308$ nm, 20 ns pulse). Part of the valve body and the left wall of the cylinder are visible in the picture. The maximum flow speed in the annular jet entering the cylinder is about 10 m/s. Also shown is an example of the later image of the tagged regions after a 50 μs delay. For this time delay, the maximum displacement of tagged regions is about 8 px (≈ 500 μm). Image pairs such as those in Fig. 5.166 are used to determine the instantaneous radial and axial velocity components in this flow field. An example of the instantaneous velocity field and the structure of the intake flow in this geometry are shown in Fig. 5.167 along with the average velocity field based on 320 realizations. The instantaneous flow map shows a highly unsteady intake annular jet, which has an undulating appearance with opposite sign large scale vortical structures on its two sides. The mean flow map indicates a large-scale region of recirculation in the upper left corner of the engine cylinder, a feature typical of an IC engine flow field. These data have also been used to derive other properties of the flow such as the instantaneous and average vorticity fields and velocity fluctuations [5.635].

Fig. 5.168 The optically accessible research engine and a typical MTV grid in the nitrogen/biacetyl flow within the engine cylinder (after *Koochesfahani* et al. [5.639])

Velocity Field During Late Compression in a Motored IC Engine

One of the main obstacles in optimizing combustion in gasoline-fueled internal combustion engines is the large cycle-to-cycle variation in in-cylinder flow and mixing characteristics. Cycle-to-cycle variability puts constraints on the lean limits of combustion. In this study velocity field data are obtained using MTV during late compression of an internal combustion engine, the most critical time of the four-stroke cycle. Such data are highly sought after since the state of the

flow just before the firing of the spark plug directly influences the subsequent combustion and emission production.

The measurements are conducted in an optically accessible motored research engine shown in Fig. 5.168. The cylinder is made from quartz and the flat-head piston face is modified for optical access through a quartz window. A typical MTV grid generated within the engine cylinder is also shown in Fig. 5.168. Measurements are made at late compression at a position of 270 crank angle degree (CAD), as the piston approaches the top dead

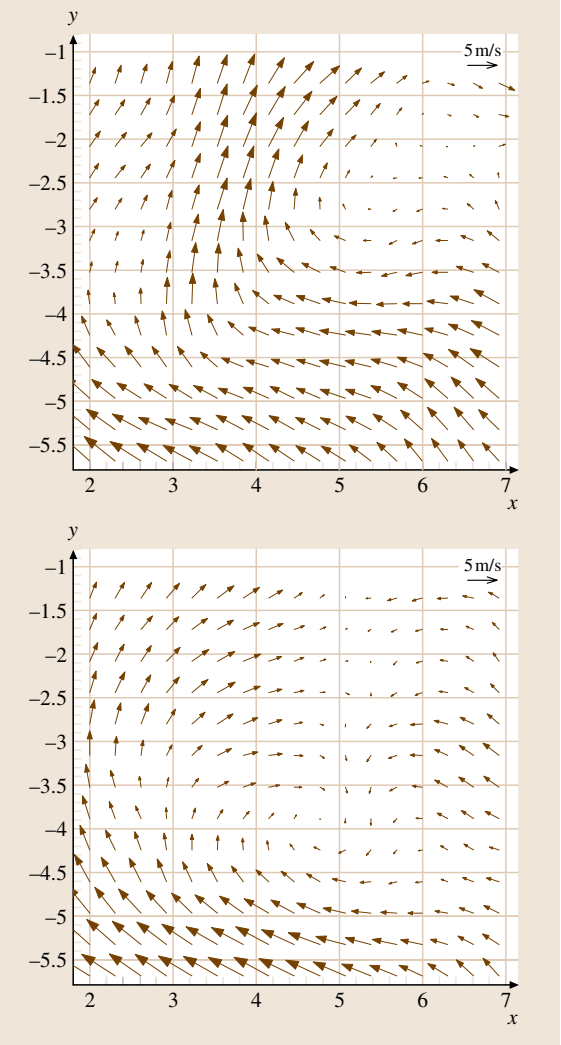

Fig. 5.170 Two instantaneous realizations at 270 CAD showing the large cycle-to-cycle variability of the flow field (after *Goh* [5.638])

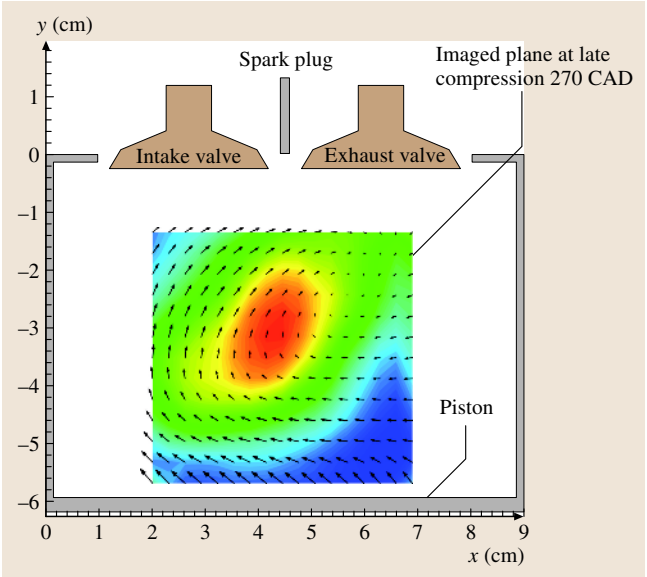

Fig. 5.169 The position of the imaged plane at 270 CAD (after *Goh* [5.638])

center (TDC) of the engine, with the engine running at 600 rpm. For the conditions described here, and the engine compression ratio of nearly 10, the gas temperature can reach a value as high as 600 K. The measurements

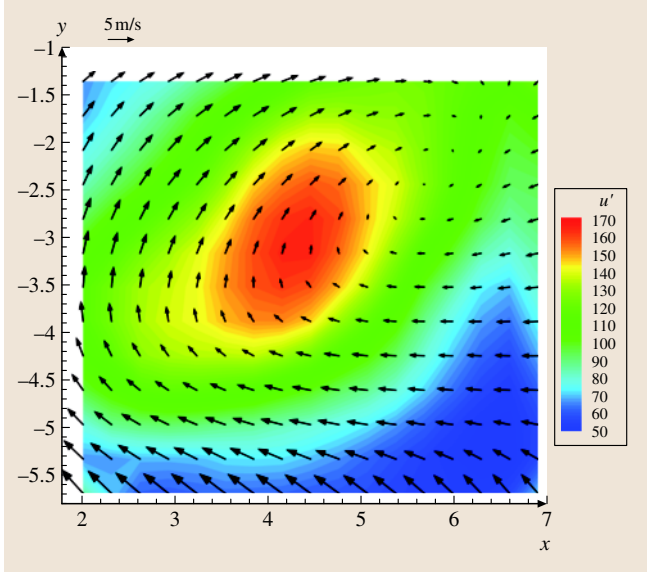

Fig. 5.171 Maps of the ensemble-averaged velocity field and the rms fluctuation of the horizontal component of the velocity u' (in cm/s). Colors denote rms fluctuation level (after *Goh* [5.638])

consist of 500 independent realizations of the velocity map at the same crack angle (270 CAD) at the mid-tumble-plane. The position of the imaged plane over which the velocity maps are obtained is given in Fig. 5.169. The details of this work can be found in *Goh* [5.638].

Two samples of the instantaneous velocity field, for two different engine cycles, are shown in Fig. 5.170. It is clear the flow pattern is significantly different between these two realizations, an indication of the large cycle-to-cycle variability of the flow. The maps of the ensemble-averaged velocity field and the rms fluctuation of the horizontal velocity component are computed from 500 such realizations (Fig. 5.171). As expected for a flow with large cycle-to-cycle variation, the mean velocity field shows little resemblance to the instantaneous field; the local fluctuation level can be higher than the mean by several hundred percent. The data shown in Figs. 5.170 and 5.171 are the first cycle-resolved velocity measurements that use molecular tracers rather than particles to determine flow velocities in a piston-engine assembly. Such measurements have been used to advance the understanding and quantification of cycle-to-cycle variability in an internal combustion engine, and to find methods for reducing it [5.638].

5.4.4 Summary and Conclusions

Molecular tagging velocimetry has seen significant advances as a result of improvements in laser and detector technologies, imaging techniques, data analysis methods, and chemical design and synthesis of novel molecular structures. These advances are expected to continue. The MTV approach has continuously evolved and its use is steadily increasing in both fundamental flow studies and applied engineering measurements.

5.5 Vorticity

Vorticity ($\nabla \times \vec{\nabla}$) is recognized as a primitive variable of considerable interest in fluid dynamics. However, its time-resolved measurement has significantly lagged behind the development of velocity and pressure measurement techniques. The necessity to obtain a measure of the *curl of the velocity*, that is, to accurately measure velocity differences over very small distances, has been a formidable challenge. Two presentations of hot-wire probe techniques are presented to guide the reader in the selection of a suitable measurement technique for a given application.

It is also appropriate to note the capacity to obtain well-resolved, single images of the vorticity component normal to the image plane using molecular tagging velocimetry is presented in Sect. 5.4. Particle image velocimetry (Sect. 5.3.3) techniques can also give a measure of the vorticity although their spatial resolution does not typically allow as fine a resolution of the scales of the vorticity field.

Most of the experimental work carried out in the past on turbulent flows has focused on acquiring velocity information on various types of flow configurations, which has been used to enhance our understanding of the underlying physics of these flows. The velocity field, however, is not well suited for defining and identifying organized structures in time-dependent vortical flows because the streamlines and pathlines are completely different in two different inertial frames of reference. Better understanding of the nature of turbulent structures and vortex motions of turbulent flows, particularly in the high-wavenumber region, often requires spatially and temporarily resolved measurements of gradients of fluid-mechanical quantities such as velocity or pressure. The availability of such measurements will lead to information on important quantities such as the structure function of velocity or pressure, the vorticity, the rate-of-strain tensor and its matrix invariants, and the dissipation rate of turbulent kinetic energy.

Lighthill [5.685] in his wide-ranging introduction to boundary-layer theory is credited as being the first researcher to emphasize the role of vorticity for the better understanding of fluid-dynamics phenomena. His work provided an extensive description of vorticity dynamics in a variety of flows by using vorticity as a primary variable.

Vorticity characterizes the rotation rate of a fluid particle. In the case of constant-density incompressible flows, vorticity is acquired by a pressure gradient introduced at a physical surface. The pressure gradient at the surface is balanced by the stress gradient,

which is related to the vorticity flux entering the flow. Thus the existence of vorticity generally indicates that viscous effects are important. In turbulent flows vorticity is the key to improving our understanding of the mechanisms that control the motion of the large-scale structures and the mechanisms by which irrotational fluid lumps gain rotational motion through the action of viscosity and thereby entrain ambient fluid into the flow field.

5.5.1 Optical Techniques in Strophometry – Vorticity Measurements Methods

Although measurements of instantaneous vorticity, particularly in unsteady or separated turbulent flows, are very much in demand, such data are scarce at present due to the extreme difficulties involved in such measurements. In most of the available techniques Taylor's hypothesis is invoked, the validity of which has not yet been justified for the case of separated flows. Recent techniques in hot-wire and hot-films anemometry can measure several components of the vorticity vector [5.686–693]. Hot-wire techniques have been extended to measure three-dimensional vorticity in vortex-dominated flows such as those over delta wings [5.689] and in compressible turbulence with or without the presence of shock waves [5.694–696]. However, these techniques are intrusive and invoke Taylor's hypothesis. In addition, hot-wires and hot-films are insensitive to the large changes in velocity direction that are present in separated flows and flows with high turbulence intensity.

In the context of the present work the term *strophometry* is defined as the science and technology involved in the measurement of fluid rotation, being a derivative of the Greek word strophe ($\sigma\tau\rho o\phi\acute{\eta}$) that literally means rotation. This definition is extended to include measurements of any spatial gradient of a given quantity or one or more velocity gradients.

Background Information

For an observer traveling with the local velocity at a given point inside the flow, the geometry of the instantaneous flow pattern at some point in the neighborhood can be described, to first order, using the terminology of the critical-point theory of *Perry* and *Chong* [5.697]. According to this theory, the local flow topology can be classified according to the nature of the eigenvalues λ of the velocity gradient tensor $A_{ij} = \partial v_i/\partial x_j$, which are the roots of the cubic equation

$$\det(A_{ij} - \lambda\delta_{ij}) = \lambda^3 + P\lambda^2 + Q\lambda + R = 0\,,$$

where the coefficients P, Q, and R are the invariants of the tensor since their values are unchanged by rotation of the coordinate frame. These invariants are $P = -\mathrm{tr}(A)$, $Q = 1/2[P^2 - \mathrm{tr}(A^2)]$ and $R = -\det(A)$.

The velocity gradient tensor (A_{ij}) can be decomposed, not uniquely, into a symmetric and antisymmetric part. Specifically, these two parts are the rate-of-strain tensor, $S_{ij} = 1/2(\partial v_i/\partial x_j + \partial v_j/\partial x_i)$ and the-rate-of-rotation tensor, $R_{ij} = 1/2(\partial v_i/\partial x_j - \partial v_j/\partial x_i) = 1/2\varepsilon_{ijk}\Omega_k$, where Ω_k is the vorticity vector; Ω_k is defined as the curl of the velocity vector

$$\Omega_k = \varepsilon_{ijk}\frac{\partial v_i}{\partial x_j} \tag{5.306}$$

and ε_{ijk} is the alternating unit vector. At each point in the flow field we may imagine a spherical fluid particle whose motion can be decomposed into translation, expansion, shearing, and rotation. The vorticity can be interpreted as just twice the instantaneous solid-body-like rotation rate of the fluid particles along the principle axes in the fluid where there exists no shear deformation. We may alternatively interpret the vorticity as the circulation per unit area of a surface perpendicular to the vorticity field.

Why is vorticity so important in understanding the dynamics of turbulent fluid flow? Insight into this may be gained by looking at the equation describing the transport of vorticity [5.696]

$$\frac{\mathrm{d}\Omega_i}{\mathrm{d}t} = S_{ik}\Omega_k - \Omega_i S_{kk} + \varepsilon_{iqn}\frac{1}{\rho^2}\frac{\partial\rho}{\partial x_q}\frac{\partial p}{\partial x_\eta} + \varepsilon_{iqn}\frac{\partial}{\partial x_q}\left(\frac{1}{\rho}\frac{\partial\tau_{\eta j}}{\partial x_j}\right)\,. \tag{5.307}$$

This transport equation indicates that, for an observer moving with the flow, the rate of change of the vorticity component Ω_i of a particle is provided by four dynamically significant processes, namely that of stretching or compression and reorientation or tilting by the strain S_{ik}, vorticity generation through dilatation, baroclinic generation through the interaction of pressure and density gradients, and viscous effects expressed by the viscous stress term. The term $S_{ik}\Omega_k$ consists of one stretching or compression component and two tilting components. This term has been illuminated mostly through numerical work and appears to play an important role in the various physical processes involved in turbulent flows. If the viscous term can be ignored when

its magnitude is small, then the change of vorticity of a fluid element in a Lagrangian frame of reference can be entirely attributed to vortex stretching and/or tilting, to dilatational effects, and to baroclinic torque.

In the case of barotropic fluids, the pressure does not enter directly into the equation, unlike the transport equation for momentum, leading to some simplification in interpretation and computation. The reason for this is that the pressure acts through the center of mass of particles and does not produce rotation; rotation is produced by the viscous shearing stresses acting tangentially at the surface of the particles. However, the pressure gradients associated with the velocity field are necessary for the diffusion of vorticity into the flow at solid surfaces. The diffusion of the vorticity is a relatively slow process governed by the same diffusivity constant, the kinematic viscosity, as that for momentum. This is shown by considering the momentum equation evaluated at the wall, where the velocity vector is identically zero because of the nonslip conditions. In this case the momentum equation is reduced to $\partial p/\partial x_i|_{\text{wall}} = \rho\partial\tau_{ki}/\partial x_k|_{\text{wall}}$ which is equivalent to

$$\left.\frac{\partial p}{\partial x_i}\right|_{\text{wall}} = -\mu\varepsilon_{ijk}\left.\frac{\partial\Omega_k}{\partial x_j}\right|_{\text{wall}} . \qquad (5.308)$$

The term $-\partial\Omega_k/\partial x_j|_{\text{wall}}$ is the vorticity flux density, a term first introduced by *Lighthill* [5.685], who defined it for two-dimensional flows by analogy to the Fourier heat conduction as $-\nu\partial\Omega_k/\partial x_j|_{\text{wall}}$. The term vorticity flux describes the rate of vorticity production *at the wall*, which then enters the flow. In that sense it is more important to know the amount of vorticity entering the flow than the amount of vorticity at the wall. Figure 5.172 depicts the mechanism of vorticity change of a small fluid element moving toward the wall. A pressure gradient tangential to the boundary causes the fluid to change its rotation due to the nonslip conditions at the wall. A fluid element with initial vorticity $\Omega_{\text{in}} < 0$ enters the positive-pressure-gradient wall region and acquires a positive vorticity change $\Delta\Omega_y$ that changes its vorticity to the output vorticity $\Omega_{\text{out}} > 0$. According to *Andreopoulos* and *Agui* [5.698] the vorticity change shed from the solid boundary and sensed at a nearby location inside the flow at a distance Δy from the wall, to a first-order approximation, will be $\Delta\Omega_z = -(\partial\Omega_z/\partial y)_{\text{w}}\Delta y = \frac{1}{\mu}(\partial p/\partial x)_{\text{w}}\Delta y$ and $\Delta\Omega_x = -(\partial\Omega_x/\partial y)_{\text{w}}\Delta y = -\frac{1}{\mu}(\partial p/\partial z)_{\text{w}}\Delta y$. Since $\Delta y > 0$ always, the signs of $\partial p/\partial x$ and $\partial p/\partial z$ determine whether the wall acts as a source or sink of vorticity. Spatially and time-resolved measurements of the vorticity flux terms $\partial\Omega_x/\partial y$ and $\partial\Omega_z/\partial y$ in a two-dimensional boundary layer have been obtained in the work by *Andreopoulos* and *Agui* [5.698].

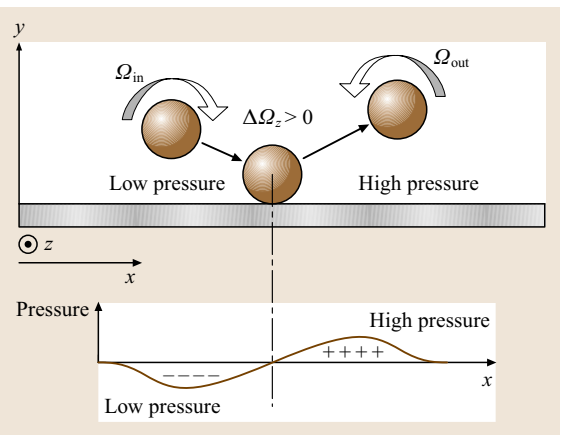

Fig. 5.172 Lighthill's mechanism of vorticity change at the wall beneath a flow

Physics of the Structure Function

There is a remarkable similarity and considerable overlap in the way velocity or pressure gradients are estimated and the way the structure functions of velocity or pressure are obtained, although they are defined quite differently. The velocity or pressure gradients, $\partial v_i/\partial r_j$ or $\partial p/\partial r_j$, respectively, are local quantities defined at one point inside the flow field, whereas the transfer function is defined as the difference between the values of velocity or pressure at two points of the flow field. Specifically the structure function is defined, before time averaging, as $\Delta v_i = v(r + \Delta r_j) - v(r)$ for velocity and $\Delta p = p(r + \Delta r_j) - p(r)$ for pressure.

For small separations Δr_j and after considering Taylor's expansion, these relations become $\Delta v_i = v(r + \Delta r_j) - v(r) = \partial v_i/\partial r_j \Delta r_j$ and $\Delta p_i = p(r + \Delta r_j) - p(r) = \partial p/\partial r_j \Delta r_j$, respectively.

In practice, the velocity or pressure gradients are obtained from the value of the corresponding structure function as the separation distance Δr_j tends to a very small value. Thus, the velocity or pressure gradients defined at one point are estimated from the difference of velocity or pressure values at two different but nearby points. In that respect the velocity or pressure gradients and the structure functions of velocity or pressure are interrelated and the underlying physics behind their behavior may be the same.

Let us assume that the differential $\Delta Q = Q(r + \Delta r) - Q(r)$ of a quantity $Q(r)$ is required to be esti-

mated at a position r. In this case, two measurements of the quantity Q at close locations r and $r+\Delta r$, are usually attempted. ΔQ is a fluctuating quantity and if we consider the time average $\overline{\Delta Q^2}$ then the structure function is defined as

$$\overline{\Delta Q^2} = \overline{[Q(r+\Delta r)-Q(r)]^2} = \overline{Q(r)^2}\left[(1-\rho)^2+2\rho(1-R_{\Delta r})\right], \quad (5.309)$$

where ρ is the ratio $\rho^2 = \overline{Q^2(r+\Delta r)}/\overline{Q^2(r)}$ and $R_{\Delta r}$ is the correlation coefficient $R_{\Delta r} = R_{r,r+\Delta r} = \frac{\overline{Q(r)Q(r+\Delta r)}}{[\overline{Q^2(r)}]^{1/2}[\overline{Q^2(r+\Delta r)}]^{1/2}}$, not to be confused with the rate-of-rotation tensor.

Thus for the rms of a gradient we obtain

$$\left(\frac{\overline{\Delta Q^2}}{\Delta r^2}\right)^{1/2} = \frac{[\overline{Q(r)^2}]^{1/2}}{\Delta r}\left[(1-\rho)^2+2\rho(1-R_{\Delta r})\right]^{1/2}. \quad (5.310)$$

The quantity Q could be, for instance, one component of the velocity vector or pressure or even one vorticity component. The relation (5.310) indicates that the rms of the quantity $\Delta Q/\Delta r$ depends, among other quantities, on $(1-\rho)$ and $(1-R_{\Delta r})$. The first quantity $(1-\rho)$ is a measure of the inhomogeneity of the turbulence intensities, while the second one $(1-R_{\Delta r})$ indicates the decorrelation between the two fluctuations of Q at r and $r+\Delta r$. It can be argued that, for small separations Δr, in most flows either $2\rho(1-R_{\Delta r}) \gg (1-\rho)^2$ or $\rho \approx 1$ is valid. In low-speed incompressible boundary layers, for instance, the ratio $2\rho(1-R_{\Delta r})/(1-\rho)^2$ is close to 150 at a location just outside the viscous sublayer for $\Delta r = \Delta x_2^+ = 16$, where x_2 is the wall normal direction. In another example: isotropic turbulence behind rectangular grids $\rho \approx 1$ [5.694]. It is, therefore, reasonable to assume that $(\overline{\Delta Q^2}/\Delta r^2)^{1/2} = [\overline{Q(r)^2}]^{1/2}/\Delta r[2\rho(1-R_{\Delta r})]^{1/2}$, which suggests that most contributions to $\Delta Q/\Delta r$ come from the uncorrelated parts of the two signals, $Q(r)$ and $Q(r+\Delta r)$. Thus the rms of $(\overline{\Delta Q^2}/\Delta r^2)^{1/2}$ between two perfectly correlated signals ($R_{\Delta r}=1$) is vanishing. In turbulent flows it is known that the existence of small-scale turbulence decreases $R_{\Delta r}$. In that context there will always be a nonzero $(\overline{\Delta Q^2}/\Delta r^2)^{1/2}$ since $R_{\Delta r} < 1$ for $\Delta r > 0$. On the other hand two sinusoidal signals with a phase shift between them φ, i. e., $y_1 = A_1 e^{i\omega t}$ and $y_2 = A_2 e^{i(\omega t+\varphi)}$, will also result in a correlation coefficient $R_{\Delta r} < 1$ since $R_{\Delta r} = \cos\varphi$. In all cases other than $\varphi = 0$, $R_{\Delta r} < 1$ and $(\overline{\Delta Q^2}/\Delta r^2)^{1/2}$ reaches nonzero values. For $\varphi = 180°$ $(1-R_{\Delta r})$ reaches a maximum value of 2 and therefore $(\overline{\Delta Q^2}/\Delta r^2)^{1/2} = 2(\overline{Q(r)^2})^{1/2}/\Delta r$. From this example it can be concluded that contributions to $\Delta Q/\Delta r$ come mostly from the uncorrelated parts of the flow or from the out-of-phase events. Small-size eddies represented in the high-wavenumber part of the spectrum are known to be weakly correlated with each other and therefore in the present context they represent contributions to $\Delta Q/\Delta r$ from the uncorrelated parts of the flow.

The limit of (5.310) when Δr approaches zero is also of interest in the present considerations since it is related to the potentially available spatial resolution. In this case $R_{\Delta r}|_{\Delta r\to 0} = 1$ and $\rho|_{\Delta r\to 0} = 1$ and thus the limit appears to become indefinite. After applying the Hôpital rule the following relation can be obtained $\lim_{\Delta r\to 0}(\overline{\Delta Q^2}/\Delta r^2) \approx -[\overline{Q(r)^2}]\{\partial^2 R/\partial(\Delta r)^2 - [\partial\rho/\partial(\Delta r)]^2\}$ where $\partial^2 R/\partial(\Delta r)^2$ is the curvature of the cross-correlation function R, at the origin. Thus a Taylor microscale λ can be defined as $(\partial^2 R/\partial(\Delta r)^2]_{\Delta r\to 0} = -1/\lambda^2$ and therefore $(\overline{\Delta Q^2}/\Delta r^2)_{\Delta r\to 0} \approx [\overline{Q(r)^2}]/\lambda^2\{1+\lambda^2[\partial\rho/\partial(\Delta r)]^2\}$.

General Requirements

The measurement of one or more components of vorticity in turbulent flows of research and technical interest has been a long-held, but elusive, goal of fluid-mechanics instrument developers and researchers. The review article by *Wallace* and *Foss* [5.81] provides a detailed account of the available techniques, as of that date, used to measure vorticity and compare existing data. The majority of the techniques are based on thermal anemometry or optical methods. The present Section will address issues related to optical techniques, which possess several advantages and some limitations with respect to those based on thermal anemometry. Optical techniques are non-intrusive, are sensitive to large changes in velocity direction and most do not require any calibration. These characteristics make them ideal for use in separated flows and flows with large turbulence intensities where the use of intrusive methods is prohibited where recirculating effects are present. Most of these optical techniques are based on detecting the light scattered by particles imbedded in the flow. In that respect, seeding the flow with appropriate particles that follow the fluid motion very closely is critical (Sect. 5.3.1). It should be noted here that, for gas flows in which seed must be added and in which the flow does not recirculate, adding particles can be far more intrusive than a hot-wire probe.

There are several requirements that determine the performance of each technique beyond its basic idea and the principles upon which it is based.

Formal Derivation in Implicit Formulations. There is a need for a formal definition of the measured quantities, either the vorticity components Ω_k or velocity gradient tensor terms A_{ij}. Specifically, there are two common ways to derive vorticity. In the first method, measurements of velocity components at nearby locations are obtained and used in a finite-difference scheme to derive vorticity. In the second method measurements of microcirculation around a small area are obtained and vorticity is computed as circulation density.

The first definition is based on a Taylor's series expansion of velocity in a nearby location, which to a first-order approximation becomes $v_i(r_j + \Delta r_j) = v_i(r_j) + \Delta r_j \partial v_i/\partial r_j + \ldots$

For r_j in the y-direction and $\Delta r_j = (0, \Delta y, 0)$ this becomes $v_i(y + \Delta y) \approx v_i(y) + \Delta y \partial v_i/\partial y$, which yields the following relation to compute the velocity gradient $\partial v_i/\partial y \approx [v_i(y + \Delta y) - v_i(y)/\Delta y]$. This relation will also define the uncertainties in the measurement of the velocity gradient.

The second method of estimating vorticity is due to *Foss* and co-workers [5.699, 700] who developed a hot-wire technique for the measurement of the transverse vorticity component. The technique involves the measurement of the microcirculation Γ around a small, finite domain of area ΔS normal to the flow. The estimated vorticity appears to be computed through the relation $\langle \Omega_z \rangle = \Gamma/\Delta S$.

These two methods are not the only ones in use. There is no need to have a computational formalism for vorticity when it is estimated explicitly. For instance, direct estimate of vorticity through measurements of fluid rotation does not require vorticity computation through an implicit scheme [5.701].

Spatial and Temporal Resolution. The spatial and temporal resolution of any probe affects the accuracy of measurements of time-dependent velocity gradients A_{ij} or vorticity components Ω_k. This resolution depends on the optical arrangement of the technique, the hardware used to generate the measuring probe volume and to process the signals, and the particles used as light scatterers and their arrival rate in the measuring locations. Thus the technique has a typical characteristic length scale L_p that is usually associated with the separation distance between the sensing areas and a time scale T_p, which depends mostly on the speed of data acquisition or burst processor. The technique should be able to resolve the small scales that exist in a given flow, which appear to be the Kolmogorov viscous scales $\eta = \nu^{3/4}\varepsilon^{-1/4}$ for length and $T_\varepsilon = \nu^{1/2}\varepsilon^{-1/2}$ for time, where ε is the dissipation rate of turbulent kinetic energy and ν is the kinematic viscosity. L_p and T_p should be less than η and T_ε, respectively, in order to capture contributions from the smallest eddies, which are responsible for most of the content of vorticity or velocity gradient since small eddies are uncorrelated [see relation (5.310)]. *Wyngaard* [5.702] was the first to evaluate the problem of spatial resolution of hot-wire-based vorticity techniques and found that no attenuation occurred for $L_\mathrm{p}/\eta = 1$, while substantial attenuation of vorticity was evident for $L_\mathrm{p}/\eta > 3.3$. The review by *Wallace* and *Foss* [5.81] concludes that reasonable estimates of velocity gradients can be obtained without attenuation for $L_\mathrm{p}/\eta < 2$–4.

Although L_p has to be as small as possible it can not be minimized independently from other parameters such as the speckle noise. Errors due to noise in the measurements amplify as the length scale decreases. There is certainly an optimum length intermediate between attenuation and amplification of noise.

Determining η requires a good estimate of the turbulent kinetic energy dissipation rate E, which is very difficult to measure directly in a laboratory. Previous studies obtained the value of E by making assumptions to reduce some of the terms in the expression of the total dissipation rate [5.694]:

$$E = \tau_{ij} S_{ij} = 2\mu S_{ij} S_{ij} - \frac{2}{3}\mu S_{kk} S_{kk} \,. \tag{5.311}$$

The second term on the right-hand side of this relation represents the additional contribution of compressibility to the dissipation rate of kinetic energy. This term disappears in the case of incompressible flow. Since this term is always positive, the negative sign in front may erroneously suggest that compressibility reduces dissipation. This is incorrect because the term $S_{ij} S_{ij}$ also contains contributions from dilatation effects, which can be revealed if one considers that

$$S_{ij} S_{ij} = \frac{1}{2}\Omega_k \Omega_k + \frac{\partial v_i}{\partial x_j}\frac{\partial v_j}{\partial x_i} \,. \tag{5.312}$$

The second term on the right-hand side represents the inhomogeneous contribution in the case of incompressible flows. In the case of compressible flows, terms related to dilatation can be extracted, and the instantaneous total dissipation rate then becomes

$$E = \mu\Omega_k\Omega_k + 2\mu\left(\frac{\partial v_i}{\partial x_j}\frac{\partial v_j}{\partial x_i} - S_{kk}S_{kk}\right) + \frac{4}{3}\mu S_{kk} S_{kk} \,. \tag{5.313}$$

The third term on the right-hand side describes the direct effects of compressibility, i. e., dilatation on the

dissipation rate. The first and the last terms on the right-hand side of the last relation are quadratic with positive coefficients and positive signs and are therefore always positive. The second term on the right-hand side indicates the contributions to the dissipation rate by the purely nonhomogeneous part of the flow. Its time-averaged contribution disappears in homogeneous flows. This term, in principle, can obtain negative values and thus can reduce the dissipation rate. This does not violate the second law of thermodynamics as long as the total dissipation remains positive at any point in space and time.

The estimates that are usually provided for E, particularly those based on indirect methods, may be very misleading. An experiment with poor spatial resolution will result in attenuation of all measured turbulent quantities including the dissipation rate, which will indicate high η and therefore high resolution.

It should be mentioned here, however, that there is increasing evidence provided by *Tsinober* et al. [5.693] and *Honkan* and *Andreopoulos* [5.689] that the Taylor microscale λ should be used to determine the spatial resolution in vorticity measurements. It has been shown in Sect. 5.3, that in the limit of vanishing separation Δx_j between the measurement locations, the rms of the fluctuations of one velocity gradient $\partial v_i/\partial x_j$ is given by $\lim_{\Delta x_j \to 0} \overline{(\Delta v_i/\Delta x_j)}^2 = \overline{u_i^2}/\lambda_{ij}^2\{1 + \lambda_{ij}^2[\partial\rho/\partial(\Delta x_j)]^2\}$, where λ_{ij} is the Taylor microscale. If the gradient, $\partial\rho/\partial\Delta x_j$, which indicates the degree of variation of the rms of velocity fluctuations, is much smaller than $1/\lambda_{ij}^2$ then the relation $\lim_{\Delta x_j \to 0} \overline{(\Delta v_i/\Delta x_j)}^2 = \overline{u_i^2}/\lambda_{ij}^2$ provides the best estimate for ideal resolution when Δx_j tends to zero. In that respect the ratio L_p/λ_{ij} should be less than 1.

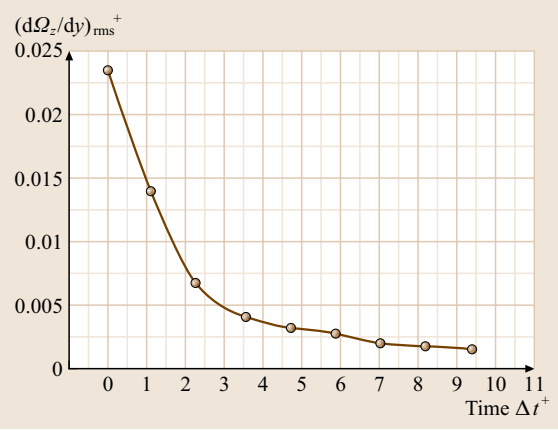

Fig. 5.173 The effect of temporal resolution on rms vorticity flux are made nondimensional by inner wall scaling (after *Andreopoulos* and *Agui* [5.698])

Although the statistics of fluctuations of individual velocity components do not require increased temporal resolution, cross-correlation/shear stress and velocity gradients/vorticity measurements require a high degree of coincidence of particles at different locations inside the probe volume. This can be achieved through a high rate of particles, which results in practically continuous signals. The resolution in time basically depends on the rate of arrivals of particles in the probe volume and on the data-processing rate of the hardware.

An example of the effect of temporal resolution on the statistical results of vorticity flux is obtained from the data of *Andreopoulos* and *Agui* [5.698]. Vorticity flux is computed by (5.308) by subtracting two pressure signals obtained at very close locations that are about 0.8 mm or $\Delta x^+ = 6$ apart. Artificial sampling times Δt were produced by skipping by various numbers equally sampled data digitized at rates substantially faster than the Kolmogorov frequency $1/T_\varepsilon$. The results plotted in Fig. 5.173, show a substantial dependence of the rms of vorticity flux on the temporal resolution Δt.

As the Reynolds number of the flow increases its spatial and temporal scales decrease and therefore, if the size of the measuring volume and data-acquisition rate remain unchanged, it is expected that the spatial and temporal resolution of the measuring technique will deteriorate.

Validation. Eventually the developed technique has to be validated in a real flow that will provide a good test bed for evaluation of its performance. In the past, velocity gradient/vorticity measurement techniques were tested in laminar flows that possessed known rotational flow characteristics very close to those predicted by theory. Although such tests are adequate to demonstrate the basic principles of the techniques, they are insufficient in evaluating or predicting the performance of the probe in a real turbulent flow where a wide range of flow scales is present and resolution issues are an important part of the overall assessment. In that respect, it may be better to test the technique in a canonical turbulent flow such as a two-dimensional, zero-pressure-gradient boundary layer over a smooth wall, a two-dimensional shear layer, or isotropic homogeneous grid-generated turbulence. The bulk and turbulent characteristics of canonical flows are well known and existing data are well documented and adequately tabulated. Unfortunately, velocity gradient/vorticity data are not always available and therefore

a comparison with previous velocity gradient/vorticity data is not possible, except in some cases of incompressible boundary-layer flows, free shear layer flows or grid-turbulence-generated flows where such data exist. The preceding taxonomy of flows also includes compressible grid-generated turbulence interaction with shock waves.

Existing Techniques and Their Classification

The inherent difficulties of velocity gradient/vorticity measurements, which require high spatial and temporal resolution in turbulent flow fields, have only recently been substantially overcome.

Laser speckle strophometry (LSS) or particle image velocimetry (PIV) techniques are non-intrusive but cannot in general provide adequate time-history information. In addition slight out-of-plane motion of the scattering particles due to flow three-dimensionality results in different speckle patterns (speckle decorrelation). In particle image velocimetry, crossing of the flowing particles paths in highly fluctuating flows may cause ambiguity in the detection scheme. PIV is also limited by spatial resolution loss due to averaging from the correlation schemes. Although the resolution of a typical CCD camera may typically be $1\,\mathrm{k}\times 1\,\mathrm{k}$ px, subregions of 32×32 px known as interrogation areas are usually considered to validate a local velocity measurement. According to *Arik* [5.703] in a typical PIV setup approximately 10 particles are needed to validate a velocity vector measurement and 10 velocity vectors are needed to evaluate a vorticity vector. Thus approximately 100 particles are needed to evaluate a vorticity vector, a number which results in 30 to 40 particles for each of the three vorticity components.

Lourenco et al. [5.704] used PIV techniques to obtain one-component vorticity measurements in a jet flow. *Meinhart* and *Adrian* [5.705] used PIV to measure the near-wall vortical structure of low-speed boundary layers with reasonable spatial resolution.

Laser speckle strophometric methods have been developed by *Breyer* et al. [5.706], *Kriegs* et al. [5.707], and *Kriegs* and *Staude* [5.708]. In these techniques the speckle pattern, which is the result of the diffraction of a plane wave produced by a random grating, is basically affected by the flow velocity gradient while the translation of the grating caused by the constant flow velocity will not affect the pattern.

These authors applied their double-pulse strophometric technique to obtain direct measurements of the quantities $\partial v/\partial x + \partial v/\partial y$, $\partial v/\partial x - \partial v/\partial y$ and $\partial v/\partial z$ in a channel flow with Reynolds number based on the channel width in the range of 2250–6700. This information was used to obtain statistics of the $\partial v/\partial y$ gradient.

Holographic particle image velocimetry (HPIV) was used by *Zhang* et al. [5.709] to obtain velocity gradient measurements in a square duct flow with moderate resolution. A polarization-based approach with dual-plane particle image velocimetry (DSPIV) has been used by *Kähler* [5.710], *Ganapathisubramani* et al. [5.711] and *Hu* et al. [5.712] to obtain vorticity measurements in boundary-layer flows and in a lobed jet mixer. A two-frequency DSPIV was applied in jet flows to measure all nine components of the velocity gradient tensor with resolution of about six Kolmogorov length scales [5.713]. These recent works based on PIV techniques have demonstrated the potential to provide measurements of vorticity with excellent spatial resolution. At the moment, their temporal resolution is rather limited, which does not however affect the process of statistical averaging. In the following a description of optical techniques which have been used to measure one velocity gradient/vorticity at a single point with reasonable success will be provided. These techniques can be classified as direct or indirect, depending on whether vorticity is obtained from the measurement of fluid particles rotation or from the measurement of individual velocity gradients inside the flow field.

One of the first direct measurements of vorticity was obtained by *Frish* and *Webb* [5.701] by measuring the solid rotations of tiny transparent spherical beads with

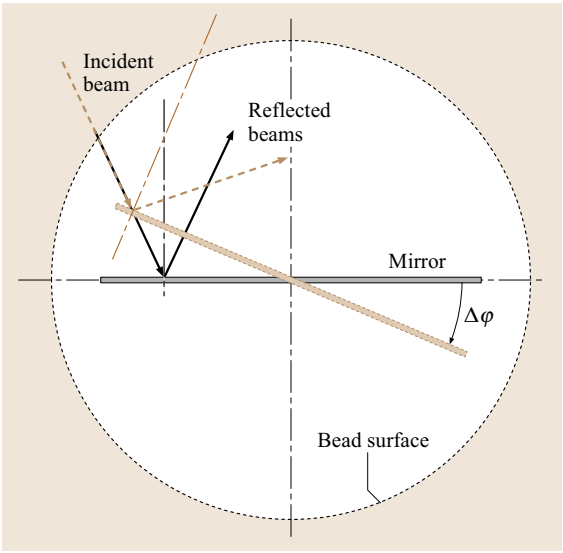

Fig. 5.174 The effect of mirror rotation on beam reflection as in the technique by *Frish* and *Webb* [5.701]

a diameter of 25 μm, each containing embedded planar crystal mirrors specially developed for this purpose, suspended in a refractive-index-matched liquid.

The flows and the beads were illuminated by a laser light and the rate of rotation of the reflected light, which is proportional to vorticity, was measured directly. Figure 5.174 depicts the effect of a rotating mirror on the direction of the reflected beam. If the mirror is rotated by an angle $\Delta\varphi$ within an infinitesimally small time Δt then its angular velocity will be $\omega = \Delta\varphi/\Delta t$ and the incident and reflected angles of the light beams are α_i and α_r, respectively, then each angle will change by the same amount $\Delta\varphi$, and the angle between the reflected and incident beams will change by $2\Delta\varphi$. For a fixed $\Delta\varphi$ the measurement of Δt can lead to the determination of the rate of rotation, which is half of the vorticity. The spatial resolution of the technique, which is determined by the size of the beads, is considered to be very good. However, the complexity of this technique and the requirement for matched refractive index prohibit its use in air.

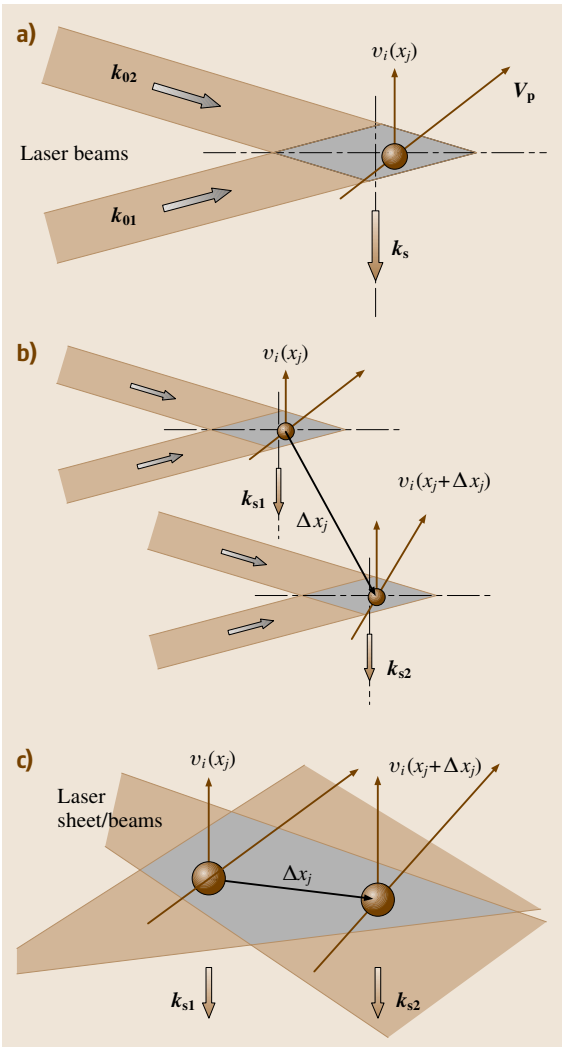

Fig. 5.175 **(a)** Typical fringe pattern in LDA. **(b)** Configuration for the measurement of one velocity gradient $\partial U_i/\partial x_j$. **(c)** Configuration for the measurement of the cross-correlation of velocity components

Most of the techniques used to obtain indirect measurements of vorticity take advantage of the Doppler effect and have configurations similar to those used in laser Doppler anemometry (LDA). In typical dual-beam configurations for velocity measurements, two laser beams cross each other to form the measuring/probe volume with the fringe pattern, as shown in Fig. 5.175a. Receiving optics can be aligned in any direction since the Doppler frequency shift Δf_D is independent of the k_s direction. The velocity component normal to the fringe orientation $v_i(x_j)$ can be obtained by measuring $\Delta f_D = \boldsymbol{V}\cdot(\boldsymbol{k}_{01} - \boldsymbol{k}_{02})/2\pi$, where $\boldsymbol{k}_{01}$ and $\boldsymbol{k}_{02}$ are the wavenumber vectors along the two incident beams forming the measurement volume.

A natural extension of the traditional single-point LDA measurement of one velocity component to obtain one velocity gradient is shown in Fig. 5.175b, where two independent probe volumes are formed at a distance Δx_j apart to measure two velocity components in the same direction, $v_i(x_j)$ and $v_i(x_j + \Delta x_j)$, respectively. The velocity gradient $\partial v_i/\partial x_j$ can be estimated through the finite-difference relation $\partial v_i/\partial x_j \approx \Delta v_i/\Delta x_j \approx v_i(x_j + \Delta x_j) - v_i(x_j)/\Delta x_j$. For one-component vorticity measurements, simultaneous measurements of the two velocity gradients are required.

This configuration has been used by *Lang* and *Dimotakis* [5.714] and *Lang* [5.715] to obtain measurements of one component of vorticity in a two-dimensional shear layer. Two probe volumes, separated by $\Delta y = 1.9$ mm, were aligned in the y-direction to measure the $\partial v/\partial y$ gradient and another two probe volumes separated by $\Delta x = 1.9$ mm were aligned in the x-direction to measure the $\partial V/\partial x$ gradient. Thus eight beams were required to measure the spanwise vorticity component $\Omega_z = \partial V/\partial x - \partial U/\partial y$, which was estimated as $\Omega_z = (V_2 - V_1)/\Delta x - (U_2 - U_1)/\Delta y$. Mean and rms values of Ω_z were obtained. The lack of estimates for the dissipation rate of turbulent kinetic energy prevented direct evaluation of the spatial resolution of this technique. A similar arrangement has been used by *Romano* et al. [5.716] to measure velocity structure functions

in a channel flow where two completely different LDA systems were used.

Instead of generating two distinct probe volumes to obtain two velocity estimates at nearby locations, an alternative method is to form a single probe volume with focus at two distinct points inside the volume. The advantage of the latter approach is that fewer optical components are required. It has already been used for cross-correlation measurements in space [5.719,720] and for simultaneous velocity measurements at several points by using an elongated control volume generated by the intersection of two *sheet* beams formed by passing the beams through two cylindrical lenses (Fig. 5.175c) as described by *Nakatani* et al. [5.721]. The light intensity is reduced significantly in this arrangement of two interfering sheets and therefore the signal-to-noise ratio is deteriorated.

The LAVOR (laser vorticity probe) method proposed by *Agui* and *Andreopoulos* [5.717,718] uses two parallel laser beams focused with a long-focal-length lens to generate a moderately narrow probe volume defined by the region of intersection of the two beams. The velocity at two different locations inside the probe volume is measured. There are several advantages to this approach over the *sheet* beam approach. These include fewer optical components, simple alignment of the optics, smaller windows for optical access, and better use of laser intensity.

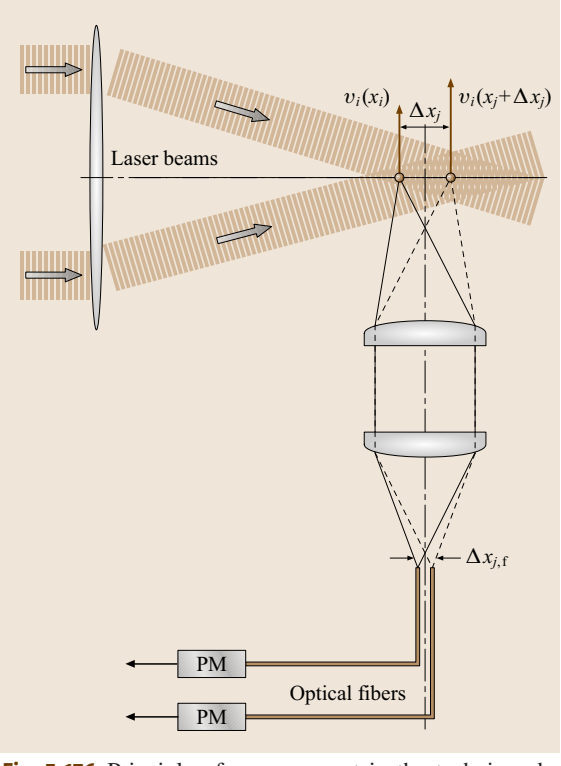

Fig. 5.176 Principle of measurement in the technique by *Agui* and *Andreopoulos* [5.717,718]. PM: photomultiplier

A schematic drawing of the principle is shown in Fig. 5.176. The measurement locations within the probe volume are defined by imaging the entire probe volume onto the optical fibers located on the opposite side of the receiving optics. Therefore, scattered light will be collected from two distant locations within the probe volume. Scattered light from the two points on the probe volume is designed to enter the acceptance cone of the optical fibers. The distance Δx_j between the two measurement points can be adjusted to match the spatial resolution requirements. No magnification through the lenses was used in this application and therefore the distance between the two fibers $\Delta x_{j,f}$ was the same as the distance Δx_j. The distance of the fibers $\Delta x_{j,f}$ can be of the order of 1 mm and, for the case where the two fibers are very close together, the distance between the two points in the probe volume will be on the order of 0.3–1 mm. The value of Δx_j sets the spatial resolution of the probe and has to be compared to the Kolmogorov length scale of the turbulent flow under investigation $\eta = (\nu^3/\varepsilon)^{1/4}$, where ε is the dissipation rate of turbulent kinetic energy, if the smallest viscous scales are be resolved [5.702,722]. It should be noted that, although the resultant probe volume is large, the spatial resolution is defined by the intersection of the probe volume and the image of the optical fiber ends. The aforementioned range of the spatial resolution is not unrealistic; it is based on the experimental results of *Johns* et al. [5.720] and *Fraser* et al. [5.719]. The authors in the first reference succeeded in making spatial correlation measurements between velocity components at different locations as close as 70 μm and without *crosstalk* between the scattered light by the two particles present at the measurement volume.

The uniqueness of the LAVOR technique for vorticity measurements lies in the use of

1. a small control volume imaged onto the core of a fiber
2. fiber optics that allows high spatial resolution and
3. fewer optical components.

An extremely fast digital data-acquisition device was used, which allows *instantaneous* processing of the burst signal with a high mean rate of 78 000 bursts/s by using a record length of 64 points to digitize the individual

bursts. This value determines the temporal resolution of the new technique. In addition to vorticity, measurements of velocity components are also obtained at the same time so that an additional mapping of the velocity flow field is not necessary.

The implementation of the previously described idea for measurements of vorticity is shown in Figs. 5.177a,b. For measurement of one vorticity component, the determination of the two velocity gradients $\partial v_2/\partial x_1$ and $\partial v_1/\partial x_2$ is required. Therefore, the probe volumes have to be oriented appropriately to coincide with the x_1–x_2 plane. It should be emphasized that the measured vorticity Ω_3 is invariant with rotation of both probe volumes about the x_3-axis, which is normal to the x_1–x_2 plane. Scattered light collected through the receiving optics enters the fibers through a module located on the focal plane. The fiber-optics module with the arrangement of the four fiber cable ends is shown in Fig. 5.177c. It should be noted that the x_1–x_2 plane coincides with the focal plane of the arrangement of the receiving optics.

An appreciation of the advantages of the LAVOR technique can be obtained if one compares it with the arrangement adopted by *Romano* et al. [5.716] to measure velocity transfer functions in channel flows that required the use of instrumentation, equipment, and optical components equivalent to two different LDA systems.

A second category of single-point velocity gradient/vorticity measurement techniques exists that are not based on the interference of two laser beams and the scattering light of a particle moving through the fringes realized on the surface of the photodetector. This category includes techniques that use laser Doppler signals from two particles illuminated by two different light beams. *Durst* et al. [5.723] in panel 3.26 of that book show that the introduction of phase variation with time caused by the movement of light-scattering particles will yield signals that originate from different particles illuminated by different light beams (Fig. 5.178a). An equation for the light intensity at the surface of the photomultiplier has been derived for the case of two beams that have the same wavelength, which shows that the intensity will vary with time and cause the photodetector to respond to the Doppler frequency, which is a function of the relative velocity of the two particles if their position is known. If the two beams are parallel, the directions of the two scattering waves are the same, and the photodetector is orientated in the same direction and positioned halfway between the two beams then the Doppler shift Δf_D is proportional to the velocity difference. No measurements have been presented to validate the proposed technique.

The idea of heterodyning of the scattered light from two particles was explored by *Hanson* [5.724] and more recently by *Ötügen* et al. [5.725] and *Yao* et al. [5.726]. Hanson's heterodyning arrangement uses an optical filter to define the relative separation of two particles, which requires the fabrication of miniature spatial gratings and rings with geometries tailored to the specific flows under investigation. His technique, which has been tested in a cylindrical laminar Couette flow, is insensitive to the sign of velocity gradient.

The technique by *Ötügen* et al. [5.725], shown schematically in Fig. 5.178b, resolves the sign of the velocity gradient by using a Bragg cell to shift the fre-

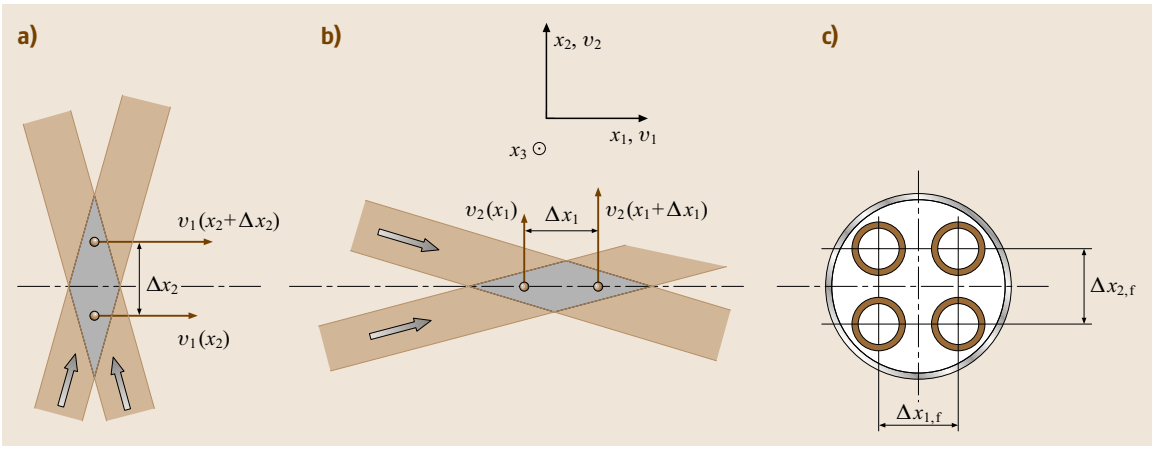

Fig. 5.177 **(a)** Beam orientation for the measurement of $\partial v_1/\partial x_2$. **(b)** Beam orientation for the measurement of $\partial v_2/\partial x_1$. **(c)** Fiber optics module

quency of one laser beam and has been tested in the laminar flow formed between two concentric cylinders with one of them rotating. *Yao*'s et al. [5.726] technique, which is quite similar to that of Ötügen et al., has been tested successfully in a laminar channel flow.

If only one particle is present in one of the two targeted locations, its Doppler effect will be lost within the much larger frequency of the laser beam that goes undetected by the photomultiplier. Only when both particles are present is there cancelation of the original laser frequency and is the beat frequency detected.

The technique by Ötügen et al. originally used two different arrangements to collect scattered light from the two particles in the measurement volume. The two scattered light paths were recombined by a beam combiner before they enter the photomultiplier. This technique has been further developed recently and a single arrangement of collecting optics has been used in which both particles appear to be practically on the same focal plane because of the close proximity of the two laser beams. The technique has been used to carry out measurements of vorticity in the turbulent boundary layer of a small closed-loop water tunnel [5.727] and in the turbulent shear layers behind a splitter plate placed in the same wind tunnel [5.728]. Each of the shear layers had a thickness of about 4 mm and the distances Δx and Δy between the two particles for each of the two pair of beams were $\Delta x = 0.7$ mm and $\Delta y = 1$ mm. Thus the ratio of the large flow scale to the separation distance Δx or Δy is 4–6, which is considered inadequate to resolve even the large-scale contributions to the vorticity let alone the contributions of small scales of the size of the Kolmogorov viscous scales, which was estimated to be 0.047–0.067 mm. This is a shortcoming of the test flow and the size of the water-tunnel facility rather than of the technique itself, which appears to be very promising. In fact, in their boundary-layer experiments the boundary-layer thickness was about 40 mm and the separation distances were reduced to $\Delta x = 0.4$ mm and $\Delta y = 0.78$ mm. In this case, the Kolmogorov length scales appear to be of the order of 0.03–0.07 mm in the region close to the wall. Thus the ratio $\Delta x/\eta$ is in the range 13–23, which can be considered reasonably small but inadequate.

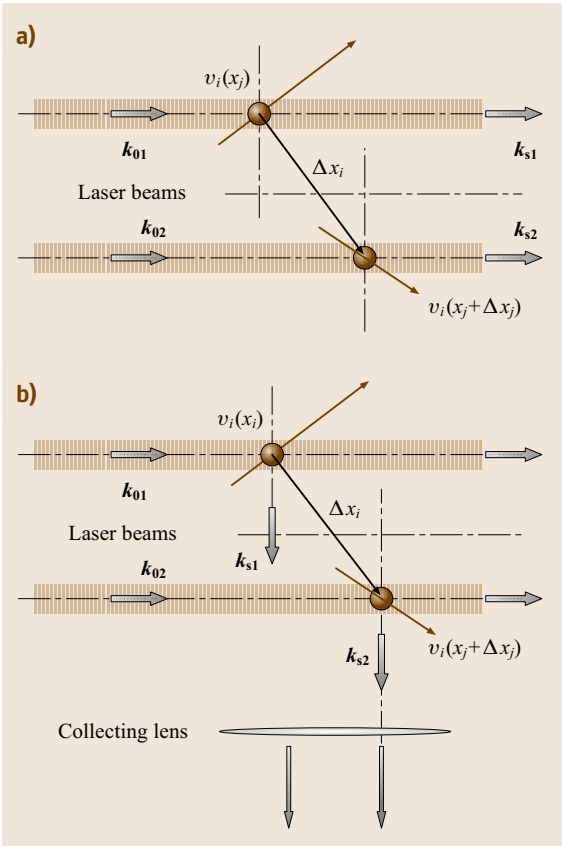

Fig. 5.178 **(a)** *Durst* et al. [5.723] proposal for velocity difference measurements. **(b)** *Ötügen* et al. [5.725] technique for velocity difference measurements

In all these techniques that estimate the velocity gradient through the heterodyning of the scattered light from two different particles, the velocity field cannot be measured simultaneously with the velocity gradient, which requires separate measurements. In this respect, the inability of these methods to provide information about the velocity field at the same time as the velocity gradient measurements may be considered a drawback.

It is also evident from the description above that many of the techniques have been validated in a laminar flow environment. This is a first step in a full evaluation plan that should be followed up with testing in a turbulent flow where documentation of the flow-field quantities exists.

Particle Rates and Temporal Resolution

Although the statistics of fluctuations of individual velocity components do not require increased temporal resolution, cross-correlation/shear stress and velocity gradients/vorticity measurements require a high degree of coincidence of particles at different locations in the probe volume. This can be achieved, to a certain extent, through high rate of particles arriving at the measurement locations. If P_A $(0 \le P_A \le 1)$ is the probability of having one particle at a given location A and P_B

($0 \le P_B \le 1$) is the probability of having one particle at a second location B then the probability of having two particles at the same time in locations A and B is $P(A \cap B) = P_A \times P_B$, provided that these two events are independent of each other [5.729]. This results in a value of $P(A \cap B)$ that is smaller than either P_A or P_B. If the presence of four particles at the same time at four different locations A, B, C, and D is required, called coincidence in the present context, then the probability of this event is P^4 where $P = P_A = P_B = P_C = P_D$. For a typical $P = 0.5$ then $P^4 = 0.0625$, a value eight times less than P.

Increasing the particle concentration so that there is always at least one pair of particles in the measuring volume can increase the coincidence and therefore the data rate. Further increase in particles concentration may result in the presence of more than one particle inside the measuring volume, which can cause interference due to multiple light scattering. In addition, the presence of too many particles will affect the flow field itself, which may become a slurry.

As the Reynolds number of the particular flow increases, turbulence fluctuations will increase and therefore turbulent diffusion, a process that is responsible for transporting particles into the measurement volume, will increase and therefore the particle arrival rate will increase. However, the residence time of each particle will be shorter and the rate of validation will decrease because the coincidence criteria will not be met. In effect, achieving high rates of validated particles present at various locations of the flow field at the same time becomes increasingly difficult and, if this is compounded with the requirement to have continuous signal, it is close to impossible.

The resolution in time of the measurements depends basically on the rate of arrivals of particles in the probe volume and on the data processing rate of the hardware. Since most burst-type processors can process data at a rate of about 200 000 bursts/s, which is considered adequate for temporal resolution of flows up to low subsonic Mach numbers, the temporal resolution is entirely dependent on the rate of particle arrivals at the focusing points.

To demonstrate several of the typical issues involved in optical strophometry, the LAVOR technique of *Agui* and *Andreopoulos* [5.718] will be described in more detail than above. This technique has been used to obtain measurements of the spanwise vorticity in the near-wall region of a two-dimensional boundary layer configured in the CCNY (City College New York) low-speed wind tunnel, which has a $1.2\,m \times 1.2 \times 8.4\,m$ working section. Three different experiments were carried out at Reynolds numbers $Re_\theta = 2700$, 3900 and 5400. This test flow has been extensively investigated and data of all turbulent quantities, including three-dimensional time-resolved vorticity obtained by subminiature multi hot-wire techniques, are well documented in several publications [5.689, 730]. Thus a direct comparison of the LAVOR data with the hot-wire data of vorticity will be more meaningful since both have been obtained in the same facility under similar flow conditions.

The flow was seeded with 1–3 μm-diameter particles produced by an oil-based smoke machine that was

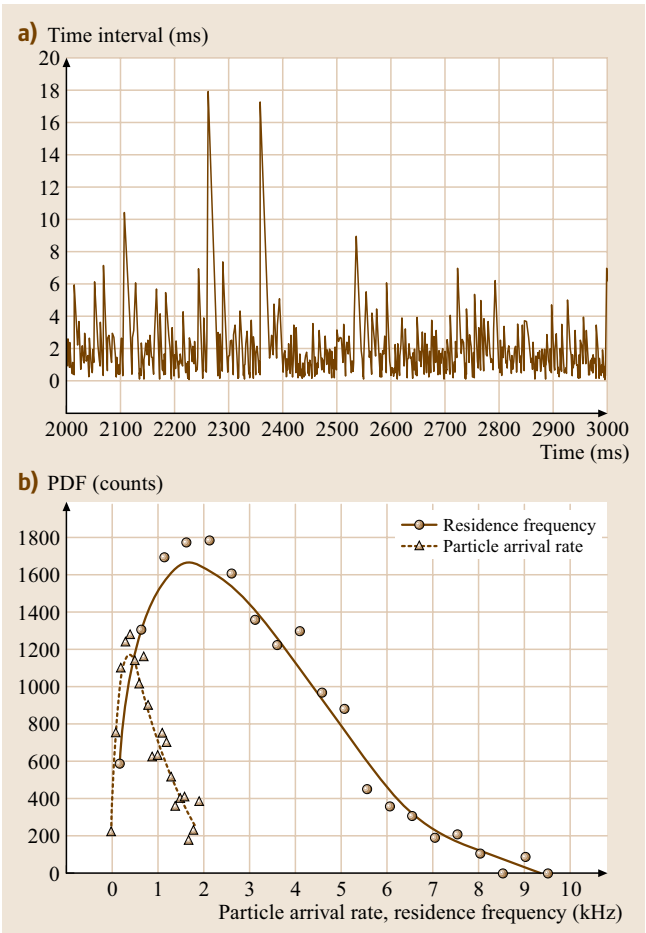

Fig. 5.179 **(a)** Typical time record of time intervals between successive particle arrivals (after *Agui* and *Andreopoulos* [5.718]). **(b)** Typical probability density function (PDF) of particle arrival rates (number/s), F_p and the inverse of the residence time in the probe volume $F_R = 1/T_R$ in the experiments by *Agui* and *Andreopoulos* [5.718]

introduced into the boundary layer through a hole in the wall about 1.8 m or 12.6δ upstream of the measuring location. The particle size, pinhole-fiber diameter, the size of the probe volume, and the separation distance between focusing points on the probe volume were the most important dimensions to be optimized in the LAVOR probe for good spatial resolution. The size of the focusing point, determined by the image of the fiber/pinhole diameter, was 100 µm, which defined the spatial resolution of velocity measurements. As mentioned earlier, the separation distance between the focusing locations on the probe volume determines the spatial resolution of the measurements of velocity gradients, i. e., vorticity. This separation in the case of the $\mathrm{Re}_\theta = 2700$ flow was about three Kolmogorov microscale units and was based on the case that this separation distance was 1.0 mm, which appeared to be the upper bound of the estimates. This resolution is about 35% better than that in the experiments of *Balint* et al. [5.731] and *Honkan* [5.690]. As a result of improved resolution, the uncertainty in measurements of vorticity due to unresolved scales is estimated to be considerably below the 9% estimate predicted by the theory of *Ewing* and *George* [5.732].

In this boundary-layer flow, the frequency scale of the Kolmogorov-size eddies $f_\varepsilon = (\varepsilon/\nu)^{1/2}$, which can be considered the maximum frequency anticipated in the flow, is about 250 Hz [5.690,731]. This indicates that adequate temporal resolution can be achieved with a rate of 250 bursts/s. Figure 5.179a shows a record of the time interval between successive particle arrivals T_p. The bursts produced by these particles have been validated by the burst processors. It can be seen that most of the time intervals are between 1 and 5 ms, which indicates a data rate much faster than 200 Hz. The validated particle data rate, defined as $F_\mathrm{p} = 1/T_\mathrm{p}$, has a probability density function (PDF), which is shown in Fig. 5.179b. It appears that the most probable value is about 450 particles per second, which is higher than the Kolmogorov frequency of the dissipative scales f_ε and about half the frequency in near-wall viscous units, u_τ^2/ν, which is approximately 1 kHz. Thus the data density in the dissipative scale is $F_\mathrm{p}/f_\varepsilon \approx 1$–2. At the same time the particle residence time T_R is smaller than the time between particles T_p. This is also shown in Fig. 5.179b where the PDF of the frequency $F_\mathrm{R} = 1/T_\mathrm{R}$ is plotted for direct comparison with the PDF of particle rate F_p. The most probable value of F_R appears to be 2.2 kHz, which is substantially larger than the most probable value of the particle rate.

Time coincidence in this case was realized within a time window t_c, which in this case was taken as the inverse of the maximum frequency of the flow $1/f_\varepsilon$, usually characteristic of the dissipative range of scales. This was facilitated in the data-processing software by interpolating between successive bursts separated by a time $\Delta t < t_\mathrm{c}$. When this time Δt was greater than t_c signal dropout occurred. Figure 5.180a shows a schematic of the interpolation algorithm used to analyze the data.

The statistical results obtained in the work of *Agui* and *Andreopoulos* [5.718] are not very sensitive to small or large changes in t_c. Figure 5.180b shows the results of a sensitivity analysis of the quantities $\overline{\Omega_3}$, and $(\overline{\omega_3^2})^{1/2}$ when the ratio of $t_\mathrm{c}/T_\varepsilon$ obtains values in the range 0.1–1.4. The data were obtained at $x_2^+ = 9.58$ and are presented as normalized differences from the value of the corresponding quantity Q at $t_\mathrm{c}/T_\varepsilon = 1$, which was finally adopted, i. e., $\Delta Q/Q = [Q(t_\mathrm{c}) - Q(T_\varepsilon)]/Q(t_\mathrm{c})$, where Q is either of the two previously mentioned quantities. The results show less than 4% variation in any of the quantities shown above for a 130% variation in $t_\mathrm{c}/T_\varepsilon$. These typical results suggest that there is no appreciable sensitivity of $\overline{\Omega_3}$, and $(\overline{\omega_3^2})^{1/2}$ to changes in the coincidence window $t_\mathrm{c}/T_\varepsilon$.

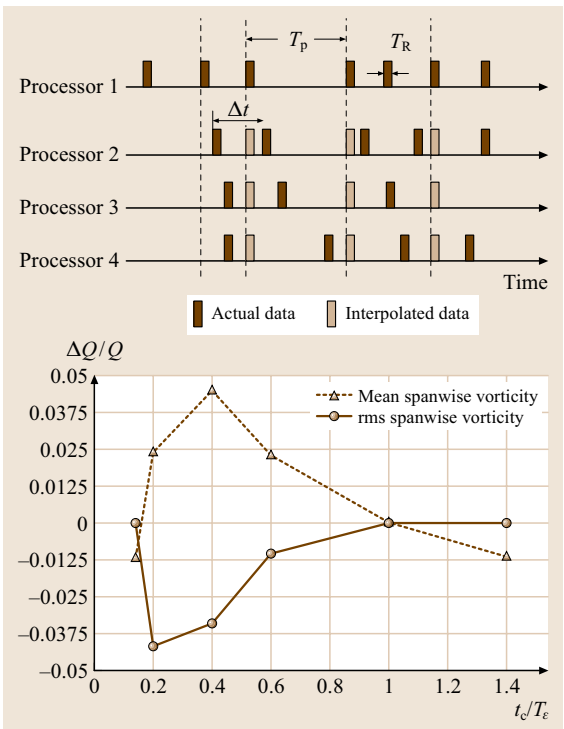

Fig. 5.180 **(a)** Interpolation scheme used in *Agui* and *Andreopoulos* [5.718]. *Black*: actual data; *grey*: interpolated data. **(b)** The effects of the coincidence window t_c on vorticity statistics (after *Agui* and *Andreopoulos* [5.718])

Uncertainties in Determining the Separation Distance for Optical Methods

In order to compute the vorticity component Ω_3 from the measured velocity differences, the distance between the two particles should be known. Although the focusing area can be determined rather well, the distance between the two particles cannot be considered as constant because the particle sizes are much smaller than the diameters of the two areas and they may not cross through the centers of the respective areas. Figure 5.181a illustrates the probe volume with two particles entering it at different locations. The actual distance between the two particles Δx_j is bounded in the following range $\Delta x_F - D_F \le \Delta x_j \le \Delta x_F + D_F$ where Δx_F is the fixed distance between the centers of the two fiber images and D_F is the diameter of the fiber image, which in the case of the work of Agui and Andreopoulos was about 0.1 mm, a value very close to half the maximum width of the probe volume. Although on average it is expected that $\overline{\Delta x_F} \approx \overline{\Delta x_j}$, instantaneous values of Δx_j can vary by $\pm D_F$ (at most) since particles can cross the probe volume without passing through the center of the fiber image. Thus the ratio of $\pm D_F/\Delta x_j$ can provide the lower and upper bounds of the estimate of the uncertainties involved in the determination of the separation distance between the two particles. Typically the distance Δx_j can be of the order of 1 mm or a fraction of that and can be fixed in advance. In this respect, it is expected that $D_F/\Delta x_j = 0.1$. *Agui* and *Andreopoulos* [5.718] attempted to reduce this uncertainty further in two different ways: first, by estimating the relative position of the particle entering the fiber image by taking into account its residence-time information and velocity as well as its local direction θ determined from the measurement of the other velocity component, and second, by filtering out data with residence traveling distance L_R within the image of the fibers, which is considerably less than the diameter D_F.

The first technique accounts for some variation in Δx_j. The associated procedure is better illustrated in Fig. 5.181b where only one image of the fiber is considered, which is assumed to be circular. The path of a particle entering at a point A_{in} with coordinates (x_1^{in}, x_2^{in}) and exiting the probe volume at A_{out} with coordinates (x_1^{out}, x_2^{out}) is also shown in this figure. The coordinate system has its origin at the centroid of the probe volume. Since the location and therefore the coordinates of the particle change during the residency time, a decision has to be made as to which location will be selected to compute the value of Δx_j. It appears that the most plausible location is the mid distance between the entry and exit points (x_1^m, x_2^m). Geometrical considerations indicate that $x_1^m = x_1^{in} - 1/2 L_R \tan\theta$ where L_R in the normal distance between A_{in} and $A_{out}(x_2^{in} - x_2^{out})$, which can be estimated through the residency time T_R and the measured local velocity v_2. Thus $x_2^{in} - x_2^{out} = L_R = v_2 T_R$ and the estimated offset location of the particle coordinate in the x_1 direction is

$$\delta x_j = \cos\theta \left[\frac{D_F^2}{4} + \left(\frac{L_R}{2\cos\theta} \right)^2 \right]^{1/2} = \left(\frac{D_F^2}{4}\cos^2\theta + \frac{L_R^2}{4} \right)^{1/2} . \quad (5.314)$$

The angle θ is the local direction of the particle at A_{in} defined as $\theta = \tan^{-1}(v_1/v_2)$. The value of v_1 at this location is not known. An estimate of this velocity component is available at the origin of the coordinate system, which was obtained at the other probe volume. This estimate of v_1 can be used in evaluating the previous equation without accounting for a possible variation along the x_1.

In order to gain some insight into the contributing terms of the previous equation, *Agui* and *Andreopoulos* [5.718] computed values of the residency distance L_R and their PDF is shown in Fig. 5.181c. L_R cannot exceed the diameter of the image of the fiber within the probe volume D_F, which was about 0.1 mm. The data of Fig. 5.181c clearly show that the majority of the events take place at $L_R \approx D_F$. The data also show that there exist contributions from events with $L_R < D_F$. The PDF drops steeply for values of $L_R > D_F$. The data indicate that the useful range of L_R is between $0.001\,\text{mm} < L_R < 0.165\,\text{mm}$ the upper bound of which is slightly higher that the anticipated 0.1 mm. It appears that events with values close to the two limits of this range contribute insignificantly to the statistical data.

In the second method used to reduce the uncertainty in Δx_j, events with values of L_R outside the range $0.016\,\text{mm} < \Delta x_j < 0.14\,\text{mm}$ were filtered out from the statistics.

The drawback of the first technique is that the depth of field of the fiber end images has been ignored in these considerations. In addition, there is an ambiguity in determining the sign of δx_j under these assumptions. The disadvantage of the second procedure is that by filtering out events with data, which correspond to particles crossing the fiber end image at locations away from its

center, the resultant time series of the processed data contain more signal dropouts than before. It appears, however, that both corrections, when applied to the acquired data, have minor effect on the statistical results. Mean and rms vorticity values are reduced by 1–2% only. The reason is that the number of events affected by the corrections is rather small in comparison to the total number of realizations. If the fixed distance between the two fibers is reduced to 0.4 mm the effect of both corrections is expected to be greater than in the case of $\Delta x_j = 1$ mm. As a result of these considerations, the data of *Agui* and *Andreopoulos* [5.718] have not been corrected to reduce the uncertainty in the fiber separation Δx_j. In addition, no corrections due to the velocity bias have been applied to their data.

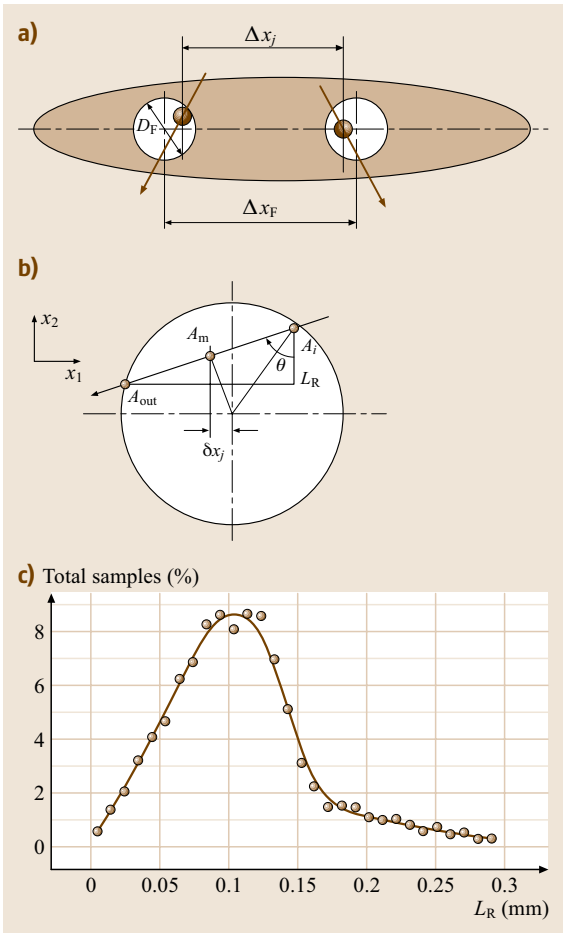

Fig. 5.181 **(a)** Schematic of two distinct focal regions and particle crossings on the same probe volume. **(b)** Geometrical details of particle crossings on half probe volume. **(c)** Typical probability density function of the transient/residence distance inside the probe volume in the experiments by *Agui* and *Andreopoulos* [5.718]

Uncertainty Estimates of Velocity Gradients Measurements

Direct estimates of the uncertainties associated with the measurements of velocity gradients can be obtained by considering the propagation of the uncertainties in the measurement of each quantity involved in the process. Following the example of *Honkan* and *Andreopoulos* [5.689], a typical velocity gradient is measured by the following approximation:

$$\frac{\partial v_i^+}{\partial x_j^+} \cong \frac{v_i(x_j + \Delta x_j) - v_i(x_j)}{\Delta x_j} T_v = F \,, \qquad (5.315)$$

where T_v is an appropriate time scale to normalize velocity gradients, which in the case of wall-bounded flows can be the viscous time scale in the near-wall region, $T_v = \nu/u_\tau^2$ with u_τ being the friction velocity.

For the typical test case of *Agui* and *Andreopoulos* [5.718], the uncertainties in the measurements of $v_i(x_j)$ and $v_i(x_j + \Delta x_j)$ can be assumed to be the same, $\Delta v_i(x_j) = \Delta v_i(x_j + \Delta x_j) = \Delta v$, and if the uncertainty in the estimate of Δx_j is $\Delta(\Delta x_j)$, then the relative uncertainty $\Delta F/F$ for the case of wall-bounded flows will be given by

$$\frac{\Delta F}{F} = \left\{ 2 \left[\frac{\Delta v}{v_i(x_j) - v_i(x_j + \Delta x_j)} \right]^2 + \left[\frac{\Delta(\Delta x_j)}{(\Delta x_j)} \right]^2 + 4 \left(\frac{\Delta u_\tau}{u_\tau} \right)^2 \right\}^{1/2} . \qquad (5.316)$$

As can be seen from this relation, the factor 4 in front of the third term on the right-hand side makes the uncertainty in the measurement of the friction velocity u_τ one of the major contributors to the total uncertainty. A typical uncertainty of 5% is assumed in determining u_τ.

The relative uncertainty shown in (5.316) has typically been estimated in the viscous sublayer where F is maximum. *Agui* and *Andreopoulos* [5.718] suggest that a typical value of the uncertainty Δv is 1%, which corresponds to about 0.01 m/s while a typical velocity difference is $\overline{v_1(x_j)} - \overline{v_j(x_j + \Delta x_j)} = u_\tau \Delta x_2^+ = 0.2$ m/s, where $\Delta x_2^+ = 1.6$ (the probe size). A typical value of the uncertainty in estimating the distance Δx_j is 2%, a value based on the results of the sensitivity analysis described earlier. Thus the uncertainty $\Delta F/F$ appears to be about 11% in the viscous sublayer. The relative un-

certainty $\Delta F/F$ increases as the distance away from the wall increases because the absolute value of F decreases.

Comparison of Mean Velocity-Gradient Data in Boundary-Layer Flows

A comparison between the mean velocity gradient and the derivative of the mean velocity profile is a good indicator of the probe's ability to measure at least one velocity gradient with sufficient accuracy. An attempt has been made here to compare several results obtained by different techniques in different facilities in boundary-layer or channel flow experiments.

Figure 5.182 shows the distribution of the mean velocity gradient $\overline{\partial U_1^+/\partial x_2^+}$ (negative $\overline{\Omega_3^+}$) across the boundary layer. Table 5.7 lists some of the bulk characteristics of the various datasets used in the present comparison. The data of *Honkan* and *Andreopoulos* [5.689], *Briassulis* et al. [5.694], and *Agui* and *Andreopoulos* [5.718] were obtained in the same wind-tunnel facility at CCNY. The data of *Agui* and *Andreopoulos* [5.718] were obtained with the optical technique LAVOR and the results shown in Fig. 5.182 are those measured at the centroid of the probe by time-averaging its instantaneous values. These data can be directly compared with the data of *Honkan* and *Andreopoulos* [5.689]. The two datasets agree very well in the buffer region while the LAVOR data appear to be slightly higher in the logarithmic region.

On the same figure the data of the mean velocity derivative are plotted; were obtained by differentiating *Spalding*'s [5.733] formula for the mean velocity distribution in the near-wall region, including the buffer zone and the logarithmic region. In addition, the data of mean velocity derivative in the logarithmic region, $1/\kappa x_2^+$, where κ is the so-called von Kármán constant, are also plotted for comparison. The data obtained by differentiating the near-wall velocity measurements of *Purtell* et al. [5.734] and *Andreopoulos* et al. [5.735] have also been plotted in the same figure. Purtell et al.'s mean velocity data show no Re_θ effect in the near-wall region and therefore the deduced mean velocity-gradient data are independent of Re_θ. The data of Andreopoulos et al. correspond to $\mathrm{Re}_\theta = 3624$.

The LAVOR data are also compared with the hot-wire data of *Balint* et al. [5.731]. It appears that the agreement of the LAVOR data with those of Balint et al. and with Spalding's formula in the buffer region is very satisfactory. Both data sets are also in very good agreement with the data obtained from the relation of the logarithmic law in the region of its validity. The data of Purtell et al. are lower than those predicted by Spalding's correlation while the data of Andreopoulos et al. are closer to Spalding's prediction in the upper edge of the buffer layer and close to Purtell's data at the upper edge of the viscous sublayer. However, if one considers that the uncertainty introduced in deducing these data and the uncertainty band associated with Spalding's formula, which originates from a modest 5% uncertainty in the initial mean velocity measurements, the agreement of the LAVOR measurements with existing data and correlations is quite satisfactory. It should also be pointed out that Spalding's relation should be reconsidered in light of recent demonstrations of limitations of the classical law-of-the-wall for the viscous sublayer. *Bradshaw* and *Huang* [5.736], for instance, have shown that integration of the total shear stress expression yields $\partial\overline{U_1}/\partial x_2^+ = 1 - A(x_2^+)^3$, where $A = \overline{\partial u_1/\partial x_2 \partial p/\partial x_2}$. The value of this coefficient, as suggested by *Mansour* et al. [5.737], is 1.4×10^{-3} and the whole subtracting term represents the contribution of the turbulent part of the total shear stress if the latter is independent of the wall distance in the viscous sublayer. Based on this relation the velocity gradient appears to be lower than that calculated from Spalding's formula (Fig. 5.182).

The data of *Su* and *Ötügen* [5.738] obtained in a water tunnel agree reasonably well with the rest of the data. The high-Reynolds-number data of *Breyer* et al. [5.706] ($\mathrm{Re}_h = 100\,000$) are substantially higher than the rest of the data in the near-wall region. The low-Reynolds-number data ($\mathrm{Re}_h = 3500$) show better agreement with the majority of the data under comparison in the near-wall region. In general, most of

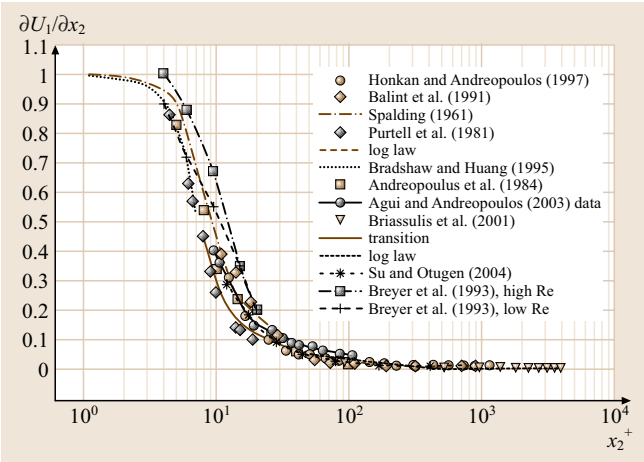

Fig. 5.182 Comparison of mean velocity gradient data obtained in boundary-layer flows by various experimental techniques

Table 5.7 Principal parameters of various experiments providing rms vorticity data

Datasets	Re_θ	Resolution L_p/η	L_p^+	Measurement technique	Measured quantities
[5.718]	2790	< 4	< 6	Optical	Ω_3
[5.696]	3900 5400	5 6	13 19	Optical	Ω_3
[5.731]	2685	6	11	Hot wire	$\Omega_1, \Omega_2, \Omega_3; S_{ij}$
[5.689]	2790	7	12	Hot wire	$\Omega_1, \Omega_2, \Omega_3; S_{ij}$, full dissipation
[5.739]	1450	6	–	Hot wire	Ω_3
[5.705]	2270	–	15	Optical, PIV	Ω_3
[5.705]	6450	–	20	Optical, PIV	Ω_3
[5.740]	1100 2870 4850	0.6–1.5 0.9–3.4 1.7–7.0	1.95 4.75 7.82	Hot wire	Ω_3
[5.741]	5×10^6	–	< 6	Hot wire	Ω_3
[5.738]	1837	17	26	Optical	Ω_3
[5.706]	(Re_h) 3500 6700 100 000	2 4	–	Optical, laser speckle	$\partial v/\partial x + \partial v/\partial y$, $\partial v/\partial x - \partial v/\partial y$, and $\partial v/\partial z$

the data agree reasonably well with each other in the region $x_2^+ > 80$ while there are substantial differences in the closer region to the wall with $x_2^+ < 80$ where most of the intensive vortical activities take place. Thus the best test for the method is how well it works in the near-wall region of the boundary-layer flow.

Comparison of Fluctuating Vorticity Statistical Data in Boundary Layers

Comparison of various data sets that describe the distribution of the rms spanwise vorticity fluctuations is shown in Fig. 5.183a plotted against x_2^+ and normalized by u_τ^2/ν. The data sets under comparison are listed in Table 5.7 together with their spatial resolution estimates. In addition to these experimental data, the DNS results of *Spalart* [5.742] obtained at a rather low $Re_\theta = 1400$ and by *Kim* et al. [5.743] are also plotted for comparison. The data of *Rajagopalan* and *Antonia* [5.739] and *Meinhart* and *Adrian* [5.705] obtained by PIV techniques with a spatial resolution of about $\Delta x^+ = 20$ are also plotted on the same figure. It should be mentioned that all the data sets, with the exception of Meinhart and Adrian and Su and Ötügen, agree remarkably well in the region $x_2^+ > 60$. Considerable differences, however, seem to exist in the near-wall region. The LAVOR data of *Agui* and *Andreopoulos* [5.718] seem to be substantially higher than any of the other measurements. The data by *Klewicki* [5.740] obtained at $Re_\theta = 2870$ are reasonably close to the LAVOR data but start to deviate in the buffer region with $x_2^+ < 20$ where differences of up to 15% can be observed.

Comparison with data obtained in other facilities under different conditions is meaningful only when appropriate scaling is available. The work of *Balint* et al. [5.731] and *Honkan* and *Andreopoulos* [5.689] clearly indicated that current scaling ideas based on inner, outer, or mixed-layer parameters failed to collapse velocity gradient/vorticity data. The data of *Honkan* and *Andreopoulos* [5.689], however, have been obtained in the same wind tunnel under exactly the same flow conditions as the LAVOR measurements. This allows a direct comparison in the absence of any problem due to inadequate scaling. It appears that the LAVOR data are higher than the hot-wire data in the $x_2^+ < 60$ region. One possible reason for this behavior is the higher spatial resolution of the LAVOR technique and its non-intrusive character.

There are two more parameters to be considered for a meaningful comparison of the various data sets. First is the accuracy in the measurements of vorticity and the uncertainty in measuring u_τ, which as discussed later appears to be one of the most dominant contributors to the overall uncertainty. Unfortunately the overall issue of accuracy in the measurements of vorticity is not addressed in detail in the published literature and information on uncertainty in the measurements of u_τ is not available for the majority of datasets. Second is the effect of Re_θ which, as will be shown in the next Section, is yet to be established. There is evidence suggesting that ω_3^+-rms

increases with increasing Re_θ. However, quantitatively this effect is not strong enough to explain the rather substantial differences between the various datasets shown in Fig. 5.183a. Most probably these differences are attributed to the combined effects of different accuracies involved in each of the techniques applied including those due to spatial resolution, the lack of appropriate scaling, and the effects of Re_θ.

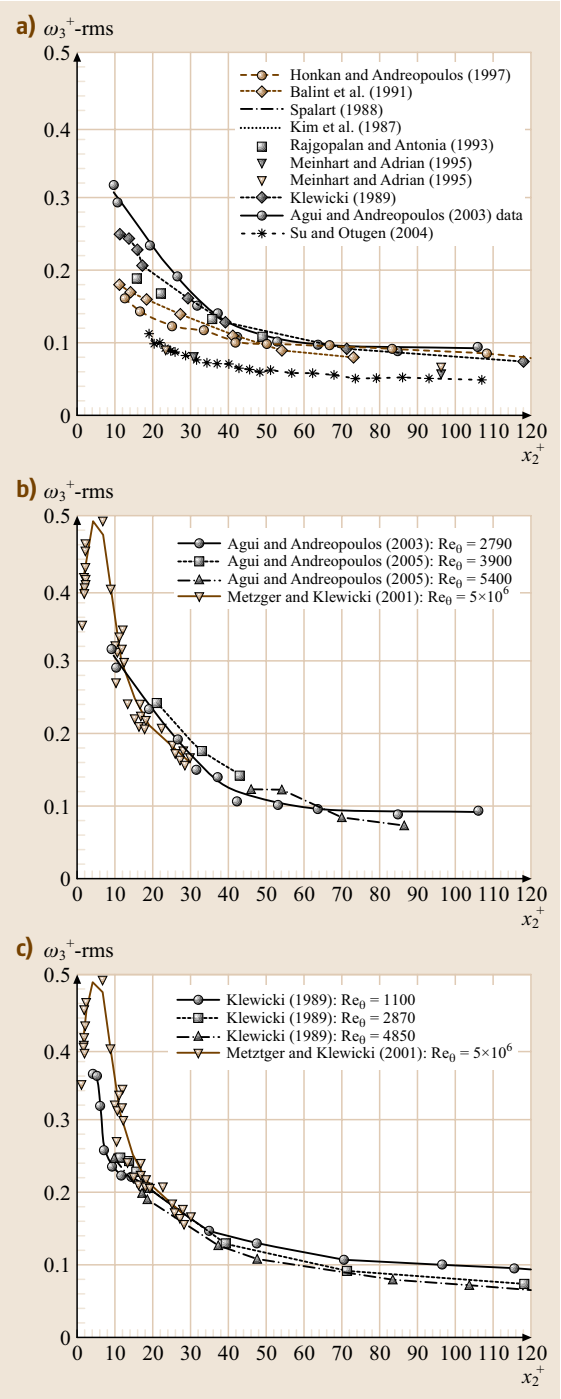

Reynolds-Number Effects

The effect of Reynolds number on statistical properties of velocity fluctuations in turbulent flows is always of interest, since most opractical engineering flows are in the high-Reynolds-number regime and most laboratory data have been obtained in low-Reynolds-number flows. Reynolds-number effects on vorticity statistics have yet to be demonstrated experimentally. Some rms data for the quantities $\partial v/\partial x + \partial v/\partial y$, $\partial v/\partial x - \partial v/\partial y$, and $\partial v/\partial z$ obtained by *Kriegs* et al. [5.707] show no effect for Reynolds numbers of 2600–4000. In the work of *Kriegs* and *Strude* [5.708] the rms data for $\partial v/\partial x + \partial v/\partial y$ seem to increase slightly in the near-wall region, with increasing Reynolds number from 2250 to 6700, while the rms data of the quantity $\partial v/\partial z$ decrease with increasing Re.

Figure 5.183b shows the rms of the spanwise vorticity fluctuations at three different values of Re_θ obtained by *Agui* and *Andreopoulos* [5.744] by using their LAVOR techniques. Although the spatial resolution is reduced with increasing Re_θ (Table 5.7) it remains reasonably acceptable at $Re_\theta = 3900$ and 5400. There is some evidence that indicates that ω_3-rms increases slightly with increasing Re_θ in the near-wall region. There is a modest increase of about 20% of ω_3-rms for a Re_θ increase of 39% at $x_2^+ = 30$. In the case of $Re_\theta = 5400$, no data in the near-wall region are available and therefore the Re effect shown in the case of $Re_\theta = 3900$ cannot be corroborated.

The high-Reynolds-number data of *Metzger* and *Klewicki* [5.741] obtained in the atmospheric boundary layer developed over the salt flats of the Great Salt Lake Desert are also plotted for comparison in Fig. 5.183b. These data appear to be higher than the present ones within the viscous sublayer and lower in the outer part of the buffer zone and the beginning of the logarithmic region. Thus the picture that emerges from this comparison is that, in the buffer and the viscous sublayer, the rms of the spanwise vorticity

Fig. 5.183 **(a)** Comparison of rms data for spanwise vorticity fluctuations obtained in boundary-layer flows by various experimental techniques. **(b,c)** Effects of Reynolds number on the vorticity statistics in a boundary layer. **(b)** After *Agui* and *Andreopoulos* [5.696]; **(c)** After *Klewicki* [5.740]

fluctuations increases with increasing Re_θ. This dependency is considerably reduced and reverses away from the wall.

Quite similar behavior is exhibited by the data of *Klewicki* [5.740], obtained in a wind tunnel at three different values of Re_θ. For clarity these data have been plotted in Fig. 5.183c separately to those shown in Fig. 5.183b. These data agree well with the data of *Agui* and *Andreopoulos* [5.744]. A comparison with the high-Re_θ data of *Metzger* and *Klewicki* [5.741] clearly suggests a rather strong dependency of vorticity fluctuations on Re_θ in the viscous sublayer and the buffer region.

Concluding Remarks

The importance of vorticity, velocity gradient tensor, rate-of-strain tensor, and wall vorticity flux was discussed first in the context of the structure function in the present contribution, followed by a discussion of the general requirements of strophometric techniques. Of paramount significance amongst these are the issues of the temporal and spatial resolution of the probe volume for the measuring technique and its validation in a turbulent flow field. Several optical techniques used in strophometry were described in detail. The major advantage of optical techniques over those based on hot wires is that they are non-intrusive in the flow field and are therefore suitable for separated flows or flows with relatively high variation in the pitch or yaw angles of the instantaneous velocity vector. In canonical turbulent boundary-layer flows, for instance, the rms of the pitch and yaw angles is about 9° very close to the wall [5.689], which for a Gaussian distribution with 3 rms range variation indicates a range of 0 to 54. In that respect, hot-wire techniques with sensitivity to pitch/yaw angle variation in this range can be effective in channel or boundary-layer-type flows. The non-intrusive nature of the optical techniques always has to be considered in relation to possible disturbances introduced by seeding since adding particles can alter the flow substantially.

A comparison of data measured in boundary-layer or channel flows using optical techniques with measurements obtained by other means was attempted to evaluate their performance.

The value of each of these techniques can be estimated by considering its cost, complexity, and performance. Most of the optical techniques developed to date have demonstrated capabilities in measuring only one component of the vorticity vector. Future work and development should focus on:

1. Increasing the spatial and temporal resolution of the techniques so that reliable time-dependent strophometric data can be obtained in high-Reynolds-number flows
2. Increasing the capabilities to measure more than one vorticity component
3. Decreasing the cost of hardware and level of complexity of the techniques
4. Applying present techniques to a wide range of flows.

5.5.2 High-Resolution Dual-Plane Stereo PIV (DSPIV)

One of the main motivations behind the continuing development of advanced measurement methods in fluid mechanics is the need for experimental studies of turbulent flows, where the wide range of length and time scales involved in the fluid motion creates one of the most demanding challenges in all of measurement science. Researchers in fluid mechanics are increasingly seeking to address issues regarding intermediate and small scales of inhomogeneous turbulence of the type encountered in practical turbulent shear flows. Unlike homogeneous isotropic or uniformly sheared turbulence in periodic domains, spatially developing turbulent shear flows at large Reynolds numbers cannot be readily studied by direct simulation. At the same time, new measurement capabilities are beginning to provide experimental access to flow information that had previously been accessible only by simulations. These include multiple-sensor hot-wire probes that provide single-point time-series data for various key turbulence quantities, such as the time-varying vorticity and strain rate components, as well as the enstrophy and the dissipation rate. In parallel, these data are being augmented with new multidimensional optical measurement methods that are providing two-, three- and even four-dimensional data for velocity gradient fields that are essential to understanding the intermediate and small scales of turbulent shear flows. Collectively, these techniques are beginning to provide a direct experimental measurement capability that, at least in the near term, may provide the most practical way to obtain the detailed structure, statistics, similarity and scaling properties of gradient quantities in turbulent shear flows at a level of resolution and detail that has traditionally been associated only with direct numerical simulations.

The fields of principal interest for understanding the precise structure and dynamics of inhomogeneous turbulence in spatially developing turbulent shear flows are

all derived from the nine simultaneous components of the velocity gradient tensor field $\partial u_i/\partial x_j(\boldsymbol{x}, t)$, given by

$$\frac{\partial u_i}{\partial x_j} = \begin{pmatrix} \partial u/\partial x & \partial u/\partial y & \partial u/\partial z \\ \partial v/\partial x & \partial v/\partial y & \partial v/\partial z \\ \partial w/\partial x & \partial w/\partial y & \partial w/\partial z \end{pmatrix} \tag{5.317}$$

The components of this tensor determine the three components of the vorticity vector

$$\omega_x = \left(\frac{\partial w}{\partial y} - \frac{\partial v}{\partial z}\right) ,$$
$$\omega_y = \left(\frac{\partial u}{\partial z} - \frac{\partial w}{\partial x}\right) ,$$
$$\omega_z = \left(\frac{\partial v}{\partial x} - \frac{\partial u}{\partial y}\right) ,$$

the three normal components of the strain rate tensor

$$S_{xx} = \left(\frac{\partial u}{\partial x}\right) ,$$
$$S_{yy} = \left(\frac{\partial v}{\partial y}\right) ,$$
$$S_{zz} = \left(\frac{\partial w}{\partial z}\right) ,$$

and the three shear components of the strain rate tensor

$$S_{xy} = \frac{1}{2}\left(\frac{\partial u}{\partial y} + \frac{\partial v}{\partial x}\right) ,$$
$$S_{yz} = \frac{1}{2}\left(\frac{\partial v}{\partial z} + \frac{\partial w}{\partial y}\right) ,$$
$$S_{zy} = \frac{1}{2}\left(\frac{\partial w}{\partial x} + \frac{\partial u}{\partial z}\right) .$$

The strain rate and vorticity components can be written as

$$S_{ij} \equiv \frac{1}{2}\left(\frac{\partial u_i}{\partial x_j} + \frac{\partial u_j}{\partial x_i}\right) \quad \text{and}$$
$$\omega_k \equiv \frac{1}{2}\left(\frac{\partial u_j}{\partial x_i} - \frac{\partial u_i}{\partial x_j}\right)\varepsilon_{ijk} .$$

Of these, specific interest is often directed at such gradient fields as the enstrophy $\boldsymbol{\omega}_i\boldsymbol{\omega}_i$, the enstrophy production rate $\boldsymbol{\omega}_i S_{ij}\boldsymbol{\omega}_i$, and the kinetic-energy dissipation rate $2\nu S_{ij}S_{ij}$, and in their properties at the quasi-universal intermediate and small scales of turbulent shear flows.

Numerous studies have sought to develop accurate ways of measuring these nine quantities simultaneously in turbulent flows, including single-point probe-based measurements [5.81, 687, 693] as well as various multidimensional imaging techniques. Most of the latter methods are based on particle imaging approaches. Classical particle image velocimetry (PIV) allows measurement of two in-plane velocity components, which provide access to four of the nine velocity gradient tensor components. These permit formation of three of the six components of the strain rate tensor and a single vorticity component. Stereo PIV additionally provides the out-of-plane velocity component, thereby giving access to two further velocity gradient components, however these do not provide any additional strain rate or vorticity components. Particle tracking velocimetry (PTV) provides three-component velocity fields throughout a three-dimensional volume, allowing access to all nine components of $\partial u_i/\partial x_j$, but the large particle separations needed for accurate tracking typically prevent gradient measurements at the small scales of turbulence. The most extensive velocity gradient measurements in turbulent flows to date have come from holographic particle image velocimetry (HPIV) [5.709], although the resolution in those measurements is typically larger than the smallest scales in the turbulent flow. Indirect measurements of $\partial u_i/\partial x_j$ via scalar imaging velocimetry (SIV) are based on three-dimensional laser-induced fluorescence imaging of a scalar field [5.745,746] and inversion of the conserved scalar transport equation to obtain the underlying three-component velocity field [5.747, 748]. This allows highly resolved measurements of all nine simultaneous components of the velocity gradients at the intermediate and small scales of a turbulent flow, but requires smoothness and continuity constraints in the inversion to obtain the velocity field.

Dual-plane stereo particle image velocimetry (DSPIV) is based on two separate stereo PIV measurements that provide all three components of velocity in two parallel light-sheet planes. This allows all nine components of $\partial u_i/\partial x_j$ to be calculated from the measured velocities in the two planes, with the resolution determined largely by the thickness and spacing of the light-sheet planes and the size of the PIV correlation window. The approach requires separating the light scattered by particles in the two light-sheet planes onto two independent stereo camera pairs. A polarization-based approach, in which the two light sheets were arranged with orthogonal polarizations so that each stereo camera pair saw the scattered light from only one of the sheets, was introduced in [5.749]. This has been used to measure comparatively large-scale features of the flow in a turbulent boundary layer [5.750, 751], and the same technique has been used to investigate large-scale features of a lobed jet mixer [5.752]. A related polarization-based dual-plane approach that combines

stereo PIV and conventional PIV, with continuity used to estimate the out-of-plane gradient component, has been used to study features of a turbulent boundary layer [5.753]. These studies all investigated specific aspects of these flows, and did not seek to resolve or study velocity gradients on the quasi-universal intermediate and small scales of turbulent shear flows. Moreover, maintaining the orthogonal polarization in the Mie scattered light requires the scattering particles to be spherical, and as a consequence these studies used fine liquid droplets as seed particles. This can be done in isothermal flows, but in exothermic reacting turbulent shear flows such liquid droplets do not survive and the polarization-based method cannot be used.

A two-frequency DSPIV approach [5.713, 754, 755] allows traditional solid metal oxide particles to be used as the seed, thereby permitting measurements in reacting as well as nonreacting turbulent shear flows. This approach is based on measurements in two differentially spaced light-sheet planes, using two different laser frequencies in conjunction with filters to separate the light scattered from the seed particles onto the individual stereo camera pairs. The differential spacing of the two stereo PIV planes allows resolution of all nine components of the $\partial u_i/\partial x_j$ fields down to the local inner (viscous) scale of the turbulent flow, permitting highly-resolved experimental studies of the quasi-universal intermediate and small scales of nonreacting and exothermically reacting turbulent shear flows.

DSPIV Measurement Setup

As indicated in Fig. 5.184, the two-frequency DSPIV method [5.713] is based on two simultaneous, independent stereo PIV measurements in two differentially spaced light-sheet planes. Two different light-sheet frequencies are used in conjunction with appropriate optical filters to separate the scattered light from particles seeded in the flow onto two independent stereo PIV camera pairs. The two-frequency system involves four Nd:YAG lasers, of which two are sequentially triggered to create the double pulses for the light sheets of wavelength 532 nm and the other two, also sequentially triggered at the same two instants of time, pump two pulsed dye lasers that provide the light sheets of wavelength 635 nm. Light scattered from 0.5 μm aluminum oxide seed particles is recorded on four 12 bit 1280 × 1024 px PIV cameras. A typical field of view of 15.5 × 12.5 mm is achieved using Sigma 70–300 f/4-5.6 APO macro lenses. The 532 nm and 635 nm stereo camera pairs each have narrow-band optical filters that block the scattered light from the other light sheet. The four cameras are arranged in an asymmetric angular-displacement forward–forward imaging configuration

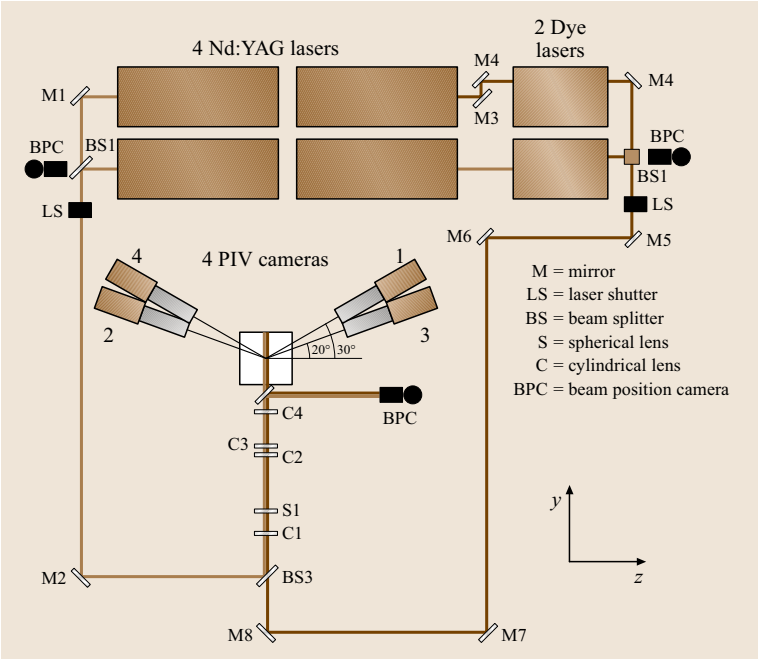

Fig. 5.184 Experimental arrangement for two-frequency dual-plane stereo PIV measurements (after [5.713])

with a 50° included angle satisfying the Scheimpflug condition. The small field of view required for high-resolution measurements and the long focal length of the camera lens necessitate large-f-number imaging to obtain sufficiently focused particle images across the entire field of view. Precise alignment of the object, lens, and image planes requires custom-designed camera mounts to maintain a coincident field of view for all four cameras. Calibration of this imaging arrangement is based on a transparent precision calibration target [5.713] that provides registration of all four cameras to a common reference frame, as well as the mapping from the object planes to each of the four image planes to correct for distortions due to the variable magnification across each image. Particle images are processed with an adaptive multipass technique using 32×32 px interrogation boxes with no overlap in the final vector fields. This provides the same in-plane resolution between vectors as the out-of-plane resolution between the planes. More-detailed descriptions of this two-frequency DSPIV setup can be found in [5.713].

Light-Sheet Characterization

The thickness, spacing, and two-axis parallelism of the two pairs of light sheets are of central importance to the resolution and accuracy of DSPIV measurements. The four laser beams are initially aligned without the sheet-forming optics to be coincident to within ±25 μm over the entire optical path, as verified optically using CCD cameras, and only then formed into light sheets by inserting the spherical and cylindrical lenses. Prior to each measurement, transmitted light from a knife edge traversed across each sheet is measured with a photodiode to assess the characteristics of the four light sheets quantitatively [5.713]. An error-function fit to each resulting profile is differentiated to obtain a Gaussian sheet-normal intensity profile. The three lowest-order moments of this profile allow the sheet centerline position and the local $1/e^2$ thickness of each laser sheet to be determined. This procedure is repeated at 16 vertical positions along each sheet in the center of the field of view, as well as at the right and left edges, to characterize the four light sheets over the entire field of view, as shown in Fig. 5.185. Typical results verify actual thicknesses of 400 ± 20 μm in the two 532 nm light sheets and 800 ± 20 μm in the two 635 nm light sheets. Sheet noncoincidence in each light-sheet pair is typically less than 40 μm, and less than 1° of nonparallelism can be achieved between the 532 nm and 635 nm light-sheet pairs. This procedure also quantitatively confirms the 400 ± 20 μm separation between the two light-sheet pairs that matches the out-of-plane spatial resolution to the in-plane resolution of the measurements.

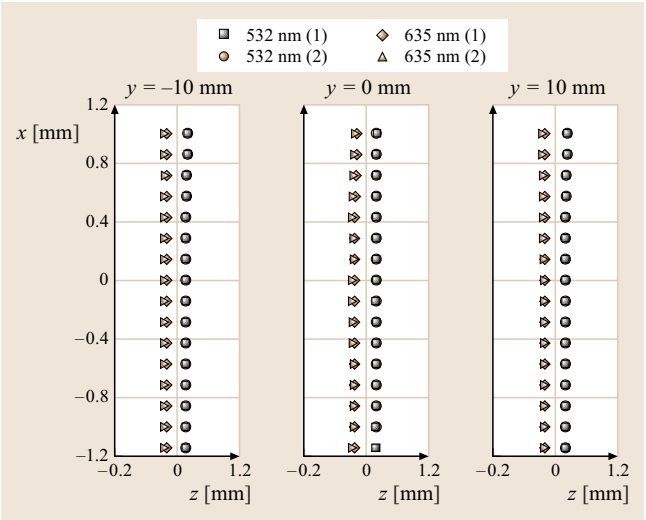

Fig. 5.185 Characterization of coincidence, two-axis parallelism and separation of the two light-sheet pairs (after [5.713])

Relative Measurement Resolution

The light sheet characteristics alone do not determine the spatial resolution achieved in any dual-plane measurement. Four principal factors collectively contribute to the spatial resolution of these DSPIV measurements:

1. the light-sheet thicknesses and separation
2. the PIV correlation window size
3. the typical bad-vector replacement region size
4. the PIV smoothing filter scale.

As noted before, typical achievable laser sheet thicknesses are $\Delta_1 \approx 400\,\mu m$ and $\Delta_1 \approx 800\,\mu m$ in the 523 nm and 635 nm light sheets, respectively. The 32×32 px PIV correlation window, together with the pixel size and magnification ratio, effectively filters the velocity field at a scale of $\Delta_2 \approx 400\,\mu m$. From the vector-to-vector spacing, the typical bad-vector replacement scale $\Delta_3 \approx 800\,\mu m$ is applied to approximately 5% of the vectors, and the median filter applied to the velocities in the final processing stage is at a scale of $\Delta_4 \approx 800\,\mu m$. Since these contributions to the net resolution are independent, the resulting velocity gradient fields are resolved to a length scale of $\Delta_{net} = (\Delta_1^2 + \Delta_2^2 + \Delta_3^2 + \Delta_4^2)^{1/2} \approx 1100\,\mu m$.

To assess the relative resolution of any such measurement, the spatial resolution Δ_{net} can be compared

with the local Kolmogorov scale $\lambda_K \equiv (\nu^3/\varepsilon)^{1/4}$, defined in terms of the viscosity ν and the local mean dissipation rate ε in homogeneous isotropic turbulence and applied to turbulent shear flows via the assumption of local isotropy. For the DSPIV measurement results shown herein, at $Re_\delta = 6000$ and 30 000, the respective Kolmogorov scales λ_K are 210 μm and 108 μm, giving a relative resolution of $\Delta_{net}/\lambda_K \approx 5.2$ at the lower Reynolds number. Here Re_δ is the local outer-scale Reynolds number $Re_\delta \equiv u_c\delta/\nu$, where u_c and δ are the local velocity and length scales, respectively, in the local mean velocity profile that characterize the peak mean shear. In turbulent jets, u_c and δ are, respectively, the local centerline mean velocity and local flow width. The corresponding inner (viscous) length $\lambda_\nu \approx 5.9\,\lambda_K$ is the local strain-limited viscous diffusion scale on which gradient fields in turbulent flows are concentrated by the competing effects of strain and viscous diffusion [5.756, 757]. At $Re_\delta = 6000$ and 30 000 the λ_ν values are 1240 μm and 640 μm, with the resulting $\Delta_{net}/\lambda_\nu \approx 0.89$ at the lower Reynolds number.

Velocity Gradient Calculation

From the measured velocity component values (u, v, w) at each point in the two differentially spaced z-planes, the in-plane components of the velocity gradient tensor $\partial u_i/\partial x_j$ can be obtained from central differences in the x- and y-directions, and the out-of-plane components obtained from one-sided differences along the z-direction. However, this would only make use of the measured velocities at six of the 18 points available in the 3×3×2 template around each point. If instead the natural pixel-based coordinate frame is rotated by $\pm\pi/4$ along the z-axis, or by $\pm\tan^{-1}(1/2)$ along the x- and y-axes, then separate evaluations of the gradient components can be obtained in each rotated frame and projected back onto the original frame. Averaging the resulting velocity gradient components obtained from all the frames produces a differencing stencil that makes use of all 18 points around each point. This provides a reduction of random error in the gradient components without significantly degrading the net spatial resolution in the resulting derivative fields. This can be contrasted to an explicit filter applied to the velocity gradients in the original frame, which for the same error reduction would lead to a substantial degradation in resolution.

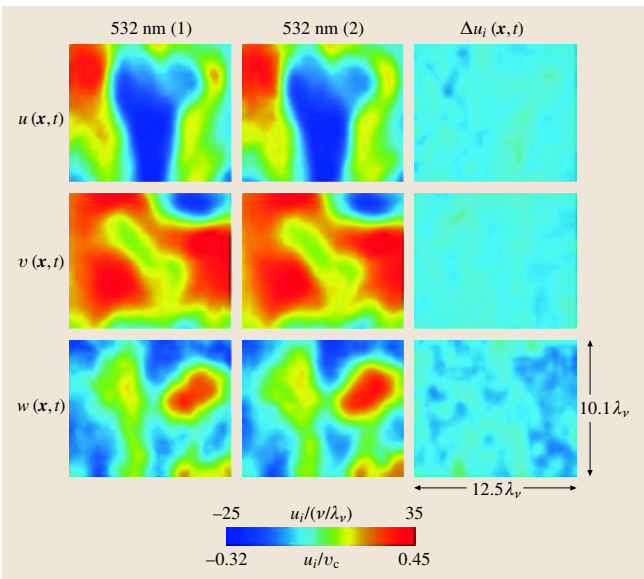

Fig. 5.186 Typical single-plane validation test showing $u_i(\boldsymbol{x}, t)$ velocity component fields measured in the same light-sheet plane by both stereo camera pairs (*left* and *middle*), and differences $\Delta u_i(\boldsymbol{x}, t)$ (*right*) on same color scale; note that $\lambda_\nu \approx 5.9\,\lambda_K$, as described in the text (after [5.758])

Single-Plane Validations

Although it is always possible to differentiate any measured velocity field to produce a matrix of derivative values, it is an entirely different matter to verify that these derivatives represent the true velocity gradient tensor components in the flow. Since high-resolution measurements of velocity gradients necessarily involve differences between nearly equal measured velocity values, it is possible for the resulting derivatives to be completely dominated by errors in the original measured velocities and thus not reflect the true velocity gradients to any significant accuracy. Avoiding this requires considerable effort to minimize even small errors in the velocity measurements, along with careful assessments of the relative errors in the resulting velocity differences to validate the tensor of derivative values. The most fundamental of such validation tests is based on single-plane imaging [5.758], in which both stereo camera pairs in the DSPIV system are arranged to image the same particle field in the same double-pulsed light sheet, so that $\Delta z \equiv 0$. In principle, the velocity fields from the two camera pairs should then be identical, and differences in the two independently measured velocity fields thus provide a quantitative assessment of the accuracy with which velocity gradients can be measured. Typical results from such single-plane imaging assessments are shown in Figs. 5.186 and 5.187, where the measurements are from the centerline of an axisymmetric turbulent jet at $Re_\delta = 6000$. Figure 5.186 shows the

instantaneous velocity component fields $u_i(\boldsymbol{x}, t)$ from the two stereo camera pairs when both image the same 532 nm light sheet, as well as the differences $\Delta u_i(\boldsymbol{x}, t)$ between these two independent measurements, shown on the same color scale. It is apparent that the differences Δu_i are far smaller than the velocity component values themselves, reflecting the comparatively high accuracy that can be obtained in such DSPIV measurements once numerous error sources have been addressed. The distributions of the measured Δu_i values obtained over many such instantaneous realizations are shown in Fig. 5.187. Relative errors, given by the ratio of rms values of Δu_i and u_i, are found to be 6.5% for the u- and v-components and 10.5% for the w-components, with the latter being slightly larger due to the inherently higher errors in measuring the out-of-plane velocity component with stereo PIV systems.

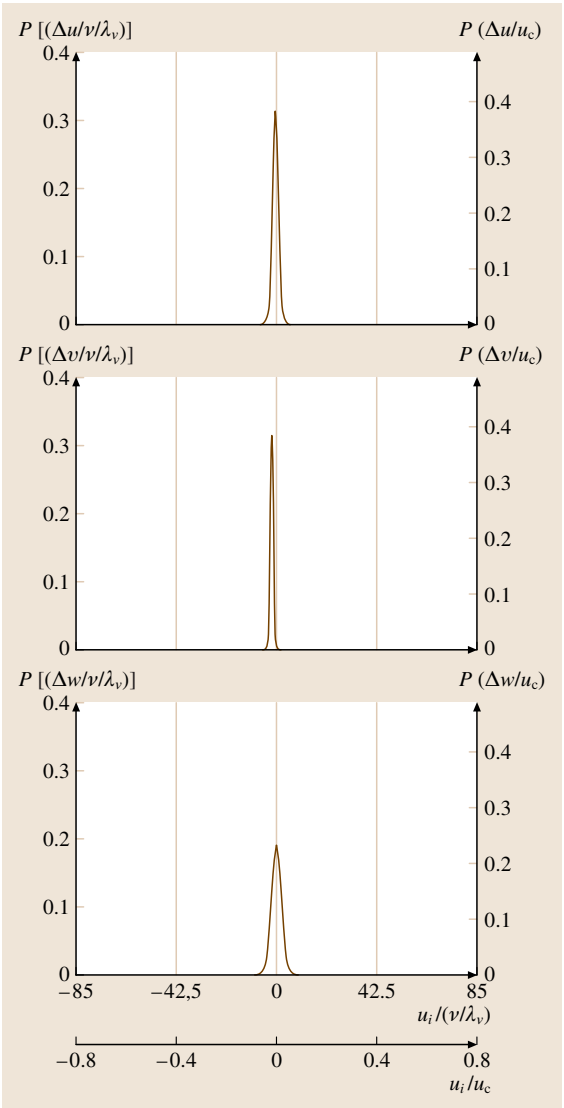

Fig. 5.187 Distributions of velocity component differences from single-plane validations tests of the type in Fig. 5.186, shown normalized on inner- and outer-scale variables (after [5.758])

Coincident-Plane Validations

The additional errors due to light-sheet positioning inaccuracies and the separate formation of 532 nm and 635 nm light-sheet pairs can be obtained from coincident-plane imaging tests [5.758]. In this case, the velocity component fields obtained from the two stereo camera pairs are compared when separate 532 nm and 635 nm light sheets are created and positioned with the optical alignment system to be as nearly coincident as experimentally feasible, i. e., $\Delta z \approx 0$. Typical results from such coincident-plane imaging assessments are shown in Figs. 5.188 and 5.189. In principle, the $u_i(\boldsymbol{x}, t)$ fields from the 532 nm and 635 nm camera pairs should again be identical, with differences being due to the errors addressed before and the additional errors introduced by the independent dual light-sheet genera-

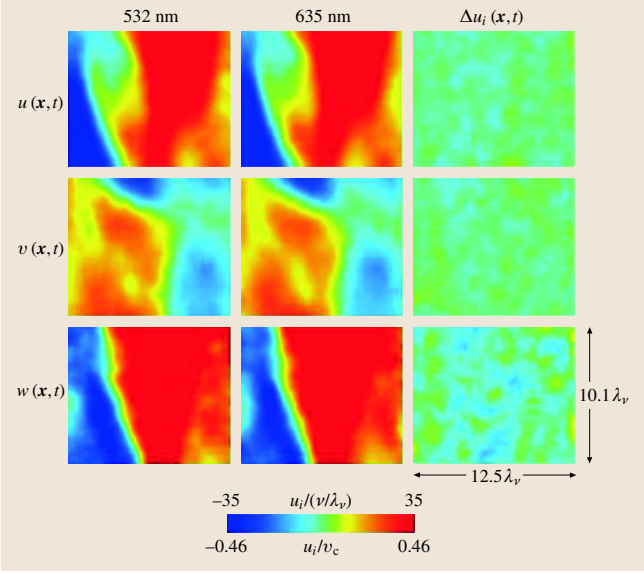

Fig. 5.188 Typical coincident-plane validations, showing $u_i(\boldsymbol{x}, t)$ velocity component fields measured in two coincident light-sheet planes by the two stereo camera pairs (*left* and *middle*), and differences $\Delta u_i(\boldsymbol{x}, t)$ (*right*) shown on the same color scale (after [5.758])

tion and positioning. It is apparent that the differences Δu_i in Fig. 5.188 are again far smaller than the velocity component values themselves, indicating that the additional errors due to separate light-sheet formation and positioning inaccuracies are substantially smaller than the errors already inherent to stereo imaging of the finite-thickness light sheets. The distributions of the measured Δu_i values from many such realizations are shown in Fig. 5.189. In this case, the elative errors are found to be 8–9% for the u- and v-components, and 16% for the w-components, verifying that the errors due to the dual light-sheet formation and positioning procedure are measurable, but are substantially smaller than those inherent in stereo PIV imaging. The results from these coincident-plane validation tests also demonstrate that further efforts to improve the light-sheet formation and positioning procedures would provide only marginal improvements in the accuracy of the velocity gradient measurements. Recent advances in mapping calibrations for stereo PIV systems [5.759, 760] may provide a way to reduce this limiting accuracy in stereo PIV measurements.

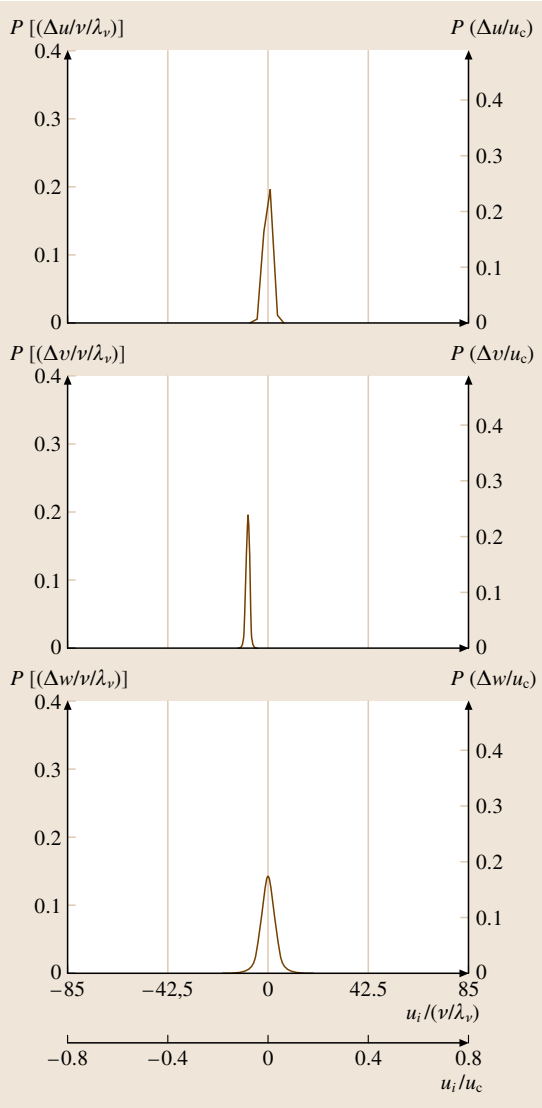

Fig. 5.189 Distributions of velocity component differences from coincident-plane validations tests of the type in Fig. 5.188, shown on inner- and outer-scale variables. Compare with Fig. 5.187 (after [5.758])

Separated-Plane Validations

The accuracy of all nine simultaneously measured velocity gradient components $\partial u_i/\partial x_j$ can be further assessed in separated-plane validation tests [5.758, 761]. The two stereo camera pairs are now arranged to image separate 532 nm and 635 nm light-sheet pairs with a differential spacing $\Delta z \approx 400\,\mu$m that matches the in-plane separation between adjacent vectors. An example of all three simultaneously measured instantaneous velocity component fields $u_i(\boldsymbol{x}, t)$ in the two differentially spaced light sheets is given at the top in Fig. 5.190. The two velocity fields should now no longer be identical due to the differential z-spacing, which gives rise to the z-derivatives in the velocity gradient components.

Figure 5.190 also shows all nine simultaneous $\partial u_i/\partial x_j$ components measured in the same flow as above. Perhaps the most stringent validation test that can be applied to any measurement of the full velocity gradient tensor is the extent to which the measured components satisfy the zero-divergence requirement from continuity in the velocity field. The resulting distribution of divergences is shown in Fig. 5.191, where the measured divergence values are normalized by the local instantaneous norm of the velocity gradient tensor, giving the relative error in the measured velocity gradients. Note that at locations where the gradients are small, this relative divergence error will be relatively large, since these errors result primarily from measurement uncertainties that are independent of the velocity gradient values. The divergence values can be compared with the distributions of the velocity gradients measured at $\mathrm{Re}_\delta = 6000$ and 30 000, corresponding to $\mathrm{Re}_\lambda = 44$ and 113, in the same flow, shown in Fig. 5.192. Ratios of the rms divergence errors to rms values of the measured on- and off-diagonal gradient components $\partial u_i/\partial x_j$

are 11.7% and 8.9%, respectively, consistent with accuracies inferred from the single- and coincident-plane validation tests.

Numerous further tests based on the similarity, scaling, and isotropy implied by classical turbulence theory allow further validation of any measurement of the velocity gradient tensor in turbulent flows [5.761]. Examples of such validations for DSPIV measurements obtained at $\mathrm{Re}_\delta = 6000$ and 30 000 are seen in distributions of the velocity gradient components in Fig. 5.192 and in the principal strain rates and vorticity components in Fig. 5.193. In each case, isotropy requires the inner-scaled distributions shown in each panel to be identical. On the semi-logarithmic axes it can be verified that such similarity extends in the measured results even to the rare-event tails of these distributions.

Velocity Gradient Field Measurements

Figure 5.194a–c show typical examples of the instantaneous enstrophy field $\boldsymbol{\omega}_i\boldsymbol{\omega}_i$, the enstrophy production rate field $\boldsymbol{\omega}_i S_{ij}\boldsymbol{\omega}_i$, and the kinetic-energy dissipation rate field $2\nu S_{ij}S_{ij}$ obtained from such DSPIV measurements at $\mathrm{Re}_\delta = 6000$ and 30 000 on the centerline of an axisymmetric turbulent jet. The relative size of each plane is given in terms of the inner (viscous) length scale λ_ν. Note that the enstrophy and dissipation rate fields are second-order gradient quantities that scale, respectively, with local outer variables as $(u_c/\delta)^2\mathrm{Re}_\delta$ and (u_c^3/δ). In contrast, the enstrophy production rate is a third-order gradient field and thus scales as $(u_c/\delta)^3\mathrm{Re}_\delta^{3/2}$. Distributions of each of these quantities obtained from over 1000 such instantaneous measured realizations [5.761] verify these outer-variable scalings as well as the similarity in the corresponding inner-variable scalings with ν and λ_ν, and provide further validations of the DSPIV measurement results for these fields. Fields of the type in Fig. 5.194 are of central importance to understanding the structure and dynamics of turbulence at the quasi-universal intermediate and small scales in inhomogeneous turbulent shear flows. Various aspects of these fields, including their precise scale-similarity properties [5.761], are likely to play a key role in developing improved subgrid-scale models for more-accurate large-eddy simulations of practical turbulent shear flows. To date the inability to access these fields in inhomogeneous turbulence has been a major factor hindering the development of such models. The advent of multidimensional measurement techniques such as DSPIV that are capable of giving accurate and highly resolved access to these fields is likely to be a significant step toward developing more-accurate physically based models of turbulence for such simulations.

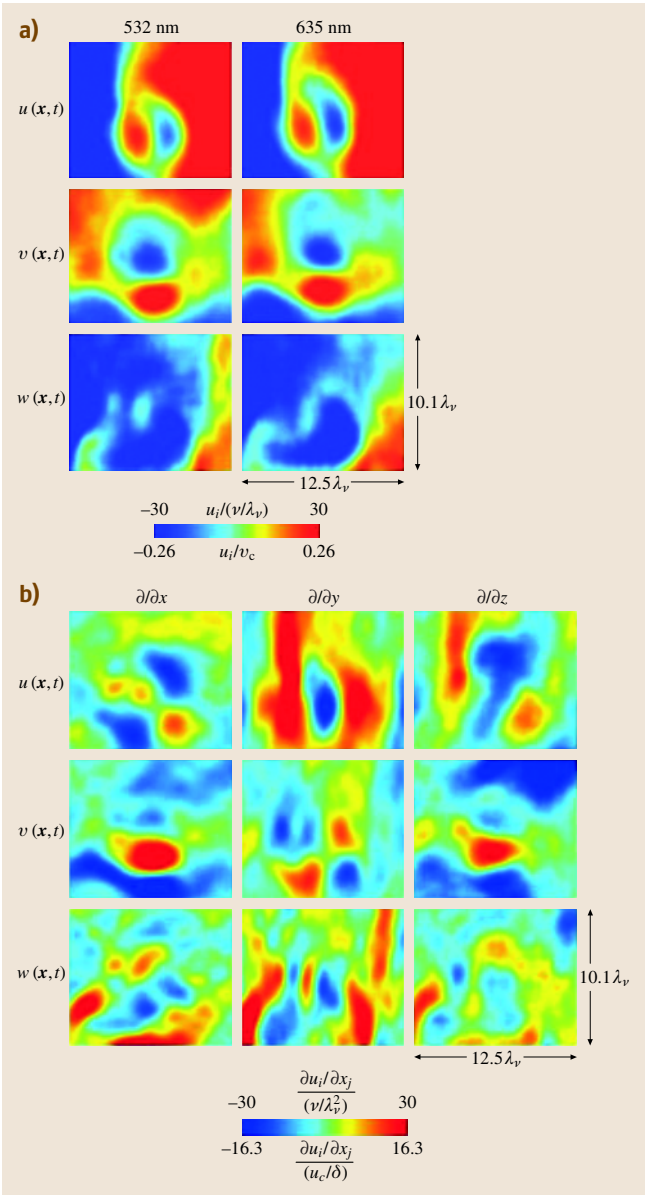

Fig. 5.190a,b Typical separated-plane DSPIV measurements, showing $u_i(\boldsymbol{x}, t)$ velocity component fields measured in the two differentially spaced light-sheet planes by the two stereo camera pairs **(a)**, and the resulting nine components **(b)** of the velocity gradient tensor field $\partial u_i/\partial x_j$, with normalizations on the inner- and outer-scale variables (after [5.758])

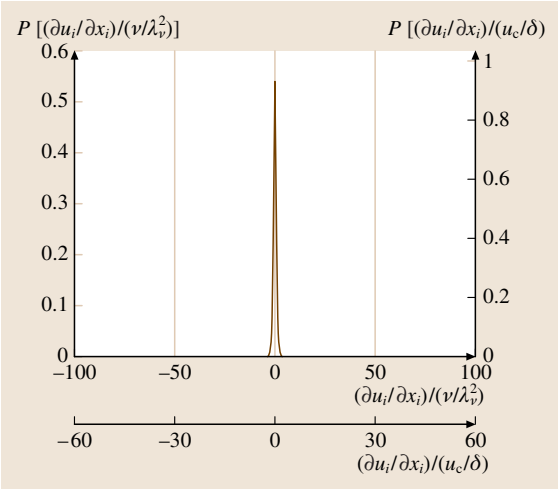

Fig. 5.191 Distribution of the measured divergence errors from separated-plane DSPIV measurements, obtained by summing the principal values of the strain rate tensor S_{ij} from the measured velocity gradient tensor field $\partial u_i/\partial x_j$, shown normalized on inner- and outer-scale variables. Compare with the range of gradient values in Fig. 5.192 (after [5.758])

Summary

DSPIV measurements of the type described here allow highly resolved direct experimental access to all nine simultaneous velocity gradient component fields $\partial u_i/\partial x_j$ on the intermediate and small scales of fully developed turbulent shear flows under conditions that are, at present, well beyond the reach of direct numerical simulations. Proper design of the DSPIV setup allows accurate measurements of the structure, statistics, similarity, and scaling of key gradient fields in such inhomogeneous shear flow turbulence, including the vorticity vector field, the strain rate tensor field, and the true kinetic-energy dissipation rate field. Proper differential spacing of the two stereo PIV light-sheet planes, as well as precise characterization of the thickness, coincidence, and two-axis parallelism of these sheets over the entire field of view, permits resolution of the velocity gradient tensor down to the local inner (viscous) length scale of the turbulent flow. Careful validations of such dual-plane measurements are possible through single- and coincident-plane tests, as well as through separated-plane measurements of the velocity divergence and further tests of the similarity, isotropy, and Re scaling in the measured gradient components and various fields derived from them. Results from such tests have established the accuracy of these fields from DSPIV measurements of the type described here. Moreover the two-frequency DSPIV method described here allows use of solid metal oxide seed particles to permit such highly resolved measurements in both nonreacting and exothermically reacting turbulent shear flows. For the foreseeable future, direct experimental measurements based on high-resolution imaging methods such as DSPIV will likely provide the only practical means for investigating the structure, statistics, similarity, and scaling properties of key gradient fields in spatially developing turbulent shear flows at a level of resolution and detail that has traditionally been associated only with direct numerical simulations.

5.5.3 Measurements of the Vorticity Vector and Other Velocity Gradient Tensor-Based Turbulence Properties

To know the vorticity vector and the strain rate tensor it is necessary to simultaneously determine the instantaneous velocity gradients of all three velocity components in the coordinate axes directions: $\partial U_i/\partial x$, $\partial U_i/\partial y$, $\partial U_i/\partial z$ ($U_1 = U$, $U_2 = V$, $U_3 = W$). Although only six velocity gradients (four cross-stream and two streamwise) have to be known to determine the vorticity vector, the four cross-stream gradients needed cannot be measured accurately with hot-wire anemometry if the other two cross-stream gradients are neglected. In order to determine the velocity gradients experimentally with a finite-difference approximation, the velocity vector has to be measured at two points closely separated in the coordinate directions. To measure three velocity vector components with hot-wire anemometry, it is necessary to use an array of at least three sensors. By separating these arrays in the y and z coordinate directions at an appropriate distance, the six cross-stream velocity gradients, $\partial U_i/\partial y$, $\partial U_i/\partial z$, can be determined with a minimum of nine sensors. Determination of the three streamwise gradients, $\partial U_i/\partial x$, using hot-wire anemometry is possible by employing *Taylor*'s [5.762] hypothesis. Depending on the number of sensors, their orientation in the probe arrays, and the position of the arrays with respect to the coordinate axes, several types of vorticity probes have been developed to date.

Geometrical Configurations of Three-Component Vorticity Probes

Nine-Sensor Probes. The first attempt to measure all three components of the vorticity vector simultaneously was made by *Wassman* and *Wallace* [5.763], who used a nine-sensor probe. It was configured in three identi-

cal arrays with three sensors in each array. To make the probe as compact as possible, the supporting prong at the center of each array was common to the three sensors. They solved the problem of crosstalk between the electrical circuits due to the common prongs, but they did not develop the probe to an operational level that permitted accurate measurements of three-dimensional velocity and vorticity fields.

T-Configuration. The nine-sensor probe idea was developed further and a version capable of simultaneously measuring all three vorticity components with reasonable accuracy was brought to operational status by *Vukoslavčević* et al. [5.687]. This design consisted of three T-configured arrays, each containing three sensors inclined at 45° to the probe axis, as shown in Fig. 5.195. Two of the sensors form a V-shaped array in the x–z plane and the third sensor is oriented at the same angle in the x–y plane. The extent of the sensing area was 1.7 mm vertically and 2.2 mm horizontally, with a distance between the array centers of approximately 1.2 mm in the y- and z-directions. The distance h between the prongs supporting each sensor was 0.5 mm. The diameters of the tungsten sensors were 2.5 μm and

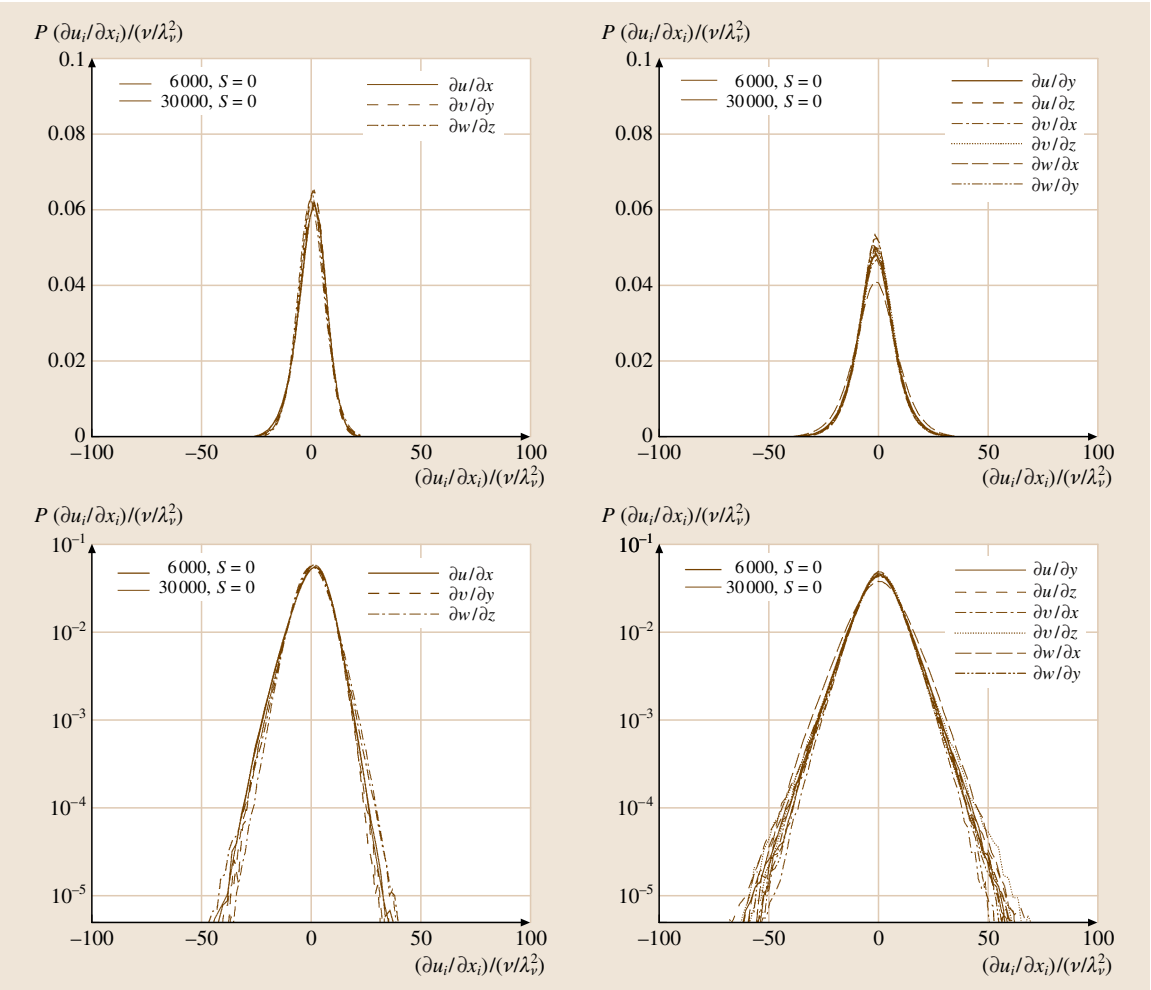

Fig. 5.192 Distributions of on-diagonal (*left*) and off-diagonal (*right*) components of inner-scaled velocity gradients $\partial u_i/\partial x_j$ measured via DSPIV in a turbulent shear flow at $\mathrm{Re}_\delta = 6000$ and 30 000 ($\mathrm{Re}_\lambda = 44$ and 113), in linear (*top*) and semilogarithmic (*bottom*) axes. Note the agreement with the similarity and scaling of isotropic turbulence (after [5.761])

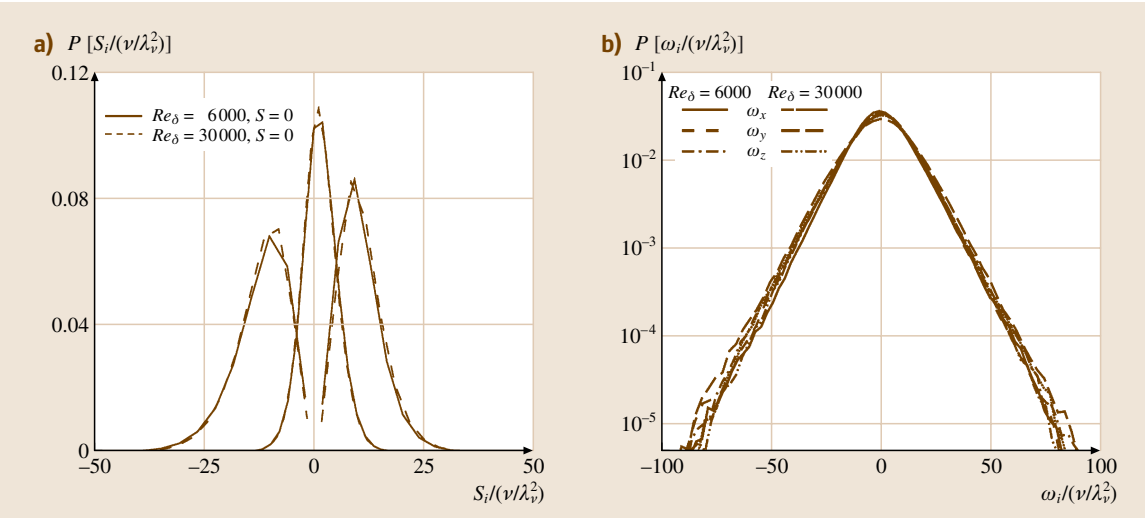

Fig. 5.193a,b Further validations of velocity gradient components $\partial u_i/\partial x_j$ measured via DSPIV in a turbulent shear flow at $\mathrm{Re}_\delta = 6000$ and 30 000 ($\mathrm{Re}_\lambda = 44$ and 113), showing the distributions of the principal strain rates **(a)** and vorticity components **(b)**. Note the excellent agreement with the requirements of isotropy and inner-scale similarity from classical theory (after [5.761])

their lengths were about 0.7 mm, giving an aspect ratio of about 280.

The length of the prongs from their tip to the base where they are glued together was 25 mm, and the base diameter was about 3.2 mm. This gives a ratio of about 8, which was large enough to avoid a very serious influence on the flow at the location of the sensors by the probe shaft as indicated by the inviscid flow considerations discussed later.

Orthogonal Configuration. *Honkan* [5.690], *Andreopoulos* and *Honkan* [5.691] and *Honkan* and *Andreopoulos* [5.689] also constructed a nine-sensor probe capable of simultaneously measuring all three vorticity components. This probe consisted of a set of three triple-sensor arrays as sketched in Fig. 5.196. The sensors in each array are mutually orthogonal to each other. They are oriented at approximately 54.7° to the probe axis and placed in meridian planes at 120° with respect to each other. For this probe each sensor was supported by a separate pair of prongs, eliminating any possibility of electrical crosstalk between the hot-wire circuits.

The total extent of the sensing region of this probe was about 4 mm across the flow, with the array centers located at the corners of an equilateral triangle with sides approximately 2.46 mm long. The array centers were separated by 2.46 mm in the y-direction and 2.13 mm in the z-direction. The distance between the supporting prongs of each sensor was 0.8 mm. The diameters of the platinum-plated tungsten sensors was 2.5 μm, and their lengths were about 0.8 mm, giving a sensor aspect ratio of about 320.

The length of the prongs of this probe from their tips to the base where they were glued together was approximately 10 mm, while the base occupied a space approximately 5 mm in diameter. This gives a ratio of only 2, so there was a possible influence of the probe shaft on the flow at the location of the sensors.

Twelve-Sensor Probes. *Tsinober* et al. [5.693] constructed a 12-sensor probe with the configuration sketched in Fig. 5.197. They added an additional tungsten sensor of 2.5 mm diameter to each array of the nine-sensor T-configuration probe and used separate pairs of prongs for each sensor, making a total of 12 sensors supported by 24 prongs.

The extent of the sensing region of this probe was 2.3 mm vertically and horizontally, with distances between the array centers of 1.4 mm and 0.4 mm between the supporting prongs of each sensor. The diameter of the tungsten sensors, inclined at 45° to the probe axis, was 2.5 μm, and their length was about 0.56 mm, giving an aspect ratio of about 224.

The length of the prongs, from their tip to the base where they are glued together, is approximately 20 mm while the base occupied a space approximately 3 mm in

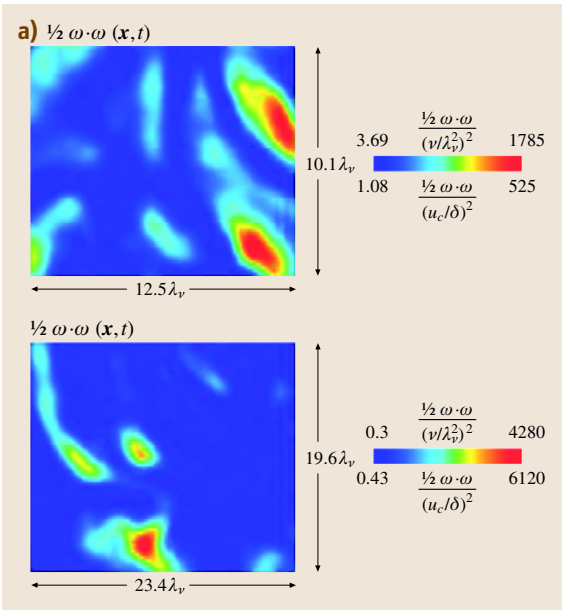

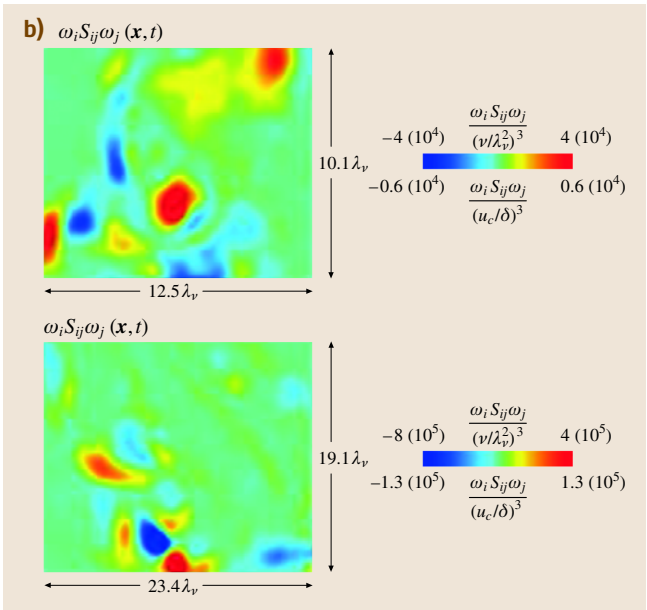

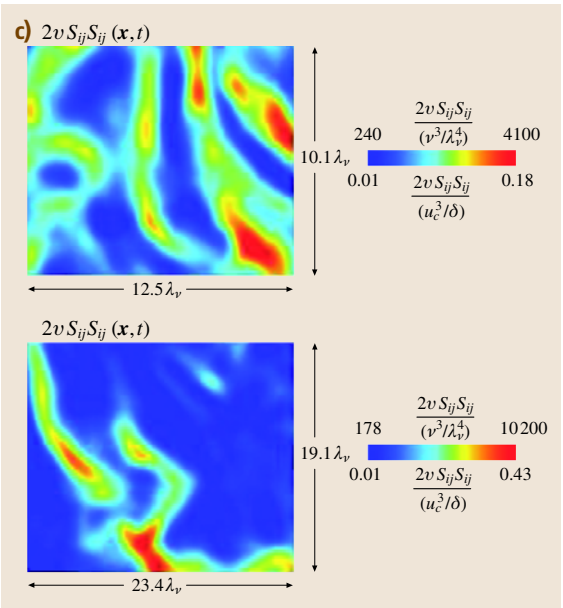

Fig. 5.194a–c Typical results from DSPIV measurements at quasi-universal intermediate and small scales of turbulent shear flows, showing **(a)** the enstrophy field, **(b)** the enstrophy-production-rate field, and **(c)** the kinetic-energy dissipation rate field obtained from measured velocity gradient components $\partial u_i/\partial x_j$ at $\mathrm{Re}_\delta = 6000$ and 30 000 ($\mathrm{Re}_\lambda = 44$ and 113). Values are shown normalized on inner- and outer-scale variables (after [5.761]) **(a)** Enstrophy fields at $\mathrm{Re}_\delta = 6000$ (*top*) and 30 000 (*bottom*) ($\mathrm{Re}_\lambda = 44$ and 113) **(b)** Enstrophy production rate fields at $\mathrm{Re}_\delta = 6000$ (*top*) and 30 000 (*bottom*) ($\mathrm{Re}_\lambda = 44$ and 113) **(c)**Dissipation rate fields at $\mathrm{Re}_\delta = 6000$ (*top*) and 30 000 (*bottom*) ($\mathrm{Re}_\lambda = 44$ and 113)

diameter, giving an aspect ratio of about 6.7. Thus there was possibly a small influence of the probe shaft on the flow at the location of the sensors.

Tsinober et al. [5.693] and *Kholmyansky* et al. [5.764] also used a 21-sensor probe consisting of five arrays of four hot-wires as well as one cold-wire positioned upstream of the central array to measure the temperature, as shown in the photograph in Fig. 5.197b. The most recent version of this probe has 25 sensors: one cold and four hot sensors for each of the five arrays. The prongs of the central array are longer than those of the surrounding arrays, so its sensors are positioned further upstream than those of the outer arrays. With this probe *Galanti* et al. [5.765] avoided having to use Taylor's hypothesis to obtain the streamwise gradients by differencing the velocity components obtained from the central array with the average of those from the four surrounding arrays. Of course, avoiding Taylor's hypothesis in this manner is at the cost of having to use this spatially averaged information for the estimation of streamwise gradients, $\partial U_i/\partial x$. It is also at the cost of the lower spatial resolution of this probe compared to probes with fewer sensors.

Nguyen [5.766] and *Marasli* et al. [5.767] used a 12-sensor probe with a similar array configuration to that of *Tsinober* et al. [5.693] but with a different arrangement of the arrays and a different data-reduction procedure. The probe design and signal data-reduction procedure are explained in detail by *Vukoslavčević* and *Wallace* [5.768].

The total extent of the sensing area of this probe was 2.20 mm in the y-direction and 2.40 mm in the z-direction, with an average distance between the array centers of approximately 1.14 mm in the y-direction and 1.32 mm in the z-direction. The distance between the supporting prongs of each sensor, inclined at 45° to the probe axis, was 0.44 mm. The diameter of the tungsten sensors was 2.5 µm, and their length was about 0.62 mm, giving an aspect ratio of about 250.

The length of the prongs from their tip to the base, where they are glued together, is approximately 33 mm while the base occupied a space approximately 3.6 mm in diameter, giving a ratio of 9. This is large enough to avoid most of the influence of the probe shaft on the flow at the probe sensors, as indicated by the inviscid flow considerations discussed later.

Eight-Sensor Probe. *Zhu* and *Antonia* [5.769], *Antonia* et al. [5.770] and *Antonia* et al. [5.771] have analyzed, constructed and used an eight-sensor probe capable of simultaneously measuring all three vorticity components. The probe consists of the four X-wire arrays shown in Fig. 5.199.

Each array can measure two velocity components providing the information necessary to determine the four cross-stream velocity gradients. In contrast to the nine- and 12-sensor configurations described above, the binormal velocity component cooling the sensors of this eight-sensor probe has to be neglected. Two arrays are positioned with horizontal orientations while the other two are in vertical orientations. The sensors in each array

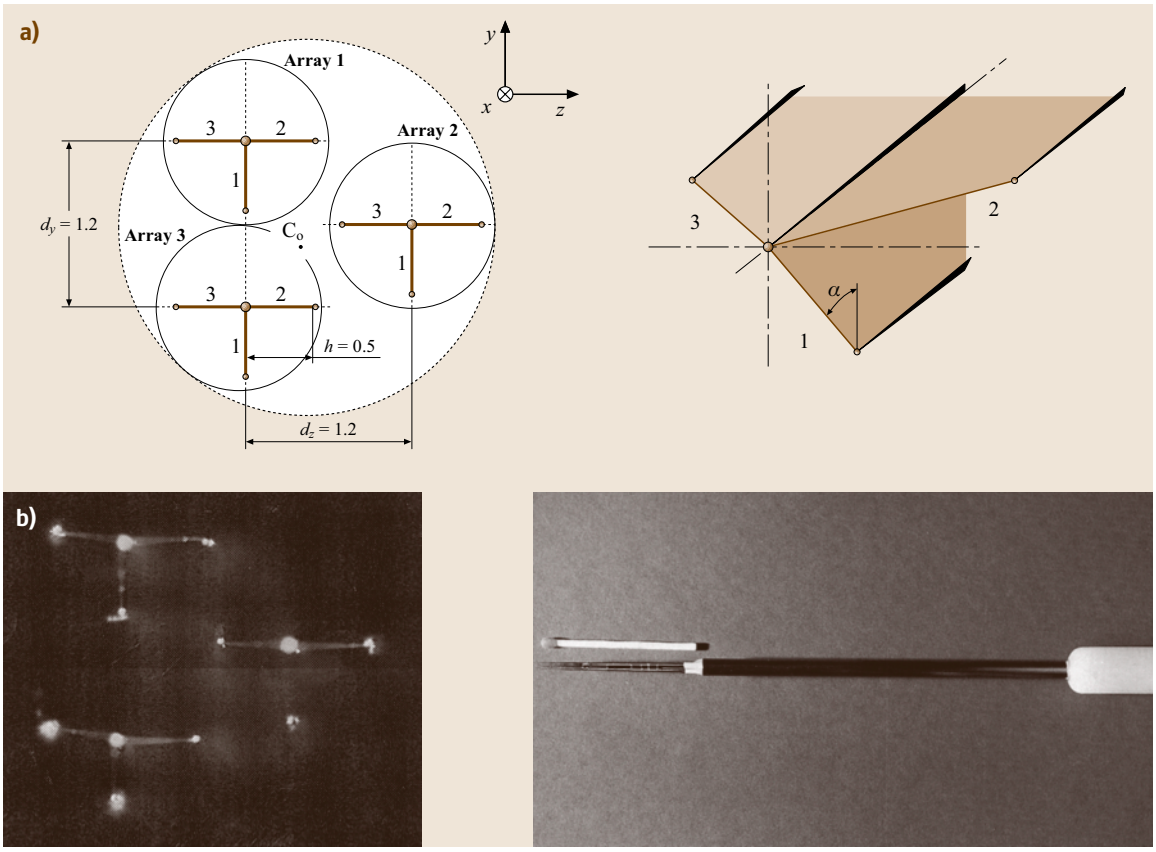

Fig. 5.195 **(a)** Sketch of the front view of a nine-sensor T-configuration probe and schematic view of one of its arrays. Dimensions in mm. **(b)** Photographs of the nine-sensor probe of *Vukoslavčević* et al. [5.687] (courtesy CUP)

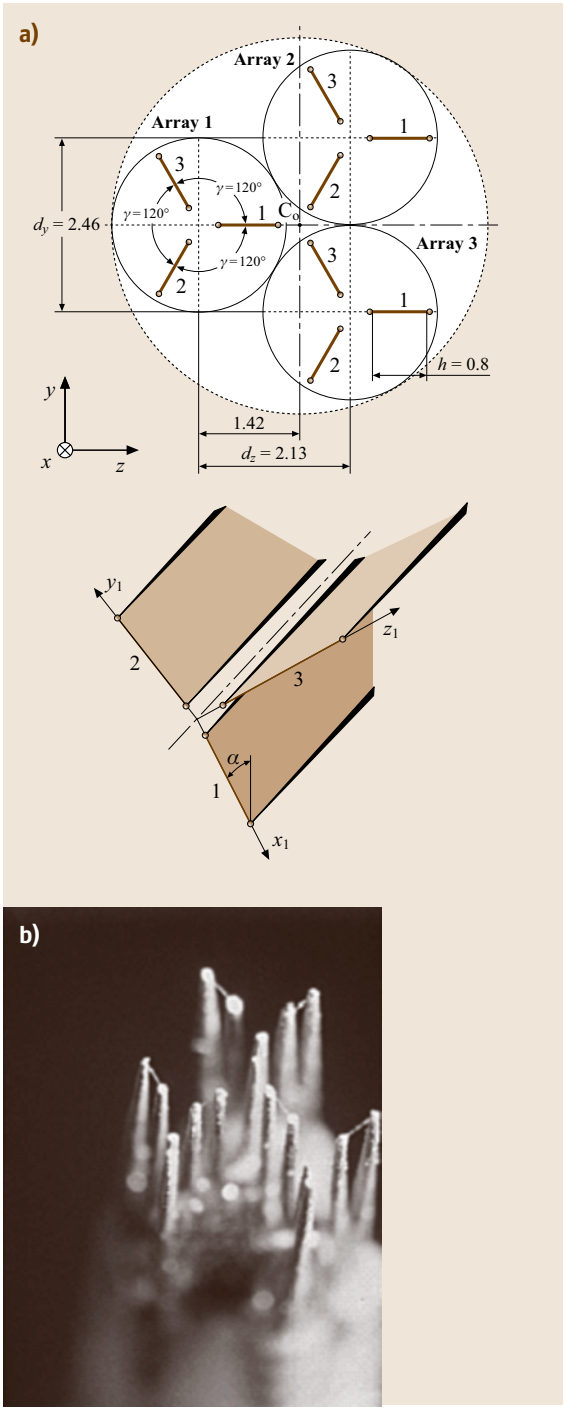

Fig. 5.196 **(a)** Sketch of the front view of a nine-sensor probe with orthogonally configured sensors and schematic view of one of its arrays. Dimensions in mm. **(b)** Photograph of an orthogonally configured nine-sensor probe of *Honkan* and *Andreopoulos* [5.689] (courtesy CUP)

are inclined at 45° to the probe axis. The separation between the two inclined wires in each X-array is 0.6 mm.

The separations between the centers of the X-arrays are $d_y = 2.1$ mm in the y-direction and $d_z = 2.2$ mm in the z-direction. All the sensors were etched from a Wollaston (Pt–10%Rh) wire to an active length of 0.5 mm. The diameters of the wires were 2.5 μm, giving an aspect ratio of about 200. The extent of the sensing area of the probe was 2.8 mm vertically and 2.7 mm horizontally.

Probe Fabrication Method

Fabrication of these vorticity probes is very difficult because of their small size, complex design, and fragility. The main problem is to fit 12, 18, 24, or even more supporting prongs into the smallest feasible space, while still satisfying the accuracy as well as spatial resolution criteria. Arranging the prongs with very small distances between them may result in two difficult problems to be overcome: preventing electrical shorting between the prongs or between the prongs and the probe body and maintaining the prongs in place so that they keep the desired array geometry. Several technical solutions and various prong materials have been tried.

For the first version of the nine-sensor probe [5.687], a tungsten rod of about 0.25 mm diameter was used for the prongs. The prongs were chemically tapered from their original diameter to a tip diameter of about 50 μm. Although using a common prong for each array for this probe reduced the aerodynamic disturbances to the flow, it introduced some electrical crosstalk between the anemometer circuits. To make this crosstalk insignificant and to avoid instabilities from the anemometer bridge circuits, the common prong resistance should be less than about 0.1 Ω. To reduce the resistance without unduly increasing the common prong diameter, each common prong was first plated with copper. Then the tips of all the prongs were plated with a thin layer of nickel to facilitate welding of the tungsten sensors to the prongs. The four prongs of each array were drawn through round four-bore ceramic insulating tubes with a 1.6 mm outside diameter, and then placed in a stainless-steel tube with one flat side in order to bring the probe as close as possible to the wall. The ends of the prongs were soldered to copper stranded wire with gold-plated connectors on the other end. The ceramic tubes were sealed into the outer stainless-steal tube with epoxy. The prong tips were manipulated under a measuring micro-

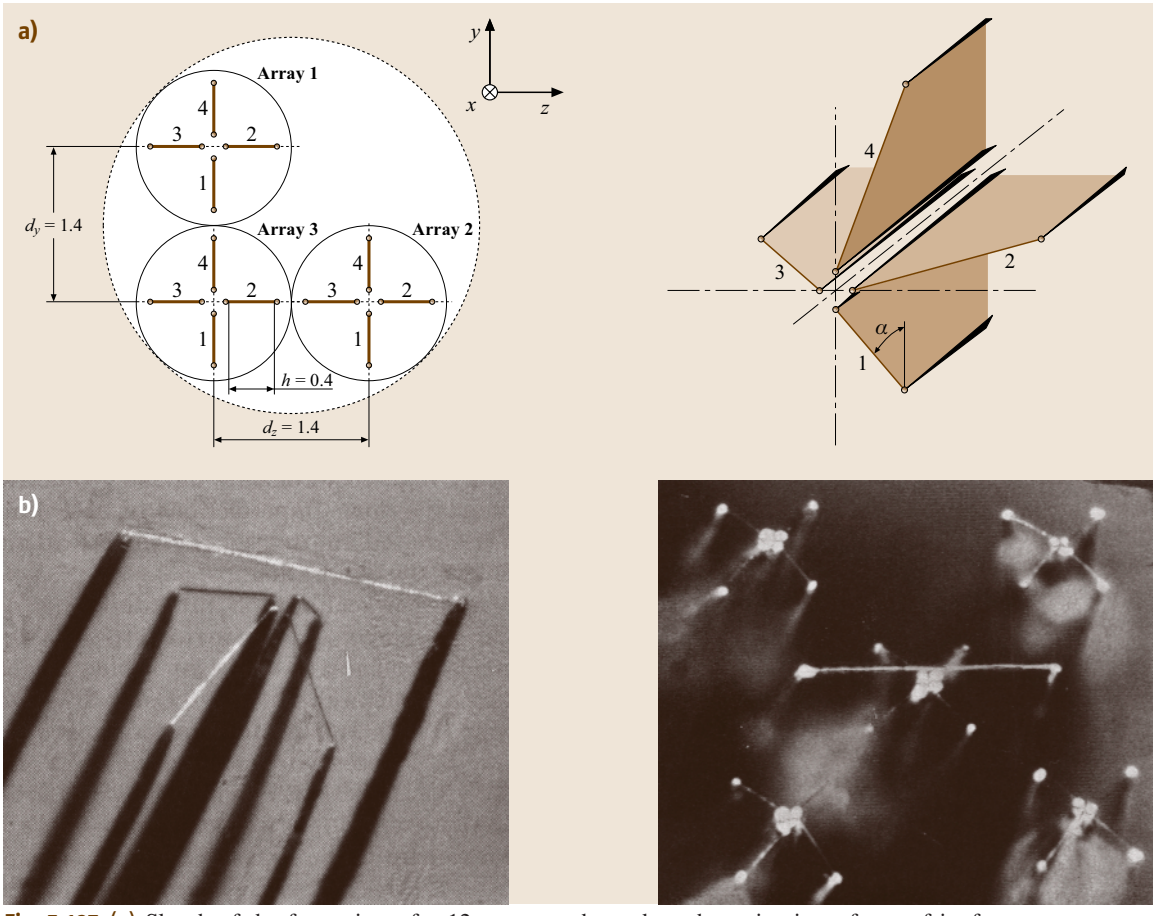

Fig. 5.197 **(a)** Sketch of the front view of a 12-sensor probe and a schematic view of one of its four-sensor arrays. Dimensions in mm. **(b)** Photograph of one array and of the 21-sensor probe of *Tsinober* et al. [5.693] (courtesy CUP)

scope into their proper geometric positions within about a ±0.01 mm tolerance. After nickel plating the prongs, the 2.5 μm-diameter unsheathed tungsten sensor wires were welded to the tips. The relative position of the prong tips and the sensor wires are shown in Fig. 5.195.

The main problem with the design of the nine-sensor probe with common central prongs was to make these central prongs small enough to avoid flow blockage but also to have resistances close to zero to avoid crosstalk between the sensors and circuit instabilities. It was difficult to reach these goals simultaneously.

To avoid this problem, *Tsinober* et al. [5.693] used four separated tiny prongs, put together to form the central prongs, in place of common prongs for each array of their 12-sensor vorticity probe. The prongs were made of tungsten wire, tapered at the tip to a 20 μm diameter, insulated by Teflon, glued together with a tip separation of 80 μm and plated with nickel or tin. They were positioned using 30 μm microspacers. A special manipulator was used to carry and position short pieces of sensor wire for welding to the tips of the prongs.

The tungsten prongs were replaced with stainless-steel prongs of the same dimension (0.25 mm) for the 12-sensor probe of *Vukoslavčević* and *Wallace* [5.768], shown in Fig. 5.198, in order to avoid both the crosstalk problem caused by common prongs and the tedious plating procedure. The resistance of a stainless-steel prong is well over the critical value of 0.1 Ω, even when it is plated to a reasonable thickness. Therefore, in place of the common prongs, four separate prongs were used in the center of each array. These prongs were tapered to a tip diameter of less than 50 μm and then drawn through four-bore ceramic tubes of 1.23 mm outside diameter.

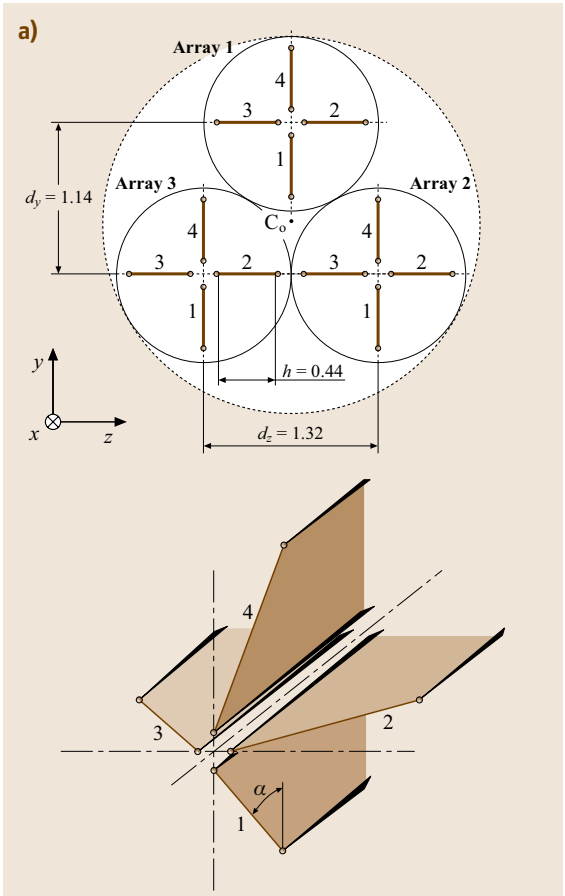

Three ceramic tubes were glued together, forming the centers of each of the three arrays of the 12-sensor probe. The rest of the 12 surrounding prongs were positioned

Fig. 5.198 **(a)** Sketch of the front view of a twelve-sensor probe of *Vukoslavčević* and *Wallace* [5.768] and a schematic view of one of its four-sensor arrays. **(b)** Photograph of the twelve-sensor probe of *Vukoslavčević* and *Wallace* [5.768] (shown in *Bernard* and *Wallace* [5.772], courtesy Wiley)

around these ceramic tubes using constant-diameter fishing line as a spacer. The whole assembly was drawn into a plastic tube of 3.6 mm outside diameter and then placed in a stainless-steal tube of 4.6 mm outside diameter. Although the number of prongs was doubled compared to the nine-sensor probe, the probe dimensions were only slightly increased. This was made possible using thinner ceramic tubes for the central prongs and placing the outside prongs around them. The prongs were positioned under a measuring microscope with an accuracy of ±0.01 mm, which was the most tedious part of this approach.

For the nine-sensor orthogonal probe of *Honkan* [5.690] and *Honkan* and *Andreopoulos* [5.689] a separate two-hole, 1.23 mm-diameter ceramic tube was used for each pair of prongs. Two 0.25 mm-diameter stainless-steel prongs, tapered at one end electrolytically to a diameter of 190 μm, were inserted into a ceramic tube and glued at one end. Using a special rig, two prongs were made simultaneously flat to mount the sensor at the required angle of 54.6° to the probe axis. This process was repeated for the eight other sensor elements. A second jig was used to position three of these elements to form one array of the triple orthogonal probe and the third one to put all three arrays together in the desired position. The unit was then inserted into a thin-walled brass tube. Miniature-sized gold connectors were used to connect the prongs and shielded wire leads. In this way the

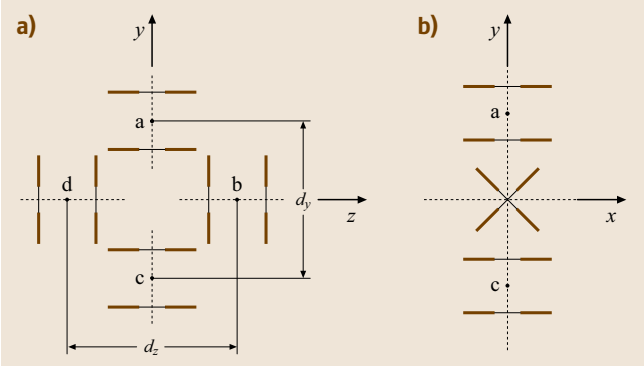

Fig. 5.199a,b Sketches of the front and side view of an eight-sensor probe of *Zhu* and *Antonia* [5.769] (courtesy of Inst. of Phys.): **(a)** streamwise view, and **(b)** cross-stream view

crosstalk problem was resolved and the plating process avoided. This method of positioning the prongs seems to be more convenient compared to the approach described above, but the dimensions of the probe body were much larger due to the use of nine separate ceramic tubes.

Spatial Resolution

Because measuring velocity gradients with hot-wire sensors to determine vorticity components requires the determination of the velocity vector at least at two points in the flow simultaneously, the spatial resolution of such probes is a serious problem that must be addressed. To measure the velocity vector accurately at a given point in a turbulent flow field, the sensors and their arrays should be as small as possible. Additionally, the distances between arrays must also be as small as possible. Unfortunately, small sensor and array sizes can result in thermal interference and inadequate sensor response. If the spacing is too small the effects of noise can overwhelm the velocity gradient signal. These issues are discussed in some detail by *Wallace* and *Foss* [5.81] and will be summarized here.

A hot-wire sensor cannot resolve motions of turbulent coherent structures that have scales smaller in size than its length [5.776]. In order to resolve the nonuniform velocity field of a vortex structure, a hot-wire probe must be much smaller than the spatial scale of that structure. This is not easy to achieve with multisensor vorticity probes. Whether a probe is capable of resolving the smallest structures in the flow depends on the ratio of its dimensions to the *Kolmogorov* [5.777] length scale η.

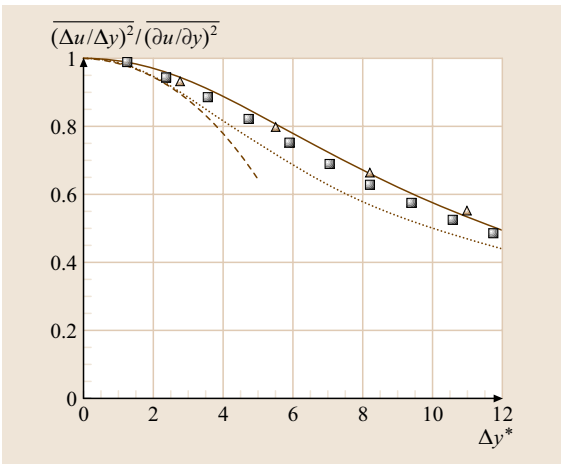

Fig. 5.200 Attenuation of the *measured* velocity gradient due to the separation distance $\Delta y^* = \Delta y/\eta$ over which the velocity difference is determined. DNS: (*triangles*) $R_\tau = 180$, (*squares*) $R_\tau = 400$; Wyngaard's analysis (*dotted line*) with *Pao*'s spectrum [5.773], (*solid line*) with DNS spectrum, (*dashed line*) truncated by *Hussein* and *George* [5.774] with Pao's spectrum. (After *Antonia* et al. [5.775])

Wyngaard [5.702] analyzed the response of the Kovasznay-type probe, designed to measure the streamwise component of vorticity Ω_x. He assumed isotropic turbulence and the theoretical three-dimensional velocity spectrum of *Pao* [5.773] and investigated the attenuation due to finite sensor length L and sensor separation S. He found that the ratio of measured to the true variance $\overline{\Omega_x^2}$ decreases sharply as η/L decreased. It is essentially 1.0 for $\eta/L = 1$, and drops to 0.86 for $\eta/L = 0.32$. Serious attenuation occurs for smaller values of η/L. He concluded that the ratio of η/L should not be smaller than 0.3, as was later confirmed by *Browne* et al. [5.778]. He also found that S/L has a strong influence on the measurement results. His analysis of the effect of S/L was performed for a fixed value of $\eta/L = 0.32$. The value of $S/L = 0.7$ provided the best probe response, while wider sensor spacing resulted in attenuation in the variance of Ω_x. *Klewicki* and *Falco* [5.692] used a hot-wire probe that enabled systematic variation of the separation of two parallel sensors. Their investigation showed that, for a Reynolds number based on the momentum thickness of 1010 in a turbulent boundary layer, the variance of the velocity gradient just above the buffer layer is attenuated by 5% for $S/\eta = 3.3$.

Antonia et al. [5.775] performed parallel sensor probe analysis to investigate the spatial resolution of velocity gradient measurements. They used the DNS data of *Kim* et al. [5.743] and *Moser* et al. [5.779] at the centerline of a turbulent channel flow simulation, with $R_\tau = 180$ and 400, where $R_\tau = u_\tau b/\nu$, $u_\tau = \sqrt{\tau_w/\rho}$ is the friction velocity, b is the channel half width, τ_w is the wall shear stress and ρ is the fluid density. They determined the *measured* velocity gradient $\Delta u/\Delta y$ by dividing the difference between two simulated streamwise velocity component values, separated in the cross-stream direction by a distance $\Delta y = S$, by the *true* velocity gradient $\partial u/\partial y$ determined with spectral differentiation using Chebychev polynomials. The ratios of the variances of the *measured* and *true* velocity gradients are compared with previous predictions in Fig. 5.200 This ratio decreased with increasing sensor separation, as had been predicted and experimentally confirmed previously. It is clear that the sensor separation should not exceed 2–4 Kolmogorov lengths to determine the velocity gradients with reasonable accuracy.

However, decreasing the distance between the sensors causes another serious problem. The errors in the gradient measurements increase greatly for small sensor separations for three reasons. The percentage error in the velocity differences, the numerator in $\Delta u/\Delta y$ determined from the velocities measured at each of the two sensors, becomes larger with decreasing sensor separation. This is because these differences are between large numbers that approach the same value as the sensors come very close together. Furthermore, the temperature fields of each of the sensors can begin to influence the other sensor. In addition the percentage error in the determination of the separation distance, the denominator in $\Delta u/\Delta y$, also rapidly increases as the separation distance decreases. An example from *Antonia* et al. [5.775] of the errors that can creep into the finite-difference approximation of velocity gradients for very small sensor separations is strikingly clear, as shown in Fig. 5.201.

In this figure, the errors in the velocity gradient variances that were observed in the DNS analysis of the *measured* velocity gradient finite-difference approximation $\Delta u/\Delta y$ are compared to physical measurements by a real hot-wire probe with variable sensor separations $\Delta y^* = \Delta y/\eta$. For small values of $\Delta y^* < 2$, the measured variance values are increasingly overestimated, resulting in a large gradient measurement error. This error primarily depends on the accuracy of the velocity measurements as well as the accuracy of the sensor separation measurements, as explained above, and can differ from one experiment to the other.

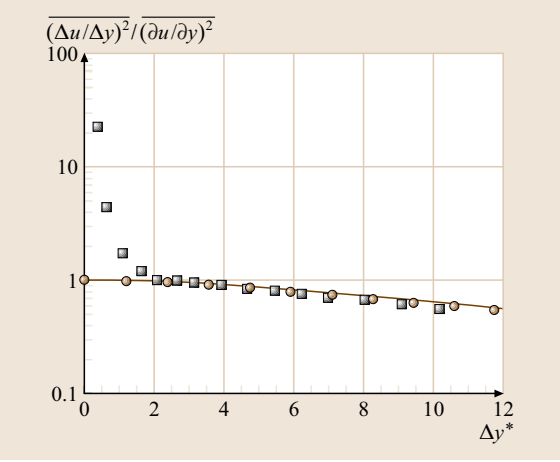

Fig. 5.201 Comparison of experimental (*squares*) and DNS (*circles*) *measured* estimates of velocity gradient variance to DNS *true* values showing the dependence on the separation distance $\Delta y^* = \Delta y/\eta$ over which the velocity difference is determined. Wyngaard's analysis with DNS spectrum (*solid line*) is also shown. (After *Antonia* et al. [5.775])

Most of the discussion thus far has been about measurements of velocity gradients or vorticity with specific probe configurations. Therefore, for other probe configurations this discussion should only be used as a general guide. Final decisions about the probe dimensions of any other configuration depend on many probe and flow parameters that must be considered individually.

There are several characteristic lengths to be considered for probe configurations designed to measure all three vorticity components: the sensor length, the separation between the sensors within an array, and the separation between the arrays in the y- and z-directions. The choices of these lengths have to be made in a manner consistent with one of the crucial assumptions required for these probes, viz. that the velocity gradients are constant over the probe sensing volume. It is very hard to meet this condition in turbulent flows, especially in flows with high mean velocity gradients such as in the wall region of turbulent boundary layers. In this case, the dimension of the probe in the wall normal direction should be smaller than in the lateral direction.

To avoid disturbing the flow too seriously by the probe body, the distance from the tips of the prongs to their base should also be sufficiently long. A rule of thumb often used by probe designers, based on a potential flow calculation, is that this length should be about 10 times the diameter of the probe body. This requirement is not easy to meet. Prongs that are too long easily vibrate in a turbulent flow, making the probe too fragile and subject to sensor breakage. The minimum diameter of the probe body is determined by the number of prongs to be placed within it while maintaining insulation between them.

The nine-sensor probe of *Vukoslavčević* et al. [5.687] and the 12-sensor probe of *Vukoslavčević* and *Wallace* [5.768] were used in a boundary-layer flow with the same characteristics. At $y^+ = 11.2$, which was the closest measurement location that the probe could be placed from the wall, they estimated the Kolmogorov microscale to be $\eta = 0.19$ mm. Thus the ratio of the Kolmogorov microscale to the sensor length was $\eta/l = 0.27$ for the nine-sensor probe and $\eta/l = 0.31$ for the 12-sensor probe. An equivalent of the sensor separation S in the *Wyngaard* [5.776] spatial resolution analysis of the Kovasznay-type probe are the separations d_y and d_z of the array centers for the vorticity probes discussed here. For the nine-sensor probe of *Vukoslavčević* et al. [5.687], $d_y/\eta = d_z/\eta = 6.3$. For the 12-sensor

probe of *Vukoslavčević* and *Wallace* [5.768], $d_y/\eta = 6.0$ and $d_z/\eta = 6.9$.

This same 12-sensor probe was used by *Nguyen* [5.766] and *Marasli* et al. [5.767] to measure the three velocity and vorticity components simultaneously in the intermediate wake of a circular cylinder with Reynolds number $\mathrm{Re_d} = 2000$ and $x/d = 30$. For this experiment d is the cylinder diameter and x is the distance downstream from the cylinder. At this location the Kolmogorov microscale was 0.2–0.4 mm, so that, in the worse case, this probe resolved the small scales as well as in the boundary-layer experiment of *Vukoslavčević* and *Wallace* [5.768] near the wall.

The same probe also was used by *Loucks* [5.780] in a two-stream mixing layer. Again in this experiment all the components of the velocity and vorticity vectors were measured simultaneously. Measurements were made at three Reynolds numbers based on the momentum thickness: $R_\theta = 432$ at a location before the mixing transition and at two stations downstream where the flow was self-similar and $R_\theta = 1792$ and 2483, respectively. At the highest Reynolds number the Kolmogorov microscale had its smallest value of 0.4 mm. Thus in this flow $\eta/l = 0.65$, $d_y/\eta = 2.9$, and $d_z/\eta = 3.3$.

Comparing these values with the spatial resolution analysis given at the beginning of this section, it is clear that the required ratio of the Kolmogorov microscale to sensor length $\eta/l \geq 0.3$ was met in all the flows in which these probes were used. The ratios of the Kolmogorov microscale to the array separations, d_y/η and $d_z/\eta \approx 2$–4, required for good spatial resolution while maintaining reasonable accuracy, was satisfied when the 12-sensor probe was used in the mixing-layer experiment and was reasonably close to these recommended values in the wake experiment and in the boundary-layer experiment discussed above. For the positions further from the wall in the boundary layer and at other positions in the cylinder wake, η becomes larger, giving better spatial resolution. From these considerations, it seems that this 12-sensor probe was capable of resolving all but the smallest scales in the turbulent boundary-layer, wake, and mixing-layers flows in which it has been used.

The nine-sensor probe of *Honkan* [5.690] and *Honkan* and *Andreopoulos* [5.689] was used in a similar boundary-layer flow with a Kolmogorow microscale of $\eta = 0.2$ mm at $y^+ = 12.5$. Thus $\eta/l = 0.25$, $d_y/\eta = 12.30$, and $d_z/\eta = 10.65$.

The spatial resolution of the 12-sensor probe of *Tsinober* et al. [5.693] would have been slightly less than that of *Vukoslavčević* and *Wallace* [5.768] at comparable locations close to the wall in a boundary layer with a similar Reynolds number. However, the closest measurements they made in their boundary layer with their probe were further out in the logarithmic layer, where the Kolmogorov microscale was 0.5 mm.

The eight-sensor probe of *Antonia* et al. [5.770] and *Antonia* et al. [5.771] was used in decaying grid turbulence with Kolmogorov microscale values of 0.17–0.4 mm at different distances from the grid. Thus the ratio of the Kolmogorov microscale to the sensor length was in the range $0.34 < \eta/l < 0.8$, while the array center separations were in the range $5.7 < d_z/\eta < 13$, depending on the distance from the grid. The array center separations of this probe are limited by the sensor lengths and the separations of the prongs. The method of *Zhu* and *Antonia* [5.769], developed to correct velocity gradients spectra for insufficient spatial resolution, was used with this eight-sensor probe. If welded wires were used for the sensors of this design instead of Wollaston etched wires, the probe could be made at least half the size, giving better spatial resolution.

With the same sensor length and prong separation and the same type of fabrication, the nine-sensor T-configuration probe will have a better spatial resolution than the nine-sensor orthogonal-configuration probe or the 12-sensor probes. However, this is not the only design consideration. As will be discussed later, the situation is just the opposite with regard to the uniqueness domain of the probes. The uniqueness domain of a 12-sensor probe is almost double that of the nine-sensor T-configuration probe. How to trade off between these two design considerations depends on the type of flow.

Determination of Cross-Stream Velocity Gradients

Two basically different approaches have been used to determine the cross-stream velocity gradient components. One is based on the assumption that the velocity gradients can be neglected over each array, assuming that the effective velocity cooling each sensor is the same within an array, but that it changes between the arrays. In addition, for the eight-sensor probe the influence of the binormal velocity component on the sensor in each array must also be neglected to measure the other two velocity components.

The other approach is based on the assumption that a different effective velocity acts at the center of each sensor. In this case the velocity gradients over the arrays are not neglected. The only necessary assumption in this second approach is that the velocity gradient components are constant over the entire probe sensing area.

This assumption can also be applied to the eight-sensor probe, but in this case two cross-stream velocity gradients have to be neglected. The first approach is much simpler but less accurate. The second approach is more accurate but requires a rather complex mathematical procedure. Different models describing sensor cooling and relating the effective cooling velocities to the anemometer voltage outputs can be utilized with both approaches. For the approach where the velocity gradients over the arrays are neglected, a direct method can also be used in which the velocity vector is mapped to the voltage outputs for each array.

The Sensor Response Equation. A general form of the sensor response equation is

$$F(E, U_e) = 0\,, \tag{5.318}$$

where E is the anemometer voltage output and U_e is the velocity effectively cooling the sensor. The simplest forms of this expression are the well-known King's law

$$E^2 = A + BU_e^n\,, \tag{5.319}$$

and a higher-order polynomial fit,

$$\sum_{p=1}^{5} b_p E^{p-1} = U_e^2\,. \tag{5.320}$$

One of the most accurate expressions for the effective cooling velocity in a three-dimensional flow field is that proposed by *Jorgensen* [5.781],

$$U_e^2 = U_n^2 + k^2 U_t^2 + h^2 U_b^2\,, \tag{5.321}$$

where U_n, U_t, and U_b are the orthogonal components of the velocity vector with respect to the sensor coordinate system, i. e., normal, tangential, and binormal to the sensor, while k and h are the so-called yaw and pitch coefficients. Another expression,

$$U_e^2 = U_{ne}^2 + h^2 U_b^2\,, \tag{5.322}$$

based on the effective sensor angle, introduced by *Bradshaw* [5.782] for X-array probes, has also been successfully extended to three-velocity-component measurements. In this case, the influence of the tangent cooling component U_t is incorporated into the normal component in the plane of the sensor and its prongs U_{ne} defined with respect to an effective sensor inclination angle. This effective angle is determined in the calibration procedure. The influence of the binormal velocity component is taken into account in the same way as in Jogensen's cooling law given in (5.321).

Data-Reduction Algorithms.

Nine-Sensor Probe. *Vukoslavčević* et al. [5.687] developed a special numerical algorithm for their nine-sensor T-configuration probe that made use of King's law (5.319) and the effective cooling velocity (5.322) concept. Relating the velocity components U_{ne} and U_b in the orthogonal coordinate system to U, V, and W, the components in probe coordinate system, the following expressions for the effective cooling velocity U_{eij} of the j-th sensor in the i-th array (i, $j = 1, 2, 3$) can be derived for the sensors in the x–y and x–z planes, respectively:

$$U_{eij}^2 = (U_{ij}\cos\alpha_{eij} + V_{ij}\sin\alpha_{eij})^2 + h_{ij}^2 W_{ij}^2 \tag{5.323}$$

and

$$U_{eij}^2 = (U_{ij}\cos\alpha_{eij} \pm W_{ij}\sin\alpha_{eij})^2 + h_{ij}^2 V_{ij}^2\,. \tag{5.324}$$

U_{eij} can be expressed in terms of the three velocity components U_0, V_0, and W_0 at the probe center C_0 (Fig. 5.195), the six cross-stream velocity gradients (in the plane normal to the probe axis passing through the sensor centers), the distance projected on this plane between the probe center and the center of each sensor, the individual sensor effective angle α_{eij}, and the pitch coefficients h_{ij}. To do this the velocity components U_0, V_0, and W_0 were expanded to first order in a Taylor series about C_0, and the effective cooling velocity was related to the voltage output using King's law. This gave the following set of nine nonlinear algebraic equations with three velocity and six cross-stream velocity gradient component unknowns:

$$\begin{aligned}
&\left(\frac{E_{ij}^2 - A_{ij}}{B_{ij}}\right)^{\frac{2}{n}} \\
&= \left[K_{ij1}\left(U_0 + C_{ij1}\frac{\partial U}{\partial z} + C_{ij2}\frac{\partial U}{\partial y}\right)\right. \\
&\quad \left. + K_{ij2}\left(V_0 + C_{ij3}\frac{\partial V}{\partial z} + C_{ij4}\frac{\partial V}{\partial y}\right)\right]^2 \\
&\quad + \left[K_{ij3}\left(W_0 + C_{ij5}\frac{\partial W}{\partial z} + C_{ij6}\frac{\partial W}{\partial y}\right)\right]^2\,.
\end{aligned} \tag{5.325}$$

For this equation, the cross-stream velocity component V is exchanged with W for the sensors $j = 2, 3$ (Fig. 5.195).

The 27 coefficients K_{ijk}, the nine coefficients A_{ij}, and the nine coefficients B_{ij} had to be determined experimentally from calibration. The constants K_{ij1}, by their nature, are cosines of the effective angles α_{eij}, the K_{ij2} coefficients are sines of the effective angles, while

the K_{ij3} coefficients account for aerodynamic blockage (pitch coefficients h_{ij}). The C_{ijl} ($l = 1, 2, 3, 4, 5, 6$) constants can be expressed as positive or negative fractions of the projected prong spacing h for a given probe geometry. The probe was calibrated in a uniform (gradient-free) flow using a mechanism to pitch and yaw the probe in the range where it gives a unique solution. Assuming an optimal value of 0.4–0.5 for the exponent n in King's Law, varying the speed magnitude for zero pitch and yaw angle and using a least-squares fit, the coefficients A_{ij} and the products $B_{ij}(K_{ij1})^{n/2}$ were found. The coefficients K_{ij1}, K_{ij2} and K_{ij3} can be determined for the sensor in the vertical or horizontal planes by yawing or pitching the probe. The equations that have to be solved to find the unknown calibration coefficients are linear.

Although various algorithms are available, a new numerical algorithm was developed to solve the system of nine nonlinear algebraic (5.325) for the unknown velocity components at the probe center and the six velocity gradients in the cross-stream direction. The method was based on a successive iteration procedure that converged after a few iterations. The probe has to be used inside the solution uniqueness range, otherwise multiple real roots can appear. This issue will be discussed in detail below.

The advantage of this solution approach used for the nine-sensor T-configuration probe is that the velocity variation over each array does not have to be neglected and the sensor inclination angles α do not have to be measured. The calibration procedure is rather simple, but the sensors have to be positioned in the horizontal or vertical planes as accurately as possible.

In their first solution method, *Honkan* [5.690] and *Honkan* and *Andreopoulos* [5.689] assumed that the velocity gradients, over each array of their nine-sensor probe with an orthogonal geometrical configuration, could be neglected and that only gradients between the arrays had to be taken into account. In this way the problem is reduced to the problem of velocity measurements with a triple-sensor orthogonal probe. The velocity gradients can then be estimated by finite differences, knowing the velocity at each array center and the separation distance between the array centers. They analyzed two possibilities for defining the response of the three arrays of their nine-sensor probe: direct mapping through a look-up table and the determination of the cooling law of each sensor.

The first approach directly relates the velocity vector to the voltage outputs for each array. The data are used to form a look-up table which maps, one-to-one, each set of three voltages, E_{i1}, E_{i2}, and E_{i3}, for each array, to a corresponding velocity vector, defined by its magnitude Q and its pitch and yaw angles φ and ϑ with respect to the probe coordinate system.

$$|E_{i1}, E_{i2}, E_{i3}| \Leftrightarrow |Q, \varphi, \vartheta| \,. \tag{5.326}$$

The advantages of this approach are that there is no need to assume any type of cooling law for the sensors, and no knowledge of the exact array geometry is required. The disadvantage is that the method requires a large number of calibration data in order to achieve high resolution. This large number of calibration points is set by the desirability of having the voltage difference ΔE_{ik} between two successive points to be of the order of the instrument resolution in order to achieve the optimum accuracy. Various methods can be used to interpolate for cases where optimum data resolution is not obtained. The uniqueness domain can be determined using an approach proposed by *Vrettos* [5.783]. Of course, as mentioned above, an inherent and serious disadvantage of this approach is that it must be assumed that the velocity vector field across each array is constant.

The second data analysis approach of *Honkan* [5.690] and *Honkan* and *Andreopoulos* [5.689] is based on determining a cooling law describing the response of each sensor. The effective cooling velocities for the i-th array are expressed as the system of algebraic nonlinear equations:

$$\begin{aligned}
U_{ei1}^2 &= H_{i1}^2 U_{li}^2 + K_{i1}^2 V_{li}^2 + M_{i1}^2 W_{li}^2 \,, \\
U_{ei2}^2 &= H_{i2}^2 U_{li}^2 + K_{i2}^2 V_{li}^2 + M_{i2}^2 W_{li}^2 \,, \\
U_{ei3}^2 &= H_{i3}^2 U_{li}^2 + K_{i3}^2 V_{li}^2 + M_{i3}^2 W_{li}^2 \,,
\end{aligned} \tag{5.327}$$

where U_l, V_l, and W_l are the velocity components in a local coordinate system x_l, y_l, z_l with its origin attached to the tip of an array and its axes along the sensors, as shown in Fig. 5.196.

These expressions are similar to Jorgensen's (5.321) cooling law. However, they are equivalent to Jorgensen's cooling law only for a special orientation of the prongs for which the velocity component along one of the sensors is normal to the second one and binormal to the third one. This was not the case for their probe.

Using the King's law fit (5.319), this system of equations can be expressed in matrix form as

$$\begin{vmatrix} \left[\left(E_{i1}^2 - A_{i1}\right)/B_{i1}\right]^{2/ni1} \\ \left[\left(E_{i2}^2 - A_{i2}\right)/B_{i2}\right]^{2/ni2} \\ \left[\left(E_{i3}^2 - A_{i3}\right)/B_{i3}\right]^{2/ni3} \end{vmatrix} = \begin{vmatrix} H_{i1}^2 & K_{i1}^2 & M_{i1}^2 \\ H_{i2}^2 & K_{i2}^2 & M_{i2}^2 \\ H_{i3}^2 & K_{i3}^2 & M_{i3}^2 \end{vmatrix} \begin{vmatrix} U_{li}^2 \\ V_{li}^2 \\ W_{li}^2 \end{vmatrix} \,. \tag{5.328}$$

The system (5.328) is linear in $U_{\mathrm{l}i}^2$, $V_{\mathrm{l}i}^2$, and $W_{\mathrm{l}i}^2$ and can easily be solved for each array. The coefficients A_{i1} and B_{i1} can be determined using a calibration procedure by varying the speed magnitude with zero pitch and yaw angle and assuming the coefficient n_{ij} to be in the range 0.45–0.5. The values of the matrix coefficients H_{ij}, K_{ij}, and M_{ij} can be found by appropriately pitching and yawing the probe. Only the positive values of $U_{\mathrm{l}i}$, $V_{\mathrm{l}i}$, and $W_{\mathrm{l}i}$ can be inside the probe uniqueness range, as will be discussed below.

The velocity components U_i, V_i, and W_i in the probe coordinate system x, y, z shown in Fig. 5.196, and the velocity components $U_{\mathrm{l}i}$, $V_{\mathrm{l}i}$ and $W_{\mathrm{l}i}$ in the local coordinate systems of each array are linearly related by

$$\begin{vmatrix} U_i \\ V_i \\ W_i \end{vmatrix} = \begin{vmatrix} p_{i1} & p_{i2} & p_{i3} \\ q_{i1} & q_{i2} & q_{i3} \\ r_{i1} & r_{i2} & r_{i3} \end{vmatrix} \begin{vmatrix} U_{\mathrm{l}i} \\ V_{\mathrm{l}i} \\ W_{\mathrm{l}i} \end{vmatrix} , \tag{5.329}$$

where the coefficients p_{ij}, q_{ij}, and r_{ij} are the combinations of the cosine and sines of angle α and γ shown in Fig. 5.196. After solving the system (5.328) for $U_{\mathrm{l}i}$, $V_{\mathrm{l}i}$, and $W_{\mathrm{l}i}$, the velocity components U_i, V_i, and W_i can be found from the (5.329) for each array and then the six velocity gradients in the y–z plane can be calculated.

Using a similar approach to that of *Vukoslavčević* et al. [5.687], *Honkan* and *Andreopoulos* [5.689] modified this solution method so that the assumption of constant velocity over each array was no longer needed. They concluded that this was a more-accurate method, because it usually is not reasonable to assume that no velocity gradients exist over the sensing areas of the arrays while determining the gradients between array centers. This assumption would only be reasonable if the size of the arrays were much smaller than the distances between the centers of the arrays, which was not the case for any of the probes described here.

Twelve-Sensor Probe. *Tsinober* et al. [5.693] also assumed that the velocity gradients were constant over each of the three arrays of four sensors forming their 12-sensor probe. They considered each four-sensor array as a combination of four three-sensor arrays. The instantaneous velocity vectors obtained from each of the four subarrays were used to form a mean for the four-sensor array at each instant. This mean was taken to be the true value of the instantaneous velocity vector at the four-sensor array. They also used direct mapping with a look-up table to relate the velocity vector and voltage output for each array. The advantage of adding a fourth sensor to each array of the nine-sensor probe to increase the uniqueness range, as will be discussed below, was not utilized with this solution method. As was discussed above, assuming that no velocity gradients exist over the sensing areas of the arrays while determining the gradients between array centers calls into question the accuracy of this method. This is because the size of the arrays of this probe is about the same as the distances between the centers of the arrays.

The advantage of the fourth sensor, related to the uniqueness range, was discussed by *Vukoslavčević* and *Wallace* [5.768]. As in the case of the nine-sensor probe, they assumed a flow field which instantaneously varies across the sensing area of the probe so that each sensor experiences a different velocity vector. Based on their previous experience with the nine-sensor probe, they found that, for the low velocities in the near-wall region of turbulent boundary layer, the polynomial fit (5.320) and *Jorgensen*'s [5.781] expression (5.321) give better results than King's law (5.319) and the effective-angle (5.322) approach. Replacing the orthogonal velocity components U_{n}, U_{t}, and U_{b} in Jorgensen's expression (5.321) with the U, V, and W velocity components in the probe coordinate system x, y, z and equating it to the polynomial (5.320), the following expressions for the response of the j-th ($j = 1$–4) sensor of the i-th ($i = 1$–3) array is obtained

$$\begin{aligned} &\sum_{n=1}^{5} b_{ijn} E_{ij}^{n-1} \\ &= a_{ij1} U_{ij}^2 + a_{ij2} V_{ij}^2 + a_{ij3} W_{ij}^2 \\ &\quad + a_{ij4} U_{ij} V_{ij} + a_{ij5} U_{ij} W_{ij} + a_{ij6} V_{ij} W_{ij} \, . \end{aligned} \tag{5.330}$$

The coefficients a_{ijk} depend on the probe geometry, the flow distortion by the prongs and thermal effects. In fact, they are products of the sines and cosines of the angles α and of the pitch and yaw coefficients, h and k, of each sensor. Dividing by a_{ij1} and taking $A_{ijk} = a_{ijk}/a_{ij1}$ and $B_{ijn} = b_{ijn}/a_{ij1}$, (5.330) becomes

$$\begin{aligned} &\sum_{n=1}^{5} B_{ijn} E_{ij}^{n-1} \\ &= U_{ij}^2 + A_{ij1} V_{ij}^2 + A_{ij2} W_{ij}^2 \\ &\quad + A_{ij3} U_{ij} V_{ij} + A_{ij4} U_{ij} W_{ij} + A_{ij5} V_{ij} W_{ij} \, . \end{aligned} \tag{5.331}$$

None of the coefficients in this equation need to be known in advance; they can be determined in a calibration procedure. By placing the probe in a nominally irrotational and uniform calibration jet flow and pitching and yawing it, an optimal number m of different flow realizations, $U_{ij} = U_{0m}$, $V_{ij} = V_{0m}$, and $W_{ij} = W_{0m}$, can

be induced. These known flow realizations and measured voltages yield a corresponding number of linear equations (5.331) with the A_{ijk} and B_{ijn} coefficients unknown. The number of equations should, of course, be equal to or greater than the number of unknown calibration coefficients for each sensor, requiring at least 10 flow realizations. The method of least squares can be used to minimize the measurement error.

As for the case of the nine-sensor probe, the velocity components U_{ij}, V_{ij}, and W_{ij} can be defined in terms of the velocity components U_0, V_0, and W_0 at the probe center C_0 (Fig. 5.198), their gradients in the plane normal to the probe axis passing through the sensor centers, and the distances c_{ij} and d_{ij} in the y- and z-directions between C_0 and the centers of each sensor.

Expanding the velocity components U_0, V_0, and W_0 to first order in a Taylor series about C_0 results in the following 12 nonlinear algebraic equations with nine velocity and cross-stream velocity gradients unknowns:

$$\begin{aligned}
&\sum_{n=1}^{5} B_{ijn} E_{ij}^{n-1} \\
&= (U_0 + gU_{ij})^2 + A_{ij1}(V_0 + gV_{ij})^2 \\
&\quad + A_{ij2}(W_0 + gW_{ij})^2 + A_{ij3}(U_0 + gU_{ij})(V_0 + gV_{ij}) \\
&\quad + A_{ij4}(U_0 + gU_{ij})(W_0 + gW_{ij}) \\
&\quad + A_{ij5}(V_0 + gV_{ij})(W_0 + gW_{ij}) \,, \qquad (5.332)
\end{aligned}$$

where

$$gU_{ij} = c_{ij}\frac{\partial U}{\partial y} + d_{ij}\frac{\partial U}{\partial z}$$

and with U replaced by V and W for gV_{ij} and gW_{ij}.

A special numerical algorithm was developed to solve these equations. For each array, it chooses the three sensor response equations, out of the four available, that give the maximum uniqueness range. In addition to obtaining the maximum possible uniqueness range, a second advantage of this method is that knowing the exact orientation of the sensors is not required. In order to define the velocity gradient, the only thing that must be known (and with good accuracy) is the spacing between the sensor centers. These distances are determined with a measuring microscope.

Nguyen [5.766] and *Marasli* et al. [5.767] used the same response equations as those by *Vukoslavčević* and *Wallace* [5.768] but their iterative solution method employed a minimization of the least-squared error from all 12 sensors. How this method affects the uniqueness range of the probe has not been analyzed.

Eight-Sensor Probe. The data-reduction mechanism of the eight-sensor probe is the simplest of all those described here. Any of the well-known methods developed for X-arrays probes can be used in this case. The assumption of *Antonia* et al. [5.770] and *Antonia* et al. [5.771] that the velocity field is constant across each array but that it varies between arrays is not necessary. This assumption can be questionable in high-gradient flows, bearing in mind that the ratio of the sensor separations to the separations between arrays is about 0.3. Assuming a constant-gradient flow field over the whole probe sensing area will make the response equations more complex, but they can be easily solved using a successive iteration procedure similar to the one developed for the nine- and 12-sensor probes. However, it is necessary to neglect the binormal component cooling each sensor and, therefore, its gradients when only eight sensors are used.

Streamwise Velocity Gradients

Using the data obtained with the nine- or 12-sensor probes, three velocity components and six velocity gradients in the cross-stream directions can be obtained. However, only four of the cross-stream gradients can be obtained with the eight-sensor probe. The streamwise gradients have to be evaluated using an alternate method.

A common method is to apply *Taylor*'s [5.762] hypothesis that the turbulent flow pattern is *frozen* for a sufficiently short time interval as it passes the probe at a fixed point in space with a convection speed U_c. Under this hypothesis, the streamwise gradient of any instantaneous velocity component U_i can be expressed as

$$\frac{\partial U_i}{\partial x} = -\frac{1}{U_c}\frac{\partial U_i}{\partial t} \,. \qquad (5.333)$$

The convection velocity U_c is usually taken as the local mean velocity $\overline{U}$ or as the local instantaneous velocity U, giving the following forms of Taylor's hypothesis:

$$\frac{\partial U_i}{\partial x} = -\frac{1}{\overline{U}}\frac{\partial U_i}{\partial t} \qquad (5.334)$$

or

$$\frac{\partial U_i}{\partial x} = -\frac{1}{U}\frac{\partial U_i}{\partial t} \,. \qquad (5.335)$$

Another approach is based on the assumption that an instantaneous property φ of a material fluid particle does not change along its Lagrangian path during a sufficiently small time interval so that the material derivative $\mathrm{D}\varphi/\mathrm{D}t = 0$. Under this assumption the momentum equation reduces to a refined form of Taylor's hypothesis

given by

$$\frac{\partial U_i}{\partial x} = -\frac{1}{U}\left(\frac{\partial U_i}{\partial t} + V\frac{\partial U_i}{\partial y} + W\frac{\partial U_i}{\partial z}\right) . \qquad (5.336)$$

It is clear from the momentum equation that this expression is strictly valid only if the pressure forces negate the viscous forces, and its accuracy depends on the degree to which this is true.

The streamwise gradient $\partial U/\partial x$ can also be determined from the continuity equation for incompressible fluid flow

$$\frac{\partial U}{\partial x} = -\left(\frac{\partial V}{\partial y} + \frac{\partial W}{\partial z}\right) . \qquad (5.337)$$

This exact expression can be employed to test the different forms of Taylor's hypothesis used to determine the streamwise velocity gradient.

All three equations, (5.334), (5.335) and (5.336) have been analyzed by evaluating the magnitude of the terms in the momentum equation. They have been tested using experimental and numerical data for different types of turbulent flows. For a turbulent flow field that is convected locally in the x-direction by the mean streamwise velocity $\overline{U}$ ($\overline{V} \approx 0$, $\overline{W} \approx 0$, $\partial\overline{U}/\partial z = 0$), the refined Taylor hypothesis expression takes the form

$$\frac{\partial U_i}{\partial x} = -\frac{1}{\overline{U}}\left(\frac{\partial U_i}{\partial t} + v\frac{\partial u_i}{\partial y} + w\frac{\partial u_i}{\partial z} + v\frac{\partial \overline{U}_i}{\partial y}\right) , \qquad (5.338)$$

where u_i are the velocity fluctuations about the mean values and v and w are components in the cross-stream directions. The last three terms in this equation are small for a sufficiently small turbulence level. In that case, the refined (5.336) and classical form (5.335) of Taylor's hypothesis give similar results.

The momentum equation can be rewritten in the following form

$$\begin{aligned}&\frac{\partial U_i}{\partial t} + \overline{U}\frac{\partial u_i}{\partial x} + \left(u\frac{\partial u_i}{\partial x} + v\frac{\partial u_i}{\partial y} + w\frac{\partial u_i}{\partial z}\right)\\ &\quad -\left[\frac{\partial}{\partial x}(\overline{uu}) + \frac{\partial}{\partial y}(\overline{uv}) + \frac{\partial}{\partial z}(\overline{uw})\right]\\ &\quad + u\frac{\partial \overline{U}_i}{\partial x} + v\frac{\partial \overline{U}_i}{\partial y} + w\frac{\partial \overline{U}_i}{\partial z} + \frac{1}{\rho}\frac{\partial p}{\partial x_i}\\ &\quad - \nu\left(\frac{\partial^2 u_i}{\partial x^2} + \frac{\partial^2 u_i}{\partial y^2} + \frac{\partial^2 u_i}{\partial z^2}\right) = 0 , \end{aligned} \qquad (5.339)$$

where p are the pressure fluctuations about the mean values. This form of the momentum equation is convenient to analyze the magnitude of the terms to be neglected in order to test the accuracy of Taylor's hypothesis for a given type of flow. An analysis of the order of magnitude of these terms is given by *Heskestad* [5.784]. He found that the terms $u_j(\partial\overline{U}_i/\partial x_j)$ are always small compared to $\overline{U}(\partial u_i/\partial x)$, and that the $(\partial/\partial x_i)\overline{u_i u_j}$ terms are also small compared to $u_j\partial u_i/\partial x_j$ if the Taylor microscale λ is quite small compared to some characteristic length L so that $\partial u_i/\partial t \gg \lambda/L$. Neglecting the viscous terms $\nu\partial^2 u_i/\partial x_k^2$, which he did on the grounds that viscous forces do not greatly affect the large-scale motion of the flow associated with its momentum, the momentum equation (5.339) reduces to the form

$$\frac{\partial u_i}{\partial x} = -\frac{1}{U}\left(\frac{\partial U_i}{\partial t} + v\frac{\partial u_i}{\partial y} + w\frac{\partial u_i}{\partial z} + \frac{1}{\rho}\frac{\partial p}{\partial x_i}\right) . \qquad (5.340)$$

In the case of boundary-layer flow, where $\partial\overline{U}/\partial x \approx 0$, this expression differs from the generalized Taylor's hypothesis (5.338) only because it includes the pressure fluctuation gradient, and because *Heskestad* [5.784] considered the $v(\partial\overline{U}/\partial y)$ term in (5.338) to be negligible. *Batchelor* [5.785] estimated that, in an isotropic field, the ratio of the mean square pressure gradient to a typical mean square inertia term is inversely proportional to the Reynolds number $\mathrm{Re}_\lambda = \lambda u/L$. If this is the case, only for $\mathrm{Re}_\lambda > 1000$ can the pressure terms be neglected and the streamwise gradients be evaluated from the generalized Taylor hypothesis (5.336) with sufficient accuracy.

Piomelli et al. [5.786] used direct numerical simulation (DNS) and large-eddy simulation (LES) data from turbulent channel flows as well as the experimental boundary-layer data of *Balint* [5.787] to extend the numerical study of Taylor's hypothesis initiated by *Hussain* et al. [5.788]. They compared the rms of the streamwise velocity gradient obtained directly from the LES and used the classical (5.334) as well as the refined form (5.336) of Taylor's hypothesis. Very good agreement was found above the buffer layer. By comparing $\partial U_i/\partial t$ with $\overline{U}\partial U_i/\partial x$ from the LES, high phase coherence between these two signals was observed above the buffer layer as evidenced by correlation coefficient values of 0.95 or higher everywhere in this region of the flow for all three streamwise velocity gradients. The amplitudes of these two signals were also similar in this region of the flow, as evidenced by their similar rms levels. In interpreting these results, one should keep in mind that in LES only the larger-scales are computed accurately, while the smaller ones are modeled. The influence of the small scales obviously affect the velocity derivatives. To assess the importance of the neglected small scales, the rms intensities of the velocity gradients were compared

to those obtained from DNS and from the experimental data of *Balint* [5.787]. Above the buffer layer, the agreement between the LES and the experimental rms values, which were determined with comparable resolution, was very good, while both sets of values are somewhat lower than those of the DNS due to insufficient resolution.

Kim and *Hussain* [5.790] investigated the propagation speed of velocity, vorticity, and pressure fluctuations from a turbulent channel flow DNS simulation. This investigation has obvious implications for Taylor's hypothesis, as they pointed out. They found, surprisingly, that the propagation velocity is very close to the local mean velocity except in the near-wall region, i. e., the viscous and buffer layers, where it has a nearly constant value of about 10 u_τ. The relative lack of agreement seen by *Piomelli* et al. [5.786] between the amplitudes of $\partial U_i/\partial t$ and $\overline{U}\partial U_i/\partial x$ in and below the buffer layer, as indicated by their rms values there, can be explained by the fact that turbulence fluctuations are not convected with the mean velocity in this region near the wall. Use of a more-appropriate convection velocity in the near-wall region of bounded flows will clearly improve the ability of the Taylor's hypothesis time–space transformation to provide adequate estimates of streamwise gradients.

A comparison of the streamwise gradient $\partial U/\partial x$ evaluated using the continuity equation and different forms of Taylor's hypothesis was given by *Loucks* [5.780]. The time series, shown in Fig. 5.202, was obtained from the boundary-layer data of *Ong* [5.789] using a nine-sensor probe in the logarithmic layer at $y^+ = 89$.

The time series of the two forms of Taylor's hypothesis match extremely well in both phase and amplitude. They can hardly be distinguished from each other. They both also track fairly closely in phase and shape with the continuity equation. However, the amplitudes of the Taylor's hypothesis signals deviate from that of the continuity equation signal during some short intervals of the time series shown. *Loucks'* [5.780] further analysis of this data, as well as the data taken by a 12-sensor probe in a plane mixing layer, have shown that these differences between $\partial U/\partial x$ obtained from continuity and from Taylor's hypothesis are not an effect of the data sampling rate. We have determined that this amplitude disagreement in the boundary-layer data of *Ong* [5.789] can be much reduced by a judicious choice of the Taylor's hypothesis convection velocity, viz. by using a convection velocity of (0.6–0.7) $\overline{U}$ near the wall. This is consistent with the findings of *Kim* and *Hussain* [5.790] mentioned above.

To compare the phase shifts of the different signals, *Loucks* [5.780] calculated the cross-correlation coefficients shown in Fig. 5.203, where R_1, R_2 and R_3 are the cross-correlation of $\partial U/\partial x$ obtained from continuity (5.337) with the various forms of Taylor's hypothesis given by (5.334), (5.336) and with (5.336), where $\overline{U}$ was used as the convection velocity in place of U.

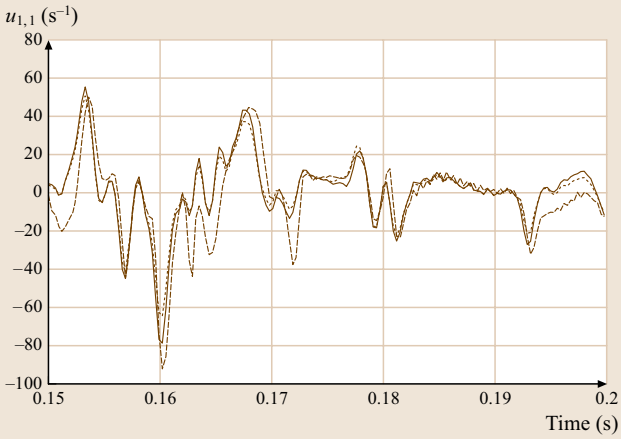

Fig. 5.202 A time series of the streamwise velocity gradient from *Loucks* [5.780] using the boundary-layer data of *Ong* [5.789] at y^+=89: continuity equation (5.337) (*dashed line*), Taylor hypothesis (5.334) (*solid line*), and refined Taylor hypothesis (5.336) (*dotted line*)

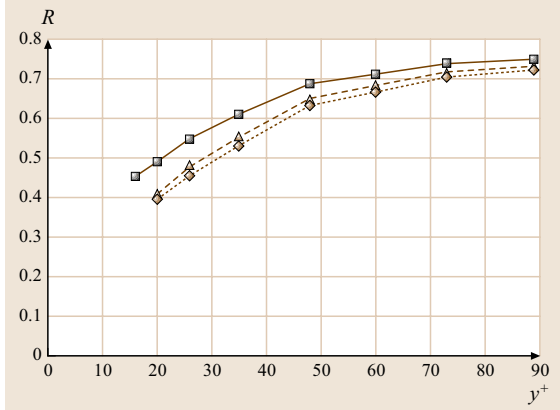

Fig. 5.203 Correlation coefficients of the streamwise velocity gradients from *Loucks* [5.780] using the boundary-layer data of *Ong* [5.789] at $y^+ = 89$: continuity (5.337) with Taylor's hypothesis (5.334) (*squares*), continuity (5.337) with refined Taylor's hypothesis (5.336) (*circles*), and continuity (5.337) with refined Taylor's hypothesis (5.336) but using $\overline{U}$ as the convection velocity (*triangles*)

Although all three coefficients are close to each other, surprisingly the highest correlation was obtained using the classical form of the Taylor hypothesis. Similar results were obtained in the mixing-layer flow.

To summarize, it can be stated that Taylor's hypothesis can be used to approximate streamwise gradients with an accuracy that improves with distance from the wall for bounded flows and with increasing mean velocity in mixing-layer flows. Adding the additional terms for the refined form of Taylor's hypothesis does not improve the accuracy. For all the flows mentioned here for which Taylor's hypothesis was examined, the Taylor microscale Reynolds number Re_λ was in the range 500–700. These are large values, but are still smaller than the criterion of *Heskestad* [5.784].

Uniqueness Range

It is well known that different fluid velocity vectors, as illustrated in Fig. 5.204, can produce the same hot-wire response. For any number of heated sensors included in a hot-wire probe, multiple solutions of the sensors' response equations can be obtained, and different velocity vectors can be determined from any specific set of anemometer output signals. This is the well-known *uniqueness* or *rectification* problem referred to by *Tutu* and *Chevray* [5.792].

Fortunately, there is a solution domain, known as the *uniqueness domain*, where the velocity vector can be uniquely determined for a given probe. The uniqueness domain of a multiple-sensor probe is shown schematically in Fig. 5.204b. The outer boundary of this domain can be described by the largest angle, φ_{cr}, defined as the angle between the probe axis, shown in Fig. 5.204b, and the velocity vector $\boldsymbol{U}_{cr}$ at the edge of the domain. Within this domain the fluid velocity vector $\boldsymbol{U}$ can be uniquely determined. The geometrical form of such a domain is usually an asymmetric conical surface for which φ_{cr} is a function of the angle θ, which specifies the orientation of the meridian plane containing $\boldsymbol{U}_{cr}$. Its shape varies, depending primarily on the number of sensors and their configuration. However, the *uniqueness range* is more commonly represented by the symmetric cone, shown in Fig. 5.204b, the half angle ε of which is defined as the minimum value of the angle φ_{cr}. Inside this cone there is a unique solution independent of the rotation of the probe around its axis. Thus hot-wire probes should only be used in flows with velocity vectors contained within the uniqueness cone. Otherwise, at least two fluid velocity vectors will give the same output signals, and there is no way to recognize which of them really exists in a given flow. The uniqueness range of a vorticity probe is the same as the uniqueness range of its arrays.

To date, a variety of investigations about the uniqueness range of different hot-wire probe configurations and their signal interpretation procedures have been published. An illustrative graphical representation, based on the *cosine law*, of the response of an ideal, infinitely long, hot-wire sensor to possible fluid velocity vector directions was given by *Willmarth* [5.793]. In the case of a three-sensor probe, there can be up to eight intersection points between the three cylindrical surfaces that represent three-probe sensor responses.

Detailed numerical and graphical analyses of the uniqueness domain of three- and four-sensor probes have been carried out by many researchers; one such survey can be found in *Vukoslavčević* et al. [5.791]. They also analyzed the uniqueness domain and derived analytical expressions defining the uniqueness range of three-

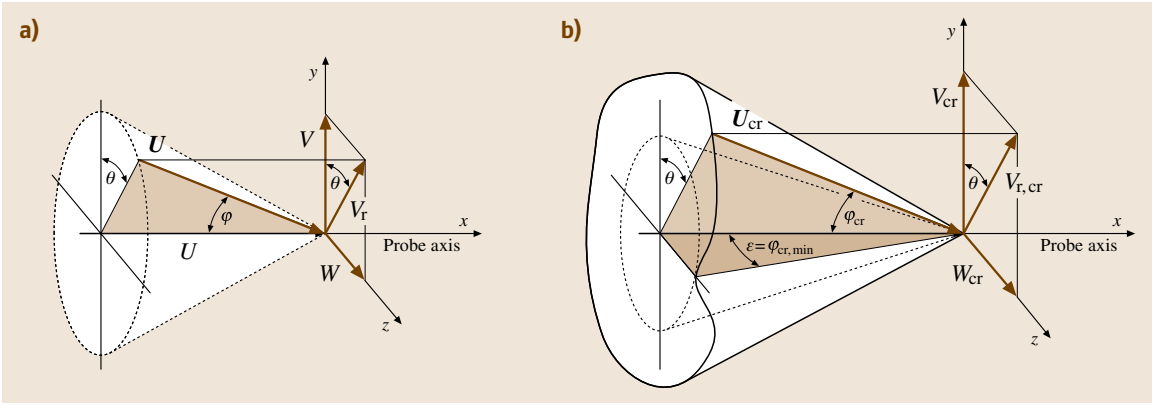

Fig. 5.204 **(a)** Velocity vector in Cartesian and spherical coordinates. **(b)** The uniqueness domain and uniqueness cone of a multisensor hot-wire probe. (After *Vukoslavčević* et al. [5.791], courtesy Inst. of Physics)

and four-sensor probes. These expressions are based on the effective angle approach (5.322) or on the effective cooling velocity (5.321) described by Jorgensen's law.

For the nine-sensor T-configuration probe, shown in Fig. 5.195, or one of its arrays, the half angle ε of the uniqueness cone corresponds to the meridian plane $\theta = 0°$ ($W = 0$) and is given by

$$\varepsilon = \varphi_{\mathrm{cr,min}} = a \tan\left[\frac{\sin 2\alpha_\mathrm{e}}{2h^2}\right] . \qquad (5.341)$$

A maximum value of $\varepsilon = 26.56°$ can be achieved for the case of an ideal sensor response ($\alpha = \alpha_\mathrm{e}$, $h = 1$) and a sensor inclination angle of $\alpha = 45°$. For any other value of angle α the uniqueness range will decrease. In the case of a nine-sensor orthogonal-configuration probe or one of its arrays, shown in Fig. 5.196, the half cone angle ε corresponds to meridian planes containing any of the sensors and their supporting prongs and is defined by

$$\varepsilon = \varphi_{\mathrm{cr,min}} = a \tan\left(\frac{\sin 2\alpha_\mathrm{e}}{h^2 + \sin^2\alpha_\mathrm{e}}\right) , \qquad (5.342)$$

with a maximum value of $\varepsilon = 35.26°$ for an ideal sensor response ($\alpha = \alpha_\mathrm{e}$, $h = 1$) and a sensor inclination angle of $\alpha = 35.26°$. As for the nine-sensor T-configuration probe, the uniqueness range will decrease for any other value of the sensor inclination angle α.

Two expressions were derived for the 12-sensor probe shown in Fig. 5.198 or for one of its four-sensor arrays. One is based on the effective-angle approach and is given by

$$\varepsilon = \varphi_{\mathrm{cr,min}} = a \tan\left(\frac{\sqrt{2}\cos\alpha_\mathrm{e}}{\sqrt{\sin^2\alpha_\mathrm{e} + h^2}}\right) . \qquad (5.343)$$

The other is based on Jorgensen's cooling law and is given by

$$\varepsilon = \varphi_{\mathrm{cr,min}} = a \tan\sqrt{\frac{2(\cos^2\alpha + k\sin^2\alpha)}{\sin^2\alpha + k^2\cos^2\alpha + h^2}} . \qquad (5.344)$$

Both of these correspond to the same meridian planes $\theta = \pm 45°$ and $\theta = \pm 135°$ ($W = \pm V$). For the case of an ideal sensor response ($\alpha = \alpha_\mathrm{e}, k = 0, h = 1$), they reduce to the same form

$$\varphi_{\mathrm{cr1,2}} = a \tan\left(\frac{\sqrt{2}\cos\alpha}{\sqrt{\sin^2\alpha + 1}}\right) , \qquad (5.345)$$

which was first derived by *Pailhas* and *Cousteix* [5.794] and gives a value of $\varepsilon = 39.23°$ for $\alpha = 45°$.

It is therefore clear that the 12-sensor probe has the highest value of the uniqueness half cone angle with a value of $\varepsilon = 39.23°$, compared to $\varepsilon = 26.56°$ and $\varepsilon = 35.26°$ for nine-sensor T-configuration and nine-sensor orthogonal-configuration probes, respectively. In addition, in contrast to the nine-sensor configurations, this value can be further increased by decreasing the sensor inclination angle α, as can be seen in Fig. 5.205 where ε is shown for different values of the pitch coefficient h and the sensor inclination angle α_e.

If the wire angle is decreased to the value $\alpha = 35.26°$ that corresponds to the nine-sensor orthogonal probe, the uniqueness half cone angle will be $\varepsilon = 45.0°$, which is about 9° higher than for the case of the nine-sensor orthogonal probe and about 18° higher than for the nine-sensor T-configuration probe. Unfortunately, decreasing the sensor inclination angle α decreases the sensitivity of the probe to the cross-stream velocity components.

All four expressions, (5.341), (5.342), (5.343), and (5.344), clearly show that for real sensor responses the uniqueness range cone half-angle ε decreases with an increase of the pitch coefficient h. In addition, the same trend can also be seen in Fig. 5.205 for the 12-sensor probe.

In order to achieve the maximum possible value of the uniqueness range cone half-angle for the 12-sensor probe shown in Fig. 5.198, an appropriate choice of three out of the four available sensors has to be made for each array, as explained in *Vukoslavčević* and *Wallace* [5.768]. Each array of a 12-sensor probe can be viewed as a combination of two subarrays of

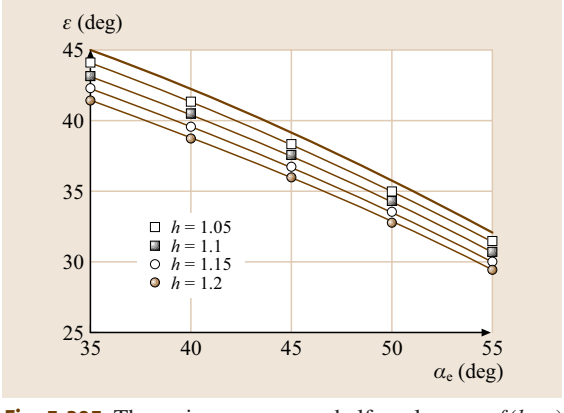

Fig. 5.205 The uniqueness cone half-angles $\varepsilon = f(h, \alpha)$ for a 12-senor probe for $h = 1$ (*lines*), $h = 1.05$ (*open square*), $h = 1.1$ (*filled square*), $h = 1.15$ (*open circle*), and $h = 1.2$ (*filled circle*). (After *Vukoslavčević* et al. [5.791], courtesy Inst. of Physics)

three-sensors in the T-configuration. For example, one subarray is formed by sensors 1, 2, and 3 in the geometrical arrangement of the arrays of the nine-sensor probe shown in Fig. 5.195, and the other is formed by sensors 2, 3, and 4 corresponding to the same three-sensor subarray configuration rotated by 180°. For a triple-sensor array, shown in Fig. 5.195, there are, in fact, two minimums of the critical angle φ_{cr}. The first is in the range $|\theta| \leq 90°$, or $V \leq 0$ and the second is in the range $90° \leq \theta \leq 180°$, or $V \geq 0$. For the combination of sensors 1, 2, and 3 the first (smaller) minimum is given by (5.341) and the second (higher) one by (5.343) and (5.344). The situation is reversed for the combination of sensors 2, 3, and 4. The higher ε corresponds to $V \geq 0$ or $90° \leq \theta \leq 180°$ and the lower one to $V \leq 0$ or $|\theta| \leq 90°$. This means that, in order to achieve the higher value for the uniqueness range cone half-angle given by (5.343) or (5.344), a choice of sensors 1, 2,and 3 has to be made for negative values of V, and sensors 2, 3, and 4 have to be chosen for positive V. However, the value of the V velocity component is not known in advance. The procedure can be started by any arbitrary initial choice and then updated depending on the sign of V. The same conclusion can be drawn from the subarray sensor combinations 1, 2, and 4 and 1, 3, and 4, together with the sign of the W velocity component.

In the case of the mapping approach using a look-up table, the only condition for which the mapping given by (5.326) is unique is given by

$$J = \begin{vmatrix} \partial E_{i1}/\partial Q & \partial E_{i2}/\partial Q & \partial E_{i3}/\partial Q \\ \partial E_{i1}/\partial \varphi & \partial E_{i2}/\partial \varphi & \partial E_{i3}/\partial \varphi \\ \partial E_{i1}/\partial \vartheta & \partial E_{i2}/\partial \vartheta & \partial E_{i3}/\partial \vartheta \end{vmatrix} \neq 0 \,. \qquad (5.346)$$

The nine elements of this Jacobian J are the sensitivities of each sensor. The partial derivatives can be found by using the finite-difference method at the successive points obtained in a calibration procedure. If J does not change sign at any point inside a domain, a unique measurement of the velocity vector can be obtained in that domain. The first attempt to verify the uniqueness of this type for an orthogonal triple hot-wire was given by *Vrettos* [5.783]. This condition is very general and can be applied to any type of probe configuration.

Examples of Measurements with Multisensor Hot-wire Probes

The probes described above have been used to measure the vorticity components as well as other important velocity gradient-based properties of turbulence such as the strain rate $S_{ij} = \partial u_i/\partial x_j + \partial u_j/\partial x_i$, the dissipation rate $\varepsilon = 2\langle S_{ij} S_{ij} \rangle$, and the helicity density $U_i \cdot \Omega_j$ in grid turbulence as well as in turbulent boundary layers, wakes, jets and mixing layers [5.689, 690, 693, 730, 731, 764, 766–768, 770, 771, 780, 787, 789, 795–805]. Here a few representative examples from the rich variety of the results from these measurements will be shown. In Fig. 5.206, the distribution of enstrophy, $0.5\overline{\omega_i \omega_i}$, measured in turbulent boundary layers with several of these probes is compared to the distribution obtained from a direct numerical simulation (DNS) by *Spalart* [5.742] of a turbulent boundary layer and of a turbulent channel flow by *Moser* et al. [5.806].

Here the comparison data are all from boundary-layer experiments or DNS with Reynolds numbers given in terms of the momentum thickness θ and the freestream velocity U_∞, with the exception of the channel flow DNS of Moser et al. where the Reynolds number is given in terms of half the channel width and the friction velocity u_τ. The experimental profiles show the same monotonic increase of the enstrophy as the wall is approached as seen in the DNS profiles. However, all the experimental data fall below the two DNS profiles except for the data of *Ong* and *Wallace* [5.803] after the normalizing velocity scale u_τ has been corrected. This correction, discussed thoroughly in *Ong* and *Wallace* [5.803], is appropriate, because using the Clauser method to determine u_τ, as was done for all the experimental data shown here, results in significantly overestimated values. Furthermore, because u_τ^4 is used in the normalization of $0.5\overline{\omega_i \omega_i}$, this error in the normalizing scale is greatly amplified.

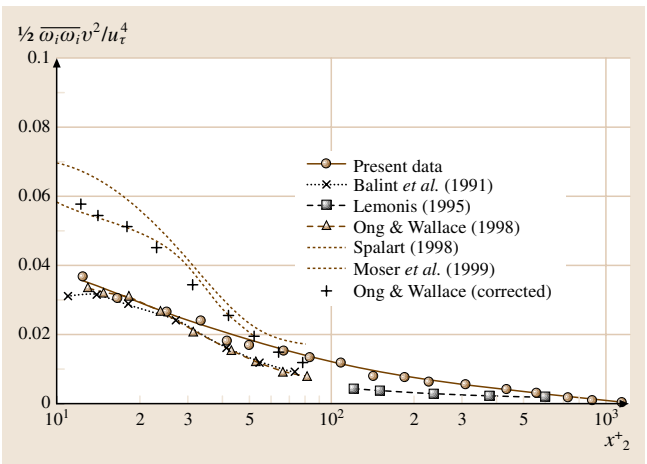

Fig. 5.206 Normalized enstrophy, $0.5\overline{\omega_i \omega_i}/u_\tau^4$, measured in turbulent boundary layers with vorticity probes and compared to simulation results. (After *Andreopoulos* and *Honkan* [5.730], courtesy CUP)

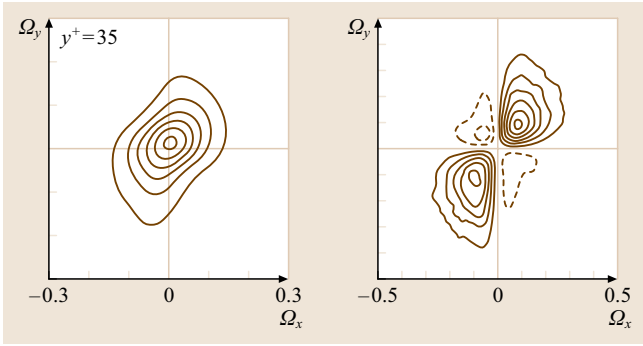

Fig. 5.207 Joint PDF and covariance integrand of the vorticity components Ω_x and Ω_y in a turbulent boundary layer at $\mathrm{Re}_\theta = 1070$ (after *Ong* and *Wallace* [5.803], courtesy CUP)

The joint probability density function (JPDF) of the streamwise and spanwise components of vorticity $P(\Omega_x, \Omega_y)$ reveals interesting characteristics of the vortical structure of turbulent shear flows. For example, the left-hand plot of $P(\Omega_x, \Omega_y)$ in Fig. 5.207 is of data taken just above the buffer layer in the turbulent boundary-layer experiment of *Ong* and *Wallace* [5.803]. The inclination of the major axis of the JPDF into the first and third quadrants of the hodograph plane implies a preference for these vorticity components to occur simultaneously with like signs, either both plus or both minus. This is even more evident in the right-hand plot of the covariance integrand, $\Omega_x \Omega_y P(\Omega_x, \Omega_y)$, where it is seen that the occurrence of like signs of these two components (first and third quadrants) dominates the value of the covariance, $\overline{\Omega_x \Omega_y}$. In fact, as *Ong* and *Wallace* [5.803] point out, the peak values of the contours in the first and third quadrants of the covariance integrand plots can be used to find the projections on the x–y plane of the angles of orientation of the vortex filaments that most contribute to the covariance $\overline{\Omega_x \Omega_y}$ at this y^+ location. These characteristics of the JPDF and covariance integrand are consistent with the prevalent view that the bounded flows are made up of organized, but often asymmetric, *hairpin* vortices, inclined downstream in the x–y plane.

In addition to simultaneous measurement of the vorticity vector components, the fact that these probes provide good estimates of the complete velocity gradient tensor, with the exception of the eight-sensor probe, make them useful in determining several other fundamental properties of turbulence. For example, all the terms of the turbulent dissipation rate are available. Figure 5.208 shows time series obtained by *Folz* [5.801] in an experiment carried out in the near-surface layer of the atmospheric boundary layer over the Utah salt flats with a 12-sensor probe like the one described in Fig. 5.198. The full dissipation rate signal ε is compared to approximations in which

1. the inhomogeneous cross-product terms are neglected so that $\varepsilon \sim 2\nu \sum_i \sum_j (\partial u_i/\partial x_j)^2$,
2. the enstrophy is used as a surrogate so that, $\varepsilon \sim \zeta/\nu = (1/\nu)\omega_i \omega_i$, and
3. isotropy is assumed so that $\varepsilon \sim 15\nu(\partial u/\partial x)^2$.

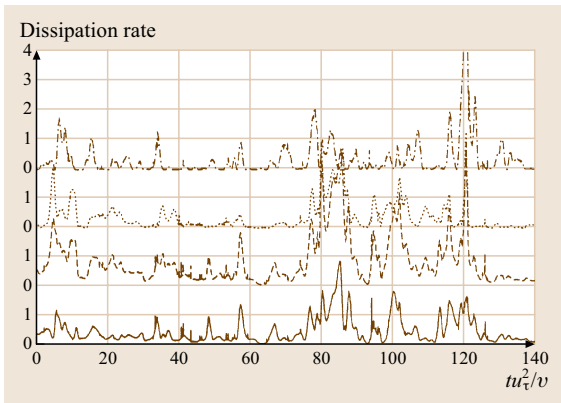

Fig. 5.208 Time series of differences between full dissipation rate, $\varepsilon = 2S_{ij}S_{ij}$ (*solid line*), and three approximations to ε at $y^+ = 45$ in the atmospheric surface layer over the Utah salt flats: homogeneous, $2\nu \sum_i \sum_j (\partial u_i/\partial x_j)^2$ (*dashed line*); entropy, ζ/ν (*dotted line*); and isotropic, $15\nu(\partial u/\partial x)^2$ (*dot-dashed line*). (After *Folz* [5.801])

There are significant differences in both the amplitude and phase between the time series of each of these approximations of the dissipation rate and the full dissipation rate ε.

A strong alignment of the vorticity vector with the intermediate eigenvector of the rate-of-strain tensor, α_i for $i = 2$, was observed by *Tsinober* et al. [5.693] in both turbulent grid flow and in a turbulent boundary layer at $y/\delta = 0.2$, as seen in Fig. 5.209. This striking result is in agreement with numerical simulations by *Ashurst* et al. [5.807], but its physical significance is still unexplained.

The decay of the vorticity component variances measured by *Antonia* et al. [5.770] in grid turbulence is shown in Fig. 5.210, where it is compared to an isotropic estimate of their decay. Each of the components decays at the same rate as the isotropic estimate, providing convincing evidence that the vorticity field, which is dominated by high wavenumbers, is isotropic in this grid flow.

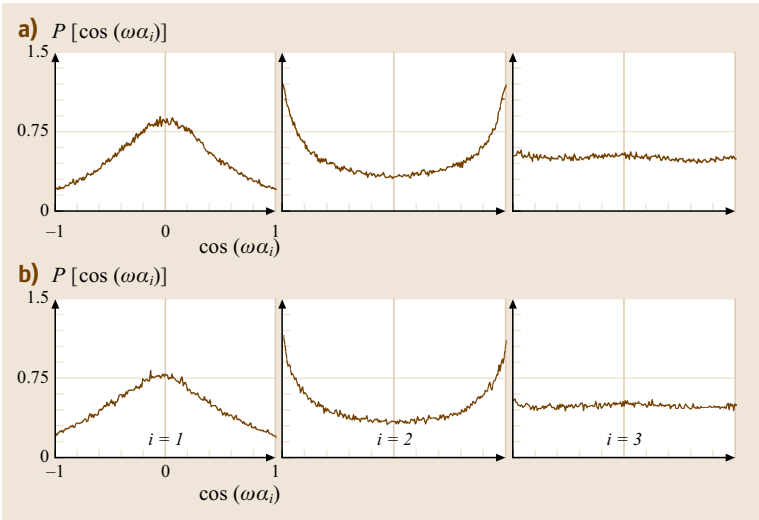

Fig. 5.209a,b Probability density functions of the cosine of the angle between the vorticity vector and the eigenvectors of the rate-of-strain tensor: $\alpha_2 < \alpha_2 < \alpha_3$; **(a)** grid flow at $x/M = 30$ and **(b)** boundary layer at $y/\delta = 0.2$. (After *Tsinober* et al. [5.693], courtesy CUP)

Summary

Only within the last 20 years has knowledge of the important properties of turbulence defined by the velocity gradient tensor, including the vorticity vector, become accessible by experimental measurements and numerical simulations. This access has enabled the examination of the structural characteristics of turbulence and the related transport processes for a rich variety of flows, as well as the testing of previously unverifiable turbulence theories. The development and use of multisensor hot-wire probes to obtain this knowledge has been an important part of this progress in turbulence research.

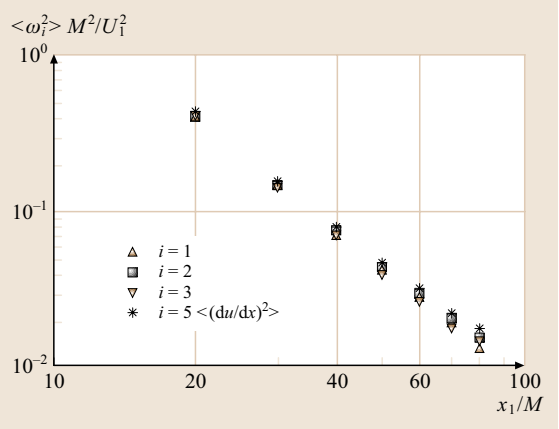

Fig. 5.210 Decay of the vorticity component variances with downstream distance in grid turbulence compared with isotropic decay. (After *Antonia* et al. [5.770], courtesy CUP)

5.5.4 Transverse Vorticity Measurements with a Four-Sensor Hot-Wire Probe

This section describes the use of a four-sensor hot wire probe that is capable of measuring time series of two components of velocity (u, v) and a single component of vorticity that is perpendicular to the measured velocities (ω_z). The original probe design and processing algorithm were developed by Foss and coworkers, and can be found in *Foss* and *Haw* [5.808], *Wallace* and *Foss* [5.81]. Measurements from this sensor are presented in, for example, *Foss* [5.809] and *Morris* and *Foss* [5.810].

A three-view drawing of the basic probe geometry is shown in Fig. 5.211. A perspective view is shown in Fig. 5.212 for clarity. Two of the sensors are parallel with

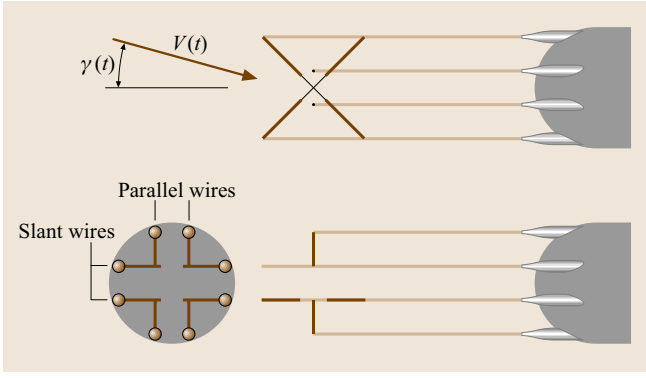

Fig. 5.211 Three-view drawing of the probe and coordinate system. Note that the wire thicknesses are not to scale

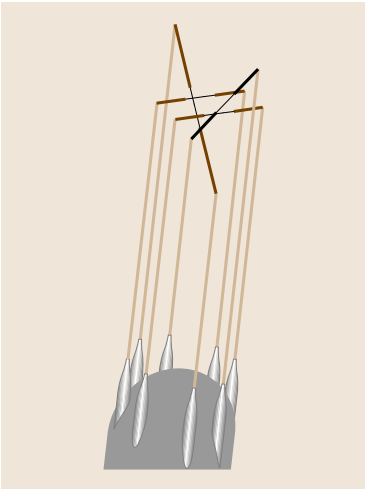

Fig. 5.212 Perspective view of the probe geometry

1–1.5 mm spacing. The remaining two sensors are configured as a standard X-wire probe, and placed through the two parallel sensors as shown. The result is a nominal measurement domain that is of the order 1 mm^3 in size. The definition of the approach velocity vector is shown in the coordinate system of the probe in Fig. 5.211. The component of velocity normal to the plane shown at the top of Fig. 5.211 is assumed to be small.

The sensors are typically created using tungsten wire with a nominal 5 μm diameter. Copper plating aerodynamically isolates the 1 mm active portion of the sensor from the support prongs. The copper plating is typically hand soldered to the supports using a multi-degree-of-freedom traverse to position the sensor over the prongs. Note that a significant challenge in the manufacture of the probe is to *thread* the fourth wire through the others. That is, the first three sensors can be positioned on the support prongs without difficulty but, due to the geometry, the fourth wire cannot be positioned without threading it through the others. This can be accomplished by first fixing the fourth wire to a small support needle.

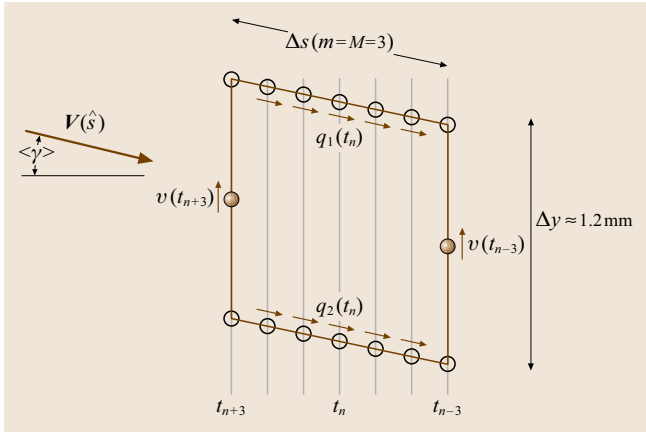

Fig. 5.213 Schematic of the microcirculation domain for the evaluation of (5.348) assuming $M = 3$

Algorithm

The time series output from the probe includes the magnitude of velocity in the *plane of the probe* as determined by the two straight wires q_1, q_2 and the angle γ determined from the X-array. Note that the symbol $q = (u^2 + v^2)^{1/2}$ is used since these sensors essentially respond to the velocity magnitudes that are perpendicular to their axes. The X-array, which could provide both u and v, is only necessary to provide the instantaneous flow angle γ. Methods for calibrating single-sensor hot-wires and X-array probes are given in Sect. 5.2. The component of vorticity to be calculated from the hot-wire signals is given by

$$\omega_z = \frac{\partial v}{\partial x} - \frac{\partial u}{\partial y} \,. \tag{5.347}$$

Rather than approximating the spatial velocity derivatives directly, an integral approach will be presented based on the circulation

$$\langle \omega_z \rangle_\mu = \frac{1}{A_\mu} \oint \boldsymbol{V}\, \mathrm{d}\boldsymbol{s} \,. \tag{5.348}$$

That is, the probe is used to evaluate a spatially averaged vorticity over a defined microcirculation domain of area A_μ by evaluating this circulation integral. The objective of the processing algorithm is to use the outputs from the hot-wire sensors (q_1, q_2, γ) to create a convected domain where (5.348) can be evaluated. A schematic of the domain of integration is shown in Fig. 5.213.

The domain is defined by the streamwise ($\hat{s}$) and probe-normal ($\hat{y}$) directions. In short, the time series of the flow speed provides the definition of a convected domain. The circulation integral can be evaluated given that the two parallel wires provide the velocity on the *top* and *bottom* of the region, and the X-wire probe provides a single estimate of the vertical component at both the fore and aft sides of the domain.

The domain is created using the time series $q_1(t_n)$ and $q_2(t_n)$ with the assumption of a local (in time) Taylor's hypothesis. The height of the domain Δy is specified by the distance between the parallel wires. The length of the domain Δs is created from a convected length that is nominally the same dimension: $\Delta s \approx \Delta y$.

However, the definition of the convected length in the streamwise direction is limited to discrete time record values set by the acquisition frequency. Specifically, the value of Δs is evaluated at time t_n as:

$$\Delta s_n(m) = \sum_{i=n-m}^{n+m} \left[\frac{q_1(t_i) + q_2(t_i)}{2} \right] \Delta t \,. \qquad (5.349)$$

where Δt is the inverse of the data-acquisition frequency, and the convection velocity is defined as the mean from the two parallel sensors. The size of Δs is established by increasing the dummy variable m until $\Delta s_n(m) > \Delta y$. The smallest value of m to satisfy this inequality is denoted by $m = M$.

Note that the circulation domain is centered on the time series point t_n, and is expanded M data points in both directions. The total number of data points used $(2M+1)$ for each calculation time (t_n) depends on the instantaneous flow speed. The data-acquisition frequency must be large enough that a minimum number of time series points are included for each evaluation of the integral given in (5.348). Specifically, $f_{\text{acq}} > 2MU/\Delta y$, where U is the minimum velocity expected in the time series, and M should be at least 3.

Note that the evaluation of the domain length defined in (5.349) assumes that the angle γ is constant over the time period that defines the ≈ 1 mm convected length. The variability in $\gamma(t)$ from the averaged value in this time period, $\langle \gamma_n \rangle$ (shown in Fig. 5.213), can be accounted for by including the factor $\cos[\gamma(t) - \langle \gamma_n \rangle]$ in the summation of (5.349). However, this correction is nearly unity in practice, and does not affect the definition of the convected length.

Once the microdomain has been *created* at time record t_n, the average vorticity is calculated from the circulation around the domain. The magnitude of the velocity can be projected onto the *top* of the microdomain as $q_1 \cos(\gamma - \langle \gamma \rangle)$ and then integrated along the length. The discrete representation is given by

$$\langle q_1(t_n) \rangle = \frac{1}{2M-1} \sum_{i=n-M}^{n+M} q_1(t_i) w_i \cos[\gamma(t_i) - \langle \gamma \rangle] \,. \qquad (5.350)$$

The weighting variable is defined as $w_i = 0.5$ if $i = \pm M$ and 1 otherwise, which properly accounts for the numerical integration at the end points of the domain.

The quantity $\langle q_2(t_n) \rangle$ should be evaluated similarly for the *bottom* of the domain. Again, the cosine factors in these expressions can typically be ignored without a significant loss of accuracy, although this should be evaluated for a given measurement environment. The velocity component in the y-direction is calculated from

$$v(t_{n\pm M}) = \frac{q_1(t_{n\pm M}) + q_2(t_{n\pm M})}{2} \sin(\gamma_{n\pm M}) \qquad (5.351)$$

at both the upstream and downstream sides of the domain.

For each point of the time series (n), the vorticity is calculated from:

$$\langle \omega_n \rangle = \frac{1}{(\Delta s)(\Delta y)} \oint (\boldsymbol{V}\, \mathrm{d}\boldsymbol{s}) = \frac{v(t_{n+M}) - v(t_{n-M})}{\Delta s} - \frac{\langle q_2 \rangle - \langle q_1 \rangle}{\Delta y} \,. \qquad (5.352)$$

Following the evaluation of $\langle \omega_n \rangle$ at time t_n, the time step is incremented, and the algorithm is repeated, beginning with a new evaluation of Δs. Given the relatively high acquisition frequency required for the evaluation of the circulation domain, it is often desirable to down-sample the vorticity by skipping to the next time step as $t_{n+\langle M \rangle}$, where $\langle M \rangle$ is the average value of M that is anticipated.

Uncertainty

The ability of the probe and algorithm to recover a time series of the fluid vorticity accurately depends highly on the specific application and implementation of the technique. This section will provide a summary of possible errors and suggested methods to minimize their effects.

An important consideration for any hot-wire-based technique is proper calibration. Typically the probe is calibrated to a velocity reference that is derived from a pressure measurement as described in Sect. 5.2. With the vorticity probe, the calibration errors can be minimized by utilizing a two-step calibration procedure. First, the two parallel sensors are calibrated and fitted. The sensor with the lower standard deviation of error is then used as the master, to which the other parallel sensor and the X-wire are calibrated. This will inherently minimize calibration differences between the two parallel sensors [the difference being of obvious importance in (5.352)].

A second consideration is the effect of electronic noise on the measurement. This is of particular importance due to the relatively high-frequency response that is required. As noted earlier, the number of points needed to create the microcirculation domain should be nominally greater than six. For example, a probe with $\Delta y = 1.0$ mm and a velocity of 10 m/s requires an acquisition frequency of 60 kHz. Note that this implies the requirement that the anemometer circuitry have a frequency response at least as high. The ef-

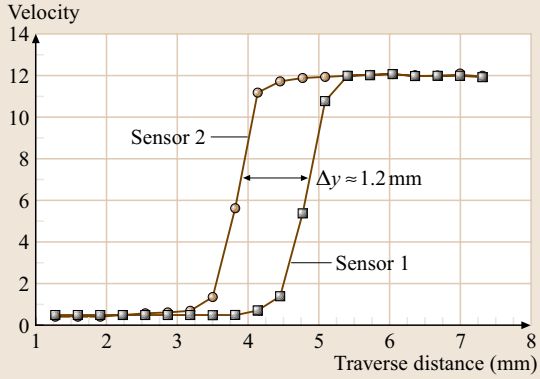

Fig. 5.214 Results from traversing the probe through a laminar shear layer. The displacement in the mean velocity curves allows the evaluation of Δy

fects of electronic noise can be minimized by using the highest-quality anemometer circuitry available, and by using an appropriately defined analog filter to reduce the contamination of high-frequency noise that is not representative of the fluid velocity fluctuations. If an analog filter is not used, then the acquisition frequency should be set sufficiently high that the integration procedure effectively filters out any high-frequency contamination. That is, $M > 10$ should be a nominal requirement.

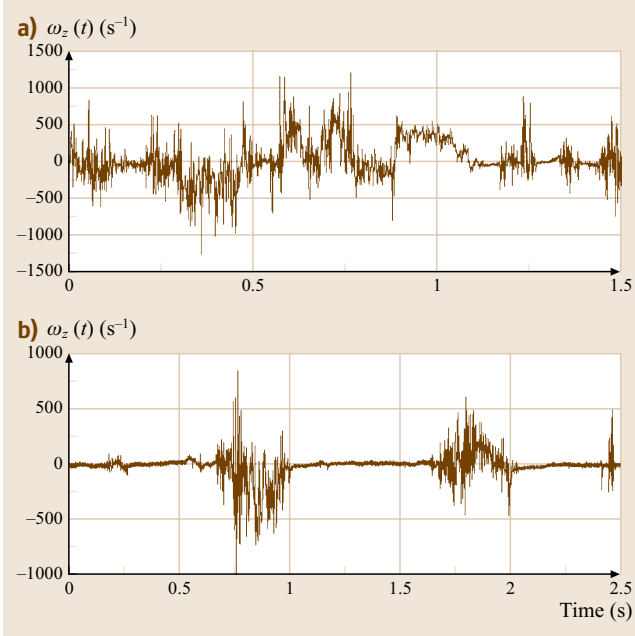

Fig. 5.215a,b Example time series of spanwise vorticity from the center of a shear layer **(a)** and the edge of a shear layer **(b)**

A source of potential error in the magnitude of the recovered vorticity is uncertainty in the distance between the parallel wires Δy. Although the support prongs may be positioned at a nominal separation, the operation of hand soldering the wires to the prongs typically results in a relatively large variability in the actual sensor placement. An effective method to determine the sensor separation is to traverse a calibrated probe through a laminar shear layer with a large mean velocity gradient. If the traversal is executed with sufficiently small spatial increments, the two parallel wires will provide identical mean velocity profiles, with a lateral shift that is equal to the probe spacing. An example is shown in Fig. 5.214. A sample probe was traversed in increments of 0.32 mm across the shear layer on one side of a calibration jet. The two sensors clearly measure an identical velocity profile that is shifted spatially, which provides an estimate of the true Δy.

As an example of the net uncertainty in the vorticity measurement, consider a probe with $\Delta y = 1.0$ mm, and a calibration range of 1–15 m/s. A typical uncertainty in the mean velocity in this range is of order 20 mm/s, with a *noise* level of about 10 mm/s. The error in the mean vorticity will then be of order $20\,\mathrm{s}^{-1}$, with a noise level of about $10\,\mathrm{s}^{-1}$. This clearly makes the technique unreliable for the recovery of the mean vorticity in many applications. However, many turbulent flows have fluctuations in vorticity that are in the range of several hundred inverse seconds in which case these errors amount to only a few percent of the total vorticity variance.

A final consideration for the uncertainty is the assumption of Taylor's hypothesis in the algorithm. Although viscous effects are often negligible in turbulent shear flows, strong pressure gradients will affect the sensors's response. Specifically, the algorithm described will result in a nonzero vorticity if the probe is subjected to a potential flow in which local streamline curvature is strong compared to the probe size. Although this effect is difficult to quantify, it is typically not considered to be as important as the calibration and electronic noise errors.

Sample Results

A recent investigation of the vorticity field of a single stream shear layer serves as an example of the use of the vorticity probe [5.811]. The flow field is also described in detail in *Morris* and *Foss* [5.812]. Essentially, the single stream shear layer, or *half-jet*, is a planar flow with a freestream on one side ($v_o = 7.1$ m/s), and a perpen-

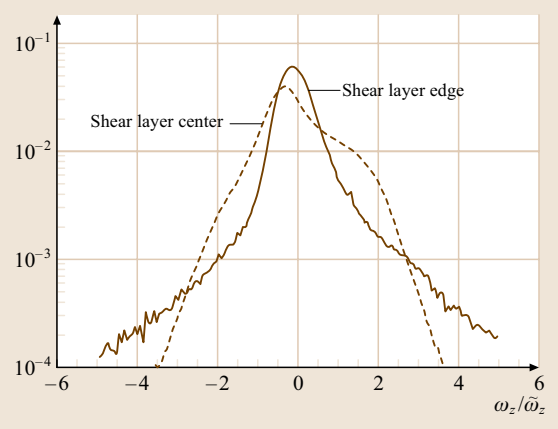

Fig. 5.216 Two examples of the vorticity PDF taken from a single stream shear layer

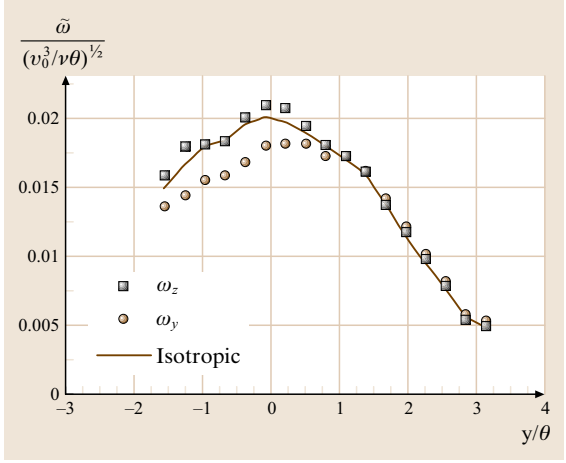

Fig. 5.217 An example profile of the rms value of two components of vorticity in a single stream shear layer. Note that the ordinate is normalized by the local momentum thickness (θ), and the vorticity is normalized by the freestream velocity (v_o), the viscosity (ν), and θ. The isotropic values were evaluated from (5.353)

dicular entrainment on the low-speed side with a speed of approximately $0.035v_o$. The coordinate system of the shear layer is specified such that x represents the streamwise direction, y represents the direction perpendicular to the plane of the shear layer, and z is the direction of spanwise homogeneity.

Two example time records of the spanwise vorticity field are given in Fig. 5.215. These data were acquired at a streamwise distance of 684 times the momentum thickness of the boundary layer at separation (9.8 mm). The first time record was acquired at a position in the center of the shear layer where the flow is fully turbulent. The rms value of the vorticity time series $\tilde{\omega}_z$ was $184\,s^{-1}$, compared to the mean shear $\partial\overline{u}/\partial y = 9\,s^{-1}$.

The second of the time records was acquired at a location near the high-speed edge of the shear layer where the flow is convectively intermittent. Specifically, relatively long periods of low vorticity levels representative of the freestream are interrupted by bursts of high levels of vorticity that contain significant high-frequency content. The rms value of the vorticity time series at this location was $\tilde{\omega}_z = 50\,s^{-1}$, compared to a nominal mean shear of zero.

From the vorticity time series, a number of stochastic measures can be computed, including spectral distributions and probability distribution functions (PDF). As an example, the complete time records from the spatial locations of Fig. 5.215 were used to compute their respective distributions (Fig. 5.216). These data show a number of interesting characteristics, most notably an exponential decrease in the PDF observed as a linear region in the semilogarithmic plot for $\omega_z/\tilde{\omega}_z > 2$. Similar features have been observed in computational solutions to isotropic turbulence [5.813].

Lastly, the vorticity probe was traversed across the shear layer in order to quantify the spatial distributions of the vorticity moments. In Fig. 5.217, the rms value of vorticity, both spanwise ($\tilde{\omega}_z$) and transverse ($\tilde{\omega}_y$), are shown with the predicted values based on single-velocity-component measurements using isotropic relations. Specifically, the time series record from one of the parallel sensors was used with Taylor's frozen-flow hypothesis to estimate the spatial derivative $\partial u/\partial x$, from which the rms vorticity was calculated [5.814] as

$$\tilde{\omega}_z^2 = 5\nu\overline{\left(\frac{\partial u}{\partial x}\right)^2}\,. \tag{5.353}$$

The agreement between the expression and the directly measured rms vorticity values shown in Fig. 5.217 is generally quite good. Although (5.353) is exact only in homogeneous and isotropic turbulence, agreement between the rms value of the vorticity time series and (5.353) can serve to verify that the probe and computer algorithm are working correctly as long as the subject flow field is not too far from equilibrium.

5.6 Thermal Transient Anemometer (TTA)

The TTA has been developed to obtain the time- and space-averaged values of the temperature and the density–velocity product of the flow through a designated area which, in this presentation, will be termed a *cell*. The complete area of interest, or segment of the total area of interest, may be used to define a cell. The former would describe, for example, the separate passages of an automotive climate control system; the latter would describe, as a second example, the 4×4 cells at the aft location of an automotive radiator. See *Foss* et al. [5.815–817] for the initial publication of this technique.

5.6.1 Operational Description

Figure 5.218 presents the multi-X pattern of the cells in a typical TTA frame. In this image, the small-diameter (≈ 0.1–0.2 mm) tungsten wire makes 15 spans across the cell width. Figure 5.218b also shows the tether locations where the tungsten wire is secured in a teflon retaining plug. In each case, the cells are intended to provide a complete representation of the flow rate and temperature for the area of interest. The 3×4 frame of Fig. 5.218 was prepared to cover the face of an automotive radiator.

Once fabricated, the resistance of the cell is measured at ambient temperature (R_a) and this value serves as the reference condition for the temperature measurement. Specifically, given (5.355) from Sect. 5.2 and

$$R_w = R_a[1 + \chi(T_w - T_a)] , \qquad (5.354)$$

the resistance of the cell (R_w) permits the temperature to be determined. Note that χ is the temperature coefficient of resistance. This is the first measurement made in the operation of the TTA.

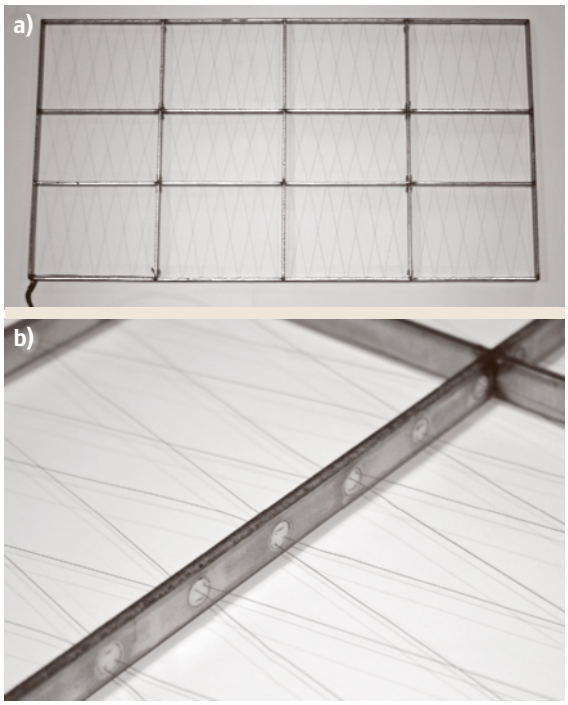

Fig. 5.218a,b A 3×4 TTA frame. **(a)** The complete frame. **(b)** A detailed view to show the tether plugs

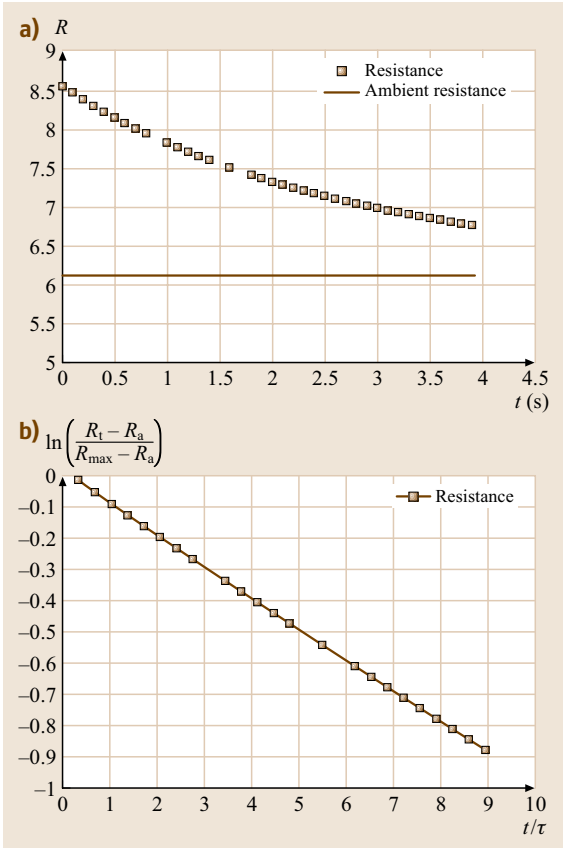

Fig. 5.219a,b $R_w(t)$ from a velocity calibration data set shown using: **(a)** algebraic coordinates, and **(b)** logarithmic–linear coordinates

The circuitry of the TTA then elevates the wire's temperature by delivering current until the wire's resistance achieves the preset value: R_{hot}. Heat transfer, as described by (5.358) in Sect. 5.2.1, results in the decrease of $R_w(t)$ from R_{hot} to R_a. Specifically, adopting a simplified lumped-parameter analysis, the temperature of the wire during the cool-down period is described as

$$mc\frac{dT_w}{dt} = -\left[hA_p(T_w - T_a) + 2k_w A_c \left|\frac{dT}{dx}\right|_{0,L}\right], \tag{5.355}$$

where m is the mass of the wire, c is its specific heat, h is the convective cooling coefficient, $A_p = \pi Ld$ is the perimeter area, k_w is the sensor's thermal conductivity, $A_c = \pi d^2/4$ is the cross-sectional area of the wire, and 0, L show the locations where the wire is tethered to the teflon plugs.

A modeling strategy, which has to be complemented with experimental data, is to characterize the conduction terms by an arbitrary length, $L(T_a)$, and a constant multiplier, λ, such that

$$2k_w A_c \left|\frac{dT}{dx}\right|_{0,L} = \lambda k_w A_c \frac{(T - T_a)}{L}. \tag{5.356}$$

The designation $L(T_a)$ is made to recognize that the *effective conduction length* may be a function of the ambient temperature. Similarly, k_w is a known function of temperature and this will be incorporated into the conduction term of response question (5.360).

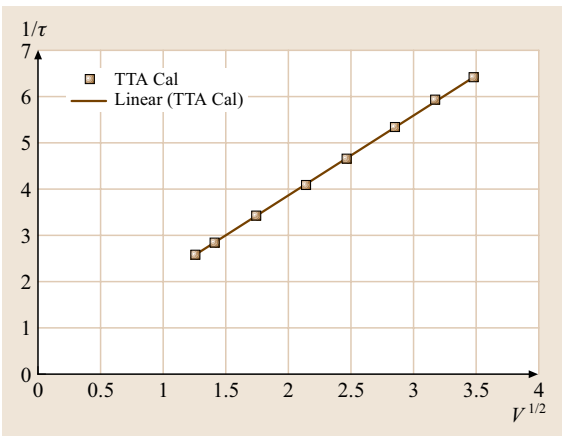

Fig. 5.220 Representative velocity calibration data for the cell of Fig. 5.219

Given the definition of the Nusselt number (Nu), the convection term can be written as

$$hA_p(T_w - T_a) = \left[\frac{\mathrm{Nu}k_f}{d}\right](T_w - T_a). \tag{5.357}$$

The nominal temperatures and the calibration and use of the TTA in air means that the influence of the Prandtl number on Nu can be neglected. Hence, the standard relationship for a cylinder heat-transfer problem

$$\mathrm{Nu} = C\left(\frac{Vd}{\nu}\right)^{0.5}, \tag{5.358}$$

can be used in (5.357) with the result

$$\text{convection term} = \frac{Ck_f}{d^{0.5}\nu_f^{0.5}}V^{0.5}. \tag{5.359}$$

Hence, (5.355) can be written as

$$\frac{d(T_w - T_a)}{(T_w - T_a)} = -\left\{A\left[\frac{k_w(T_a)}{k_w(T_{a-cal})}\right] + \frac{Bk_f}{\nu_f^{0.5}}V^{0.5}\right\}dt \tag{5.360}$$

or

$$\frac{T_w - T_a}{T_{hot} - T_a} = \exp\left(-\frac{t}{\tau}\right), \tag{5.361}$$

where

$$\frac{1}{\tau} = \left\{A\left[\frac{k_w(T_a)}{k_w(T_{a-cal})}\right] + \frac{Bk_f}{\nu_f^{0.5}}V^{0.5}\right\}. \tag{5.362}$$

5.6.2 Representative Results

The $R_w(t)$ values from a velocity calibration are shown in Fig. 5.219. The tungsten sensor wire diameter was 0.175 mm for these data. The standard deviation between the measured values and the exponential fit was 0.69 ms. Hence, these data provided $\tau = (293 \pm 0.69)$ ms.

Figure 5.220 shows the balance of the calibration results for the cell of Fig. 5.219. These data are displayed as suggested by (5.362). The standard deviation of the fitted equation to the separate (τ, V) data pairs is 0.0118 m/s. This *small* value attests to the veracity of (5.362) to represent the effective cooling of the sensor wire at the calibration temperature.

5.7 Sonic Anemometry/Thermometry

5.7.1 Definition

Similar to hot-wire anemometry and LDA, ultrasonic anemometry (or, as it is more commonly in the literature, sonic anemometry) is a measurement technique that is used to obtain multiple components of instantaneous velocity at a point in space.

In addition to the three velocity components, most modern sonic anemometers also provide virtual temperature (T_v) measurements. The virtual temperature is the temperature at which dry air has the same density as moist air at the same pressure [5.818]. Using this definition, a convenient form of the equation of state may be written as $P = \rho R_d T_v$, where P is total pressure of air including moisture (Pa), ρ is the total density of air (kg/m^3) and R_d is the gas constant for dry air (287 J/(kg K)) [5.819]. The virtual temperature is given by $T_v = T(1+0.61q)$, where T is the absolute temperature. Here, $q = M_w/(M_w + M_d)$ is the specific humidity, defined as the ratio of the mass of moist air (M_w) to the total mass of air ($M_w + M_d$).

Sonic anemometer/thermometers (SATs) are very robust: they have no moving parts, require infrequent calibration, and can operate in harsh atmospheric environmental conditions. SATs can be left out in the field for extended periods of time with little maintenance compared to hot-wire, cup, and propeller anemometers. These qualities combined with the fact that the length and time scales that are resolved with current sonic anemometer technology are quite large (compared to fast-response engineering techniques) have made this technique popular with researchers probing the atmospheric boundary layer [5.820]. While sonic anemometers are quite robust, the response of sonic anemometers could be affected by intense rain, severe contamination (dirt, dust, etc.), ice formation, and structural vibrations. All of these effects are areas of current research efforts [5.821]. Table 5.8 provides a comparison of the main characteristics of the following three traditional atmospheric boundary-layer measuring techniques: sonic, cup, and propeller anemometers.

In recent years, many researchers have used SATs in conjunction with other instrumentation to calculate covariances using so-called eddy correlation or eddy covariance techniques. The SAT allows correlations of velocity components and the virtual temperature to be readily computed. For example, useful quantities such as Reynolds stresses ($\overline{u_i' u_j'}$) and turbulent heat fluxes ($\overline{u_i' T_v'}$) are easily calculated from the time series output from the SAT. Additional physical quantities such as the vertical turbulent concentration fluxes of CO_2 and water vapor are regularly measured using this technique [5.822] For example, gas sensors can be collocated with a SAT to allow quantities such as $\overline{u_i' \chi'}$ to be calculated (where χ represents the concentration of the tracer gas). As a result of the ability to calculate such useful quantities, SAT use has spread to a variety of applications including air quality [5.823, 824], wind energy [5.825, 826], urban boundary layer [5.827, 828], forest canopy and agriculture [5.829], hydrological [5.830], and trace-gas budget studies (often related to global climate change [5.831]). Additionally, SATs have been used as an option for exploration of extraterrestrial atmospheres [5.832, 833], and low-pressure gas anemometry. There is also a flow meter technique based on sonic anemometry [5.834].

The type of sonic anemometry described in this section has been used by engineers and micrometeorologists since the late 1950s [5.835]. Historically two types of sonic anemometers have been used, pulse and continuous wave. Pulse anemometers measure time delays between ultrasonic pulses (defined as having frequencies > 20 kHz) while continuous-wave anemometers measure phase shifts [5.836–838]. Using this technol-

Table 5.8 Summary of the main operational characteristics of sonic, cup, and propeller anemometers

System	Calibration	Maintenance	Sampling frequency	Three components of wind speed?	Temperature measurement
Sonic anemometer/ thermometer	Initial	Cleaning	Up to 100 Hz	Yes (for three-path models)	Yes (sonic temperature)
	Sonics present some weaknesses that are considered in the text				
Cup anemometer	Periodic	Intense	Distance constant > 1 m	No	No
	Mobile parts, slow response, influenced by turbulence, influenced by vertical velocity components.				
Propeller anemometer	Periodic	Moderate	Distance constant > 1 m	Estimate for three-probe configurations	No
	Mobile parts, slow response, influenced by turbulence and misalignment				

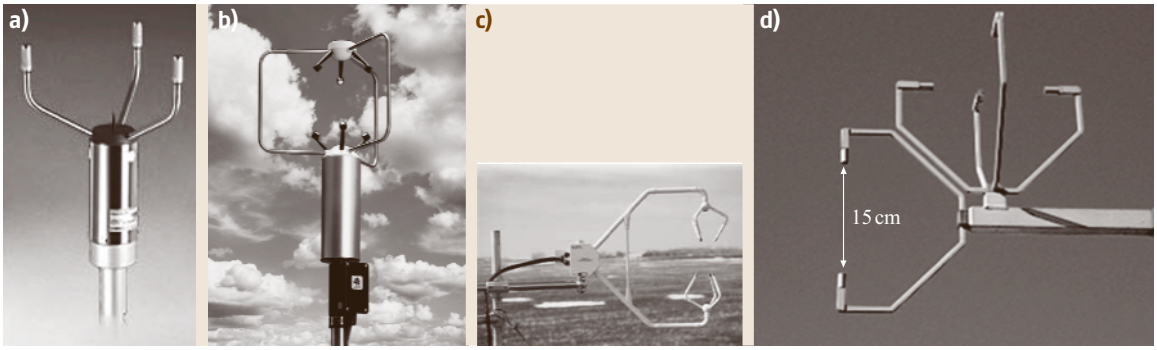

Fig. 5.221a–d Various sonic anemometer configurations: **(a)** 2-D sonic anemometer with vertical mounting base, **(b)** 3-D SAT with vertical mounting base, **(c)** 3-D SAT with horizontal mounting nonorthogonal pulse paths, **(d)** 3-D SAT with horizontal mounting and orthogonal pulse paths. Photographs are courtesy of **(a)** Vaisala, Inc. **(b)** RM Young Company, **(c)** Campbell Scientific, Inc. and **(d)** Applied Technologies, Inc.

ogy, a SAT measures a *line-averaged* velocity of the flow field along the acoustic path. The line averaging represents the main limitation to the instrument's frequency response [5.818]. Today most manufacturers use pulse-based anemometers. Figure 5.221 shows four different sonic anemometers currently in manufacture, with varying path lengths and probe configurations.

5.7.2 Measurement Principles

Most modern sonic anemometers determine velocity components along a known path length by measuring the difference in transit times of acoustic pulses sent simultaneously in opposite directions between two sensors. Multiple paths oriented at various angles allow for the measurement of multiple components of the velocity vector. A number of excellent sources exist that describe the fundamental principles of sonic anemometers [5.818, 836, 839]. For most devices, the ultrasonic pulse is generated using piezoelectric transducers that act as both the transmitter and receiver. In some particular cases, when a sonic anemometer is used in other atmospheres (i. e., gases different than air or different conditions, leading to different sound speed) the transducer technology may differ. Piezoelectric transducers present an acoustic impedance on the order of $1.2\times10^7\,\mathrm{kg/m^2s}$, whereas the Earth's air presents an acoustic impedance of $400\,\mathrm{kg/m^2s}$. According to [5.832], the ratio of these values results in an acceptable attenuation of an ultrasound signal when it is transmitted from a piezoelectric sensor in the Earth's atmosphere. However, for instance in the Martian case, the impedance ratio would be unacceptable; the extremely low acoustic impedance of the Martian atmosphere ($3\,\mathrm{kg/m^2s}$) would lead to extreme attenuation of the ultrasound signal transmitted from a piezoelectric sensor. In this case, capacitive transducers with acoustic impedances of $1000\,\mathrm{kg/m^2s}$ can be used as an alternative to piezoelectric transducers.

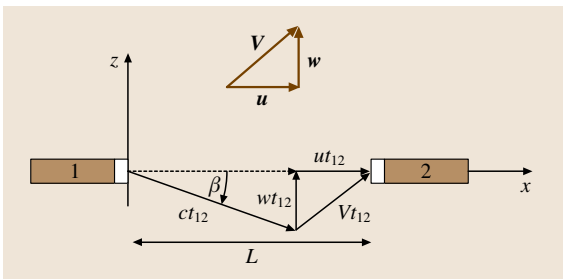

Fig. 5.222 2-D schematic of the ray vectors associated with an ultrasonic pulse being sent from the transmitter (1) to the receiver (2) in a steady, uniform velocity field

The description given here is for an ultrasonic pulse-type anemometer and is adapted from *Kaimal* [5.836], *Kaimal* and *Finnigan* [5.818] and *Cuerva* and *Sanz-Andres* [5.839]. The basic principles of operation are best understood by considering a steady, uniform, 2-D flow field with an along-path velocity component of u and a velocity component normal to the path of w, as shown in Fig. 5.222. The time of flight for a pulse sent from transducer 1 to traverse to transducer 2 will be denoted by t_{12}. Similarly a pulse sent from transducer 2 to 1 will have a time of flight t_{21}. The following equation may be written using the ray vectors shown in Fig. 5.222 for a pulse being transmitted from sensor 1 to 2:

$$ct_{12}\cos\beta + ut_{12} = L\,, \tag{5.363}$$

where, $\sin\beta = w/c$, c is the speed of sound, and L is the distance between transducers 1 and 2. A similar equation may be written for a pulse traveling from sensor 2 to 1. The associated times of flight are then

$$t_{12} = \frac{L}{c\cos\beta + u} \tag{5.364}$$

and

$$t_{21} = \frac{L}{c\cos\beta - u} \,. \tag{5.365}$$

The transmitted time difference is then

$$\Delta t = t_{21} - t_{12} = \frac{2uL}{c^2\cos^2\beta - u^2} \,. \tag{5.366}$$

Substituting $\sin^2\beta + \cos^2\beta = 1$ and $u^2 + w^2 = V^2$ gives

$$\Delta t = \frac{2uL}{c^2 - V^2} \,. \tag{5.367}$$

For small-Mach-number flow, $V \ll c$, the along-path wind component simplifies to

$$u = \frac{c^2}{2L}\Delta t \,. \tag{5.368}$$

Equation (5.368) requires the speed of sound to be estimated. Following [5.836], the effect of temperature and water-vapor content can be accounted for by approximating the speed of sound as $c^2 = C_T T(1 + 0.32e/p)$, where T is the absolute temperature (K), e is the vapor pressure of water in air, $C_T = 403\,\mathrm{m^2/s^2\,K}$ and p is the atmospheric pressure. The virtual temperature is approximated as $T_v = T(1 + 0.32e/p)$ so that $c^2 = C_T T_v$. This can be related to the familiar definition of the speed of sound given by $c^2 = \gamma p/\rho$, where $\gamma = C_p/C_v$ is the ratio of specific heats at constant pressure and volume, and ρ is the density of air ($\mathrm{kg/m^3}$). Substituting the ideal gas relationship with the virtual temperature, $p = \rho R_d T_v$, yields $c^2 = \gamma R_d T_v$.

Most SATs however, use a single path to send pulses simultaneously from sensor 1 to 2 and from sensor 2 to 1. These instruments use electronics to subtract time inverses directly, namely

$$\frac{1}{t_{12}} - \frac{1}{t_{21}} = \frac{2u}{L} \,. \tag{5.369}$$

This yields the velocity along the path without the need to calculate the speed of sound separately. The resulting equation for the velocity is simply

$$u = \frac{L}{2}\left(\frac{1}{t_{12}} - \frac{1}{t_{21}}\right) \,. \tag{5.370}$$

It should be noted that, in a real configuration, the pulses are not sent simultaneously because of physical limitations (it is technically impossible for a sensor to act as both an emitter and receiver simultaneously). In practice there is a time delay between shots (z_B) that is on the order of 0.001 s, depending on the manufacturer. The effect of this time delay between pulses must be taken into account when a sonic anemometer measures the turbulence velocity and temperature spectra [5.839].

As shown in *Kaimal* and *Finnigan* [5.818] the time-inverses method also allows the speed of sound to be calculated directly, hence providing an estimate of the virtual temperature. Squaring the sum of the inverse flight times yields

$$\left(\frac{1}{t_{12}} + \frac{1}{t_{21}}\right)^2 = \frac{4c^2}{L^2}\cos^2\beta = \frac{4c^2}{L^2}\left(1 - \frac{w^2}{c^2}\right) \,. \tag{5.371}$$

Equation (5.371) can then be solved for the speed of sound,

$$c^2 = \frac{L^2}{4}\left(\frac{1}{t_{12}} + \frac{1}{t_{21}}\right)^2 + w^2 \,. \tag{5.372}$$

Using the approximation derived above, $c^2 = C_T T_v$ yields the following expression for the virtual temperature

$$T_v = \frac{L^2}{4C_T}\left(\frac{1}{t_{12}} + \frac{1}{t_{21}}\right)^2 + \frac{w^2}{403} \,. \tag{5.373}$$

For a multicomponent anemometer, w in (5.373) can be calculated using the velocity components from the other axes of the anemometer. The exact formulation

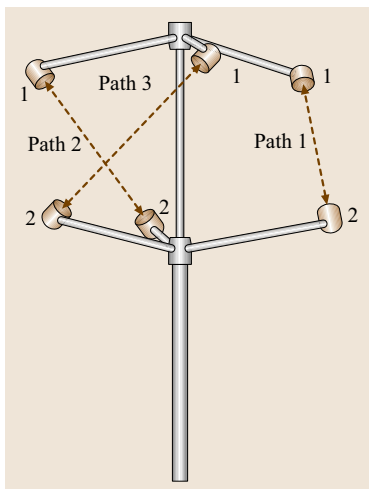

Fig. 5.223 Schematic of a commercial 3-D sonic anemometer indicating the three pathlines

Table 5.9 Pulse sequence and timing for a METEK USA-1 sonic anemometer. The activated path refers to the paths shown in Fig. 5.223, while the path sense refers to the transmitter-to-receiver communication shown in Fig. 5.222

Activated path	Path sense	Time (ms)
1	1-2	z_B 1.14
1	2-1	z_B 1.14
2	1-2	z_B 1.14
2	2-1	z_B 1.14
3	1-2	z_B 1.14
3	2-1	z_B 1.14
Electronic and computation		z_E 0.88

for w depends on the geometry of the SAT axes. This temperature is actually the sonic temperature (the temperature reported by the SAT) but for most applications represents the virtual temperature quite well [5.840]. As noted by [5.841], most SATs actually determine sonic temperature as an average over multiple paths. In that case, (5.373) represents the sonic temperature obtained for one path.

For a three-path sonic anemometer (Fig. 5.223), a full sequence leading to a complete measurement of the wind-speed vector consists of at least six shots of ultrasound pulses, two pulses per acoustic path. The time required to compute the wind-speed vector from individual path measurements is limited by the time delay z_B between consecutive pulses and the time after the sixth pulse z_E required to reset the electronics. Table 5.9 shows a typical pulse sequence, which lasts $6z_B + z_E = 7.72$ ms [5.842].

In general, SATs do not provide the direct measurements from the individual pulse sequence. Instead they carry out averaging processes on them. These processes, normally called *block averaging*, are manufacturer dependent. A typical scheme for this process is included in Table 5.10.

5.7.3 Device Characteristics, Accuracy, and Limitations

Most SATs attributes vary across manufactures. Typical sensor measurement paths are approximately 0.10–0.20 m. The velocity range of most sensors is approximately ±30 m/s with velocity accuracies in the range of ±0.02–0.05 m/s. Temperature accuracy tends to vary much more significantly over a range of ±0.1–2.0 °C. The sampling frequency range is typically up to about 100 Hz. Some manufactures also allow for oversampling of wind components and output of an average filtered signal at a lower frequency, as discussed above, via a block averaging process (Table 5.10).

Table 5.10 Typical pulse firing sequence and block averaging for a gill wind research sonic anemometer. The time delay between pulses is $z_B = 0.001$ s; the data delivery speed is 168 samples/s

Path	Pulse sense	Start time	End time
Path 1	1–2	0	z_B
	2–1	z_B	$2z_B$
Path 2	1–2	$2z_B$	$3z_B$
	2–1	$3z_B$	$4z_B$
Path 3	1–2	$4z_B$	$5z_B$
	2–1	$5z_B$	$6z_B$

Mode	Averaged measurements	Final number of averaged measurements delivered (true number of samples per second)
1	8	21 (168/8)
2	3	56 (168/3)

The frequency response of a SAT is limited by the attenuation in the spatial response imposed by line averaging along a path. *Kaimal* [5.818] and *Kaimal* and *Finnigan* [5.818] have suggested as a *rule of thumb* that the low-pass filtering attenuation distortions are confined to spectral wavelengths $\lambda < 2\pi L$. If the paths of sensors are separated (e.g., nonintersecting paths, as in Fig. 5.221d) then, the response of the turbulent fluxes (e.g., $\overline{u_i' T_v'}$ or $\overline{u_i' u_j'}$) calculated between the sensors is compromised if $\lambda < 2\pi s$, where s is the separation distance between the midpoints of the pulse paths. For a typical SAT with intersecting sensor paths and a sensor separation of $L = 0.10$ m (e.g., Fig. 5.221c), spectral attenuation will occur for wavelengths less than about 0.63 m. Using Taylor's frozen turbulence hypothesis to express this limit in terms of frequency for $L = 0.1$ m and a typical wind speed of $u = 10$ m/s leads to a limiting frequency of $f = u/(2\pi L) \approx 15.9$ Hz.

These *rules of thumb* were developed assuming a homogeneous turbulent velocity field [5.843]. *Cuerva* and *Sanz-Andres* [5.839] have investigated the effect of this assumption on measurements made on more-realistic flow fields. In particular, they investigated line-averaging effects for a nonsteady, nonuniform velocity field through the sensor. They found that the flow Mach number and the time delay between pulses increases the wavelength at which spectral attenuation begins. In some cases, the combination of line averaging and geometry effects leads to overestimation of the spectra instead of spectral attenuation.

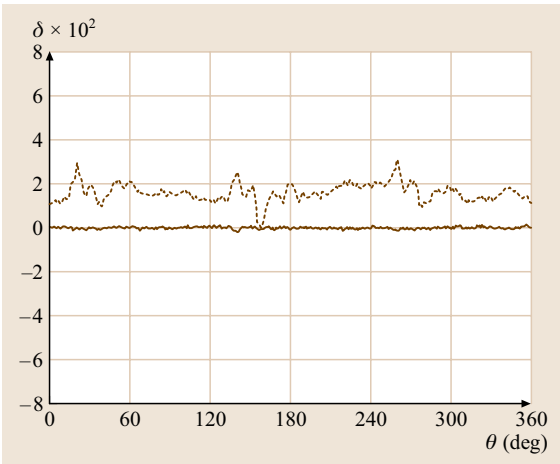

Fig. 5.224 Difference between the measured wind-speed magnitude $|\boldsymbol{u}|^{\mathrm{M}}$ and the actual magnitude $|\boldsymbol{u}|$ as a percentage of the actual one (represented as δ) versus the incidence angle θ. The *dotted line* represents the uncorrected response (0–3%) of the anemometer and the *solid line* the corrected response after calibration in wind tunnel [5.848]

As a result of the line averaging, care must be taken when placing the sensors near surfaces. For use in the atmospheric surface layer, the minimum distance between the center of the probe and the ground has been suggested to be $z_{\min} = 8\pi L$ [5.844]. *Wamser* et al. [5.845] however, showed that the maximum attenuation occurs in the vertical velocity variance near the ground and that the $z_{\min}$ restriction can be relaxed down to about $z_{\min} = 4L$, or just less than one meter for most SATs over flat terrain. Additionally, depending on the application, the block averaging process can lead to non-negligible effects of the determination of turbulence properties [5.846, 847].

The effect of aerodynamic disturbances associated with the acoustic path supporting structures on the measurement of averaged characteristics of the wind-speed vector must be considered. This effect is highly manufacturer dependent [5.849]. Figure 5.224 shows the corrections in the measurement of the average value of the total magnitude of the wind speed as a function of the angle of incidence of the wind-speed vector for a commercial sonic anemometer unit. These corrections are easily determined by a calibration process and can be implemented internally (by the manufacturer) or during postprocessing by the user.

In general, it can be stated that two phenomena:

1. aerodynamic interference in the acoustic paths due to supporting structures
2. the line-averaging process

make the sonic anemometer response non-isotropic (i. e., directional), both when measuring averaged and turbulent magnitudes. The characteristics of this directional response depend on the sensor design.

Coordinate Transformation Methods

The alignment of a SAT is of great importance since misalignment produces a deviation between the assumed probe coordinate system and the actual one. SATs are often aligned in the field such that the y-axis points northward, the x-axis eastward, and the z-axis normal to the surface. Another common horizontal alignment technique is to orient the anemometer to limit flow distortion as much as possible based on the expected winds. Alignment is typically accomplished

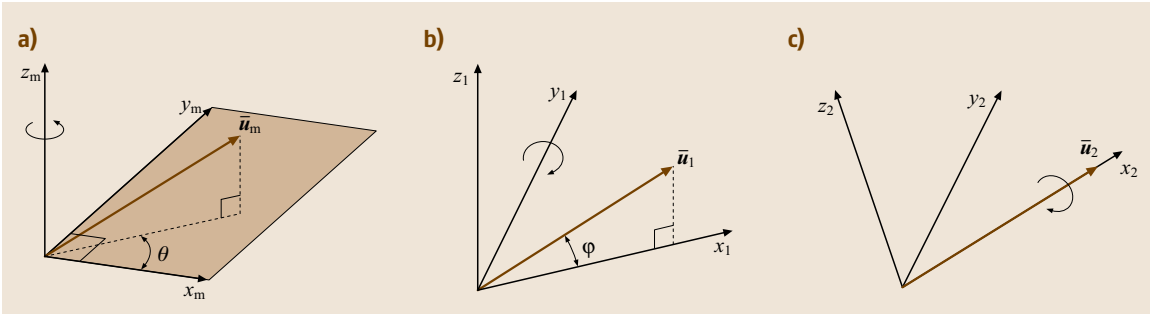

Fig. 5.225a–c Schematic of the coordinate rotation technique showing **(a)** the first rotation θ about the z_{m} axis (yaw), **(b)** the second rotation φ about the y_1 axis (pitch) and **(c)** the final rotation ψ about the x_2 axis (roll). $\overline{\boldsymbol{u}}_{\mathrm{m}} = (\overline{u}_{\mathrm{m}}, \overline{v}_{\mathrm{m}}, \overline{w}_{\mathrm{m}})$, $\overline{\boldsymbol{u}}_1 = (\overline{u}_1, 0, \overline{w}_1)$, $\overline{\boldsymbol{u}}_2 = (\overline{u}_2, 0, 0)$ are the average velocity vectors referred to in the sonic anemometer coordinate system $(x_{\mathrm{m}}, y_{\mathrm{m}}, z_{\mathrm{m}})$, after the first rotation with a reference system (x_1, y_1, z_1), and the second rotation with a reference system (x_2, y_2, z_2), respectively

using tools such as inclinometers, compasses, global positioning units, and levels. Unfortunately, some level of misalignment is unavoidable and causes the various components of the velocity field to be incorrectly redistributed. As noted by [5.850], this can be particularly problematic when calculating velocity covariances over sloping terrain where the SAT is usually either aligned with the vertical component normal to the slope or leveled. *Wilczak* et al. [5.850] review several correction/coordinate transformation algorithms that are useful for sonic anemometers. Following [5.818, 850] and [5.851] the most widely used coordinate transformation technique is presented below, followed by *Wilczak* et al.'s [5.850] alternative method. These methods transform velocities in the measured coordinate system into a streamline coordinate system. This operation is very useful for comparing wind-tunnel data or theory to atmospheric surface layer data. It is also particularly useful for investigating turbulent surface exchanges such as the turbulent vertical flux of momentum or a scalar (e.g., $\overline{u_i' \chi'}$ or $\overline{u_i' u_j'}$). The coordinate transformations are most appropriate over horizontally homogeneous, uniformly sloping terrain (e.g., in the inertial layer above forests, buildings, fields, etc.).

A transformation of the measured coordinate system into a streamline coordinate system is a transformation between two orthogonal coordinates systems and is shown schematically in Fig. 5.225. This is a rotation operation that can be represented in matrix form as

$$\begin{pmatrix} u_\mathrm{f} \\ v_\mathrm{f} \\ w_\mathrm{f} \end{pmatrix} = \boldsymbol{A} \begin{pmatrix} u_\mathrm{m} \\ v_\mathrm{m} \\ w_\mathrm{m} \end{pmatrix} , \quad \boldsymbol{A} = \boldsymbol{T} \cdot \boldsymbol{S} \cdot \boldsymbol{R} , \tag{5.374}$$

where u_m, v_m, and w_m are the instantaneous velocity components in the measured sonic coordinate system, and u_f, v_f, and w_f are the final instantaneous velocity components after the transformation. As noted by *Sozzi* [5.851], a method to obtain an approximation of $\boldsymbol{A}$ is to combine one or more rotations in order to align the coordinate system axes in which the measurements where made (x_m, y_m, z_m with unit vectors $\boldsymbol{i}_\mathrm{m}$, $\boldsymbol{j}_\mathrm{m}$, and $\boldsymbol{k}_\mathrm{m}$) with the tangent, binormal, and principal normal of the local streamline (x_f, y_f, z_f with unit vectors $\boldsymbol{i}_\mathrm{f}$, $\boldsymbol{j}_\mathrm{f}$, and $\boldsymbol{k}_\mathrm{f}$) as shown in Fig. 5.226 using

$$\boldsymbol{T} = \begin{pmatrix} 1 & 0 & 0 \\ 0 & \cos\psi & \sin\psi \\ 0 & -\sin\psi & \cos\psi \end{pmatrix} ,$$

$$\boldsymbol{S} = \begin{pmatrix} \cos\varphi & 0 & \sin\varphi \\ 0 & 1 & 0 \\ -\sin\varphi & 0 & \cos\varphi \end{pmatrix} ,$$

$$\boldsymbol{R} = \begin{pmatrix} \cos\theta & \sin\theta & 0 \\ -\sin\theta & \cos\theta & 0 \\ 0 & 0 & 1 \end{pmatrix} .$$

Here, ψ, φ, and θ are the roll, pitch, and yaw rotation angles, respectively, taken as positive counterclockwise about each axis. The principal normal is defined by the direction in which the streamline is curving most rapidly [5.818]. Often in practice the estimation procedure is further simplified with a rougher estimate that only consists of the first two rotations, or a so-called double rotation, first about the z_m axis and then about the y_1 axis.

The procedure is typically broken up into three rotation operations. If x_m, y_m, z_m is the measuring coordinate system of the sonic anemometer, the first operation is a rotation about the vertical (z_m) axis that aligns the new x-coordinate with the mean streamwise wind direction, i. e., $(x_\mathrm{m}, y_\mathrm{m}, z_\mathrm{m}) \rightarrow (x_1, y_1, z_1)$ so that the mean spanwise velocity is zero:

$$\begin{pmatrix} u_1 \\ v_1 \\ w_1 \end{pmatrix} = \boldsymbol{R} \begin{pmatrix} u_\mathrm{m} \\ v_\mathrm{m} \\ w_\mathrm{m} \end{pmatrix}$$

or,

$$\begin{aligned} u_1 &= u_\mathrm{m} \cos\theta + v_\mathrm{m} \sin\theta , \\ v_1 &= -u_\mathrm{m} \sin\theta + v_\mathrm{m} \cos\theta , \\ w_1 &= w_\mathrm{m} , \end{aligned} \tag{5.375}$$

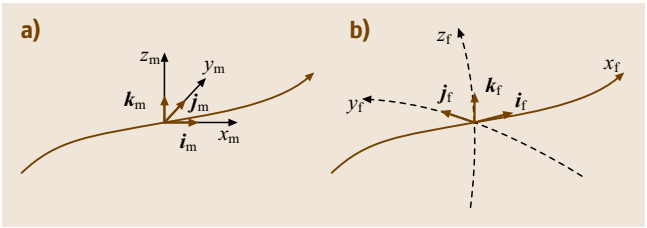

Fig. 5.226a,b Schematic of (a) a streamline passing through the sonic anemometer coordinate system and (b) the streamline coordinate system as discussed in the text (after [5.852]). $\boldsymbol{i}_\mathrm{f}$ is tangent to the streamline, $\boldsymbol{j}_\mathrm{f}$ is binormal to the streamline, and $\boldsymbol{k}_\mathrm{f}$ is normal to the streamline. As noted by *Finnigan* [5.852], the z_f coordinate lines are tangent to the field of $\boldsymbol{k}_\mathrm{f}$ vectors, the y_f coordinate lines are tangent to the field of $\boldsymbol{j}_\mathrm{f}$ vectors, and the streamlines form the x_f coordinates

where

$$\theta = \tan^{-1}\left(\frac{\overline{v}_\mathrm{m}}{\overline{u}_\mathrm{m}}\right), \quad \sin\theta = \frac{\overline{v}_\mathrm{m}}{\sqrt{\overline{u}_\mathrm{m}^2 + \overline{v}_\mathrm{m}^2}} \quad \text{and}$$

$$\cos\theta = \frac{\overline{u}_\mathrm{m}}{\sqrt{\overline{u}_\mathrm{m}^2 + \overline{v}_\mathrm{m}^2}} . \tag{5.376}$$

In these equations, $\overline{v}_\mathrm{m}$ and $\overline{u}_\mathrm{m}$ are mean velocities in the measured sonic anemometer coordinate system. Therefore, the transformation is based on the choice of the mean velocity. This should be an ensemble average, however, practically it is usually estimated with time averages. After the first rotation, $\overline{v}_1 = 0$ by definition. Once θ is determined, either the time series can be rotated using (5.375) or the following equations for mean flow and turbulent stresses can be used

$$\begin{aligned}
\overline{u}_1 &= \overline{u}_\mathrm{m}\cos\theta + \overline{v}_\mathrm{m}\sin\theta , \\
\overline{v}_1 &= -\overline{u}_\mathrm{m}\sin\theta + \overline{v}_\mathrm{m}\cos\theta , \\
\overline{w}_1 &= \overline{w}_\mathrm{m} , \qquad (5.377) \\
\overline{u'^2_1} &= \overline{u'^2_\mathrm{m}}\cos^2\theta + \overline{v'^2_\mathrm{m}}\sin^2\theta + 2\overline{u'_\mathrm{m}v'_\mathrm{m}}\sin\theta\cos\theta , \\
\overline{v'^2_1} &= \overline{u'^2_\mathrm{m}}\sin^2\theta + \overline{v'^2_\mathrm{m}}\cos^2\theta - 2\overline{u'_\mathrm{m}v'_\mathrm{m}}\sin\theta\cos\theta , \\
\overline{w'^2_1} &= \overline{w'^2_\mathrm{m}} , \qquad (5.378) \\
\overline{u'_1v'_1} &= \overline{u'_\mathrm{m}v'_\mathrm{m}}(\cos^2\theta - \sin^2\theta) \\
&\quad + \sin\theta\cos\theta\left(\overline{v'^2_\mathrm{m}} - \overline{u'^2_\mathrm{m}}\right) , \\
\overline{u'_1w'_1} &= \overline{u'_\mathrm{m}w'_\mathrm{m}}\cos\theta + \overline{v'_\mathrm{m}w'_\mathrm{m}}\sin\theta , \\
\overline{v'_1w'_1} &= -\overline{u'_\mathrm{m}w'_\mathrm{m}}\sin\theta + \overline{v'_\mathrm{m}w'_\mathrm{m}}\cos\theta . \qquad (5.379)
\end{aligned}$$

As shown in Fig. 5.225b, the second rotation is about the y_1 axis and forces $\overline{w}_2 = 0$. The velocities are given by

$$\begin{aligned}
u_2 &= u_1\cos\varphi + w_1\sin\varphi , \\
v_2 &= v_1 \\
w_2 &= -u_1\sin\varphi + w_1\cos\varphi , \qquad (5.380)
\end{aligned}$$

where

$$\varphi = \tan^{-1}\left(\frac{\overline{w}_1}{\overline{u}_1}\right) ,$$

$$\sin\varphi = \frac{\overline{w}_1}{\sqrt{\overline{u}_1^2 + \overline{w}_1^2}} \quad \text{and}$$

$$\cos\varphi = \frac{\overline{u}_1}{\sqrt{\overline{u}_1^2 + \overline{w}_1^2}} . \tag{5.381}$$

Equations similar to (5.377–5.379) can then be easily obtained. This completes the double rotation and aligns x_2 with the mean wind direction. The last rotation or triple rotation rotates the coordinate system such that the final z-axis is normal to the mean wind trajectory [5.851] (Fig. 5.224b). According to [5.850] there are an infinite number of rotations that satisfy $\overline{v}_\mathrm{f} = \overline{w}_\mathrm{f} = 0$. It has been suggested that the approximation $\overline{v'_\mathrm{f}w'_\mathrm{f}} = 0$ can be made over flat land [5.818, 853]. If this is done, the following equations result:

$$\begin{aligned}
u_\mathrm{f} &= u_2 , \\
v_\mathrm{f} &= v_2\cos\psi + w_2\sin\psi , \\
w_\mathrm{f} &= -v_2\sin\psi + w_2\cos\psi , \qquad (5.382)
\end{aligned}$$

where

$$\psi = \frac{1}{2}\tan^{-1}\left(\frac{2\overline{v'_2w'_2}}{\overline{v'^2_2} - \overline{w'^2_2}}\right) . \tag{5.383}$$

Since the third rotation is based on a strong (and likely incorrect for complex flow) constraint on the turbulent stress, it should be used with extreme caution. *Finnigan* [5.852] recommends that the third rotation should not be applied but that the general procedure should be used.

Planar Fit Method

As an alternative, *Wilczak* et al. [5.850] suggest a *planar-fit* technique to determine the pitch and roll angles of the anemometer, which reduces the error associated with the second and third rotations described above. The method uses average velocity vectors from an ensemble of averaging periods to define a new best-fit x–y plane using multiple linear regression. This plane is defined by a pitch and roll angle with respect to the sonic anemometer coordinate system similar to that described above. This regression forces the average vertical velocity to be zero (i. e., $\overline{w}_\mathrm{pf} = 0$). First, the planar-fit velocity components are determined through a partial rotation, namely

$$\begin{pmatrix} u_\mathrm{pf} \\ v_\mathrm{pf} \\ w_\mathrm{pf} \end{pmatrix} = \boldsymbol{T}(\psi_\mathrm{pf})\cdot\boldsymbol{S}(\varphi_\mathrm{pf})\cdot\begin{pmatrix} u_\mathrm{m} \\ v_\mathrm{m} \\ w_\mathrm{m} \end{pmatrix} = \boldsymbol{P}\cdot\begin{pmatrix} u_\mathrm{m} \\ v_\mathrm{m} \\ w_\mathrm{m} \end{pmatrix} , \tag{5.384}$$

where $\boldsymbol{P} = \boldsymbol{T}(\psi_\mathrm{pf})\boldsymbol{S}(\varphi_\mathrm{pf})$ and the planar-fit pitch (φ_pf) and roll (ψ_pf) angles are determined from a least-squares fitting of the mean velocity vectors to a single plain. The final rotated velocities ($\overline{u}_\mathrm{f} \neq 0$, $\overline{v}_\mathrm{f} = 0$ and $\overline{w}_\mathrm{f} = 0$) are obtained by rotating the planar-fit velocities through the

appropriate yaw angle θ_{pf} using (5.385) as

$$\begin{pmatrix} u_{\mathrm{f}} \\ v_{\mathrm{f}} \\ w_{\mathrm{f}} \end{pmatrix} = \boldsymbol{R}(\theta_{\mathrm{pf}}) \cdot \begin{pmatrix} u_{\mathrm{pf}} \\ v_{\mathrm{pf}} \\ w_{\mathrm{pf}} \end{pmatrix} , \tag{5.385}$$

where

$$\theta_{\mathrm{pf}} = \tan^{-1}\left(\frac{\overline{v}_{\mathrm{pf}}}{\overline{u}_{\mathrm{pf}}}\right) . \tag{5.386}$$

Here, $\overline{u}_{\mathrm{pf}}$ and $\overline{v}_{\mathrm{pf}}$ represent average values taken for each averaging period. To determine the planar-fit pitch (φ_{pf}) and roll (ψ_{pf}) angles [5.850] consider a modified version of (5.384) for the mean velocities that includes a mean offset error vector $\boldsymbol{a}$ associated with the error in the measured velocities associated with the instrument

$$\begin{pmatrix} \overline{u}_{\mathrm{pf}} \\ \overline{v}_{\mathrm{pf}} \\ \overline{w}_{\mathrm{pf}} \end{pmatrix} = \begin{pmatrix} p_{11} & p_{12} & p_{13} \\ p_{21} & p_{22} & p_{23} \\ p_{31} & p_{32} & p_{33} \end{pmatrix} \begin{pmatrix} \overline{u}_{\mathrm{m}} - a_1 \\ \overline{v}_{\mathrm{m}} - a_2 \\ \overline{w}_{\mathrm{m}} - a_3 \end{pmatrix} . \tag{5.387}$$

Wilczak et al. [5.850] show that the $\overline{u}$ and $\overline{v}$ biases are usually much smaller than the $\overline{w}$ bias. Consequently, their method only contains a mean offset in the vertical velocity. This is done by setting the last equation in (5.387) to zero (i. e., $\overline{w}_{\mathrm{pf}} = 0$) and rearranging to obtain

$$\overline{w}_{\mathrm{m}} = a_3 - \frac{p_{31}}{p_{33}}\overline{u}_{\mathrm{m}} - \frac{p_{32}}{p_{33}}\overline{v}_{\mathrm{m}} \tag{5.388}$$

that is,

$$\overline{w}_{\mathrm{m}} = b_0 + b_1\overline{u}_{\mathrm{m}} + b_2\overline{v}_{\mathrm{m}} . \tag{5.389}$$

The b coefficients are then solved for by minimizing the function S,

$$S = \sum_{i=1}^{N} \left(\overline{w}_{m,i} - b_0 - b_1\overline{u}_{m,i} - b_2\overline{v}_{m,i}\right)^2 , \tag{5.390}$$

where $\overline{u}_{m,i}$, $\overline{v}_{m,i}$, and $\overline{w}_{m,i}$ are the components of the mean velocities measured by the sonic anemometer for each averaging period. Taking the partial derivative of (5.390) with respect to b_0, b_1, and b_2 and setting the resulting equations each equal to zero yields the following system of equations:

$$\begin{pmatrix} N & \sum_i \overline{u}_{m,i} & \sum_i \overline{v}_{m,i} \\ \sum_i \overline{u}_{m,i} & \sum_i \overline{u}^2_{m,i} & \sum_i \overline{u}_{m,i}\overline{v}_{m,i} \\ \sum_i \overline{v}_{m,i} & \sum_i \overline{u}_{m,i}\overline{v}_{m,i} & \sum_i \overline{v}^2_{m,i} \end{pmatrix} \begin{pmatrix} b_0 \\ b_1 \\ b_2 \end{pmatrix} = \begin{pmatrix} \sum_i \overline{w}_{m,i} \\ \sum_i \overline{u}_{m,i}\overline{w}_{m,i} \\ \sum_i \overline{v}_{m,i}\overline{w}_{m,i} \end{pmatrix} .$$

The b_i coefficients can easily be obtained using a standard matrix-inversion technique. The planar-fit pitch and roll angles are then calculated using the following equations that are obtained by combining (5.389) and the orthogonality condition (i. e., $p_{31} + p_{32} + p_{33} = 1$) as

$$p_{31} = \frac{-b_1}{\sqrt{b_1^2 + b_2^2 + 1}} = -\cos\psi_{\mathrm{pf}} \sin\varphi_{\mathrm{pf}} ,$$

$$p_{32} = \frac{-b_2}{\sqrt{b_1^2 + b_2^2 + 1}} = -\sin\psi_{\mathrm{pf}} ,$$

$$p_{33} = \frac{1}{\sqrt{b_1^2 + b_2^2 + 1}} = \cos\psi_{\mathrm{pf}} \cos\varphi_{\mathrm{pf}} ,$$

$$\sin\psi_{\mathrm{pf}} = -p_{32} ,$$

$$\sin\varphi_{\mathrm{pf}} = \frac{b_1}{\sqrt{b_1^2 + 1}} ,$$

$$\cos\psi_{\mathrm{pf}} = \sqrt{\frac{b_1^2 + 1}{b_1^2 + b_2^2 + 1}} ,$$

$$\cos\varphi_{\mathrm{pf}} = \frac{1}{\sqrt{b_1^2 + 1}} .$$

The planar-fit pitch and roll angles can now be substituted into (5.384) to solve for u_{pf}, v_{pf}, and w_{pf}. The last step is to solve for the final rotated velocities using (5.385).

Other Sensor Issues

While, it has been observed that thermal expansion of SATs has a negligible effect on accuracy [5.836], the sensors and supports of SATs create wakes that interfere with the flow field being measured and result in a velocity deficit error. Aerodynamic distortion on the acoustic path is not only due to wake effects but also due to blockage effects, leading to acceleration in certain parts of the acoustic path regions [5.849]. Horizontally mounted SATs (Fig. 5.221c,d) are usually pointed into the mean wind and have a restricted range of permissible wind angles to avoid the wakes of the sensor and mounting equipment. Vertically mounted SATs (Fig. 5.221a,b) are often axisymmetric but have supports that induce wake effects. Also, any mean vertical winds will cause significant flow distortion due to the base. Many manufacturers include corrections that are meant for specific anemometer orientations to account for wake-shadowing effects of the sensor supports. These usually assume that the mean flow is horizontal and are not valid for flow with significant mean verti-

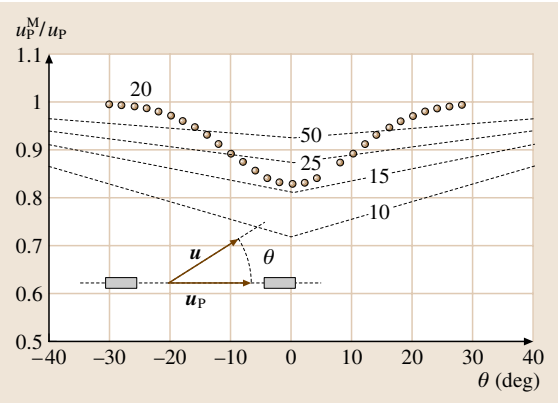

Fig. 5.227 Normalized velocity attenuation u_P^M/u_P (where $\boldsymbol{u}_P$ is the projection of the wind vector $\boldsymbol{u}$ onto the pulse path) from transducer shadowing in a sonic anemometer (with orthogonal probe axes) shown as a function of wind direction (θ) for various values of L/a (10–50) (after [5.818, 854]). Here, a is the diameter of the transducer, L is the separation distance between transducers

cal velocity components. Shadowing effects have also been investigated in the literature [5.849, 854–859]. Figure 5.227 is an example of the corrections that can be applied to particular SATs. With more sensors being used in environments with a nonhorizontal mean flow (e.g., urban flow and complex terrain), this topic has become an important issue. In particular it has been shown that introducing an angle of attack to the sonic anemometer can cause large errors in mean velocities and turbulent fluxes [5.860]. Additional calibration data over a full range of wind angles is necessary to alleviate this problem. It should be remarked that, in extremely poor designs, certain sonic anemometer geometries may lead to undefined measured wind speed values (i. e., one measurement corresponding to multiple wind values) as described in [5.861].

Temperature measurements from the SAT are sensitive to moisture content [5.841] and cross-stream velocity and should be corrected [5.862]. *Schotanus* et al. [5.863] and *Liu* et al. [5.841] have proposed corrections. Some manufacturers include correction algorithms that can be run online or implemented in postprocessing. *Liu* et al. [5.841] have provided correction information for several specific types of sonic anemometers including the Campbell Scientific CSAT3, the Metek USA-1 and the Gill Instrument Solent R2, R3, R31, and HS.

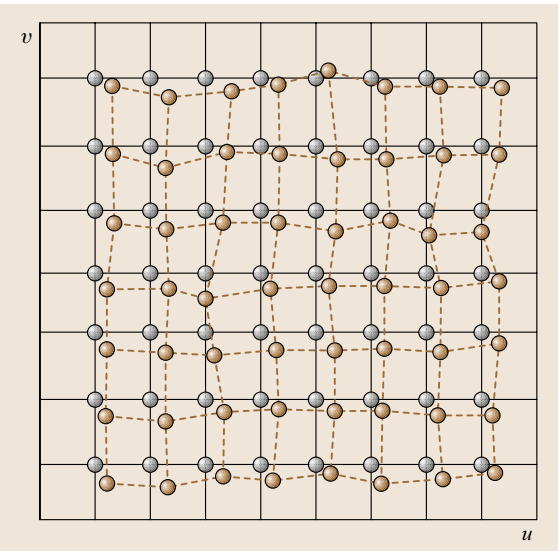

Fig. 5.228 Schematic of the results from a two-dimensional calibration. The graphical relation $f_{cal} : \mathbb{R}^2 \to \mathbb{R}^2$ is presented. The grey dots represent the wind-tunnel measurements (real values of u and v), whereas the brown dots represent the values measured by the sonic anemometer (measured values of u and v)

5.7.4 Data-Acquisition Requirements

Most SATs have data-acquisition electronics built into the instrument on a mounting arm or in an included electronics box. Communication with the electronics typically takes place through a modem-type communication protocol using a PC terminal (e.g., via an RS-232 serial port) or a data logger. Some manufacturers use proprietary digital communication protocols (e.g., SDI (synchronous digital interface) for Vaisala, Inc. and SDM (synchronous devices for measurement) for Campbell Scientific, Inc.) that give the best instrument performance. These digital communication techniques allow for external instrument triggering. In addition, most manufacturers' electronics can be programmed to output analog signals.

5.7.5 Use and Calibration Procedures

One of the biggest advantages of SATs is that they typically only require an initial calibration. Usually, SATs only need to be recalibrated if the sensors have been disturbed (for example, causing the pulse path distance L to be changed). Some models require regular zeroing in a still/anechoic chamber [5.821, 864]. In general, prior to instrument deployment, checking the zero of

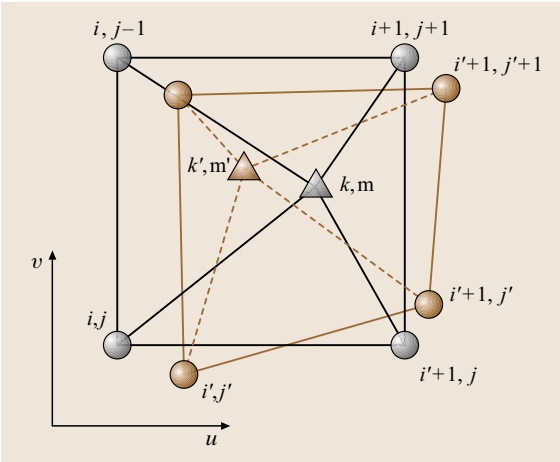

Fig. 5.229 Schematic of the correction process of a sonic measurement. The grey dots represent the real values of the wind speed determined during calibration in wind tunnel, the brown dots represent the values of u and v measured by the sonic anemometer during calibration, the grey triangle represents the values of u and v measured in the field, and the white triangle represents the values of the interpolated (corrected after calibration) u and v

the instrument in a still chamber is a good practice. If the path distance has changed, SATs are usually calibrated using a reference standard (e.g., Pitot-static or hot-wire probe) in a wind tunnel. Calibration method specifications are proposed in the literature [5.821,864]. However, a need for a uniform systematic calibration method still exists. The calibration of a sonic anemometer involves the determination of the function $\boldsymbol{f}_{\text{cal}} : \mathbb{R}^3 \to \mathbb{R}^3$ for a number of different values of wind speed magnitude $|\boldsymbol{u}|$, wind direction (or horizontal incidence angle) θ, and vertical angle of incidence α, which may give rise to a large number of calibration points. For example, a typical full calibration may consist of $N_u \times N_\theta \times N_\alpha = 10 \times 40 \times 10 = 4000$ calibration points. From these experimental relations between the real and measured wind speed vectors (u, v, w) [or equivalent vector magnitudes $(|\boldsymbol{u}|, \theta, \alpha)$] a proper fit to the function $\boldsymbol{f}_{\text{cal}} : \mathbb{R}^3 \to \mathbb{R}^3$ that can be applied to correct future measurements must be determined.

The authors have explored linear interpolation methods to reduce the information contained in the calibration test. The philosophy behind this method can be more easily illustrated if a two-dimensional calibration is considered. If only the variation of two components of the wind speed are evaluated (i. e., the two horizontal components u and v), the relation between the measured and real values can be represented graphically as in Figs. 5.228 and 5.229, where the white dots represent the calibration values for the vector (u, v) and the grey dots the corresponding measured values $(u^{\text{M}}, v^{\text{M}})$. (A similar scheme with a different data process is presented in [5.857].)

An enlargement of the schematic shown in Fig. 5.228 is represented in Fig. 5.229. The white triangle represents the interpolated (corrected after calibration) value of the measured vector $(u^{\text{M}}, v^{\text{M}})$. This calibrated value is obtained in this case by a linear calibration function $\boldsymbol{f}^{\text{l}}_{\text{cal}} : \mathbb{R}^2 \to \mathbb{R}^2$ so that the corrected vector is obtained as

$$\begin{aligned}(\boldsymbol{u}_{k,\text{m}})^{\text{M}}_{\text{C}} &= \left(u^{\text{M}}_{k,\text{m}}, v^{\text{M}}_{k,\text{m}}\right)_{\text{C}} \\ &= \boldsymbol{f}^{\text{l}}_{\text{cal}}(\boldsymbol{u}_{k',\text{m}'}; \boldsymbol{u}_{i,j}, \boldsymbol{u}_{i',j'}, \boldsymbol{u}_{i+1,j}, \boldsymbol{u}_{i'+1,j} \\ &\quad \ldots \boldsymbol{u}_{i'+1,j'+1}) \,. \end{aligned} \tag{5.391}$$

To avoid cross contamination of the velocity components, extreme care needs to be taken during mounting and leveling SATs. Over level terrain, bubble indicators are useful for leveling. However, over sloping terrain users must determine if the sensor is to be placed parallel to the slope or oriented with respect to the gravitational vector. In addition, sensors should be placed to maximize the useful range of measurements by minimizing tower and sensor distortion by orienting the sensor into the predominant wind direction. Quality control routines are used in postprocessing to remove or mark data with winds that have been disturbed by the tower.

Finally, wet sensors, rain, snow, icing, and debris on sensors degrade the ultrasonic signal. Most manufactures have heated sensors that are intended for cold weather use to prevent icing.

5.7.6 Manufacturers and Costs

A number of manufacturers exist around the world including: Vaisala, Inc., RM Young Company, Applied Technologies, Inc., Campbell Scientific, Inc., Metek GmbH, and Gill Instruments Ltd. Anemometer cost varies significantly. 2-D SATs are less expensive than 3-D devices, typically costing $ 1000–3000. The price range of 3-D SATs is approximately $ 2000–8000. The prices generally vary with accuracy and additional sensor options and do not include data loggers or laptop computers for data storage.

5.7.7 Device Comparison

SATs provide a number of advantages for making point measurements in flows with length scales of interest

that are greater than $O(1\,\mathrm{m})$ for frequencies less than $O(10\,\mathrm{Hz})$. Over this range, they provide much better response than traditional meteorological instruments such as cup-and-vane or propeller anemometers [5.820, 844, 865] (Table 5.8). SATs are much easier to operate and much more robust than traditional engineering laboratory equipment such as LDA, PIV, or hot-wire anemometry. However, for investigating high-frequency turbulence at the smallest length scales, traditional engineering laboratory equipment must be employed.

References

5.1 S.H. Chue: Pressure probes for fluid measurement, Prog. Aerosp. Sci. **16**, 147–223 (1975)

5.2 D.W. Bryer, R.C. Pankhurst: *Pressure Probe Methods for Determining Wind Speed and Flow Direction* (Her Majesty's Stationery Office, London 1971)

5.3 H. Pitot: Déscription d'une machine pour mesurer la vitesse des eaux courantes et le sillage desvaisseaux. In: *Mémoires de L'Académie des Sciences* (L'Académie des Sciences, Paris 1732)

5.4 H.W. Liepmann, A. Roshko: *Elements of Gas Dynamics* (Wiley, New York 1957)

5.5 R.C. Pankhurst, D.W. Holder: *Wind-Tunnel Technique* (Sir Isaac Pitman, London 1952)

5.6 F. S. Sherman: New experiments on impact pressure interpretation in supersonic and subsonic rarified airstreams, Tech. Note *2995*, (NACA, Washington 1953)

5.7 C.W. Hurd, K.P. Chesky, A.H. Shapiro: Influence of viscous effects on impact tubes, J. Appl. Mech. **20**(2), 254–256 (1953)

5.8 M. Barker: On the use of very small Pitot-tubes for measuring wind velocities, Proc. R. Soc. London, Vol. 101 (1922) 435–445

5.9 F.A. MacMillan: Viscous effects on Pitot tubes in shear flow, J. R. Aeronaut. Soc. **58**, 837–839 (1954)

5.10 F.A. MacMillan: Viscous effects on flattened Pitot tubes at low speeds, J. R. Aeronaut. Soc. **58**, 837–839 (1954)

5.11 W. G. S. Lester: The flow past a Pitot tube at low Reynolds numbers, Rep. Memor. *3240*, Aero. Res. Council (1961)

5.12 E.U. Repik: Measuring the velocity in a boundary layer with a total-head Pitot tube, J. Eng. Phys. Thermophys. **22**(3), 357–360 (1972)

5.13 N.P. Mikhailova, E.U. Repik: Effect of viscosity on Pitot tube readings at low flow speeds, Izv. Akad. Nauk. SSSR **1**, 136–139 (1976)

5.14 M. V. Zagarola: *Mean-flow scaling of turbulent pipe flow*. Ph.D. Thesis (Princeton University, Princeton 1996)

5.15 K. G. Merriam, E. R. Spaulding: Comparative tests of Pitot-static tubes, Tech. Note *546* (NACA, Washington 1935)

5.16 F. Homann: The effect of high viscosity on the flow around a cylinder and a sphere, Tech. Mem. *1334* (NACA, Washington 1952)

5.17 J.L. Potter, A.B. Bailey: Pressures in the stagnation regions of blunt bodies in rarified flow, AIAA J. **2**(4), 743–745 (1964)

5.18 S. Goldstein: A note on the measurement of total head and static pressure in a turbulent stream, Proc. R. Soc. London A **155**(886), 570–575 (1936)

5.19 T. Christiansen, P. Bradshaw: Effect of turbulence on pressure probes, J. Phys. E Sci. Instrum. **14**, 992–997 (1981)

5.20 S. Tavoularis, M. Szymczak: Displacement effects of square-ended Pitot tubes in shear flows, Exp. Fluids **7**, 33–37 (1989)

5.21 V. Ozarapoglu: *Measurements in incompressible turbulent flows*. Ph.D. Thesis (Université Laval, Quebec 1973)

5.22 J. Dickinson: *Turbulent Skin Friction Techniques* (Laval University, Quebec 1975)

5.23 B.J. McKeon, J. Li, W. Jiang, J.F. Morrison, A.J. Smits: Pitot probe corrections in high Reynolds number fully developed turbulent pipe flow, Meas. Sci. Technol. **14**, 1449–1458 (2003)

5.24 J. P. Monty: *Developments in smooth wall turbulent duct flows*. Ph.D. Thesis (University of Melbourne, Australia 2005)

5.25 B. J. McKeon: *High Reynolds number turbulent pipe flow*. Ph.D. Thesis (Princeton University, Princeton 2003)

5.26 I.M. Hall: The displacement effect of a sphere in two-dimensional shear flow, J. Fluid Mech. **1**, 142–162 (1956)

5.27 M.J. Lighthill: Contributions to the theory of the Pitot-tube displacement effect, J. Fluid Mech. **1**, 493–512 (1957)

5.28 F. A. MacMillan: Experiments on Pitot tubes in shear flow, Rep. Memor. *3028*, Aero. Res. Council. (1956)

5.29 A. Quarmby, H.K. Das: Displacement effect on Pitot tubes with rectangular mouths, Aeronaut. Q. **20**, 129–139 (1969)

5.30 P.O.A. Davies: The behaviour of a Pitot tube in transverse shear, J. Fluid Mech. **3**, 441–456 (1958)

5.31 A. D. Young, J. N. Maas: The behaviour of a Pitot-tube in a transverse total-pressure gradient, Rep. Memor. *1770*, Aero. Res. Council (1936)

5.32 J.L. Livesey, J.D. Jackson, C.J. Southern: The static-hole error problem: an experimental investigation of errors for holes of varying diameters and depths, Aircr. Eng. **34**, 43–47 (1962)

5.33 E.U. Repik, V.K. Kuzenkov, N.P. Mikhailova: Influence of velocity gradient and wall proximity on the readings of a Pitot tube in measurement of surface friction and velocity distribution in a turbulent boundary layer, J. Eng. Phys. Thermophys. **48**(6), 642–649 (1985)

5.34 V.C. Patel: Calibration of the Preston tube and limitations on its use in pressure gradients, J. Fluid Mech. **23**, 185–206 (1965)

5.35 C.W. Hubbard: Investigation of errors of Pitot tubes, Trans. ASME **61**, 477–492 (1939)

5.36 A. Pope, J.J. Harper: *Low-Speed Wind Tunnel Testing* (Wiley, New York 1966)

5.37 R. Shaw: The influence of hole dimensions on static pressure measurements, J. Fluid Mech. **7**, 550–564 (1960)

5.38 B.J. McKeon, A.J. Smits: Static pressure correction in high Reynolds number fully developed turbulent pipe flow, Meas. Sci. Technol. **13**, 1608–1614 (2002)

5.39 B. Chebbi, S. Tavoularis: Pitot-static tube response at very low Reynolds numbers, Phys. Fluids **3**(3), 481–483 (1991)

5.40 G.G. Zilliac: Calibration of seven-hole pressure probes for use in fluid flows with large angularity, Tech. Mem. *102200* (NASA, Washington 1989)

5.41 D. Sumner: A comparison of data-reduction methods for a seven-hole probe, J. Fluid Eng. **124**, 523–527 (2002)

5.42 C. Venkateswara Babu, M. Govardhan, N. Sitaram: A method of calibration of a seven-hole pressure probe for measuring highly three-dimensional flows, Meas. Sci. Technol. **9**, 468–476 (1998)

5.43 A.A. Gerner, C.L. Maurer, R.W. Gallington: Nonnulling seven-hole probes for high angle flow measurement, Exp. Fluids **2**, 95–103 (1984)

5.44 T.T. Takahashi: Measurement of air flow characteristics using seven-hole cone probes, Tech. Mem. *112-194* (NASA, Washington 1997)

5.45 S. Corrsin: Turbulence: Experimental methods. In: *Handbuch der Physik/Encyclopedia of Physics VIII/2*, ed. by S. Flügge (Springer, Berlin, Heidelberg 1963) pp. 524–590

5.46 P. Bradshaw: *An Introduction to Turbulence and its Measurements* (Pergamon, Oxford 1975)

5.47 J.O. Hinze: *Turbulence* (McGraw-Hill, New York 1975)

5.48 R.F. Blackwelder: Hot-wire and hot-film anemometers. In: *Methods of Experimental Physics: Fluid Dynamics*, Vol. 18, ed. by R.J. Emrich (Academic, New York 1981) pp. 259–314

5.49 A.E. Perry: *Hot-Wire Anemometry* (Clarendon, Oxford 1982)

5.50 L.M. Fingerson, P. Freymuth: Thermal anemometers. In: *Fluid Mechanics Measurements*, Vol. 4, ed. by R.J. Goldstein (Hemisphere, Washington 1983) pp. 99–154

5.51 C.G. Lomas: *Fundamentals of Hot-Wire Anemometry* (Cambridge Univ. Press, Cambridge 1986)

5.52 H.H. Bruun: *Hot-Wire Anemometry* (Oxford Scientific, Oxford 1995)

5.53 I. Lekakis: Calibration and signal interpretation for single and multiple hot-wire/hot-film probes, Meas. Sci. Technol. **7**, 1313–1333 (1996)

5.54 G. Comte-Bellot: Hot-wire anemometry, Ann. Rev. Fluid Mech. **8**, 209–231 (1976)

5.55 G. Comte-Bellot: Hot-wire anemometry. In: *Handbook of Fluid Dynamics*, ed. by R.W. Johnson (CRC, Boca Raton 1998) pp. 34.1–34.29

5.56 G. Comte-Bellot: Les méthodes de mesure physique de la turbulence, J. Phys. **37**(Suppl. C1), 67–78 (1976)

5.57 T. Tsuji, Y. Nagano, M. Tagawa: Frequency response and instantaneous temperature profile of cold-wire sensors for fluid temperature fluctuation measurements, Exp. Fluids **13**, 171–178 (1992)

5.58 P.O.A.L. Davies, M.J. Fisher: Heat transfer from electrically heated cylinders, Proc. R. Soc. London A, Vol. 280 (1964) 486–527

5.59 J. Laufer, R. McClellan: Measurements of heat transfer from fine wires in supersonic flows, J. Fluid Mech. **1**, 276–289 (1956)

5.60 J. Fraden: *Handbook of Modern Sensors* (Springer-AIP, Berlin, New York 2004)

5.61 A.D. McConnell, S. Uma, K.E. Goodson: Thermal conductivity of doped polysilicon layers, J. MEMS **0654**, 1–11 (2001)

5.62 Q. Lin, F. Jiang, X.Q. Wang, Y. Xu, Z. Han, Y.C. Tai, J. Lew, C.M. Ho: Experiments and simulations of MEMS thermal sensors for wall-shear stress measurements in aerodynamic control applications, J. Micromech. Microeng. **14**, 1640–1649 (2004)

5.63 T. Ebefors, E. Kälvesten, G. Stemme: Three dimensional silicon triple-hot-wire anemometer based on polyimide joints, IEEE Int. Workshop on Micro Electro Mechanical System, Vol. MEMS'98 (1998) 25–29

5.64 T. Ebefors: *Polyimide V-groove joints for three-dimensional silicon transducers*. Ph.D. Thesis (Royal Institute of Technology, Stockholm 2000)

5.65 A. van Dijk, F.T.M. Nieuwstadt: The calibration of (multi) hot-wire probes. 1. Temperature calibration, Exp. Fluids **36**, 540–549 (2004)

5.66 J. Lemay, A. Benaïssa: Improvement of cold-wire response for measurement of temperature dissipation, Exp. Fluids **31**, 347–356 (2001)

5.67 R.W. Derksen, R.S. Azad: An examination of hot-wire length corrections, Phys. Fluids **26**, 1751–1754 (1983)

5.68 G. Comte-Bellot, A. Strohl, E. Alcaraz: On aerodynamic disturbances caused by hot-wire probes, J. Appl. Mech. **38**, 767–774 (1971)

5.69 A. Strohl, G. Comte-Bellot: Aerodynamic effects due to configuration of X-wire anemometers, J. Appl. Mech. **40**, 661–666 (1973)

5.70 W.W. Willmarth, L.K. Sharma: Study of turbulent structure with hot wires smaller than the viscous length, J. Fluid Mech. **142**, 121–149 (1984)

5.71 P.M. Ligrani, P. Bradshaw: Subminiature hot-wire sensors: development and use, J. Phys. E Sci. Instrum. **20**, 323–332 (1987)

5.72 F. Jiang, Y.C. Tai, C.M. Ho, W.J. Li: A micromachined polysilicon hot-wire anemometer, Solid State Sensor and Actuator Workshop (1994) 264–267

5.73 B. Castaing, B. Chabaud, B. Hébral: Hot-wire anemometer operating at cryogenic temperature, Rev. Sci. Instrum. **63**, 4167–4173 (1992)

5.74 F. Jiang, Y.C. Tai, R. Karen, M. Gaustenauer, C.H. Ho: Theoretical and experimental studies of micromachined hot-wire anemometers, Intern. Electron. Devices Meeting (1994) 139–142

5.75 J.M. Österlund, A.V. Johansson: Dynamic behavior of hot-wire probes in turbulent boundary layers. In: *Advances in Turbulence*, ed. by R. Benzi (Kluwer, Dordrecht 1995) pp. 398–402

5.76 G. Comte-Bellot: Écoulement turbulent entre deux parois planes parallèles, Publ. Sci. Tech. Min. Air Paris **419**, 1–159 (1965), [previously: Contribution à l'étude de la turbulence de conduite, Ph.D. Thesis (Univ. Grenoble, Grenoble 1963), No 315, translated into English by P. Bradshaw: Turbulent flows between parallel walls, A.R.C. 31609 FM 4102 (1969)]

5.77 C. Bailly, G. Comte-Bellot: *Turbulence* (CNRS, Paris 2003)

5.78 M. Hishida, Y. Nagano: Turbulence measurements with symmetrically bent V-shaped hot-wires. Part 1: Principles of Operation, J. Fluid Eng. Trans. ASME **110**, 264–269 (1988)

5.79 M. Hishida, Y. Nagano: Turbulence measurements with symmetrically bent V-shaped hot-wires. Part 2: Measuring velocity components and turbulent shear stresses, J. Fluid Eng. Trans. ASME **110**, 270–274 (1988)

5.80 A. van Dijk, F.T.M. Nieuwstadt: The calibration of (multi) hot-wire probes. 2. Velocity calibration, Exp. Fluids **36**, 550–564 (2004)

5.81 J.M. Wallace, J.F. Foss: The measurement of vorticity in turbulent flows, Ann. Rev. Fluid. Mech. **27**, 469–514 (1995)

5.82 M. Sunyach: *Contribution à l'étude des frontières d'écoulements turbulents libres*. Thèse d'Etat (Univ. Lyon, Lyon 1971), No. 1971-37 (in French)

5.83 C.H.P. Chen, R.F. Blackwelder: Large-scale motion in a turbulent boundary layer: a study using temperature contamination, J. Fluid Mech. **89**, 1–31 (1978)

5.84 H.S. Kang, S. Chester, C. Meneveau: Decaying turbulence in an active-grid-generated flow and comparisons with large-eddy simulation, J. Fluid Mech. **480**, 129–160 (2003)

5.85 J. Delville, L. Ukeiley, L. Cordier, J.P. Bonnet, M. Glauser: Examination of large-scale structures in a turbulent plane mixing layer. Part 1. Proper orthogonal decomposition, J. Fluid Mech. **391**, 91–122 (1999)

5.86 J.H. Citriniti, W.K. George: Reconstruction of the global velocity field in the axisymmetric mixing layer utilizing the proper orthogonal decomposition, J. Fluid Mech. **418**, 137–166 (2000)

5.87 R.M. Hall, C.J. Obara, D.L. Carraway, C.B. Johnson, R.E. Wright Jr, P.F. Covell, M. Azzazy: Comparisons of boundary-layer transition measurement techniques at supersonic Mach numbers, AIAA J. **29**, 865–871 (1991)

5.88 T.R. Moes, G.R. Sarma, S.M. Mangalam: Flight demonstration of a shock location sensor using constant voltage hot-film anemometry, NASA Tech. Memo **4806** (1997)

5.89 R.J. Adrian, R.E. Johnson, B.G. Jones, P. Merati, A.T.C. Tung: Aerodynamic disturbances of hot-wire probes and directional sensitivity, J. Phys. E Sci. Instrum. **17**, 62–71 (1984)

5.90 B.J. Hoole, J.R. Calvert: The use of a hot-wire anemometer in turbulent flow, J. R. Aeronaut. Soc. **71**, 511–512 (1967)

5.91 L.S.G. Kovasznay: Turbulence in supersonic flow, J. Aeronaut. Sci. **20**, 657–675 (1953)

5.92 J.-P. Bonnet J.P.: *Etude théorique et expérimentale de la turbulence dans un sillage supersonique*. Thèse d'Etat (Univ. Poitiers, Poitiers 1982), No. 355

5.93 C.M. Ho, Y.C. Tai: Micro-electro-mechanical-systems (MEMS) and fluid flows, Ann. Rev. Fluid Mech. **30**, 579–612 (1998)

5.94 W.H. MacAdams: *Heat Transmission* (McGraw-Hill, New York 1954)

5.95 B.G. Van der Hegge Zijnen: Modified correlation formulae for the heat transfers by natural and by forced convection from horizontal cylinders, Appl. Sci. Res. **6**, 129–140 (1956)

5.96 D.C. Collis, M.J. Williams: Two-dimensional convection from heated wires at low Reynolds numbers, J. Fluid Mech. **6**, 357–384 (1959)

5.97 L.J.S. Bradbury, I.P. Castro: Some comments on heat transfer laws for fine wire, J. Fluid Mech. **51**, 487–495 (1972)

5.98 H. Kramers: Heat transfer from spheres to flowing media, Physica **XII**(2-3), 61–80 (1946)

5.99 G.E. Andrews, D. Bradley, G.F. Hundy: Hot wire anemometer calibration for measurements of small gas velocities, Int. J. Heat Mass Transf. **15**, 1765–1786 (1972)

5.100 M.V. Morkovin: Fluctuations and hot-wire anemometry in compresible flows, Wind Tunnel AGARDographs Ser. **24**, 1–102 (1956)

5.101 F.M. White: *Viscous Fluid Flow* (McGraw-Hill, New York 1991)

5.102 S.C.R. Dennis, J.D. Hudson, N. Smith: Steady laminar forced convection from a circular cylinder at low Reynolds numbers, Phys. Fluids **11**, 933–940 (1968)

5.103 E.R.G. Eckert, R.M. Drake Jr: *Analysis of Heat and Mass Transfer* (Hemisphere, Washington 1987)

5.104 J.G. Knudsen, D.L. Katz: *Fluid Dynamics and Heat Transfer* (McGraw-Hill, New York 1958)

5.105 M.S. Uberoi, S. Corrsin: Spectra and diffusion in a round turbulent jet, NACA Rep. **1040** (1951)

5.106 A.P. Hatton, D.D. James, H.W. Swire: Combined forced and natural convection with low-speed air flow over horizontal cylinders, J. Fluid Mech. **42**, 17–31 (1970)

5.107 W.M. Pitts, B.J. McCaffrey: Response behaviour of hot wires and films to flows of different gases, J. Fluid Mech. **169**, 465–512 (1986)

5.108 E.F. Spina, C.B. McGinley: Constant-temperature anemometry in hypersonic flow: critical issues and sample results, Exp. Fluids **17**, 365–374 (1994)

5.109 T.G. Elizarova, I.A. Shirokov, S. Montero: Numerical simulation of shock-wave structure for argon and helium, Phys. Fluids **17**, 068101 (2005)

5.110 J.C. Hill, C.A. Sleicher: Convective heat transfer from small cylinders to mercury, Int. J. Heat Mass Transf. **12**, 1595–1604 (1969)

5.111 J.C. Hill, C.A. Sleicher: Directional sensitivity of hot-films sensors in liquid metals, Rev. Sci. Instrum. **42**, 1461–1468 (1971)

5.112 B. Gebhart, L. Pera: Mixed convection from horizontal cylinders, J. Fluid Mech. **45**, 49–64 (1971)

5.113 K.A. Smith, E.W. Merrill, H.S. Mickley, P.S. Virk: Anomalous Pitot tube and hot film measurements in dilute polymer solutions, Chem. Eng. Sci. **22**, 619–626 (1967)

5.114 D.F. James, A.J. Acosta: Laminar flow of dilute polymer solutions around circular cylinders, J. Fluid Mech. **42**, 269–288 (1970)

5.115 J.L. Lumley: Drag reduction in turbulent flow by polymer additives, J. Polym. Sci. Macromol. Rev. **7**, 263–290 (1973)

5.116 L.S.G. Kovasznay: The hot-wire anemometry in supersonic flow, J. Aeronaut. Sci. **17**, 565–584 (1950)

5.117 M.V. Morkovin, R.E. Phinney: *Extended Applications of Hot-wire Anemometry to High-speed Turbulent Boundary Layers* (John Hopkins Univ., Baltimore 1958)

5.118 W.G. Spangenberg: Heat-loss characteristics of hot-wire anemometers at various densities in transonic and supersonic flow, NACA Tech. Note **3381** (1955)

5.119 C.F. Dewey Jr: Hot wire measurements in low Reynolds number hypersonic flows, J. Am. Rocket Soc. **28**, 1709–1718 (1961)

5.120 C.F. Dewey Jr: A correlation of convective heat transfer and recovery temperature data for cylinders in compressible flow, Int. J. Heat Mass Transf. **8**, 245–252 (1965)

5.121 L.V. Baldwin, V.A. Sandborn, J.C. Laurence: Heat transfer from transverse and yawed cylinders in continuum, slip, and free molecule air flows, J. Heat Transf. Trans. ASME **82**, 77–86 (1960)

5.122 J. Gaviglio: Sur les méthodes de l'anémométrie par fil chaud des écoulements turbulents compressibles de gaz, J. Mécanique **2**, 449–498 (1978)

5.123 S. Barre, P. Dupont, J.P. Dussauge: Hot-wire measurements in turbulent transonic flows, Eur. J. Mech. B Fluids **11**(4), 439–454 (1992)

5.124 P.C. Stainback, K.A. Nagabushana: Review of hot-wire anemometry techniques and the range of their applicability. In: *Thermal Anemometry*, Vol. FED167, ed. by ASME (ASME, New York 1993) pp. 93–133

5.125 A.J. Smits, K. Hayakawa, K.C. Muck: Constant temperature hot-wire anemometer practice in supersonic flows. Part 1: The normal wire, Exp. Fluids **1**, 83–92 (1983)

5.126 J. Weiss, H. Knauss, S. Wagner: Experimental determination of the free-stream disturbance field in a short-duration supersonic wind tunnel, Exp. Fluids **35**, 291–302 (2003)

5.127 G. Comte-Bellot, G.R. Sarma: Constant voltage anemometer practice in supersonic flows, AIAA J. **39**, 261–270 (2001)

5.128 J.R. Stalder, G. Goodwin, M.O. Creager: Heat transfer to bodies in a high-speed rarefied-gas stream, NACA Tech. Note **2438** (1951)

5.129 N. Chokani, A.N. Shiplyuk, A.A. Sidorenko, C.B. McGinley: Comparison between a hybrid constant-current anemometer and constant-voltage anemometer in hypersonic flow, 34th AIAA Fluid Dynamics Conf (AIAA, 2004) , , AIAA Paper 2004-2248

5.130 M.V. Scadron, I. Warshasky: Experimental determination of time constants and Nusselt numbers for bare-wire thermocouples in high-velocity air streams and analytical approximation of conduction and radiation errors, NACA Tech. Note **2599** (1952)

5.131 P. Dupont, J.F. Debieve: A hot wire method for measuring turbulence in transonic or supersonic heated flows, Exp. Fluids **13**, 84–90 (1992)

5.132 C.C. Horstman, W.C. Rose: Hot-wire anemometry in transonic flow, AIAA J. **15**, 395–401 (1977)

5.133 G.S. Jones, P.C. Stainback, C.D. Harris, C.W. Brooks, S.J. Clukey: Flow quality measurements for the Langley 8-foot transonic pressure tunnel LFC experiment, AIAA Paper, Vol. 89-0150 (1989)

5.134 G.S. Jones: Wind tunnel requirements for hot-wire calibrations, AIAA Paper **94-2534** (1994)

5.135 W.C. Rose: Turbulence measurements in a compressible boundary layer, AIAA J. **12**, 1060–1064 (1974)

5.136 D.A. Walker, W.F. Ng, M.D. Walker: Experimental comparison of two hot-wire techniques in supersonic flow, AIAA J. **27**, 1074–1080 (1989)

5.137 J.D. Norris, N. Chokani: Rapid scanning of overheat ratios using a constant voltage anemometer, AIAA J. **41**, 1619–1621 (2003)

5.138 D.R. Smith, A.J. Smits: Simultaneous measurements of velocity and temperature fluctuations in the boundary layer of a supersonic flow, Exp. Therm. Fluid Sci. **7**, 221–229 (1993)

5.139 M.V. Morkovin: Effects of compressibility on turbulent flows, Colloque CNRS, Vol. 108 (1962) 367–380

5.140 J. Gaviglio: Reynolds analogies and experimental study of heat tranfer in the supersonic boundary layer, Int. J. Heat Mass Transf. **30**, 911–926 (1987)

5.141 J. Weiss, H. Knauss, S. Wagner, N.D. Chokani, G. Comte-Bellot, A. Kosinov: Comparative measurements in M=2.54 flow using constant-temperature and constant-voltage anemometers, 41st AIAA Aerospace Sci. Meeting and Exhibit (2003) , , AIAA Paper 2003-1277

5.142 A.J. Smits, J.P. Dussauge: Hot-wire anemometry in supersonic flow, AGARDograph **315**, 5.1–5.14 (1989)

5.143 A.D. Kosinov, N.V. Semionov, Y.G. Yermolaev: Disturbances in test section of T-325 supersonic wind tunnel, Russ. Acad. Sci. Novosibirsk ITAM Rep. **6-99** (1999)

5.144 C.L. Ko, D.K. McLaughlin, T.R. Troutt: Supersonic hot-wire fluctuation data analysis with a conduction end-loss correction, J. Phys. E Sci. Instrum. **11**, 488–494 (1978)

5.145 I. Kidron: Measurement of the transfer function of hot-wire and hot-film turbulence transducers, IEEE Trans. Instrum. Meas. **15**(3), 76–81 (1966)

5.146 B.J. Bellhouse, D.L. Schultz: The determination of fluctuating velocity in air with heated thin film gauges, J. Fluid Mech. **29**, 289–295 (1967)

5.147 J.F. Brison, G. Charnay, G. Comte-Bellot: Calcul des transferts thermiques entre film chaud et substrat par un modèle à deux dimensions : prévision de la réponse dynamique des sondes usuelles, Int. J. Heat Mass Transf. **22**, 111–119 (1978)

5.148 G.R. Sarma: Transfer function analysis of the constant voltage anemometer, Rev. Sci. Instrum. **69**, 2385–2391 (1998)

5.149 G.R. Sarma: Analysis of a constant voltage anemometer circuit, IEEE Instrum. Meas. Technol. Conf. **1993**, 731–736 (1993)

5.150 C.A. Reimann, N. Chokani, G.R. Sarma: Improved calibration methods for a constant voltage anemometer-operated hot-wire in hypersonic flow, 41th AIAA Aerospace Sci. Meeting and Exhibit (2003) , , AIAA Paper 2003-0976

5.151 G. Comte-Bellot, J.P. Schon: Harmoniques créés par excitation paramétrique dans les anémomètres à fil chaud à intensité constante, Int. J. Heat Mass Transf. **12**, 1661–1677 (1969)

5.152 F.H. Champagne, C.A. Sleicher, O.H. Wehrmann: Turbulence measurements with inclined hot-wires, J. Fluid Mech. **28**, 153–175 (1967)

5.153 R. Betchov: L'influence de la conduction thermique sur les anémomètres à fils chauds, Proc. K Ned. Akad. Wet., Vol. 51 (1948) 721–730

5.154 R.G. Lord: Hot-wire probe end-loss corrections in low density flows, J. Phys. E Sci. Instrum. **7**, 56–60 (1974)

5.155 S.C. Morris, J.F. Foss: Transient thermal response of a hot-wire anemometer, Meas. Sci. Technol. **14**, 251–259 (2003)

5.156 J.D. Li, B.J. McKeon, W. Jiang, J.F. Morrison, A.J. Smits: The response of hot wires in high Reynolds-number turbulent pipe flow, Meas. Sci. Technol. **15**, 789–798 (2004)

5.157 L. Löfdahl, V. Chernoray, S. Haasl, G. Stemme, M. Sen: Characteristics of a hot-wire microsensor for time-dependent wall shear stress measurements, Exp. Fluids **35**, 240–251 (2003)

5.158 K. Bremhorst, L. Krebs, D.B. Gilmore: The frequency response of hot-wire anemometer sensors to heating current fluctuations, Int. J. Heat Mass Transf. **20**, 315–322 (1977)

5.159 R.G. Lord: The dynamic behaviour of hot-wire anemometers with conduction end losses, J. Phys. E Sci. Instrum. **14**, 573–578 (1981)

5.160 A.C.M. Beljaars: Dynamic behaviour of the constant temperature anemometer due to thermal inertia of the wire, Appl. Sci. Res. **32**, 509–518 (1976)

5.161 J.D. Li: Dynamic response of constant temperature hot-wire system in turbulence velocity measurements, Meas. Sci. Technol. **15**, 1835–1847 (2004)

5.162 H. Tennekes, J.L. Lumley: *A First Course in Turbulence* (MIT Press, Cambridge 1972)

5.163 H.L. Dryden, G.B. Schubauer, W.C. Mock Jr, H.K. Skramstad: Measurements of intensity and scale of wind-tunnel turbulence and their relation to the critical Reynolds number of spheres, NACA Tech. Rep. **581** (1937)

5.164 F.N. Frenkiel: Effects of wire length in turbulence investigations with a hot-wire anemometer, Aeronaut. Q. **V**, 1–24 (1954)

5.165 J.C. Wyngaard: Measurement of small-scale turbulence structure with hot-wires, J. Phys. E Sci. Instrum. **1**(Serie 2), 1105–1108 (1968)

5.166 M.S. Uberoi, L.S.G. Kovasznay: On mapping and measurement of random fields, Q. Appl. Math. **10**, 375–393 (1953)

5.167 D. Ewing, H.J. Hussein, W.K. George: Spatial resolution of parallel hot-wire probes for derivative measurements, Exp. Therm. Fluid Sci. **11**, 155–173 (1995)

5.168 J.W. Elsner, P. Domagala, W. Elsner: Effect of finite spatial resolution of hot-wire anemometry on measurements of turbulence energy dissipation, Meas. Sci. Technol. **4**, 517–523 (1993)

5.169 J.C. Wyngaard: Spatial resolution of the vorticity meter and other hot-wire arrays, J. Phys. E Sci. Instrum. **2**(Serie 2), 983–987 (1969)

5.170 R.A. Antonia, D.A. Shah, L.W.B. Browne: Spectra of velocity derivatives in a turbulent wake, Phys. Fluids **30**, 3455–3462 (1987)

5.171 R.A. Antonia, J. Mi: Corrections for velocity and temperature derivatives in turbulent flows, Exp. Fluids **14**, 203–208 (1993)

5.172 Y. Suzuki, N. Kasagi: Evaluation of hot-wire measurements in wall shear turbulence using a direct numerical simulation database, Exp. Therm. Fluid Sci. **5**, 66–77 (1992)

5.173 T. Zhou, R.A. Antonia, L.P. Chua: Performance of a probe for measuring turbulent energy and temperature dissipation rates, Exp. Fluids **33**, 334–345 (2002)

5.174 L.W.B. Browne, R.A. Antonia, D.A. Shah: Selection of wires and wire spacing for X-wires, Exp. Fluids **6**, 286–288 (1988)

5.175 P.M. Ligrani, P. Bradshaw: Spatial resolution and measurement of turbulence in the viscous sublayer using subminiature hot-wire probes, Exp. Fluids **5**, 407–417 (1987)

5.176 A.V. Johansson, P.H. Alfredsson: Effects of imperfect spatial resolution on measurements of wall-bounded turbulent shear flows, J. Fluid Mech. **137**, 409–421 (1983)

5.177 J.C. Klewicki, R.E. Falco: On accurately measuring statistics associated with small-scale structure in turbulent boundary layers using hot-wire probes, J. Fluid Mech. **219**, 119–142 (1990)

5.178 P. Moin, P.R. Spalart: Contributions of numerical simulation data base to the physics, modeling, and measurement of turbulence, NASA Tech. Memo **100022** (1987)

5.179 R.A. Antonia, Y. Zhu, J. Kim: On the measurement of lateral velocity derivatives in turbulent flows, Exp. Fluids **15**, 65–69 (1993)

5.180 R.A. Antonia, Y. Zhu, J. Kim: Corrections for spatial velocity derivatives in a turbulent shear flow, Exp. Fluids **16**, 411–416 (1994)

5.181 E. Huguenard, A. Magnan, A. Planiol: Les appareils à fils chauds, leur application à l'étude des mouvements atmosphériques, Serv. Technol. Aeronaut. Paris **32**, 1–66 (1926)

5.182 L.F.G. Simmons, A. Bailey: A hot-wire instrument for measuring speed and direction of airflow, Phil Mag S7 **13**(3), 81–96 (1927)

5.183 L.V. King: The linear hot-wire anemometer and its application in technical physics, J. Franklin I. **181**, 1–25 (1916)

5.184 J.S.G. Thomas: The hot-wire anemometer: its application to the investigation of the velocity of gases in pipes, Phil Mag S6 **233**(39), 505–534 (1920)

5.185 E.G. Richardson: *Les appareils à fil chaud, leurs applications dans la mécanique expérimentale des fluides* (Gauthier-Villars, Paris 1934)

5.186 H.L. Dryden, A.M. Kuethe: The measurement of fluctuations of air speed by the hot-wire anemometer, NACA Rep. **320** (1929)

5.187 V.V. Repkov, A.N. Shiplyuk, A.A. Sidorenko, V.A. Lebiga, A.Y. Pak, V.N. Zinoviev: Contant current anemometer with built-in microcontroller, Int. Conf. Meth. Aerophys. Res (Nonparel, Novosibirsk 2004) 4.247–4.249

5.188 I. Kidron: The signal-to-noise ratios of constant-current and constant-temperature hot-wire anemometers, IEEE Trans. Instrum. Meas. **16**(1), 68–73 (1967)

5.189 P. Freymuth: Noise in hot-wire anemometers, Rev. Sci. Instrum. **39**, 550–557 (1968)

5.190 D. Bestion, J. Gaviglio, J.P. Bonnet: Comparison between constant-current and constant-temperature hot-wire anemometers in high speed flows, Rev. Sci. Instrum. **54**, 1513–1524 (1983)

5.191 K. Bremhorst, L.J.W. Graham: A fully compensated hot/cold wire anemometer system for unsteady flow velocity and temperature measurements, Meas. Sci. Technol. **1**, 425–430 (1990)

5.192 G. Asch: *Les capteurs en instrumentation industrielle* (Dunod, Paris 2006)

5.193 M. Ziegler: The construction of a hot wire anemometer with linear scale and negligible lag, Verh. K. Akad. Wet. **15**, 3–22 (1934)

5.194 J.R. Weske: A hot-wire circuit with very small time lag, NACA Tech. Rep. **881** (1943)

5.195 E. Ossofsky: Constant temperature operation of the hot-wire anemometer at high frequency, Rev. Sci. Instrum. **19**, 881–889 (1948)

5.196 J.C. Wyngaard, J.L. Lumley: A constant temperature hot-wire anemometer, J. Sci. Instrum. **44**, 363–365 (1967)

5.197 P. Freymuth: Feedback control theory for constant-temperature hot-wire anemometers, Rev. Sci. Instrum. **38**, 677–681 (1967)

5.198 Davis M.R., Davies P.O.A.L.: *The physical characteristics of hot-wire anemometers*, Tech. Rep. 2 (Univ. Southampton, Southampton 1968)

5.199 A.E. Perry, G.L. Morrison: A study of the constant-temperature hot-wire anemometer, J. Fluid Mech. **47**, 577–599 (1971)

5.200 N.B. Wood: A method for determination and control of the frequency response of the constant-temperature hot-wire anemometer, J. Fluid Mech. **67**, 769–786 (1975)

5.201 P. Freymuth: Frequency response and electronic testing for constant-temperature hot-wire anemometers, J. Phys. E Sci. Instrum. **10**, 705–710 (1977)

5.202 P. Freymuth: On higher order dynamics of constant-temperature hot-wire anemometers, Meas. Sci. Technol. **9**, 534–535 (1998)

5.203 J.H. Watmuff: An investigation of the constant-temperature hot-wire anemometer, Exp. Therm. Fluid Sci. **11**, 117–134 (1995)

5.204 L.M. Fingerson: Thermal anemometry, current state, and future directions, Rev. Sci. Instrum. **65**, 285–300 (1994)

5.205 F.E. Jorgensen: The computer-controlled constant-temperature anemometer. Aspects of set-up, probe calibration, data acquisition and data conversion, Meas. Sci. Technol. **7**, 1378–1387 (1996)

5.206 G. Comte-Bellot: Anémométrie à fil chaud (cas des fluides incompressibles). In: *Techniques de Mesure dans les Écoulements*, ed. by CEA/EDF (Eyrolles, Paris 1974) pp. 117–198

5.207 P. Freymuth: The effect of varying resistance ratio on the behaviour of constant-temperature hot-wire anemometers, J. Phys. E Sci. Instrum. **14**, 1373 (1981)

5.208 P. Freymuth: Second or third order control theory for constant-temperature hot-wire anemometers?, Exp. Fluids **23**, 175–176 (1997)

5.209 B.C. Khoo, Y.T. Chew, C.J. Teo, C.P. Lim: The dynamic response of a hot-wire anemometer: III. Voltage-perturbation versus velocity-perturbation testing for near-wall hot-wire/film probes, Meas. Sci. Technol. **10**, 152–169 (1999)

5.210 C.J. Teo, B.C. Khoo, Y.T. Chew: The dynamic response of a hot-wire anemometer: IV. Sine-wave voltage perturbation testing for near-wall hot-wire/film probes and the presence of low-high frequency response characteristics, Meas. Sci. Technol. **12**, 37–51 (2001)

5.211 P. Freymuth: Interpretations in the control theory of thermal anemometers, Meas. Sci. Technol. **8**, 174–177 (1997)

5.212 J. Weiss, H. Knauss, S. Wagner: Method for the determination of frequency response and signal to noise ratio for constant-temperature hot-wire anemometers, Rev. Sci. Instrum. **72**, 1904–1909 (2001)

5.213 J. Weiss, N. Chokani, G. Comte-Bellot: Constant-temperature and constant-voltage anemometer use in a Mach 2.5 flow, AIAA J. **43**, 1140–1143 (2005)

5.214 G. Comte-Bellot, G.R. Sarma, T. Faure, J.P. Dussauge, P. Dupont, J.F. Debiève: Performance studies of the constant voltage anemometer in a Mach 2.3 boundary layer, ICIASF 99 (1999) 40.1–40.9

5.215 J. Weiss: Effect of bridge imbalance on the estimation of sensitivity coefficients for constant-temperature hot-wire anemometers, Meas. Sci. Technol. **14**, 1373–1380 (2003)

5.216 S.G. Saddoughi, S.V. Veeravalli: Hot-wire anemometry behaviour at very high frequencies, Meas. Sci. Technol. **7**, 1297–1300 (1996)

5.217 P. Freymuth: Nonlinear control theory for constant-temperature hot-wire anemometers, Rev. Sci. Instrum. **40**, 258–262 (1969)

5.218 G.R. Sarma: Flow Rate Measuring Apparitus, US Patent 5,074,147 (1991)

5.219 S.M. Mangalam, G.R. Sarma, S. Kuppa, L.R. Kubendran: A new approach to high-speed flow measurements using constant voltage anemometry, 17th Aerospace Ground Testing Conf (1992) , , AIAA Paper 92-3957

5.220 J.T. Lachowicz, N. Chokani, S.P. Wilkinson: Boundary-layer stability measurements in a hypersonic quiet tunnel, AIAA J. **34**, 2496–2500 (1996)

5.221 J. Weiss, G. Comte-Bellot: Electronic noise in a constant voltage anemometer, Rev. Sci. Instrum. **75**, 1290–1296 (2004)

5.222 M.A. Kegerise, E.F. Spina: A comparative study of constant-voltage and constant-temperature hot-wire anemometers, Partl: The static response, Exp. Fluids **19**, 154–164 (2000)

5.223 M.A. Kegerise, E.F. Spina: A comparative study of constant-voltage and constant-temperature hot-wire anemometers, Part II: The dynamic response, Exp. Fluids **19**, 165–177 (2000)

5.224 G.R. Sarma, R.W. Lankes: Automated constant voltage anemometer with in situ measurements of overheat and time constant of the hot-wire, Rev. Sci. Instrum. **70**, 2384–2386 (1999)

5.225 G.R. Sarma, G. Comte-Bellot, T. Faure: Software corrected hot wire thermal lag for the constant voltage anemometer featuring a constant bandwidth at the selected compensation setting, Rev. Sci. Instrum. **69**, 3223–3231 (1998)

5.226 S. Kuppa, G.R. Sarma, S.M. Mangalam: Effect of thermal inertia on the frequency response of constant voltage hot-wire anemometer and its compensation, ASME Fluid Meas. Instrum. Forum, Vol. FED 161 (1993) 67–73

5.227 G. Comte-Bellot, J. Weiss, J.C. Béra: Lead-resistance effects in a constant voltage anemometer, Rev. Sci. Instrum. **75**, 2075–2081 (2004)

5.228 A.E. Blanchard, J.T. Lachowicz, S.P. Wilkinson: NASA Langley Mach 6 quiet wind-tunnel performance, AIAA J. **35**, 23–28 (1997)

5.229 G. Comte-Bellot, J. Weiss, J.C. Béra: Control of the dynamic non-linearity in a constant voltage anemometer, Bull. Am. Phys. Soc. **50**(9), 189 (2005)

5.230 A.A. Abdel-Rahman, G.J. Hitchman, P.R. Slawson, A.B. Strong: An X-array hot-wire technique for heated turbulent flows of low velocity, J. Phys. E Sci. Instrum. **22**, 638–644 (1989)

5.231 H.H. Bruun, M.A. Khan, H.H. Al-Kayiem, A.A. Fardad: Velocity calibration relationships for hot-wire anemometry, J. Phys. E Sci. Instrum. **21**, 225–232 (1988)

5.232 L.V. King: On the convection of heat from small cylinders in a stream of fluid: determination of the convection constants of small platinum wires with applications to hot-wire anemometry, Phil. Trans. R. Soc. Lond. Ser. A **214**, 373–432 (1914)

5.233 A. Baille: *Lois de refroidissement des fils chauds aux faibles vitesses*. Ph.D. Thesis, (Univ. Aix-Marseille, Aix-Marseille 1971), (in French)

5.234 S.S. Tewari, Y. Jaluria: Calibration of constant-temperature hot-wire anemometers for very low velocities in air, Rev. Sci. Instrum. **61**, 3834–3845 (1990)

5.235 B.C. Khoo, Y.T. Chew, C.P. Lim: The flow between a rotating and a stationary disc: application to near-wall hot-wire calibration, Meas. Sci. Technol. **9**, 650–658 (1998)

5.236 R.E. De Haan: The dynamic calibration of a hot wire by means of a sound wave, Appl. Sci. Res. **24**, 335–353 (1971)

5.237 R.P. Dring, B. Gebhart: Hot-wire anemometer calibration for measurements at very low velocity, ASME J. Heat Transf. **91**, 241–244 (1969)

5.238 Y.T. Chew, S.M. Ha: The directional sensitivities of crossed and triple hot-wire probes, J. Phys. E Sci. Instrum. **21**, 613–620 (1988)

5.239 G. Comte-Bellot: Hot-wire and hot-film anemometers. In: *Measurements of Unsteady Fluid Dyn. Phen.*, ed. by B.E. Richards (Hemisphere, Washington 1977) pp. 123–162

5.240 R.M. Lueptow, K.S. Breuer, J.H. Haritonidis: Computer-aided calibration of X-probes using a look-up table, Exp. Fluids **6**, 115–118 (1988)

5.241 F.D. Johnson, H. Eckelmann: A variable angle method of calibration for X-probes applied to wall-bounded turbulent shear flow, Exp. Fluids **2**, 121–130 (1984)

5.242 Y.T. Chew, S.M. Ha: A. critical evaluation of the explicit data analysis algorithm for a crossed wire anemometer in highly turbulent isotropic flow, Meas. Sci. Technol. **1**, 775–781 (1990)

5.243 W.W. Willmarth, T.J. Bogar: Survey and new measurements of turbulent structure near the wall, Phys. Fluids **20S**, 9–21 (1977)

5.244 W.W. Willmarth: Geometric interpretation of the possible velocity vectors obtained with multiple sensors, Phys. Fluids **28**, 462–465 (1985)

5.245 P. Burattini, R.A. Antonia: The effect of different X-wire calibration schemes on some turbulence statistics, Exp. Fluids **38**, 80–89 (2005)

5.246 H.H. Bruun, C. Tropea: The calibration of inclined hot-wire probes, J. Phys. E Sci. Instrum. **18**, 405–413 (1985)

5.247 J.G. Kawall, M. Shokr, J.F. Keffer: A digital technique for the simultaneous measurement of streamwise and lateral velocities in turbulent flows, J. Fluid Mech. **133**, 83–112 (1983)

5.248 I.C. Lekakis, R.J. Adrian, B.G. Jones: Measurement of velocity vectors with orthogonal and non-orthogonal triple-sensor probes, Exp. Fluids **7**, 228–240 (1989)

5.249 L.W.B. Browne, R.A. Antonia, L.P. Chua: Calibration of X-probes for turbulent flow measurements, Exp. Fluids **7**, 201–208 (1989)

5.250 B. Lakshminarayana, R. Davino: Sensitivity of three sensor hot wire probe to yaw and pitch angle variation, J. Fluid Eng. Trans. ASME **110**, 120–122 (1988)

5.251 L. Pompeo, H. Thomann: Quadrupole hot-wire probes in a simulated wall flow, Exp. Fluids **14**, 145–152 (1993)

5.252 G. Pailhas, J. Cousteix: Méthodes d'exploitation des données d'une sonde anémométrique à quatre fils chauds, Rech. Aérospatiale **2**, 161–168 (1986)

5.253 K. Döbbeling, B. Lenze, W. Leuckel: Computer-aided calibration and measurements with a quadruple hotwire probe, Exp. Fluids **8**, 257–262 (1990)

5.254 M. Samet, S. Einav: A hot-wire technique for simultaneous measurements of instantaneous velocities in 3D flows, J. Phys. E Sci. Instrum. **20**, 683–690 (1987)

5.255 T.J. Gieseke, Y.G. Guezennec: An experimental approach to the calibration and use of triple hot-wire probes, Exp. Fluids **14**, 305–315 (1993)

5.256 G. Lemonis, T. Dracos: A new calibration and data reduction method for turbulence measurement by multihotwire probes, Exp. Fluids **18**, 319–328 (1995)

5.257 K. Döbbeling, B. Lenze, W. Leuckel: Basic considerations concerning the construction and usage of multiple hot-wire probes for highly turbulent three-dimensional flows, Meas. Sci. Technol. **1**, 924–933 (1990)

5.258 P. Lavoie, A. Pollard: Uncertainty analysis of four-sensor hot-wires and their data-reduction schemes used in the near field of a turbulent jet, Exp. Fluids **34**, 358–370 (2003)

5.259 J. Cousteix, J.C. Juillen: Jauges à fil chaud pour la mesure du frottement pariétal: réalisation, étalonnage, applications, Rech. Aérospatiale **3**, 207–218 (1982)

5.260 J.H. Haritonidis: The measurement of wall shear stress. In: *Advances in Fluid Mechanic Measurements*, Vol. 45, ed. by M. Gad-el-Hak (Springer, Berlin, Heidelberg 1989) pp. 229–261

5.261 W.J. Cook, T.H. Giddings, J.D. Murphy: Response of hot-element wall shear-stress gages in laminar oscillating flows, AIAA J. **26**, 706–713 (1988)

5.262 W.J. Cook: Response of hot-element wall shear stress gages in unsteady turbulent flows, AIAA J. **32**, 1464–1471 (1994)

5.263 J.B. Huang, F.K. Jiang, Y.C. Tai, C.M. Ho: A micro-electro-mechanical-system-based thermal shear-stress sensor with self-frequency compensation, Meas. Sci. Technol. **10**, 687–696 (1999)

5.264 H. Schlichting, K. Gersten: *Boundary Layer Theory* (McGraw-Hill, New York 2000)

5.265 W. Nitsche, C. Haberland: Ein vereinfachtes Eichverfahren für Hitzdrahtanemometer (Einzelpunkteichung), Z. Flugwiss. Weltraumforsch. **8**, 264–270 (1984), (in German)

5.266 G.L. Brown, R.F. Davey: The calibration of hot-films for skin friction measurement, Rev. Sci. Instrum. **42**, 1729–1731 (1971)

5.267 K.D. Cole, J.V. Beck: Conjugated heat transfer from a hot-film probe for transient air flow, J. Heat Transf. Trans. ASME **110**, 290–296 (1988)

5.268 J.K. Reichert, R.S. Azad: Wall shear stress measurement with a hot film in a variable temperature flow, Rev. Sci. Instrum. **48**, 341–345 (1977)

5.269 P.H. Alfredsson, A.V. Johansson, J.H. Haritonidis, H. Eckelmann: The fluctuating wall-shear stress and the velocity field in the viscous sublayer, Phys. Fluids **31**, 1026–1033 (1988)

5.270 R.I. Tanner: Theory of a thermal fluxmeter in a shear flow, J. Appl. Mech. **34**, 801–805 (1967)

5.271 G.R. Sarma, T. Moes: Demonstration of skin friction measurements featuring in situ estimation of conduction loss using constant voltage anemometers and surface hot-films, Rev. Sci. Instrum. **76**, 055102 (2005)

5.272 S.M. Mangalam: Real-time extraction of hydrodynamic flow characteristics using surface signatures, IEEE J. Oceanic Eng. **29**, 622–630 (2004)

5.273 J.D. Ruedi, H. Nagib, J. Österlund, P.A. Monkewitz: Evaluation of three techniques for wall-shear measurements in three-dimensional flows, Exp. Fluids **35**, 389–396 (2003)

5.274 M.J. Lighthill: The response of laminar skin friction and heat transfer to fluctuations in the stream velocity, Proc. R. Soc. London A, Vol. 224 (1954) 1–23

5.275 O. Desgeorges, T. Lee, F. Kafyeke: Multiple hot-film array calibration and skin friction measurement, Exp. Fluids **32**, 37–43 (2002)

5.276 A.M. Koppius, G.R.M. Trines: The dependence of hot-wire calibration on gas temperature at low Reynolds numbers, Int. J. Heat Mass Transf. **19**, 967–974 (1972)

5.277 R. Thünker, W. Nitsche, M. Swoboda: Hot-wire, hot-film and surface hot-film applications in strongly temperature loaded flows, ICIASF, Vol. 89 (1989)

5.278 L. Meyer: Calibration of a three-wire probe for measurements in nonisothermal flow, Exp. Therm. Fluid Sci. **5**, 260–267 (1992)

5.279 S.F. Benjamin, C.A. Roberts: Measuring flow velocity at elevated temperature with a hot wire anemometer calibrated in cold flow, Int. J. Heat Mass Transf. **45**, 703–706 (2002)

5.280 J.M. Cimbala, W.J. Park: A direct hot-wire calibration technique to account for ambient temperature drift in incompressible flow, Exp. Fluids **8**, 299–300 (1990)

5.281 M. Kostka, V. Vasanta Ram: On the effects of fluid temperature on hot wire characteristics. Part 1: Results of experiments, Exp. Fluids **13**, 155–162 (1992)

5.282 V. Vasanta Ram: On the effects of fluid temperature on hot wire characteristics. Part 2: Foundations of a rational theory, Exp. Fluids **13**, 267–278 (1992)

5.283 K. Hollasch, B. Gebhart: Calibration of constant-temperature hot-wire anemometers at low velocities in water with variable fluid temperature, ASME J. Heat Transf. **94**, 17–22 (1972)

5.284 R.E. Drubka, J. Tan-atichat, H.M. Nagib: Analysis of temperature compensating circuits for hot-wires and hot-films, DISA Inf. **22**, 5–14 (1977)

5.285 G.R. Sarma, G. Comte-Bellot: Automated constant voltage anemometer for measurements with fluid temperature drifts, Rev. Sci. Instrum. **73**, 1313–1317 (2002)

5.286 G.E. Truzzi, G.R. Sarma, N. Chokani: Constant voltage anemometer operated hot wire at subsonic speeds over wide overheats in unstady flows, Rev. Sci. Instrum. **73**, 4363–4368 (2002)

5.287 S. Corrsin: Extended applications of the hot-wire anemometer, Rev. Sci. Instrum. **18**, 469–471 (1947)

5.288 T.T. Yeh, C.W. Van Atta: Spectral transfer of scalar and velocity fields in heated-grid turbulence, J. Fluid Mech. **58**, 233–261 (1973)

5.289 L. Fulachier: Hot-wire measurements in low speed heated flows, Proc. Dyn. Flow Conf. DISA, ed. by B.W. Hansen (1979) 465–487

5.290 P. Paranthoen, C. Petit, J.C. Lecordier: The effect of the thermal prong-wire interaction on the response of a cold wire in gaseous flows (air, argon, helium), J. Fluid Mech. **124**, 457–473 (1982)

5.291 L.W.B. Browne, R.A. Antonia, A.J. Chambers: Effect of the separation between cold wires on the spatial derivatives of temperature in a turbulent flow, Bound.-Lay. Meteorol. **27**, 129–139 (1983)

5.292 L. Mydlarski, Z. Warhaft: Passive scalar statistics in high-Peclet-number grid turbulence, J. Fluid Mech. **358**, 135–175 (1998)

5.293 M. Tagawa, K. Kato, Y. Ohta: Response compensation of fine-wire temperature sensors, Rev. Sci. Instrum. **76**, 094904 (2005)

5.294 P. Mestayer, P. Chambaud: Some limitations to measurements of turbulence micro-structure with hot and cold wires, Bound.-Lay. Meteorol. **16**, 311–329 (1979)

5.295 S.-C. Lin, S.-C. Lin: Study of strong temperature mixing in subsonic grid turbulence, Phys. Fluids **16**, 1587–1598 (1971)

5.296 S. Tavoularis: A circuit for the measurement of instantaneous temperature in heated turbulent flows, J. Phys. E Sci. Instrum. **11**, 21–23 (1978)

5.297 R.A. Antonia, L.W.B. Browne, A.J. Chambers: Determination of time constants of cold wires, Rev. Sci. Instrum. **52**, 1382–1385 (1981)

5.298 J.C. LaRue, T. Deaton, C.H. Gibson: Measurement of high-frequency turbulent temperature, Rev. Sci. Instrum. **46**, 757–764 (1975)

5.299 L. Fulachier, R. Dumas: Spectral analogy between temperature and velocity fluctuations in a turbulent boundary layer, J. Fluid Mech. **77**, 257–277 (1976)

5.300 G. Huelsz, E. Ramos: Temperature measurements inside the oscillatory boundary layer produced by acoustic waves, J. Acoust. Soc. Am. **103**, 1532–1537 (1998)

5.301 L.S.G. Kovasznay, M.S. Uberoi, S. Corrsin: The transformation between one- and three- dimensional power spectra for an isotropic scalar fluctuation field, Phys. Rev. **76**, 1263–1264 (1949)

5.302 A.E. Perry, A.J. Smits, M.S. Chong: The effects of certain low frequency phenomena on the calibration of hot wires, J. Fluid Mech. **90**, 415–431 (1979)

5.303 P. Paranthoen, J.C. Lecordier: Mesures de température dans les écoulements turbulents, Rev. Gen. Therm. **35**, 283–308 (1996)

5.304 D.W. Artt, A. Brown: The simultaneous measurement of velocity and temperature, J. Phys. E Sci. Instrum. **4**, 72–74 (1971)

5.305 G. Comte-Bellot, J. Mathieu: Sur la détermination expérimentale des coefficients de sensibilité aux fluctuations de vitesse et de température des anémomètres à fil chaud, CR Acad. Sci. Paris **246**, 3219–3222 (1958)

5.306 J.P. Bonnet, M.A. Knani: Calibration and use of inclined hot-wires in a supersonic turbulent wake, Exp. Fluids **6**, 179–188 (1988)

5.307 S. Candel: *Mécanique des fluides* (Dunod, Paris 1995)

5.308 W. Konrad, A.J. Smits: Reynolds stress measurements in a three-dimensional supersonic turbulent boundary layer, Proc. ASME Symp. Therm. Anemometry, Vol. FED 167 (1993) 219–230

5.309 E.M. Fernando, J.F. Donovan, A.J. Smits: The calibration and operation of a constant-temperature anemometer crossed-wire probe in supersonic flow, Proc. ASME Symp. Thermal Anemometry, Vol. FED 53 (1987) 43–49

5.310 A.J. Smits, K.C. Muck: Constant temperature hot-wire anemometer practice in supersonic flows. Part 2: The inclined wire, Exp. Fluids **2**, 33–41 (1984)

5.311 E. Reshotko, I.E. Beckwith: Compressible laminar boundary layer over a yawed infinite cylinder with heat transfer and arbitrary Prandtl number, NACA Tech. Rep. **1379** (1957)

5.312 W.C. Rose, D.A. Johnson: Turbulence in a shock-wave boundary-layer interaction, AIAA J. **13**, 884–889 (1975)

5.313 D.A. Johnson, W.C. Rose: Laser velocimeter and hot-wire anemometer comparison in a supersonic boundary layer, AIAA J. **13**, 512–515 (1975)

5.314 P. Bradshaw: Compressible turbulent shear layers, Ann. Rev. Fluid Mech. **9**, 33–54 (1977)

5.315 E.F. Spina, A.J. Smits, S.K. Robinson: The physics of supersonic turbulent boundary layers, Ann. Rev. Fluid Mech. **26**, 287–319 (1994)

5.316 F.R. Payne, J.L. Lumley: One-dimensional spectra derived from an airborne hot-wire anemometer, Q. J. R. Meteorol. Soc. **92**, 397–401 (1966)

5.317 C.M. Sheih, H. Tennekes, J.L. Lumley: Airborne hot-wire measurements of the small-scale structure of atmospheric turbulence, Phys. Fluids **14**, 201–215 (1971)

5.318 N.R. Panchapakesan, J.L. Lumley: Turbulence measurements in axisymmetric jets of air and helium. Part 1. Air jet, J. Fluid Mech. **246**, 197–223 (1993)

5.319 N.R. Panchapakesan, J.L. Lumley: Turbulence measurements in axisymmetric jets of air and helium. Part 2. Helium jet, J. Fluid Mech. **246**, 225–247 (1993)

5.320 R.M. Kelso, T.T. Lim, A.E. Perry: A novel flying hot-wire system, Exp. Fluids **16**, 181–186 (1994)

5.321 D. Coles, A.J. Wadcock: Flying-hot-wire study of flow past an NACA 4412 airfoil at maximum lift, AIAA J. **17**, 321–329 (1979)

5.322 B. Cantwell, D. Coles: An experimental study of entrainment and transport in the turbulent near wake of a circular cylinder, J. Fluid Mech. **136**, 321–374 (1983)

5.323 M.D. Walker, M.R. Maxey: A whirling hot-wire anemometer with optical data transmission, J. Phys. E Sci. Instrum. **18**, 516–521 (1985)

5.324 H.J. Hussein, S.P. Capp, W.K. George: Velocity measurements in a high-Reynolds-number, momentum-conserving, axisymmetric, turbulent jet, J. Fluid Mech. **258**, 31–75 (1994)

5.325 B.E. Thomson, J.H. Whitelaw: Flying hot-wire anemometry, Exp. Fluids **2**, 47–56 (1984)

5.326 H.H. Al-Kayiem, H.H. Bruun: Evaluation of a flying X hot-wire probe system, Meas. Sci. Technol. **2**, 374–380 (1991)

5.327 L.J. Otten, A.L. Pavel, W.E. Finley, W.C. Rose: A survey of recent atmospheric turbulence measurements from a subsonic aircraft, AIAA Paper **81-0298** (1981)

5.328 M. Jaroch: Development and testing of pulsed-wire probes for measuring fluctuating quantities in highly turbulent flows, Exp. Fluids **3**, 315–322 (1985)

5.329 I.P. Castro, A. Haque: The stucture of a turbulent shear layer bounding a reversed flow region, J. Fluid Mech. **179**, 439–468 (1987)

5.330 I.P. Castro, M. Dianat: Pulsed wire velocity anemometry near walls, Exp. Fluids **8**, 343–352 (1990)

5.331 L.J.S. Bradbury, I.P. Castro: A pulsed-wire technique for velocity measurements in highly turbulent flows, J. Fluid Mech. **49**, 657–691 (1971)

5.332 R.V. Westphal, J.K. Eaton, J.P. Johnston: A new probe for measurement of velocity and wall shear stress in unsteady, reversing flow, J. Fluid Eng. Trans. ASME **103**, 478–482 (1981)

5.333 M. Jaroch, A. Dahm: A new pulsed-wire probe for measuring the Reynolds stresses in the plane containing the main shear direction of a turbulent shear flow, J. Phys. E Sci. Instrum. **21**, 1085–1094 (1988)

5.334 P.M. Handford, P. Bradshaw: The pulsed-wire anemometer, Exp. Fluids **7**, 125–132 (1989)

5.335 I.P. Castro, B.S. Cheun: The measurement of Reynolds stresses with a pulsed-wire anemometer, J. Fluid Mech. **118**, 41–58 (1982)

5.336 L.J.S. Bradbury: Measurements with a pulsed-wire and a hot-wire anemometer in the highly turbulent wake of a normal flat plate, J. Fluid Mech. **77**, 473–497 (1976)

5.337 B. Venås, H. Abrahamsson, P.Å. Krogstad, L. Löfdahl: Pulsed hot-wire measurements in two- and three-dimensional wall jets, Exp. Fluids **27**, 210–218 (1999)

5.338 P. Calvet, F. Liousse: Mesures locales de températures, pressions et vitesses au moyen de capteurs thermorésistants chauffés par impulsions, Rev. Gen. Therm. **114**, 527–542 (1971)

5.339 E. Mathioulakis, M. Grignon, J.G. Poloniecki: A pulsed-wire technique for velocity and temperature measurements in natural convection flows, Exp. Fluids **18**, 82–86 (1994)

5.340 M. Grignon, E. Mathioulakis, P. Ngae, J.G. Poloniecki: Pulsed-wire technique for velocity measurements in natural convection flows – a numerical optimisation tool, Int. J. Heat Mass Transf. **41**, 3121–3129 (1998)

5.341 D. Li, K.S. Gow: The development of a pulsed multi-element hot-wire anemometer, Meas. Sci. Technol. **6**, 1175–1185 (1995)

5.342 J.F. Foss, D.G. Bohl, T.J. Hicks: The pulse width modulated-constant temperature anemometer, Meas. Sci. Technol. **7**, 1388–1395 (1996)

5.343 J.F. Foss, T.J. Hicks: Processing time series data (velocity, shear stress) from the pulse width modulated-constant temperature anemometer (PWM-CTA). In: *19th ICIASF IEEE*, ed. by M.P. Wernet (IEEE, Piscataway 2001) pp. 448–453

5.344 T.J. Hicks, J.K. Schwannecke, M.J. Norconk, A.M. Hellum, J.F. Foss: The evolved 100 kHz PWM-CTA. In: *20th ICIASF*, ed. by R.H. Engler (IEEE, Piscataway 2003)

5.345 J.-L. Breton: *Dissipation thermique de fils chauds soumis à des impulsions calorifique*. Thèse Spécialité (Univ. Paul Sabatier, Toulouse 1972)

5.346 J.F. Foss, R.C. Haw: Transverse vorticity measurements using a compact array of four sensors. In: *The Heuristics of Thermal Anemometry*, Vol. FED97, ed. by D.E. Stock, S.A. Sherif, A.J. Smits (ASME, New York 1990) pp. 71–76

5.347 S.-C. Morris: *The Velocity and Vorticity Fields of a Single Stream Shear Layer*, Ph.D. Thesis (Michigan State University, East Lansing 2002)

5.348 C. Crowe, M. Sommerfeld, Y. Tsuji: *Multiphase Flows with Droplets and Particles* (CRC, Boca Raton 1998)

5.349 A.T. Hjemfelt, L.F. Mockros: Motion of discrete particles in a turbulent fluid, Appl. Sci. Res. **16**, 149–161 (1966)

5.350 B.T. Chao: Turbulent transport behavior of small particles in a turbulent fluid, Österr. Ingenieurarch. **19**, 7 (1964)

5.351 R. Mei: Velocity fidelity of flow tracer particles, Exp. Fluids **22**, 1–13 (1996)

5.352 A. Melling: Tracer particles and seeding for particle image velocimetry, Meas. Sci. Technol. **8**, 1406–1416 (1997)

5.353 F. Scarano, B.W. van Oudheusden: Planar velocity measurements of a two-dimensional compressible wake, Exp. Fluids **34**, 430–441 (2003)

5.354 R.P. Dring: Sizing criteria for laser anemometry particles, J. Fluid Eng. Trans. ASME **104**, 15–17 (1982)

5.355 G. Tedeschi, H. Gouin, M. Elena: Motion of tracer particles in supersonic flows, Exp. Fluids **26**, 288–296 (1999)

5.356 H.-E. Albrecht, M. Borys, N. Damaschke, C. Tropea: *Laser Doppler and Phase Doppler Measurement Techniques* (Springer, Berlin, Heidelberg 2003)

5.357 C.D. Meinhart, S.T. Wereley, J.G. Santiago: PIV measurements of a microchannel flow, Exp. Fluids **27**, 414–419 (1999)

5.358 G. Rottenkolber, R. Meier, O. Schäfer, S. Wachter, K. Dullenkopf, S. Wittig: Phase discrimination inside a spray: LDV measurements using fluorescent seeding particles (FLDV). In: *Laser Techniques for Fluid Mechanics*, ed. by R.J. Adrian, D.F.G. Durao, F. Durst, M.V. Heitor, M. Maedo, J.H. Whiteclaw (Springer, Berlin, Heidelberg 2002) pp. 511–526

5.359 C. Helsper, L. Mölter: Erzeugung von Prüfaerosolen für die Kalibrierung von optischen partikelmessverfahren nach VDI 3491, Tech. Mess. **56**, 229–234 (1989), (in German)

5.360 D. Dabiri, M. Gharib: Digital particle image thermometry: The method and implementation, Exp. Fluids **11**, 77–86 (1991)

5.361 A. Günther, P.R. von Rohr: Influence of the optical configuration on temperature measurements with fluid-dispersed TLCs, Exp. Fluids **32**, 533–541 (2002)

5.362 G. Rottenkolber, R. Meier, O. Schäfer, S. Wachter, K. Dullenkopf, S. Wittig: Combined PDA and LDV measurements: Phase discrimination inside a spray using fluorescent seeding particles, Proc. 10th Int. Symp. Appl. Laser Technol. Fluid Mech. Lisbon (2000) , paper 31.1

5.363 D. Sinclair, V.K. LaMer: Light scattering as a measure of particle size in aerosols: The production of monodisperse aerosols, Chem. Rev. **44**, 245–267 (1949)

5.364 A. Lefebvre: *Atomisation and Sprays* (Hemisphere, New York 1989)

5.365 W.-H. Echols, J.-A. Young: Studies of air-operated aerosol generators, NRL Rep. *5929* (US Naval Res. Lab., Washington 1963)

5.366 : Proc. London Math. Soc., Vol. 10 (1878) 4

5.367 G. Brenn, F. Durst, C. Tropea: Monodisperse sprays for various purposes – their production and characteristics, Part. Part. Syst. Charact. **13**, 179–185 (1996)

5.368 N. Paone, G.M. Revel, E. Nino: Velocity measurement in high turbulent premixed flames by a PIV measurement system, Proc. 8th Int. Symp. Appl. Laser Technol. Fluid Mech. Lisbon (1996) , , paper 3.4

5.369 M. Glass, I.M. Kennedy: An improved seeding method for high temperature laser Doppler velocimetry, Combust. Flame **49**, 155–162 (1977)

5.370 D.J. Anderson, C.A. Greated, J.D.C. Jones, G. Nimmo, S. Wiseall: Fibre optic PIV studies in an industrial combustor, Proc. 8th Int. Symp. Appl. Laser Technol. Fluid Mech. Lisbon (1996) , , paper 18.4

5.371 J.K. Agarwal, E.M. Johnson: Generating aerosol for laser velocimeter seeding, TSI Quart. **VII** (1981)

5.372 F. Scarano, B.W. van Oudheusden, W.J. Bannink, M. Bsibsi: Experimental investigation of supersonic base flow plume interaction by means of particle image velocimetry, 5th Eur. Symp. Aerothermodyn. Space Vehicles Cologne (2004)

5.373 Y. Yeh, H.Z. Cummins: Localized fluid flow measurements with a He-Ne laser spectrometer, Appl. Phys. Lett. **4**, 176–179 (1964)

5.374 B. Lehmann: Geschwindigkeitsmessung mit Laser-Doppler-Anemometer Verfahren, Wissenschaftliche Berichte AERG-Telefunken **41**, 141–145 (1968), (in German)

5.375 H.D. vom Stein, H.J. Pfeifer: A Doppler difference method for velocity measurements, Metrologia **5**, 59–61 (1969)

5.376 B. Lehmann, H. Nobach, C. Tropea: Measurement of acceleration using the laser Doppler technique, Meas. Sci. Technol. **13**(9), 1367–1381 (2002)

5.377 W. Feller: *An Introduction to Probability Theory and Its Applications*, Vol. I (Wiley, New York 1971)

5.378 P. Buchhave, W.K. George Jr, J.L. Lumley: The measurement of turbulence with the laser-Doppler anemometer, Ann. Rev. Fluid. Mech. **11**, 443–504 (1979)

5.379 L.H. Benedict, H. Nobach, C. Tropea: Estimation of turbulent velocity spectra from laser Doppler data, Meas. Sci. Technol. **11**, 1089–1104 (2000)

5.380 H.R.E. van Maanen, H. Nobach, L.H. Benedict: Improved estimator for the slotted autocorrelation function of randomly sampled LDA data, Meas. Sci. Technol. **10**, L4–L7 (1999)

5.381 H.E. Nobach Müller, C. Tropea: Efficient estimation of power spectral density from laser Doppler anemometer data, Exp. Fluids **24**, 499–509 (1998)

5.382 W.T. Mayo Jr, M.T. Shay, S. Ritter: Digital estimation of turbulence power spectra from burst counter LDV data, Proc. 2nd Int. Workshop on Laser Velocimetry (Purdue Univ., 1974) 16–26

5.383 H.R.E. van Maanen, M.J. Tummers: Estimation of the auto correlation function of turbulent velocity fluctuations using the slotting technique with local normalization, Proc. 8th Int. Symp. Appl. Laser Technol. Fluid Mech. Lisbon, ed. by R.J. Adrian, D.F.G. Durao, F. Durst, M.V. Heitor, M. Maeda, J.H. Whitelaw (1996) , , paper 36.4

5.384 R.J. Adrian, C.S. Yao: Power spectra of fluid velocities measured by laser Doppler velocimetry, Exp. Fluids **5**, 17–28 (1987)

5.385 E. Müller, H. Nobach, C. Tropea: LDA signal reconstruction: application to moment and spectral estimation, Proc. 7th Int. Symp. Appl. Laser Technol. Fluid Mech. Lisbon, ed. by R.J. Adrian, D.F.G. Durao, F. Durst, M.V. Heitor, M. Maedo, J.H. Whiteclaw (1994) , , paper 23.2

5.386 H. Nobach, E. Müller, C. Tropea: Refined reconstruction techniques for LDA data analysis, Proc. 8th Int. Symp. Appl. Laser Technol. Fluid Mech. Lisbon, ed. by R.J. Adrian, D.F.G. Durao, F. Durst, M.V. Heitor, M. Maedo, J.H. Whiteclaw (1996) , , paper 36.2

5.387 W. Merzkirch: *Flow Visualization* (Academic, Orlando 1987)

5.388 M. Van Dyke: *An Album of Fluid Motion* (Parabolic, Stanford 1982)

5.389 G.L. Brown, A. Roshko: On density effects and large structure in turbulent mixing layers, J. Fluid Mech. **64**, 775–816 (1974)

5.390 B.J. Cantwell: Organized motion in turbulent flow, Ann. Rev. Fluid Mech. **13**, 457–515 (1981)

5.391 A.K.M.F. Hussain: Coherent structures and turbulence, J. Fluid Mech. **173**, 303–356 (1986)

5.392 L. Hesselink: Digital image processing in flow visualization, Ann. Rev. Fluid Mech. **20**, 421–486 (1988)

5.393 R.J. Adrian: Particle-imaging techniques for experimental fluid mechanics, Ann. Rev. Fluid Mech. **23**, 261–304 (1991)

5.394 R.J. Adrian: Twenty years of particle image velocimetry, Exp. Fluids **39**, 159–169 (2005)

5.395 H.T. Kim, S.J. Kline, W.C. Reynolds: The production of turbulence near a smooth wall in a turbulent boundary layer, J. Fluid Mech. **50**, 133 (1971)

5.396 J. Westerweel: *Particle Image Velocimetry – Theory and Application* (Delft Univ. Press, Delft 1993)

5.397 M. Stanislas, K. Okamoto, C.J. Kähler, J. Westerweel: Main results of the second international PIV challenge, Exp. Fluids **39**, 170–191 (2005)

5.398 W. Kühn, J. Kompenhans, J.C. Monnier: Full scale PIV test in an industrial facility. In: *Particle Image Velocimetry – Progress Towards Industrial Application*, ed. by M. Stanislas, J. Kompenhans, J. Westerweel (Kluwer, Dordrecht 2000) pp. 91–150

5.399 F. Scarano, C. van Wijk, L.L.M. Veldhuis: Traversing field of view and AR-PIV for mid-field wake vortex investigation in a towing tank, Exp. Fluids **33**, 950–961 (2002)

5.400 T. Hori, J. Sakakibara: High-speed scanning stereoscopic PIV for 3D vorticity measurement in liquids, Meas. Sci. Technol. **15**, 1067–1078 (2004)

5.401 F. Scarano, G.E. Elsinga, E. Bocci, B.W. van Oudheusden: Investigation of 3-D coherent structures in the turbulent cylinder wake using Tomo-PIV, 13th Int. Symp. Appl. Laser Tech. Fluid Mech., Lisbon (2006)

5.402 C. Brucker: 3-D scanning-particle-image-velocimetry: Technique and application to a spherical cap wake flow, Appl. Sci. Res. **56**, 157–79 (1996)

5.403 S.F. Herrmann, K.D. Hinsch: Light-in-flight holographic particle image velocimetry for wind-tunnel applications, Meas. Sci. Technol. **15**, 613–621 (2004)

5.404 G.E. Elsinga, B. Wieneke, F. Scarano, B.W. van Oudheusden: Tomographic particle image velocimetry, Exp. Fluids **41**, 933–947 (2006)

5.405 J. Haertig, M. Havermann, C. Rey, A. George: Particle image velocimetry in Mach 3.5 and 4.5 shock-tunnel flows, AIAA J. **40**, 1056 (2002)

5.406 J.R. Hove, R.W. Köster, A.S. Forouhar, G. Acevedo-Bolton, S.E. Fraser, M. Gharib: Intracardiac fluid forces are an essential epigenetic factor for embryonic cardiogenesis, Nature **421**, 172–177 (2003)

5.407 P. Vennemann: In vivo micro particle image velocimetry measurements of blood-plasma in the embryonic avian heart, J. Biomech. **39**, 1191–1200 (2006)

5.408 C. Fukushima, L. Aanen, J. Westerweel: Investigation of the mixing process in an axisymmetric turbulent jet using PIV and LIF. In: *Laser Techniques for Fluid Mechanics*, ed. by R.J. Adrian, D.F.G. Durao, M.V. Heitor, M. Maeda, C. Tropea, J.H. Whitelaw (Springer, Heidelberg, Berlin 2002) pp. 339–356

5.409 E. Delnoij, J. Westerweel, N.G. Deen, J.A.M. Kuipers, W.P.M. van Swaaij: Ensemble correlation PIV applied

to bubble plumes rising in a bubble column, Chem. Eng. Sci. **54**, 5159–5171 (1999)
5.410 K.T. Kiger, C. Pan: PIV technique for the simultaneous measurement of dilute two-phase flows, J. Fluid Eng. **122**, 811–818 (2000)
5.411 D.A. Khalitov, E.K. Longmire: Simultaneous two-phase PIV by two-parameter phase discrimination, Exp. Fluids **32**, 252–268 (2002)
5.412 R. Lindken, W. Merzkirch: A novel PIV technique for measurements in multiphase flows and its application to two-phase bubbly flows, Exp. Fluids **33**, 814–825 (2002)
5.413 C. Poelma, J. Westerweel, G. Ooms: Turbulence statistics from optical whole field measurements in particle-laden turbulence, Exp. Fluids **40**, 347–363 (2006)
5.414 J. Westerweel: Fundamentals of digital particle image velocimetry, Meas. Sci. Technol. **8**, 1379 (1997)
5.415 J.W. Goodman: *Introduction to Fourier Optics* (McGraw-Hill, New York 1968)
5.416 M.G. Olsen, R.J. Adrian: Out-of-focus effects on particle image visibility and correlation in microscopic particle image velocimetry, Exp. Fluids **29**, S166–S147 (2000)
5.417 A.K. Prasad: Stereoscopic particle image velocimetry, Exp. Fluids **29**, 103 (2000)
5.418 C. Willert: Stereoscopic digital particle image velocimetry for application in wind tunnel flows, Meas. Sci. Technol. **8**, 353 (1997)
5.419 C.W.H. van Doorne, J. Westerweel: Measurement of laminar, transitional and turbulent pipe flow using stereoscopic-PIV, Exp. Fluids **42**, 259–279 (2007)
5.420 J. Westerweel, J. van Oord: Stereoscopic PIV measurement in a turbulent boundary layer. In: *Particle Image Velocimetry: Progress Towards Industrial Application*, ed. by M. Stanislas, J. Kompenhans, J. Westerweel (Kluwer, Dordrecht 2000) pp. 459–478
5.421 S.M. Soloff: Distortion compensation for generalized stereoscopic particle image velocimetry, Meas. Sci. Technol. **8**, 1441 (1997)
5.422 S.J.M. Coudert, J.P. Schon: Back-projection algorithm with misalignment corrections for 2D3C stereoscopic PIV, Meas. Sci. Technol. **12**, 1371 (2001)
5.423 B. Wieneke: Stereo-PIV using self-calibration on particle images, Exp. Fluids **39**, 267–280 (2005)
5.424 A. Rosenfeld, A.C. Kak: *Digital Picture Processing*, 2nd edn. (Academic, Orlando 1982)
5.425 A.K. Jain: *Fundamentals of Digital Image Processing* (Prentice-Hall, Englewood Cliffs 1989)
5.426 A.V. Oppenheim, A.S. Willsky, S. Hamid, S.H. Nawab: *Signals and Systems* (Prentice-Hall, Englewood Cliffs 1983)
5.427 J. Westerweel: Effect of sensor geometry on the performance of PIV interrogation. In: *Laser Techniques Applied to Fluid Mechanics*, ed. by R.J. Adrian, D.F.G. Durao, F. Durst, M.V. Heitor, M. Maedo, J.H. Whitelaw (Springer, Berlin, Heidelberg 2000) pp. 37–55
5.428 K.E. Meyer, J. Westerweel: Advection velocities of flow structures estimated from particle image velocimetry measurements in a pipe, Exp. Fluids **29**, S237 (2000)
5.429 C. Freek, J.M.M. Sousa, W. Hentschel, W. Merzkirch: On the accuracy of a MJPEG-based digital image compression PIV system, Exp. Fluids **27**, 310 (1999)
5.430 Y.G. Guezennec, N. Kiritsis: Statistical investigation of errors in particle image velocimetry, Exp. Fluids **10**, 138 (1990)
5.431 R.D. Keane, R.J. Adrian, Y. Zhang: Super-resolution particle imaging velocimetry, Meas. Sci. Technol. **6**, 754–768 (1995)
5.432 R.J. Adrian: Statistical properties of particle image velocimetry measurements in turbulent flow. In: *Laser Anemometry in Fluid Mechanics*, Vol. III, ed. by D.F.G. Durao, R.J. Adrian, T. Asanuma, F. Durst, J.H. Whitelaw (1988) pp. 115–129
5.433 J. Westerweel: Theoretical analysis of the measurement precision in particle image velocimetry, Exp. Fluids **29**, S3 (2000)
5.434 R.D. Keane, R.J. Adrian: Optimization of particle image velocimeters. Part I: Double-pulsed systems, Meas. Sci. Technol. **1**, 1202 (1990)
5.435 H.T. Huang, H.F. Fielder, J.J. Wang: Limitation and improvement of PIV, Part II. particle image distortion, a novel technique, Exp. Fluids **15**, 263–273 (1993)
5.436 R.D. Keane, R.J. Adrian: Optimization of particle image velocimeters. Part II: Multiple-pulsed systems, Meas. Sci. Technol. **2**, 963 (1991)
5.437 R.D. Keane, R.J. Adrian: Theory of cross-correlation analysis of PIV images, Appl. Sci. Res. **49**, 191 (1992)
5.438 J. Westerweel: Measurement of fully-developed turbulent pipe flow with digital particle image velocimetry, Exp. Fluids **20**, 165 (1996)
5.439 J. Westerweel: The effect of a discrete window offset on the accuracy of cross-correlation analysis of digital PIV recordings, Exp. Fluids **23**, 20 (1997)
5.440 O. Ronneberger: *Messung aller drei Geschwindigkeitskomponenten mit Hilfe der Particle Image Velocimetry mittels einer Kamera und zweier paralleler Lichtschnitte*, Diploma Thesis (Georg-August-Universitât, Göttingen 1998)
5.441 E.O. Brigham: *The Fast Fourier Transform and Its Applications* (Prentice-Hall, Englewood Cliffs 1988)
5.442 C.E. Willert, M. Gharib: Digital particle image velocimetry, Exp. Fluids **10**, 181 (1991)
5.443 M.B. Priestley: *Spectral Analysis and Time Series* (Academic, San Diego 1992)
5.444 A.K. Prasad, R.J. Adrian, C.C. Landreth, P.W. Offutt: Effect of resolution on the speed and accuracy of particle image velocimetry interrogation, Exp. Fluids **13**, 105–116 (1992)
5.445 K.T. Christensen: The influence of peak-locking errors on turbulence statistics computed from PIV ensembles, Exp. Fluids **36**, 484 (2004)

5.446 A.M. Fincham, G. Delerce: Advanced optimization of correlation imaging velocimetry algorithms, Exp. Fluids **29**, S013–S022 (2000)

5.447 C.E. Willert: The fully digital evaluation of photographic PIV recordings, Appl. Sci. Res. **56**, 79 (1996)

5.448 N. Bobroff: Position measurement with a resolution and noise-limited instrument, Rev. Sci. Instrum. **57**, 1152 (1986)

5.449 D.P. Hart: Sparse array image correlation, Proc. 8th Int. Symp. Appl. Laser Tech. Fluid Mech. Lisbon (1996)

5.450 J.M. Foucaut, B. Miliat, N. Perenne, M. Stanislas: Characterization of different PIV algorithms using the EUROPIV synthetic image generator and real images from a turbulent boundary layer. In: *Particle Image Velocimetry: Recent Improvements*, ed. by M. Stanislas, J. Westerweel, J. Kompenhans (Springer, Heidelberg, Berlin 2004) pp. 163–185

5.451 C.D. Meinhart, S.T. Wereley, J.G. Santiago: A PIV algorithm for estimating time-averaged velocity fields, J. Fluid Eng. **122**, 285–289 (2000)

5.452 D.P. Hart: PIV error correction, Exp. Fluids **29**, 13–22. (2000)

5.453 M.P. Wernet: Symmetric phase only filtering: a new paradigm for DPIV data processing, Meas. Sci. Technol. **16**, 601–618 (2005)

5.454 F. Scarano: Iterative image deformation methods in PIV, Meas. Sci. Technol. **13**, R1–R19 (2002)

5.455 B. Lecordier: Etude de l'interaction de la propagation d'une flamme premelangee avec le champ aerodynamique, par association de la tomographie Laser et de la Velocimetrie par Images de particules. These de doctorat (Universite de Rouen, Rouen 1997)

5.456 S.T. Wereley, C.D. Meinhart: Second-order accurate particle image velocimetry, Exp. Fluids **31**, 258 (2001)

5.457 P.T. Tokumaru, P.E. Dimotakis: Image correlation velocimetry, Exp. Fluids **19**, 1–15 (1995)

5.458 F. Scarano: A super-resolution PIV interrogation approach by means of velocity 2nd derivatives correlation, Meas. Sci. Technol. **15**, 475–486 (2004)

5.459 F.F.J. Schrijer, F. Scarano: Effect of predictor-corrector filtering on the stability and spatial resolution of iterative PIV interrogation, Exp. Fluids, (in press) (2007)

5.460 F. Scarano, F.F.J. Schrijer: Effect of predictor filtering on the stability and spatial resolution of iterative PIV interrogation, 5th International Symposium on PIV, Caltech Pasadena (2005)

5.461 J. Nogueira, A. Lecuona, P.A. Rodriguez: Local field correction PIV, implemented by means of simple algorithms, and multigrid versions, Meas. Sci. Technol. **12**, 1911 (2001)

5.462 J. Westerweel, F. Scarano: A universal detection criterion for the median test, Exp. Fluids **39**(6), 1096–1100 (2005)

5.463 J. Westerweel: Efficient detection of spurious vectors in particle image velocimetry data sets, Exp. Fluids **16**, 236–247 (1994)

5.464 L. Lourenco, A. Krothapalli: On the accuracy of velocity and vorticity measurements with PIV, Exp. Fluids **18**, 421–428 (1995)

5.465 S. Abrahamson, S. Lonnes: Uncertainty in calculating vorticity from 2D velocity fields using circulation and least-squares approaches, Exp. Fluids **20**, 10–20 (1995)

5.466 A. Fouras, J. Soria: Accuracy of out of plane vorticity measurements derived from in-plane velocity field data, Exp. Fluids **25**, 409–430 (1998)

5.467 M. Raffel, C. Willert, S. Wereley, J. Kompenhans: *Particle Image Velocimetry – a practical guide* (Springer, Berlin, Heidelberg 2007)

5.468 J.M. Foucaut, M. Stansislas: Some considerations on the accuracy and frequency response of some derivative filters applied to particle image velocimetry fields, Meas. Sci. Technol. **13**, 1058–1071 (2002)

5.469 G.K. Batchelor: *An Introduction to Fluid Mechanics* (Cambridge Univ. Press, Cambridge 1967)

5.470 C.C. Landreth, R.J. Adrian: Measurement and refinement of velocity data using high image density analysis in particle image velocimetry. In: *Applications of Laser Anemometry to Fluid Mechanics*, ed. by D.F.G. Durao, R.J. Adrian, M. Maeda, F. Durst, J.H. Whitelaw (Springer, Berlin 1990) pp. 484–497

5.471 C.C. Landreth, R.J. Adrian: Impingement of a low Reynolds number turbulent circular jet onto a flat plate at normal incidence, Exp. Fluids **9**, 74–84 (1990)

5.472 J.N. Forkey, W.R. Lempert, R.B. Miles: Corrected and calibrated I2 absorption model at frequency-doubled Nd:YAG laser wavelengths, Appl. Opt. **36**(27), 6729–6738 (1997)

5.473 H. Komine: System for measuring velocity field of fluid flow utilizing a laser-Doppler spectral image converter, US Patent 4,919,536 (1990)

5.474 H. Komine, S.J. Brosnan, A.B. Litton, E.A. Stappaerts: Real-time Doppler global velocimetry, AIAA Paper, Vol. 91-0337 (1991)

5.475 J.F. Meyers, H. Komine: Doppler global velocimetry – A new way to look at velocity. In: *Laser Anemometry: Advances and Applications*, ed. by A. Dybbs, B. Ghorashi (ASME, New York 1991)

5.476 J.F. Meyers: Doppler global velocimetry – The next generation?, AIAA Paper, Vol. 92-3897 (1992)

5.477 J.W. Lee, J.F. Meyers, A.A. Cavone, K.E. Suzuki: Doppler global velocimetry measurements of the vortical flow above an F/A-18, AIAA Paper, Vol. 93-0414 (1993)

5.478 J.F. Meyers: Development of Doppler global velocimetry as a flow diagnostics tool, Measurement in Fluids and Combustion Systems, Special Issue, Meas. Sci. Technol. **6**(6), 769–783 (1995)

5.479 J.F. Meyers, J.W. Lee, R.J. Schwartz: Characterization of measurement error sources in Doppler global velocimetry, Meas. Sci. Technol. **12**, 1–12 (2001)

5.480 M.S. Reinath: Doppler global velocimeter development for large wind tunnels, Meas. Sci. Technol. **12**, 432–441 (2001)

5.481 R.L. McKenzie: Planar Doppler velocimetry for large-scale wind tunnel applications, AGARD Fluid Dynamics Panel 81st Meeting and Symposium on Advanced Aerodynamic Measurement Technology Seattle (1997) , , paper 9

5.482 R.L. McKenzie, M.S. Reinath: Planar Doppler velocimetry dapabilities at low speeds and its application to a full-scale rotor flow, AIAA Paper, Vol. 2000-2292 (2000)

5.483 T.J. Beutner, G. Elliott, A. Mosedale, C. Carter: Doppler Global velocimetry applications in large scale facilities, AIAA Paper, Vol. 98-2608 (1998)

5.484 G.S. Elliott, T.J. Beutner: Molecular Filter Based Planar Doppler Velocimetry, Prog. Aerosp. Sci. **35**, 799–845 (1999)

5.485 G.S. Elliott, T.J. Beutner, C.D. Carter: Application of planar Doppler velocimetry wind tunnel testing, AIAA Paper, Vol. 2000-0412 (2000)

5.486 R.-M. Kremer, E.-J. Korevaar, S.-H. Bloom: Laser radar device, US Patent 5,267,010 (1993)

5.487 S.H. Bloom, P.A. Searcy, K. Choi, R. Kremer, E. Korevaar: Helicopter plume detection by using an ultranarrow-band noncoherent laser Doppler velocimeter, Opt. Lett. **18**, 244–246 (1993)

5.488 R.B. Miles, J.N. Forkey, W.R. Lempert: Filtered Rayleigh scattering measurements in supersonic/hypersonic facilities, AIAA Paper, Vol. 92-3894 (1992)

5.489 J.N. Forkey, N.D. Finkelstein, W.R. Lempert, R.B. Miles: Control of experimental uncertainties in filtered Rayleigh scattering measurements, AIAA Paper, Vol. 95-0298 (1995)

5.490 M.W. Smith, G.B. Northam, J.P. Dummond: Application of absorption filter planar Doppler velocimetry to sonic and supersonic Jets, AIAA J. **34**, 434–441 (1996)

5.491 M.W. Smith: Application of a planar Doppler velocimetry system to a high Reynolds number compressible jet, AIAA Paper, Vol. 98-0428 (1998)

5.492 G.S. Elliott, M. Samimy, S.A. Arnette: A molecular filter based velocimetry technique for high speed flows, Exp. Fluids **18**, 107–118 (1994)

5.493 P.S. Clancy, M. Samimy, W.R. Erskine: Planar Doppler velocimetry: three-component velocimetry in supersonic jets, AIAA Paper, Vol. 98-0506 (1998)

5.494 N.J. Quinlan, R.W. Ainsworth, B.J. Bellhouse, R.J. Manners, S.J. Thorpe: Application of Doppler global velocimetry to supersonic gas-particle flows in drug delivery. In: *GALA 7th International Conference on Laser Anemometry – Advances and Applications*, ed. by B. Ruck (GALA, Karlsruhe 1997), , paper 21-1

5.495 I. Röhle, R. Schodl: Evaluation of the Accuracy of the Doppler Global Technique, Proc. Optical Methods and Data Processing in Heat and Fluid Flow London (1994) 155–161

5.496 I. Röhle: Three-dimensional Doppler global velocimetry in the flow of a fuel spray nozzle and in the wake region of a car, Flow Meas. Instrum. **7**, 287–294 (1996)

5.497 I. Röhle, R. Schodl, P. Voigt, C. Willert: Recent developments and applications of quantitative laser light sheet measuring techniques in turbomachinery components, Meas. Sci. Technol. **11**, 1023–1035 (2000)

5.498 C. Willert, E. Blümcke, M. Beversdorff, W. Unger: Application of phase-averaging Doppler global velocimetry to engine exhaust flows, 10th Int. Symp. Appl. Laser Tech. Fluid Mech. Lisbon (2000) , , paper 35-2

5.499 M. Fischer, J. Heinze, K. Matthias, I. Roehle: Doppler global velocimetry in flames using a new developed, frequency stabilized, tunable, long pulse YAG laser, 10th Int. Symp. Appl. Laser Tech. Fluid Mech. Lisbon (2000) , , paper 35-3

5.500 D.S. Nobes, H.D. Ford, R.P. Tatam: Three dimensional planar Doppler velocimetry using imaging fibre bundles, AIAA Paper, Vol. 2002-0692 (2002)

5.501 C. Willert, G. Stockhausen, J. Klinner, M. Beversdorff, J. Quest, U. Jansen, M. Raffel: On the development of Doppler global velocimetry for cryogenic wind tunnels, IEEE 20th ICIASF (IEEE, New York 2003)

5.502 J. Kuhlman, S. Naylor, K. James, S. Ramanath: Accuracy study of a 2-component point Doppler velocimeter (pDv), AIAA Paper, Vol. 97-1916 (1997)

5.503 J. Kuhlman, P. Collins, T. Scarberry: Two-component point Doppler velocimetry data in circular jets, Meas. Sci. Technol. **12**, 395–408 (2001)

5.504 J. Kuhlman, P. Collins: Circular jet 2-component point Doppler velocimetry (pDv) Velocity Data, AIAA Paper, Vol. 2000-2296 (2000)

5.505 J. Crafton, N.M. Messersmith, J.P. Sullivan: Filtered Doppler velocimetry: development of a point system, AIAA Paper, Vol. 98-0509 (1998)

5.506 W. Förster, G. Karpinsky, H. Krain, I. Röhle, R. Schodl: 3-component-Doppler-laser-two-focus velocimetry applied to a transonic centrifugal compressor, 10th Int. Symp. Appl. Laser Tech. Fluid Mech. Lisbon (2000) , , paper 7-2

5.507 M.P. Wernet: Planar particle imaging Doppler velocimetry, a 3-component velocity measurement technique, AIAA Paper, Vol. 2004-0022 (2004)

5.508 D.H. Thompson: A tracer particle fluid velocity meter incorporating a laser, J. Sci. Instrum. **1**, 929–932 (1968)

5.509 L.H. Tanner: Particle timing laser velocity meter, Opt. Laser Technol. **5**, 108–110 (1973)

5.510 L. Lading: Analysis of a laser correlation anemometer, Proc. 3rd Symp. Turbulence in Liquids (1973) 205–219

5.511 R. Schodl: Ein neues optisches Geschwindigkeitsmessverfahren: Laser-Zweistrahlverfahren, DFVLR-Nachrichten **12**, 506–508 (1973), , (in German)

5.512 L. Lading: Comparing a laser Doppler anemometer with a laser correlation anemometer, Proc. Conf. Engineering Uses of Coherent Optics Glasgow (1975) 19–36

5.513 L. Lading: The time-of-flight laser anemometer, AGARD CP **193**, 23 (1976)

5.514 A.E. Smart: Special problems of laser anemometry in difficult applications, AGARD Lecture Ser. **90** (1977)

5.515 W. T. Mayo Jr., A. E. Smart: Comparison of data from the transit time velocimeter with other systems now in use for velocity measurements, AED-TR-79-32, Final Report on Contract F40500-78-C-002 (1979)

5.516 W.T. Mayo Jr., A.E. Smart, T.E. Hunt: Laser transit anemometer with microcomputer and special digital electronics: measurements in supersonic flows, 8th ICIASF (1979)

5.517 K.G. Barlett, C.Y. She: Single particle correlated time-of-flight velocimeter for remote wind speed measurement, Opt. Lett. **1**, 175 (1977)

5.518 R.G.W. Brown, E.R. Pike: A combined laser Doppler and time of flight anemometer, Opt. Laser Technol. **10**(6), 317–319 (1978)

5.519 C.Y. She, R.F. Lelley: Scalling law and photon-count distribution of a laser time-of-flight velocimeter, J. Opt. Soc. Am. **72**, 365–371 (1982)

5.520 R.G.W. Brown: Velocimetry signals and data reduction in simulation and practice. In: *Photon Correlation Techniques*, ed. by E.O. Schulz-du Bois (Springer, Berlin, New York 1983)

5.521 M.N. Bross: Transit laser anemometry data reduction for flow in industrial turbomaschinery, Proc. 3rd Int. Conf. Photon Correlation Techniques in Fluid Mechanics Cambridge (1979)

5.522 R. Schodl: A laser dual beam method for flow measurement in turbomaschines, ASME Paper, Vol. 74-GT-159 (1974)

5.523 R. Schodl: Laser-two-focus velocimetry for use in aero engines. Laser optical measurement methods for aero engine research and development, AGARD-LS **90**, 4.1–4.34 (1977)

5.524 R. Schodl: Development of the laser-two-focus method for nonintrusive measurement of flow vectors particularly in turbomachines, ESA-TT **528** (1979)

5.525 R. Schodl: A laser-two-focus velocimetry for automatic flow vector measurements in the rotating components of turbomachines, Measurement Methods in Rotating Components of Turbomachinery (ASME, New York 1980)

5.526 L. Lading: Spatial Filtering in Laser Anemometry, Proc. of the 4th Symp. Turbulence in Liquids (1975)

5.527 U. Schricker: *Optimierung der Messsignalaufbereitung der Datensammlung für das Laser-Zwei-Fokus-Geschwindigkeitsmessverfahren* (Inst. F. Strahlantriebe und Turboarbeitsmaschinen, Aachen 1979)

5.528 R. Schodl: Comparison of signal processing by correlation and by pulse-fair timing in laser dual focus velocimetry, Proc. Symp. Long Range and Optical Velocity Measurements (1980)

5.529 P.W. McDonald: A comparison between measured and computed flow fields in a transonic compressor rotor, Trans. ASME J. Eng. Power **102**(4), 883–891 (1980)

5.530 L. Maretto, M. Troilo: A dual focus fiber optic anemometer for measurements in wet stream, Measuring Techniques in Transonic and Supersonic Flows in Cascades and Turbomachines (Ecole Centrale de Lyon, Ecully 1981)

5.531 L. Lading: Estimating time and time-lag in time-of-flight velocimetry, Appl. Opt. **22**(22), 3637–3643 (1983)

5.532 R. Schodl: Laser-two-focus velocimetry, Advanced Instrumentation for Aero Engine Components, AGARD-CP-399 (AGARD, Philadelphia 1986) 7

5.533 S. Yasu, T. Tamaki, S. Nagno: Measurements of flow field within an axial flow fan using a laser two focus velocimeter, Int. Gas Turbine Congress Tokyo (1983) , , paper 83-Tokyo-IGTC-49

5.534 L. Fottner, J. Lichtfuss: Design of transonic compressor cascade for minimal shock losses and comparison with test results, Viscous Effects in Turbomachines, AGARD CP 351 (1983)

5.535 G. Janssens., J. Labbe: Two focus laser velocimeter applied to measurements in an experimental centrifugal compressor, ICIASF, Vol. 83 (1983) 251–254

5.536 H. Hayami, Y. Senoo, H. Ueki: Flow in the inducer of a centrifugal compressor measured with a laser velocimeter, ASME Paper, Vol. 84-GT-74 (1984)

5.537 M.M. Ross: *DFVLR/Leicester University/GEC Laser Anemometer Experiments at the High Speed Aerodynamics Laboratory, Leicester University* (Whetstone, Leicester 1978)

5.538 J.C. Erdmann: Particle statistics in transit velocimetry. In: *Photon Correlation Techniques*, ed. by E.O. Schulz-du Bois (Springer, Berlin, New York 1983) pp. 168–191

5.539 J.B. Attis: Statistical aspects of signal processing in laser transit velocimetry, Conf. Photon Correlation Techniques in Fluid Mechanics Standford (1980)

5.540 R. Schodl: Laser-two-focus velocimetry: Two and three dimensional techniques, VKI Lecture Series on Advanced Measurement Techniques, D/1998/0238/455, VKI LS 1998-06 (1998)

5.541 W. Förster: Laser-2-focus data analysis using a nonlinear regression model, 16 ICIASF Symp. Dayton (1995)

5.542 H. Selbach: Laser-2-Fokus Geschwindigkeitsmessverfahren. In: *Lasermethoden in der Strömungsmesstechnik*, ed. by B. Ruck (AT Fachverlag, Stuttgart 1990), , (in German)

5.543 J.D. Trolinger, J.J. Ginouy: Laser applications in flow diagnostics, AGARD-AG **296** (1988)

5.544 W. M. Humphreys Jr., W. E. Hunter Jr.: Estimating laser transit anemometry noise performance capabilities. Presented at the 13th ICIASF 89 in Göttingen, Germany (1989)

5.545 R. Schodl, W. Förster: A multi-color fiberoptic laser-two-focus velocimeter for 3-dimensional flow analysis, Fourth Int. Symp. Appl. Laser Anemometry to Fluid Mechanics Lisbon (1988)

5.546 I. Roehle, R. Schodl: Method for measuring flow vectors in gas flow, UK Patent GB 2 295 670 A (1995)

5.547 I. Röhle: Three dimensional Doppler global velocimetry in the flow of a fuel spray nozzle and in the wake region of a car, Flow Meas. Instrum. **7**(3/4), 287–294 (1996)

5.548 R. Schodl, W. Förster, G. Karpinsky, I. Röhle: 3-component-doppler global laser-two-focus velocimetry applied to a transonic centrifugal compressor, 10th Int. Symp. Appl. Laser Tech. Fluid Mech. Lisbon (2000)

5.549 H. Krain: High pressure ratio centrifugal compressor with transonic flow, Proc. 3rd ASME/JSME Conference San Francisco, FEDSM99-7801 (1999) 9

5.550 C.P. Gendrich, D.G. Bohl, M.M. Koochesfahani: Whole-field measurements of unsteady separation in a vortex ring/wall interaction, AIAA Paper, Vol. 97-1780 (1997)

5.551 D. Bohl, M. Koochesfahani, B. Olson: Development of stereoscopic molecular tagging velocimetry, Exp. Fluids **30**, 302–308 (2001)

5.552 R.E. Falco, D.G. Nocera: Quantitative multipoint measurements and visualization of dense solid-liquid flows using laser induced photochemical anemometry (LIPA). In: *Particulate Two-Phase Flow*, ed. by M.C. Rocco (Butterworth-Heinemann, London 1993) pp. 59–126

5.553 M.M. Koochesfahani, R.K. Cohn, C.P. Gendrich, D.G. Nocera: Molecular tagging diagnostics for the study of kinematics and mixing in liquid phase flows, Proc. Eighth Int. Symp. Appl. Laser Tech. Fluids Mech. Lisbon, Vol. I (1996) 1–12

5.554 M.M. Koochesfahani: Molecular tagging velocimetry (MTV): Progress and applications, AIAA Paper, Vol. 1999-3786 (1999)

5.555 W.R. Lempert, S.R. Harris: Molecular tagging velocimetry. In: *Flow Visualization – Techniques and Examples*, ed. by A.J. Smits, T.T. Lim (Imperial College Press, London 2000) pp. 73–92

5.556 M.M. Koochesfahani (Ed.): Special Feature: Molecular Tagging Velocimetry, Meas. Sci. Technol. **11**(9), 1235–1300 (2000)

5.557 V. Balzani, V. Carassiti: *Photochemistry of Coordination Compounds* (Academic, London 1970)

5.558 L.S. Forster: Photophysical processes – energy levels and spectra. In: *Concepts of Inorganic Photochemistry*, ed. by A.W. Adamson, P.D. Fleischauer (Wiley-Interscience, New York 1975) pp. 1–35

5.559 R.P. Wayne: *Principles and Applications of Photochemistry* (Oxford Univ. Press, Oxford 1980)

5.560 J. Jortner, S.A. Rice, R.M. Hochstrasser: Radiationless transitions in photochemistry, Adv. Photochem. **7**, 149–309 (1969)

5.561 K.F. Freed: Radiationless transitions in molecules, Acc. Chem. Res. **11**, 74–80 (1978)

5.562 S.H. Lin (Ed.): *Radiationless Transitions* (Academic, New York 1980)

5.563 N.J. Turro: *Modern Molecular Photochemistry* (Benjamin/Cummings, Menlo Park 1978)

5.564 V. Balzani, L. Moggi, M.F. Manfrin, F. Bolletta: Quenching and sensitization processes of coordination compounds, Coord. Chem. Rev. **15**, 321–433 (1975)

5.565 Miller S.: *Photochemical reaction for the study of velocity patterns and profiles*. B.A.Sc. Thesis (University of Toronto, Ontario 1962)

5.566 A.T. Popovich, R.L. Hummel: A new method for nondisturbing turbulent flow measurement very close to a wall, Chem. Eng. Soc. **22**, 21–25 (1967)

5.567 F. Frantisak, A. Palade de Iribarne, J.W. Smith, R.L. Hummel: Nondisturbing tracer technique for quantitative measurements in turbulent flows, Ind. Eng. Chem. Fund. **8**, 160–167 (1969)

5.568 R.L. Hummel: Nondisturbing flow measurement using a photochromic tracer technique. High speed photography, Proc. SPIE **97**, 302–307 (1976)

5.569 M. Ojha, R.S.C. Cobbold, K.W. Johnston, R. Hummel: Pulsatile flow through constricted tubes: an experimental investigation using photochromic tracer methods, J. Fluid Mech. **203**, 173–197 (1989)

5.570 R.E. Falco, C.C. Chu: Measurement of two-dimensional fluid dynamic quantities using a photochromic grid tracing technique, Proc. SPIE **814**, 706–710 (1987)

5.571 E. Merzbacher: *Quantum Mechanics* (Wiley, New York 1970)

5.572 V.N. Yurechko, Y.S. Ryazantsev: Fluid motion investigation by photochromic flow visualization technique, Exp. Therm. Fluid Sci. **4**, 273–288 (1991)

5.573 A. D'Arco, J.C. Charmet, M. Cloitre: Nouvelle technique de marquage d'ecoulement par utilisation de molecules photochromes, Rev. Phys. Appl. **17**, 89–93 (1982)

5.574 C.C. Chu, Y.Y. Liao: A quantitative study of the flow around an impulsively started circular cylinder, Exp. Fluids **13**, 137–146 (1992)

5.575 C.C. Chu, C.T. Wang, C.H. Hsieh: An experimental investigation of vortex motions near surfaces, Phys. Fluids **5**(3), 662–676 (1993)

5.576 P. Zalzal, M. Ojha, C.R. Ethier, R.S.C. Cobbold, K.W. Johnston: Visualization of transitional pipe flow using photochromic tracer method, Phys. Fluids **6**, 2003–2010 (1994)

5.577 C.C. Chu, C.T. Wang, C.C. Chang, R.Y. Chang, W.T. Chang: Head-on collision of two coaxial vortex rings: experimental and computation, J. Fluid Mech. **296**, 39–71 (1995)

5.578 G.G. Couch, K.W. Johnston, M. Ohja: Full-field flow visualization and velocity measurement with a photochromic grid method, Meas. Sci. Technol. **7**(9), 1238–1246 (1996)

5.579 H. Park, J.A. Moore, O. Trass, M. Ojha: Laser photochromic velocimetry estimation of the vorticity and pressure field – two-dimensional flow in a curved vessel, Exp. Fluids **26**, 55–62 (1999)

5.580 R. Miles, C. Cohen, J. Conners, P. Howard, S. Huang, E. Markovitz, G. Russell: Velocity measurements by vibrational tagging and fluorescent probing of oxygen, Opt. Lett. **12**(11), 861–863 (1987)

5.581 R.B. Miles, J.J. Connors, E.C. Markovitz, P.J. Howard, G.J. Roth: Instantaneous profiles and turbulence statistics of supersonic free shear layers by Raman Excitation plus Laser-Induced Electronic Fluorescence (RELIEF) velocity tagging of oxygen, Exp. Fluids **8**, 17–24 (1989)

5.582 R.B. Miles, J.E. Connors Markovitz, P. Howard, G. Roth: Instantaneous supersonic velocity profiles in an underexpanded sonic air jet by oxygen flow tagging, Phys. Fluids **1**(2), 389–393 (1989)

5.583 R.B. Miles, D. Zhou, B. Zhang, W.R. Lempert, Z.S. She: Fundamental turbulence measurements by RELIEF flow tagging, AIAA J. **31**(3), 447–452 (1993)

5.584 R.B. Miles, W.R. Lempert: Quantitative flow visualization in unseeded flows, Ann. Rev. Fluid Mech. **29**, 285–326 (1997)

5.585 D.A. Long: *Raman Spectroscopy* (McGraw-Hill, New York 1977)

5.586 R. Frey, J. Lukasik, J. Ducuing: Tunable Raman excitation and vibrational relaxation in diatomic molecules, Chem. Phys. Lett. **14**(4), 514–517 (1972)

5.587 R.L. McKenzie: Progress in laser spectroscopic techniques for aerodynamic measurements: an overview, AIAA J. **31**, 465–477 (1993)

5.588 G. Herzberg: *Molecular Spectra and Molecular Structure: Spectra of Diatomic Molecules*, 2nd edn. (van Nostrand, New York 1950)

5.589 M.W. Feast: Emission Schumann–Runge O2 bands, Nature **162**, 214–215 (1948)

5.590 A. Noullez, G. Wallace, W. Lempert, R.B. Miles, U. Frisch: Transverse velocity increments in turbulent flow using the RELIEF technique, J. Fluid Mech. **339**, 287–307 (1997)

5.591 R.B. Miles, J. Grinstead, R.H. Kohl, G. Diskin: The RELIEF flow tagging technique and its application in engine testing facilities and for helium-air mixing studies, Meas. Sci. Technol. **11**(2), 1272–1281 (2000)

5.592 W.R. Lempert, K. Magee, P. Ronney, K.R. Gee, R.P. Haughland: Flow tagging velocimetry in incompressible flow using photo-activated nonintrusive tracking of molecular motion (PHANTOMM), Exp. Fluids **18**, 249–257 (1995)

5.593 S.R. Harris, W.R. Lempert, L. Hersh, C.L. Burcham, A. Saville, R.B. Miles, K. Gee, R.P. Haughland: Quantitative measurements on internal circulation in droplets using flow tagging velocimetry, AIAA J. **34**(3), 449–454 (1996)

5.594 S.R. Harris, R.B. Miles, W.R. Lempert: Observations of fluid flow produced in a closed cylinder by a rotating lid using the PHANTOMM (Photo-Activated Non Intrusive Tracking of Molecular Motion) flow tagging technique, Proc. Eighth Int. Symp. Appl. Laser Tech. Fluid Mech. Lisbon (1996) 1–9

5.595 M. Biage, S.R. Harris, W.R. Lempert, A.J. Smits: Quantitative velocity measurements in turbulent Taylor-Couette flow by PHANTOMM flow tagging, Proc. Eighth Int. Symp. Appl. Laser Tech. Fluid Mech. Lisbon (1996) 1–8

5.596 P.H. Paul, M.G. Garguilo, D.J. Rakestraw: Imaging of pressure and electrokinetically driven flows through open capillaries, Anal. Chem. **70**, 2459–2467 (1998)

5.597 W.R. Lempert, S.R. Harris: Flow tagging velocimetry using caged dye photo-activated fluorophores, Meas. Sci. Technol. **11**(9), 1251–1258 (2000)

5.598 J.S. Park, H.J. Kim, K.D. Kihm: Molecular tagging fluorescence velocimetry (MTFV) for Lagrangian flow field mapping inside evaporating meniscus: potential use for micro-scale applications, J. Flow Visual. Image Process. **8**, 177–187 (2001)

5.599 D. Sinton, X. Xuan, D. Li: Thermally induced velocity gradients in electroosmotic microchannel flows: the cooling influence of optical infrastructure, Exp. Fluids **37**, 872–882 (2004)

5.600 J.A. McCray, D.R. Trentham: Properties and uses of photoreactive caged compounds, Ann. Rev. Biophys. Chem. **18**, 239–270 (1989)

5.601 L.R. Boedeker: Velocity measurements by H2 O photolysis and laser-induced fluorescence of OH, Opt. Lett. **14**(10), 473–475 (1989)

5.602 L. Goss, T. Chen, D. Trump, B. Sarka, A. Nejad: Flow tagging velocimetry using UV- photodissociation of water vapor, AIAA Paper, Vol. 91-0355 (1991)

5.603 G. Meijer, J.J. ter Meulen, P. Andresen, A. Bath: Sensitive quantum state selective detection of H2 O and D2 O by (2+1)-resonance enhanced multiphoton ionization, J. Chem. Phys. **85**, 6914–6922 (1986)

5.604 R.J. Exton, M.E. Hillard: Raman Doppler velocimetry – A unified approach for measuring molecular-flow velocity, temperature, and pressure, Appl. Opt. **25**, 14–21 (1986)

5.605 L. Goss, T. Chen, D. Schommer, A. Nejad: Laser diagnostics for velocity measurements in supersonic combusting environments, AIAA Paper, Vol. 92-0008 (1992)

5.606 J.A. Wehrmeyer, L.A. Ribarov, D.A. Oguss, F. Batliwala, R.W. Pitz, P.A. DeBarber: Flow tagging velocimetry for low and high temperature flowfields, AIAA Paper **99-0646** (1999)

5.607 J.A. Wehrmeyer, L.A. Ribarov, D.A. Oguss, R.W. Pitz: Flame flow tagging velocimetry with 193 nm H2 O photodissociation, Appl. Opt. **38**, 6912–6917 (1999)

5.608 R.W. Pitz, J.A. Wehrmeyer, L.A. Ribarov, D.A. Oguss, F. Batliwala, P.A. DeBarber, S. Deusch, P.E. Dimo-

takis: Unseeded molecular flow tagging in cold and hot flows using ozone and hydroxyl tagging velocimetry, Meas. Sci. Technol. **11**(9), 1259–1271 (2000)
5.609 R.W. Pitz, M.D. Lahr, Z.W. Douglas, J.A. Wehrmeyer, S. Hu, C.D. Carter, K.-Y. Hsu, C. Lum, M.M. Koochesfahani: Hydroxyl tagging velocimetry in a supersonic flow over a cavity, Appl. Opt. **44**(31), 6692–6700 (2005)
5.610 L.A. Ribarov, J.A. Wehrmeyer, R.W. Pitz, R.A. Yetter: Hydroxyl tagging velocimetry (HTV) in experimental airflows, Appl. Phys. B **74**, 175–183 (2002)
5.611 L.A. Ribarov, J.A. Wehrmeyer, S. Hu, R.W. Pitz: Multiline hydroxyl tagging velocimetry measurements in reacting and nonreacting experimental flows, Exp. Fluids **37**, 65–74 (2004)
5.612 R.W. Pitz, T.M. Brown, S.P. Nandula, P.A. Skaggs, P.A. DeBarber, M.S. Brown, J. Segall: Unseeded velocity measurement by ozone tagging velocimetry, Opt. Lett. **21**(10), 755–757 (1996)
5.613 L.A. Ribarov, J.A. Wehrmeyer, F. Batliwala, R.W. Pitz, P.A. DeBarber: Ozone tagging velocimetry using narrowband excimer lasers, AIAA J. **37**(6), 708–714 (1999)
5.614 C. Orlemann, C. Schulz, J. Wolfrum: NO-flow tagging by photodissociation of NO2. A new approach for measuring small-scale flow structures, Chem. Phys. Lett. **307**(1–2), 15–20 (1999)
5.615 S. Krüger, G. Grünefeld: Stereoscopic flow-tagging velocimetry, Appl. Phys. B **69**, 509–512 (1999)
5.616 S. Krüger, G. Grünefeld: Gas-phase velocity field measurements in dense sprays by laser-based flow tagging, Appl. Phys. B **70**, 463–466 (2000)
5.617 N.J. Dam, R.J.H. Klein-Douwel, N.M. Sijtsema, J.J. ter Meulen: Nitric oxide flow tagging in unseeded air, Opt. Lett. **26**, 36–38 (2001)
5.618 N.M. Sijtsema, N.J. Dam, R.J.H. Klein-Douwel, J.J. ter Meulen: Air photolysis and recombination tracking: A new molecular tagging velocimetry scheme, AIAA J. **40**(6), 1061–1064 (2002)
5.619 W.P.N. van der Laan, R.A.L. Tolboom, N.J. Dam, J.J. ter Meulen: Molecular tagging velocimetry in the wake of an object in supersonic flow, Exp. Fluids **34**, 531–533 (2003)
5.620 P. Barker, A. Thomas, H. Rubinsztein-Dunlop, P. Ljungberg: Velocity measurements by flow tagging employing laser-enhanced ionisation and laser induced fluorescence, Spectrochim. Acta B **50**, 1301–1310 (1995)
5.621 H. Rubinsztein-Dunlop, B. Littleton, P. Barker, P. Ljungberg, Y. Malmsten: Ionic strontium fluorescence as a method for flow tagging velocimetry, Exp. Fluids **30**, 36–42 (2001)
5.622 M.-M. Koochesfahani: *Experiments on turbulent mixing and chemical reactions in a liquid mixing layer*. Ph.D. Thesis (California Institute of Technology, Pasadena 1984)
5.623 J.P. Crimaldi: The effect of photobleaching and velocity fluctuations on single-point LIF measurements, Exp. Fluids **23**, 325–330 (1997)
5.624 G.R. Wang, H.E. Fiedler: On high spatial resolution scalar measurement with LIF. Part 1: Photobleaching and thermal blooming, Exp. Fluids **29**, 257–264 (2000)
5.625 J. Rička: Photobleaching velocimetry, Exp. Fluids **5**, 381–384 (1987)
5.626 K.F. Schrum, J.M. Lancaster, S.E. Johnston, S.D. Gilman: Monitoring electroosmotic flow by periodic photobleaching of a dilute, neutral fluorophore, Anal. Chem. **72**, 4317–4321 (2000)
5.627 B.P. Mosier, J.I. Molho, J.G. Santiago: Photobleached-fluorescence imaging of microflows, Exp. Fluids **33**, 545–554 (2002)
5.628 G.R. Wang: Laser induced fluorescence photobleaching anemometer for microfluidic devices, Lab. Chip. **5**, 450–456 (2005)
5.629 B. Hiller, R.A. Booman, C. Hassa, R.K. Hanson: Velocity visualization in gas flows using laser-induced phosphorescence of biacetyl, Rev. Sci. Instrum. **55**, 1964–1967 (1984)
5.630 H.S. Lowry: Velocity measurements using the laser-induced phosphorescence of biacetyl, AIAA Paper, Vol. 87-1529 (1987)
5.631 J.B. Liu, Q. Pan, C.S. Liu, J.R. Shi: Principles of flow field diagnostics by laser induced biacetyl phosphorescence, Exp. Fluids **6**, 505–513 (1988)
5.632 H.S. Hilbert, R.E. Falco: Measurements of flows during scavenging in a two-stroke engine, SAE Tech. Paper **910671** (1991)
5.633 B. Stier, M.M. Koochesfahani: Molecular tagging velocimetry in gas phase and its application to jet flows, ASME Paper, Vol. FEDSM97-3687 (1997)
5.634 B. Stier, M.M. Koochesfahani: Whole field MTV measurements in a steady flow rig model on an IC engine, SAE Tech. Paper **980481** (1998)
5.635 B. Stier, M.M. Koochesfahani: Molecular tagging velocimetry (MTV) measurements in gas phase flows, Exp. Fluids **26**(4), 297–304 (1999)
5.636 H.G. Hascher, M. Novak, K. Lee, H. Schock, H. Rezaei, M.M. Koochesfahani: An evaluation of IC-engine flow with the use of modern in-cylinder measuring techniques, AIAA Paper, Vol. 98-3455 (1998)
5.637 E.M. Thurlow, J.C. Klewicki: Experimental study of turbulent Poiseuille–Couette flow, Phys. Fluids **12**(4), 865–875 (2000)
5.638 A.-C.-H. Goh: *Active flow control for maximizing performance of spark-ignited stratified charge engines*. M.S. Thesis (Michigan State University, East Lansing 2001)
5.639 M.M. Koochesfahani, A.C. Goh, H.J. Schock: Molecular Tagging Velocimetry (MTV) and its automotive applications. In: *The Aerodynamics of Heavy Vehicles: Trucks, Busses, and Trains*, Lecture Notes in Applied and Computational Mechanics, Vol. 19, ed. by R. McCallen, F. Browand, J. Ross (Springer, Heidelberg, Berlin 2004) pp. 143–155

5.640 W.R. Lempert, N. Jiang, S. Sethuram, M. Samimy: Molecular tagging velocimetry measurements in supersonic microjets, AIAA J. **40**, 1065–1070 (2002)

5.641 W.R. Lempert, M. Boehm, N. Jiang, S. Gimelshein, D. Levin: Comparison of molecular tagging velocimetry data and direct simulation Monte Carlo simulations in supersonic micro jet flows, Exp. Fluids **34**, 403–411 (2003)

5.642 Z. Pikramenou, J.-A. Yu, R.B. Lessard, A. Ponce, P.A. Wong, D.G. Nocera: Luminescence from supramolecules triggered by the molecular recognition of substrates, Coord. Chem. Rev. **132**, 181–194 (1994)

5.643 M.A. Mortellaro, D.G. Nocera: A turn-on for optical sensing, Chem. Tech. **26**, 17–23 (1996)

5.644 M.A. Mortellaro, D.G. Nocera: A supramolecular chemosensor for aromatic hydrocarbons, J. Am. Chem. Soc. **118**, 7414–7415 (1996)

5.645 D.G. Nocera: Not just another pretty shape, New Sci. **149**, 24–27 (1996)

5.646 C.M. Rudzinski, D.G. Nocera: Buckets of light, Opt. Sensors Switches **7**, 1–90 (2001)

5.647 V. Balzani, F. Bolletta, F. Scandola: Vertical and "nonvertical" energy transfer processes – a general classical treatment, J. Am. Chem. Soc. **102**, 2152–2163 (1980)

5.648 J.F. Endicott: Manipulation of superexchange couplings, Acc. Chem. Res. **21**, 59–66 (1988)

5.649 W. Horrocks, M. Albin: Lanthanide ion luminescence in coordination chemistry and biochemistry, Prog. Inorg. Chem. **30**, 1–104 (1983)

5.650 J.-C.G. Bünzli: Luminescent probes. In: *Lanthanide Probes in Life, Chemical and Earth Sciences*, ed. by J.-G.C. Bünzli, G.R. Choppin (Elsevier, Amsterdam 1988) pp. 219–293

5.651 J.-A. Yu, R.B. Lessard, D.G. Nocera: Direct observation of intramolecular energy transfer from a Î² -diketonate to terbium(III) ion encapsulated in a cryptand, Chem. Phys. Lett. **187**, 263–268 (1991)

5.652 V. Balzani, F. Scandola: *Supramolecular Photochemistry* (Ellis-Horwood, Chichester 1991)

5.653 G. Wenz: Cyclodextrins as building blocks for supramolecular structures and functional units, Angew. Chem. Int. Edit. **33**, 803–822 (1994)

5.654 A. Ponce, P.A. Wong, J.J. Way, D.G. Nocera: Intense phosphorescence triggered by alcohols upon formation of a cyclodextrin ternary complex, J. Phys. Chem. **97**, 11137–11142 (1993)

5.655 W.K. Hartmann, M.H.B. Gray, A. Ponce, D.G. Nocera: Substrate induced phosphorescence from cyclodextrin lumophore host-guest complexes, Inorg. Chim. Acta **243**, 239–248 (1996)

5.656 H. Hu, C. Lum, M.M. Koochesfahani: Molecular tagging thermometry with adjustable temperature sensitivity, Exp. Fluids **40**, 753–763 (2006)

5.657 H. Hu, M.M. Koochesfahani: Molecular tagging velocimetry and thermometry technique and its application to the wake of a heated cylinder, Meas. Sci. Technol. **17**, 1269–1281 (2006)

5.658 S.-R. Harris: *Quantitative measurements in a lid driven, cylindrical cavity using the PHANTOMM flow tagging technique*. Ph.D. Thesis (Princeton University, Princeton 1999)

5.659 M.M. Koochesfahani, D. Bohl: Molecular tagging visualization and velocimetry of the flow at the trailing edge of an oscillating airfoil, Proc. 10th Int. Symp. Flow Visualization Kyoto (2002) , , paper F0453

5.660 R.B. Hill, J.C. Klewicki: Data reduction methods for flow tagging velocity measurements, Exp. Fluids **20**(3), 142–152 (1996)

5.661 J.C. Klewicki, R.B. Hill: Laminar boundary layer response to rotation of a finite diameter surface patch, Phys. Fluids **15**(1), 101–111 (2003)

5.662 R. Sadr, J.C. Klewicki: Flow field characteristics in the near field region of particle-laden coaxial jets, Exp. Fluids **39**, 885–894 (2005)

5.663 K. Wirtz, M.M. Koochesfahani, J.J. McGrath, A. Benard: Molecular tagging velocimetry applied to buoyancy-driven convective phenomena during solidification, ASME Paper, Vol. HTD-361-4 (1998) 103

5.664 C. Lum, M.M. Koochesfahani, J.J. McGrath: Measurements of the velocity field with MTV during the solidification of an alloy analog with mushy region, ASME/IMECE2001 Paper, Vol. HTD-24222 (2001)

5.665 C. Lum: *Velocity field measurement for a unidirectional solidification of an ammonium chloride (NH4 Cl) solution using molecular tagging velocimetry (MTV)*. M.S. Thesis (Michigan State University, East Lansing 2001)

5.666 D.-G. Bohl: *Experimental Study of the 2-D and 3-D Structure of a Concentrated Line Vortex Array*. Ph.D. Thesis (Michigan State University, East Lansing 2002)

5.667 D.G. Bohl, M.M. Koochesfahani: MTV measurements of axial flow in a concentrated vortex core, Phys. Fluids **16**(11), 4185–4191 (2004)

5.668 D. Maynes, A.R. Webb: Velocity profile characterization in sub-millimeter diameter tubes using molecular tagging velocimetry, Exp. Fluids **32**, 3–15 (2002)

5.669 C. Lum: *An experimental study of pressure- and electroosmotically-driven flows in microchannels with surface modifications*. Ph.D. Thesis (Michigan State University, East Lansing 2005)

5.670 R.-K. Cohn: *Effect of forcing on the vorticity field in a confined wake*. Ph.D. Thesis (Michigan State University, East Lansing 1999)

5.671 C.P. Gendrich, M.M. Koochesfahani, D.G. Nocera: Molecular tagging velocimetry and other novel applications of a new phosphorescent supramolecule, Exp. Fluids **23**(5), 361–372 (1997)

5.672 C.-P. Gendrich: *Dynamic stall of rapidly pitching airfoils: MTV experiments and Navier–Stokes simulations*. Ph.D. Thesis (Michigan State University, East Lansing 1998)

5.673 R.K. Cohn, M.M. Koochesfahani: Vorticity field evolution in a forced wake, Proc. 1st Int. Symp. Turbulence and Shear Flow Phenomena Santa Barbara, ed. by S. Banerjee, J.K. Eaton (1999) 901–906

5.674 M. Koochesfahani, R. Cohn, C. MacKinnon: Simultaneous whole-field measurements of velocity and concentration fields using combined MTV and LIF, Meas. Sci. Technol. **11**(9), 1289–1300 (2000)

5.675 R. Sadr, J.C. Klewicki: An experimental investigation of the near-field flow development in coaxial jets, Phys. Fluids **15**(5), 1233–1246 (2003)

5.676 R. Sadr, J.C. Klewicki: A spline-based technique for estimating flow velocities using two-camera multiline MTV, Exp. Fluids **35**, 257–261 (2003)

5.677 C.P. Gendrich, M.M. Koochesfahani: A spatial correlation technique for estimating velocity fields using Molecular Tagging Velocimetry (MTV), Exp. Fluids **22**(1), 67–77 (1996)

5.678 Q. Zheng, J.C. Klewicki: A fast data reduction algorithm for molecular tagging velocimetry: the decoupled spatial correlation technique, Meas. Sci. Technol. **11**(9), 1282–1288 (2000)

5.679 P.T. Tokumaru, P.E. Dimotakis: Image correlation velocimetry, Exp. Fluids **19**, 1–15 (1995)

5.680 R.K. Cohn, M.M. Koochesfahani: The accuracy of remapping irregularly spaced velocity data onto a regular grid and the computation of vorticity, Exp. Fluids **29**, S61–S69 (2000)

5.681 J.E. Guilkey, K.R. Gee, P.A. McMurtry, J.C. Klewicki: Use of caged fluorescent dyes for the study of turbulent passive scalar mixing, Exp. Fluids **21**, 237–242 (1996)

5.682 L. Hansen, J.E. Guilkey, P.A. McMurtry, J.C. Klewicki: The use of photoactivatable fluorophores in the study of turbulent pipe mixing: effects of inlet geometry, Meas. Sci. Technol. **11**(9), 1235–1250 (2000)

5.683 S.L. Thomson, D. Maynes: Spatially resolved temperature measurements in a liquid using laser induced phosphorescence, J. Fluid Eng. **123**, 293–302 (2001)

5.684 H. Hu, M.M. Koochesfahani: A novel technique for quantitative temperature mapping in liquid by measuring the lifetime of laser induced phosphorescence, J. Visual. Jpn. **6**(2), 143–153 (2003)

5.685 M.J. Lighthill: Chap. II. In: *Laminar Boundary Layer*, ed. by L. Rosenhead (Oxford University, Oxford 1963)

5.686 J.M. Wallace: The measurement of vorticity in turbulent flows, 9th Biannual Symposium on Turbulence (1984)

5.687 P. Vukoslavcevic, J.M. Wallace, J. Balint: The velocity and vorticity vector fields of a turbulent boundary layer, Part I. Simultaneous measurement by hot-wire anemometry, J. Fluid Mech. **228**, 25–51 (1991)

5.688 A. Honkan, J. Andreopoulos: Experimental investigation of time-resolved vorticity in two dimensional turbulent boundary layer flows, AIAA Paper, Vol. 93-2910 (1993)

5.689 A. Honkan, Y. Andreopoulos: Vorticity, strain rate and dissipation characteristics in the near wall region of turbulent boundary layers, J. Fluid Mech. **350**, 29–26 (1997)

5.690 A. Honkan: *An experimental study of the vortical structure of turbulent flows*. Ph.D. Thesis (City University of New York, New York 1994)

5.691 Y. Andreopoulos, A. Honkan: Experimental techniques for highly resolved measurements of rotation, strain and dissipation-rate tensors in turbulent flows, Meas. Sci. Technol. **7**, 1462–1476 (1996)

5.692 J.C. Klewicki, R.E. Falco: On accurately measuring statistics associated with small- scale structure in turbulent boundary layers using hot wire probes, J. Fluid Mech. **219**, 119–142 (1990)

5.693 A. Tsinober, E. Kit, T. Dracos: Experimental investigation of the field of velocity gradients in turbulent flows, J. Fluid Mech. **242**, 169–192 (1992)

5.694 G. Briassulis, J. Agui, Y. Andreopoulos: The structure of weakly compressible grid turbulence, J. Fluid Mech. **432**, 219–283 (2001)

5.695 Y. Andreopoulos, J.H. Agui, G. Briassulis: Shock wave-turbulence interactions, Ann. Rev. Fluid Mech. **32**, 309–345 (2000)

5.696 J.H. Agui, G. Briassulis, Y. Andreopoulos: Studies of interactions of a propagating shock wave with decaying grid turbulence: velocity and vorticity field, J. Fluid Mech. **524**, 143–195 (2005)

5.697 A.E. Perry, M.S. Chong: A description of eddying motions and flow patterns using critical point concepts, Ann. Rev. Fluid Mech. **19**, 125–155 (1987)

5.698 J. Andreopoulos, J.H. Agui: Wall-vorticity flux dynamics in a two-dimensional turbulent boundary layer, J. Fluid Mech. **309**, 45–84 (1996)

5.699 J.F. Foss: Accuracy and uncertainty in transverse vorticity measurements, Bull. Am. Phys. Soc. **21**, 1237 (1976), (abstract)

5.700 J.F. Foss: Advanced techniques for transverse vorticity measurements, Proc. Biennial Symp. Turbulence (1981) 208–218

5.701 M.B. Frish, W.W. Webb: Direct measurements by Optical Probe, J. Fluid Mech. **107**, 173–185 (1981)

5.702 J.C. Wyngaard: Spatial resolution of the vorticity meter and other hot-wire arrays, J. Phys. E Sci. Instrum. **2**, 983–987 (1969)

5.703 E.B. Arik: Current status of particle image velocimetry and laser Doppler anemometry instrumentation. In: *Flow at Ultra High Reynolds and Rayleigh Numbers: A Status Report*, ed. by R.J. Donnelly, K.R. Sreenivasan (Springer, Berlin, New York 1998) pp. 138–158

5.704 L. Lourenco, A. Krothapalli: The role of photographic parameters in Laser-Speckle of particle image displacement velocimetry, Exp. Fluids **5**, 23–31 (1987)

5.705 C.D. Meinhart, R.J. Adrian: Measurements of the zero-pressure-gradient turbulent boundary layer using particle image velocimetry, AIAA Paper, Vol. 95-0789 (1995)

5.706 H. Breyer, H. Kriegs, U. Schmidt, W. Staude: The measurement of velocity gradients in fluid flow by

laser light scattering, Part 1: Mean gradients, Exp. Fluids **15**, 200–208 (1993)
5.707 H. Kriegs, R. Schulz, W. Staude: The measurement of velocity gradients in fluid flow by laser light scattering, Part 2: Statistical properties of gradients, Exp. Fluids **15**, 240–246 (1993)
5.708 H. Kriegs, W. Staude: A laser-pulse technique for the measurement of time-resolved velocity gradients in fluid flow, Meas. Sci. Technol. **6**, 653 (1995)
5.709 J. Zhang, B. Tao, J. Katz: Turbulent flow measurement in a square duct with hybrid holographic PIV, Exp. Fluids **23**, 373–381 (1997)
5.710 C.J. Kähler: Investigation of the spatio-temporal flow structure in the buffer region of a turbulent boundary layer by means of multiplane stereo PIV, Exp. Fluids **36**, 114–130 (2004)
5.711 B. Ganapathisubramani, E.K. Longmire, I. Marusic, S. Pothos: Dual-plane PIV technique to resolve complete velocity gradient tensor in a turbulent boundary layer, Exp. Fluids **32**(2), 222–231 (2004)
5.712 H. Hu, T. Saga, T. Kobayashi, N. Taniguchi, M. Yasuki: Dual-plane stereoscopic particle image velocimetry: System setup and its application on a lobed jet mixing flow, Exp. Fluids **31**, 277–293 (2001)
5.713 J.A. Mullin, W.J.A. Dahm: Dual-plane stereo particle image velocimetry (DSPIV) for measuring velocity gradient fields at intermediate and small scales of turbulent flows, Exp. Fluids **38**, 185–196 (2005)
5.714 D.B. Lang, P.E. Dimotakis: Vorticity measurements in a two-dimensional shear-layer, Bull. Am. Phys. Soc. **29**(9), 1556 (1984)
5.715 D.-B. Lang: *Laser Doppler velocity and vorticity measurements in turbulent shear layers*. Ph.D. Thesis (Caltech, Pasadena 1985)
5.716 G.P. Romano, R.A. Antonia, T. Zhou: Evaluation of LDA temporal and spatial velocity structure functions in a low Reynolds number turbulent channel flow, Exp. Fluids **27**, 368–377 (1999)
5.717 J.H. Agui, J. Andreopoulos: Development of a New LASER Vorticity Probe-LAVOR. Fluids Engineering Division of ASME, Int. Symp. Laser Anemometry, Vol. FED191, ed. by T.T. Huang, M.V. Ötügen (1994) 11–19
5.718 J.H. Agui, Y. Andreopoulos: A new laser vorticity probe – LAVOR: its development and validation in a turbulent boundary layer, Exp. Fluids **34**, 192–205 (2003)
5.719 R.A. Fraser, P.G. Felton, F.V. Bracco, D.A. Santavica: Preliminary turbulence length scale measurements in a motored IC engine, SAE Tech. Paper **860021** (1986)
5.720 R.J.R. Johns, G.F. Pitcher, E. Winkelhofer: Measurement of spatial correlations in a turbulent flow with a two-dimensional backscatter LDA system, 3rd Int. Symp. Applications of Laser Anemometry to Fluid Mechanics Lisbon (1986)
5.721 N. Nakatani, M.E. Tokita, M.E. Mocgowa, T. Yamada: Simultaneous measurement of flow velocity variations at several points with multi-point LDV, Int. Conf. Laser Anemometry Manchester (1986)
5.722 A.A. Kolmogorov: The Local Structure of Turbulence in Incompressible Viscous Fluid for Very Large Reynolds Numbers, CR Akad. Sci. SSSR **30**, 301–306 (1941)
5.723 F. Durst, A. Melling, J.H. Whitelaw: *Principles and Practice of Laser-Doppler Anemometry* (Academic, New York 1981)
5.724 S.G. Hanson: Application of the laser gradient anemometer (LGA) for fluid flow measurements, 2nd Symp. Applications of Laser Anemometry to Fluid Mechanics Lisbon (1984)
5.725 M.V. Ötügen, W.-J. Su, G. Papadopoulos: A New Laser-Based Method for Strain Rate and Vorticity Measurements, Meas. Sci. Technol. **9**, 267–274 (1998)
5.726 S. Yao, P. Tong, B. Ackerson: Proposal and testing of a fiber optic based measurements of flow vorticity, Appl. Opt. **40**(24), 4022–4027 (2001)
5.727 V.P. Stepaniuk, C. Tarau, M.V. Ötügen, W.-J. Su: Evaluation of a laser velocity gradient probe and measurements in a boundary layer, Exp. Fluids **36**, 510–513 (2004)
5.728 V.P. Stepaniuk, W.-J. Su, C. Tarau, M.V. Ötügen: Measurements in turbulent shear layers using a laser vorticity probe, AIAA Paper, Vol. 2004-1223 (2004)
5.729 L. Blank: *Statistical Procedures for Engineering, Management and Science* (McGraw-Hill, New York 1980)
5.730 Y. Andreopoulos, A. Honkan: An experimental study of the dissipative and vortical motion in turbulent boundary layers, J. Fluid Mech. **439**, 131–163 (2001)
5.731 J. Balint, J.M. Wallace, P. Vukoslavcevic: The velocity and vorticity vector fields of a turbulent boundary layer, Part 2 Statistical Properties, J. Fluid Mech. **228**, 53–86 (1991)
5.732 D. Ewing, W.-K. George: Private communication (1993)
5.733 D.B. Spalding: A single formula for the law of the wall, J. Appl. Mech. **28**, 455–458 (1961)
5.734 L.P. Purtell, P.S. Klebanoff, F.T. Buckley: Turbulent boundary layer at low Reynolds number, Phys. Fluids **24**(5), 802–811 (1981)
5.735 J. Andreopoulos, F. Durst, Z. Zaric', J. Jovanovic: Influence of Reynolds number on Characteristics of Turbulent Wall Boundary Layers, Exp. Fluids **2**, 7–16 (1984)
5.736 P. Bradshaw, G.P. Huang: The law of the wall in turbulent flow, Proc. R. Soc. London A, Vol. 451 (1995) 165–188
5.737 N.N. Mansour, J. Kim, P. Moin: Reynolds-stress and dissipation-rate budgets in a turbulent channel flow, J. Fluid Mech. **194**, 15–44 (1988)
5.738 W.-J. Su, M.-V. Ötügen: Private communication (2004)
5.739 S. Rajagopalan, R.H. Antonia: RMS spanwise vorticity measurements in a turbulent boundary layer, Exp. Fluids **14**, 142–144 (1993)

5.740 J.-C. Klewicki: *On the interactions between the inner and outer region motions in turbulent boundary layers*. Ph.D. Thesis (Michigan State University, East Lansing 1989)

5.741 M.M. Metzger, J.C. Klewicki: A comparative study of near-wall turbulence in high and low Reynolds number boundary layers, Phys. Fluids **13**(3), 692–701 (2001)

5.742 P.R. Spalart: Direct simulation of a turbulent boundary layer up to R_θ = 1410, J. Fluid Mech. **187**, 61–98 (1988)

5.743 J. Kim, P. Moin, R. Moser: Turbulence statistics in fully developed channel flow at low Reynolds number, J. Fluid Mech. **177**, 133–166 (1987)

5.744 J.-H. Agui, Y. Andreopoulos: Reynolds number effects on vorticity statistics (2005) (in preparation)

5.745 W.J.A. Dahm, K.B. Southerland, K.A. Buch: Direct, high resolution, four-dimensional measurements of the fine scale structure of Sc >> 1 molecular mixing in turbulent flows, Phys. Fluids **3**, 1115–1127 (1991)

5.746 W.J.A. Dahm, L.K. Su, K.B. Southerland: A scalar imaging velocimetry technique for four-dimensional velocity field measurements in turbulent flows, Phys. Fluids **4**, 2191–2206 (1992)

5.747 L.K. Su, W.J.A. Dahm: Scalar imaging velocimetry measurements of the velocity gradient tensor field at the dissipative scales of turbulent flows, Part I: Assessment of errors, Phys. Fluids **8**, 1869–1882 (1996)

5.748 L.K. Su, W.J.A. Dahm: Scalar imaging velocimetry measurements of the velocity gradient tensor field at the dissipative scales of turbulent flows, Part II: Experimental results, Phys. Fluids **8**, 1883–1906 (1996)

5.749 C.J. Kähler, J. Kompenhans: Multiple plane stereo PIV: Technical realization and fluid-mechanical significance, Proc. 3rd Int. Workshop on PIV Santa Barbara (1999)

5.750 C.J. Kähler, M. Stanislas, J. Kompenhans: Spatio-temporal flow structure investigation of near-wall turbulence by means of multiplane stereo particle image velocimetry, Proc. 11th Int. Symp. Appl. Laser Tech. Fluid Mech. Lisbon (2002)

5.751 C.J. Kähler: Investigation of the spatio-temporal flow structure in the buffer region of a turbulent boundary layer by means of multiplane stereo PIV, Exp. Fluids **36**, 114–130 (2004)

5.752 H. Hu, T. Saga, T. Kobayashi, N. Taniguchi, M. Yasuki: Dual-plane stereoscopic particle image velocimetry: System setup and its application on a lobed jet mixing flow, Exp. Fluids **31**, 277–293 (2001)

5.753 B. Ganapathisubramani, E.K. Longmire, I. Marusic, S. Pothos: Dual-plane PIV technique to resolve complete velocity gradient tensor in a turbulent boundary layer, Proc. 12th Int. Symp. Appl. Laser Tech. Fluid Mech. Lisbon (2004)

5.754 J.A. Mullin, W.J.A. Dahm: Highly-resolved three-dimensional velocity measurements via dual-plane stereo particle image velocimetry (DSPIV) in turbulent flows, AIAA Paper, Vol. 2002-0290 (2002)

5.755 J.A. Mullin, W.J.A. Dahm: Direct experimental measurements of velocity gradient fields in turbulent flows via high-resolution frequency-based dual-plane stereo PIV (DSPIV), Proc. 12th Int. Symp. Appl. Laser Tech. Fluid Mech. Lisbon (2004)

5.756 K.A. Buch, W.J.A. Dahm: Experimental study of the fine-scale structure of conserved scalar mixing in turbulent flows, Part 1. Sc >> 1, J. Fluid Mech. **317**, 21–71 (1996)

5.757 K.A. Buch, W.J.A. Dahm: Experimental study of the fine-scale structure of conserved scalar mixing in turbulent flows, Part 2. Sc $\approx$ 1, J. Fluid Mech. **364**, 1–29 (1998)

5.758 J.A. Mullin, W.J.A. Dahm: Dual-plane stereo particle image velocimetry measurements of velocity gradient tensor fields in turbulent shear flow. Part 1: Accuracy assessments, Phys. Fluids **18**(3), 035101 (2006)

5.759 D.C. Bjorkquist: Stereoscopic PIV calibration verification, Proc. 11th Int. Symp. Appl. Laser Tech. Fluid Mech. Lisbon (2002)

5.760 B. Wiener: Stereo-PIV using self-calibration on particle images, Proc. 5th Int. Symp. Particle Image Velocimetry Busman (2003)

5.761 J.A. Mullin, W.J.A. Dahm: Dual-plane stereo particle image velocimetry measurements of velocity gradient tensor fields in turbulent shear flow. Part 2: Experimental results, Phys. Fluids **18**(3), 035102 (2006)

5.762 G.I. Taylor: Production and disipation of vorticity in a turbulent fluid, Proc. R. Soc. London **164**, 15–23 (1938)

5.763 W.W. Wassman, J.M. Wallace: Measurement of vorticity in turbulent shear flow, Bull. Am. Phys. Soc. **24**, 1142 (1979)

5.764 M. Kholmyansky, A. Tsinober, S. Yorish: Velocity derivatives in the atmospheric turbulent flow at Re_λ =104, Phys. Fluids **13**, 311–314 (2001)

5.765 B. Galanti, G. Gulitsky, M. Kholmyansky, A. Tsinober, S. Yorish: Adv. in Turbulence X. In: *Proc. 10th European Turb. Conf*, ed. by H.I. Andersson, P.Å. Krogstad (CIMNE, Barcelona 2004)

5.766 P.-N. Nguyen: *Simultaneous measurements of the velocity and vorticity vector fields in the turbulent near wake of a circular cylinder*. Ph.D. Thesis (Univ. of Maryland, College Park 1993)

5.767 B. Marasli, P. Nguyen, J.M. Wallace: A calibration technique for multiple-sensor hot- wire probes and its application to vorticity measurements in the wake of a circular cylinder, Exp. Fluids **15**, 209–218 (1993)

5.768 P. Vukoslavcevic, J.M. Wallace: A 12-sensor hot-wire probe to measure the velocity and vorticity vectors in turbulent flow, Meas. Sci. Technol. **7**, 1451–1461 (1996)

5.769 Y. Zhu, R.A. Antonia: Spatial resolution of a 4-X-wire vorticity probe, Meas. Sci. Technol. **7**, 1492–1497 (1996)

5.770 R.A. Antonia, T. Zhou, Y. Zhu: Three-component vorticity measurements in a turbulent grid flow, J. Fluid Mech. **374**, 29–57 (1998)

5.771 R.A. Antonia, P. Orlandi, T. Zhou: Assessment of a three-component vorticity probe in decaying turbulence, Exp. Fluids **33**, 384–390 (2002)

5.772 P.S. Bernard, J.M. Wallace: *Turbulent Flow: Analysis, Measurement and Prediction* (Wiley, Hoboken 2002)

5.773 Y.N. Pao: Structure of turbulent velocity and scalar fields of large wave numbers, Phys. Fluids **8**, 1063–1075 (1965)

5.774 H.J. Hussein, W.K. George: Influence of wire spacing on derivative measurements with parallel hot-wire probes, Forum on Turbulent Flow, Vol. 94 (1990) 121–124

5.775 R.A. Antonia, Y. Zhu, J. Kim: On the measurement of lateral velocity derivatives in turbulent flows, Exp. Fluids **15**, 65–69 (1993)

5.776 J.C. Wyngaard: Measurement of small-scale turbulence structure with hot-wires, J. Phys. E Sci. Instrum. **1**, 1105–1108 (1968)

5.777 A.N. Kolmogorov: Dissipation of energy in locally isotropic turbulence, CR Acad. Sci. URSS **32**, 19–21 (1941)

5.778 L.W.B. Browne, R.A. Antonia, D.A. Shah: Selection of wires and wire spacing for X- wires, Exp. Fluids **6**, 286–288 (1988)

5.779 R.D. Moser, J. Kim, N.N. Mansour: Direct numerical simulation of turbulent channel flow up to Re=590, Phys. Fluids **11**, 943–945 (1989)

5.780 R.-B. Loucks: *An Experimental Investigation of the Velocity and Vorticity Fields in a Plane Mixing Layer*. Ph.D. Thesis (Univ. of Maryland, College Park 1998)

5.781 F.E. Jorgensen: Directional sensitivity of wire and fiber film probes, DISA Inf. **11**, 31–37 (1971)

5.782 P. Bradshaw: *An Introduction to Turbulence and Its Measurements* (Pergamon, New York 1971)

5.783 N. Vrettos: *Experimentelle Untersuchung der Ausbreitung von Kulturmschwaden im Windkanal*. Studienarbeit (Univ. of Karlsruhe, Karlsruhe 1984) (in German)

5.784 G. Heskestad: A generalized Taylor hypothesis with application for high Reynolds number turbulent shear flows, Trans. ASME **87**, 735–739 (1965)

5.785 G.K. Batchelor: Pressure fluctuations in isotropic turbulence, Proc. Cambridge Phil. Soc., Vol. 47 (1951) 359

5.786 U. Piomelli, J.L. Balint, J.M. Wallace: On the validity of Taylor Hypothesis for wall bounded flows, Phys. Fluids **3**, 609–611 (1988)

5.787 J.-L. Balint: *Contribution de l'Etude de la Structure Tourbillionaire d'une Couche Limite Turbulente au Moyen d'une Sonde a Neuf Fils Chaude Measurant le Rotationnel*. Docteur d'Etat en Sciences (Ecole Centrale de Lyon, Lyon 1986), in French

5.788 F. Hussain, K. Jeong, J. Kim: Structure of turbulent shear flows, Proc. Summer Prog. Ctr. Turb. Res. Stanford Univ./NASA Ames (1987) 273–290

5.789 L. Ong: *Visualization of turbulent flows with simultaneous velocity and vorticity measurements*. Ph.D. Thesis (Univ. of Maryland, College Park 1992)

5.790 J. Kim, F. Hussain: Propagation velocity of perturbations in turbulent channel flow, Phys. Fluids **3**, 695–706 (1993)

5.791 P. Vukoslavcevic, D. Petrovic, J.M. Wallace: An analytical approach to the uniqueness problem of hot-wire probes to measure simultaneously three velocity components, Meas. Sci. Technol. **15**, 1848–1854 (2004)

5.792 N.K. Tutu, R. Chevray: Cross wire anemometer in high intensity turbulence, J. Fluid Mech. **71**, 785–800 (1975)

5.793 W.W. Willmarth: Geometrical interpretation of the possible velocity vectors obtained with multiple sensor probes, Phys. Fluids **28**, 462–465 (1985)

5.794 G. Pailhas, J. Coustex: Methode d'explotation des donnes d'une sonde anemometrique a quatre fils chauds, Rech. Aerospatiale **2**, 161–168 (1986)

5.795 E. Kit, A. Tsinober, J.L. Balint, J.M. Wallace, E. Levich: An experimental study of helicity related properties of turbulent flow past a grid, Phys. Fluids **30**, 3323–3325 (1988)

5.796 J.M. Wallace, J.L. Balint, L. Ong: An experimental study of helicity density in turbulent flow, Phys. Fluids **4**, 2013–2026 (1992)

5.797 S. Menon: *A study of velocity and vorticity statistics in an axisymmetric jet*. M.S. Thesis (Univ. of Houston, Houston 1993)

5.798 J.J. Gorski, J.M. Wallace, P.S. Bernard: The enstrophy equation budget of bounded turbulent shear flows, Phys. Fluids **6**, 3197–3199 (1994)

5.799 L. Ong, J.M. Wallace: Local isotrophy of the vorticity field in a boundary layer at high Reynolds number. In: *Advances in Turbulence*, Vol. V, ed. by R. Benzi (Springer, Berlin, Heidelberg 1995) pp. 392–397

5.800 G.-C. Lemonis: *An experimental study of the vector fields of velocity and vorticity in turbulent flows*. Ph.D. Thesis (Swiss Federal Institute of Technology, Zurich 1995)

5.801 A. Folz: *An experimental study of the near-surface turbulence in the atmospheric boundary layer*. Ph D. Thesis (Univ. of Maryland, College Park 1997)

5.802 A. Tsinober, L. Shtilman, H. Vaisburd: A study of vortex stretching and enstrophy generation in numerical and laboratory turbulence, Fluid Dyn. Res. **21**, 477–494 (1997)

5.803 L. Ong, J.M. Wallace: Joint probability density analysis of the structure and dynamics of the vorticity field of a turbulent boundary layer, J. Fluid Mech. **367**, 291–328 (1998)

5.804 B. Galanti, A. Tsinober: Self-amplification of the field of velocity derivatives in quasi-isotropic turbulence, Phys. Fluids **12**, 3097–3099 (2001)

5.805 N. Li: *Passive scalar dispersion in a turbulent mixing layer*. Ph.D. Thesis (Univ. of Maryland, College Park 2004)

5.806 J.-N. Kim: *Wirbelstärkemessungen in einer turbulenten Scherschicht*. Dr.-Ing. Thesis (Tech. Univ. Berlin, Berlin 1989)

5.807 W.T. Ashurst, A.R. Kerstein, R.A. Kerr, C.H. Gibson: Alignment of vorticity and scalar gradient with strain rate in simulated Navier-Stokes turbulence, Phys. Fluids **30**, 2343–2353 (1987)

5.808 J.F. Foss, R.C. Haw: Transverse vorticity measurements using a compact array of four sensors, ASME **FED 97**, 71–76 (1990)

5.809 J.F. Foss: Vorticity considerations and planar shear layers, Exp. Therm. Fluid Sci. **8**, 260–270 (1994)

5.810 S.C. Morris, J.F. Foss: Vorticity spectra in high Reynolds number anisotropic turbulence, Phys. Fluids **17**, 088102 (2005)

5.811 S.-C. Morris: *The velocity and vorticity fields of a single stream shear layer*. Ph.D. Thesis (Michigan State University, East Lansing 2002)

5.812 S.C. Morris, J.F. Foss: Boundary layer to shear layer – the transition region, J. Fluid Mech. **494**, 187 (2003)

5.813 K. Sreenivasan, A. Juneja, A. Suri: Scaling properties of circulation in moderate Reynolds number turbulent wakes, Phys. Rev. Lett. **75**, 433 (1995)

5.814 G. Batchelor: *Homogeneous Turbulence* (Cambridge Univ. Press, Cambridge 1954)

5.815 J.F. Foss, J.K. Schwannecke, A.R. Lawrenz, M.W. Mets, S.C. Treat, M.D. Dusel: The thermal transient anemometer, Meas. Sci. Technol. **15**, 2248–2255 (2004)

5.816 J.F. Foss, J.A. Peabody, M.J. Norconk, A.R. Lawrenz: Ambient temperature an free stream turbulence effects on the thermal transient anemometer, Meas. Sci. Technol. **17**, 2519–2526 (2006)

5.817 J.F. Foss: Thermal transient anemometer having sensing cell assembly, US Patent 7051599 (2006)

5.818 J.C. Kaimal, J.J. Finnigan: *Atmospheric Boundary Layer Flows: Their Structure and Measurement* (Oxford Univ. Press, New York 1994)

5.819 J.D. Anderson: *Modern Compressible Flow: With Historical Perspective*, 2nd edn. (McGraw-Hill, New York 1990)

5.820 J. Wyngaard: Cup, propeller, vane, and sonic anemometers in turbulence research, Ann. Rev. Fluid Mech. **13**, 399 (1981)

5.821 VDI-Guideline (Ed.): Turbulence measurement with sonic anemometers, VDI *3786*, Part 12 (VDI, Düsseldorf 1994)

5.822 M. Aubinet, A. Grelle, A. Ibrom, U. Rannik, J. Moncrieff, T. Foken, A.S. Kowalski, P.H. Martin, P. Berbigier, C. Bernhofer, R. Clement, J. Elbers, A. Granier, T. Grunwald, K. Morgenstern, K. Pilegaard, C. Rebmann, W. Snijders, R. Valentini, T. Vesala, A.H. Fitter, D.G. Raffaelli: Estimates of the annual net carbon and water exchange of forests: the EUROFLUX methodology, Adv. Ecol. Res. **30**, 113 (2000)

5.823 B. Duan, C.W. Fairall, D.W. Thomson: Eddy correlation measurements of the dry deposition of particles in wintertime, J. Appl. Meteorol. **27**, 642 (1988)

5.824 B.B. Hicks, D.R. Matt, R.T. McMillen: A micrometeorological investigation of surface exchange of 03, S02 and N02: A case study, Bound.-Lay. Meteorol. **47**, 127 (1988)

5.825 A. Cuerva, S. López-Díez, D. Bercebal: Higher level descriptions of sites and wind turbines by means of principal component analysis, Proc. European Wind Energy Conference (James James Sciences, London 1999) 663

5.826 A. Fragoulis: The complex terrain wind environment and its effects on the power output and loading of wind turbines, Aerospace Sciences Meeting and Exhibit, AIAA (1997) 33–40

5.827 M.W. Rotach, S.-E. Gryning, E. Batchvarova, A. Christen, R. Vogt: Pollutant dispersion close to an urban surface: The BUBBLE tracer experiment, Meteorol. Atmos. Phys. **87**, 39 (2004)

5.828 N. Kato, T. Ohkuma, J.R. Kim, H. Marukawa, Y.J. Niihori: Full scale measurements of wind velocity in two urban areas using an ultrasonic anemometer, Wind Eng. Aerodyn. **88**, 67–78 (1992)

5.829 J. Finnigan: Turbulence in plant canopies, Ann. Rev. Fluid Mech. **32**, 519–571 (2000)

5.830 R.M. Petrone, J.S. Price, J.M. Waddington, H. Von Waldow: Effects of a changing surface cover on the moisture and energy exchange of a restored peatland, J. Hydrol. **295**, 198–210 (2004)

5.831 X. Lee, W. Massman, B. Law (Eds.): *Handbook of Micrometeorology: A Guide for Surface Flux Measurement and Analysis* (Kluwer Academic, Dordrecht 2004)

5.832 D. Banfield, R. Dissly, A.D. Toigo, P.J. Gierasch, W.R. Dagle, D. Schindel, D.A. Hutchins, B.T. Khuri-Yakub: Mars acoustic anometer – eddy fluxes, Proc. 6th Int. Conf. Mars (2003) 3144

5.833 A. Cuerva, A. Sanz-Andres: Sonic anemometry of planetary atmospheres, J. Geophys. Res. Planets **108**, 5029 (2003), (DOI:10.1029/2002JE001944)

5.834 J.G. Webster: *Instrumentation and Sensors Handbook* (CRC, Boca Raton 1999)

5.835 V.-E. Suomi: Energy budget studies and development of the sonic anemometer for spectrum, AFCRC Tech. Rep. *56-274* (University of Wisconsin, 1957)

5.836 F. Dobson, L. Hasse, R. Davis: *Air-Sea Interaction – Instruments and Methods* (Plenum, New York 1982)

5.837 H.L. Fox, Bolt, Beranek, Newman (Eds.): AFCRL 68-0180 (1968)

5.838 S.E. Larson, F.W. Weller, J.A. Businger: Continuous wave sonic anemometer for investigation of atmospheric turbulence, J. Appl. Meteorol. **18**, 562–568 (1979)

5.839 A. Cuerva, A. Sanz-Andres: On the sonic anemometer measurement theory, J. Wind Eng. Aerodyn. **88**, 25–55 (2000)

5.840 J.C. Kaimal, J.E. Gaynor: Another look at sonic thermometry, Bound.-Lay. Meteorol. **56**, 401–410 (1991)

5.841 H. Liu, G. Peters, T. Foken: New equations for sonic temperature variance and buoyancy heat flux with an omnidirectional sonic anemometer, Bound.-Lay. Meteorol. **100**, 459 (2001)

5.842 A. Cuerva, A. Sanz-Andres, J. Navarro: On multiple-path sonic anemometer measurement theory, Exp. Fluids **34**, 345–357 (2003)

5.843 J.C. Kaimal, J.C. Wyngaard, D.A. Haugen: Deriving power spectra from a three-component sonic anemometer, J. Appl. Meteorol. **7**, 827–837 (1968)

5.844 H. Lenschow: *Probing the Atmospheric Boundary Layer* (Am. Meteorol. Soc., Boston 1986)

5.845 C. Wamser: The frequency response of sonic anemometers, Bound.-Lay. Meteorol. **84**, 231 (1997)

5.846 K. Henjes, P.K. Taylor, M.J. Yelland: Effect of pulse averaging on sonic anemometer spectra, J. Atmos. Ocean. Technol. **16**, 181–184 (1999)

5.847 A. Cuerva, A. Sanz-Andres: Steps to reach a safe scenario with sonic anemometers as standard sensor for wind measurements in wind energy, Proc. European Wind Energy Conference Nice (James James, London 1999) 649

5.848 A. Cuerva, A. Sanz-Andrés, S. Franchini: The role of ultrasonic anemometry in wind engineering. In: *Fourth European African Conf. Wind Engineering*, ed. by J. Náprstek, C. Ficher (ITAM AS CR, Prague 2005), , paper 152

5.849 A. Wieser, F. Fielder, U. Corsmeier: The influence of the sensor design on wind measurements with sonic anemometer systems, J. Atmosph. Ocean. Technol. **18**, 1585–1608 (2001)

5.850 J.M. Wilczak, S.P. Oncley, S.A. Stage: Sonic anemometer tilt correction algorithms, Bound.-Lay. Meteorol. **99**, 127–150 (2001)

5.851 R. Sozzi, M. Favaron: Sonic anemometry and thermometry: theoretical basis and dataprocessing software, Environ. Softw. **11**, 259–270 (1996)

5.852 J.J. Finnigan: A re-evaluation of long-term flux measurement techniques, Part II: Coordinate systems, Bound.-Lay. Meteorol. **113**, 1–41 (2004)

5.853 R.T. McMillan: An eddy correlation technique with extended applicability to non-simple terrain, Bound.-Lay. Meteorol. **43**, 231 (1988)

5.854 J.C. Wyngaard, S.-F. Zhang: Transducer-shadow effects on turbulence spectra measured by sonic anemometer, J. Atmosph. Ocean. Technol. **2**, 548 (1985)

5.855 J.A. Murray, J.C. Klewicki, C.A. Biltoft: An experimental investigation of sonic anemometer wake blockage effects, ASME, Vol. FED 161 (1993) 43

5.856 A. Grelle, A. Lindroth: Flow distortion by a solent sonic anemometer: Wind tunnel calibration and its assessment for flux measurement over forest field, J. Atmosph. Ocean. Technol. **11**, 1529 (1994)

5.857 C. Kraan, W.A. Oost: A new way of anemometer calibration and its application to a sonic anemometer, J. Atmosph. Ocean. Technol. **6**, 516 (1989)

5.858 D. Heinemann, D. Langner, U. Stabe, H. Waldl (Ed.), R. Watson: Measurement and correction of ultrasonic anemometer errors and impact on turbulence measurements, European Wind Energy Conference Dublin (1998) 409

5.859 N.G. Mortensen, J. Højstrup: The solent sonic – response and associated errors, Symp. Meteorology Observation and Instrumentation (Am. Meteorol. Soc., Boston 1992) 501

5.860 M.K. van der Molen, J.H.C. Gash, J.A. Elbers: Sonic Anemometer cosine response and flux measurement: II The effect of introducing an angle of attack dependent calibration, Agric. For. Meteorol. **122**, 95 (2004)

5.861 A. Cuerva, A. Sanz-Andres, O. Lopez: Singularities and un-definitions in the calibration functions of sonic anemometers, J. Atmosph. Ocean. Technol. **21**, 1868 (2004)

5.862 J. Wyngaard: Transducer-shadow effects on turbulence spectra measured by sonic anemometers, J. Atmosph. Ocean. Technol. **2**, 548 (1985)

5.863 P. Schotanus, F.T.M. Nieuwstadt, H.A.R. De Bruin: Temperature measurement with a sonic anemometer and its application to heat and moisture fluxes, Bound.-Lay. Meteorol. **26**, 81 (1983)

5.864 ISO: *Meteorology–Sonic anemometer/thermometers – Acceptance test methods for mean wind measurements*, Vol. 16622, 1st edn. (ISO, 2001)

5.865 S. Cervenka (Ed.): Selection of an Anemometer For Measurement of Wind Turbulence, ECN-I-92-029 DE92 557290 (Energieonderzoek Centrum Nederland, 1992)